Advances in Polymer Technology

Design and Engineering of Polymer Systems for Bioapplications

Lead Guest Editor: Samira Hosseini
Guest Editors: Margarita S. Dominguez, Grissel T. De Santiago, Marco Lopez, Ernesto Di Maio, and María J. G. Celma

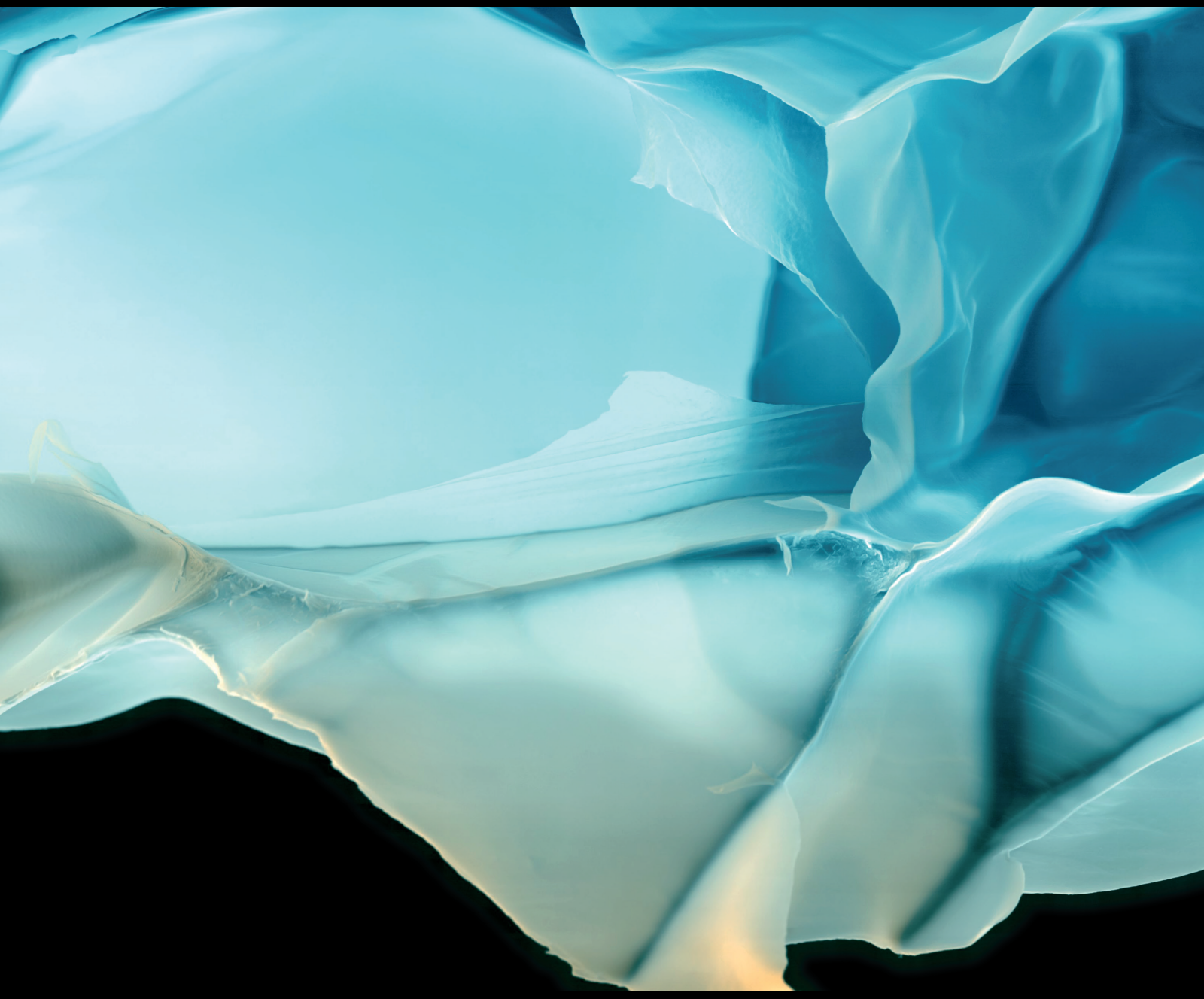

Design and Engineering of Polymer Systems for Bioapplications

Advances in Polymer Technology

Design and Engineering of Polymer Systems for Bioapplications

Lead Guest Editor: Samira Hosseini
Guest Editors: Margarita S. Dominguez, Grissel T. De Santiago, Marco Lopez, Ernesto Di Maio, and María J. G. Celma

Contents

Development and Characterization of PEGylated Chromatographic Monoliths as a Novel Platform for the Separation of PEGylated RNase a Isomers

Calef Sánchez-Trasviña, Marco Rito-Palomares, and José González-Valdez

Research Article (10 pages), Article ID 5067028, Volume 2019 (2019)

Hindawi
Advances in Polymer Technology
Volume 2021, Article ID 8816564, 24 pages
https://doi.org/10.1155/2021/8816564

Review Article

Latest Updates on the Advancement of Polymer-Based Biomicroelectromechanical Systems for Animal Cell Studies

Ricardo Garcia-Ramirez,[1] Ana S. Cerda-Kipper,[1] Damaris Alvarez,[1] Sofia Reveles-Huizar,[1] Jorge A. Garza-Abdala,[1] and Samira Hosseini [1,2]

[1]*Tecnologico de Monterrey, Writing Lab, Institute for the Future of Education, Monterrey, 64849 NL, Mexico*
[2]*Tecnologico de Monterrey, Institute for the Future of Education, Institute for the Future of Education, Monterrey, 64849 NL, Mexico*

Correspondence should be addressed to Samira Hosseini; samira.hosseini@tec.mx

Received 1 September 2020; Revised 6 March 2021; Accepted 24 March 2021; Published 7 April 2021

Academic Editor: Kinga Pielichowska

Biological sciences have reached the fundamental unit of life: the cell. Ever-growing field of Biological Microelectromechanical Systems (BioMEMSs) is providing new frontiers in both fundamental cell research and various practical applications in cell-related studies. Among various functions of BioMEMS devices, some of the most fundamental processes that can be carried out in such platforms include cell sorting, cell separation, cell isolation or trapping, cell pairing, cell-cell communication, cell differentiation, cell identification, and cell culture. In this article, we review each mentioned application in great details highlighting the latest advancements in fabrication strategy, mechanism of operation, and application of these tools. Moreover, the review article covers the shortcomings of each specific application which can open windows of opportunity for improvement of these devices.

1. Introduction

The analytical platforms that facilitate growing, monitoring, analyzing, and manipulating cells are essential to the advancements of the biological and biomedical fields [1]. In cell-related studies, it is of vital importance to be able to identify, isolate, sort and separate, culture, pair, and record the differentiation and communications of cells. While 2-dimensional (2D) *in vitro* platforms enable a certain degree of progress, they fall short in mimicking the microenvironment the cells experience within a living body [2]. Moreover, cell studies within traditional petri dish commonly require large sample volume and various external equipment to support the experiments. Biological Microelectromechanical Systems (BioMEMSs) have emerged as great alternatives to facilitate cell studies for multiple applications. These devices are compact and portable while operating on small sample volume and offering automatization of multiple processes.

Application of BioMEMS in cell-related studies allows metering, dilution, flow switching, particle separation, mixing, pumping, incubation of reaction mixtures, and dispensing or injecting cells for different procedures [2]. BioMEMS closely mimics microenvironment of cells by incorporating the necessary stimulations of physical, electrical, chemical, and mechanical natures that cells need in order to grow and respond to their surroundings. The intrinsic properties of cells including size, shape, deformability, and charge play a crucial role in physically manipulating them [3, 4]. These devices rely on several forces including electrical, magnetic, mechanical, hydrodynamic, and centrifugal forces to manipulate cells for intended applications. Fabrication of BioMEMS commonly follows the standard soft or hard lithography techniques often combined with lift-off, wet etching, replica modeling, and 3-dimensional (3D) printing. Polymers, in particular, have played a significant role in fabrication of these devices as they lend remarkable characteristics to the device including flexibility, transparency, lightweight, ease of fabrication, and cost-effectiveness [5].

In this review article, the latest advancements of polymer-based BioMEMS in cell-related studies are summarized. In

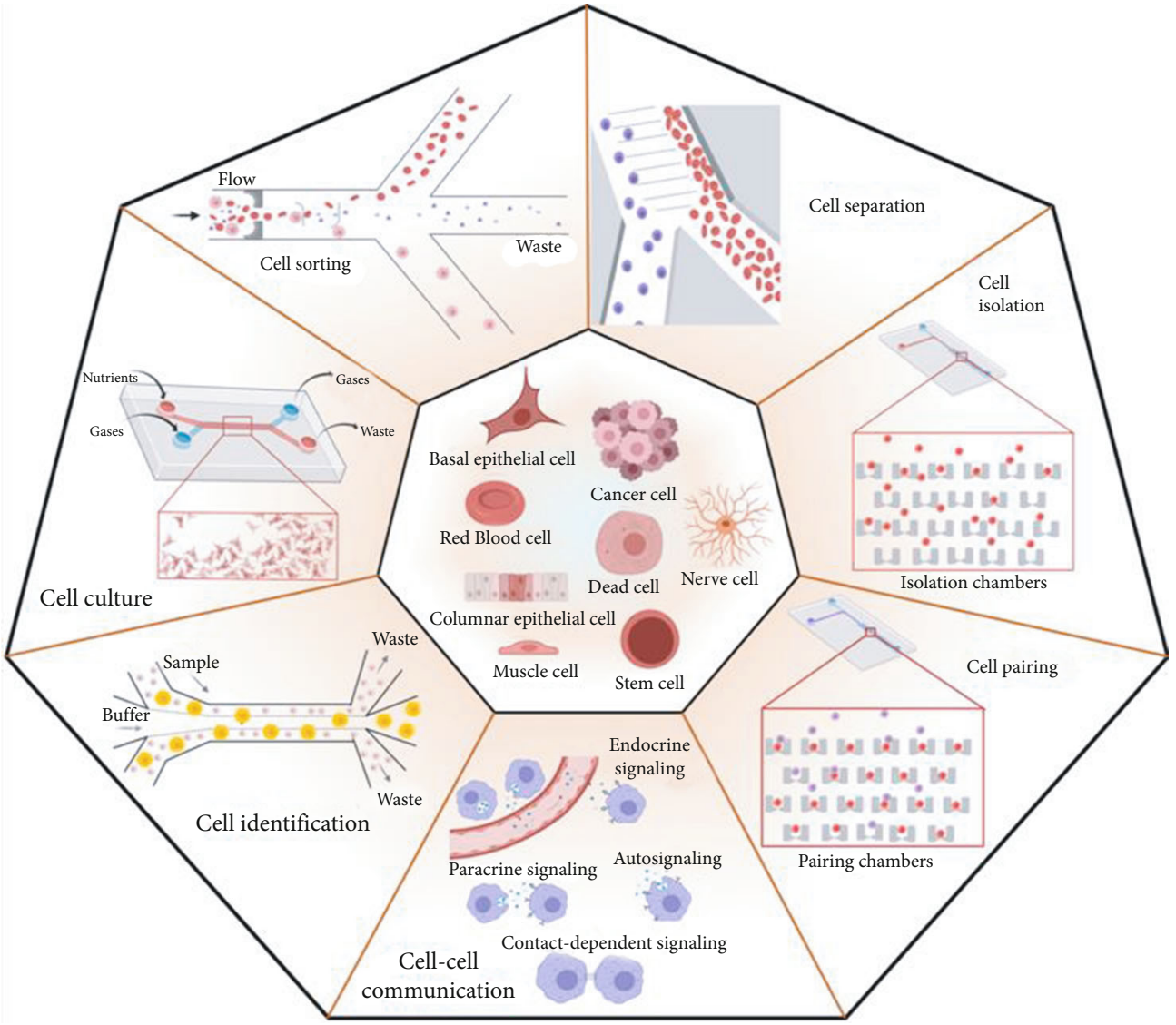

Figure 1: Cell-related applications of BioMEMS: cell sorting, cell separation, cell isolation, cell pairing, cell-cell communication, cell identification, and cell culture.

specific, applications such as cell sorting, cell separation, cell isolation or trapping, cell pairing, cell-cell communication, cell differentiation and identification, and cell culture in latest designs of BioMEMS are thoroughly reviewed (Figure 1). Each field of study includes the latest updates of the BioMEMS along with their main components, the fabrication strategy, the mechanism of operation, and the specifics of each platform. The review article also covers limitations and shortcoming of BioMEMS in cell-related studies with specific emphasis on the applications of interest.

2. BioMEMS in Cell Sorting

Accurate and high-throughput particle/cell sorting is a critical step in various protocols in biology, biotechnology, and medicine [6]. Nowadays, conventional technologies are capable of providing high-efficiency sorting in a short timescale. Recent advances in BioMEMS have allowed the development of miniaturized devices offering similar capabilities as those provided by commercial cell sorting platforms [7]. Cell sorting on BioMEMS provides several advantages, including the reduction of the equipment size, eliminating potential hazardous aerosols, simplifying complex protocols, and multiplexing several steps [8]. BioMEMSs dedicated to particle or cell sorting are capable of integrating time-consuming and labor-intensive experimental procedures into compact integrated pieces of equipment. These devices manipulate small sample volumes that allow examining individual cells or particles of interest [6, 9]. Table 1 presents some of the latest applications of BioMEMS devices in cell sorting in detail providing the components of the device, the fabrication strategy, and the mechanism of operation, in addition to the specific and remarks for these devices.

The intrinsic physical properties of the target cells are often used to achieve controlled cell sorting. The use of external charges or forces is introduced to BioMEMS in order to

Table 1: Recent BioMEMS platforms for particle/cell sorting including the type of the platform, the main components, the fabrication strategy, the mechanism of operation, and the specifics of each platform.

BioMEMS platform	Main components	Fabrication strategy	Mechanism of operation	Specifics	Ref.
Microfluidic-based Raman ACS	Laser beam laser tweezer Raman microscopy PDMS-based microfluidic device	Standard soft lithography technique	Raman effect takes place when light illuminates a certain region of the microdevice. The photon interaction perturbs the electron configuration of the molecule to an unstable virtual state during the photon scattering, yielding the differences between particles.	The laser tweezers enable trapping of individual cells at the focus of the laser beam.	[15]
Micro/nanomotors for cancer cell targeting	Synthesized PS Janus particles	Wet etching and photolithography	The micromotors were designed to harness local H_2O_2 produced by cancer cells to convert chemical energy into mechanical propulsion while targeting specific cancer cells.	The design needs to overcome the low Reynolds number and Brownian motion, which work together against the motor's locomotion.	[14]
Centrifugal microfluidic Chip	Charge-based microchannel flow	Standard soft lithography	By applying a voltage to the cells, monodisperse droplets were generated and manipulated.	The device encapsulates and sorts cells in one single step.	[10]
Single-molecule tracing microfluidic chip	Microchannels Acoustic wave transducer		Acoustic waves push specific particles into cavities depending on their size and deformability.	The device can be used for organic and inorganic particle separation.	[11]
3D carbon-DEP microfluidic chip	3D-carbon electrodes voltage signal generator	Two-step photolithography process	DEP was used to separate death from live monocytes using 3D carbon electrodes. A voltage was applied to create an electric field. Live monocyte cells reacted to the attraction force and were trapped in the electric fields near the electrodes while dead cells remain unresponsive.	The strategy offers a contact-free procedure leading to more accurate analytical results.	[17]
DEP microfluidic chip	ITO electrodes Function generator Power supply Syringe pump Microfluidic device	Standard soft lithography	Following the channels, the cells were carried to the tumor-trapping zone, where tumor cells could not continue traveling through the device outlet due to their size and deformability.	The device is capable to induce cell sorting based on DEP by encapsulating particles in droplets and applying a voltage potential in a single step.	[18]
Microfluidic-based Raman ACS optofluidic platform	Raman microspectroscopy Laser beams Laser tweezers PDMS-based microfluidic device	Standard soft lithography	Cells from a sample fluid were flown into a microfluidic device and focused in the vertical and horizontal directions by two sheath flows. Cells captured by the optical tweezers were moved to the sample-free stream for spectrum measurement. Cells of interest were released into the collection outlet for further cultivation.	The device is capable of sorting four model bacteria while demonstrated a sorting accuracy of 98%, high-throughput performance by sorting up to 500 cells per hour, and compatibility with cultivation after collection of the cells.	[16]
DEP microfluidic chip	Au/Ti electrodes Function generator Power supply Syringe pump PDMS-based microfluidic device	Standard soft lithography, physical vapor deposition, and D.C. sputtering	A sample was injected in the microfluidic chip at a constant rate, following through the channels; the cells of interest were subjected to DEP forces and trapped in different areas.	The device is capable of separating three kinds of circulating cells. The proposed model for DEP-based cell stretching enables the integration of more reliable geometries that can potentially optimize the use of DEP for cell sorting.	[20]

Table 1: Continued.

BioMEMS platform	Main components	Fabrication strategy	Mechanism of operation	Specifics	Ref.
DEP microfluidic chip with conductive PDMS	Ag-PDMS-based electrodes Power supply PDMS microfluidic chip	Standard soft lithography and multilayer lithography	Sorting was achieved by DEP forces while a solution of cells passed through the microfluidic device.	The device utilizes Ag-PDMS electrodes in a simple fabrication process. DEP is utilized at low DC voltages of less than 15 Vpp with a high frequency.	[19]

ACS: activated cell sorting; Ag-PDMS: silver-polydimethylsiloxane; CTCs: circulating tumor cells; DEP: dielectrophoresis; H_2O_2: hydrogen peroxide; ITO: indium tin oxide; LOC: Lab-on-a-Chip; PDMS: polydimethyl siloxane; PS: polystyrene; RACS: Raman activated cell sorting; Vpp: peak to peak voltage (Vpp); 3D: three dimensional.

achieve a fine sorting of particles. A microscale centrifugal technology called centrifugal microfluidic chip (CMC) was developed by Yu et al. The authors describe a device capable of classifying immune cells from the blood cells based on their charge and performing a cell analysis *in situ*. The CMC consists of a glass-sandwich channel-layer assembly with an integrated polydimethylsiloxane (PDMS) layer along with microfluidic channels that connect the two glass layers. This glass-sandwich approach was used to enhance the CMC mechanical properties and minimize the deformation of the PDMS channels at higher centrifugation speeds. Since the glass tensile strength is higher than that of PDMS, the authors were able to achieve an acceleration of 1,000 g without damaging the microfluidic PDMS channels while enabling a higher recovery of peripheral blood mononuclear cells (PBMC). A simple 10-minute centrifuge step was necessary to reach purity and recovery levels above 95% for PBMC [10]. This implementation yields several applications related to the automatization of blood sample assays and could potentially be utilized to develop point-of-care (POC) devices for rapid diagnostics.

A device capable of controlling the movement of different particles using surface acoustic waves (SAWs) was developed by Lin et al. [9]. The device employed a digital transducer to generate different sound waves that enabled the movement of particles of specific sizes in predefined pathways. The sound waves directed the particles into separate cavities, enabling the individual analysis of these targeted particles [9]. The PDMS chamber of the device was fabricated on a silicon (Si) mold etched by deep reactive ion etching and molded using conventional soft lithography techniques. Demolding from the Si wafer was achieved by finalizing the etching process with a passivation step to yield a hydrophobic surface layer on the PDMS. Diverse sound waves can be generated providing a basis for the device to work with an extensive range of particles (inorganic and organic), thus allowing it to be used for several applications related to cell studies including cell differentiation and stress research, among others [9].

Another example of a BioMEMS applying SAW for cell sorting is the work of Ding and Huang which utilized tunable standing surface acoustic waves (SSAWs) in a continuous flow to separate white blood cells. The main difference between the proposed work of Lin et al. and this work is the use of the acoustic radiation force to directly manipulate cells, rather than affecting the fluids [11]. The authors described the use of a single-layer PDMS channel and a piezoelectric substrate with a pair of interdigitated transducers as part of the device. PDMS is often used as the preferred polymer for BioMEMS and cell studies due to its beneficial features including optical transparency, biocompatibility, low autofluorescence, deformability, low electromagnetic energy dissipation, and high dielectric strength, among others [12]. Nevertheless, it has been reported that the thickness of PDMS walls could directly affect the transmission of the SAW. For that reason, it is recommended that microfluidic channel walls to be as thin as possible to enhance the efficiency of the SAW-based devices [13].

BioMEMS devices focused on particle or cell sorting are an enabling technology to automate and integrate multistep operations. The use of MEMS technologies significantly reduces the total time of an assay in applications related to diagnostics and drug-delivery systems (DDS). Gao et al. described a technique for cell sorting based on micro/nanomotors, which were equipped with *in situ* energy conversion that made them capable of autonomous movement. The ability of some cancer cells to mutate, inhibit antiproteases, and result in metastasis involves generating oxidative stress by producing an elevated level of hydrogen peroxide (H_2O_2). The authors used this fact as the principle for designing the device. The micromotors were designed to harness local H_2O_2 produced by cancer cells to convert chemical energy into mechanical propulsion while targeting specific cancer cells. Presented mechanism with the propelled navigation allows micro/nanomotors to act as highly diffusive delivery vehicles that promote cancer cell targeting with possible applications related to DDS and cancer diagnostics by the aim of specific biomarkers [14].

The single-cell Raman spectra (SCRS) is often utilized to characterize phenotypic changes and functions of cells of interest. Song et al. described the development of a Raman activated cell sorting (RACS) device with no external labeling [15]. Furthermore, Lee and colleagues in 2019 described a Raman-based cell sorting technique with 3D microfluidics. In this work, a 3D hydrodynamic focusing microfluidic system for a fully automated, continuous Raman activated cell sorting (3D-RACS) was described. The system consisted of 3D printed detection chambers that have been integrated within a PDMS-based sorting unit. The device demonstrated the ability to precisely position cells in the detection chamber

for Raman measurements and sorting from 1 μm to 10 μm cell sizes [16].

Another sorting approach that uses a label-free method and has been continuously used due to its relevant characteristics is dielectrophoresis (DEP). DEP is often referred to as one of the most utilized sorting methods since it preserves cell viability, employs intrinsic properties of cells, is contact-free, and provides high-yield for the downstream analysis of the cells [17]. Yildizhan et al. proposed a PDMS chip with 3D carbon electrodes for the separation of monocyte cells. The work introduced the integration of 3D electrodes based on carbonization of SU8 by pyrolysis and the utilization of lower electrical impulses due to the conductivity of the carbon-based electrodes. The device demonstrated the DEP separation of live and dead human U937 monocyte cells from a mixture of cell suspension [17]. Another device that utilized DEP as a sorting technique was proposed by Hung et al. in which a device combined droplet microfluidics and DEP. The authors reported the formation of droplets and encapsulation of particles of interest. The following DEP sorting and manipulation of droplets were achieved based on the dielectrical charges of the encapsulated materials [18]. Another work that utilized modified electrodes was demonstrated by Nie et al. The authors used AgPDMS as the material for the integrated microelectrodes. Such design in the conducting-PDMS electrodes has exploited the polymer doped with Ag to enable the DEP-based bidirectional cell sliding and sorting by mirroring the unidirectional track to incorporate more parallel flow streams [19]. Hosseini et al. proposed a different DEP-based sorting device in which optimized conditions were developed based on cell stretching and lumped mechanical modeling. The authors showed how an optimized electrode design can highly increase the sorting of different cell types in a single fluid. The study proposed a model for cell elongation and verified the experimental results. The model was examined for three kinds of circulating cells, namely, erythrocyte, PBMC, and breast cancer cell line (T-47D). Although the authors utilized regular Au/Ti electrodes as the base for the DEP device, the optimized geometry of the structures paired with a SU8 insulator layer in a PDMS channel provided label-free analysis for a large variety of cells with different sizes and properties [20].

3. BioMEMS in Cell Separation

Cell separation refers to the process of splitting a specific cell population from others within a biological sample, for instance, circulating tumor cells (CTCs) from blood or a particular tissue. This process is fundamental to acquire analytes of interest within a single fluid [4]. Multiple systems can be used in order to achieve the separation of different cell populations. In BioMEMS, different transport processes can be performed in microfluidic devices; hence, a number of microfluidic features are used for fluid transfer for the specific purpose of cell separation [21]. Similar to cell sorting, developed approaches for sell separation highly rely on intrinsic properties of the target cells including size, shape, charge, and deformability. In Table 2, we provide some of the latest techniques developed for cell separation within BioMEMS.

Several Lab-on-a-Chip (LOC) devices have been utilized in order to separate cells or particles based on their size. A device for size-based separation was reported in 2013 by Geislinger and Franke. The separation process benefited from hydrodynamic effects on Reynolds number (Re) to divide the cells based on their size and deformability (Table 2). The microfluidic was reported to be a suitable candidate for sorting CTCs from a mixture including red blood cells (RBCs) [22]. The authors reported possible applications of this device in cancer diagnostics and therapeutics. Moreover, Hvichia et al. described a microscale separation platform that consisted of a stepped physical structure that decreased progressively in the dimensions of the fluidic path through which the cells traveled. This process allowed capturing viable CTCs [23]. The application of microfluidics for cell separation in liquid biopsies is also a prominent and recurrent theme in deformability-based cell separation (Figure 2). In particular, CTCs have a deformability characteristic which is a key indicator for metastasis and noninvasive diagnosis of cancer [23].

Charge-based cell separation techniques employ the electrical properties of cells and/or the medium that contains them in order to cause a displacement [6]. This approach is especially useful to sort out and separate target cells from a homogeneous solution since low concentrations and similarities in shape and size can make this task difficult [24]. Song et al. proposed an array of oblique interdigitated gold electrodes within a PDMS-based BioMEMS for the continuous sorting of stem cells in a homogeneous mixture of cells (Table 2). This facilitated further applications of this device in differentiation of target cells and cell-cell studies [25]. These technologies enable scientists to generate new diagnostic tools that could considerably shorten the time needed for bioanalytical assays.

Another technology that has been used for cell separation in BioMEMS is inertial microfluidics. In inertial microfluidic devices, cells can be manipulated and separated by using hydrodynamic forces of the carrier fluid in the channel to focus particles in certain bands. This passive manipulation relies on the microchannel characteristics and the intrinsic hydrodynamic effects of the target cells [26]. By using polyvinyl chloride (PVC), Zhu et al. described a polymer-film inertial microfluidic jigsaw (PIMJ) sorter for rare cell separation. The proposed device was fabricated by assembling laser-patterned polymer-film layers of different thicknesses and assembling it as a jigsaw puzzle. A high recovery ratio of more than 90% was achieved for the separation of rare tumor cells from white blood cells (WBCs) [26].One of the main advantages of this system was the easy fabrication method, as opposed to conventional PDMS-based microchips. The authors highlighted the ease of fabrication by simple assembly of multiple layers to form a 3D structure on the same plane, enabling a faster production of devices with complex geometries without the need of a clean room facility. Razavi et al. described an inertial microfluidic device based on 3D printing with a right-angled triangular cross-section. Made from poly(methyl methacrylate) (PMMA), the device was

Table 2: Recent BioMEMS platforms for cell separation including the type of the platform, the main components, the fabrication strategy, the mechanism of operation, and the specifics of each platform.

BioMEMS platform	Main components	Fabrication strategy	Mechanism of operation	Specifics	Ref.
Noninertial hydrodynamic lift-induced cell sorting device	Syringe pumps Microfluidic chip Voltage source		The separation process took advantage of size and deformability as intrinsic biomarkers were induced by a hydrodynamic effect at very low Re, separating the target cells by their size.	The device is capable of sorting MV3-melanoma cells from an RBC suspension at a high hematocrit level. The mechanism of sorting is gentle compared to other label-free techniques.	[22]
Parsortix™ system for cell capture	Plastic molding containing a stepped separation structure and microchannels Heat-bonded thin plastic cover	Standard soft lithography	The system used a microfluidic cassette that captured cells based on their size and deformability. The sample passes through a fluidic path leading to flow distribution channels and over the stepped separator.	Cell size must be known for the system to be able to capture them. The device does not depend on antibody affinity.	[23]
Continuous-flow microfluidic DEP chip	Oblique interdigitated electrode array AC frequency generator Syringe pumps Microfluidic chip		The devices used DEP to force the target cells to flow in a determined path.	The device facilitated the continuous label-free cell separation.	[25]
Paper-based extraction device	Paper-based valve Sponge-based buffer storage	3D printing using a photopolymer resin	Separation was achieved by the combination of high affinity between the negatively charged particles of interest and the positively charged glass fiber.	The device can be used in resource-limited settings.	[87]
Microfluidic chip with a ratchet mechanism coupled with a hydrodynamic concentrator	2D microscale funnel membrane-based Microvalves	Standard PDMS multilayer soft lithography fabrication techniques	The device used oscillatory flow to manipulate cancer cells and leukocytes and performed a throughput separation.	The device has the ability to refresh the filter microstructure after each separation.	[88]
Inertial focusing LOC	Rectangular microchannel Serpentine microchannels Fluidic resistors	Standard soft lithography techniques with PDMS	The device operated a high-throughput separation by multichannel shape-based sorting of the microalga using inertial focusing techniques.	The device is cost-effective and label-free.	[95]
Elasto-inertial pinched flow fractionation microfluidic platform	Asymmetric T-shaped microchannels Syringe pumps		Continuous separation of particles of equal volume by exploiting the elasto-inertial lift-induced particle viscoelastic fluids. The device uses particle's rotational movements controlled by the zig-zag shape of the induced microchannel.	The device offered a label-free separation.	[96]
Polymer-film inertial microfluidic jigsaw sorter	A trapezoidal spiral inertial microfluidic sorter chip Syringe pump	Laser cutting Plasma-activated bonding	The device utilized a syringe pump to inject the cell suspension at specific flow rates. The cells were separated by inertial forces and recovered in different outlets.	The device demonstrates a complete separation of the binary particles with a minimum size difference of 2 μm. The device was successfully applied for the separation of rare CTCs from the blood samples.	[26]
3D printed inertial microfluidic device	3D printed device PMMA sheet Syringe pump	DLP 3D printing Pressure-sensitive adhesive bonding	The device utilized the inertial forces to separate different cell lines.	Through this strategy, fabrication of a right-angled triangular cross-section was possible.	[27]

Table 2: Continued.

BioMEMS platform	Main components	Fabrication strategy	Mechanism of operation	Specifics	Ref.
Acoustofluidic chip for nano/microparticle separation	PDMS-based chip SAW transducer Function generator Amplifier Syringe pump	Photolithography Standard soft lithography techniques with PDMS	Hydrodynamic focusing was applied allowing particles to enter consistently into the same position in the acoustic field, and once the SAW field was applied, particles were deflected and separated into different streams.	Particles with a wide size range from 200 nm to 10 μm can be separated with this device.	[28]

CTCs: circulating tumor cells; DEP: dielectrophoresis; DLP: digital light processing; LOC: Lab-on-a-Chip; PDMS: polydimethyl siloxane; PMMA: poly(methyl methacrylate); RBCs: red blood cells; Re: Reynolds number; SAW: surface acoustic wave ; 3D: three-dimensional; 2D: two-dimensional.

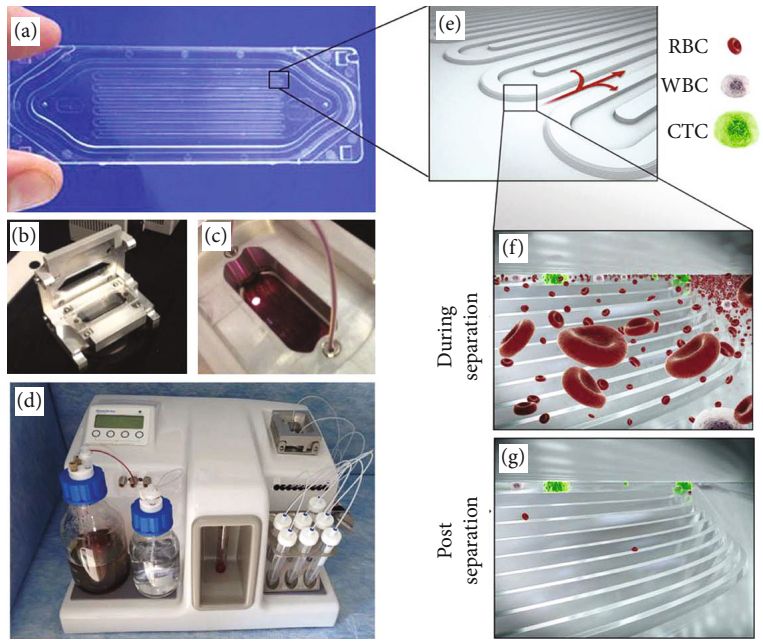

Figure 2: The microfluidic device for the (a–g) cell capture process shows the device and the progression of capturing CTCs [23], ©2016, National Library of Medicine.

capable of separating target cells without altering the cell activity which made it a safe method for biological assays [27]. Alike the work of Zhu et al., the authors also described the challenges of manufacturing PDMS-based devices and the new possibilities that alternative polymers could give to the BioMEMS devices.

As previously discussed in the cell sorting section, SAW is a technique often utilized in BioMEMS devices. Zhao et al. described a disposable PDMS acoustofluidic chip for nano/-microparticle separation [28]. The authors demonstrated the use of a hybrid channel design with hard and soft materials and tilted-angle standing SAWs. The disposable part of the device was the PDMS-based chip with the channels, while the interdigital transducers (IDTs) were reused multiple times. The device was capable of differentiating and successfully separating bacteria from RBCs with a purity of 96%. The hybrid hard/soft PDMS channels were employed to minimize the acoustic attenuation factor that PDMS causes in SAW. This control was achieved by utilizing a low thickness PDMS bottom enclosure [28].

4. BioMEMS in Cell Isolation/Trapping

In molecular and cellular biology research, cell isolation and trapping are essential steps for accurate and precise analysis of specific cell types which subsequently allow exploiting particular cell properties and cell categorization [29]. Highly efficient cell isolation and trapping could open various windows of opportunity to the areas of drug discovery, cancer genomics, cell separation, confinement, and controllable transfection of cells [30]. Table 3 provides an overview of the latest advancements made over the past five years highlighting the specific interface between BioMEMS and cell isolation/trapping.

Centrifugation enables fluids with different densities to sediment into layers of increasing density under the influence of gravitational forces [29]. Espulgar et al. proposed a PDMS-based centrifugal microfluidic device to trap single cells with controlled separation distance allowing studying of cell growth, coupling, decoupling, and beating in a rapid manner [31]. Other examples of PDMS cell trapping device include

Table 3: Recent BioMEMS platforms for cell isolation/trapping including the type of the platform, the main components, the fabrication strategy, the mechanism of operation, and the specifics of each platform.

BioMEMS platform	Main components	Fabrication strategy	Mechanism of operation	Specifics	Ref.
Centrifugal microfluidic chip	Microfluidic chip Acrylic plastic plates with silicon tubes Filtering channels Focusing channels Trapping channels	Lithography methods Standard photolithography technique	The device applied centrifugal force to isolate the cells.	The device does not need large equipment for cell manipulation.	[31]
Planar p-DEP chip	P-DEP chip TPIDA electrodes (A-IDA and B-IDA electrodes) Microfluidic channels Microwell array		Cells were trapped by applying AC signal into the electrodes. The paired cells in each microwell could be pushed together into a U-shaped microbaffle by liquid flow through a capillary-sized channel, resulting in single isolation and subsequent cell-cell contact.	The device is facile and accurate.	[32]
3D cell rotation BioMEMS platform	V-shaped pillars Microchannels C-PDMS electrodes ITO electrode Controllable 3D cell rotation	Photolithography and wet etching methods	Cell medium would be streamed along with the flow, and only one cell was trapped at the opening of the V-shaped pillars, subsequently back-flowed, and stabilized inside the chamber.	The strategy offered a low-cost device with straightforward approach that had a better control over cell trapping and isolation.	[34]
Flow-through LOC	Gold electrodes PDMS microfluidic channel DEP trap	Standard photolithography and lift-off techniques	Cells were trapped at the constant flow with the continuous application of the electric field. The n-DEP allowed trapping the cells independent of gravity.	The device offered control over unwanted lysis. It involved simultaneous n-DEP trapping and AC electroporation.	[30]
Microfluidic cell trap array	Microfluidic channel Hydrodynamic sieve-like trap system	Photolithography technique	The cells were flowed in, and single cells were trapped on the protein micropatterns by the sieve-like traps.	The device used passive trapping suitable for preserving cell viability.	[35]
Microfluidic device with integrated pipettes	Microfluidic network of 60 loops Bypass channel Cavities Trap Pipettes	Soft lithography process	The cell-drug mixture was injected into the grid, and the device trapped individual cells within the array of cavities and immobilized them.	The devices presented control over the distribution of cells/clusters. It involves a downstream assay for capturing rare CTCs.	[36]
Microfluidic device	Syringe pump Magnetic stirring bar Micropillar array Fluorescence microscope	Photolithography and soft lithography techniques	The cells were kept in suspension through a magnetic stirring bar, while the cell mixture or blood sample was pumped through the device.	It is a noninvasive device for monitoring the response to cancer treatments.	[37]
1D cell migratory assay	Hydrodynamic trap microfluidic channels Microtracks Stamped substrates Laser ablated substrates	Multilayer photolithography process	Cells were seeded at low flow rate onto the patterned microtracks and trapped by hydrodynamic barriers.	Microtracks allowed guiding cell migration with high predictability and precise positioning.	[38]

Table 3: Continued.

BioMEMS platform	Main components	Fabrication strategy	Mechanism of operation	Specifics	Ref.
Semiautomated microfluidic cell-based biosensor	Fluid channels Pneumatic valves Fluid crossed-channel structure Control channels	Rapid prototyping technique	A controllable pneumatic trap was used to encapsulate and discharge suspended cells.	In this device, the chemical stimulation to cell was achieved by flexible hydrodynamic gating.	[39]
Hydrodynamic Snaring Array	V-shaped weirs U-shape dwelling region Microcultivation system 96-well plates	Microelectrochemical process, inductively coupled plasma etching, and photolithography	Single cells were trapped and manipulated within a high flow and low-pressure area that reconcentrated the streamline via a V-shaped weir that loaded the cells, pushing them precisely into the dwelling region due to the void and wedge structures.	The device is capable of trapping single cells in 10 s. Additionally, it allows for long-term cultivation.	[40]
Porous-microwell trapping-system	Sieved microwell array Microfluidic two-layered channel	Slit channel lithography	Particles were directed along the top channel and captured in the microwells. A shielding flow along the sides of the top channel was used to guide the flow directly over the wells, and untrapped particles were sieved along the flow path.	In this device, well occupancy and trapping were improved.	[41]
Polymer-based porous microcapsules	Microcapsules with shells and asymmetrical distributed funnel-shaped pores	Droplet microfluidic technology and chemical phase separation process	The pores' geometry and bacteria's motility drive the bacteria to enter the microcapsule cavity.	The surrounding liquid environment safeguards the bacteria while adding bactericide into the cavities greatly enhanced the efficiency of the system.	[42]

AC: alternating current; C-PDMS: carbon-black-PDMS; CTCs: circulating tumor cells; DUV: deep ultraviolet illumination; DLD: deterministic lateral displacement; Au: gold; ITO: indium tin oxide; IDA: interdigitated array; LOC: Lab-on-a-chip; n-DEP: negative dielectrophoresis; C4F8: octafluorocyclobutane; PDMS: polydimethyl siloxane; PolyMUMP: polysilicon multiuser surface micromachining process; p-DEP: positive dielectrophoresis; Ti: titanium; TPIDA: two-pair interdigitated array.

DEP, a versatile method for cell manipulation due to its compatibility with cells, label-free nature, simplicity, and integration of *in situ* cell measurements [32]. DEP enables the manipulation of individual living cells by regulating electrical signals applied to the electrodes [33]. Different designs and electrode arrangements were reported for such devices. Among these proposed strategies, positive dielectrophoresis (p-DEP) offers a facile method for cell trapping which can be further used for cell communications and a precise cell pairing in cell fusion [32]. Negative dielectrophoresis (n-DEP) provides a better control over unwanted lysis and simultaneous analysis of alternate current (AC) electroporation of single cells (Figure 3) [30]. Moreover, a coupling of different techniques such as hydrodynamics and DEP enables single-cell loading, cell rotation, and consequently sell isolation [34].

Another simple yet effective example of polymer-based BioMEMS was proposed by Lin et al. for accurate and controlled isolation of single cells on protein micropatterns. This PDMS microfluidic device incorporated aligning sieve-like trap arrays in a microfluidic channel to control the type, the amount, and the arrangement of nearby cells [35] (Table 3). Bithi and Vanapalli presented a pipette-based microfluidic cell isolation (MCI) device for operating single-cell drug assays. The PDMS device was developed for handling and manipulating rare types of cells and to compartmentalize such cell samples [36]. Another example was a PDMS microfluidic device that immobilized tumor cells on the surface of the microchannels by the aim of capture agents. Functionalized with aptamer-antibody, the microchannel of this device promoted a strong bond between the substrate and the cells which allowed isolation (Table 3) [37]. Hisey et al. proposed a BioMEMS that hydrodynamically seeded single cancer cells onto polystyrene (PS) microtracks benefiting from topographical cues and encouraging migratory cell behavior. The device improved the reproducibility of cell trapping and enhanced the clinical applicability of *in vitro* single-cell migration assays. This device benefited from automatic analysis of single-cell migration behavior to predict treatment outcomes and antimetastasis drug screening [38]. In another study, a multiarray microchip developed by Huang et al. allowed studying mechanically induced physiological changes in cells through a side-stretching mechanism and a controllable pneumatic trap which were used to encapsulate and discharge suspended cells (Table 3). This PDMS device has shown promises in molecular processes and tissue reshaping applications [39].

Chiang et al. were able to trap a single cell in 10 s with a hydrodynamic snaring array (Table 3), enabling a stable perfusion culture microenvironment. Furthermore, the authors presented a unique microstructural design method. Their particular approach of V-blocking and voids enabled new

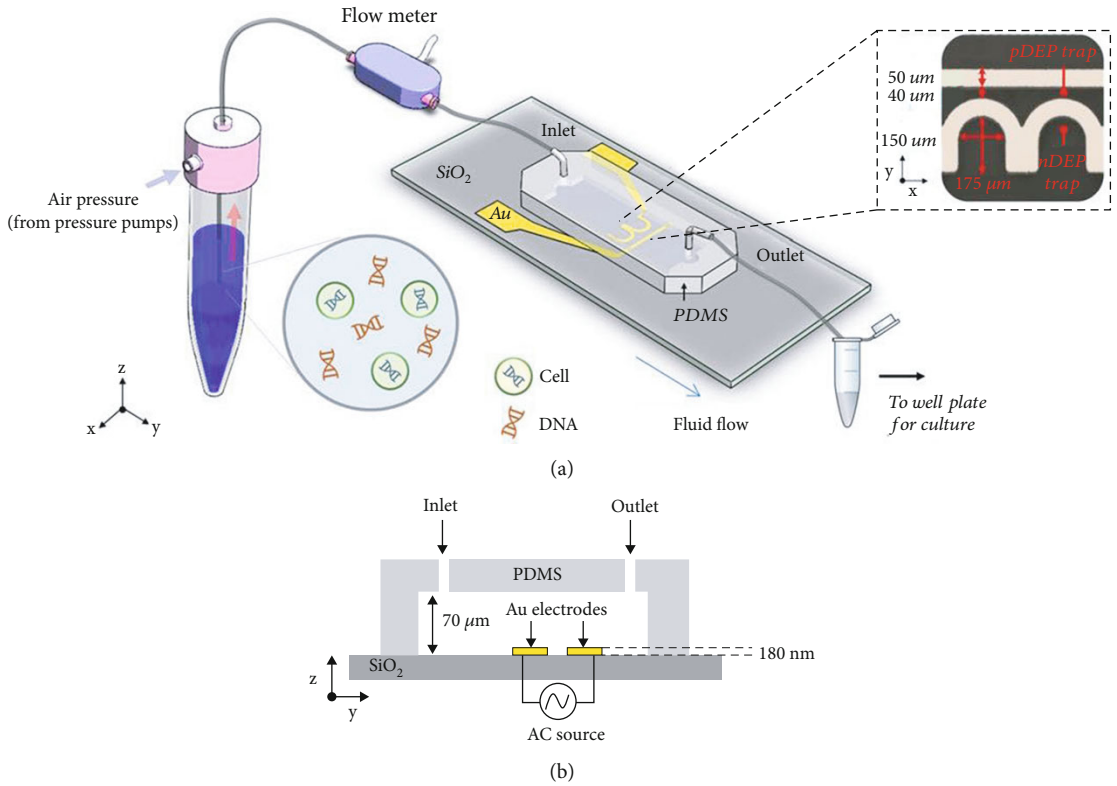

Figure 3: (a) An overview of the BioMEMS platform made from PDMS and gold electrodes and (b) a cross-section view of the trapping chamber [30], ©2019, Nature Publishing Group.

techniques to trap various cell types and different cell sizes. Additionally, the authors demonstrated an independent cultural environment in each PDMS well, showing great promise for interaction studies among single and multiple cells [40]. Other studies have also benefited from hydrodynamic forces. Romita et al. have utilized hydrodynamic forces as a main driving force to capture cells and to exclude the need for sedimentation time. The authors developed sieved microwells with open pores at the bottom, enabling crossflow trapping within a double-layered PDMS microfluidic device, in a simple two-step fabrication process, as seen in Table 3. This device opened new channels to improve capture ability and well occupancy, showing great promise for single-cell analysis. Moreover, its versatile fabrication methods allowed the device to be adaptable into a wide range of sizes and shapes [41]. Scientists use various geometric designs to isolate cells in devices. For instance, in the case of Luo et al. the authors developed polymer-based porous microcapsules to capture, trap, and isolate bacteria (Table 3). In this study, poly(DL-lactide-coglycolide) (PLGA) and poly(L-lactide)-b-poly(ethylene glycol) (PLA-b-PEG) were sued to create the microcapsules while polyvinylpyrrolidone (PVP) served as surfactant. The asymmetric porous geometry in combination with the bacteria's own motility greatly diminishes the need for nutrient source or chemical components to entice the bacteria, thus reducing bacterial toxicity to surrounding cells. This device has shown great promises as an alternative to reduce bacterial contamination in liquids for environmental studies [42].

5. BioMEMS in Cell Pairing

Cell pairing facilitates a better comprehension of cell-cell communication mechanisms and therefore is a key to understanding most physiological and pathological disorders of multicellular organisms. Cell pairing triggers the fusion between cells, a unique tool to combine genetic and epigenetic information of two different cell types. Since the 1960s, this methodology has been commonly used to identify transacting factors that affect gene expression and antibody-producing hybridoma generation [43]. Cell paring has proven to be an excellent strategy for biological studies such as cell fusion and cell-cell communications. Cell pairing approaches commonly rely on initially trapping individual cells (explained in the previous section) followed by introducing the second cell type to the system which allows the two trapped cells to pair [44]. Table 4 provides an overview of the latest advancements of recent years highlighting the specific BioMEMS developed for cell pairing applications.

Li et al. demonstrated a strategy that used centrifugal force to hydrodynamically trap and pair cells for analysis over an extended period of time [44]. The method enabled a higher density of cell pairing units in a straightforward, rapid, and simple operation while remaining friendly to cells. Furthermore, the device allowed both homotypic and heterotypic cell pairing, accompanied by long-term on-chip coculture for the analysis of intercellular interactions. The BioMEMS device proposed in this study proved to be a robust tool in biological applications and a controllable

Table 4: Recent BioMEMS platforms for cell pairing including the type of the platform, the main components, the fabrication strategy, the mechanism of operation, and the specifics of each platform.

BioMEMS platform	Main components	Fabrication strategy	Mechanism of operation	Specifics	Ref.
Centrifugal hydrodynamic microfluidic chip	Cell chamber array Hydrodynamic-assisted single-cell traps	Standard soft lithography methods	Individual cells were hydrodynamically trapped and relocated into cell chambers by centrifugation of transient storage. Subsequently, a second cell could be captured and trapped in the structure of the device.	By this selective manipulation, the device could trap three or more single cells in one cell chamber. Moreover, the design gave more available spatial space to the cells and without chamber-chamber crosstalk.	[44]
Hydrodynamic microfluidic chip	Hydrodynamic trap Oil-isolated microchambers		Cells flowed by hydrostatic pressure, and the corresponding traps were occupied. Subsequently, residual cells were washed away, and a different cell suspension was added sequentially.	High efficiency and single-cell accuracy were offered in this device with minimize chance of cross-contamination.	[45]
Mechanical parylene slide system	PRF Tweezers Glass substrate SU-8 comb layer PDMS box PDMS cover Syringe pump		Tweezers were used to control the trapping area, where PFR on the comb layer was slide to open positions and cells were trapped along the PFR. Subsequently, another cell could be trapped through the same strategy.	The mechanism allowed the control of the amount and order of lined-up cells; however, the cell pairing system depended on wettability of the surfaces.	[46]
Microfluidic deformability-based device	PDMS hydrodynamic traps Flow-through channel Syringe pumps		The cells were captured in the single-cell traps by passive hydrodynamics and pipetting. Once saturation was reached, additional cells traveled through the trap with an increased flow. Thus, the second load of cells were introduced to the device and were passively transferred into the larger traps with the captured cells.	Sequential trapping and pairing of cells with similar and diverse sizes were possible. In this platform, the cell fusion was achieved using biological, chemical, and physical biological, chemical, and physical stimuli.	[47]
Droplet-based microfluidic platform	Sorting chip Collection chip Electroosmotic pump Syringe pumps		Before encapsulation, each cell type was stained with different fluorescent dyes. Afterward, emulsions were injected into the device and a refilling pump was used to withdraw droplets that did not trigger sorting. The positive droplets were collected into the chip, and trapping was monitored.	The device mimics a niche environment enabling pairing and cell-cell interactions at the single-cell level. It does not require specific solutions for cells of different sizes.	[48]
Multifunction-integrated microfluidic device	IDA electrodes Microwells	Standard lift-off process, soft lithography technique, and mold-replica modeling	P-DEP was applied to attract two cells into the trenches. n-DEP force was then activated to achieve cell pairing.	Either electrical or chemical stimuli can be used for cell fusion allowing flexibility and multi-fusion.	[50]
Droplet-based multifunctional microfluidic platform	Pneumatic microvalve Droplet trap chamber Lateral bypass channels	Multilayer soft lithography using PDMS	The array operates in a FIFO manner. The generated droplets were carried by the continuous oil phase into the FIFO storage unit and sequentially captured in the traps to form a library of immobilized droplets. After filling the trap array, selected droplets were moved to the merging chamber, where controlled droplet fusion was induced.	The entire procedure was accomplished in several minutes.	[51]

Table 4: Continued.

BioMEMS platform	Main components	Fabrication strategy	Mechanism of operation	Specifics	Ref.
Droplet microfluidic platform	Droplet microfluidic system 3D electrodes Microfluidic channels Droplet cultivation channel	2PP microfabrication Multilayer soft lithography using PDMS	Vertical droplet cultivation was reflowed into a planar droplet reflow channel remaining tightly packed. Subsequently, the train of water-in-oil emulsion droplets flowed into the aqueous flow, and the carrier oil was cleaved into the first train of droplets which generated a second water-in-oil emulsion droplet, resulting in their pairing.	Droplets had the capacity to encapsulate cells from a large library to generate droplet libraries, while the paired cells remained closely connected.	[49]
HL-Chip	Microwell platform Dual-well HL-Chip	Soft lithography	Objects were precisely positioned and loaded into the array and briefly centrifuged until the occupancy was achieved. The dual-well structure contributed to pairing.	The device permitted design arrays of defined cell/object combinations for different analysis and material retrieval.	[52]

2PP: two-photon photolithography; AC: alternating current; FIFO: first-in, first-out; HL-Chip: hierarchical loading microwell chip; IDA: interdigital array (IDA); n-DEP: negative dielectrophoresis; PRF: parylene rail films; PDMS: polydimethyl siloxane; p-DEP: positive dielectrophoresis.

model for complex biological system studies which successfully handled fragile cells.

Hydrodynamic principles were also used for the development of a microfluidic chip that facilitated cell pairing in controlled environments with highly efficient trapping and pairing without the aid of external equipment. Cells, in this device, flowed by hydrostatic pressure and the corresponding traps were occupied. Subsequently, residual cells were washed away, and a different cell suspension was added sequentially in order to pair the predetermined cells. While the chance of cross-contamination was limited, the device offered a slightly low throughput [45]. Abe et al. demonstrated a cell pairing system suitable for mounting and positioning and manipulating cells by mechanically sliding a parylene rail films (PRF). Furthermore, the PDMS-based device could control the trapping sites, and by repetition, it enabled pairing multiple cells in a specific order within the device (Table 4). The proposed system could be applicable in studies of cell-cell interactions, cell fusion, and coculture aimed at drug discovery [46].

Cell pairing is essential for cell fusion, a natural process that occurs during embryogenesis and immune responses. Classic fusion methods depend on random cell pairings therefore lack control over cell-cell contacts [47]. In order to address this shortcoming, microfluidic devices of different classes were developed for controlled pairing of partner cells [47, 48]. Dura et al. developed a PDMS-based cell pairing device for sequential trapping and pairing multiple cells. This device employed passive hydrodynamics and flow-induced deformation to capture the cells (Table 4). The proposed device applied biological, chemical, and physical stimuli to pair cells of similar and diverse sizes [47]. Hu *et al.* presented a droplet-based microfluidic device for cell pairing based on dual-color sorting. This device was fabricated by using PDMS:SU8 with 10 : 1 ratio on silicon wafer. A refilling pump was incorporated in this device to withdraw droplets that did not trigger the sorting mechanism. This pairing method facilitated unique collection and analysis of droplets with two different cells (stained with different dyes) within a robust tool for screening and manipulating cells [48].

Furthermore, Zhang et al. presented an integrated multilayer droplet microfluidic platform capable of handling a large number of droplets of different sizes, allowing to operate large-scale multistep droplet processing (Table 4). The platform had minimal error during the assays and could even handle large droplet sizes (known to be difficult to manipulate). The study presented two significant innovations: (1) the usage of curved microstructures and (2) a new droplet cleaving scheme. The first permitted consistent droplet reflows (in both planar and vertical directions), and the latter facilitated automatic droplet pairing. This strategy allowed continuous aqueous-phase flow and cleavage of the water-in-oil emulsion droplets, permitting sequential manipulation. This versatile PDMS-based device enabled droplet generation, reflow, cleaving, pairing, and cocultivation [49].

A PDMS microfluidic device for cell capturing, pairing, fusion, transfer, and culture was developed by He et al. [50]. The device incorporated capture wells and electrodes which operated by the aim of DEP (Figure 2). A p-DEP was applied to attract two cells into the trenches within capture wells, and a n-DEP was then activated to achieve cell pairing. When cells were fused, they were transferred for on-chip culture by flipping the device (Figure 4).

This simple-structured multifunctional device offers various cell-related operations with compatibility and flexibility [50]. Another multifunctional PDMS microfluidic platform was developed by Babahosseini *et al.* offering droplet generation, capture, storage, and selective merging of the target droplets. The droplets used in this study were of different sizes containing individual cells of different types and pairing of diverse ranges of cells within discrete droplets [51]. More recently, Zhou et al. were able to pair and align functionalized beads and different types of cells utilizing a hierarchical loading microwell chip (HL-Chip) (Table 4). The PDMS-based

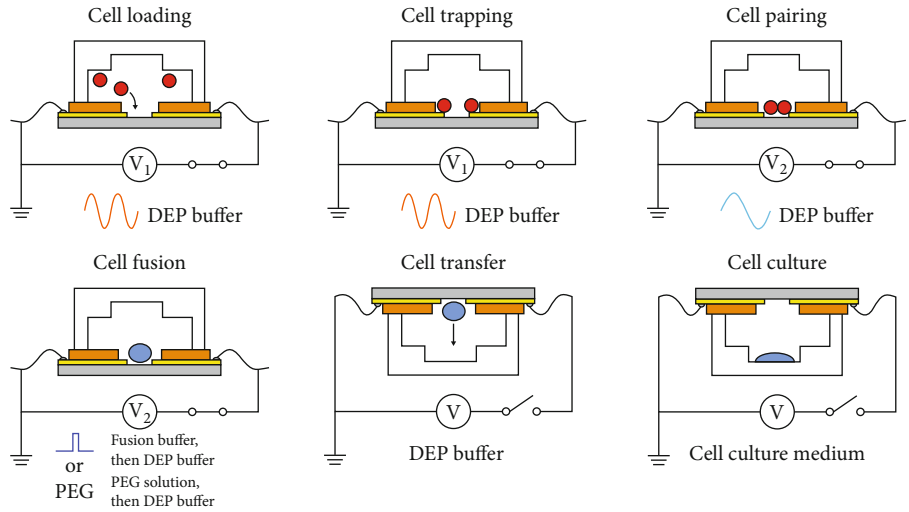

Figure 4: The schematic representation of the device and its functions in different applications. With permission [50], ©2019, American Institute of Physics.

device presented high precision and efficiency in pairing and aligning cell beads adjacent to each other. The authors claimed that the HL-Chip technology could be a powerful microtool as it enabled quantitative and simultaneous detection, retrieval of desired single cells, and high-throughput and single-cell loading efficiency whilst remaining easy to handle [52].

6. BioMEMS in Cell-Cell Communication

Communication between cells is of particular importance in multicellular organisms [53, 54]. The interaction between cells regulates different processes, including cell proliferation, apoptosis, differentiation, and response to stimuli, among others. Moreover, errors in communication pathways can lead to diseases including cancer, autoimmune disorders, and diabetes [53]. Due to their complexity, cell communication mechanisms remain poorly understood. Microfluidic platforms can provide an *in vivo*-mimicked environment where studies of intercellular communication are performed offering advantages over other systems including a precise control of dynamic perfusion, extracellular chemical environment, cell arrangement, and single-cell manipulation [5, 8]. The results from these studies can be translated into new applications in the areas of drug screening, tissue engineering, and for understanding the nature of different diseases.

One of the main applications of BioMEMS is in studying cell-to-cell interactions between tumor cells and various types of target cells [55]. Ma et al. developed a PDMS microfluidic device that promoted indirect interactions between fibroblasts and tumor cells. The proposed platform enabled the study of the interaction between different types of cells in a single device including the interactions of human embryonic lung fibroblasts (HFL-1) with either carcinoma cells (HepG2, ACC-M, and ACC-2) or healthy epithelial cells (GES-1) (Figure 5). The results of the study revealed that the site-directed migration and transdifferentiation of embryonic fibroblasts only occur in the presence of carcinoma cells [56]. Similarly, Fang et al. created a unidirectional microfluidic chip with the same purpose of studying indirect cell interactions between either invasive or noninvasive breast cancer tumor cells (MDA-MB-231, MCF-7) and fibroblasts (MRC-5). The proposed device was made combining both soft lithography and traditional lithography techniques, and it was comprised of a PDMS piece with two culture chambers and two surrounding media channels. Both culture channels were connected by the medium transport channels, which carried the used medium of one culture chamber to its counterpart, hence enabling the unidirectional and noncontact communication between the cells. The communications between both types of tumor cells resulted in a major conversion rate from the invasive breast cancer tumor cells (MDA-MB-231) [57]. Further, approaches to the study of the indirect cell interactions between cancerous and target cells include passive diffusion. Rahman et al. generated a two-layer microfluidic culture device, made from a bottom layer of agarose (3%) and a top layer of PDMS to facilitate chemical diffusion. The culture and media supply channels were in the top PDMS layer. Breast cancer cells (MDA-MB-231) and adipose-derived stem cells (ASCs) were cultured in their respective channels, and media was supplied via their neighboring outer channels to reduce shear stress. The coculture proved to have a positive effect on MDA-MB-231 cell growth and proliferation, suggesting that ASCs provide a supportive environment for the breast cancer cells [58].

Other microdevices that are based on interconnected cell culture chambers have also been employed in cancer cell migration assays and motility studies [59] as well as chemotherapy testing applications [60, 61]. Table 5 provides a thorough overview of some of the latest strategies developed for studying cell-cell communication.

Another important aspect that can be carefully studied in microdevices is neural development and dysfunctions [55]. Taylor et al. presented a PDMS-based device that simulated synapses on-chip, where rat hippocampal neurons were used

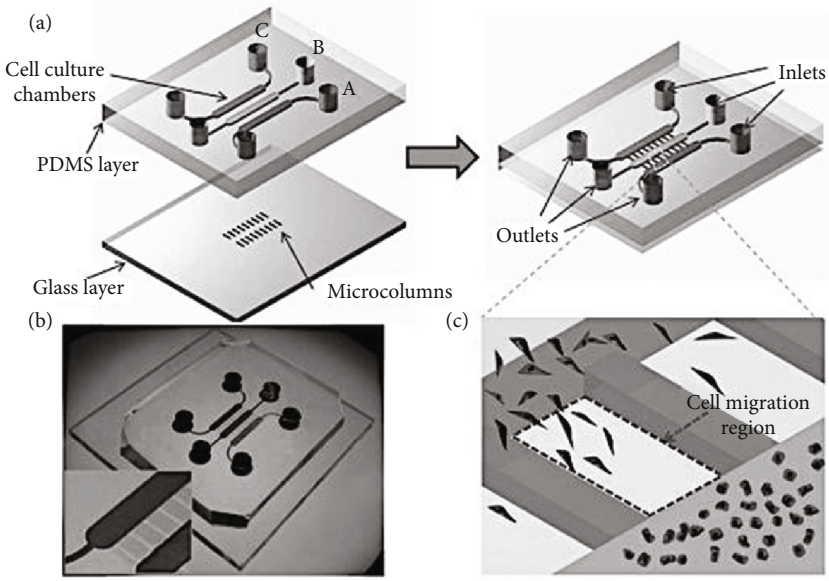

Figure 5: The schematic representation of the BioMEMS in direct contact with cells. With permission [56], ©2010, Wiley Online Library.

to form synapses in a microarray to study the effect of chemical injuries. One significant advantage of the proposed platform was that it manipulated, both fluidically and genetically, two neuronal populations in an independent manner [62]. Schneider et al. developed a multiscale PDMS chip that permitted cell culture and cell-cell communication of neuronal progenitor cells. Their microreactor enabled cell stimulation by assembling patterned protein surfaces inside individual wells. The authors combined the use of polymer and glass substrate, to benefit from easy 3D fabrication, and chip's mountability. This device used substrates patterned with biomolecules allowing communication through narrow channels, while permitting cells to be cultured spatially separated from each other. Moreover, by this design, cells were prevented from migrating the cell soma, while permitting physical contact with neighboring cells. This microreactor showed great promise as a compartmentalized culture system. Furthermore, the experiments demonstrated that cell-cell communication of physically stimulated separated cells can be feasible [63].

Other devices, such as microfluidic platforms and coculture systems, have been used to study interactions between neurons and other cells as well [64, 65]. BioMEMSs are powerful tools for controlling and analyzing cell-cell interactions/communication at different levels of complexity. However, most of the available technologies are still at a proof-of-concept stage. Future efforts should be made to use microfluidic chips to generate more human-like biological microenvironments.

7. BioMEMS in Cell Differentiation and Identification

Different BioMEMS have been developed for cell differentiation and identification. Cell differentiation is an important phenomenon that occurs numerous times in the process of multicellular formation within organisms as it alters from a simple eukaryotic cell to a more complex structure such as tissues or different cell types. Differentiation remains as one of the main functions of cells throughout tissue repair and cell turnover. The studying of cell differentiation is, therefore, vital in various biological-related fields.

For cell differentiation, Bilican et al. presented a focusing-free microfluidic device and tested the device for the differentiation of RBCs and lymphocytes. In this PDMS device, a current between the external electrodes was generated by an AC signal. In the absence of the particles, the output current was zero. In the presence of the particles, however, the positive output voltage increased. This device was capable of differentiating the target cells, even when the cells were similar size range. Additionally, the platform had the potential to be used in hematological diseases such as malaria or anemia [66]. Another PDMS device was developed by Ong et al. proposing a pump-free microfluidic platform to achieve the long-term differentiation of HepaRG cells into hepatocyte-like-cells (HLCs) and presented potential to develop *in vitro* liver models on a simple platform [67]. Table 6 provides a thorough overview of some of the latest strategies developed for studying cell differentiation within BioMEMS.

Alternatively, cell differentiation can be performed benefiting from the electromagnetic properties of cells. Jupe et al. developed a flexural plate-wave (FPW) sensor capable of detecting respiratory infectious viral diseases at newborns. In this strategy, an oscillation of 23 to 30 MHz was applied to cells which caused their binding to the surface of the device. The attached cells to the surface produced a mass gain used for differentiation. The sensor was designed to be highly specific, capturing only molecules that are complementary to the target cell [68]. Gajasinghe et al. presented an electrical impedance spectroscopy-based PDMS-based device for studying tumor cells [69]. Using impedance measurement, the recorded ΔR_c values depended on cell size. This

Table 5: Recent BioMEMS platforms for cell-cell communication including the type of the platform, the main components, the fabrication strategy, the mechanism of operation, and the specifics of each platform.

BioMEMS platform	Main components	Fabrication strategy	Mechanism of operation	Specifics	Ref.
Microfluidic device for indirect contact coculture	Two layers of multiple cell culture chambers Parallel layer of migration regions	Wet etching method	Human liver carcinoma cells and human embryonic lung fibroblast cells were introduced into two culture chambers, and culture medium was infused into a third chamber.	Indirect coculture with tumor cells was performed in this device. As a result, direct migration and transdifferentiation were observed.	[56]
On-chip coculture system	Center end-closed channels Cell culture chambers Microchannels		Melanoma cells and immune cells from the spleen of wild type and deficient knockout for interferon regulatory factor 8 mice were cocultured for one week and monitored by fluorescence microscopy and time-lapse recordings.	The device monitored the interactions between cancer and immune cells of immune competence vs. immunodeficiency.	[59]
Microfluidic device for chemical and physical contact	Cell culture chambers Migration microchannel	Standard photolithography method	Human peripheral blood mononuclear cells or alternative mouse splenocytes were loaded into one chamber and treated and untreated tumor cells into another chamber. The cells were carefully monitored by time-lapse recordings.	FPR1 promoted interactions between dying cancer cells and leukocytes.	[61]
Microfluidic device for tumor simulation	Cell culture chambers Hydrogel barriers		Human bladder cancer cells, macrophages, fibroblasts, and HUVECs were cultivated inside the chambers and monitored by inverted microscopy.	The device incorporated simulation system for screening of different chemotherapeutic agents.	[60]
Synapses on-chip	Microgrooves Chambers Perfusion channel	Soft lithography method	Rat hippocampal neurons were plated in the two compartments, cultured, and then infected with either a GFP- or RFP-Sindbis virus in order to visualize potential connections.	The device incorporated simulation system to access and manipulate synaptic regions.	[62]
Axon and glia coculture system	Two compartments Central channels	Standard photolithography	Neurons and glial cells were cultured in separate chambers. Only neuronal processes (especially axons) could enter the glial side through the central channels.	The device allowed the studying of the signaling pathways between neurons and glia.	[64]
Macro-micro-nano system	Cell-seeding compartments Nanochannel array	Two-step photolithography process	Osteocyte-like cells and motor neurons were cultured on the device for 7 days and heated from one side. The concentrations of extracellular ATP and ATP receptor were measured to quantify the response of the cells.	The device measured the signal response of osteocytes and neurons to heat shock.	[97]
Multicompartment neuron-glia coculture platform	Circular soma compartment Satellite axon/glia compartments Microchannels	Micromilling, hot embossing, and soft lithography methods	Dissected primary neuron cells were loaded into the soma compartment. After 14–17 days of culture. When a dense axonal layer inside the axon/glia compartments was formed, oligodendrocyte progenitor cells and astrocytes were loaded on top of the isolated axon layer.	The device facilitated the studying of the central nervous system axonal biology and axon–glia interactions.	[65]

Table 5: Continued.

BioMEMS platform	Main components	Fabrication strategy	Mechanism of operation	Specifics	Ref.
PDMS chip	PDMS chip Microreactor 100 mesoscale open wells Microscale deep channels	Soft lithography method and UV lithography	Cells were cultured in adjacent wells in the microreactor. Cell-cell communication was possible via the interconnecting channels of neighboring wells.	The microstructure system allows both spatially separated cocultivation and specific treatment of cells.	[63]
Unidirectional microfluidic chip	Two culture chambers Two surrounded medium channels	Traditional photolithography and soft lithography	Cells were cultured in separate culture chambers, and their respective secretions traveled through the medium channels to the opposing culture chambers.	The device facilitated the study of communication and conversion between healthy and cancerous cells.	[57]
Two-layer microfluidic device	PDMS layer Two culture channels Two media supply channels Agarose layer	Traditional photolithography, soft lithography, and PDMS replication	Breast cancer cells and human adipose stromal cells were cultured in the inner culture channels while fresh media was supplied by the outer channels. The spacing between the media and the cell channels allowed the delivery of fresh media and cellular crosstalk via passive diffusion.	The delivery of fresh media via a separate channel reduced the risk of the cells' exposure to shear stress.	[58]

ATP: adenosine triphosphate; FPR1: formyl peptide receptor 1; HUVECs: human umbilical vein endothelial cells; PDMS: polydimethylsiloxane.

noninvasive device had an effectiveness of 93.2% without the need for functionalization or cell labeling.

Lui et al. used the electromagnetic properties of cells to identify and count the cells in situ. In this single-cell detection sensor, three electrodes were divided the straight microchannels into two consecutive stage microcoulter. When the cells passed through the microcoulter, each cell generated voltage pulses and by using the magnetic beads, the target-cell was identified. This detection method has shown the potential to be used in drug screening and stem cell population analysis [70]. Ghassemi et al. performed the detection of CTC through impedance spectroscopy. The PDMS-based microfluidic device had two main channels for delivery and constriction. The cell suspension was inserted into the delivery channel and was subsequently sent to the constriction channel to measure the cell's impedance. Finally, this system not only differentiated normal and cancer cells with more than 90% accuracy, but also has potential to identify different types of cancer [71]. Huang et al. developed an in situ single-cell recognition system (ISCRS) in order to extract a single-adhered-cell and perform the analysis of its phosphatidylcholine (PC) compositions through mass spectrometry (MS). This methodology used the U87-MG cells (U87), human hepatoma (HepG2) cells, human epithelial colorectal adenocarcinoma (Caco-2) cells, and human umbilical vein endothelial cells (HUVEC) for the single-cell identification and classification. The single-cell probe, which is the main component for the analytical system, was fabricated from PDMS using standard soft lithography techniques. The ISCRS consisted of four steps: flow injection, observation, operation, and detection system. Once the cell's mass data was collected, the cell identification was done by the application of a linear discriminant analysis (LDA). The device has shown an accuracy rate of 91.8% for cell classification. This methodology has potential for cell identification and auxiliary disease diagnosis [72]. Zhu et al. proved that cells stained with gold nanorods (GNRs) could be detected and stimulated simultaneously due to femtosecond-laser irradiation. While the laser could cause necrosis of apoptosis, the effect could be controlled by adjusting the laser focusing. The ideal exposure duration was found to be around 1 and 2 ms/cell. This PDMS-based microfluidic device showed that photostimulation could be useful for cell detection [73].

8. BioMEMS in Cell Culture

Cell culture is a fundamental step in most cell-related studies. It is a process of growing and monitoring various aspects of cells in a laboratory environment. While traditional 2D cultures performed in petri dish may fail to mimic the microenvironment of cells, the 3D cell culture setups within BioMEMS present carefully controlled conditions, which are similar to those of cells' natural environment [74]. BioMEMSs for cell culture also provide controlled temperature, continuous supply of nutrients, and monitored gas exchange. Various advancements of BioMEMS in 3D cell culture have made significant contributions to the areas of *in vitro* disease modeling, pharmaceutical industries, drug testing, gene expression, drug toxicology, and diagnosis, among others.

As previously mentioned, a precise monitoring of culture conditions is of vital importance which, in turn, initiated development of novel strategies for 3D cell culture. These new developments cover a range of advancements from the shape of the culture chambers [75–77] to the fabrication materials [76, 78]. The temperature, in particular, plays a great role as it should remain homogeneous across the device

Table 6: Recent BioMEMS platforms for cell differentiation and identification including the type of the platform, the main components, the fabrication strategy, the mechanism of operation, and the specifics of each platform.

BioMEMS platform	Main components	Fabrication strategy	Mechanism of operation	Specifics	Ref.
μIFC	Au and Cr electrodes	Conventional soft lithography technique	A current between the external electrodes was generated by an AC signal. In the absence of particles, the output current was zero. In the presence of the particle, however, the positive output voltage increased. When the particle reached the second electrode, the negative output voltage was recorded.	Differentiation was possible even when the cells had similar sizes.	[66]
Pump-free microfluidic platform	PDMS-based microfluidic device Micropillars Valve control	Soft lithography and DRIE	A pump-free perfusion system was used for long-term differentiation. A passive pumping system was implemented to control medium perfusion in a constant flow rate.	The differentiation was achieved within 14 days. The device had a derivation efficiency of 92%.	[67]
Frequency shift-based POC device	FPW sensor Comb-like IDT electrodes	Five photolithographic steps based on photomask-set	Oscillations (23-30 MHz) were introduced to the device and caused the biomolecules to bind to the surface. The attached cells to the surface produced a mass gain.	The device binds only to one type of chemokine and repels others.	[68]
Electrical impedance spectroscopy-based LOC	Silicon wafers and PDMS	Photolithography and anisotropic etching	Impedance measurements were done at 750 kHz and 10 MHz. Since the cells were of different sizes, the detected ΔR_c values depended on the size of cells. Finally, opacity could be used to differentiate cell lines.	This noninvasive device has an effectiveness of 93.2%. The method requires no functionalization or cell labeling.	[69]
Impedance measurement-based microfluidic device	PDMS Microchannels Bypass channels Coplanar electrodes	Soft lithography and lift-off	The first path in this device was a trap while the second path was a bypass channel. When the trap was empty, a cell would be driven into the trap. Once the trap was occupied by a cell, the flow-through path would block. Therefore, the next cell would be driven into the bypass channel and enter the next available trap.	The device could monitor dynamic changes in electrical properties of individual cells over long periods of time.	[91]
Single-cell detection sensor	External magnet Electrodes Microcoulter counter Microfluidic chip	Standard soft lithography	The sensor was able to detect single cells due to their magnetic properties. Three electrodes were used and divided the straight microchannels into two consecutive stage microcoulter. When the cells passed through the microcoulter, each cell generated a voltage pulse and by using the magnetic beads, the target cells were identified.	The device identifies and counts cells *in situ* while measuring the size of each cell individually.	[70]
Impedance-based CTC detector	PDMS Syringe pump Sensors Planar electrodes	Photolithography and lift-off	The "off-chip" device had an embedded pair of planar electrodes. The impedance was obtained in the surrounding of the medium. When the CTC was detected, an impedance peak was obtained. When the "on-chip" device detected a CTC in the constriction channel, a peak was deviated from a constant baseline.	Differentiation was achieved with 90% of success. The system has the potential for detecting different types of cancer.	[71]
ISCRS	PDMS ESI-QTOF-MS Syringe pump	Standard soft lithography	The target cell was captured due to the probe's adjustment.	The accuracy of the classification was 91.8%.	[72]

Table 6: Continued.

BioMEMS platform	Main components	Fabrication strategy	Mechanism of operation	Specifics	Ref.
Photostimulation-based LOC	PDMS Gold nanorods	Standard soft lithography	GNRs were added into the cell buffer, and photostimulation was performed. Subsequently, the solution of suspended cells and oil was injected into the chip, and the cells created a single-cell laminar flow. Lastly, the cells were delivered into a petri dish for culture and analysis.	The necrosis of apoptosis can be controlled by the laser focusing.	[73]

AC: alternating current; R_c: cell's resistance; CTCs: circulating tumor cells; Cr: chromium; CMOS: complementary metal-oxide-semiconductor; DRIE: deep reactive ion etching; ESI-QTOF-MS: electrospray quadrupole time of flight mass spectrometer; FPW: flexural plate-wave; Au: gold; GNR: gold nanorods; IDT: interdigital transducer; ISCRS: *in situ* single-cell recognition system; LOC: Lab-on-a-chip; μIFC: microfluidic-based impedance flow cytometer; PDMS: polydimethyl siloxane; POC: point-of-care.

for optimal growth [79]. It poses a challenge as the system may heat up and cool down faster due to its size. Numerous efforts in temperature surveillance and control techniques have been proposed and explored using microfluidic approaches. These strategies include microheaters [80], temperature sensors, and integrated incubator [81]. Mäki et al. fabricated a device for indirect temperature measurement during cell culture [81]. This PDMS-based device incorporated a proportional-integral (PI) controller and a temperature sensor plate (TSP). The PDMS device was made of two PDMS layers and a glass lid. Six culture chambers were punched on the top PDMS layer and were irreversibly merged with the bottom layer using oxygen plasma treatment. The PI control system implemented sensors to detect the temperature of the cell culture wells and to generate a response from the closed-loop temperature control system. The platform was proven to successfully control the temperature inside and outside the culture system [81].

Nutrient depletion is a common issue in small-sized cell culture platforms. Different approaches have attempted to offer better control over these key elements [82]. In general, mammalian cells require oxygen in order to grow. Therefore, the oxygen consumption rate (OCR) is yet another important parameter to measure and control in such devices [83]. Bunge et al. developed a 3D cell culture platform for long-term cell cultivation and monitoring [82]. The culture chamber was located at the center of the device surrounded by two porous hydrogel walls, which provided a constant supply of nutrients and gases from neighboring channels [82]. A μrespirometer for monitoring OCR was also proposed by the same authors [84]. The device was fabricated using a glass wafer and a silicone piece with DRIYE-etched channels. The Madin-Darby Canine Kidney cells (MDCK) were cultured inside this device, and the oxygen concentration was recorded by the aim of platinum(II)-5,10,15,20-tetrakis-(2,3,4,5,6-pentafluorphenyl)-porphyrin (PtTFPP) fluorescent dye within a PS-matrix. The glass and silicon segments of the device were oxygen-impermeable. With a low drift rate, a long-term measurement of oxygen consumption was, therefore, possible [84].

Additionally, biocompatibility accounts for one of the priorities of cell culture BioMEMS. PDMS is by far the most popular material for soft lithography and fabrication of cell culture devices as it projects great biocompatibility. However, its stability and cell adhesion properties have not been described as optimal. As a replacement, Dabaghi et al. proposed the use of polydopamine (PDA) coating prior to the application of the traditional collagen coat to improve the overall cell attachment and proliferation. Two PDA coating methods were implemented including dynamic and static coating methods. In dynamic coating, the PDA solution passed through the device with a peristaltic pump versus the static coating in which the microfluidic device was filled with the PDA solution. Human bronchial epithelial cells (HBECs) were cultured in devices with both types of coating application and showed no significant differences in cell attachment [85].

Specific cell types are more challenging to culture *in vitro*. Stem cells are recognized to be one of the most difficult types of cells to culture *in vitro* since they tend to differentiate if they are not successfully kept under conditions similar to the *in vivo* environments. One of the solutions to this challenge is the use of microdroplets as culture chambers. Carreras et al. proposed the use of a PMMA-based microfluidic device that generated a double-layered microdroplet bead to culture hematopoietic stem cells (HSCs) from bone marrow. This proposed method showed almost no differentiation, with few exceptions over the culture time, proving that microdroplet-based microfluidic can be a possible alternative for stem cell culture [86].

More recent cell culture approaches include the use of alternative polymer materials such as SJI-001. This alternative offers a lower autofluorescence emission hence suitable for fluorescence-based applications. The authors tested the use of SJI-001 as a component for microfluidic devices and as a potential cell scaffold. The proposed microfluidic device was fabricated using both traditional lithography and soft lithography techniques. The walls of the device were PDMS-based, and the SJI-001 or SU-8 was used for the bottom layers. HeLa cells expressing green fluorescent protein-fused histone H2B (HeLa-H2B-GFP) were cultured in both devices for 9 days, from which the SJI-001-based platform presented better adherence rate and proliferation times than its traditional counterpart [78].

Table 7: Recent BioMEMS platforms for cell culture including the type of the platform, the main components, the fabrication strategy, the mechanism of operation, and the specifics of each platform.

BioMEMS platform	Main components	Fabrication strategy	Mechanism of operation	Specifics	Refs.
Indirect temperature measurement LOC	Heating system Temperature sensor plate PDMS chamber Electrodes	Soft lithography	The PI control system implemented porous sensors to detect the temperature of the cell culture wells and to generate a response from the closed-loop temperature control system.	The platform enables temperature control inside and outside the culture system.	[81]
Microheater chip for cell culture	Microheater Culture chambers Electrical probes	Soft lithography and laser direct-write methods	A precise square voltage pulse was applied to the electrical probes in order to generate a heating response from the thermal stimulator.	The device supports a wide range of temperatures (37-100°C).	[80]
μRespirometer LOC	PS matrix Glass wafer Microsensor film	DRIE, powder blasting, and UV excitation processes	μRespirometer determined the OCR of mammalian cells. The film was integrated into a closed microfluidic chip made of oxygen-impermeable materials.	The integrated device allowed continuous fluorescent measurement over 12 hours.	[84]
Butterfly-shaped microchip	Main channel Test channel Fluid reservoir	Standard photolithography	The main channel width was constant at some places and increased linearly at other regions. The test channels were all positioned at different distances from each other relative to the main channel. The device was used to determine whether there was a distance-dependent interaction between a cell type and a factor.	The device was compatible with different cell types and mixtures.	[98]
Long-term on-chip culture	Five inlets Channels 3D printed holder	Photolithography and wet etching	The culture chamber was located at the center of the device surrounded by two porous hydrogel walls, which provided the nutrients and gases from neighboring channels.	The device required no external equipment and provided no shear stress on the cells.	[82]
LEGO inspired modular microfluidic	Three building blocks	Conventional lithography on a soft lithography mold	The building blocks could be interlocked via tongue and groove connections and by an interference fit vertical connections. To assemble the double-layer blocks, the microwells were attached to their respective tubing, coupled and hollowed to form an O-ring-free sealed microfluidic system.	The device is stiff enough to allow manual coupling of the pieces, and yet, its deformability accommodates the interferences.	[75]
Gelatin-based microfluidic cell culture chip	PMMA PDMS Glass NOA GEL-D gelatin film	Soft lithography	The culture chambers were sealed with their respective GEL-D gelatin film which allowed materials of different natures (PMMA, PDMS, and glass) to be attached to each other and interact with cells.	The chips were found to be resistant to pressure (up to 0.7 MPa) and exposure to organic solvent, as well as temperature (up to 70°C)	[76]
Multilayered-architecture microfluidic array	Pneumatic layers Porous membranes 3D culture layer Fluidic layers	Conventional lithography and soft lithography	The porous membrane allowed the cell interaction with either different drugs individually or simultaneously due to the incorporated top and bottom valves.	The device enables dual drug testing on the same cell culture chamber and is suitable for scaled-up drug testing.	[77]

Table 7: Continued.

BioMEMS platform	Main components	Fabrication strategy	Mechanism of operation	Specifics	Refs.
Closed microfluidic cell culture system	Battery Peristaltic pump Microchannel (PDMS, SJI-001) Reservoir	Conventional lithography and soft lithography	Cells seeded inside the microchannel were cultured for long periods with a controlled flow rate due to the peristatic pump.	SJI-001 was used at the bottom of the microchannel, which improved the overall cell adhesion rate in comparison to the conventional counterpart.	[78]
Microdroplet-based microfluidic system	4 inlets Mixing area Outlet	PMMA laser engraving, drill pressing	Double-layered microdroplets were generated by hydrodynamic focusing, and flows were driven by gravity.	Most cells remained undifferentiated, with slight lymphoid and myeloid exceptions.	[86]
PDMS-PDA treated microfluidic device	Inlet Outlet Microchannel (PDMS, PDA)	Soft lithography and PDA coating	The culture microchannel had a PDA and a collagen coat in order to improve cell attachment. PDA interacts with the amine groups and covalently binds them into the PDMS surface.	The strategy improved cell attachment and stability.	[85]

DRIE: deep reactive ion etching; LOC: Lab-on-a-chip; NOA: Norland optical adhesive; OCR: oxygen consumption rate; PDMS: polydimethyl siloxane; PMMA: poly(methyl methacrylate); PI: proportional-integral; GEL: Reversible gelatin-based; 3D: three-dimensional; PDA: polydopamine.

BioMEMSs are powerful tools that have permitted culturing different cell lines that would otherwise be challenging to culture and analyze by traditional methods due to their specific requirements. Table 7 provides some of the latest advancements of 3D cell culture BioMEMS aimed at controlling the cells' microenvironment for effective culture and monitoring of cells.

9. Limitations of BioMEMS in Cell-Related Studies

While numerous proof-of-concept studies are available for the use of BioMEMS devices in cell-related studies, implementation of these techniques as a widely accepted conventional approach faces serious challenges. Among the general shortcomings of BioMEMS devices, the complexity of operation is a significant obstacle preventing the widespread use of these tools. The high costs of MEMS research facilities create a burden which further limits these devices to reach their full potentials. While these miniaturized devices are compact and portable, they still require external heating, pumping, and tubing equipment to operate. Apart from the general shortcoming of BioMEMS, they fall short when certain aspects of cell studies are concerned.

Cell sorting in BioMEMS often enables higher control and a fine automatization of the process. Nevertheless, there exist certain limitations that could thwart the desired functionality and outcomes of BioMEMS devices. The need for cell labeling could potentially restrict the number of cells or particles that can be sorted by these devices [18]. Some sorting mechanisms rely on DEP which is reported to have low efficiency in cell lysing as often a high voltage is needed to enable DEP [17]. While several complex microfluidic platforms for cell sorting are reported, only a small number of them can be used directly for whole blood, saliva, or other samples. Such systems commonly need external bulky setups, elaborated designs for purification, or manual intermediate purification steps prior to sorting [10].

Cell separation is a fundamental step in the majority of cell-related studies to acquire analytes of interest from a single heterogeneous fluid. Performing cell separation in BioMEMS devices, however, poses certain challenges. One of the drawbacks of size-based cell separation is that the size of the target cells must be known beforehand. This is while the fluid might contain other cells that are in the same size range as the target cells [23]. The purification step that is often needed prior to cell separation involves manual addition of reagents into the device which may lead to errors [87]. Furthermore, the high cost of implementing equipment, the inconsistent isolation efficiency, and the possible degradation of cell viability/functionality in the separation process are reported as constraining factors in this application [88].

Cell isolation and/or trapping is another essential step in cell-related studies. BioMEMS commonly uses passive capturing or hydrodynamic force for cell isolation and/or trapping purposes [32, 35, 38, 89]. These techniques face challenges including selective capturing of cells and further release of the trapped cells. Other category of BioMEMS relies on mechanisms including DEP [30], micropipettes [36], or optical tweezers [46], which can be harmful to the cells and often hard to maintain their dynamic and chemical stimuli while positioning the cells [36, 89].

Pairing methods often require external forces and sophisticated equipment while the undesirable effect of heat in the involving steps of operating a BioMEMS may impact the cells and complicate the long-term studying of pairing [44]. DEP, electric field, and magnetic force are commonly applied to cell pairing devices which may induce potential to damage cells as high field strength encourages disruptions in the cell, leading to unwanted lysis [30, 34, 44]. In specific designs were the cells are initially positioned in wells of opposite sides, applying an electric field may, in fact, trap the cells even

further in their positions and act against pairing [32]. A careful control over the electric field and optimization of electrodes into a planar structure are, therefore, crucial steps in cell pairing [32, 34]. In addition, sequential trapping commonly involves complicated 3D fabrication techniques. Such devices are reported to lack sufficient throughput, and trapping three or more cells can be challenging [46]. Moreover, in some of these designs, the spatial positioning of cells which leads to pairing in a specific order might be very challenging to achieve.

Cell-cell communication is the basis of various diseases including cancer, autoimmune disorders, and diabetes [53]. A careful analysis of communication between cells is, therefore, crucial for understanding the nature of these illnesses. The major limitation of BioMEMS which is aimed at cell-cell communication is the complex microenvironments which they need to reproduce in order to accurately mimic the physiological models [55, 90]. Other challenges involve the simultaneous culture of multiple cell types, parallelization, and automation of the process [55].

Cell differentiation and/or identification BioMEMS typically relies on techniques such as impedance flow cytometry, which has the limitation of identifying cells through nonspecific electrical properties [70]. Impedance-based flow cytometers are also unable to track temporal changes in properties of individual cells [91]. Human stem cell-derived differentiation in a BioMEMS requires hepatocyte culture platform and long-term culture for robust applications [67]. Furthermore, some BioMEMSs apply dynamic bioreactors to differentiate cells which could introduce hydrodynamic shear stress hence decreasing the cell viability [92].

Cell culture is one of the most fundamental protocols performed in BioMEMS for all cell-related studies. However, this basic step also suffers from certain limitations of these devices. Majority of the BioMEMS platforms are made of PDMS through soft lithography fabrication process. PDMS, however, can absorb molecules and interfere with the assay [93]. Moreover, current 3D culture devices have a major limitation of implementing barriers between fluids and cells to eliminate shear stress on the cells due to fluid flow and long-term culture [94]. Perfusion of more than one growth medium which is sometimes required when coculturing multiple cell lines can also pose a great challenge in such devices.

10. Conclusions

BioMEMS enables new possibilities for monitoring, accommodating, and modulating cell units in unprecedented ways alongside with new prospects of development of integrated devices that can automatize and significantly improve the current tools for biological studies. In this review article, the latest developments of BioMEMS platforms for cell-related studies are covered with specific emphasis on cell sorting, cell separation, cell isolation or trapping, cell pairing, cell-cell communication, cell differentiation and identification, and cell culture. For each cell-related application, we review not only the advancement of such devices, but also the main components of the device, the fabrication strategies, and the mechanism of operation, as well as remarks on each platform. This review also summarizes some of the general and specific shortcomings of the BioMEMS platforms in cell-related studies which can further advance the optimization process of these tools.

Conflicts of Interest

The authors declare no conflict of interest.

Authors' Contributions

S.H. proposed the topic and outlines of the review paper. R.G., A.S.C., D.A., S.R., and J.A.G. performed the literature review and wrote the draft. R.G. and A.S.C. wrote the analytical sections and edited the entire draft. S.H. supervised the work and shaped up the manuscript.

Acknowledgments

The authors would also like to acknowledge the financial and technical support of Writing Lab, Institute for the Future of Education, Tecnologico de Monterrey, Mexico.

References

[1] Y. Yanagida, "MEMS/NEMS-based devices for bio-measurements," *Electrochemistry*, vol. 85, no. 9, pp. 572–579, 2017.

[2] S. Saliterman, *Fundamentals of BioMEMS and Medical Microdevices*, Wiley, 2006.

[3] E. W. K. Young and D. J. Beebe, "Fundamentals of microfluidic cell culture in controlled microenvironments," *Chemical Society Reviews*, vol. 39, no. 3, pp. 1036–1048, 2010.

[4] M. J. Tomlinson, S. Tomlinson, X. B. Yang, and J. Kirkham, "Cell separation: terminology and practical considerations," *Journal of Tissue Engineering*, vol. 4, 14 pages, 2013.

[5] S. Hosseini, F. Ibrahim, I. Djordjevic, and L. H. Koole, "Recent advances in surface functionalization techniques on polymethacrylate materials for optical biosensor applications," *Analyst*, vol. 139, no. 12, pp. 2933–2943, 2014.

[6] C. Wyatt Shields IV, C. D. Reyes, and G. P. López, "Microfluidic cell sorting: a review of the advances in the separation of cells from debulking to rare cell isolation," *Lab on a Chip*, vol. 15, no. 5, pp. 1230–1249, 2015.

[7] M. E. Piyasena and S. W. Graves, "The intersection of flow cytometry with microfluidics and microfabrication," *Lab on a Chip*, vol. 14, no. 6, pp. 1044–1059, 2014.

[8] J. El-Ali, P. K. Sorger, and K. F. Jensen, "Cells on chips," *Nature*, vol. 442, no. 7101, pp. 403–411, 2006.

[9] L. Lin, Q. Chen, and J. Sun, "Micro/nanofluidics-enabled single-cell biochemical analysis," *TrAC Trends in Analytical Chemistry*, vol. 99, pp. 66–74, 2018.

[10] Z. T. F. Yu, J. G. Joseph, S. X. Liu et al., "Centrifugal microfluidics for sorting immune cells from whole blood," *Sensors and Actuators B: Chemical*, vol. 245, pp. 1050–1061, 2017.

[11] X. Ding and T. J. Huang, "Microfluidic manipulation and sorting of particles using tunable standing surface acoustic wave," Google Patents, March 2017.

[12] R. Garcia-Ramirez and S. Hosseini, "History of Biomicroelectromechanical Systems (BioMEMS)," in *BioMEMS*, Springer, Singapore, 2021.

[13] M. C. Jo and R. Guldiken, "Effects of polydimethylsiloxane (PDMS) microchannels on surface acoustic wave- based microfluidic devices," *Microelectronic Engineering*, vol. 113, pp. 98–104, 2014.

[14] W. Gao, B. E.-F. de Ávila, L. Zhang, and J. Wang, "Targeting and isolation of cancer cells using micro/nanomotors," *Advanced Drug Delivery Reviews*, vol. 125, pp. 94–101, 2018.

[15] Y. Song, H. Yin, and W. E. Huang, "Raman activated cell sorting," *Current Opinion in Chemical Biology*, vol. 33, pp. 1–8, 2016.

[16] K. S. Lee, M. Palatinszky, F. C. Pereira et al., "An automated Raman-based platform for the sorting of live cells by functional properties," *Nature Microbiology*, vol. 4, no. 6, pp. 1035–1048, 2019.

[17] Y. Yildizhan, N. Erdem, M. Islam, R. Martinez-Duarte, and M. Elitas, "Dielectrophoretic separation of live and dead monocytes using 3D carbon-electrodes," *Sensors*, vol. 17, no. 11, p. 2691, 2017.

[18] S. Hung, C. H. Hsu, and C. Chen, "Cell sorting in microfluidic systems using dielectrophoresis," in *IEEE 15th International Conference on Nanotechnology (IEEE-NANO)*, pp. 872–875, Rome, Italy, 2015.

[19] X. Nie, Y. Luo, P. Shen, C. Han, D. Yu, and X. Xing, "High-throughput dielectrophoretic cell sorting assisted by cell sliding on scalable electrode tracks made of conducting-PDMS," *Sensors and Actuators B: Chemical*, vol. 327, article 128873, 2021.

[20] I. I. Hosseini, M. Moghimi Zand, A. A. Ebadi, and M. Fathipour, "Cell properties assessment using optimized dielectrophoresis-based cell stretching and lumped mechanical modeling," *Scientific Reports*, vol. 11, no. 1, p. 2341, 2021.

[21] S. Barkam, S. Saraf, and S. Seal, "Fabricated micro-nano devices for in vivo and in vitro biomedical applications," *Wiley Interdisciplinary Reviews: Nanomedicine and Nanobiotechnology*, vol. 5, no. 6, pp. 544–568, 2013.

[22] T. M. Geislinger and T. Franke, "Sorting of circulating tumor cells (MV3-melanoma) and red blood cells using non-inertial lift," *Biomicrofluidics*, vol. 7, no. 4, p. 044120, 2013.

[23] G. E. Hvichia, Z. Parveen, C. Wagner et al., "A novel microfluidic platform for size and deformability based separation and the subsequent molecular characterization of viable circulating tumor cells," *International Journal of Cancer*, vol. 138, no. 12, pp. 2894–2904, 2016.

[24] A. Salmanzadeh, "Isolation of rare cells through their dielectrophoretic signature," *Journal of Membrane Science & Technology*, vol. 3, no. 1, pp. 1–4, 2013.

[25] H. Song, J. M. Rosano, Y. Wang et al., "Continuous-flow sorting of stem cells and differentiation products based on dielectrophoresis," *Lab on a Chip*, vol. 15, no. 5, pp. 1320–1328, 2015.

[26] Z. Zhu, D. Wu, S. Li et al., "A polymer-film inertial microfluidic sorter fabricated by jigsaw puzzle method for precise size-based cell separation," *Analytica Chimica Acta*, vol. 1143, pp. 306–314, 2021.

[27] S. Razavi Bazaz, O. Rouhi, M. A. Raoufi et al., "3D printing of inertial microfluidic devices," *Scientific Reports*, vol. 10, no. 5929, pp. 1–14, 2020.

[28] S. Zhao, M. Wu, S. Yang et al., "A disposable acoustofluidic chip for nano/microparticle separation using unidirectional acoustic transducers," *Lab on a Chip*, vol. 20, no. 7, pp. 1298–1308, 2020.

[29] C. Yousuff, E. Ho, K. Ismail Hussain, and N. Hamid, "Microfluidic platform for cell isolation and manipulation based on cell properties," *Micromachines*, vol. 8, no. 1, p. 15, 2017.

[30] M. Punjiya, H. R. Nejad, J. Mathews, M. Levin, and S. Sonkusale, "A flow through device for simultaneous dielectrophoretic cell trapping and AC electroporation," *Scientific Reports*, vol. 9, no. 1, p. 11988, 2019.

[31] W. Espulgar, Y. Yamaguchi, W. Aoki et al., "Single cell trapping and cell-cell interaction monitoring of cardiomyocytes in a designed microfluidic chip," *Sensors and Actuators B: Chemical*, vol. 207, no. Part A, pp. 43–50, 2015.

[32] C. Wu, R. Chen, Y. Liu, Z. Yu, Y. Jiang, and X. Cheng, "A planar dielectrophoresis-based chip for high-throughput cell pairing," *Lab on a Chip*, vol. 17, no. 23, pp. 4008–4014, 2017.

[33] X. Guo and R. Zhu, "Controllably moving individual living cell in an array by modulating signal phase difference based on dielectrophoresis," *Biosensors & Bioelectronics*, vol. 68, pp. 529–535, 2015.

[34] L. Huang, P. Zhao, S. Bian et al., "A novel bioMEMS device for efficient on-chip single cell loading and 3D rotation," in *2017 IEEE 30th International Conference on Micro Electro Mechanical Systems (MEMS)*, pp. 490–493, Las Vegas, NV, USA, January 2017.

[35] L. Lin, Y. S. Chu, J. P. Thiery, C. T. Lim, and I. Rodriguez, "Microfluidic cell trap array for controlled positioning of single cells on adhesive micropatterns," *Lab on a Chip*, vol. 13, no. 4, pp. 714–721, 2013.

[36] S. S. Bithi and S. A. Vanapalli, "Microfluidic cell isolation technology for drug testing of single tumor cells and their clusters," *Scientific Reports*, vol. 7, no. 1, article 41707, 2017.

[37] Z. H. Fan, J. I. Varillas, J. Zhang, K. Chen, and T. J. George, "Tumor cell isolation in microfluidic devices for cancer treatment monitoring," in *2017 IEEE 30th International Conference on Micro Electro Mechanical Systems (MEMS)*, pp. 1264–1267, Las Vegas, NV, January 2017.

[38] C. L. Hisey, O. Mitxelena-Iribarren, M. Martínez-Calderón et al., "A versatile cancer cell trapping and 1D migration assay in a microfluidic device," *Biomicrofluidics*, vol. 13, no. 4, article 044105, 2019.

[39] Y. Huang, N. T. Nguyen, K. S. Lok et al., "Multiarray cell stretching platform for high-magnification real-time imaging," *Nanomedicine*, vol. 8, no. 4, pp. 543–553, 2013.

[40] Y. Y. Chiang, Y. C. Teng, Z. Y. Su, H. Y. Hsueh, and K. H. Tu, "Hydrodynamic Snaring Array for Trapping and Perfusion Culture of Single Cell," *Sensors and Actuators B: Chemical*, vol. 312, article 127966, 2020.

[41] L. Romita, S. Thompson, and D. K. Hwang, "Rapid fabrication of sieved microwells and cross-flow microparticle trapping," *Scientific Reports*, vol. 10, no. 1, p. 15687, 2020.

[42] R. Luo, S. Pashapour, O. Staufer, I. Platzman, and J. P. Spatz, "Polymer-based porous microcapsules as bacterial traps," *Advanced Functional Materials*, vol. 30, no. 17, article 1908855, 2020.

[43] A. M. Skelley, O. Kirak, H. Suh, R. Jaenisch, and J. Voldman, "Microfluidic control of cell pairing and fusion," *Nature Methods*, vol. 6, no. 2, pp. 147–152, 2009.

[44] L. Li, H. Wang, L. Huang, S. A. Michael, W. Huang, and H. Wu, "A controllable, centrifugal-based hydrodynamic microfluidic chip for cell-pairing and studying long-term communications between single cells," *Analytical Chemistry*, vol. 91, no. 24, pp. 15908–15914, 2019.

[45] J. Zhu, Y. Wang, P. Chen, H. Su, W. Du, and B. F. Liu, "Highly efficient microfluidic device for cell trapping and pairing towards cell-cell communication analysis," *Sensors and Actuators B: Chemical*, vol. 283, pp. 685–692, 2019.

[46] Y. Abe, K. Kamiya, T. Osaki, R. Kawano, N. Miki, and S. Takeuchi, "Mechanical cell pairing system by sliding parylene rails," in *2014 IEEE 27th International Conference on Micro Electro Mechanical Systems (MEMS)*, pp. 185–187, San Francisco, CA, USA, January 2014.

[47] B. Dura, Y. Liu, and J. Voldman, "Deformability-based microfluidic cell pairing and fusion," *Lab on a Chip*, vol. 14, no. 15, pp. 2783–2790, 2014.

[48] H. Hu, D. Eustace, and C. A. Merten, "Efficient cell pairing in droplets using dual-color sorting," *Lab on a Chip*, vol. 15, no. 20, pp. 3989–3993, 2015.

[49] H. Zhang, A. R. Guzman, J. A. Wippold et al., "An ultra high-efficiency droplet microfluidics platform using automatically synchronized droplet pairing and merging," *Lab on a Chip*, vol. 20, no. 21, pp. 3948–3959, 2020.

[50] W. He, L. Huang, Y. Feng, F. Liang, W. Ding, and W. Wang, "Highly integrated microfluidic device for cell pairing, fusion and culture," *Biomicrofluidics*, vol. 13, no. 5, article 054109, 2019.

[51] H. Babahosseini, T. Misteli, and D. L. Devoe, "Microfluidic on-demand droplet generation, storage, retrieval, and merging for single-cell pairing," *Lab on a Chip*, vol. 19, no. 3, pp. 493–502, 2019.

[52] Y. Zhou, N. Shao, R. Bessa de Castro et al., "Evaluation of single-cell cytokine secretion and cell-cell interactions with a hierarchical loading microwell chip," *Cell Reports*, vol. 31, no. 4, article 107574, 2020.

[53] T. Pawson, "Protein modules and signalling networks," *Nature*, vol. 373, no. 6515, pp. 573–580, 1995.

[54] F. Guo, J. B. French, P. Li et al., "Probing cell-cell communication with microfluidic devices," *Lab on a Chip*, vol. 13, no. 16, pp. 3152–3162, 2013.

[55] M. Rothbauer, H. Zirath, and P. Ertl, "Recent advances in microfluidic technologies for cell-to-cell interaction studies," *Lab on a Chip*, vol. 18, no. 2, pp. 249–270, 2018.

[56] H. Ma, T. Liu, J. Qin, and B. Lin, "Characterization of the interaction between fibroblasts and tumor cells on a microfluidic co-culture device," *Electrophoresis*, vol. 31, no. 10, pp. 1599–1605, 2010.

[57] G. Fang, H. Lu, H. Aboulkheyr Es et al., "Unidirectional intercellular communication on a microfluidic chip," *Biosensors & Bioelectronics*, vol. 175, article 112833, 2021.

[58] S. M. Rahman, J. M. Campbell, R. N. Coates et al., "Evaluation of intercellular communication between breast cancer cells and adipose-derived stem cellsviapassive diffusion in a two-layer microfluidic device," *Lab on a Chip*, vol. 20, no. 11, pp. 2009–2019, 2020.

[59] L. Businaro, G. Schiavoni, V. Lucarini et al., "Cross talk between cancer and immune cells: exploring complex dynamics in a microfluidic environment," *Lab on a Chip*, vol. 13, no. 2, pp. 229–239, 2013.

[60] P. Liu, Y. W. Cao, S. D. Zhang et al., "A bladder cancer microenvironment simulation system based on a microfluidic co-culture model," *Oncotarget*, vol. 6, no. 35, pp. 37695–37705, 2015.

[61] A. D. Blackwell, M. A. Tamayo, B. Beheim et al., "Helminth infection, fecundity, and age of first pregnancy in women," *Science*, vol. 350, no. 6263, pp. 970–972, 2015.

[62] A. Taylor, D. Dieterich, H. Ito, S. Kim, and E. M. Schuman, "Microfluidic local perfusion chambers for the visualization and manipulation of synapses," *Neuron*, vol. 66, no. 1, pp. 57–68, 2010.

[63] A. Schneider, T. Scharnweber, D. Cammann, B. Rapp, S. Giselbrecht, and C. M. Niemeyer, "Multiscale microstructure for investigation of cell–cell communication," *Small Methods*, vol. 4, no. 12, article 2000647, 2020.

[64] H. Higashimori and Y. Yang, "Imaging analysis of neuron to glia interaction in microfluidic culture platform (MCP)-based neuronal axon and glia co-culture system," *JoVE*, vol. 68, article e4448, 2012.

[65] J. Park, H. Koito, J. Li, and A. Han, "Multi-compartment neuron–glia co-culture platform for localized CNS axon–glia interaction study," *Lab on a Chip*, vol. 12, no. 18, pp. 3296–3304, 2012.

[66] I. Bilican, M. T. Guler, M. Serhatlioglu, T. Kirindi, and C. Elbuken, "Focusing-free impedimetric differentiation of red blood cells and leukemia cells: a system optimization," *Sensors and Actuators B: Chemical*, vol. 307, article 127531, 2020.

[67] L. J. Y. Ong, L. Jin, P. K. Singh et al., "A pump-free microfluidic 3D perfusion platform for the efficient differentiation of human hepatocyte-like cells," *Biotechnology and Bioengineering*, vol. 114, no. 10, pp. 2360–2370, 2017.

[68] A. Jupe, S. Kahnert, M. Figge et al., "Development of a piezoelectric flexural plate-wave (FPW) biomems-sensor for rapid point-of-care diagnostics," *NATO Science for Peace and Security Series A: Chemistry and Biology*, pp. 199–212, 2018.

[69] R. W. R. L. Gajasinghe, O. Tigli, M. Jones, and T. Ince, "Label-free tumor cell detection and differentiation based on electrical impedance spectroscopy," in *2016 IEEE SENSORS*, pp. 3–5, Orlando, FL, USA, 2017.

[70] F. Liu, K. C. Pawan, G. Zhang, and J. Zhe, "A microfluidic sensor for single cell detection in a continuous flow," in *2017 19th International Conference on Solid-State Sensors, Actuators and Microsystems (TRANSDUCERS)*, pp. 194–197, Kaohsiung, Taiwan, Jul. 2017.

[71] P. Ghassemi, X. Ren, B. M. Foster, B. A. Kerr, and M. Agah, "Post-enrichment circulating tumor cell detection and enumeration via deformability impedance cytometry," *Biosensors & Bioelectronics*, vol. 150, article 111868, 2020.

[72] Q. Huang, S. Mao, M. Khan, W. Li, Q. Zhang, and J. M. Lin, "Single-cell identification by microfluidic-based: in situ extracting and online mass spectrometric analysis of phospholipids expression," *Chemical Science*, vol. 11, no. 1, pp. 253–256, 2020.

[73] Y. Zhu, H. Xu, X. Wei, and H. He, "Single-cell detection and photostimulation on a microfluidic chip aided with gold nanorods," *Cytometry Part A*, vol. 97, no. 1, pp. 39–45, 2020.

[74] P. B. Gahan, "Molecular biology of the cell (4th edn) B. Alberts, A. Johnson, J. Lewis, K. Roberts and P. Walter (eds), Garland Science, 1463 pp., ISBN 0-8153-4072-9 (paperback) (2002)," *Cell Biochemistry and Function*, vol. 23, no. 2, pp. 150–150, 2005.

[75] X. Xie, S. Maharjan, S. Liu, Y. Zhang, and C. Livermore, "A modular, reconfigurable microfabricated assembly platform for microfluidic transport and multitype cell culture and drug Testing," *Micromachines*, vol. 11, no. 1, p. 2, 2020.

[76] G. Pitingolo, A. Riaud, C. Nastruzzi, and V. Taly, "Tunable and reversible gelatin-based bonding for microfluidic cell culture,"

Advanced Engineering Materials, vol. 21, no. 8, p. 1900145, 2019.

[77] H. C. Chang, C. H. Lin, D. Juang et al., "Multilayer architecture microfluidic network array for combinatorial drug testing on 3D-cultured cells," *Biofabrication*, vol. 11, no. 3, article 035024, 2019.

[78] H. Ueno, K. Maruo, M. Inoue, H. Kotera, and T. Suzuki, "Cell culture on low-fluorescence and high-resolution photoresist," *Micromachines*, vol. 11, no. 6, p. 571, 2020.

[79] J. E. Swain, "Decisions for the IVF laboratory: comparative analysis of embryo culture incubators," *Reproductive Biomedicine Online*, vol. 28, no. 5, pp. 535–547, 2014.

[80] D. Nieto, P. McGlynn, M. de la Fuente, R. Lopez-Lopez, and G. M. O'connor, "Laser microfabrication of a microheater chip for cell culture outside a cell incubator," *Colloids and Surfaces. B, Biointerfaces*, vol. 154, pp. 263–269, 2017.

[81] A.-J. Maki, T. Ryynanen, J. Verho, J. Kreutzer, J. Lekkala, and P. J. Kallio, "Indirect temperature measurement and control method for cell culture devices," *IEEE Transactions on Automation Science and Engineering*, vol. 15, no. 2, pp. 420–429, 2018.

[82] F. Bunge, S. van den Driesche, and M. J. Vellekoop, "Microfluidic platform for the long-term on-chip cultivation of mammalian cells for Lab-on-a-Chip applications," *Sensors*, vol. 17, no. 7, pp. 1603–1615, 2017.

[83] R. D. Guarino, L. E. Dike, T. A. Haq, J. A. Rowley, J. B. Pitner, and M. R. Timmins, "Method for determining oxygen consumption rates of static cultures from microplate measurements of pericellular dissolved oxygen concentration," *Biotechnology and Bioengineering*, vol. 86, no. 7, pp. 775–787, 2004.

[84] F. Bunge, S. van den Driesche, A. Waite, U. Mirastschijski, and M. J. Vellekoop, "μRespirometer to determine the oxygen consumption rate of mammalian cells in a microfluidic cell culture," in *2017 IEEE 30th International Conference on Micro Electro Mechanical Systems (MEMS)*, pp. 414–417, Las Vegas, NV, 2017.

[85] M. Dabaghi, S. Shahriari, N. Saraei et al., "Surface modification of PDMS-based microfluidic devices with collagen using polydopamine as a spacer to enhance primary human bronchial epithelial cell adhesion," *Micromachines*, vol. 12, no. 2, p. 132, 2021.

[86] P. Carreras, I. González, M. Gallardo et al., "Long-term human hematopoietic stem cell culture in microdroplets," *Micromachines*, vol. 12, no. 1, p. 90, 2021.

[87] R. Tang, H. Yang, J. R. Choi et al., "Paper-based device with on-chip reagent storage for rapid extraction of DNA from biological samples," *Microchimica Acta*, vol. 184, no. 7, pp. 2141–2150, 2017.

[88] B. K. Lin, S. M. McFaul, C. Jin, P. C. Black, and H. Ma, "Highly selective biomechanical separation of cancer cells from leukocytes using microfluidic ratchets and hydrodynamic concentrator," *Biomicrofluidics*, vol. 7, no. 3, article 034114, 2013.

[89] Y. Wang, J. Zhu, P. Chen et al., "A microfluidic platform with pneumatically switchable single-cell traps for selective intracellular signals probing," *Talanta*, vol. 192, pp. 431–438, 2019.

[90] B. M. Baker and C. S. Chen, "Deconstructing the third dimension – how 3D culture microenvironments alter cellular cues," *Journal of Cell Science*, vol. 125, no. 13, pp. 3015–3024, 2012.

[91] Y. Zhou, S. Basu, E. Laue, and A. A. Seshia, "Single cell studies of mouse embryonic stem cell (mESC) differentiation by electrical impedance measurements in a microfluidic device," *Biosensors & Bioelectronics*, vol. 81, pp. 249–258, 2016.

[92] C. Mckee and G. R. Chaudhry, "Advances and challenges in stem cell culture," *Colloids and Surfaces. B, Biointerfaces*, vol. 159, pp. 62–77, 2017.

[93] K. P. Valente, S. Khetani, A. R. Kolahchi, A. Sanati-nezhad, A. Suleman, and M. Akbari, "Microfluidic technologies for anticancer drug studies," *Drug Discovery Today*, vol. 22, no. 11, pp. 1654–1670, 2017.

[94] A. J. Bastiaens, J. Frimat, T. Van Nunen, and B. Schurink, "Advancing a MEMS-based 3D cell culture system for in vitro Neuro-Electrophysiological recordings," *Frontiers in Mechanical Engineering*, vol. 4, pp. 1–10, 2018.

[95] M. Li, H. E. Muñoz, K. Goda, and D. Di Carlo, "Shape-based separation of microalga _Euglena gracilis_ using inertial microfluidics," *Scientific Reports*, vol. 7, no. 1, article 10802, 2017.

[96] X. Lu and X. Xuan, "Continuous microfluidic particle separation via elasto-inertial pinched flow fractionation," *Analytical Chemistry*, vol. 87, no. 12, pp. 6389–6396, 2015.

[97] S. McCutcheon, R. Majeska, M. Schaffler, and M. Vazquez, "A multiscale fluidic device for the study of dendrite-mediated cell to cell communication," *Biomedical Microdevices*, vol. 19, no. 3, p. 71, 2017.

[98] E. Yildiz-Ozturk, S. Gulce-Iz, M. Anil, and O. Yesil-Celiktas, "Cytotoxic responses of carnosic acid and doxorubicin on breast cancer cells in butterfly-shaped microchips in comparison to 2D and 3D culture," *Cytotechnology*, vol. 69, no. 2, pp. 337–347, 2017.

Hindawi
Advances in Polymer Technology
Volume 2021, Article ID 8815006, 23 pages
https://doi.org/10.1155/2021/8815006

Review Article

Supramolecular Biopolymers for Tissue Engineering

Rosario Pérez-Pedroza,[1] **Alan Ávila-Ramírez**,[1] **Zainab Khan**,[2] **Manola Moretti**,[1] **and Charlotte A. E. Hauser**[1]

[1]*Laboratory for Nanomedicine, Division of Biological & Environmental Science & Engineering (BESE), King Abdullah University of Science and Technology (KAUST), Thuwal 23955-6900, Saudi Arabia*
[2]*Beacon Development, King Abdullah University of Science and Technology (KAUST), Thuwal 23955-6900, Saudi Arabia*

Correspondence should be addressed to Charlotte A. E. Hauser; charlotte.hauser@kaust.edu.sa

Received 16 September 2020; Revised 11 December 2020; Accepted 27 December 2020; Published 13 January 2021

Academic Editor: Grissel T. De Santiago

Supramolecular biopolymers (SBPs) are those polymeric units derived from macromolecules that can assemble with each other by noncovalent interactions. Macromolecular structures are commonly found in living systems such as proteins, DNA/RNA, and polysaccharides. Bioorganic chemistry allows the generation of sequence-specific supramolecular units like SBPs that can be tailored for novel applications in tissue engineering (TE). SBPs hold advantages over other conventional polymers previously used for TE; these materials can be easily functionalized; they are self-healing, biodegradable, stimuli-responsive, and nonimmunogenic. These characteristics are vital for the further development of current trends in TE, such as the use of pluripotent cells for organoid generation, cell-free scaffolds for tissue regeneration, patient-derived organ models, and controlled delivery systems of small molecules. In this review, we will analyse the 3 subtypes of SBPs: peptide-, nucleic acid-, and oligosaccharide-derived. Then, we will discuss the role that SBPs will be playing in TE as dynamic scaffolds, therapeutic scaffolds, and bioinks. Finally, we will describe possible outlooks of SBPs for TE.

1. Introduction

Supramolecular biopolymers (SBPs) are polymeric units derived from macromolecules that can assemble with each other by noncovalent interactions. Independent units of an SBP interact with each other to create vast structural arrays [1–3]. In fact, it is common to find supramolecular assemblies within biological systems because macromolecules intrinsically interact among each other by noncovalent bonding. Thanks to the advancement of bioorganic chemistry [4–6], researchers have been able to synthesize short strands of sequence-specific SBPs. By doing so, they can regulate the governing noncovalent forces by tuning the monomers' sequence. These changes also affect the topological features of the SBP. In other words, if the sequence changes, the weak interactions will change the microstructure and accordingly the macrostructure [1, 7, 8]. Furthermore, as sequences change, specific motifs or active sites may become available for the interaction between the material and its environment. Hence, SBPs have the potential to embody tailored materials for different applications, such as scaffolds for tissue engineering (TE).

TE and regenerative medicine are multidisciplinary fields that target the development and generation of functional tissues and organs, therapies, and technologies to renew damaged tissues. TE relies on the encapsulation and culture of cells in a scaffold that can sustain its growth to recreate the microenvironment commonly found in a tissue of interest. TE holds a grand promise for research and clinical applications. It could allow the advancement of patient-specific personalized therapies, sophisticated tissue generation, miniaturization of functional organs, accelerated therapeutic evaluation, and even reduced animal use [9]. Currently, the state-of-the-art of TE is switching from simple *in vitro* replicas of tissue sections to structurally and biologically complex models of whole organs [10–12]. Researchers are also

developing dynamic and cell-free scaffolds for regeneration [13–15], patient-derived organ models [16], and more elegant molecular delivery systems [17, 18].

SBPs have a variety of advantages when used in TE. First, their sequence is tunable when synthesized by solid-phase synthesis. Several experts have already identified interactive motifs for assembly [19–22]. Tailoring SBPs is not only limited to the polymeric unit and the structure *per se* but also includes any bioactive motifs that could be incorporated within the same unit or structure, creating multifunctional materials [23]. Furthermore, some SBPs are thermodynamically reversible, which allows them to constantly heal and reshape their structure at the nanoscale [24–26]. Hence, SBPs also allow the incorporation of controlled chemical and physical degradation mechanisms within the materials. All these characteristics allow researchers to tailor SBPs into stimuli-responsive materials, also known as smart materials [27, 28]. Finally, SBPs can combine all these smart properties into conventional materials. In summary, SBPs are easily functionalized to induce specific cell responses. Furthermore, as shown in Figure 1, the specific sequence of each monomer defines the noncovalent interaction for assembly, as well as its specific nano- and microstructure. These scaffolds can be further implemented as bioinks, drug delivery systems, and dynamic or therapeutic scaffolds.

It is important to note that the use of synthetic polymers and biopolymers was pivotal to kick-start the development of TE. Conventional polymers allowed to generate three-dimensional (3D) models that resembled natural tissue conformations, concluding that two-dimensional cell cultures are unable to recapitulate the characteristics of most tissues [29–31]. This is because conventional polymeric scaffolds support cellular seeding, proliferation, migration, and differentiation in a 3D geometry. Also, these materials allow gas and mass transport, water retention, physical support, and physical cell aligning [32, 33]. However, conventional polymers present a variety of disadvantages to novel technologies such as the use of organoids [34, 35], whole-organ engineering [36, 37], patient-specific tissue regeneration [38], and *in situ* therapeutics [39]. Specifically, conventional polymers are rarely stimuli-responsive, do not self-heal, do not degrade in a controlled manner, and are expected to trigger unwanted immune responses, unless thoroughly functionalized. Moreover, conventional polymers due to their lack of resemblance to biological molecules are not equipped with the benefits that SBPs have. Conventional polymers commonly rely on the scaffold enrichment with specific molecules, responsive moieties, or chemical functionalization by surface chemistry [40, 41]. With either approach, signals or functional moieties could have nonspecific and uncontrolled localization and delivery, requiring extra steps for the functionalization or enrichment of the polymer [42, 43]. Furthermore, a majority of the conventional polymers fails to remodel and heal themselves continuously in tune with complex cellular structures, unless coupled with self-healing systems or moieties [44, 45]. This issue becomes important when pluripotent cells are used in TE for differentiation and self-organization into multiple cell types in order to resemble the natural tissue. Different from biopolymers, conventional polymers fail to constantly remodel their nanostructure to be adapted to the growth and self-organizing of these cellular constructs [46, 47]. Similarly, the scaffolds are expected to have a controlled degradation that slowly allows cells to exchange the matrix scaffold to their own extracellular scaffold materials [48, 49]. Degradation of conventional polymers has variable kinetics, proportional to the water diffusion coefficient, rate of hydrolysis, and the thickness of the construct. All these parameters are difficult to control in order to match the degradation rate and the ECM reconstruction rate of the cells.

The concept of "supramolecular units" was coined in the 1960s by Nobel Laureate Albert Szent-Gyorgyi [50], 40 years after Hermann Staudinger's definition of a polymer [51]. Szent-Gyorgyi described the assembly of protein structures as the covalently bonded molecular bricks with "submolecular" characteristics that are interacting with each other to form supramolecular units. As mentioned previously, the interactions that define the assembly of supramolecular units are the "cooperation of hydrogen bonding and hydrophobic bonding" [52] among proteins and nucleic acids. Interestingly, in 1963, Merrifield developed the method of solid-phase peptide synthesis (SPPS), which simplified the synthesis of sequence-specific polypeptides [53–56]. Since then, similar efforts to ease the synthesis of other sequence-specific biopolymers were consequently proposed [57–59]. All these discoveries and developments allowed the synthesis of sequence-specific polypeptides, nucleic acid chains, and polysaccharides at high-purity rates, which eventually provided the versatility to use these molecules as self-assembling materials with interesting properties at the nanoscale. Currently, there is enough evidence that SBPs can be used, together with other tools, as advanced biomaterials for TE, as shown in Figure 2.

The forces driving SBPs' assembly involve several noncovalent interactions that act cooperatively. The strength and participation of each vary depending on the specific sequence of the SBPs [69, 70]. Nucleic acid-derived materials hold the simplest assembling mechanics among other SBPs, as the units interact initially by base pairing held by H-bonds. Canonical Watson-Crick base pairing and noncanonical base pairing (Hoogsteen and wobble base pairs, commonly found in RNA molecules) occur thanks to hydrogen- (H-) bonds formed among bases. All these interactions are based on the principle of complementarity [71]. However, it is widely accepted that nucleic-acid-derived SBPs can be further stabilized by π-π stacking through the aromatic structures of the nucleobases in the same backbone [72, 73]. In fact, it is the π-π interactions that stabilize the DNA structures towards the typical double-helical structure. On the other hand, RNA molecules will be mainly stabilized by the tertiary structures facilitated by the H-bonding between the bases [74].

Peptide-derived materials have a higher degree of complexity than nucleic-acid-derived materials due to the characteristics of their amino acids' side-chain residues [75–78]. One of the important parameters used to design amphiphilic peptides is the existence of a gradient of polarity [76, 79, 80]. Nonpolar residues aggregate with each other due to hydrophobic interactions, while still maintaining solubility due to the presence of polar residues. As hydrophobic interactions

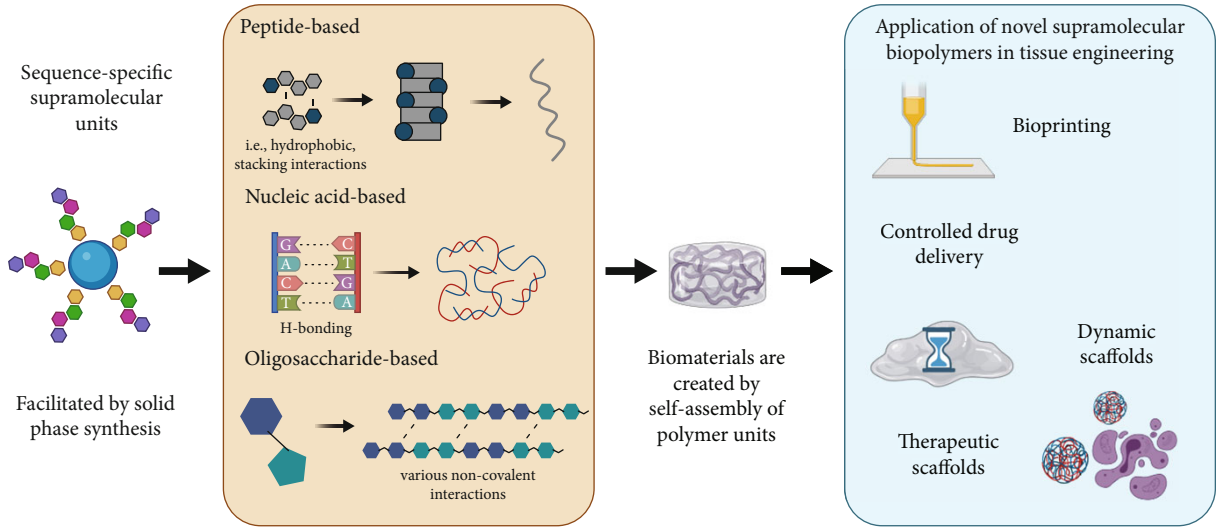

Figure 1: The technology of solid-phase synthesis eased the generation of sequence-specific units for supramolecular assemblies. These sequence-specific units interact with each other by varied noncovalent interactions, which leads to the assembly of nano- and microscopic structures that develop into macroscale sized biomaterials, such as hydrogels. These supramolecular assemblies can be used as novel biopolymers for tissue engineering, as their properties allow them to be used as bioinks, as carrier for controlled drug delivery, and as dynamic and therapeutic scaffolds.

spontaneously arise from entropy-driven changes, the use of charged and polar residues induces additional ionic interactions and H-bonding, whereas amide-π and CH-π interactions can further contribute to noncovalent interactions [81]. The velocity in which the one or other system is reached will define the characteristics of the self-assembling peptide. Generally speaking, most peptides have a cooperative and enthalpy-driven H-bonding that induces hydrophobic aggregation, plus complementary interactions that will aid on the control of hydrophobicity rates [82]. Interestingly, the assembly of peptides tends to follow a nucleation pattern. Once the energy barrier for aggregation is broken, the microstructure will assemble around already aggregated dimers.

Oligosaccharide-derived peptides have the most complex set of noncovalent interactions. Some researchers report on self-assembly mechanisms similar to those of the polymeric version of the oligosaccharide, such as ionic bonds in o-acetylated alginate [83]. However, some other SBPs include oligosaccharides modified to include an aliphatic section in the molecule. The resultant amphiphilic molecules assemble by hydrophobic interactions, like peptide-based SBPs. One of the most recognized supramolecular oligosaccharide is the family of cyclodextrins, which interact by the so-called host-guest interactions. These interactions are based on the existence of a lipophilic cavity and a hydrophilic exterior that allows for the capture of hydrophobic molecules in the inside of a donut-shaped structure [84, 85].

In this review, we want to discuss the three types of SBPs used for TE: peptide-, nucleic acid-, and oligosaccharide-derived polymers. We will point to a variety of interesting approaches that have been generated for the development of novel materials with potential applications in TE. In addition, we elaborate on the challenges in TE that could be overcome with these materials. How are these materials currently being used as dynamic and therapeutic scaffolds. Finally, we will talk about the potential of these materials in bioprinting, and we will give an outlook about the field. It is important to note that besides supramolecular biopolymers, supramolecular assemblies can also rely on organic or inorganic moieties. However, given that this field is very broad, our focus will be on the specific concepts surrounding supramolecular biopolymers (SBPs).

2. Applications

2.1. Peptide-Derived Polymers. Noncovalent interactions such as hydrophobic effects, electrostatic interactions, and π-π stacking influence peptide assembly [82]. These weak bonds affect the interactions among residues, which eventually define the formation of stable three-dimensional structures similarly as during the folding of proteins. Specific peptide compounds with a characteristic and defined sequence and short enough to make folding difficult or impossible are able to self-assemble with each other; these compounds are known as self-assembling peptides (SAP) and have been thoroughly studied for almost 30 years. Studies on peptide assembly started in the early 90s, with two peptide sequences that would naturally create simple β-sheets. The first pioneering study started with a Z-DNA-binding protein from *Saccharomyces cerevisiae*. After exploring its composition, Zhang et al. found that a repetitive motif, known as EAK16, was able to self-assemble [86, 87]. Investigations on the second self-assembling peptide ever explored started in 1993, with the study of amyloid-beta peptides that promote degeneration in Alzheimer's disease [88, 89]. Soon after, peptide aggregates were proposed as a model system to study self-assembly mechanisms [90], and by 1997, a 24-residue peptide sequence was proved capable of assembling in β-sheet plates [91]. These studies started the emergence of SAPs as potential materials for TE.

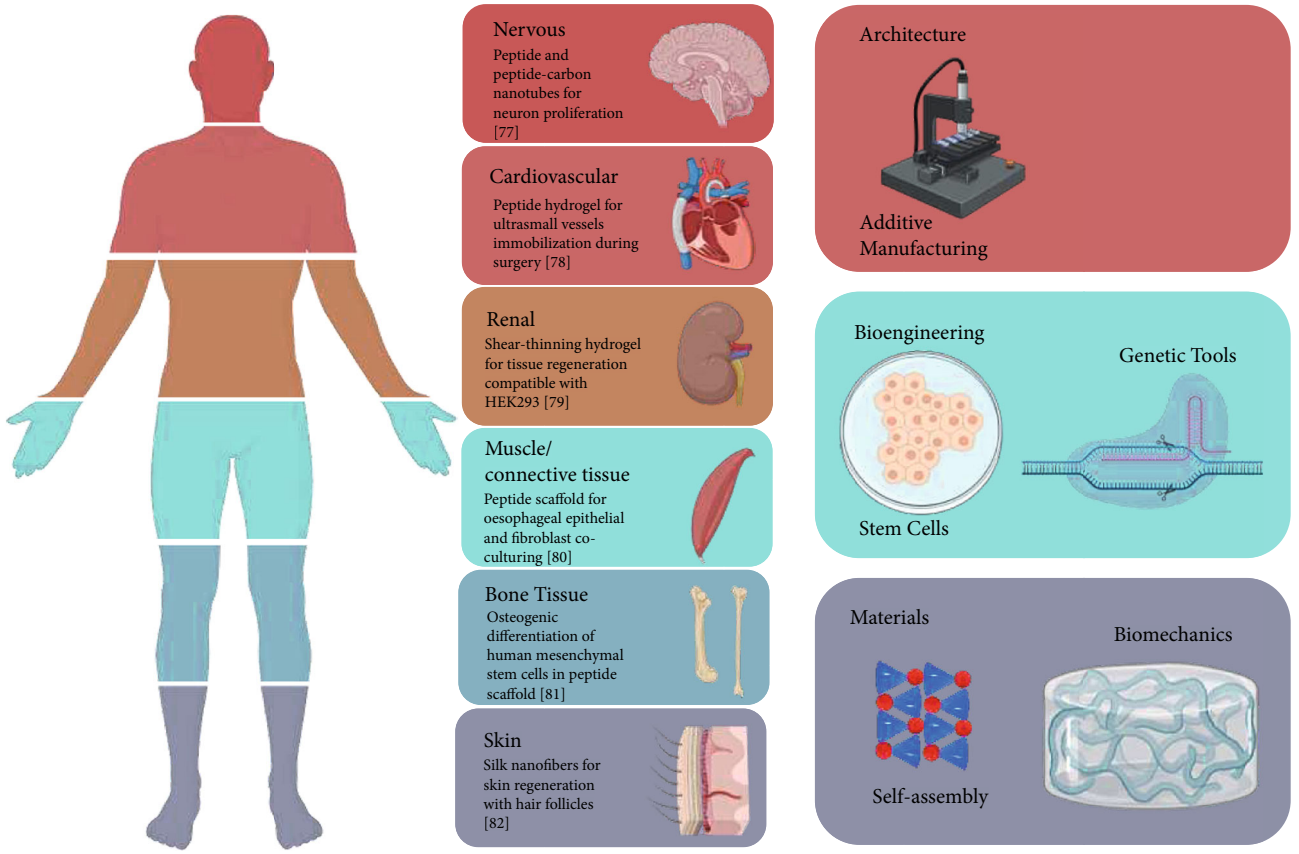

Figure 2: TE is built on the following important pillars comprised of the development of organ and tissue architecture, bioengineering techniques, and material science. SBPs are involved in all these three pillars of TE with the aim to develop tissue-specific constructs for a variety of complex human organ systems; nowadays, SBPs have proven resourceful for the proliferation of neurons [60], endothelial cells [61], kidney cells [62], fibroblasts [63], osteocytes from mesenchymal stem cells [64], and complex skin regeneration [65]. SBPs can be used cooperatively with other technologies to create versatile and smart scaffolds for TE. For instance, in order to obtain complex architectures, SBPs can be coupled with additive manufacturing techniques [66]. SBPs can also be coupled with bioengineering tools such as the use of stem cells [67] to create complex tissue-like cultures or the use of genetic tools to create active therapeutic scaffolds [68]. Finally, these materials can be designed to have triggered assembly mechanisms [26], as well as to control cell mechanics by their structural composition [23].

Evidence was given that peptides aggregate into a variety of nanostructures such as bilayers, nanotubes, nanorods, nanovesicles, nanofibers, nanobelts, and nanodonuts [2]. Hauser's work is explicitly focused on developing peptide nanofibers because of their similarity to fibril structures formed within the native extracellular matrix (ECM). For instance, the Hauser group previously designed peptide biomaterial that exhibits a fibrous structure in which individual nanofibers can extend up to one centimeter in length. To this effect, it is proposed that the use of materials that resemble the ECM may trigger specific cellular responses such as microvilli formation in intestinal epithelial cells, which is a direct response to the interaction between the cell and the surface topography [92, 93]. Indeed, fiber-forming decellularized matrices and collagen are the typical scaffolds used for the formation of intestinal villi. However, some SAPs designed by Loo et al. are among the few materials that also allow villi formation, presumably due to the nanofiber conformation of the structure (Figures 3(a)–3(c)) [66]. In fact, fiber-forming SAPs recapitulate the cellular microenvironment so that encapsulated stem cells can maintain pluripotency in long-term cultures for over 30 passages without major chromosomal mutations [67].

Moreover, the versatility of SAPs is not only limited to their biofunctionality but also to the possibility to tune their mechanical properties. Chan et al. developed an SAP in which the C-terminal residue of the hexapeptide Leu-Ile-Val-Ala-Gly-Xaa (where Xaa could be any amino acid) will determine the mechanical properties of the material, the clarity of the hydrogel, and the condensation morphology of the nanofiber without affecting the cytocompatibility of the gel (Figure 3(d)). The inclusion of an arginine residue at the C-terminus enhances gelation kinetics due to the presence of hydrogen bond donors/acceptors. However, a residue that is a weak donor/acceptor, like lysine, will allow the peptide to diffuse before condensing, permitting gelation at lower concentrations [75]. This work proves that peptide-derived SBPs are not only bioactive but can also be tuned in a bottom-up fashion by partially modifying an SAP sequence. This implication may allow the use of bioactive materials

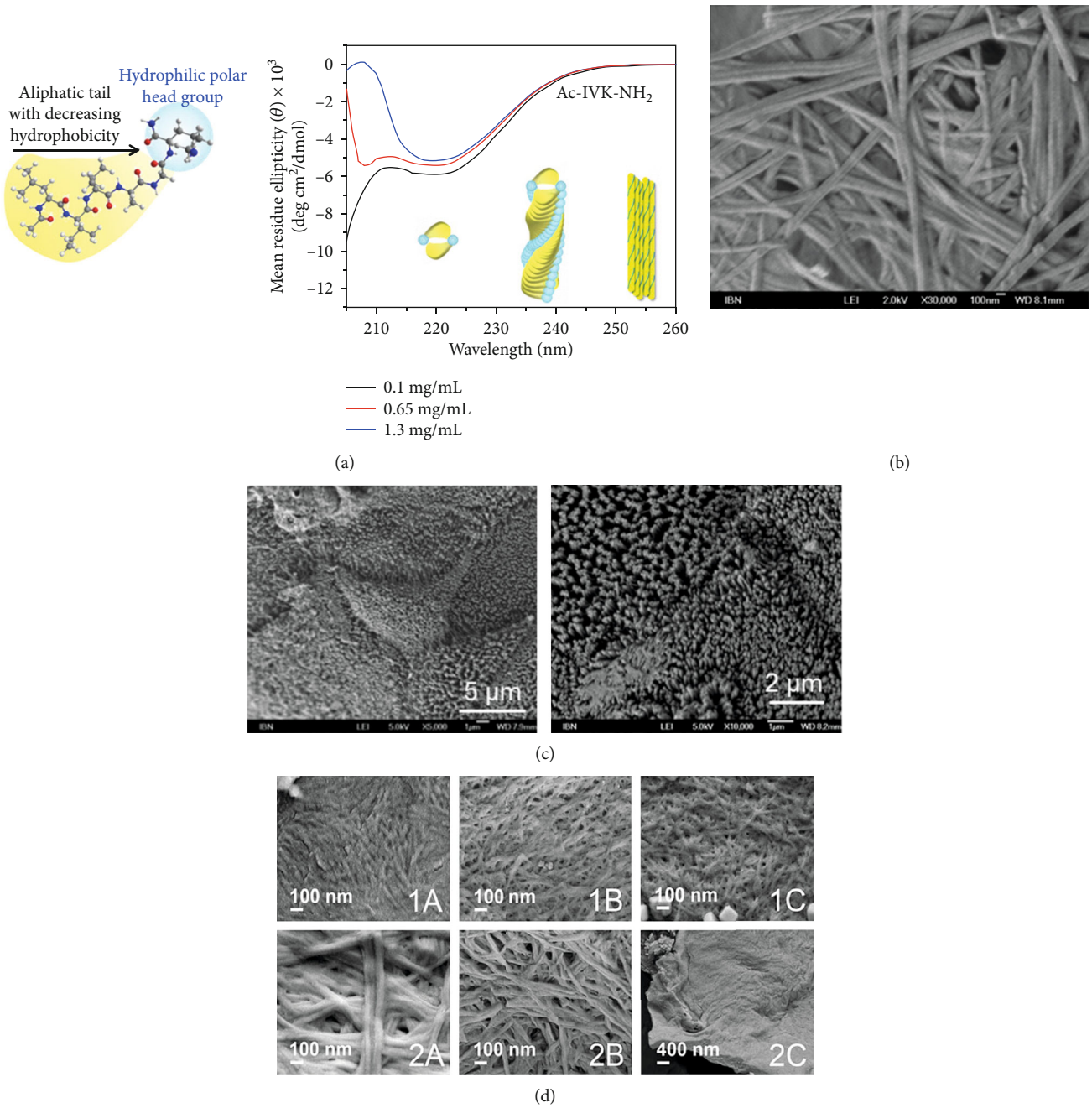

Figure 3: (a) Mechanism of assembly of aliphatic SAPs. Due to the hydrophobicity gradient in the peptide monomer, the monomers will assemble first in antiparallel pairs. Next, dimers will form intermediate α-helical structures. The nanofiber will be formed when multimers stack into stable β-fibrils. (b) Field emission scanning microscopy (FESEM) of the interconnected nanofiber structures. (c) Field emission scanning microscopy (FESEM) of Caco2 intestinal epithelial cells cultured on an SAP hydrogel. Homogeneous microvilli phenotype can be observed. (d) Topography of trimers and pentamers with different C-terminus residues. The diameter and prevalence of the individual fibers depend on the properties of the changing residue. These figures have been reproduced with permission from the American Chemical Society and Springer Nature [66, 75].

among tissues with different physicochemical and mechanical requirements. These novel approaches concerning SAPs have given advances in the pragmatic use of state-of-the-art applications for these materials as a scaffold for TE, where a considerable quantity of biomaterial extracts from animals is needed. In addition to the characteristics of SAPs mentioned above, the study of these molecules helps to design a possible library of ultrashort peptides for diverse applications to understand complex actions in medicine, such as amyloid formation. For instance, the behavioral characterization of aliphatic peptides, resembling amyloid sequences, aids to the corroboration of the natural amyloid aggregation behavior corresponding to Alzheimer's and other degenerative diseases. The Hauser model proposes an aliphatic system to

understand amyloidogenesis. Therefore, with this information, novel drugs and therapies could be developed to mitigate amyloid formation in the human body [76, 94]. The aliphatic ultrashort self-assembling peptides have been demonstrated to be suitable for a variety of interesting biomedical applications, including the use of peptide nanogels for wound healing applications in a burn wound model as well as in a full-thickness wound model [95, 96]. Furthermore, a successful injectable therapy was demonstrated when using anticancer drug-loaded peptide hydrogels for the *in vivo* injection in breast tumors. A significant shrinking of the size of the tumor was observed in a mouse model [97]. Interestingly, amyloid-like peptide aliphatic hydrogels maintained the pluripotency state of human embryonic stem cells and human-induced pluripotent stem cells (iPSCs) during culturing in the peptide scaffold for over 9 months, so far the longest reported period of time to culture sensitive human embryonic stem cells in a synthetic matrix [67]. Microfluidic technologies allow to form peptide nanoparticles for drug delivery and for the use as theranostic agents [98, 99]. Last, not least, bioimaging applications are feasible when referring to the interesting optical characteristics of these ultrashort aliphatic self-assembling peptides, making use of their nonlinear second harmonic behavior [100, 101].

A different type of SAPs is those developed by Insua and Montenegro [102]. The group proposes the use of cyclic peptides that assemble into nanotubes. Following, two exposed leucine and one tryptophan residue of the nanotubes bind and form nanosheet bilayers under acidic conditions. The remaining residues of the cyclic peptides are hydrophilic. This way, the nanosheet bilayer has a hydrophilic surface and several hydrophobic cores, suggesting potential applications as a molecular transporter and as stimuli-responsive membranes. On the other hand, Shi et al. [103] opted for the use of a phosphorylated 20-residue SAP to induce nanofiber assembly under the presence of phosphatase. In a dephosphorylated state, the SAPs fold into β-hairpin structures and stack into double layers due to the agglomeration of hydrophobic residues, resulting in a dry interface [104]. The new approach from the authors is aimed at phosphorylating the peptide in such a way that it would obstruct the generation of a hydrophobic pocket unless the residue becomes enzymatically dephosphorylated. This proves the versatility regarding nanostructures that can be achieved by the use of supramolecular peptide scaffolds.

Other approaches on peptide-derived SBPs include peptide-based assembling biomaterial with thixotropic behavior or, in other words, time-dependent shear-thinning hydrogels (Figure 4(a)) [105]. The peptides could potentially be used for active wound tissue regeneration as it maintains hydration and reduces bacterial contamination. The hydrogel is based on a construct of an Amoc (9-anthracenemethoxycarbonyl)-capped dipeptide; protected peptide-based hydrogelators show self-assembling behavior due to their hydrophobicity and aromaticity, which enhance interactions by π-π stacking. The included phenylalanine side chains are thought to be useful for imitating the ECM, and they further aid the malleability of aggregating into different nanostructures. The hydrogel can be effectively used for wound healing applications due to its biocompatible cyclic oligosaccharides inherent to cyclodextrins, which have both a hydrophobic interior and a hydrophilic exterior that mimics the ECM. On the other hand, Zheng et al. designed a silk-based nanofiber that allowed scarless skin regeneration in functional tissue. In a microsphere conformation, the nanofiber imbues and disperses mesenchymal stem cells into an injectable hydrogel to simulate paracrine signaling and induce scarless skin regeneration with hair follicles (Figures 4(b) and 4(c)) [65]. The *in vivo* studies reveal an improvement and outstanding novelty compared to other traditional biomaterial systems, presenting a reliable TE method in the applications of nanofibers for wound healing. Both works prove that macromolecule-derived supramolecular biopolymers can be modified with unconventional functional groups or may contain full proteins and even so generate specific conformations due to the weak governing interactions.

Furthermore, Kong et al. carried out a study on the oral administration of peptide drugs, hampered by their metabolic instability and limited intestinal uptake. The synthesis of a peptide with gastrointestinal-protease-resistant behavior that counteracts the interleukin-23 receptor, which has a direct effect on ulcerative colitis and Crohn's disease formation, would be an interesting development of biomaterials for oral drug-delivery purposes. Orally administrated drugs are progressively degraded during intake. For this reason, low amounts of drugs generally arrive at the desired target. The authors designed an inhibiting peptide of coagulation factor XIa that is able to resist protease degradation in the gastrointestinal tract. *In vivo* tests showed that using bacteriophages that encode for the inhibiting double-bridge peptide, more than thirty percent of the peptide remained intact with small peptide traces within the blood of the mice [106].

2.2. Nucleic Acid-Derived Polymers. The interest in DNA- and RNA-based scaffolds has been growing exponentially in the last decade. Similar to the origami technology, nucleotide-derived networks take advantage of the unique characteristics of nucleic acid polymers, i.e., pairing capability among complementary strands, sequence-dependent secondary structure, specific binding capability, controlled hybridization, and available DNA/RNA-interacting enzymes. Ever since the first DNA-containing hydrogels were reported in 1998 [107], which employed chemically modified salmon sperm DNA as a crosslinking agent in an acrylamide gel, nucleic acid-derived polymers have generated considerable interest as malleable natural biopolymers.

Novel strategies arose since the introduction of the first DNA crosslinked polyacrylamide (DNA-PA), like the switchable surface-integrated hydrogel from Kahn et al. [108]. The crosslinking mechanism is based on a hybridization chain reaction (HCR). Acrylamide chains were copolymerized with either DNA strand 1 or 3. Strand 1 can hybridize into a hairpin loop, while strand 3 binds with the partially complementary DNA strand 2, and together, they hybridize into a single hairpin unit. Using a fourth DNA strand (4) that is complementary to the toehold region of strand 1, the authors were able to develop a material that

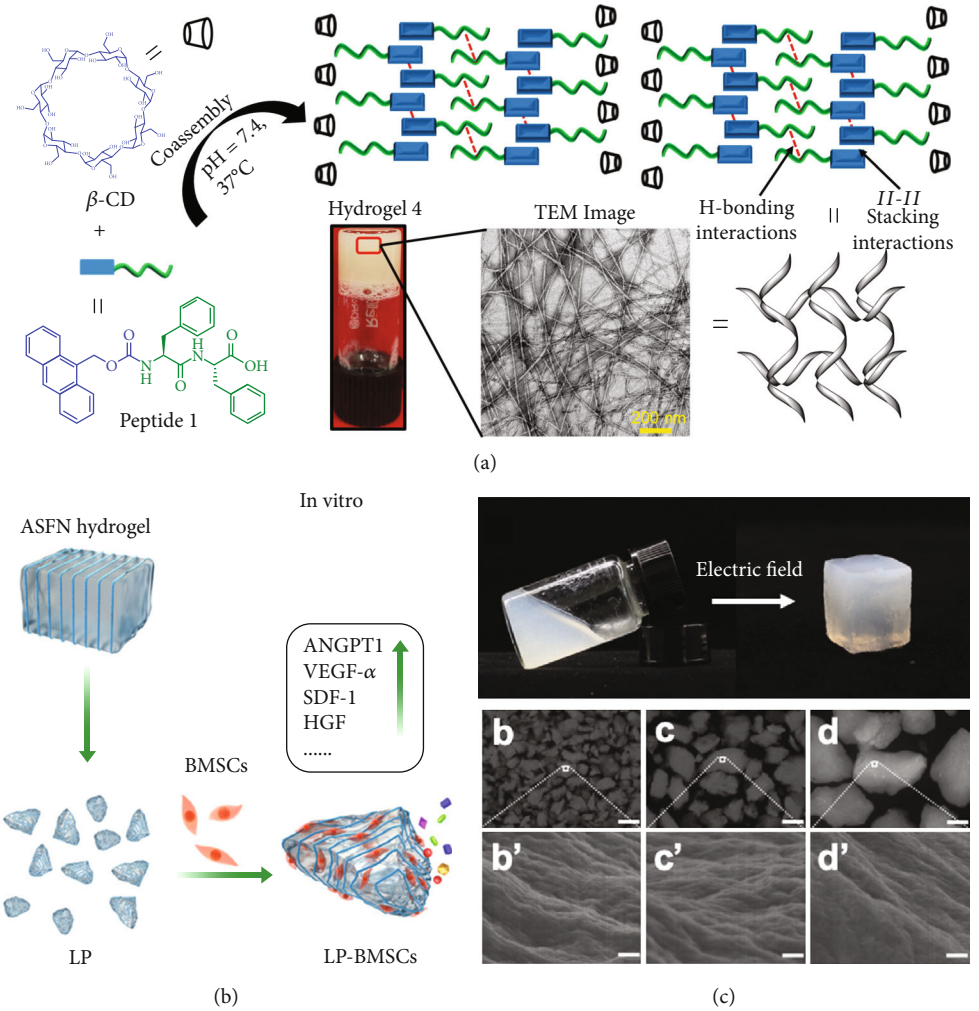

FIGURE 4: (a) Coassembly mechanism of thixotropic hydrogel. Nanofibers are a result of stacking and hydrogen bonding interactions among the residues of the monomer. The properties of the hydrogel are tuned with the use of β-cyclodextrin, in order to obstruct the assembly structure, which allows the hydrogel to be injectable. (b) A silk fibroin hydrogel was loaded with mesenchymal stem cells and growth factors that would allow cellular differentiation when bent in an *in vivo* model. (c) The hydrogel was separated with a molecular sieve, prepared under an electric field. The results show that the material retains a hierarchical, aligned structure. These figures have been reproduced with permission from the American Chemical Society and John Wiley and Sons [65, 105].

polymerizes into an Au-coated surface and simultaneously binds the two acrylamide polymers holding strand 1 or 3. Therefore, strand 4, which covers the surface, is used as an initiator for polymerization of an acrylamide gel. Additionally, the mechanical properties of the hydrogel can be enhanced more than 3-fold from 461 to 1770 Pa by adding potassium ions or 18-crown-6-ether to the system. The increase of the mechanical strength is caused by the formation and dissociation of G-quadruplexes of a fifth DNA strand copolymerized within both acrylamide chains. Although the research objective was the development of a hydrogel with on/off states for biosensing, the authors were able to design a sample material to be adapted into TE. Similar DNA-functionalized surfaces hold potential for skeletal TE where there is a demand for hard materials able to bond with soft hydrogels. The use of loop-hybridizing oligonucleotide systems for crosslinking initiation has ample applications for the crosslinking of polymers without the use or generation of cytotoxic compounds. Finally, this same system has an integrated "switch" system that signals into reversible stiffness changes which can be engineered into sensing specific cellular signals that require the release of either factors or cells, especially useful for the study of embryonic development.

DNA-derived polymers do not only serve as crosslinkers between copolymers, as is the case for DNA-acrylamide hydrogels, but can also create nanostructures or tridimensional networks among hybridized chains of DNA or RNA. These networks are not necessarily the main component of the hydrogel formulation, yet they contribute significantly to the mechanical or biological characteristics of the hydrogel. Um et al. generated branched DNA monomers able to assemble into variform DNA (namely, X, Y, and T) by ligase activity [109]. Originally planned for drug and cell release applications, this study showed the potential of nucleic acid-based hydrogels for the development of patient-

specific grafts and personalized medicine, as well as genetic and stem cell therapies in a biomaterial that is by definition biocompatible and biodegradable.

Conde et al. [68] presented an improvement in DNA-based hydrogels by developing a self-assembly RNA-based hydrogel scaffold from microRNA modulation. By the time this study was published, the use of triple helices had not been employed for other purposes than protein regulation by nuclease or repressing activity. The authors could demonstrate the versatility of the secondary structure of nucleic acid polymers to form complex functional nanostructures. Two of the three oligonucleotide sequences were therapeutic and were able to form Watson-Crick and Hoogsteen hydrogen bonds among them. A third RNA strand would bind exclusively by Hoogsteen hydrogen bonds and stabilize the complex into a triple helix. The nanoparticles would form by complexing the triple helix with a poly(amidoamine) dendrimer solely by a difference in charges. The authors proved the cellular uptake of such scaffolds and the therapeutic RNA strands' effect as a tumor suppressor miRNA.

In 2008, Wang et al. [110] developed a two monomer DNA-containing hydrogel, in which one involved a three-oligomer, Y-shaped structure, and the second one was a linear dsDNA linker. The crucial characteristic feature is the sticky ends in both monomers, which allow crosslinking among the structure and the linker. The matrix proves to permit cellular migration that can be adjusted by the inclusion of signals within the hydrogel. Also, the crosslinking mechanism of the hydrogel allows adjacent macrostructures to fuse and heal. This characteristic behavior permitted the authors to generate DNA bricks to form more complex scarless structures that adhere effectively. A similar Y-shaped structure was used by Sato [111]. However, the linker was removed, so that the structure's sticky ends would be complementary. DNA droplets formed by nucleation and grew by collision and fusion. The droplets formed via liquid-liquid phase separation, allowing the macrostructures to aggregate selectively within themselves and to sequence specific Y-shaped structures depending on the DNA concentration. The authors developed a variety of specific sequences for the sticky ends of the structures, which would differ in their thermodynamic properties. The presence of a cross-bridging motif would favor the binding among the diverse sticky-end sequences; in addition to the degradation of the complex structures by RNases, this allows the creation of complex-shaped droplets. Although this project's scope seems to tackle a drug delivery matter, it could allow the development of regenerative medicine approaches, such as bioactive molecule encapsulation within cell-free tissue-engineered vascular drafts [14, 112].

Two recent publications describe the convergence of poly(ethylene glycol) diacrylate (PEGDA)/DNA hybrid hydrogels for a cell-free system, where a physically crosslinked DNA network-based cell fishing strategy is applied. As a result, an efficient capture was observed with 3D enveloping and enzyme-triggered release of bone marrow mesenchymal stem cells. The DNA network is generated by self-assembly via a second rolling circle amplification method and by assembly of two (number of lengths) DNA strands [113, 114] (Figure 5).

Qi et al. developed shape-controlled and self-assembled hydrogels using DNA sequences to control the shape of different hydrogels with self-assembling behaviors. They have reported about hydrogel cubes with edge lengths from 1 to 30 nm. In a single reaction, 25 dimers were constructed in a high multiplex with 50 distinct hydrogel cube species. Since the cuboids display face-specific DNA glues, diverse structures are achieved in aqueous and interfacial agitation systems. Within aqueous systems, it was found that extended chains, network structures, squares, dimers, chains of fixed length, and T-junctions could be generated in relation to the assembly systems. Therefore, this approach leads to a higher definition of hydrogel morphology at the nanoscale [115].

With regard to DNA-crosslinked polymers, Du and Hill [116] worked on a thorough characterization of DNA-poly(acrylamide) PA hydrogels and their gelation kinetics. Using an N,N′-methylene(bis)acrylamide as a chemical crosslinker, the group was able to identify the mechanistic role of both fragments and, hence, proposed and analyzed the longest relaxation times in correlation to the dissociation rates. Their model allowed the evaluation of interactions of other DNA-derived gel networks, such as the one presented by Anderson et al. [117]. In this case, "click" nucleic acids were conjugated to an eight-armed poly(ethylene glycol) PEG polymer through thiol-ene mechanisms, in order to overcome the scaling faults of fully formed DNA polymers. Crosslinking of the gel occurred by Watson-Crick base pairing and allowed reversibility at high temperatures (Figure 6). This work demonstrated the versatility of DNA-linked synthetic hydrogels, although their suitability in a biological setting was not evaluated.

In recent years, there has been a growing interest in the alternative application of the Clustered Regularly Interspaced Short Palindromic Repeats (CRISPR) technology, including its potential in stimuli-responsive materials. English et al. [118] used CRISPR-associated (Cas) enzymes and engineered DNA-based hydrogels to control the mechanical properties of the materials when specific sequences were detected by the enzymatic complex. The already known DNA-PA [108] can be crosslinked using an AT-rich oligonucleotide strand that binds to two noncomplementary strands in the DNA bridges. Using a high-catalytic-efficiency Cas12 that cleaves AT-rich regions, the authors were able to induce and control the degree of bulk gel degradation by the concentration of trigger DNA. One of the most significant successes of the project is the capability of differentiation among oligonucleotide inputs, which cause individual responses in the hydrogel. Although the team successfully released both AuNPs and cells enclosed in the DNA-AP matrix, these experiments were solely a proof of concept for both TE and drug delivery assays. As the authors state, "this technology endorses the possibility of cargo release in tissue culturing after specific cellular cues." However, future work could include experiments to characterize the change of the mechanical properties as the DNA bridges are cleaved and foster the development of cellular factors detection systems, as well as the inclusion of several different oligonucleotides for stepped degradation of the artificial matrix.

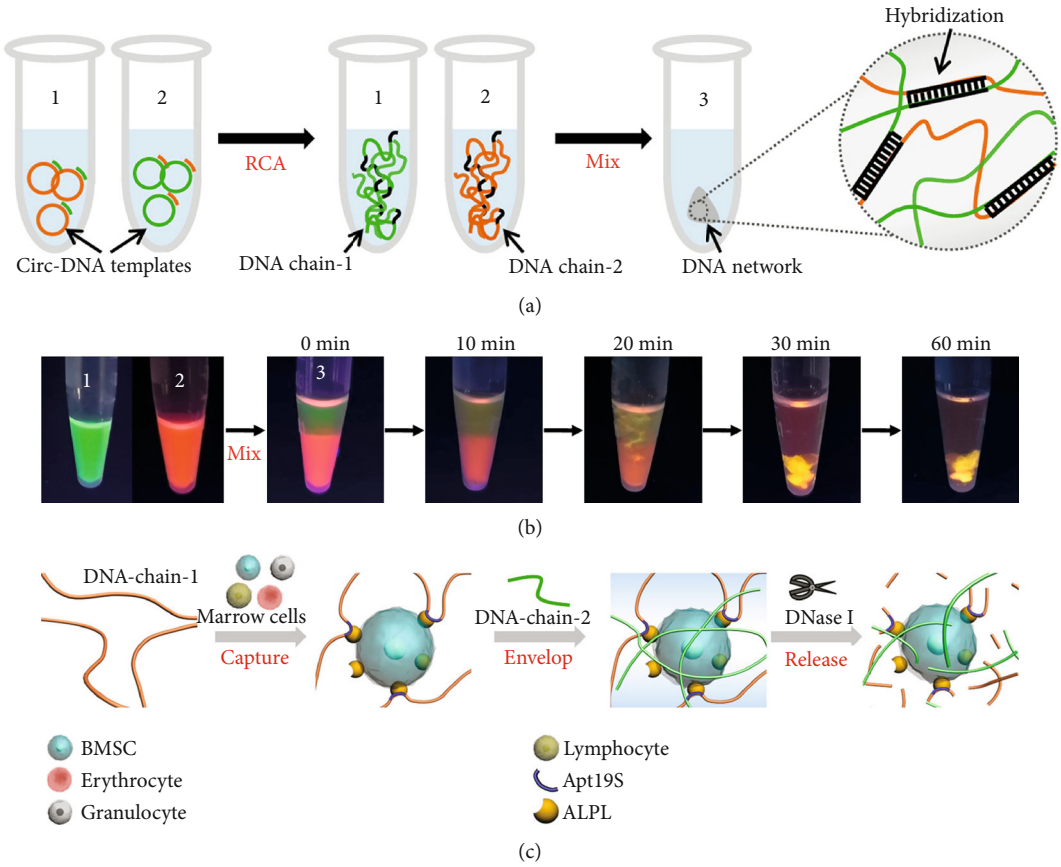

Figure 5: (a) It is possible to generate ultralong DNA chains using circular DNA templates. The strategy of elongation employed is a double rolling circle amplification (double RCA). Using two partially complementary DNA templates, the ultralong chains are able to hybridize with each other after mixing. (b) The use of stained DNA chains allows the observation of the hybridization process after being mixed. (c) The template DNA also contained aptamers that bind to a specific surface membrane protein (ALPL) of marrow cells. The authors designed a mechanism of capture and release of stem cells using the aptamer-containing ultralong DNA hydrogel and DNases for degradation of the matrix. These figures have been reproduced with permission from the American Chemical Society [114].

As specific DNA and RNA moieties bind to specific molecules, these materials can be used as low releasing systems, sensors, or inactivators. For further applications, Li et al. [119] present a comprehensive review of DNA hydrogels and microgels for other biological applications that differ from TE, such as biosensing. On the other hand, Chen et al. [120] cover a variety of strategies of DNA self-assembly for both the DNA-as-crosslinkers and DNA-as-polymer hydrogels.

2.3. Oligosaccharide-Derived Polymers. Native polysaccharides have complex architectures. They can be both homo- and copolymers, linear or branched. Depending on the crosslinking mechanisms, polysaccharides can assemble into oriented fibers or tangled networks. The intricacy behind these biopolymers is related to their biosynthesis pathways and to their usually random copolymeric structure. Polysaccharides such as alginate, cellulose, and chitin have been repeatedly employed throughout the history of TE. However, saccharides in the ECM can also be found in the form of glycosaminoglycans and proteoglycans, enhancing the complexity behind the research and development of highly characterized saccharide-derived scaffolds.

The structural complexity of glycomolecules made it difficult to synthesize natural biopolymers based on saccharides. However, as proteoglycans and glycosaminoglycans are an essential part of the ECM to which they provide cellular signals, efforts to introduce specific oligosaccharides have been implemented in TE. Although these materials are not used as the main component for a scaffold, materials biofunctionalized with structurally defined oligosaccharides pose advantages over their naïve equivalent [121]. Moreover, oligosaccharides allow us to translate the various properties of polysaccharides into soluble, less viscous, or bioactive alternatives for their use in TE [122].

Hyaluronic acid, one of the most abundant proteoglycans in the mammalian ECM, has proven to modulate endothelialization in tissues by activating intracellular signaling cascades when present as low molecular weight oligomers [123]. This phenomenon is especially crucial for artificial vascularization when blood vessels align and attach to structures that work as the basement membrane. In a recent study, Kang et al. [124] reported that HA oligosaccharides (oHA) prevent coagulation and allow platelet adhesion. The oHA, ranging from tetra- to decamers, were immobilized in collagen by reductive amination and were used to generate

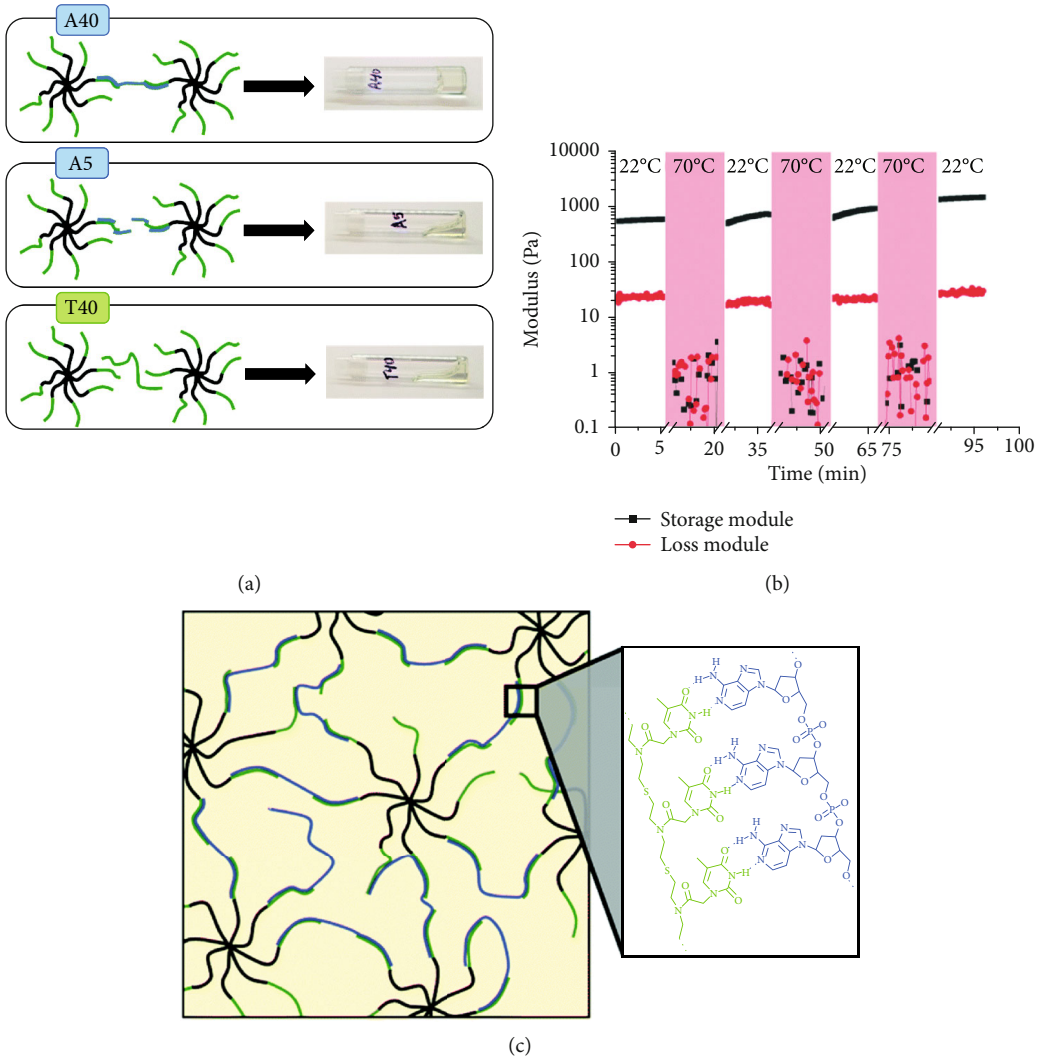

Figure 6: (a) Schematic of the "click" nucleic acids used for an 8PEG-thymine macromer crosslinking using a 40-mer adenine ssDNA, a 5-mer ssDNA adenine, and a 40-mer thymine ssDNA. It was observed that the hydrogel would crosslink only in the presence of long thymine-complementary strands. (b) When subjected to a denaturalizing temperature, the stiffness of the hydrogel decreased considerably. However, this mechanism appears to be reversible, as the mechanic properties of the material change accordingly to the input temperature. (c) As the 40-mer adenine ssDNA will anneal with the thymine strands, the crosslinker could potentially bind with multiple 8PEG-T oligomers. These figures have been reproduced with permission from the American Chemical Society [117].

electrospun nanofibers crosslinked by glutaraldehyde (GTA) vapor or 1-ethyl-3-[3-dimethylaminopropyl] carbodiimide hydrochloride (EDC). Endothelial cells seem to proliferate and migrate when embedded in an oHA-enriched collagen matrix. The same collagen/oHA matrices prepared by reductive amination have also been used in an independent study by Li et al. [125]. Due to the scaffold mineralization of hydroxyapatite, the group theorizes that oHA may enhance calcium chelation by providing new carboxyl groups (Figure 7). The presence of oHA improves the adhesion and proliferation of vascular cells while allowing osteoblast differentiation and infiltration in the nanofibers. It also proves the proficiency of collagen/oHA-based nanofibers as possible scaffolds for bone regeneration in the coming years. The inclusion of oHA in tissue scaffolds will allow the generation of bioactive matrices that may accelerate endothelialization which in turn may promote angiogenesis, a key component for the further study and development of the next generation of TE.

Similarly, chitosan oligomers, although naturally present in shells and outer skeletons of crustaceans, are known to modify the mammalian metabolic state and influence cell fate. Although not commonly employed within the principal composition of a scaffold for TE, its properties and manipulability show potential for both tissue regeneration and development of tissue grafts. Lv et al. [126] enriched a carboxymethyl chitosan/alginate hydrogel with chitosan oligosaccharide (COS), which affected the mechanical properties, gelling kinetics, and biological properties. A two-stage gelling process is observed under the coalescence of COS, when the carboxyl groups from carboxymethylcellulose (CMCS) and COS get protonated in a staggered manner. With respective pKa values of 6.5 and 5.8, electrostatic attractions are induced and the alginate matrix gets stabilized before the gelation

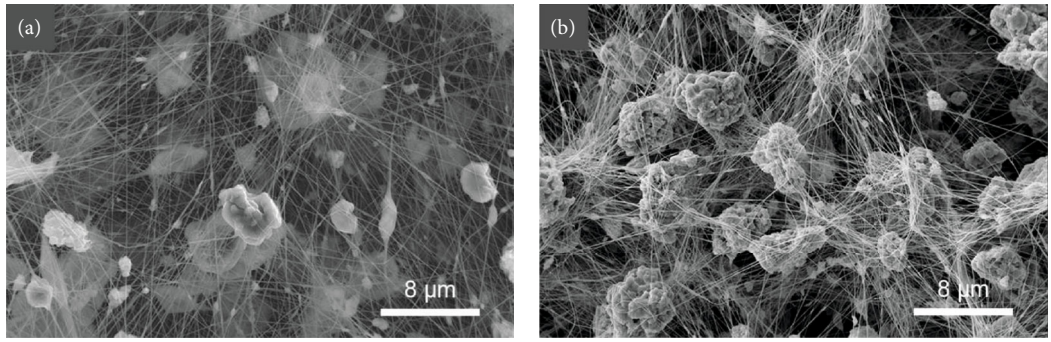

(a) (b)

Figure 7: SEM images of electrospun nanofibers of (a) collagen/HA and (b) collagen/oHA. Inorganic particles mineralize within the nanofibers, promoted by the presence of oHA. The pattern of mineralization gave rise to a change in pore size which, in turn, enhances cell migration and proliferation within the voids. These figures have been reproduced with permission from Elsevier [125].

process is finalized. Low concentrations (<0.5%) of COS showed prolonged viability of human umbilical cord mesenchymal stem cells and potential wound healing capabilities with no inflammation response and maturation of granulation tissue. Wound healing properties of chitosan have been addressed before by Sandri et al. [127]. A halloysite/COS nanocomposite was developed and tested as a wound dressing formulation for enhanced healing. COS-containing hydrogels seemed to enhance cell proliferation *in vitro*, whereas the use of the nanocomposite demonstrated the lowest lesion area *vs.* time profile when compared against the control groups. The histological analysis showed early reepithelialization and angiogenesis. COS has previously demonstrated anti-inflammatory activity by hampering the responses from lipopolysaccharides and inhibiting mitogen-activated protein kinase-dependent pathways [128, 129].

Oligosaccharide synthesis has historically been a labor-intensive, inefficient, and time-consuming synthesis method. Rather than seen as synthesized products, oligosaccharides are usually degradation products of their polymeric form. The methods used for degradation of natural carbohydrates are hydrolysis, enzymatic or chemical cleavage, and radiation, where each of these procedures has different energetic, economical, and environmental costs. However, the resultant product is usually a mixture of oligosaccharides with varying molecular weights. We rarely obtain a final carbohydrate product of a structure-specific composition. The importance behind the automation of well-defined oligosaccharides relies on the capacity to characterize and study particular carbohydrate conformations and structure-property correlations within biological events [58, 59]. The development of an automated synthesis supports the opportunity to study and characterize the effects of biologically relevant complex saccharide motifs in the cellular environment and may be used in the creation of new smart and biofunctional scaffolds to achieve more complexity with a higher degree of biological simulation (biomimetics). The earlier mentioned efforts of Peter Seeberger and coworkers strengthen the goal of creating well-defined complex carbohydrate structures by applying automated glycan synthesis [130].

3. SBPs for Tissue Engineering (TE)

As it was stated by Williams [36], "the major problems of TE were apparent from the early experiences with skin." Indeed, researchers worked hard to develop materials that replicate the nano- and microstructure of tissues, maintain their properties at physiological conditions, and are stable and biocompatible. However, TE is now reaching a new level of complexity: two-dimensional cell monolayers are moving to three-dimensional constructs (or even to four-dimensional ones) [131–133]. Cell lines are being replaced by pluripotent and patient-derived cells [134–136], and tissue grafts are evolving to organoids and whole organs [10, 16, 47, 136–141]. As such, the materials employed must improve accordingly. By now, it is evident that SBPs have an opportunity to be widely used in TE applications; their particularities have the potential to solve current challenges that TE and regenerative medicine have brought upon material design. In Table 1, we can find a comprehensive overview regarding published approaches of SBPs for a specific application within TE.

We have briefly talked about the importance of induction of cellular responses by the scaffold, where cell fate is controlled by multiple chemical and physical cues from the cellular microenvironment. Signaling molecules are biochemical cues that promote adhesion, proliferation, migration, or differentiation. It is of indispensable interest for all TE approaches to control the presence and concentration of these signaling molecules in the cellular microenvironment. In a natural matrix, these factors can constrain the ability of cells to repair, regenerate, and replace tissue. This is why controlled delivery has become one of the fundamentals for tissue regeneration [142], where the induction of response is specifically relevant for the generation of organ-like structures.

Considering entrapped small signaling molecules, cyclodextrins (CDs) are good examples, because they are known for their host-guest complexation. CDs are able to entrap small molecules in the hydrophobic core by hydrophobic interactions. Current efforts to use CDs as delivery hydrogels are focusing on the development of derivatives of CDs for controlled delivery of small molecules [143]. For instance,

Table 1: Engineered SBPs developed in the last 15 years arranged by applications on TE and regenerative medicine.

Application		Outcome	Biomolecule	Possible main interacting forces
Complex macro- and microstructures		In situ multilayer bioprinting of DNA hydrogel [186]	P-N	H-bonding
		Complex nanostructures (i.e., nanocircles) [187]	N	H-bonding, hydrophobic interactions
		Highly stable DNA fiber resistant to DNases [188]	N	H-bonding, electrostatic interactions
		DNA origami scaffold with lipid core [189]	N	H-bonding, hydrophobic interactions
		Vesicle forming DNA hydrogel [190]	N	Electrostatic and hydrophobic interactions
		Network scaffold from RNA [191]	N	H-bonding, π-π stacking
		Self-assembly peptides with fiber topology, fine-tuning capacities [192]	P	H-bonding, electrostatic interactions
		DNA hydrogel bricks [110]	N	H-bonding, electrostatic interactions
		DNA hydrogel modulated by internal stress interactions [193]	N	H-bonding, ionic bridges
Cellular scaffolds	Tissue microenvironment development	Peptide scaffold for gastrointestinal villi reconstruction [67]	P	π-π stacking, hydrophobic interactions
		Dentinogenic peptide hydrogel laden with dental pulp stem cells [194]	P	H-bonding, van der Waals and electrostatic interactions
		Osteogenic scaffold for the recapitulation of nucleus pulposus phenotype [195]	P	π-π stacking, hydrophobic interactions
		Osteogenic differentiation of human mesenchymal stem cells in peptide scaffold [64]	P	Electrostatic interactions
		Injectable alginate-peptide scaffold for osteogenic differentiation [196]	S-P	π-π stacking, hydrophobic interactions
	Bioactive	Peptide scaffold that promotes epithelial regeneration [197]	P	Hydrophobic interactions, H-bonding
		Scaffold for mesenchymal stem cell-derived extracellular vesicles release for tissue repair [62]	P	π-π stacking, hydrophobic interactions
		Peptide scaffold for oesophageal epithelial and fibroblast coculturing [63]	P	π-π stacking, hydrophobic interactions
		Peptide scaffold that promotes vascularization and innervation innately [198]	P	Hydrophobic interactions
		Peptide scaffold for proliferation and migration of human umbilical endothelial cells by localized and controlled release of H_2S [60]	P	Electrostatic interactions
		3D peptide scaffold for neuron proliferation [199]	P	H-bonding, hydrophobic interactions
		Peptide-carbon nanotube complex that promotes natural cell behavior and affects cancer cell microenvironment [200]	P	Hydrophobic, electrostatic, van der Waals interactions
		Injectable peptide for oligodendrocyte encapsulation and proliferation [201]	P	Hydrophobic interactions, π-π stacking
		Injectable hydrogel with slow degradation that allows the regeneration of native ECM [184]	P-S	Electrostatic interactions
		DOX-releasing system that also promotes dendritic cell maturation [202]	P	H-bonding, electrostatic interactions
	Stem cell culturing	Injectable peptide scaffold for embryonic stem cell culture [203]	P	π-π stacking, hydrophobic interactions

Table 1: Continued.

Application		Outcome	Biomolecule	Possible main interacting forces
Smart scaffolds	Stimuli responsive	pH-responsive DNA hydrogel [204]	N	Triple H-bonding
		pH-responsive cyclic DNA scaffold [205]	N	H-bonding
		pH-responsive alginate hydrogel functionalized with hyaluronan oligosaccharides [206]	S	H-bonding
		Glucose-responsive, insulin release system [207]	P	H-bond, hydrophobic interactions
		ATP-responsive DNA hydrogel [208]	N	H-bonding
		Enzyme-responsive, silica-coated with konjac oligosaccharide [209]	S	H-bonding, π-π stacking
		Nanotube-DNA hydrogel optothermally responsive [210]	N	H-bonding
		MicroRNA responsive, DNA hydrogel for cancer screening [211]	N	H-bonding
		Thermoresponsive beta-cyclodextrin-based hydrogel [212, 213]	S	H-bonding, hydrophobic interactions
		Light-induced release, DNA hydrogel [214]	N	H-bonding, π-π stacking
	Shape memory	Reversible, CMC-based driven by chemical and physical stimuli [215]	S	Donor-acceptor interactions
Delivery	Drug	Chitosan oligosaccharide drug delivery vehicle with enhanced membrane permeability [216]	S	Not detailed
		DNA nanosponges for drug delivery [217]	N	Electrostatic interactions
		DNA-PA hydrogel for controlled release [218]	N	Hydrophobic interaction, H-bonding
	Cell	Injectable peptide scaffold for cell delivery [219]	P	H-bonding, electrostatic interactions
	Enzyme	Water-insoluble peptide for enzyme protection [220]	P	H-bonding, π-π stacking
	Genetic material	Hydrogel for sustained RNA release [221]	N	H-bonding
		Chitosan-graft-(PEI-β-cyclodextrin) copolymers for DNA and siRNA delivery [222]	S	H-bonding, electrostatic interactions
		Cell-penetrating peptide for gene delivery [223]	P	Electrostatic interactions
		DNA hydrogel for nucleic acid delivery [224]	N	H-bonding, π-π stacking
Therapeutic	Wound regeneration	Adhesive DNA hydrogel with antimicrobial properties [61, 225]	N	H-bonding
		Hydrogel for accelerated healing [185]	P	Hydrophobic interactions
		Hydrogel with hyaluronan oligosaccharides for accelerated diabetic wound healing [206]	S	Not detailed
	Immobilization	Microsurgery assistance-hydrogel for the immobilization of ultrasmall vessels. [226]	P	π-π stacking
	Cancer therapy	Hexapod-like DNA hydrogel for photothermal immunotherapy [227]	N	Not detailed
	Immunotherapy	DNA hydrogel as a vaccine system by noncovalent binding [228]	N	Electrostatic interactions

N = nucleic acid-based material; S = oligosaccharide-based material; P = peptide-based material.

Fiorica et al. developed a hyaluronic acid/CD hydrogel for injectable localized chemotherapy [144]. The authors reported a remarkable release period of over 1 month, due to CD complexation. Furthermore, when performing *in vivo* tests, they observed a reduction on the solid tumor volume and no damage to other tissues due to the presence of the cytotoxic chemotherapy agent. Another creative approach to the use of CDs was reported in 2019 [145]. Here, the use of poly-CDs as a crosslinking agent in a solution of a tetronic-adamantane conjugate generated a shear-thinning, micelle-based hydrogel by simple mixing. Furthermore, chemotherapy drugs were loaded and successfully delivered to cellular environments at a low pH (<7.4 pH). Furthermore, besides their long-proved capability to deliver chemotherapy drugs, CD-based hydrogels have proven to be useful gene delivery agents [146]. If coupled with other small molecules, CDs may work as delivery vehicles of small signals to induce specific cell responses.

On another hand, self-assembling peptide hydrogels can also work as injectable scaffolds for controlled delivery of

small molecules. Oxaliplatin-derived peptide hydrogels showed significant growth inhibition of breast tumors in a mouse breast cancer model. Before injecting the therapeutic hydrogel for the localized therapy, the peptide hydrogel was functionalized by ligating the anticancer drug oxaliplatin via click chemistry [97]. In a very comprehensive review, Wang et al. recollect a variety of strategies to design and implement peptides for drug delivery [147]. One of the most novel efforts on peptides for drug delivery is the D3F3 forky peptide designed by Tao et al. [148]. The resultant fibers of the peptide self-assembly are able to bind to doxorubicin (DOX), a known chemotherapy drug. However, once the zinc ion concentration overcomes a threshold, the fibers will form a gel among themselves and release DOX. This mechanism was thought for controlled delivery of DOX into the prostate, where the concentration of zinc ions is significantly higher than in the bloodstream.

By definition, origami DNA is an SBP. We can easily figure out why this complex 3D structure can be used as smart delivery vehicles. Complex 3D DNA structures are evidently easier to design and synthesize which make them a versatile drug delivery tool [149, 150]. A current DNA origami drug delivery approach consisted in a bundle of nanostructures that would carry and release DOX after the detection of signal molecules by the cell and the following endocytosis of the delivery bundle. This novel approach serves as proof of concept of a stable and specific ligand-drug conjugate facilitated by a DNA origami scaffold [151].

The controlled delivery of small molecules has important implications for TE. To be more specific, we will briefly talk about vascularization, which is needed to irrigate thick constructs, as diffusion is not optimal for mass transfer over large distances (>200 μm) [152, 153]. Vascularization is a process mainly dependent on cell-ECM interactions [154–157]. One of the current approaches to solve this issue was the synthesis of a self-assembling glycosylated peptide used to mimic the highly glycosylated environment of the ECM. Coupled with a proangiogenic factor, the peptide was able to induce microvascularization *in vivo* and *in vitro* [158]. Another interesting approach is shown by an injectable gelatin hydrogel modified with a cyclodextrin motif that would entrap antioxidative molecules. The inclusion of such molecules enabled the enhanced angiogenesis *in vivo* [159]. For a more profound description of the state-of-the-art and the role of materials in angiogenesis, we recommend the review of Lee et al. [160].

Besides small molecule delivery, complex tissue development also encompasses the fabrication of complex microstructures that are anatomically relevant. Most complex organs, such as the lungs, kidneys, and glands, are formed by several branched, independent, organized cellular aggregates. In order to reproduce organ-specific microstructures, biomaterials should be versatile enough to allow the growth and self-organization of several cellular subtypes [46, 161–163]. This implies the following matrix rearrangement according to the stochastic cell growth. Self-healing SBPs form dynamic scaffolds that allow a constant ECM remodeling according to the cellular movement. A recent review on self-healing hydrogels describes several approaches using cyclodextrins and peptides [164]. Peptides have been largely explored as self-healing scaffolds [165]. A series of injectable dipeptides have shown instantaneous self-healing properties, while presenting a wide range of tunable mechanical properties. *In vivo* experiments demonstrated that this material, when used as a filler, exhibits low inflammatory responses [166].

4. Supramolecular Biopolymers for Bioprinting

Recently, additive manufacturing protocols have been optimized for diverse biofabrication needs, depending on the material's requirements and their desired morphology [167]. The design of a meaningful material is the initial crucial step for establishing a suitable scaffold in order to accommodate specific kinds of cells or tissue. Each material has limitations regarding its use for experimental and translational applications. In an effort to overcome the inherent limitations of bioinks, such as weak mechanic properties or low printing resolution, researchers have developed data processing strategies to achieve high-resolution structures [168, 169]. Currently, there is a demand for customized bioinks, as well as for hardware and software. Various emergent startup companies, such as Allevi, Cellink, and Organovo, besides many others, have developed suitable bioinks for bioprinting in combination with corresponding printing equipment. Still, the use of existing bioprinting protocols remains a constant challenge, due to the unforeseen behavior and limitations when combining biomaterials, chemical constituents, growth factors, and cells [170]. The review of Mir et al. is recommended for deeper understanding of the overall potential of bioprinting [171].

To overcome these limitations, different techniques like material extrusion [172, 173], material jetting [174–176], and vat polymerization [177, 178] (which encompasses stereolithography and two-photon polymerization) [179] were introduced. In addition, novel innovative methods have been developed such as, for instance, computed axial lithography, better known as volumetric printing, with the aim to print photocrosslinkable polymers faster and with better resolution [180]. Furthermore, recently, the use of state-of-the-art robotics for bioprinting has started. By having different-degree-of-freedom robotic arms, the robots can mimic fine human movements—in an effort to simulate human surgeons—while providing the accuracy of machines. The robots are directly used for the bioprinting of gel material, where all the detailed programming for incorporation of cells, extrusion of material, and pressure and/or velocity settings are included [66].

Additionally, as printing fidelity and reproducibility of biomaterials is required for superior performances, the use of rationally designed *ad hoc* synthetic SBPs has a clear advantage over other bioinks. This allows achieving higher accuracy in vitro, ex vivo, and in vivo, which is fundamental for punctual applications. To give an example, Muller et al. used biomaterials with solid fractions, such as bioceramics or nanoparticles for bone or cartilage tissue regeneration. Because of the presence of two different materials, the particles and the hydrogel produce inconsistent dispersion of

particles; thus, the printing or the formation of the desired morphology is difficult to achieve. The group solved this issue by the use of gellan gum methacrylate, hyaluronic acid methacrylate with hydroxyapatite crystals or particles that enhanced the ink's printability. Cryomilling of the ink components decreased its viscosity 10-fold with a shear rate of $0.1\,s^{-1}$ without compromising homogeneity and stronger interlayer adhesion between layers [181]. In another study from the same group, the designed bioink showed a mechanical improvement after dynamic covalent links between the amine and 45 nm sized silica nanoparticles that were imbued in state-of-the-art oxidized alginate. The reversible imine bonds between amines on the nanoparticles and aldehydes of oxidized alginate lead to significant enhancement of the rheological properties and better printability. The yield stress increased 5.4-fold without compromising the biocompatibility of the bioink when using 2 wt% nanoparticles [182].

Moreover, as stated before, it is preferable to avoid the use of cytotoxic crosslinkers or UV light, which can be damaging to the cells. Indeed, SBPs assembly can be triggered by different stimuli, e.g., ions, and this capability is also exploited in bioprinting. For instance, Kim and coworkers [183] designed a self-assembling saccharide-based bioink, based on competitive covalent bonding between hyaluronate and a water-soluble form of chitosan, with self-healing capability. Using acid dihydrazide, the hyaluronate and glycol chitosan forms acylhydrozane bonds. Moreover, changing the molecular weight of the hyaluronate allowed the material to change its mechanical properties and to be extruded without a postgelation system. However, neither conformational-specific oligosaccharides nor nucleic acid-derived hydrogels have been yet explored as bioinks: we expect SBP hydrogels to be used as smart and bioactive materials for bioprinting soon.

5. Conclusions and Outlook

SBPs are polymeric units that self-assemble to supramolecular scaffolds by noncovalent interactions. Because of their unique properties, they appear as promising alternatives that are able to overcome existing challenges in TE. Currently, there is a lack of robust materials that can be appropriately used for the development of organoids, whole-organ engineering, patient-specific tissue regeneration, or *in situ* therapeutics. Using interactive motifs, SBPs can be easily functionalized into bioactive materials. SBPs are also often thermodynamically reversible, which supports self-healing properties. Furthermore, these materials can include stimuli-responsive motifs.

Peptide- and nucleic acid-derived polymers have resolved a variety of issues that saccharide-derived supramolecular biopolymers did not yet resolve, such as routine procedures for characterization and elucidation of binding and annealing mechanisms. Chemically synthesized macromolecular biopolymers have the advantage of not to depend on batch-to-batch variations which can cause serious troubles when using natural-derived biopolymers. It is recommended to think about the possible implementation of SBPs in situ and engineer additional traits that may enhance its properties. For example, it would be suggested to work on nature-inspired self-assembly peptides for the generation of detection probes. A second example would be to step on the conjugation of optically active molecules to allow the detection of specific molecular phenomena, such as self-healing or annealing. Further studies could also focus on the generation of matrices with gradients of density to allow specific geographical mechanical stimuli.

Currently, a major challenge is the lack of smart synthesis methods for complex oligosaccharide structures. There is obviously a need to develop methods that will allow the generation of branched oligosaccharides. Methods to be explored include the use of glycosylases within an automated chemical polymerization. The development of novel synthesis strategies will support the generation of complex and well-characterized materials such as glycopeptides or nucleic acid/saccharide-based hydrogels. This will also give additional opportunities for the inclusion of specific signaling oligosaccharides within a matrix and will amplify the spectrum of bulk properties of the novel scaffolds and their overall tunability. Particularly regarding sugars, the development of a high-yield synthesis will unleash the potential of using saccharides with a specific confirmation as part of a scaffold that would mimic the presence of glycosaminoglycans and even proteoglycans found in the extracellular matrix. In addition, given that a high percentage of membrane proteins respond to glycosylated molecules, it is important to focus on the effect of sequence-specific oligosaccharides in order to enhance the cell-ECM interactions in materials.

Moreover, smart novel materials offer a variety of biochemical cues and physicochemical properties useful for the development of specific materials for TE. Some of these materials have already been studied under *in vivo* conditions, such as the self-healing peptide-based hydrogel from Tondera et al. [184], which did not trigger any inflammatory response when injected in mice, or a peptide-based wound dressing developed by our group [185] which not only presumably suppressed inflammatory reactions but also allowed accelerated wound healing. This suggests that the development of designer supramolecular biopolymers composed of peptides and nucleic acids may bring us closer to optimized healthcare technologies. Under these premises, it is important to promote the translation of promising SBPs into medical devices for detection of molecules, high-end and cell-free prosthesis, or topical treatments. This will certainly facilitate future applications of cell-laden or smart drug delivery TE devices based on SBPs. Another alternative will be the study of bioactive SBP scaffolds for cell-free therapies.

SBPs offer a robust and tunable platform for the creation of personalized materials for TE. However, at this moment, the design is limited to experts in polymer biochemistry. Only the design of DNA origami structures has the potential to allow nonexperts to make use of them. Therefore, future projects could also focus on the development of information technology (IT) tools to facilitate the *in silico* design of SBPs. The generation of such tools would enhance the accessibility of such materials.

Supramolecular biopolymers made from biomolecules hold several advantages over natural biopolymers or synthetic biopolymers, because they give a multitude of

structural diversity by applying rational design and combinatorial approaches. Peptide- and nucleic acid-based materials are employed for TE applications as they are relatively easy to tune due to their sequence-dependent characteristics, such as annealing time, conductivity, hydrophobicity, porosity, binding capacity, stimuli-responsiveness, and biocompatibility. Although the more complex oligosaccharide synthesis is lagging behind peptide and nucleic acid synthesis, current promising new efforts will allow the design and study of more complex oligosaccharide-based materials for TE in the same manner. Currently, designer supramolecular biopolymers are proving their efficacy as cellular scaffolds and versatile modulators of the cellular microenvironment. Further efforts for the inclusion of these materials into advanced TE and healthcare applications are expected in the years to come.

Abbreviations

SBP: Supramolecular biopolymer
SPS: Solid phase synthesis
TE: Tissue engineering
SAP: Self-assembling peptide.

Conflicts of Interest

The authors declare no conflict of interest for this paper.

Authors' Contributions

M.P.P. and A.A.R. contributed equally to the final manuscript; M.M. and Z.K. assisted with a critical revision of the article; C.A.E.H. advised on the content of the manuscript and corrected and approved the final version for publishing.

Acknowledgments

Graphical abstract was created with http://biorender.com/. Funding was provided by KAUST under baseline funds, BAS/1/1075-01-01.

References

[1] L. Wang, C. Gong, X. Yuan, and G. Wei, "Controlling the self-assembly of biomolecules into functional nanomaterials through internal interactions and external stimulations: a review," *Nanomaterials*, vol. 9, no. 2, 2019.

[2] C. A. Hauser and S. Zhang, "Designer self-assembling peptide nanofiber biological materials," *Chemical Society Reviews*, vol. 39, no. 8, pp. 2780–2790, 2010.

[3] R. Otter and P. Besenius, "Supramolecular assembly of functional peptide–polymer conjugates," *Organic & Biomolecular Chemistry*, vol. 17, no. 28, pp. 6719–6734, 2019.

[4] W. S. Marshall and R. J. Kaiser, "Recent advances in the high-speed solid phase synthesis of RNA," *Current Opinion in Chemical Biology*, vol. 8, no. 3, pp. 222–229, 2004.

[5] M. Dhanawat and S. K. Shrivastava, "Solid-phase synthesis of oligosaccharide drugs: a review," *Mini Reviews in Medicinal Chemistry*, vol. 9, no. 2, pp. 169–185, 2009.

[6] V. Mäde, S. Els-Heindl, and A. G. Beck-Sickinger, "Automated solid-phase peptide synthesis to obtain therapeutic peptides," *Beilstein Journal of Organic Chemistry*, vol. 10, pp. 1197–1212, 2014.

[7] P. Chandika, S.-Y. Heo, T.-H. Kim et al., "Recent advances in biological macromolecule based tissue-engineered composite scaffolds for cardiac tissue regeneration applications," *International Journal of Biological Macromolecules*, vol. 164, pp. 2329–2357, 2020.

[8] R. Marmorstein and M. X. Fitzgerald, "Modulation of DNA-binding domains for sequence-specific DNA recognition," *Gene*, vol. 304, pp. 1–12, 2003.

[9] R. L. Robert Lanza, J. Vacanti, A. Anthony, R. L. Robert Lanza, J. Vacanti, and A. Atala, *Principles of Tissue Engineering*, Elsevier, 5th edition, 2020.

[10] S. Sohn, M. V. Buskirk, M. J. Buckenmeyer, R. Londono, and D. Faulk, "Whole organ engineering: approaches, challenges, and future directions," *Applied Sciences*, vol. 10, no. 12, p. 4277, 2020.

[11] K. Uday Chandrika, R. Tripathi, Y. Kameshwari, N. Rangaraj, J. Mahesh Kumar, and S. Singh, "Refunctionalization of decellularized organ scaffold of pancreas by recellularization: whole organ regeneration into functional pancreas," *Tissue Engineering and Regenerative Medicine*, 2020.

[12] S. E. Park, A. Georgescu, and D. Huh, "Organoids-on-a-chip," *Science*, vol. 364, no. 6444, pp. 960–965, 2019.

[13] I. Fernández-Cervantes, N. Rodríguez-Fuentes, L. V. León-Deniz et al., "Cell-free scaffold from jellyfish Cassiopea andromeda (Cnidaria; Scyphozoa) for skin tissue engineering," *Materials Science and Engineering: C*, vol. 111, p. 110748, 2020.

[14] Z. Wang, C. Liu, Y. Xiao et al., "Remodeling of a cell-free vascular graft with nanolamellar intima into a neovessel," *ACS Nano*, vol. 13, no. 9, pp. 10576–10586, 2019.

[15] H. Kwan, E. Chisari, and W. S. Khan, "Cell-free scaffolds as a monotherapy for focal chondral knee defects," *Materials*, vol. 13, no. 2, p. 306, 2020.

[16] S. Hedayat and N. Valeri, "Patient-derived organoids: promises, hurdles and potential clinical applications," *Clinical Oncology*, vol. 32, no. 4, pp. 213–216, 2020.

[17] H. Zhang, T. Fan, W. Chen, Y. Li, and B. Wang, "Recent advances of two-dimensional materials in smart drug delivery nano-systems," *Bioactive Materials*, vol. 5, no. 4, pp. 1071–1086, 2020.

[18] M. Shahriari, V. P. Torchilin, S. M. Taghdisi, K. Abnous, M. Ramezani, and M. Alibolandi, ""Smart" self-assembled structures: toward intelligent dual responsive drug delivery systems," *Biomaterials Science*, vol. 8, no. 21, pp. 5787–5803, 2020.

[19] J. L. Beesley and D. N. Woolfson, "The *de novo* design of α-helical peptides for supramolecular self-assembly," *Current Opinion in Biotechnology*, vol. 58, pp. 175–182, 2019.

[20] K. Ariga, M. Nishikawa, T. Mori, J. Takeya, L. K. Shrestha, and J. P. Hill, "Self-assembly as a key player for materials nanoarchitectonics," *Science and Technology of Advanced Materials*, vol. 20, no. 1, pp. 51–95, 2019.

[21] W. Zhang, X. Yu, Y. Li, Z. Su, K. D. Jandt, and G. Wei, "Protein-mimetic peptide nanofibers: motif design, self-assembly synthesis, and sequence-specific biomedical applications," *Progress in Polymer Science*, vol. 80, pp. 94–124, 2018.

[22] Z. Su, R. Zhang, X.-Y. Yan et al., "The role of architectural engineering in macromolecular self-assemblies via non-

covalent interactions: a molecular LEGO approach," *Progress in Polymer Science*, vol. 103, p. 101230, 2020.

[23] B. O. Okesola, C. Redondo-Gómez, and A. Mata, "18- Multicomponent self-assembly: supramolecular design of complex hydrogels for biomedical applications," in *Self-assembling Biomaterials*, H. S. Azevedo and R. M. P. Silva, Eds., pp. 371–397, Woodhead Publishing, 2018.

[24] D. J. Pochan, J. P. Schneider, J. Kretsinger, B. Ozbas, K. Rajagopal, and L. Haines, "Thermally reversible hydrogels via intramolecular folding and consequent self-assembly of a de novo designed peptide," *Journal of the American Chemical Society*, vol. 125, no. 39, pp. 11802-11803, 2003.

[25] M. L. Daly, Y. Gao, and R. Freeman, "Encoding reversible hierarchical structures with supramolecular peptide–DNA materials," *Bioconjugate Chemistry*, vol. 30, no. 7, pp. 1864–1869, 2019.

[26] R. Freeman, ,M. Han, Z. Álvarez et al., "Reversible self-assembly of superstructured networks," *Science*, vol. 362, no. 6416, pp. 808–813, 2018.

[27] R. D. A. A. Rajapaksha, "7 - Self-assembling smart materials for biomaterials applications," in *Polymer Nanocomposite-Based Smart Materials*, R. Bouhfid, A. E. K. Qaiss, and M. Jawaid, Eds., pp. 121–147, Woodhead Publishing, 2020.

[28] N. Nandi, K. Gayen, S. Ghosh et al., "Amphiphilic peptide-based supramolecular, noncytotoxic, stimuli-responsive hydrogels with antibacterial activity," *Biomacromolecules*, vol. 18, no. 11, pp. 3621–3629, 2017.

[29] B. Guo and P. X. Ma, "Synthetic biodegradable functional polymers for tissue engineering: a brief review," *Science China Chemistry*, vol. 57, no. 4, pp. 490–500, 2014.

[30] P. Zorlutuna, N. Annabi, G. Camci-Unal et al., "Microfabricated biomaterials for engineering 3D tissues," *Advanced Materials*, vol. 24, no. 14, pp. 1782–1804, 2012.

[31] J. Kundu, F. Pati, Y. Hun Jeong, and D.-W. Cho, "Chapter 2 - biomaterials for biofabrication of 3D tissue scaffolds," in *Biofabrication*, G. Forgacs and W. Sun, Eds., pp. 23–46, William Andrew Publishing, Boston, 2013.

[32] J. L. Drury and D. J. Mooney, "Hydrogels for tissue engineering: scaffold design variables and applications," *Biomaterials*, vol. 24, no. 24, pp. 4337–4351, 2003.

[33] C. D. Spicer, "Hydrogel scaffolds for tissue engineering: the importance of polymer choice," *Polymer Chemistry*, vol. 11, no. 2, pp. 184–219, 2020.

[34] A. C. Wan, "Recapitulating Cell-Cell Interactions for Organoid Construction - Are Biomaterials Dispensable?," *Trends in Biotechnology*, vol. 34, no. 9, pp. 711–721, 2016.

[35] P. S. Thakuri, C. Liu, G. D. Luker, and H. Tavana, "Biomaterials-based approaches to tumor spheroid and organoid modeling," *Advanced Healthcare Materials*, vol. 7, no. 6, 2018.

[36] D. F. Williams, "Challenges with the development of biomaterials for sustainable tissue engineering," *Frontiers in Bioengineering and Biotechnology*, vol. 7, no. 127, 2019.

[37] A. da Silva Morais, S. Vieira, X. Zhao et al., "Advanced biomaterials and processing methods for liver regeneration: state-of-the-art and future trends," *Advanced Healthcare Materials*, vol. 9, no. 5, p. 1901435, 2020.

[38] E. A. Guzzi and M. W. Tibbitt, "Additive manufacturing of precision biomaterials," *Advanced Materials*, vol. 32, no. 13, p. 1901994, 2020.

[39] S. Abdulghani and G. R. Mitchell, "Biomaterials for in situ tissue regeneration: a review," *Biomolecules*, vol. 9, no. 11, p. 750, 2019.

[40] A. K. Gaharwar, I. Singh, and A. Khademhosseini, "Engineered biomaterials for in situ tissue regeneration," *Nature Reviews Materials*, vol. 5, no. 9, pp. 686–705, 2020.

[41] E. Mariani, G. Lisignoli, R. M. Borzì, and L. Pulsatelli, "Biomaterials: foreign bodies or tuners for the immune response?," *International Journal of Molecular Sciences*, vol. 20, no. 3, p. 636, 2019.

[42] B. A. Badeau and C. A. DeForest, "Programming stimuli-responsive behavior into biomaterials," *Annual Review of Biomedical Engineering*, vol. 21, no. 1, pp. 241–265, 2019.

[43] F. M. Fumasi, N. Stephanopoulos, and J. L. Holloway, "Reversible control of biomaterial properties for dynamically tuning cell behavior," *Journal of Applied Polymer Science*, vol. 137, no. 25, p. 49058, 2020.

[44] W. Wang, R. Narain, and H. Zeng, "Rational design of self-healing tough hydrogels: a mini review," *Frontiers in Chemistry*, vol. 6, 2018.

[45] S. D. Menikheim and E. B. Lavik, "Self-healing biomaterials: the next generation is nano," *WIREs Nanomedicine and Nanobiotechnology*, vol. 12, no. 6, p. e1641, 2020.

[46] A. Chansaenroj, S. Yodmuang, and J. N. Ferreira, "Trends in salivary gland tissue engineering: from stem cells to secretome and organoid bioprinting," *Tissue Engineering Part B: Reviews*, 2020.

[47] J. He, X. Zhang, X. Xia et al., "Organoid technology for tissue engineering," *Journal of Molecular Cell Biology*, vol. 12, no. 8, pp. 569–579, 2020.

[48] H. Zhang, L. Zhou, and W. Zhang, "Control of scaffold degradation in tissue engineering: a review," *Tissue Engineering Part B: Reviews*, vol. 20, no. 5, pp. 492–502, 2014.

[49] B. Laycock, M. Nikolić, J. M. Colwell et al., "Lifetime prediction of biodegradable polymers," *Progress in Polymer Science*, vol. 71, pp. 144–189, 2017.

[50] A. Szent-Gyorgyi, "The supra- and submolecular in biology," *Journal of Theoretical Biology*, vol. 1, no. 1, pp. 75–82, 1961.

[51] H. Staudinger, "Über polymerisation," *Berichte der deutschen chemischen Gesellschaft (A and B Series)*, vol. 53, no. 6, pp. 1073–1085, 1920.

[52] A. L. Lehninger, "Supramolecular organization of enzyme and membrane systems," *Naturwissenschaften*, vol. 53, no. 3, pp. 57–63, 1966.

[53] R. B. Merrifield, "Solid phase peptide synthesis. I. The synthesis of a tetrapeptide," *Journal of the American Chemical Society*, vol. 85, no. 14, pp. 2149–2154, 1963.

[54] D. Andreu, R. B. Merrifield, H. Steiner, and H. G. Boman, "Solid-phase synthesis of cecropin A and related peptides," *Proceedings of the National Academy of Sciences of the United States of America*, vol. 80, no. 21, pp. 6475–6479, 1983.

[55] S. Mojsov and R. B. Merrifield, "Solid-phase synthesis of crystalline glucagon," *Biochemistry*, vol. 20, no. 10, pp. 2950–2956, 2002.

[56] B. F. Gisin, R. B. Merrifield, and D. C. Tosteson, "Solid-phase synthesis of the cyclododecadepsipeptide valinomycin," *Journal of the American Chemical Society*, vol. 91, no. 10, pp. 2691–2695, 1969.

[57] H. G. Khorana, "Nucleic acid synthesis," *Pure and Applied Chemistry*, vol. 17, no. 3-4, pp. 349–382, 1968.

[58] Y. Zhu, T. Tyrikos-Ergas, K. Schiefelbein, A. Grafmuller, P. H. Seeberger, and M. Delbianco, "Automated access to well-defined ionic oligosaccharides," *Organic & Biomolecular Chemistry*, vol. 18, no. 7, pp. 1349–1353, 2020.

[59] A. A. Joseph, A. Pardo-Vargas, and P. H. Seeberger, "Total synthesis of polysaccharides by automated glycan assembly," *Journal of the American Chemical Society*\, vol. 142, no. 19, pp. 8561–8564, 2020.

[60] A. Longchamp, K. Kaur, D. Macabrey et al., "Hydrogen sulfide-releasing peptide hydrogel limits the development of intimal hyperplasia in human vein segments," *Acta Biomaterialia*, vol. 97, pp. 374–384, 2019.

[61] S. Obuobi, H. K. L. Tay, N. D. T. Tram et al., "Facile and efficient encapsulation of antimicrobial peptides via crosslinked DNA nanostructures and their application in wound therapy," *Journal of Controlled Release*, vol. 313, pp. 120–130, 2019.

[62] Y. J. Zhou, S. Liu, M. Zhao et al., "Injectable extracellular vesicle-released self-assembling peptide nanofiber hydrogel as an enhanced cell-free therapy for tissue regeneration," *Journal of Controlled Release*, vol. 316, pp. 93–104, 2019.

[63] D. Kumar, V. L. Workman, M. O'Brien et al., "Peptide hydrogels-a tissue engineering strategy for the prevention of oesophageal strictures," *Advanced Functional Materials*, vol. 27, no. 38, p. 1702424, 2017.

[64] L. A. Castillo Diaz, M. Elsawy, A. Saiani, J. E. Gough, and A. F. Miller, "Osteogenic differentiation of human mesenchymal stem cells promotes mineralization within a biodegradable peptide hydrogel," *Journal of Tissue Engineering*, vol. 7, Article ID 204173141664978, 2016.

[65] X. Zheng, Z. Ding, W. Cheng et al., "Microskin-inspired injectable MSC-laden hydrogels for scarless wound healing with hair follicles," *Advanced Healthcare Materials*, vol. 9, no. 10, p. 2000041, 2020.

[66] Y. Loo, A. Lakshmanan, M. Ni, L. L. Toh, S. Wang, and C. A. Hauser, "Peptide bioink: self-assembling nanofibrous scaffolds for three-dimensional organotypic cultures," *Nano Letters*, vol. 15, no. 10, pp. 6919–6925, 2015.

[67] Y. Loo, Y. S. Chan, I. Szczerbinska et al., "A chemically well-defined, self-assembling 3D substrate for long-term culture of human pluripotent stem cells," *ACS Applied Biomaterials*, vol. 2, no. 4, pp. 1406–1412, 2019.

[68] J. Conde, N. Oliva, M. Atilano, H. S. Song, and N. Artzi, "Self-assembled RNA-triple-helix hydrogel scaffold for microRNA modulation in the tumour microenvironment," *Nature Materials*, vol. 15, no. 3, pp. 353–363, 2016.

[69] M. S. Ekiz, G. Cinar, M. A. Khalily, and M. O. Guler, "Self-assembled peptide nanostructures for functional materials," *Nanotechnology*, vol. 27, no. 40, p. 402002, 2016.

[70] F. Herbst, D. Döhler, P. Michael, and W. H. Binder, "Self-healing polymers via supramolecular forces," *Macromolecular Rapid Communications*, vol. 34, no. 3, pp. 203–220, 2013.

[71] M. J. Hannon, "Supramolecular DNA recognition," *Chemical Society Reviews*, vol. 36, no. 2, pp. 280–295, 2007.

[72] P. Yakovchuk, E. Protozanova, and M. D. Frank-Kamenetskii, "Base-stacking and base-pairing contributions into thermal stability of the DNA double helix," *Nucleic Acids Research*, vol. 34, no. 2, pp. 564–574, 2006.

[73] P. L. Privalov and C. Crane-Robinson, "Forces maintaining the DNA double helix," *European Biophysics Journal*, vol. 49, no. 5, pp. 315–321, 2020.

[74] S. E. Butcher and A. M. Pyle, "The molecular interactions that stabilize RNA tertiary structure: RNA motifs, patterns, and networks," *Accounts of Chemical Research*, vol. 44, no. 12, pp. 1302–1311, 2011.

[75] K. H. Chan, W. H. Lee, M. Ni, Y. Loo, and C. A. E. Hauser, "C-Terminal Residue of Ultrashort Peptides Impacts on Molecular Self- Assembly, Hydrogelation, and Interaction with Small-Molecule Drugs," *Scientific Reports*, vol. 8, no. 1, 2018.

[76] C. A. E. Hauser, R. Deng, A. Mishra et al., "Natural tri- to hexapeptides self-assemble in water to amyloid -type fiber aggregates by unexpected -helical intermediate structures," *Proceedings of the National Academy of Sciences*, vol. 108, no. 4, pp. 1361–1366, 2011.

[77] J. Wang, K. Liu, R. Xing, and X. Yan, "Peptide self-assembly: thermodynamics and kinetics," *Chemical Society Reviews*, vol. 45, no. 20, pp. 5589–5604, 2016.

[78] Y. Sun and C. Kang, "Self-assembly of peptides into hydrogel," *Journal of Organic & Inorganic Chemistry*, vol. 2, no. 1, 2016.

[79] X. Zhao, F. Pan, H. Xu et al., "Molecular self-assembly and applications of designer peptide amphiphiles," *Chemical Society Reviews*, vol. 39, no. 9, pp. 3480–3498, 2010.

[80] A. Dehsorkhi, V. Castelletto, and I. W. Hamley, "Self-assembling amphiphilic peptides," *Journal of Peptide Science*, vol. 20, no. 7, pp. 453–467, 2014.

[81] M. W. Krone, C. R. Travis, G. Y. Lee, H. J. Eckvahl, K. N. Houk, and M. L. Waters, "More than π–π–π stacking: contribution of amide–π and CH–π interactions to crotonyllysine binding by the AF9 YEATS domain," *Journal of the American Chemical Society*, vol. 142, no. 40, pp. 17048–17056, 2020.

[82] Y. Liu, L. Zhang, and W. Wei, "Effect of noncovalent interaction on the self-assembly of a designed peptide and its potential use as a carrier for controlled bFGF release," *International Journal of Nanomedicine*, vol. Volume 12, pp. 659–670, 2017.

[83] W. Chanasit, Z. J. C. Gonzaga, and B. H. A. Rehm, "Analysis of the alginate O-acetylation machinery in Pseudomonas aeruginosa," *Applied Microbiology and Biotechnology*, vol. 104, no. 5, pp. 2179–2191, 2020.

[84] V. Bertacche, N. Lorenzi, D. Nava, E. Pini, and C. Sinico, "Host–guest interaction study of resveratrol with natural and modified cyclodextrins," *Journal of Inclusion Phenomena and Macrocyclic Chemistry*, vol. 55, no. 3-4, pp. 279–287, 2006.

[85] R. Challa, A. Ahuja, J. Ali, and R. Khar, "Cyclodextrins in drug delivery: an updated review," *AAPS PharmSciTech*, vol. 6, no. 2, pp. E329–E357, 2005.

[86] S. Zhang, T. Holmes, C. Lockshin, and A. Rich, "Spontaneous assembly of a self-complementary oligopeptide to form a stable macroscopic membrane," *Proceedings of the National Academy of Sciences*, vol. 90, no. 8, pp. 3334–3338, 1993.

[87] S. Zhang, C. Lockshin, A. Herbert, E. Winter, and A. Rich, "Zuotin, a putative Z-DNA binding protein in Saccharomyces cerevisiae," *The EMBO Journal*, vol. 11, no. 10, pp. 3787–3796, 1992.

[88] C. J. Pike, D. Burdick, A. J. Walencewicz, C. G. Glabe, and C. W. Cotman, "Neurodegeneration induced by beta-amyloid peptides in vitro: the role of peptide assembly state," *The Journal of Neuroscience*, vol. 13, no. 4, pp. 1676–1687, 1993.

[89] B. Soreghan, J. Kosmoski, and C. Glabe, "Surfactant properties of Alzheimer's A beta peptides and the mechanism of amyloid aggregation," *Journal of Biological Chemistry*, vol. 269, no. 46, pp. 28551–28554, 1994.

[90] R. Jayakumar, C. Jayanthy, and L. Gomathy, "Peptide aggregates: a novel model system to study self-assembly of peptides," *International Journal of Peptide and Protein Research*, vol. 45, no. 2, pp. 129–137, 1995.

[91] A. Aggeli, M. Bell, N. Boden et al., "Responsive gels formed by the spontaneous self-assembly of peptides into polymeric β-sheet tapes," *Nature*, vol. 386, no. 6622, pp. 259–262, 1997.

[92] L. Wang, S. K. Murthy, W. H. Fowle, G. A. Barabino, and R. L. Carrier, "Influence of micro-well biomimetic topography on intestinal epithelial Caco-2 cell phenotype," *Biomaterials*, vol. 30, no. 36, pp. 6825–6834, 2009.

[93] H. J. Kim, D. Huh, G. Hamilton, and D. E. Ingber, "Human gut-on-a-chip inhabited by microbial flora that experiences intestinal peristalsis-like motions and flow," *Lab on a Chip*, vol. 12, no. 12, pp. 2165–2174, 2012.

[94] A. Lakshmanan, D. W. Cheong, A. Accardo, E. Di Fabrizio, C. Riekel, and C. A. E. Hauser, "Aliphatic peptides show similar self-assembly to amyloid core sequences, challenging the importance of aromatic interactions in amyloidosis," *Proceedings of the National Academy of Sciences*, vol. 110, no. 2, pp. 519–524, 2013.

[95] Y. Loo, Y. C. Wong, E. Z. Cai et al., "Ultrashort peptide nanofibrous hydrogels for the acceleration of healing of burn wounds," *Biomaterials*, vol. 35, no. 17, pp. 4805–4814, 2014.

[96] W. Y. Seow, G. Salgado, E. B. Lane, and C. A. Hauser, "Transparent crosslinked ultrashort peptide hydrogel dressing with high shape-fidelity accelerates healing of full-thickness excision wounds," *Scientific Reports*, vol. 6, no. 1, p. 32670, 2016.

[97] M. R. Reithofer, K. H. Chan, A. Lakshmanan et al., "Ligation of anti-cancer drugs to self-assembling ultrashort peptides by click chemistry for localized therapy," *Chemical Science*, vol. 5, no. 2, pp. 625–630, 2014.

[98] S. Ghalayini, H. H. Susapto, S. Hall, K. Kahin, and C. A. E. Hauser, "Preparation and printability of ultrashort self-assembling peptide nanoparticles," *International Journal of Bioprinting*, vol. 5, no. 2, p. 239, 2019.

[99] M. Ni, G. Tresset, C. Iliescu, and C. A. E. Hauser, "Ultrashort peptide theranostic nanoparticles by microfluidic-assisted rapid solvent exchange," *IEEE Transactions on Nano-Bioscience*, vol. 19, no. 4, pp. 627–632, 2020.

[100] E. Di Fabrizio, S. Schlücker, J. Wenger et al., "Roadmap on biosensing and photonics with advanced nano-optical methods," *Journal of Optics*, vol. 18, no. 6, article 063003, 2016.

[101] M. Ni, S. Zhuo, C. Iliescu et al., "Self-assembling amyloid-like peptides as exogenous second harmonic probes for bioimaging applications," *Journal of Biophotonics*, vol. 12, no. 12, article e201900065, 2019.

[102] I. Insua and J. Montenegro, "1D to 2D self assembly of cyclic peptides," *Journal of the American Chemical Society*, vol. 142, no. 1, pp. 300–307, 2019.

[103] J. Shi, G. Fichman, and J. P. Schneider, "Enzymatic control of the conformational landscape of self-assembling peptides," *Angewandte Chemie-International Edition*, vol. 57, no. 35, pp. 11188–11192, 2018.

[104] K. Nagy-Smith, E. Moore, J. Schneider, and R. Tycko, "Molecular structure of monomorphic peptide fibrils within a kinetically trapped hydrogel network," *Proceedings of the National Academy of Sciences of the United States of America*, vol. 112, no. 32, pp. 9816–9821, 2015.

[105] P. K. Gavel, N. Kumar, H. S. Parmar, and A. K. Das, "Evaluation of a peptide-based coassembled nanofibrous and thixotropic hydrogel for dermal wound healing," *ACS Applied Bio Materials*, vol. 3, no. 5, pp. 3326–3336, 2020.

[106] X. D. Kong, J. Moriya, V. Carle et al., "De novo development of proteolytically resistant therapeutic peptides for oral administration," *Nature Biomedical Engineering*, vol. 4, no. 5, pp. 560–571, 2020.

[107] D. Umeno, T. Kano, and M. Maeda, "Affinity adsorption separation of mutagenic molecules by polyacrylamide hydrogels comprising double-stranded DNA," *Analytica Chimica Acta*, vol. 365, no. 1-3, pp. 101–108, 1998.

[108] J. S. Kahn, A. Trifonov, A. Cecconello, W. Guo, C. Fan, and I. Willner, "Integration of switchable DNA-based hydrogels with surfaces by the hybridization chain reaction," *Nano Letters*, vol. 15, no. 11, pp. 7773–7778, 2015.

[109] S. H. Um, J. B. Lee, N. Park, S. Y. Kwon, C. C. Umbach, and D. Luo, "Enzyme-catalysed assembly of DNA hydrogel," *Nature Materials*, vol. 5, no. 10, pp. 797–801, 2006.

[110] Y. J. Wang, Y. Shao, X. Ma et al., "Constructing tissuelike complex structures using cell-laden DNA hydrogel bricks," *ACS Applied Materials & Interfaces*, vol. 9, no. 14, pp. 12311–12315, 2017.

[111] Y. Sato, T. Sakamoto, and M. Takinoue, "Sequence-based engineering of dynamic functions of micrometer-sized DNA droplets," *Science Advances*, vol. 6, no. 23, article eaba3471, 2020.

[112] H. Yuan, C. Chen, Y. Liu, T. Lu, and Z. Wu, "Strategies in cell-free tissue-engineered vascular grafts," *Journal of Biomedical Materials Research Part A*, vol. 108, no. 3, pp. 426–445, 2020.

[113] J. Cui, D. Wu, Q. Sun et al., "A PEGDA/DNA hybrid hydrogel for cell-free protein synthesis," *Frontiers in Chemistry*, vol. 8, p. 28, 2020.

[114] C. Yao, H. Tang, W. Wu et al., "Double rolling circle amplification generates physically cross-linked DNA network for stem cell fishing," *Journal of the American Chemical Society*, vol. 142, no. 7, pp. 3422–3429, 2020.

[115] H. Qi, M. Ghodousi, Y. du et al., "DNA-directed self-assembly of shape-controlled hydrogels," *Nature Communications*, vol. 4, no. 1, p. 2275, 2013.

[116] C. Du and R. J. Hill, "Complementary-DNA-strand cross-linked polyacrylamide hydrogels,," *Macromolecules*, vol. 52, no. 17, pp. 6683–6697, 2019.

[117] A. J. Anderson, H. R. Culver, S. J. Bryant, and C. N. Bowman, "Viscoelastic and thermoreversible networks crosslinked by non-covalent interactions between "clickable" nucleic acid oligomers and DNA," *Polymer Chemistry*, vol. 11, no. 17, pp. 2959–2968, 2020.

[118] M. A. English, L. R. Soenksen, R. V. Gayet et al., "Programmable CRISPR-responsive smart materials," *Science*, vol. 365, no. 6455, pp. 780–785, 2019.

[119] F. Li, D. Lyu, S. Liu, and W. Guo, "DNA hydrogels and microgels for biosensing and biomedical applications," *Advanced Materials*, vol. 32, no. 3, article e1806538, 2020.

[120] J. Chen, Y. Zhu, H. Liu, and L. Wang, "Tailoring DNA self-assembly to build hydrogels," *Topics in Current Chemistry*, vol. 378, no. 2, p. 32, 2020.

[121] D. Xu, K. Arnold, and J. Liu, "Using structurally defined oligosaccharides to understand the interactions between proteins and heparan sulfate," *Current Opinion in Structural Biology*, vol. 50, pp. 155–161, 2018.

[122] A. Kumar and A. Kumar, "The virtuous potential of chitosan oligosaccharide for promising biomedical applications," *Journal of Materials Research*, vol. 35, no. 9, pp. 1123–1134, 2020.

[123] E. A. Turley, P. W. Noble, and L. Y. Bourguignon, "Signaling properties of hyaluronan receptors," *Journal of Biological Chemistry*, vol. 277, no. 7, pp. 4589–4592, 2002.

[124] L. Kang, W. Jia, M. Li et al., "Hyaluronic acid oligosaccharide-modified collagen nanofibers as vascular tissue-engineered scaffold for promoting endothelial cell proliferation," *Carbohydrate Polymers*, vol. 223, p. 115106, 2019.

[125] M. Li, X. Zhang, W. Jia et al., "Improving in vitro biocompatibility on biomimetic mineralized collagen bone materials modified with hyaluronic acid oligosaccharide," *Materials Science & Engineering. C, Materials for Biological Applications*, vol. 104, p. 110008, 2019.

[126] X. Lv, Y. Liu, S. Song et al., "Influence of chitosan oligosaccharide on the gelling and wound healing properties of injectable hydrogels based on carboxymethyl chitosan/alginate polyelectrolyte complexes," *Carbohydrate Polymers*, vol. 205, pp. 312–321, 2019.

[127] G. Sandri, C. Aguzzi, S. Rossi et al., "Halloysite and chitosan oligosaccharide nanocomposite for wound healing," *Acta Biomaterialia*, vol. 57, pp. 216–224, 2017.

[128] C. Muanprasat and V. Chatsudthipong, "Chitosan oligosaccharide: biological activities and potential therapeutic applications," *Pharmacology & Therapeutics*, vol. 170, pp. 80–97, 2017.

[129] L. Shi, B. Fang, Y. Yong et al., "Chitosan oligosaccharide-mediated attenuation of LPS-induced inflammation in IPEC-J2 cells is related to the TLR4/NF-κB signaling pathway," *Carbohydrate Polymers*, vol. 219, pp. 269–279, 2019.

[130] K. Toshima and K. Tatsuta, "Recent progress in O-glycosylation methods and its application to natural-products synthesis," *Chemical Reviews*, vol. 93, no. 4, pp. 1503–1531, 1993.

[131] K. M. Yamada and M. Sixt, "Mechanisms of 3D cell migration," *Nature Reviews Molecular Cell Biology*, vol. 20, no. 12, pp. 738–752, 2019.

[132] I. Apsite, J. M. Uribe, A. F. Posada, S. Rosenfeldt, S. Salehi, and L. Ionov, "4D biofabrication of skeletal muscle microtissues," *Biofabrication*, vol. 12, no. 1, article 015016, 2019.

[133] C. Zuppinger, "3D cardiac cell culture: a critical review of current technologies and applications," *Frontiers in Cardiovascular Medicine*, vol. 6, p. 87, 2019.

[134] B. Widholz, S. Tsitlakidis, B. Reible, A. Moghaddam, and F. Westhauser, "Pooling of patient-derived mesenchymal stromal cells reduces inter-individual confounder-associated variation without negative impact on cell viability, proliferation and osteogenic differentiation," *Cells*, vol. 8, no. 6, p. 633, 2019.

[135] M. del Carmen Ortuño-Costela, M. García-López, V. Cerrada, and M. E. Gallardo, "iPSCs: a powerful tool for skeletal muscle tissue engineering," *Journal of Cellular and Molecular Medicine*, vol. 23, no. 6, pp. 3784–3794, 2019.

[136] J. A. Brassard and M. P. Lutolf, "Engineering stem cell self-organization to build better organoids," *Cell Stem Cell*, vol. 24, no. 6, pp. 860–876, 2019.

[137] K. H. Hillebrandt, H. Everwien, N. Haep, E. Keshi, J. Pratschke, and I. M. Sauer, "Strategies based on organ decellularization and recellularization," *Transplant International*, vol. 32, no. 6, pp. 571–585, 2019.

[138] M. Mabrouk, H. H. Beherei, and D. B. Das, "Recent progress in the fabrication techniques of 3D scaffolds for tissue engineering," *Materials Science and Engineering: C*, vol. 110, article 110716, 2020.

[139] T. Tsuchiya, R. Doi, T. Obata, G. Hatachi, and T. Nagayasu, "Lung microvascular niche, repair, and engineering," *Frontiers in Bioengineering and Biotechnology*, vol. 8, no. 105, 2020.

[140] J. Rubert, P. J. Schweiger, F. Mattivi, K. Tuohy, K. B. Jensen, and A. Lunardi, "Intestinal organoids: a tool for modelling diet–microbiome–host interactions," *Trends in Endocrinology and Metabolism*, vol. 31, no. 11, pp. 848–858, 2020.

[141] A. Fatehullah, S. H. Tan, and N. Barker, "Organoids as an in vitro model of human development and disease," *Nature Cell Biology*, vol. 18, no. 3, pp. 246–254, 2016.

[142] R. Subbiah and R. E. Guldberg, "Materials science and design principles of growth factor delivery systems in tissue engineering and regenerative medicine," *Advanced Healthcare Materials*, vol. 8, no. 1, p. 1801000, 2019.

[143] W. Ha, Z. H. Wang, X. B. Zhao, and Y. P. Shi, "Reinforced supramolecular hydrogels from attapulgite and cyclodextrin pseudopolyrotaxane for sustained intra-articular drug delivery," *Macromolecular Bioscience*, p. 2000299, 2020.

[144] C. Fiorica, F. S. Palumbo, G. Pitarresi et al., "A hyaluronic acid/cyclodextrin based injectable hydrogel for local doxorubicin delivery to solid tumors," *International Journal of Pharmaceutics*, vol. 589, p. 119879, 2020.

[145] H. J. Lee, P. T. Le, H. J. Kwon, and K. D. Park, "Supramolecular assembly of tetronic–adamantane and poly (β-cyclodextrin) as injectable shear-thinning hydrogels," *Journal of Materials Chemistry B*, vol. 7, no. 21, pp. 3374–3382, 2019.

[146] A. Rey-Rico and M. Cucchiarini, "Supramolecular cyclodextrin-based hydrogels for controlled gene delivery," *Polymers*, vol. 11, no. 3, p. 514, 2019.

[147] Q. Wang, N. Jiang, B. Fu, F. Huang, and J. Liu, "Self-assembling peptide-based nanodrug delivery systems," *Biomaterials Science*, vol. 7, no. 12, pp. 4888–4911, 2019.

[148] M. Tao, J. Liu, S. He, K. Xu, and W. Zhong, "In situ hydrogelation of forky peptides in prostate tissue for drug delivery," *Soft Matter*, vol. 15, no. 20, pp. 4200–4207, 2019.

[149] Q. Zhang, Q. Jiang, N. Li et al., "DNA origami as an in vivo drug delivery vehicle for cancer therapy," *ACS Nano*, vol. 8, no. 7, pp. 6633–6643, 2014.

[150] Q. Jiang, S. Liu, J. Liu, Z.-G. Wang, and B. Ding, "Rationally designed DNA-origami nanomaterials for drug delivery in vivo," *Advanced Materials*, vol. 31, no. 45, article 1804785, 2019.

[151] Z. Ge, L. Guo, G. Wu et al., "DNA origami-enabled engineering of ligand–drug conjugates for targeted drug delivery," *Small*, vol. 16, no. 16, article 1904857, 2020.

[152] R. K. Jain, P. Au, J. Tam, D. G. Duda, and D. Fukumura, "Engineering vascularized tissue," *Nature Biotechnology*, vol. 23, no. 7, pp. 821–823, 2005.

[153] N. Asakawa, T. Shimizu, Y. Tsuda et al., "Pre-vascularization of in vitro three-dimensional tissues created by cell sheet engineering," *Biomaterials*, vol. 31, no. 14, pp. 3903–3909, 2010.

[154] K. H. Hussein, K.-M. Park, L. Yu, S.-H. Song, H.-M. Woo, and H.-H. Kwak, "Vascular reconstruction: a major challenge in developing a functional whole solid organ graft from decellularized organs," *Acta Biomaterialia*, vol. 103, pp. 68–80, 2020.

[155] L. E. Bertassoni, M. Cecconi, V. Manoharan et al., "Hydrogel bioprinted microchannel networks for vascularization of tissue engineering constructs," *Lab on a Chip*, vol. 14, no. 13, pp. 2202–2211, 2014.

[156] J. Rouwkema and A. Khademhosseini, "Vascularization and angiogenesis in tissue engineering: beyond creating static networks," *Trends in Biotechnology*, vol. 34, no. 9, pp. 733–745, 2016.

[157] M. A. Ruehle, E. A. Eastburn, S. A. LaBelle et al., "Extracellular matrix compression temporally regulates microvascular angiogenesis," *Science Advances*, vol. 6, no. 34, article eabb6351, 2020.

[158] J. Qi, Y. Yan, B. Cheng et al., "Enzymatic formation of an injectable hydrogel from a glycopeptide as a biomimetic scaffold for vascularization," *ACS Applied Materials & Interfaces*, vol. 10, no. 7, pp. 6180–6189, 2018.

[159] Y. Zheng, W. Yuan, H. Liu, S. Huang, L. Bian, and R. Guo, "Injectable supramolecular gelatin hydrogel loading of resveratrol and histatin-1 for burn wound therapy," *Biomaterials Science*, vol. 8, no. 17, pp. 4810–4820, 2020.

[160] J.-H. Lee, P. Parthiban, G.-Z. Jin, J. C. Knowles, and H.-W. Kim, "Materials roles for promoting angiogenesis in tissue regeneration," *Progress in Materials Science*, no. article 100732, 2020.

[161] T. Takebe, B. Zhang, and M. Radisic, "Synergistic engineering: organoids meet organs-on-a-chip," *Cell Stem Cell*, vol. 21, no. 3, pp. 297–300, 2017.

[162] M. J. Kratochvil, A. J. Seymour, T. L. Li, S. P. Paşca, C. J. Kuo, and S. C. Heilshorn, "Engineered materials for organoid systems," *Nature Reviews Materials*, vol. 4, no. 9, pp. 606–622, 2019.

[163] L. C. Bahlmann, A. Fokina, and M. S. Shoichet, "Dynamic bioengineered hydrogels as scaffolds for advanced stem cell and organoid culture," *MRS Communications*, vol. 7, no. 3, pp. 472–486, 2017.

[164] L. Saunders and P. X. Ma, "Self-healing supramolecular hydrogels for tissue engineering applications," *Macromolecular Bioscience*, vol. 19, no. 1, article 1800313, 2019.

[165] L. Cai, S. Liu, J. Guo, and Y.-G. Jia, "Polypeptide-based self-healing hydrogels: design and biomedical applications," *Acta Biomaterialia*, vol. 113, pp. 84–100, 2020.

[166] P. Ren, J. Li, L. Zhao et al., "Dipeptide self-assembled hydrogels with shear-thinning and instantaneous self-healing properties determined by peptide sequences," *ACS Applied Materials & Interfaces*, vol. 12, no. 19, pp. 21433–21440, 2020.

[167] W. L. Ng, C. K. Chua, and Y.-F. Shen, "Print me an organ! Why we are not there yet," *Progress in Polymer Science*, vol. 97, p. 101145, 2019.

[168] J. M. Lee, W. L. Ng, and W. Y. Yeong, "Resolution and shape in bioprinting: strategizing towards complex tissue and organ printing," *Applied Physics Reviews*, vol. 6, no. 1, article 011307, 2019.

[169] W. L. Ng, A. Chan, Y. S. Ong, and C. K. Chua, "Deep learning for fabrication and maturation of 3D bioprinted tissues and organs," *Virtual and Physical Prototyping*, vol. 15, no. 3, pp. 340–358, 2020.

[170] M. Vaidya, "Startups tout commercially 3D-printed tissue for drug screening," *Nature Medicine*, vol. 21, no. 1, p. 2, 2015.

[171] T. A. Mir, S. Iwanaga, T. Kurooka, H. Toda, S. Sakai, and M. Nakamura, "Biofabrication offers future hope for tackling various obstacles and challenges in tissue engineering and regenerative medicine: A Prospective," *International Journal of Bioprinting*, vol. 5, no. 1, 2019.

[172] I. T. Ozbolat and M. Hospodiuk, "Current advances and future perspectives in extrusion-based bioprinting," *Biomaterials*, vol. 76, pp. 321–343, 2016.

[173] C. Silva, C. J. Cortés-Rodriguez, J. Hazur, S. Reakasame, and A. R. Boccaccini, "Rational design of a triple-layered coaxial extruder system: in silico and in vitro evaluations directed toward optimizing cell viability," *International Journal of Bioprinting*, vol. 6, no. 4, 2020.

[174] H. Gudapati, M. Dey, and I. Ozbolat, "A comprehensive review on droplet-based bioprinting: past, present and future," *Biomaterials*, vol. 102, pp. 20–42, 2016.

[175] W. L. Ng, J. M. Lee, W. Y. Yeong, and M. W. Naing, "Microvalve-based bioprinting–process, bio-inks and applications," *Biomaterials Science*, vol. 5, no. 4, pp. 632–647, 2017.

[176] D. Takagi, W. Lin, T. Matsumoto et al., "High-precision 3D inkjet technology for live cell bioprinting," *International Journal of Bioprinting*, vol. 5, no. 2, 2019.

[177] W. L. Ng, J. M. Lee, M. Zhou et al., "Vat polymerization-based bioprinting—process, materials, applications and regulatory challenges," *Biofabrication*, vol. 12, no. 2, article 022001, 2020.

[178] J. Zhang, Q. Hu, S. Wang, J. Tao, and M. Gou, "Digital light processing based three-dimensional printing for medical applications," *International Journal of Bioprinting*, vol. 6, no. 1, 2020.

[179] L. Moroni, J. A. Burdick, C. Highley et al., "Biofabrication strategies for 3D in vitro models and regenerative medicine," *Nature Reviews Materials*, vol. 3, no. 5, pp. 21–37, 2018.

[180] B. E. Kelly, I. Bhattacharya, H. Heidari, M. Shusteff, C. M. Spadaccini, and H. K. Taylor, "Volumetric additive manufacturing via tomographic reconstruction," *Science*, vol. 363, no. 6431, pp. 1075–1079, 2019.

[181] M. Müller, P. Fisch, M. Molnar et al., "Development and thorough characterization of the processing steps of an ink for 3D printing for bone tissue engineering," *Materials Science & Engineering. C, Materials for Biological Applications*, vol. 108, p. 110510, 2020.

[182] M. Lee, K. Bae, C. Levinson, and M. Zenobi-Wong, "Nanocomposite bioink exploits dynamic covalent bonds between nanoparticles and polysaccharides for precision bioprinting," *Biofabrication*, vol. 12, no. 2, article 025025, 2020.

[183] S. W. Kim, D. Y. Kim, H. H. Roh, H. S. Kim, J. W. Lee, and K. Y. Lee, "Three-dimensional bioprinting of cell-laden constructs using polysaccharide-based self-healing hydrogels," *Biomacromolecules*, vol. 20, no. 5, pp. 1860–1866, 2019.

[184] C. Tondera, R. Wieduwild, E. Roder, C. Werner, Y. X. Zhang, and J. Pietzsch, "In vivo examination of an injectable hydrogel system crosslinked by peptide-oligosaccharide interaction in immunocompetent nude mice," *Advanced Functional Materials*, vol. 27, no. 15, article 1605189, 2017.

[185] W. T. Arab, A. M. Niyas, K. Seferji, H. H. Susapto, and C. A. E. Hauser, "Evaluation of peptide nanogels for accelerated wound healing in normal micropigs," *Frontiers in Nanoscience and Nanotechnology*, vol. 4, no. 4, pp. 1–9, 2018.

[186] C. Li, A. Faulkner-Jones, A. R. Dun et al., "Rapid formation of a supramolecular polypeptide-DNA hydrogel for in situ three-dimensional multilayer bioprinting," *Angewandte Chemie International Edition*, vol. 54, no. 13, pp. 3957–3961, 2015.

[187] C. M. Niemeyer, M. Adler, S. Gao, and L. Chi, "Supramolecular DNA-streptavidin nanocircles with a covalently attached oligonucleotide moiety," *Journal of Biomolecular Structure and Dynamics*, vol. 20, no. 2, pp. 223–230, 2002.

[188] C. K. Lee, S. R. Shin, S. H. Lee et al., "DNA hydrogel fiber with self-entanglement prepared by using an ionic liquid," *Angewandte Chemie-International Edition*, vol. 47, no. 13, pp. 2470–2474, 2008.

[189] S. W. Shin, K. S. Park, M. S. Jang et al., "X-DNA origami-networked core-supported lipid stratum," *Langmuir*, vol. 31, no. 3, pp. 912–916, 2015.

[190] M. C. Morán, M. G. Miguel, and B. Lindman, "DNA gel particles from single and double-tail surfactants: supramolecular assemblies and release characteristics," *Soft Matter*, vol. 7, no. 5, pp. 2001–2010, 2011.

[191] Z. Huang, G. N. Kangovi, W. Wen, S. Lee, and L. Niu, "An RNA aptamer capable of forming a hydrogel by self-assembly," *Biomacromolecules*, vol. 18, no. 7, pp. 2056–2063, 2017.

[192] J. Gao, C. Tang, M. A. Elsawy, A. M. Smith, A. F. Miller, and A. Saiani, "Controlling self-assembling peptide hydrogel properties through network topology," *Biomacromolecules*, vol. 18, no. 3, pp. 826–834, 2017.

[193] Y. Hu, J. S. Kahn, W. Guo et al., "Reversible modulation of DNA-based hydrogel shapes by internal stress interactions," *Journal of the American Chemical Society*, vol. 138, no. 49, pp. 16112–16119, 2016.

[194] P. K. Nguyen, W. Gao, S. D. Patel et al., "Self-assembly of a dentinogenic peptide hydrogel," *ACS Omega*, vol. 3, no. 6, pp. 5980–5987, 2018.

[195] S. Wan, S. Borland, S. M. Richardson, C. L. R. Merry, A. Saiani, and J. E. Gough, "Self-assembling peptide hydrogel for intervertebral disc tissue engineering," *Acta Biomaterialia*, vol. 46, pp. 29–40, 2016.

[196] M. Ghosh, M. Halperin-Sternfeld, I. Grinberg, and L. Adler-Abramovich, "Injectable alginate-peptide composite hydrogel as a scaffold for bone tissue regeneration," *Nanomaterials*, vol. 9, no. 4, 2019.

[197] N. C. Carrejo, A. N. Moore, T. L. Lopez Silva et al., "Multidomain peptide hydrogel accelerates healing of full-thickness wounds in diabetic mice," *ACS Biomaterials Science & Engineering*, vol. 4, no. 4, pp. 1386–1396, 2017.

[198] A. N. Moore, T. L. L. Silva, N. C. Carrejo, C. A. O. Marmolejo, I. C. Li, and J. D. Hartgerink, "Nanofibrous peptide hydrogel elicits angiogenesis and neurogenesis without drugs, proteins, or cells," *Biomaterials*, vol. 161, pp. 154–163, 2018.

[199] S. Motamed, M. P. Del Borgo, K. Kulkarni et al., "A self-assembling beta-peptide hydrogel for neural tissue engineering," *Soft Matter*, vol. 12, no. 8, pp. 2243–2246, 2016.

[200] M. Sheikholeslam, S. D. Wheeler, K. G. Duke, M. Marsden, M. Pritzker, and P. Chen, "Peptide and peptide-carbon nanotube hydrogels as scaffolds for tissue & 3D tumor engineering," *Acta Biomaterialia*, vol. 69, pp. 107–119, 2018.

[201] J. D. Tang, C. Mura, and K. J. Lampe, "Stimuli-responsive, pentapeptide, nanofiber hydrogel for tissue engineering," *Journal of the American Chemical Society*, vol. 141, no. 12, pp. 4886–4899, 2019.

[202] H. Jin, C. Wan, Z. Zou et al., "Tumor ablation and therapeutic immunity induction by an injectable peptide hydrogel," *ACS Nano*, vol. 12, no. 4, pp. 3295–3310, 2018.

[203] P. Hitscherich, P. K. Nguyen, A. Kannan et al., "Injectable self-assembling peptide hydrogels for tissue writing and embryonic stem cell culture," *Journal of Biomedical Nanotechnology*, vol. 14, no. 4, pp. 802–807, 2018.

[204] E. Cheng, Y. Xing, P. Chen et al., "A pH-triggered, fast-responding DNA hydrogel," *Angewandte Chemie-International Edition*, vol. 48, no. 41, pp. 7660–7663, 2009.

[205] H. Y. Jia, J. Z. Shi, Y. Shao, and D. S. Liu, "DNA hydrogels formed of bended DNA scaffolds and properties study," *Chinese Journal of Polymer Science*, vol. 35, no. 10, pp. 1307–1314, 2017.

[206] T. Wang, Y. Zheng, Y. Shi, and L. Zhao, "pH-responsive calcium alginate hydrogel laden with protamine nanoparticles and hyaluronan oligosaccharide promotes diabetic wound healing by enhancing angiogenesis and antibacterial activity," *Drug Delivery and Translational Research*, vol. 9, no. 1, pp. 227–239, 2019.

[207] X. Li, M. Fu, J. Wu et al., "pH-sensitive peptide hydrogel for glucose-responsive insulin delivery," *Acta Biomaterialia*, vol. 51, pp. 294–303, 2017.

[208] F. Wang, R.-b. Zhong, Q. Tang et al., "An ATP-responsive linear DNA hydrogel," *Acta Polymerica Sinica*, no. 5, pp. 553–558, 2018.

[209] W. Guo, C. Yang, L. Cui, H. Lin, and F. Qu, "An enzyme-responsive controlled release system of mesoporous silica coated with konjac oligosaccharide," *Langmuir*, vol. 30, no. 1, pp. 243–249, 2014.

[210] N. D. Mansukhani, L. M. Guiney, Z. Wei et al., "Optothermally reversible carbon nanotube-DNA supramolecular hybrid hydrogels," *Macromolecular Rapid Communications*, vol. 39, no. 2, article 1700587, 2018.

[211] Y. Si, L. Xu, N. Wang, J. Zheng, R. Yang, and J. Li, "Target microRNA-responsive DNA hydrogel-based surface-enhanced Raman scattering sensor arrays for microRNA-marked cancer screening," *Analytical Chemistry*, vol. 92, no. 3, pp. 2649–2655, 2020.

[212] A. Roy, P. P. Maity, A. Bose, S. Dhara, and S. Pal, "β-Cyclodextrin based pH and thermo-responsive biopolymeric hydrogel as a dual drug carrier," *Materials Chemistry Frontiers*, vol. 3, no. 3, pp. 385–393, 2019.

[213] A. Roy, P. P. Maity, S. Dhara, and S. Pal, "Biocompatible, stimuli-responsive hydrogel of chemically crosslinked β-cyclodextrin as amoxicillin carrier," *Journal of Applied Polymer Science*, vol. 135, no. 10, p. 45939, 2018.

[214] J. Song, K. Im, S. Hwang et al., "DNA hydrogel delivery vehicle for light-triggered and synergistic cancer therapy," *Nanoscale*, vol. 7, no. 21, pp. 9433–9437, 2015.

[215] Z. Li, G. Davidson-Rozenfeld, M. Vázquez-González et al., "Multi-triggered supramolecular DNA/bipyridinium dithienylethene hydrogels driven by light, redox, and chemical stimuli for shape-memory and self-healing applications," *Journal of the American Chemical Society*, vol. 140, no. 50, pp. 17691–17701, 2018.

[216] R. Huang, J. Han, R. Wang et al., "Surfactant-free solid dispersion of BCS class IV drug in an amorphous chitosan oligosaccharide matrix for concomitant dissolution in vitro - permeability increase," *European Journal of Pharmaceutical Sciences*, vol. 130, pp. 147–155, 2019.

[217] J. Wang, H. Wang, H. Wang et al., "Nonviolent self-catabolic DNAzyme nanosponges for smart anticancer drug delivery," *ACS Nano*, vol. 13, no. 5, pp. 5852–5863, 2019.

[218] D. Lyu, S. Chen, and W. Guo, "Liposome crosslinked polyacrylamide/DNA hydrogel: a smart controlled-release system for small molecular payloads," *Small*, vol. 14, no. 15, article e1704039, 2018.

[219] Y. Yamada, N. L. Patel, J. D. Kalen, and J. P. Schneider, "Design of a peptide-based electronegative hydrogel for the direct encapsulation, 3D culturing, in vivo syringe-based delivery, and long-term tissue engraftment of cells," *ACS Applied Materials & Interfaces*, vol. 11, no. 38, pp. 34688–34697, 2019.

[220] N. Singha, A. Srivastava, B. Pramanik et al., "Unusual confinement properties of a water insoluble small peptide hydrogel," *Chemical Science*, vol. 10, no. 23, pp. 5920–5928, 2019.

[221] F. Komura, K. Okuzumi, Y. Takahashi, Y. Takakura, and M. Nishikawa, "Development of RNA/DNA hydrogel targeting toll-like receptor 7/8 for sustained RNA release and potent immune activation," *Molecules*, vol. 25, no. 3, p. 728, 2020.

[222] Y. Ping, C. Liu, Z. Zhang, K. L. Liu, J. Chen, and J. Li, "Chitosan-graft-(PEI-β-cyclodextrin) copolymers and their supramolecular PEGylation for DNA and siRNA delivery," *Biomaterials*, vol. 32, no. 32, pp. 8328–8341, 2011.

[223] R. M. Raftery, D. P. Walsh, L. Blokpoel Ferreras et al., "Highly versatile cell-penetrating peptide loaded scaffold for efficient and localised gene delivery to multiple cell types: from development to application in tissue engineering," *Biomaterials*, vol. 216, p. 119277, 2019.

[224] Y. Nishida, S. Ohtsuki, Y. Araie et al., "Self-assembling DNA hydrogel-based delivery of immunoinhibitory nucleic acids to immune cells," *Nanomedicine*, vol. 12, no. 1, pp. 123–130, 2016.

[225] M. Shin, J. H. Ryu, J. P. Park, K. Kim, J. W. Yang, and H. Lee, "DNA/tannic acid hybrid gel exhibiting biodegradability, extensibility, tissue adhesiveness, and hemostatic ability," *Advanced Functional Materials*, vol. 25, no. 8, pp. 1270–1278, 2015.

[226] D. J. Smith, G. A. Brat, S. H. Medina et al., "A multiphase transitioning peptide hydrogel for suturing ultrasmall vessels," *Nature Biotechnology*, vol. 11, no. 1, pp. 95–102, 2016.

[227] T. Yata, Y. Takahashi, M. Tan et al., "DNA nanotechnology-based composite-type gold nanoparticle-immunostimulatory DNA hydrogel for tumor photothermal immunotherapy," *Biomaterials*, vol. 146, pp. 136–145, 2017.

[228] Y. Shao, Z. Y. Sun, Y. Wang, B. D. Zhang, D. Liu, and Y. M. Li, "Designable immune therapeutical vaccine system based on DNA supramolecular hydrogels," *ACS Applied Materials & Interfaces*, vol. 10, no. 11, pp. 9310–9314, 2018.

Hindawi
Advances in Polymer Technology
Volume 2020, Article ID 5462949, 9 pages
https://doi.org/10.1155/2020/5462949

Research Article

Preparation and Characterization of Liposomal Everolimus by Thin-Film Hydration Technique

Gabriela Torres-Flores,[1] Azucena Gonzalez-Horta,[2] Yadira I. Vega-Cantu,[1] Ciro Rodriguez,[1,3] and Aida Rodriguez-Garcia[4]

[1]*Tecnologico de Monterrey, Escuela de Ingeniería y Ciencias, Monterrey 64849, Mexico*
[2]*Universidad Autónoma de Nuevo León, Facultad de Ciencias Biológicas, Laboratorio de Ciencias Genómicas, San Nicolás de los Garza 66455, Mexico*
[3]*Laboratorio Nacional de Manufactura Aditiva y Digital (MADiT), Apodaca 66629, Mexico*
[4]*Universidad Autónoma de Nuevo León, Facultad de Ciencias Biológicas, Instituto de Biotecnología, San Nicolás de los Garza 66455, Mexico*

Correspondence should be addressed to Aida Rodriguez-Garcia; aidrod@hotmail.com

Gabriela Torres-Flores and Azucena Gonzalez-Horta contributed equally to this work.

Received 3 July 2020; Revised 25 September 2020; Accepted 28 September 2020; Published 10 October 2020

Academic Editor: Margarita S. Dominguez

In 10% to 40% of the cases of coronary stent implantation, patients face in-stent restenosis due to an inflammatory response, which induces artery thickening. Everolimus, a drug that inhibits growth factor-stimulated cell proliferation of endothelial cells, represents a promising alternative to prevent in-stent restenosis. In this study, everolimus was encapsulated by a film hydration technique in liposomes by using phosphatidylcholine and cholesterol at different ratios. As the ratio of cholesterol increases, it modulates the rigidity of the structure which can affect the encapsulation efficiency of the drug due to steric hindrance. Moreover, various lipid : drug ratios were tested, and it was found that as the lipid : drug ratio increases, the encapsulation efficiency also increases. This behavior is observed because everolimus is a hydrophobic drug; therefore, if the lipidic region increases, more drug can be entrapped into the liposomes. In addition, stability of the encapsulated drug was tested for 4 weeks at 4°C. Our results demonstrate that it is possible to prepare liposomal everolimus by film hydration technique followed by extrusion with high entrapment efficiency as a viable drug delivery system.

1. Introduction

Cardiovascular disease remains the leading cause of morbidities and mortality worldwide. It encompasses a broad range of conditions that affect the heart and blood vessels, many of which are related to a process called atherosclerosis. Atherosclerosis is characterized by plaques that appear in the inner layers of arteries. Despite the advances in prevention, controlling risk factors such as smoking, dietary habits, lack of exercise, and high blood pressure, atherosclerosis continues to take deadly toll globally [1]. One of the widely applied percutaneous coronary interventions (PCI) in this type of disease is the coronary stent (coronary intravascular implant) that induces artery revascularization. Despite its popularity, up to 4 out of 10 people with coronary stents present in-stent restenosis, a decrease in the diameter of the arterial lumen [2]. This phenomenon is caused by neointimal proliferation, that is an excessive propagation of the endothelial tissue in the interior area of the stent or by new atherosclerotic plaques [3]. One way to prevent this effect is by using coated stents that allow drug release (such as everolimus, sirolimus, paclitaxel, and zotarolimus) directly into the artery [4]. There are several excipients that can be used for drug release, including polymeric, nanoparticle, and liposomal coatings.

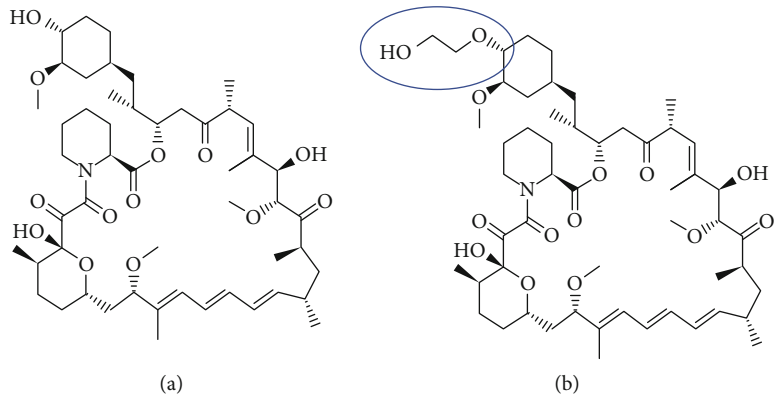

Figure 1: Drug comparison. Chemical structure of (a) sirolimus and (b) everolimus.

Liposomes are considered as one of the most used nanometric carriers in controlled release systems due to their ability to encapsulate both hydrophilic and hydrophobic drugs [5]. In addition, liposomes are used for drug release systems due to the variety of sizes, biocompatibility, ability to be directed to the site of interest, and their ability to maximize encapsulation capacity by transforming vesicles from multilamellar to unilamellar [6, 7]. Liposomes are composed of either palmitoyl oleyl phosphatidylcholine (POPC) or dioleoyl phosphatidylcholine (DOPC), which belong to the phosphatidylcholine (PC) family, the major component of animal cell membranes [8]. POPC contains one saturated and one unsaturated alkyl chain, while DOPC has two unsaturated alkyl chain; as a result, both have the same phase behaviors at 25°C. POPC has a phase transition melting temperature (T_m) of -2°C while the T_m for DOPC is -20°C; thus they are in the liquid crystalline phase. Liposomes can be grafted with polymer coating onto metal-based stents to prolong the half-life of the drugs, by allowing their gradual release and restraining the occurrence of restenosis. Antiproliferative drugs as in the first-generation stents, such as sirolimus and paclitaxel, are widely used to prevent excessive growth of endothelial tissue that could induce in-stent restenosis. However, due to their nature, they delay the process of healing of the artery, leading to a space where platelets agglomerate and cause thrombosis [9]. Due to these side effects, the use of biocompatible polymers in the second-generation drug eluting stents may present a higher safety profile, mechanical support, drug-delivery activity, and a complete bioresorption over several years, compared with those of the first generation [10]. Everolimus has been proposed to be used in second-generation coronary stents since, despite its hydrophobic nature, it is more bioavailable than sirolimus. Therefore, it has a greater capacity to be absorbed by the body as the variation in the functional group attached to carbon 40 (circled in Figure 1) increases its polarity [11].

Previously implemented methods for liposome synthesis, specifically for encapsulation of everolimus, solely concentrate on encapsulation by injection [12] and by mixing in aqueous solution [13]. Moreover, these systems and developed methods were mainly targeted at cancer treatment. Unlike previous works, the objective of this study was to develop everolimus-releasing liposomes through thin-film hydration method that could potentially be used to cover coronary stents. This method has presented greater control over size than the reports of the literature mentioned above, which is useful to regulate liberation kinetics as liposomes with smaller sizes (50 nm) tend to decompose earlier than larger vesicles since their high curvature tension leads to lower stability. Specifically, this work shows the optimization of the molar ratio between PC and cholesterol (Chol), the extent of the double bonds presents in PC, and the lipid : drug ratio for the development of stable unilamellar nanoliposomes using thin-film hydration and extrusion. This fine tuning was aimed at obtaining liposomes between 100 and 150 nm, small enough to avoid an unintended immune response and large enough to maintain liposome stability for at least 4 weeks.

2. Materials and Methods

2.1. Materials. Lipids used, cholesterol (Chol), palmitoyl-2-oleoyl-sn-glycero-phosphocholine (POPC), and 1,2-dioleoyl-sn-glycero-3-phosphocholine (DOPC) were purchased from Sigma Aldrich (St. Louis, MO, USA). Everolimus was obtained from Adooq Bioscience (Irvine, CA, USA) and organic solvents from Merck (Massachusetts, USA). On the other hand, HEPES ([4-(2-hydroxyethyl) piperazine-1-ethanesulfonic acid]) buffer and reactive grade sodium chloride were purchased from CTR Scientific S.A de C.V (Monterrey, Mex).

2.2. Methods

2.2.1. Preparation of Liposomal Everolimus. In the present work, in order to analyze the effect of drug to lipid ratio, liposomal composition of samples A, B, and C was maintained at a 9 : 1 w/w ratio of palmitoyl oleyl PC and Chol, respectively. To follow an optimization process of one factor at a time (OFAT), the lipid : drug with higher entrapment efficiency (%EE) was chosen for the optimization of the lipid composition. Therefore, the liposome composition was modified using POPC : Chol with a 7 : 3 ratio and another formulation with DOPC : Chol with a 9 : 1 ratio as Table 1 suggests. This table indicates the sample name, if the liposome was

Table 1: Experimental design for the optimization of liposomes' lipid composition and lipid : drug ratio (concentration of everolimus was maintained at 0.06 mM).

Sample	Lipidic components	Lipid ratio PC : Chol	Lipid : drug molar ratio
Blank	POPC : Chol	9 : 1	-
A	POPC : Chol	9 : 1	60 : 1
B	POPC : Chol	9 : 1	45 : 1
C	POPC : Chol	9 : 1	30 : 1
D	POPC : Chol	7 : 3	60 : 1
E	DOPC : Chol	9 : 1	60 : 1

prepared using POPC or DOPC, the ratio of either POPC or DOPC to cholesterol, and the molar ratio of everolimus versus the lipidic components, in respective columns. For reproducibility purposes, each sample was produced in triplicate.

To carry out the preparation of lipid mixtures with the absence or presence of everolimus, lipids were dissolved in chloroform : methanol in 3 : 1 v/v, while everolimus was dissolved in methanol. These solutions were mixed at different molar ratios as shown in Table 1, where the concentration of the drug was maintained at 0.06 mM (Table 1). We relied on the reports of the literature in selecting the lipid : drug ratio for sustained high entrapment efficiency of sirolimus, the drug from which everolimus is derived [14].

After solution preparation, the organic solvent was evaporated under nitrogen flow, followed by 2 hours of maintaining the samples under vacuum with a Vacufuge Plus equipment (New York, USA) to completely remove all traces of the solvent. The lipid film was then hydrated in 1 mL of buffer and 50 mM HEPES containing 30 mM NaCl pH 7 at 25°C with stirring at 1400 rpm for 2 minutes every 10 minutes during two hours with a Thermomixer Comfort (Eppendorf). The multivesicular (MLV) suspension was then extruded 12 times through 100 nm pore size nucleopore polycarbonate membranes (Whatman, UK) to produce samples with a narrow size distribution. The extrusion was carried out at 25°C to maintain vesicles above phase transition temperature using a miniextrusion kit (Avanti Polar Lipids, Alabaster, AL, USA). The entrapment efficiency of everolimus was calculated by separating the nonencapsulated from the encapsulated drugs by gel filtration chromatography using a Sephadex G75 column. During the elution, 60 fractions of 2 mL each were collected. Under these experimental conditions, the initial lipid sample was diluted 10 times as determined by phosphorous assay [15, 16].

2.2.2. Entrapment Efficiency. The entrapment efficiency (%EE) analysis was performed by UV-Vis spectroscopy Genesys 10 Thermo-Scientific (Madison, WI, USA) at 278 nm (lmax of everolimus) and interpolating the value on a calibration curve prepared for this purpose ($y = 61.859x + 0.0074$). The calibration curve was linear in the range of 0-0.006 mM with a correlation coefficient of $R^2 = 0.99871$.

The equation used to calculate the %EE is shown below, where CS is the sample concentration and 0.006 mM is the theoretical concentration of everolimus (which was diluted by a factor of ten due to the purification process). It should be noted that CS was calculated using the maximum absorbance peak from the extraction profiles of each sample.

$$\%EE = \frac{CS}{0.006} * 100 \quad (1)$$

Equation (1) was used to calculate the %EE of each sample.

2.2.3. Physicochemical Characterization of Liposomes. Size of empty and loaded liposomes and polydispersity of samples, as well as zeta potential were determined using dynamic light scattering (DLS). These parameters were studied during 4 weeks as a stability analysis using the ZetaSizer Nano equipment ZS90 (Malvern Instruments, UK). Liposomes were stored at 4°C during the course of these 4 weeks.

For infrared spectroscopy analysis, the samples were completely dried at 30°C, using an aqueous solvent group configuration with the equipment Ez-2plus (Genevac) which concentrates samples under vacuum conditions. Once dried, the samples were analyzed by ATR-FTIR spectroscopy (infrared spectroscopy by total attenuated reflectance) using a diamond crystal sample holder in a Perkin Elmer equipment Spectrum 400.

2.2.4. Morphological Characterization of Liposomes. For the morphological study of liposomes, samples were centrifuged with 30 K filters at 13,500 rpm for 15 minutes to eliminate the salts. These filters retain liposomes since they are heavier than 30 KDaltons allowing the separation of salts. Liposomes were then placed in a scanning electron microscope (SEM) sample holder and allowed to dry in a desiccator. Subsequently, the samples were coated with a 5 nm gold layer using a rotary pumped coater Quorum Q150R ES, and the morphology was observed by a Zeiss EVO MA25 SEM.

2.2.5. Statistical Analysis. Statistical analysis was performed based on an adjustment to an ANOVA of 2 variables through the GraphPad Prism 8.1.0 software. For all comparative tests, the Tukey test was used and the differences of $p < 0.05$ were considered statistically significant.

3. Results and Discussion

3.1. Characterization of Liposome Size, Polydispersity, and Stability. Liposomes were developed through thin-film hydration technique, which is the most common method for liposome preparation. Since lipidic composition and concentration could have a significant impact on developing a therapeutically efficient liposomal carrier system, we examined different parameters such as lipid-to-drug molar ratio, the increase in cholesterol, and the presence of more unsaturations in phospholipid's acyl chain. Liposomes' sizes were determined through dynamic light scattering (DLS), where it was observed that sizes were slightly greater than 100 nm, even though they were extruded by a polycarbonate filter with 0.1 μm pores, as shown in Figure 2(a). This is due to a squeezing phenomenon of liposomes through the filter. Since cholesterol has a rigid ring and an ultra-smooth face in its

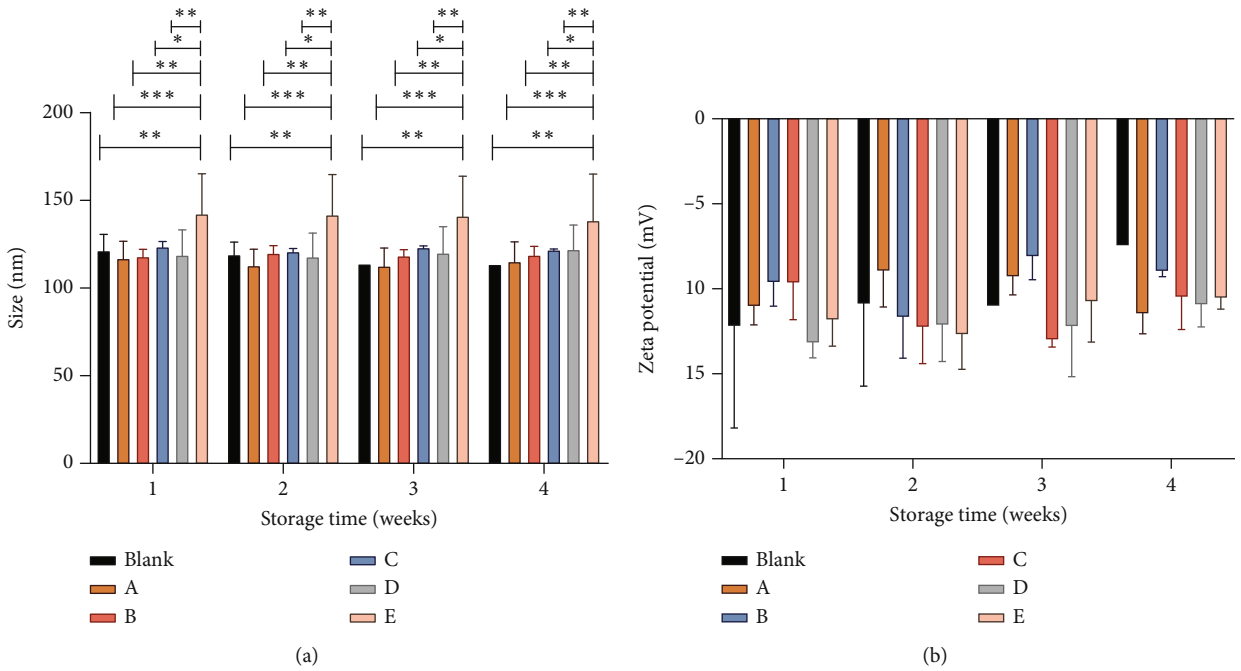

FIGURE 2: Liposomes' characterization: (a) size and (b) zeta potential. Lines are shown only when there is a significant difference between two samples, in which asterisks denote the level of significance. $^{*}p < 0.05$, $^{**}p < .001$, and $^{***}p < .0001$.

structure, the squeezing process has most likely taken place by allowing the lipids to turn quickly at the extremities [17]. This leads to lipids of high lateral mobility, as well as packed acyl chains [18]. Consequently, this contributes to the variation of sizes since the packing factor affects the intensity and duration of van der Waals forces present in liposomes. In addition, by increasing the percentage of Chol in the formulation, the coexistence of a binary phase Lo (ordered liquid) and Ld (disordered liquid) leads to discontinuities in the lipid membrane, which facilitates the structural interaction between liposomes [19]. This structural interaction propitiates vesicular aggregations which may lead to slightly bigger liposomes. However, the range of sizes obtained was close to the ideal sizes (100 nm-150 nm) for the intended application, as liposomes have to be small enough to "fool" the immune system. However, the liposomes' size should not be below 50 nm since the stability of liposomes would be compromised due to curvature tension in the vesicle. Moreover, in this specific case, samples with polydispersity index (PDI) less than 0.2 were observed, which indicates that the samples were homogeneous and stable for up to 4 weeks.

It is observed that for sample A (Table 1), the sizes decrease compared to the blank, despite being loaded with everolimus. Loading the liposomes with everolimus did not change the size. This is due to the fact that everolimus forms bonding sites between everolimus and liposomes. Therefore, interaction forces make the liposomes rather compact. Moreover, neither the drug : lipid ratio variation (samples A, B, and C) nor the increment of cholesterol in liposomes (sample D) has shown statistically different size changes (statistical analysis can be reviewed in Supplementary Information (available here)); thus, it can be concluded that these factors do not affect the liposome size. The only sample that showed a significant difference ($p \leq 0.05$) with respect to the size of the blank was sample E, which was prepared with DOPC instead of POPC. We believe that this is due to the presence of the extra double bond of DOPC which decreases the packing factor of acyl chains; thus, the sizes increase.

On the other hand, Figure 2(b) shows that the zeta potential of all liposomes, primarily composed of PC, was slightly negative (-11.28 ± 1.44) even though PC is considered a zwitterion. This is due to a 5% phosphatidic acid present in POPC and DOPC composition and the negative charge of cholesterol at pH 7 [20]. Furthermore, it was determined that the zeta potential did not show statistically significant changes from weeks 1 to 4. This indicates that liposomes are stable for the period of 1 month at 4°C, since a change in zeta potential would suggest a degradation or change in composition [21].

3.2. Chemical Analysis of Liposomes. The ATR-FTIR spectra of the blank (empty liposomes), pure everolimus, and samples A-D (loaded liposomes) are shown in Figure 3. The signal at 1741 cm^{-1} is attributed to the ester present in everolimus and in the polar head of PC [22]. The band at 1658 cm^{-1} present in both empty and loaded liposomes is attributed to the C = C bond. This last peak has been observed at a wavelength of 1645 cm^{-1} in polymeric stents coated with everolimus [23]. The peaks at 1658 and 1741 cm^{-1} are characteristic of the drug. However, the intensity of the previous two signals is lower in loaded liposomes since everolimus is dispersed within the liposome matrix. Moreover, the intensity is low due to the attenuation of ATR spectroscopy signal as a function of the thickness of the diamond crystal used in these assays. The peak at

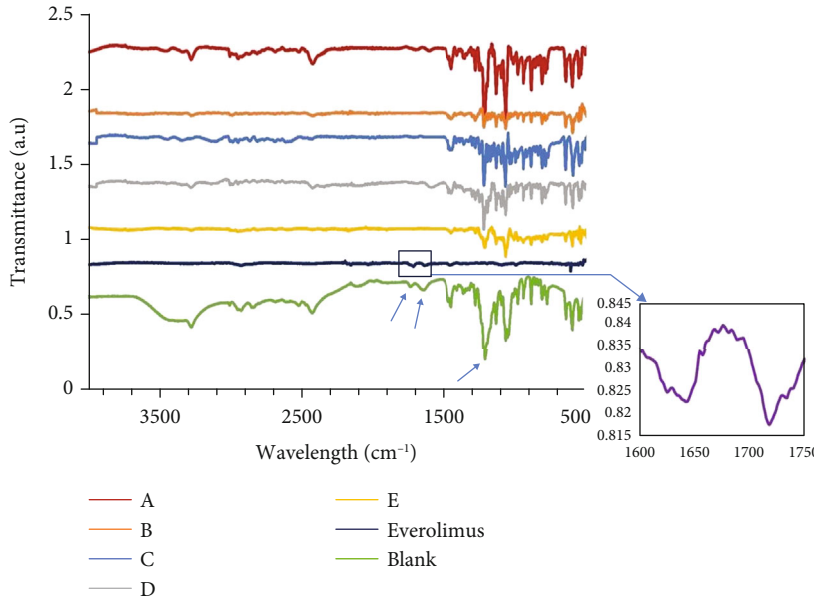

Figure 3: Functional group analysis. ATR-FTIR spectra of samples A-E, free everolimus, and blank liposomes.

1214 cm^{-1} in lipid samples represents the C-N bond of PC. It can be observed that sample A shows greater intensity than samples B and C as it has the greatest lipid : drug ratio. Similarly, in sample D, POPC decreased; therefore, the peak intensity of this particular sample is less than samples A, B, and C. In addition, it was observed that the modification from POPC to DOPC present in sample E decreased the signal intensity even though the lipid : drug rate was maintained the same. The results prove that there are no new chemical bonds between everolimus and lipids even though they interact with each other at the physical level.

3.3. Entrapment Efficiency. The %EE analysis was determined with UV-Vis spectroscopy at 278 nm, which corresponds to the active UV functional groups in everolimus. Figure 4 shows the results obtained from samples Figures 4(a)–4(e), where fraction 16 has the maximum absorbance at 278 nm and 400 nm, which indicate the absorbance of everolimus and the lipids, respectively. Subsequently, it can be observed that approximately 10 fractions are present where the absorbance at 278 nm rises again, which indicates the presence of free everolimus. This signal appears in fractions collected later compared to the peak of liposomes, as the drug has a lower molecular weight thus taking longer to leave the column which has high area within the pores of the stationary phase.

The %EE was calculated against the final concentration of everolimus, which was set to 0.006 mM due to the 10 factor of dilution that was previously stated for the purification method. The blank presented an average %EE of 11.5% even though no drug was loaded. This is due to a small variation of the dilution factor during purification. Moreover, the %EE of samples A, B, and C, in which the sole difference was the lipid : drug ratio (60 : 1, 45 : 1, and 30 : 1, respectively), has a direct relation with the composition. At a higher amount of lipid, the encapsulation efficiency increases. The highest encapsulation percentage was obtained for a lipid : drug 60 : 1 ratio, since the everolimus is hydrophobic and is trapped within the bilipid layer of liposomes. However, by decreasing the amount of lipid, the number of sites where everolimus can be trapped decreases. This trend is in accordance with a previous study regarding the encapsulation efficiency of another class of hydrophobic drug called docetaxel. In this study conducted by Pereira *et al.*, formulations with 40 : 1 and 20 : 1 lipid ratios had encapsulation efficiency of nearly 100% without significant differences [12]. In that study, however, it was necessary to increase the lipid : drug ratio to 60 : 1 to reach the encapsulation efficiencies close to 100% since everolimus is more hydrophobic than docetaxel hence requiring a greater lipid content. This comparison has led us to a relevant conclusion for liposomal formulation since it indicates that the lipid : drug ratio can be tuned depending on the nature of the encapsulated drug.

Unlike samples A, B, and C, in sample D, the amount of cholesterol was increased, reaching up to POPC : Chol of 7 : 3 ratio (Table 1). This was done to stabilize the structure of the lipid bilayer and increase the stability of the sample in biological serum for the intended application [24, 25]. However, it was found that %EE decreased to an average value of 44.13%. This is due to the fact that cholesterol is positioned within the lipid layer and therefore obstructs the drug encapsulation by 50% since everolimus is also a hydrophobic molecule which is primarily positioned within the lipid bilayer [26] (Table 2).

Formulation E was performed with a lipid : drug 60 : 1 ratio and a 9 : 1 DOPC : Chol ratio, which showed lower encapsulation percentage than sample A which is composed of the same molar ratios (lipid : drug 60 : 1 and 9 : 1 POPC). However, the difference of sample E was that the type of PC used was DOPC instead of POPC as in A-D formulations. This was done to analyze the effect of double bonds (see Figure 5) in the entrapment efficiency of everolimus, as previously reported [12]. Therefore, a comparison of %EE was made between liposomes composed of DOPC (with 2

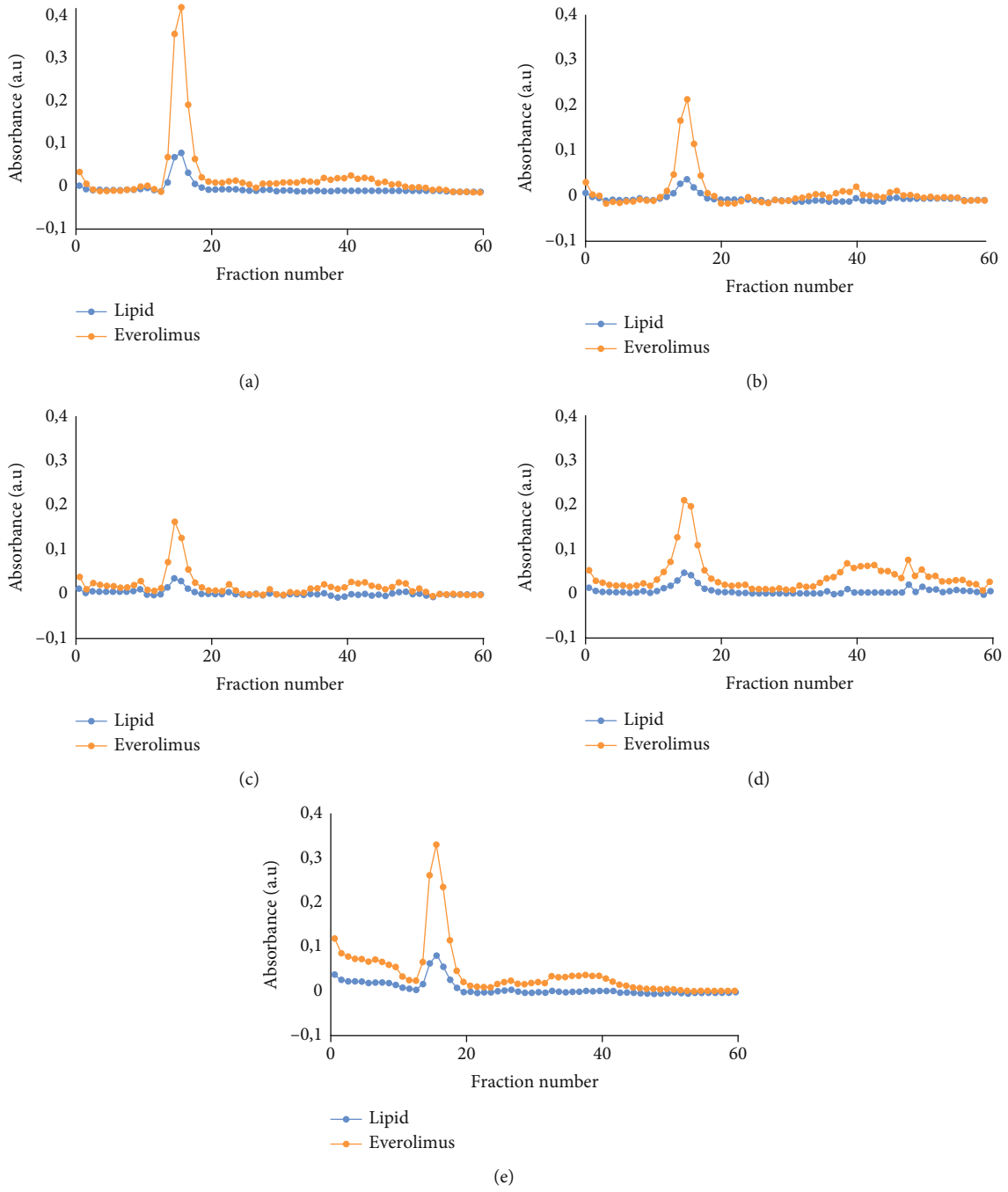

Figure 4: Entrapment analysis. UV-Vis extraction profile of samples (a), (b), (c), (d), and (e) obtained from the liposomes' purified fractions.

Table 2: Entrapment summary. Average %EE obtained by UV-Vis at 278 nm of the samples (POPC : Chol : DOPC/lipid : drug).

Sample	Entrapment efficiency (EE %)	Standard deviation
Blank	11.51	6.07
A (9 : 1 : 0/60 : 1)	92.82	2.64
B (9 : 1 : 0/45 : 1)	45.27	0.30
C (9 : 1 : 0/30 : 1)	33.68	0.66
D (3 : 7 : 0/60 : 1)	48.69	5.76
E (0 : 1:9/60 : 1)	71.89	5.18

double bonds) and POPC (with one double bond). As it can be observed in Table 2, the %EE of sample E (with DOPC) was 20% below that in sample A. This observation is relevant to understand the entrapment of everolimus in liposomes since it demonstrates that everolimus interaction is not carried out primarily in the double bonds of PC as suggested by Iwase and Maitani [27]. In that study, the %EE increases when formulation with DSPC : Chol 55 : 45 was used versus another sample composed of soy lecithin : Chol 95 : 5. This was attributed to the double bond of linoleic acid present in soy lecithin [12]. However, the formulation of DSPC : Chol 55 : 45 is estimated to have had a 14-fold lower %EE since

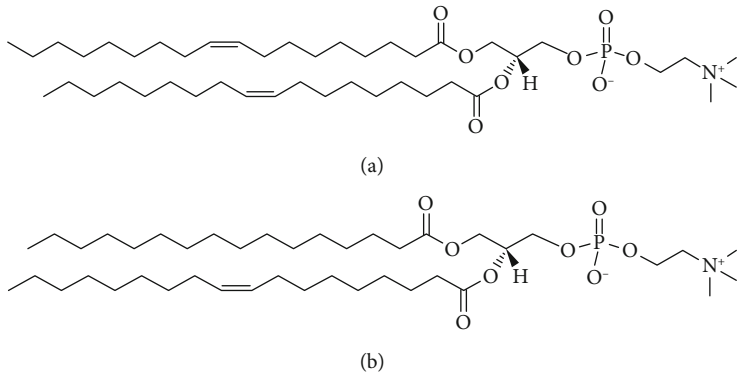

Figure 5: Chemical formula of (a) DOPC and (b) POPC.

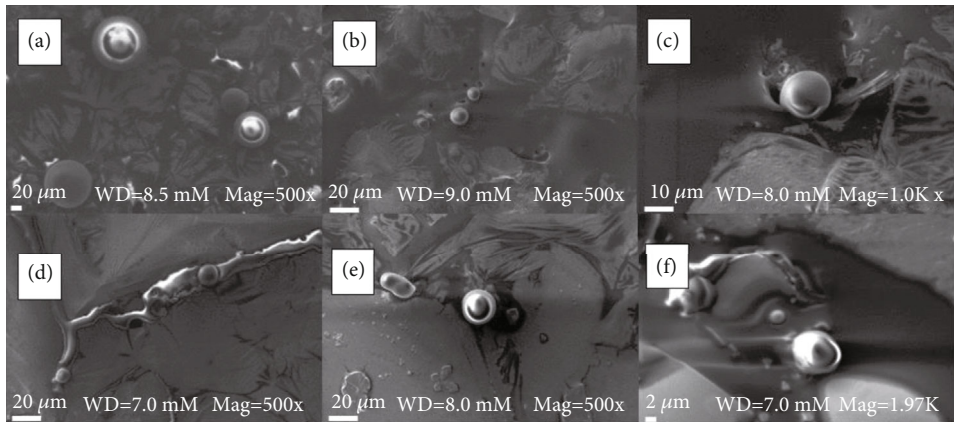

Figure 6: Morphological analysis. Images of liposomes obtained by scanning electron microscopy using an acceleration voltage of 5 kV of (a) blank, (b) sample A, (c) sample B, (d) sample C, (e) sample D, and (f) sample E.

the percentage of cholesterol in the sample DSPC : Chol 55 : 45 used by Iwase et al. was 9 times higher than the sample composed of lecithin : Chol 95 : 5 [27].

3.4. Morphological Characterization of Liposomes. The morphology of liposomes was analyzed through SEM. All samples presented a spherical shape regardless of the molar ratios of the lipid and drug or if they were loaded with everolimus or the lipidic composition of liposomes. However, the sizes observed through SEM, shown in Figure 6, were significantly larger than those observed by DLS. We believe that this is due to the tendency of liposomes to fuse in the drying process during sample preparation, as seen in Figure 6. The observed change in morphology is due to the fact that water promotes the formation of liposomes, and, when evaporated, it can deform the original structure due to its high surface tension [26, 28]. In addition, the increase in size affects the homogeneity of the sample since there is no control in size during the fusion process of liposomes. It is important to point out that the drying process can be affecting the size and shape of liposomes as well. In order to further understand the morphology and size of the loaded and preloaded liposomes, in future works, we will direct effort towards applying other techniques such as cryogenic TEM or environmental TEM, which could generate more in-depth information about morphology of liposomes and polydispersity index.

4. Conclusions

In the present work, it was determined how the lipid : drug and liposome lipid composition affect size, polydispersity index, stability, and encapsulation efficiency of the drug-loaded liposomes. Specifically, we found that the formulation with the highest %EE (95%) was a liposome with a lipid : drug 60 : 1 ratio and with a lipid composition with POPC Chol 9 : 1. It was also found that the %EE of everolimus is directly proportional to the lipid : drug ratio and inversely proportional to the amount of cholesterol and double bonds present in PC. This finding could be relevant for the encapsulation of other hydrophobic drugs in liposomes following similar compositions. The obtained results suggest that the thin layer hydration and extrusion method represents a simple and reproducible method. This allowed to study the behavior of lipid-everolimus, thus permitting the tuning of encapsulation efficiency by modulating the lipid composition. As future work, morphological characterization could be done by an environmental SEM or cryogenic TEM in order to avoid liposomal fusion and to observe single liposomes and to compare the morphology between samples. The next research efforts

will be focused to perform release kinetics analysis to determine the drug release profile and functionalize liposomes in polymers to further coat the metallic stents. The results reported in this work will be relevant for further applications of liposomes as drug delivery systems and for their use in coronary stents to prevent in-stent restenosis.

Abbreviations

PCI: Percutaneous coronary intervention
PC: Phosphatidylcholine
Chol: Cholesterol
HEPES: 4-(2-hydroxyethyl) piperazine-1-ethanesulfonic acid
POPC: Palmitoyl oleyl phosphatidylcholine
DOPC: Dioleoyl phosphatidylcholine
MLV: Multilamellar vesicle
OFAT: One factor at a time
LUV: Large unilamellar vesicle
%EE: Percentage of entrapment efficiency
PDI: Polydispersity index
L : F: Lipid to drug ratio.

Data Availability

The experimental data used to support the findings of this study are available from the corresponding author upon request.

Conflicts of Interest

The authors declare that there is no conflict of interest regarding the publication of this paper.

Authors' Contributions

G.T-F. contributed to the methodology, investigation, original draft preparation, review, and editing. A.G-H. contributed to the conceptualization, supervision, review, and editing. The founding acquisition, validation, review, and editing were done by Y.V-C. C.R. contributed to the resources. A.R-G. did the conceptualization, project administration, review, and editing. All the authors read and approved the final version prior to submission. Gabriela Torres-Flores and Azucena Gonzalez-Horta contributed equally to the work.

Acknowledgments

We are grateful to Dvorak Montiel-Condado and Abelardo Chávez-Montes who gently lent us their laboratory equipment. The technical help received from Elda Graciela Gómez, Felipe López, César Augusto García, Regina Elizabeth Vargas Mejía, and Daniel Mejia-Valdez is greatly appreciated. This work has been supported by the Advanced Manufacturing Focus Group of Tecnologico de Monterrey.

Supplementary Materials

The supplementary section is divided in two appendixes: appendix A, being tables with numerical data obtained for size, PDI, and zeta potential of liposomes and appendix B, being the statistical analysis numerical evidence of results stated in the manuscript. *(Supplementary Materials)*

References

[1] D. K. Arnett, R. S. Blumenthal, M. A. Albert et al., "2019 ACC/AHA guideline on the primary prevention of cardiovascular disease: a report of the American College of Cardiology/American Heart Association Task Force on Clinical Practice Guidelines," *Journal of the American College of Cardiology*, vol. 140, no. 11, pp. e596–e646, 2019.

[2] G. Oliva, M. Espallargues, and J. M. V. Pons, "Stents recubiertos de fármacos antiproliferativos : revisión sistemática del beneficio y estimación del impacto presupuestario," *Revista Española de Cardiología*, vol. 57, no. 7, pp. 617–628, 2004.

[3] N. A. Scott, "Restenosis following implantation of bare metal coronary stents: pathophysiology and pathways involved in the vascular response to injury," *Advanced Drug Delivery Reviews*, vol. 58, no. 3, pp. 358–376, 2006.

[4] A. S. Puranik, E. R. Dawson, and N. A. Peppas, "Recent advances in drug eluting stents," *International Journal of Pharmaceutics*, vol. 441, no. 1-2, pp. 665–679, 2013.

[5] K.-I. Joo, L. Xiao, S. Liu et al., "Crosslinked multilamellar liposomes for controlled delivery of anticancer drugs," *Biomaterials*, vol. 34, no. 12, pp. 3098–3109, 2013.

[6] S. Mallick and J. S. Choi, "Liposomes: versatile and biocompatible nanovesicles for efficient biomolecules delivery," *Journal of Nanoscience and Nanotechnology*, vol. 14, no. 1, pp. 755–765, 2014.

[7] M. Danaei, M. Dehghankhold, S. Ataei et al., "Impact of particle size and polydispersity index on the clinical applications of lipidic nanocarrier systems," *Pharmaceutics*, vol. 10, no. 2, p. 57, 2018.

[8] V. Nele, M. N. Holme, U. Kauscher, M. R. Thomas, J. J. Doutch, and M. M. Stevens, "Effect of formulation method, lipid composition, and PEGylation on vesicle lamellarity: a small-angle neutron scattering study," *Langmuir*, vol. 35, no. 18, pp. 6064–6074, 2019.

[9] Q. Wu, K. S. Huang, M. Chen, and D. J. Huang, "Rapamycin enhances platelet aggregation induced by adenosine diphosphate in vitro," *Platelets*, vol. 20, no. 6, pp. 428–431, 2009.

[10] T. Palmerini, U. Benedetto, G. Biondi-Zoccai et al., "Long-term safety of drug-eluting and bare-metal Stents," *Journal of the American College of Cardiology*, vol. 65, no. 23, pp. 2496–2507, 2015.

[11] S. Granata, A. Dalla Gassa, A. Carraro et al., "Sirolimus and everolimus pathway: reviewing candidate genes influencing their intracellular effects," *International Journal of Molecular Sciences*, vol. 17, no. 5, p. 735, 2016.

[12] S. Pereira, R. Egbu, G. Jannati, and W. T. al-Jamal, "Docetaxel-loaded liposomes: the effect of lipid composition and purification on drug encapsulation and in vitro toxicity," *International Journal of Pharmaceutics*, vol. 514, no. 1, pp. 150–159, 2016.

[13] T. B. Yu, Z. Shi, and S. H. Su, "Stable liposomal formulations of rapamycin and rapamycin derivatives for treating cancer," US Patent 2017/0065520A1, 2017.

[14] A. Haeri, S. Sadeghian, S. Rabbani, M. S. Anvari, M. A. Boroumand, and S. Dadashzadeh, "Use of remote film loading methodology to entrap sirolimus into liposomes: preparation, characterization and in vivo efficacy for treatment of restenosis," *International Journal of Pharmaceutics*, vol. 414, no. 1-2, pp. 16–27, 2011.

[15] G. Rouser, A. N. Siakotos, and A. S. Fleisher, "Quantitative analysis of phospholipids by thin-layer chromatography and phosphorus analysis of spots," *Lipids*, vol. 1, pp. 85-86, 1966.

[16] A. Gonzalez-Horta, A. Matamoros-Acosta, A. Chavez-Montes, R. Castro-Rios, and J. Lara-Arias, "Biodegradable nanoparticles loaded with tetrameric melittin: preparation and membrane disruption evaluation," *General Physiology and Biophysics*, vol. 36, no. 4, pp. 373–381, 2017.

[17] H. Martinez-Seara, T. Róg, M. Karttunen, I. Vattulainen, and R. Reigada, "Cholesterol induces specific spatial and orientational order in cholesterol/phospholipid membranes," *PLoS One*, vol. 5, no. 6, article e11162, 2010.

[18] H. Barman, M. Walch, S. Latinovic-Golic et al., "Cholesterol in negatively charged lipid bilayers modulates the effect of the antimicrobial protein granulysin," *The Journal of Membrane Biology*, vol. 212, no. 1, pp. 29–39, 2006.

[19] F. Giudice, *Caracterización estructural de liposomas y su interacción con moléculas anfifílicas de interés farmacológico*, Tesis Doctoral en Ciencias Químicas Biol Francesca Giudice Departamento de Química Biológica CIQUIBIC, 2016.

[20] J. Salcedo, A. Delgado, and F. González-Caballero, "The effect of pH on the electrical properties of the cholesterol/water interface. I. ζ potential," *Journal of Colloid and Interface Science*, vol. 133, no. 1, pp. 278–281, 1989.

[21] J. Qi, W. Zhang, X. Feng et al., "Thermal degradation of gelatin enhances its ability to bind aroma compounds: investigation of underlying mechanisms," *Food Hydrocolloids*, vol. 83, pp. 497–510, 2018.

[22] A. Mirmohseni, J. Hosseini, M. Shojaei, and S. Davaran, "Design and evaluation of mixed self-assembled monolayers for a potential use in everolimus eluting coronary stents," *Colloids and Surfaces B: Biointerfaces*, vol. 112, pp. 330–336, 2013.

[23] M. Wu, L. Kleiner, F. W. Tang, S. Hossainy, M. C. Davies, and C. J. Roberts, "Surface characterization of poly(lactic acid)/everolimus and poly(ethylene vinyl alcohol)/everolimus stents," *Drug Delivery*, vol. 17, no. 6, pp. 376–384, 2010.

[24] D. C. Drummond, C. O. Noble, M. E. Hayes, J. W. Park, and D. B. Kirpotin, "Pharmacokinetics and in vivo drug release rates in liposomal nanocarrier development," *Journal of Pharmaceutical Sciences*, vol. 97, no. 11, pp. 4696–4740, 2008.

[25] C. Kirby and G. Gregoriadis, "The effect of the cholesterol content of small unilamellar liposomes on the fate of their lipid components," *Life Sciences*, vol. 27, no. 23, pp. 2223–2230, 1980.

[26] M. A. Rouf, I. Vural, J. M. Renoir, and A. A. Hincal, "Development and characterization of liposomal formulations for rapamycin delivery and investigation of their antiproliferative effect on MCF7 cells," *Journal of Liposome Research*, vol. 19, no. 4, pp. 322–331, 2009.

[27] Y. Iwase and Y. Maitani, "Preparation and in vivo evaluation of liposomal everolimus for lung carcinoma and thyroid carcinoma," *Biological and Pharmaceutical Bulletin*, vol. 35, no. 6, pp. 975–979, 2012.

[28] S. Park, R. A. Venditti, H. Jameel, and J. J. Pawlak, "Changes in pore size distribution during the drying of cellulose fibers as measured by differential scanning calorimetry," *Carbohydrate Polymers*, vol. 66, no. 1, pp. 97–103, 2006.

Hindawi
Advances in Polymer Technology
Volume 2020, Article ID 6187048, 41 pages
https://doi.org/10.1155/2020/6187048

Review Article

3D *In Vitro* Human Organ Mimicry Devices for Drug Discovery, Development, and Assessment

Aida Rodriguez-Garcia,[1,2] Jacqueline Oliva-Ramirez,[3] Claudia Bautista-Flores,[4] and Samira Hosseini[4,5]

[1]*Universidad Autónoma de Nuevo León, Facultad de Ciencias Biológicas, Instituto de Biotecnología, Ave. Pedro de Alba S/N, Ciudad Universitaria, CP 66455, San Nicolás de los Garza, NL, Mexico*
[2]*Laboratorio Nacional de Manufactura Aditiva y Digital (MADiT), Apodaca, NL, Mexico*
[3]*Tecnológico de Monterrey, Escuela de Ingeniería y Ciencias, Ave. Lago de Guadalupe Km 3.5, Cd López Mateos, Atizapán, Estado de Mexico, Mexico*
[4]*Tecnologico de Monterrey, Escuela de Ingeniería y Ciencias, Ave. Eugenio Garza Sada 2501, Monterrey, 64849 NL, Mexico*
[5]*Tecnologico de Monterrey, Writing Lab, TecLabs, Vicerrectoría de Investigación y Transferencia de Tecnología, Monterrey, 64849 NL, Mexico*

Correspondence should be addressed to Samira Hosseini; samira.hosseini@tec.mx

Received 17 April 2020; Accepted 30 June 2020; Published 10 August 2020

Academic Editor: Mona Semsarilar

The past few decades have shown significant advancement as complex *in vitro* humanized systems have substituted animal trials and 2D *in vitro* studies. 3D humanized platforms mimic the organs of interest with their stimulations (physical, electrical, chemical, and mechanical). Organ-on-chip devices, including *in vitro* modelling of 3D organoids, 3D microfabrication, and 3D bioprinted platforms, play an essential role in drug discovery, testing, and assessment. In this article, a thorough review is provided of the latest advancements in the area of organ-on-chip devices targeting liver, kidney, lung, gut, heart, skin, and brain mimicry devices for drug discovery, development, and/or assessment. The current strategies, fabrication methods, and the specific application of each device, as well as the advantages and disadvantages, are presented for each reported platform. This comprehensive review also provides some insights on the challenges and future perspectives for the further advancement of each organ-on-chip device.

1. Introduction

Prior to testing a new drug in a clinical trial, principal phase analysis on the pharmacodynamics and pharmacokinetics takes place using animal models and/or two-dimensional (2D) *in vitro* models. Such analyses could prevent adverse drug events and predict organ toxicity and drug mechanisms prior to testing on human beings [1], while offering economic benefits and time reduction between drug discovery and clinical trials [2]. Despite the technological advancements in animal or 2D drug testing, the development and application of new therapeutic products face multiple barriers prior to clinical trials. While various animal models are genetically altered to mimic the human body for drug testing and screening, the inability to replicate key facets of the human body makes such trials limited with respect to drug efficacy and safety assessments. *In vitro* studies, on the other hand, allow a certain degree of progress, although as yet they cannot replace clinical trials on humans [3]. In particular, traditional *in vitro* analysis is incapable of mimicking the human body due to the lack of surrounding stimulations each organ undergoes in a living body or in some cases the studies are performed in different species [3, 4].

In the past few decades, more complex *in vitro* humanized systems have replaced animal studies and 2D *in vitro* analysis as they closely mimic the organ of interest and can

incorporate the necessary stimulations (physical, electrical, chemical, and mechanical) that an organ can experience. Since the advent of cell culture systems and microfabrication techniques, the organ-on-chip technology has gained momentum as one of the pioneering technologies for drug metabolism analysis [1]. Organ-on-chip devices fall under the category of microfluidics or biomicroelectromechanical system (Bio-MEMS) with main components including cells, media, tissues, and scaffolds [1, 5]. The principal approaches in in vitro organ-specific tissue modelling include three-dimensional (3D) organoids or spheroids, 3D microencapsulation within microgels, bioprinted organ platforms (e.g., cell-seeded scaffolds), and bioreactor-incorporated devices [6–8].

In vitro modelling including 3D organoids, 3D microfabrication, and 3D bioprinted platforms for several organs was presented. Such platforms fabricate human mimicry systems including the heart, kidney, lung, intestinal tract, liver, retina, bone, and brain [9]. Organ-on-chip devices facilitate drug testing on different cell lines, while multiple-organ-chip platforms study the pathways of different drugs and their efficacy on one organ in correlation with others [2]. Human-on-chip devices provide a deeper understanding of drug metabolism, pharmacokinetics, and toxicity on the human body as a unified physiological entity. Moreover, the addition of one or more biosensors for continuous monitoring of biomarkers has led to further comprehension of the metabolic changes *in situ*. The personalized medicine, in turn, could be highly promoted by organ-on-chip devices as they require a small tissue sample from the patient to replicate the organ [10]. Nonetheless, organ-on-chip and human-on-chip platforms also suffer from certain shortcomings, including the complexity of the operation due to the device size and the inconsistency of the results from one laboratory to another [11]. Undoubtedly, the microenvironmental control and monitoring to maintain the long-time cell culture without changing the microorgan's physiology and morphology are some of the major challenges yet to overcome. Moreover, the variability of the organogenesis throughout tissue development has to be carefully controlled in order to meet the expected objectives of an organ-on-chip device [12]. This review article concentrates on the latest updates of in vitro human mimicry systems for drug assessment. In that perspective, we narrow down the focus of this article to the advances of the organ physiology mimicry in on-chip devices with respect to drug discovery, development, and assessment for the selected organs: liver, kidney, lung, gut, heart, skin, and brain. Moreover, the review article provides some insights on human-on-chip devices and the application of such devices for drug assessment and screening.

2. Organ-on-Chip Strategies

2.1. Liver-on-Chip. The liver plays a critical role in drug metabolism, body homeostasis, digestion, and the elimination of toxic substances. *In vitro* human liver models are used to evaluate the metabolism and toxicity of chemical compounds and drugs and for the evaluation candidate drugs in cancer research and genetic studies [13]. Experiments can be carried out using primary cells isolated from patients or using cells from cell banks, such as the American Type Culture Collection (ATCC) [14]. Furthermore, cell culture systems allow researchers to understand drug absorption, distribution, metabolism, and excretion and to assess their pharmacokinetic and pharmacodynamic parameters. Human liver cells lose many functions in normal culture, including drug-metabolizing and drug transport activities, which are basic for drug discovery. 2D cultures have other limitations, including the alteration of cell morphology, the loss of polarity and phenotype, and the change in gene expression [15].

Current *in vitro* systems evaluate the toxicity of new drugs using different human hepatic cell lines, such as hepatocytes, liver sinusoidal endothelial cells (LSEC), human liver cells (HepG2), and a hepatic stem cell line (HepaRG). Hepatocytes are the main parenchymal cells that comprise the cell plates of the lobule, carrying out most of the metabolic functions of the liver [16]. LSEC are thin, elongated cells that are part of the reticuloendothelial system (RES) and play a role in maintaining the homeostasis and hepatic immunity [17]. HepG2 and HepaRG cells are immortalized cell lines that can be used as an alternative to primary cells for drug screening and toxicological studies. HepG2 are derived from a hepatocellular carcinoma and are frequently used for the evaluation of drug toxicity due to the expression of liver-specific enzymes and nuclear transcription factors, including p53 and Nrf2, which are essential for drug metabolism [18]. HepaRG are also derived from a hepatocellular carcinoma. These cells have two different cell morphologies; however, they can be differentiated on treatment with dimethyl sulfoxide (DMSO). Therefore, under appropriate cell culture conditions, HepaRG represents the most suitable cell line for long-term studies of a slowly metabolized drug and for determining the mechanisms associated with exposure to xenobiotics [19]. Another concept that must be considered in the evaluation of the metabolism and toxicity of drugs is drug-induced liver injury (DILI), which is associated with acute liver failure and is the main reason for the subsequent market withdrawal of approved drugs [20]. The major advances in molecular pharmacology and toxicology, hand in hand with novel strategies for development of 3D liver models, allow for the improved recreation of cell-cell interactions within their own microenvironment, as well as endowing a more permissive, tissue-like, microenvironment for long-term culture that can improve hepatotoxicity predictions [21]. Some of the latest examples of liver-on-chip platforms for drug discovery, development, and analysis are thoroughly reviewed in this article (Table 1).

2.1.1. Analysis of Drugs in Liver-on-Chip Devices. The liver plays a key role in all metabolic processes in the human body, such as body homeostasis, drug metabolism, and the detoxification of blood; therefore, an adequate liver model is a necessity for drug development [22]. Hepatocytes cultured within 2D *in vitro* models lose many functions and activities, limiting their modelling function. For that reason, 3D liver-on-a-chip models are an excellent option for *in vitro* liver analysis. The engineered hepatic tissues in 3D devices, however, should closely mimic the natural functions of the organ.

Table 1: Summary of recent advancements hepatotoxicity testing including the type of drug, the application, the applied cell lines, and the kinetics.

Drug type	Application	Applied cell lines	Kinetics	Ref(s)
Acetaminophen, clozapine, olanzapine, fialuridine, entecavir, aminophenol	Biotransformation, hepatotoxicity	Human hepatocytes from donors	7 days of culture, 48 hr stimuli	[32]
Amiodarone, acetaminophen	Hepatotoxicity due to mitochondrial respiration analysis	HepG2/C3	28 days	[39]
Acetaminophen-omeprazol, acetaminophen-rifampicina, acetaminophen-ciprofloxacin	Drug-drug interaction	HepG2, HUVEC EA.hy926, stellate, U937		[38]
Acetaminophen	Hepatoxicity	HepG2/C3	30 days	[23]
Acetaminophen, isoniazid, rifampicin	Drug-drug interaction, hepatoxicity	Lobule-like HepG2, HAEC	4 days	[136]
Diclofenac	Biotransformation	Multicellular platform: Hu8150 and HK8160	7 days	[30]
Phenacetin, diclofenac, lidocaine, ibuprofen, propranolol, prednisolone	Biotransformation variability	Human primary hepatocytes from donors	7 days	[31]
Bupropion/2-phenyl-2-(1-piperidinyl)propane), tolbutamide/sulphafenazole, omeprazole/ benzylnirvanol, testosterone/ketoconazole	Development of CYP450 inhibitors	HepaRG	24 hrs	[26]
Warfarina, dasatinib	Drug-drug interaction	HepaRG	24 hrs	[27]
Midazolam, phenacetin, acetaminophen	Biotransformation	Human primary hepatocytes	13 days	[35]
Tolbutamide, testosterone	Hepatic clearance by CYP3A1 and CYP2C11	Rat hepatocyte primary cell culture	15 days	[137]
Adaptaquin (HIF PHD inhibitors)	Hepatotoxicity	HepaRG	48 hrs	[138]
Adaptaquin and analogs	Biotransformation, hepatotoxicity	HepaRG	24 hrs	[36]
Rifampin, ketoconazole	Hepatotoxicity	Hepatic stellate cells isolated from rat	~14 days	[42]
Vitamin D	Biotransformation	HepG2 cells, RPTEC	~5 days	[139]
Vitamin E (-tocoferol)	Biosynthesis of metabolites to target 5-lipoxygenase	Human-liver-sinusoid, HepaRG cells, HUVEC, human monocyte (PBM)	~5 days	[40]
Ethanol	Detoxification and hepatotoxicity	HepG2	4 days	[24]

CYP450: cytochrome P450; HepG2/C3: human hepatocellular carcinoma/complement factor 3; HUVEC: human umbilical vein cell line; EA.hy926: endothelial cell; U937: human histiocytic lymphoma; HAEC: human aortic endothelial cell line; Hu8150: primary human hepatocytes; HK8160: human Kupffer cells; HepaRG: hepatic biprogenitor cell line; CYP3A1: cytochrome P450 3A1; CYP2C11: cytochrome P450 2C11; RPTEC: renal proximal tubule epithelial cells; PBM: peripheral blood mononuclear cells.

In order to monitor the physiology of the liver cells, some studies quantified the hepatic biomarker concentration (e.g., albumin, transferrin, alpha-1 antitrypsin, and ceruloplasmin) by the liver spheroids [10]. Also, immunophenotyping is frequently used to prove the identity or the structure of the hepatocyte, such as cytokeratin 18, MRP2 bile canalicular protein, and tight junction protein ZO-1. It is critical that these molecules maintain their expression over time [23, 24].

Prior to drug absorption within the body, metabolism of the xenobiotic agent occurs. This pathway transforms the drug into a hydrophilic molecule, which, in turn, helps during excretion. Depending on the drug, the biotransformation may occur in different organs, including the liver. There are two main phases for such biotransformation. Primarily, the molecule is modified by the addition of functional groups (hydroxy groups, epoxides, etc.). The enzymes from the family of the cytochrome 450 (CYP450) conduct these reaction processes. There are several isoforms of these molecules which may change between species. This change is essential, while there is no standard model that mimics all the isoforms. In humans, CYP3A4 catalyzes over 50% of the drugs and CYP2D6 over 20%. The second phase in the metabolic reaction process is to create a hydrophilic metabolite through the conjugation of charged groups.

The stability in the expression of CYP450 is a significant event in order to generate an efficient model. Such stability was studied by Ortega-Prieto et al. in 2018. The authors created a microbioreactor, with medium recirculation by a pneumatical micropump. The recirculation speed of the media allowed the nutrients and oxygen levels to remain stable. The primary hepatic spheroid attachment in the

microfluidic reactor was generated by a coated collagen polystyrene (PS) scaffold. The results show in primary human hepatocytes with micropump medium recirculation that the levels of CYP450 remained the same over forty days. This result represented 3-4-fold improvement compared to 2D platforms. Furthermore, a long-term hepatitis B model of infection was created by which the viral concentration over 12 days was monitored. An increase in the cytokines and immune receptors was observed when they were treated with interferon-alpha. The study was also able to predict human host responses against HBV. Moreover, with the addition of other, nonparenchymal hepatic cells, such as Kupffer cells, an efficient viral clearance was obtained. As a result, the device identified essential biomarkers at the early stages of infection [25].

The liver-on-a-chip devices also facilitate studying metabolic pathways in preclinical phases. Zakharyants et al. in 2016 and 2017 induced organoids using HepaRG cells and cultured them into a microbioreactor device with recirculating media in order to test the expression of CYP450. In the first study, the results showed the genetic expression of four isoforms of CYP450, including CYP2B6, CYP2C9, CYP2C19, and the most crucial one, CYP3A4. The authors tested several inhibitors for each isoform. The conclusion was that the 3D model recreated the regular expression of isoforms compared with static cultures. With these results, a second study was performed in which the authors tested the drug interaction of warfarin and dasatinib. Warfarin biotransformation was associated with CYP2C9 isoform, and dasatinib with CYP3A4. The study showed that the use of warfarin with compounds metabolized by the same isoform (CYP2C9) could lead to drug-drug interactions [26, 27].

Human primary hepatocytes are the cells frequently used for the analysis of drug toxicity. However, their limited *in vitro* proliferation capacity has prompted the search for alternative cells. Spheroids have been reported as a promising model to study *in vitro* hepatotoxicity, demonstrating better results than conventional 2D cell culture models. Furthermore, 3D spheroid cultures show appropriate sensitivity to analyze the biomarker's responses induced by hepatotoxic drugs. Foster et al. [28] evaluated the hepatotoxicity risk assessment of acetaminophen and fialuridine by monitoring the release of the hepatic biomarkers α-GST and miR-122. Both hepatotoxins produced dose- and time-dependent increases in miR-122 and α-GST release. These results confirm that the liver-on-a-chip model is sensitive for drug assessment [28].

During the *in vitro* culture of primary hepatocytes, many phenotype-specific functions are lost or significantly diminished. To maintain these functions, a fluidic 3D microreactor platform was introduced to preserve the metabolic activity of the human hepatocytes for more than two weeks. Long et al. [29] and Sarkar et al. [30] performed two different studies using liver-on-chip devices for preclinical studies. Both groups obtained the microdevice from CN Bio Innovations in which a pneumatic pump controlled the fluidic system and moved the media through the polyurethane membrane scaffold positioned between cells and pneumatic plates. Primary human hepatocytes (Hu8150) from healthy donors and Kupffer cells were cultured in this device. Long et al. (2016) tested the CYP450 activity under chronic inflammatory conditions and the effect of a biological drug named tocilizumab, which is a monoclonal antibody for rheumatoid arthritis. In this pathology, the inflammatory molecules decreased the CYP450 activity. The microdevice measured the drug activity and the CYP450 isoform recovery. Furthermore, the drug-drug interaction was analyzed with simvastatin [29]. Sarkar et al.'s work, on the other hand, is aimed at evaluating the biotransformation of diclofenac in the microdevice and compared the results with known *in vivo* metabolic profiles. The results showed similar metabolites for biotransformation in phases I and II, as reported within the human body. Moreover, the drug-induced toxicity measured by the protein markers, including albumin and lactate dehydrogenase (LDH), was found to be similar. By inducing inflammation, the authors created an immunocompetent model for the discovery of early biomarkers, proving the mimetic potential of 3D microfluidic devices [30].

The same bioreactor (CN Bio Innovations) also facilitated drug metabolite measurements for six different drugs. The objective of this study was to identify the variability of drug responses using four healthy hepatic cell donors. This variation refers to an individual average of intrinsic drug clearance. The device was suitable for analyzing the interdonor variability due to differential drug metabolites, LDH production for toxicity, hepatic gene expression levels, and hepatic albumin excretion [31]. Hepatic cells were the only cell types cultured in this bioreactor. This poses a shortcoming, as CYP450 isoform expression depends on the full cellular environment of the liver.

The traditional 2D human hepatocyte culture methods are reported to decrease, and eventually lose, the expression of the CYP450 isoforms [32]. In particular, the activity analysis of some isoforms of CYP450 reported in several studies has demonstrated a downregulation of CYP1A2, 2E1, and 3A4 within 14 and 28 days. These results suggest that microfluidic devices are more sensitive than the current 2D plate-based cultures [33]. A report from Proctor et al. [34] presents the testing of over 100 different drugs and their cytotoxicity within both 2D and 3D culture systems. The authors indicated that the 3D culture platforms allowed for easier manipulation and offered higher sensitivity than 2D cultures, while maintaining the specificity of *gold-standard* culture assays.

In microfluidic cultures, hepatocytes cultivated for 13 days have shown an increase of CYP2B6, CYP2C19, CYP2C8, CYP1A2, CYP2D6, and CYP3A4 mRNA and other molecules, including SULT1A1, UGT1A1, and HNF4a, during the kinetic analysis. This is in contrast with their Petri dish control cultures in which the increase in the number of molecules occurred only towards the end of the kinetic analysis [35, 36]. In monitoring these proteins, other studies have confirmed that a gradual, and significant, increase in CYP1A1, CYP1A2, CYP2E1, and CYP3A4 occurred using chip-based devices in comparison to 2D cultures [37].

Due to its well-known, high propensity induction of hepatotoxicity, acetaminophen is a drug that has been tested in several reports. Liver-on-a-chip devices have proven to be accurate in assessing the cytotoxic analysis and drug-drug

interaction of acetaminophen. Deng et al. [38] fabricated a 3D liver-sinusoid-on-a-chip (LSOC) by a lithographic technique using polydimethylsiloxane (PDMS) and polymethylmethacrylate (PMMA) with two polycarbonate (PC) porous membranes to mimic the microenvironment of the liver sinusoid (Figure 1). In this model, the authors introduced a multicellular culture using human hepatocellular carcinoma (HepG2) cells as a source of hepatocytes, human umbilical vein cells, human stellate cells, and human histiocytic lymphoma U937 cells to recreate the liver endothelium and stroma [38]. The drugs were perfused in the artificial blood, and cell viability was determined with methyl-thiazolyl-tetrazolium (MTT). The results showed that the hepatotoxicity of drug-drug interaction was 17.15% for acetaminophen-rifampicin, 14.88% for acetaminophen-omeprazole, and 19.74% for acetaminophen-ciprofloxacin. The results confirmed that this microfluidic liver model can be used to evaluate the hepatotoxicity of drug-drug interactions [38].

Some drugs may induce cell injury by inhibiting the mitochondrial enzyme function or even directly interrupting the respiratory complex. The tracking of oxygen consumption in this process could predict the toxic effect of these drugs. To analyze this type of metabolism, a microbioreactor with a removable inner microwell of PDMS bonded to glass coverslips was developed. The outer part of the device was fabricated with stainless steel and a top glass window. The device was equipped with a fusion touch syringe pump to perfuse the media. Each well was coated with collagen and cultured with HepG2/C3A and HeLa cells. Using a luminescence quenching assay, the authors quantified real-time oxygen, distribution of amiodarone and acetaminophen, and toxicity. When acetaminophen and amiodarone were introduced into the system, they showed the progressive inhibition of complex III of the mitochondrial electron transport chain and hepatotoxicity independent of CYP450 [39].

Pein et al. [40] fabricated a biochip with two polyethylene terephthalate (PET) porous membranes separated into upper and lower chambers and sealed with PS. The first and last microchannels contained human umbilical vein endothelial cells (HUVECs) and macrophages, and the central channel hosted the hepatic compartment with HepaRG hepatocytes and stellate cells. The device demonstrated vitamin E metabolites to act as inflammatory suppressors and elucidated the metabolic pathway. Moreover, the multicellular chip allowed for identifying the cellular features, such as chemotaxis, cytokine production, and cellular regulation, induced by the vitamin E metabolites [40].

The physiological elements measured in most of the studies that represent a healthy liver are albumin and urea production. If the concentration of either of these metabolites is impaired, it may result in hepatotoxicity. Mi et al. [41] developed a device consisting of a PDMS/glass chip with three chambers. The system consisted of an upper layer fabricated by lithography using PDMS and a lower layer of a glass slide (Figure 2(a)). The upper chamber contained the medium and the factors, while the middle and lower chambers were used for HepG2-laden collagen and HUVEC-laden collagen culture, respectively (Figures 2(b)–2(d)). The amounts of albumin and urea were evaluated over a period of 7 days after acetaminophen treatment. The results showed that albumin secretion and the urea concentration decreased with increasing acetaminophen concentration. The device achieved biomimetic functions and structure by maintaining bioactivity for seven days, while it has exhibited great potential for hepatotoxic drug screening [41].

Bhise et al. (2016) designed a platform that enables the bioprinting of hepatocyte spheroid-laden hydrogel constructs directly in the culture chamber of a bioreactor. The system consisted of three chambers divided by layers of PDMS and PMMA covered by a glass slide. Spheroids were then mixed with gelatin methacryloyl (GelMA) and printed in the middle chamber (Figures 3 and 4). The bioreactor can be disassembled to access the cells for biological assessment during the long-term culture period. The platform maintained the cultured spheroids viable and active for thirty days and represents an important step towards the fabrication of automated systems for high-throughput drug screening [23].

An important characteristic of the liver is its zonation, meaning that cells from different parts of the lobule are affected differently by structurally diverse and functionally different toxins. DILI triggered by various drug types that are metabolized in different zones of the liver is typically a cause for acute and chronic liver diseases. Weng et al. [42] fabricated a liver-on-a-chip consisting of a micropatterned collagen-coated PDMS membrane with diverter plates of polycarbonate (PC) to sandwich the membrane and a peristaltic pump for medium circulation (Figures 5(a)–5(f)). Stained primary liver cells (PLCs) were deposited on the membrane and incubated overnight (Figure 5(g)). Cells under controlled microenvironmental conditions were able to differentiate, and hepatic zonation and a dose-dependent effect of acetaminophen were observed. This device showed great potential for studying drug-induced liver injury in a more detailed manner [42].

Significant efforts have been made in developing microfluidic platforms for predicting human pharmacokinetics and pharmacodynamics using *in vitro* human models. 3D liver-on-chip models hold great potential for understanding the mechanisms of drug hepatotoxicity and for improving the *in vitro* ADME methods during drug development. Challenges such as reproducibility, 3D miniaturization of the proximal tubule, the use of appropriate materials for the device fabrication, and the stem cell differentiation are yet to be addressed for clinical applications. Cell-cell interaction and a dynamic microfluid flow have permitted mimicking the physiological environment and the maintenance of liver function. Therefore, facilitating a longer-term culture of hepatocytes which allows for the exploration of the modes of action and the biological responses to drugs and drug interactions is of great importance.

2.2. Kidney-on-Chip. The kidneys are involved in maintaining homeostasis in the several physiologic operations of the body, including the filtration and retention of essential compounds, blood pressure, and physiological pH regulation. The kidneys also mediate the excretion of waste materials, excess drugs, and their metabolites during drug metabolism. Due to these last functions, the analysis of the drug toxicity is

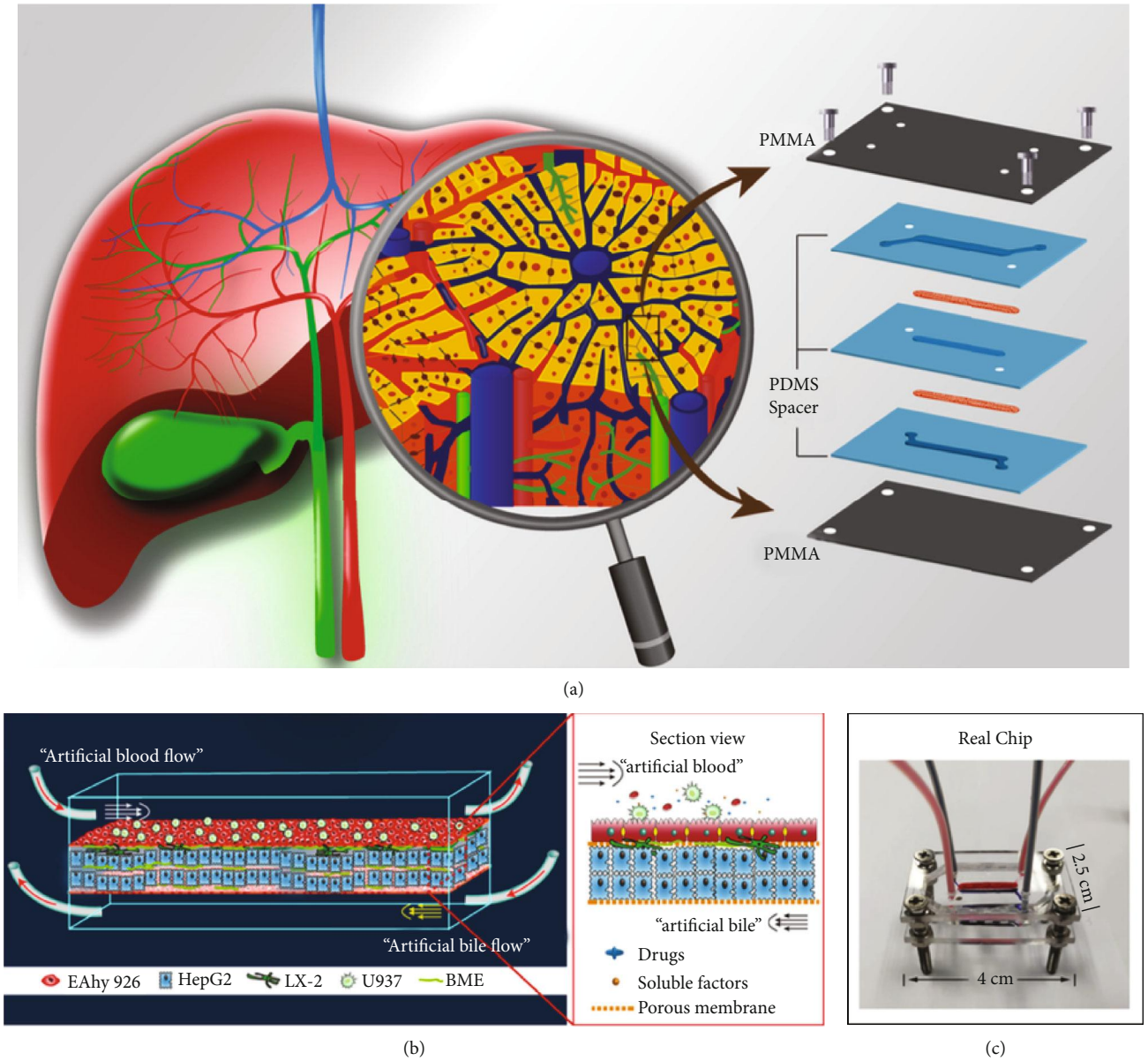

Figure 1: (a) Schematic of a liver sinusoid structure and the LSOC microdevice. Left: an illustration of the physiological structure of the liver sinusoid in the liver. Right: the design of the LSOC microdevice. (b) Schematic diagram of four cell lines seeded in the device. (c) Picture and size measurement of the chip. Reproduced (or adapted) with permission [38], ©2019, American Institute of Physics.

frequently performed within kidney model platforms [43]. The two factors that influence such excretion of waste compounds are the glomerular filtration rate (GFR) and the renal blood flow (RBF). While the primary factor delivers the drug to the kidney, the GFR eliminates the metabolites. The minimal functioning unit of a kidney is a nephron, consisting of the glomerulus, loop of Henle, and the proximal convoluted tubule. The glomerulus is where the major blood filtration process occurs. It consists of a network of capillaries through which circulating blood can be filtered in the urine, making it the most important part of the renal system. The tiniest construction element of this network is called a podocyte, a highly differentiated epithelial cell type that constitutes a major proportion of the kidney filtration barrier and regulates selective filtration. Renal function progressively reduces in the elderly, which may result in two pathologic entities: chronic kidney disease (CKD) (including glomerulonephritis, hypertensive nephrosclerosis, and diabetic nephropathy) and acute kidney disease (AKD) when blood clots or cholesterol deposits gather around the kidneys. Typically, drug excretion in these patients is impaired.

In vivo drug administration results in a complex process; the main focus of kidney-on-a-chip devices is to mimic the kidney physiology and function in order to determine the nephrotoxicity caused by the administration of different drugs [44]. In the design and development of a kidney-on-a-chip device, therefore, mimicking both factors (GFR and RBF) is of great importance. The complexity of the kidney anatomy makes it rather difficult to mimic the full organ on the chip (Figure 6). For that reason, the majority of the

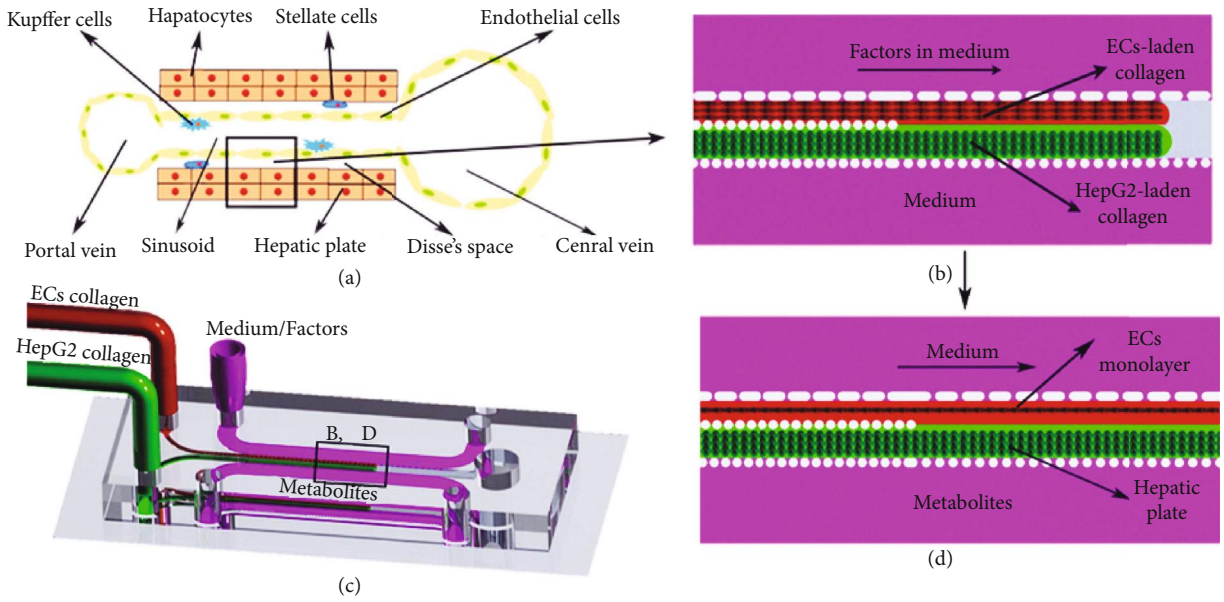

Figure 2: Formation of the biomimetic liver sinusoid on a chip. (a) Schematic diagram of a liver sinusoid. Hepatic plates and endothelial cell (EC) monolayers are the main part of this unit. (b) Injection of cell-laden collagen and medium with factors. (c) The 3D schematic diagram of collagen and medium injection process. (d) After the stimulation of factors for two days, an EC monolayer formed and medium with factors was changed to medium without factors, forming the liver sinusoid on a chip. Reproduced (or adapted) with permission [41], ©2018, IOP Science.

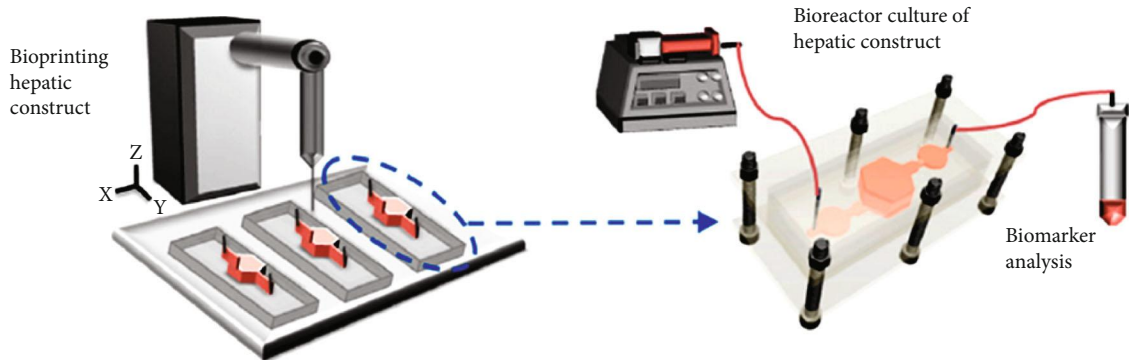

Figure 3: Schematic of the hepatic bioreactor culture platform integrated with a bioprinter and biomarker analysis module [23], ©2018, IOP Science.

studies focus on specific parts of the kidney, including the tubules or the glomerulus [45–47]. Some devices mimic solely a glomerulus-on-a-chip to measure nephrotoxicity or drug interactions, while others may mimic the renal tubular cells from a different part of the tubules in order to measure the toxicity damage or to simulate the urine flow rate.

The most common cell type used for the *in vitro* evaluation of kidney toxicity includes kidney proximal tubule epithelial cells (PTECs) [48, 49], immortalized kidney epithelial cells (HK-2) [50], dog kidney cells (MDCK), pig kidney cells (LLC-PK1) [51], and human proximal tubular epithelial cells (HPTECs) [52]. Traditional 2D culture systems or static organoid systems do not mimic the structural and functional characteristics of these cells [47, 49, 53–55]. Other studies are focused on mimicking nephrons in order to demonstrate a relationship between fluid flows and primary cell functionality [56]. With this overview, 3D models of kidney tissue that analyze human responses are essential for drug screening, disease modelling, and kidney organ engineering for tissue remodelling [56, 57]. Some of the latest examples of kidney-on-chip platforms for drug discovery, development, and analysis are thoroughly reviewed in this article (Table 2).

2.2.1. Analysis of Drugs in Kidney-on-Chip Devices. Traditional *in vitro* and *in vivo* studies using animal models are limited as there is a difference between the drug pharmacokinetics and pharmacodynamics in humans and in animals. An accurate system that identifies the nephrotoxicity of several compounds during the preclinical testing, therefore, can overcome the drawbacks of traditional models. Kidney-on-chip devices show excellent potentials in mimicking the structure and physiological environments of the organs while

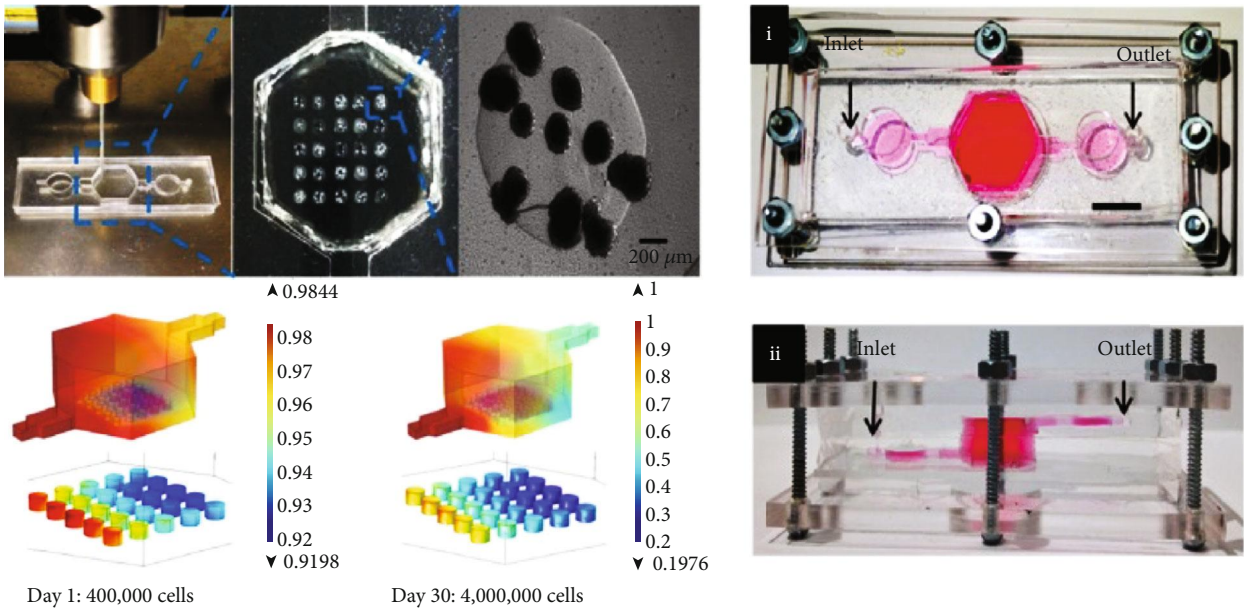

Figure 4: Bioprinting GelMA hydrogel-based hepatic construct within the bioreactor as a dot array. Top view (i) and side view (ii) of the assembled bioreactor with the inlet and outlet fluidic ports as indicated along with the oxygen concentration. Reproduced (or adapted) with permission [23], ©2018, IOP Science.

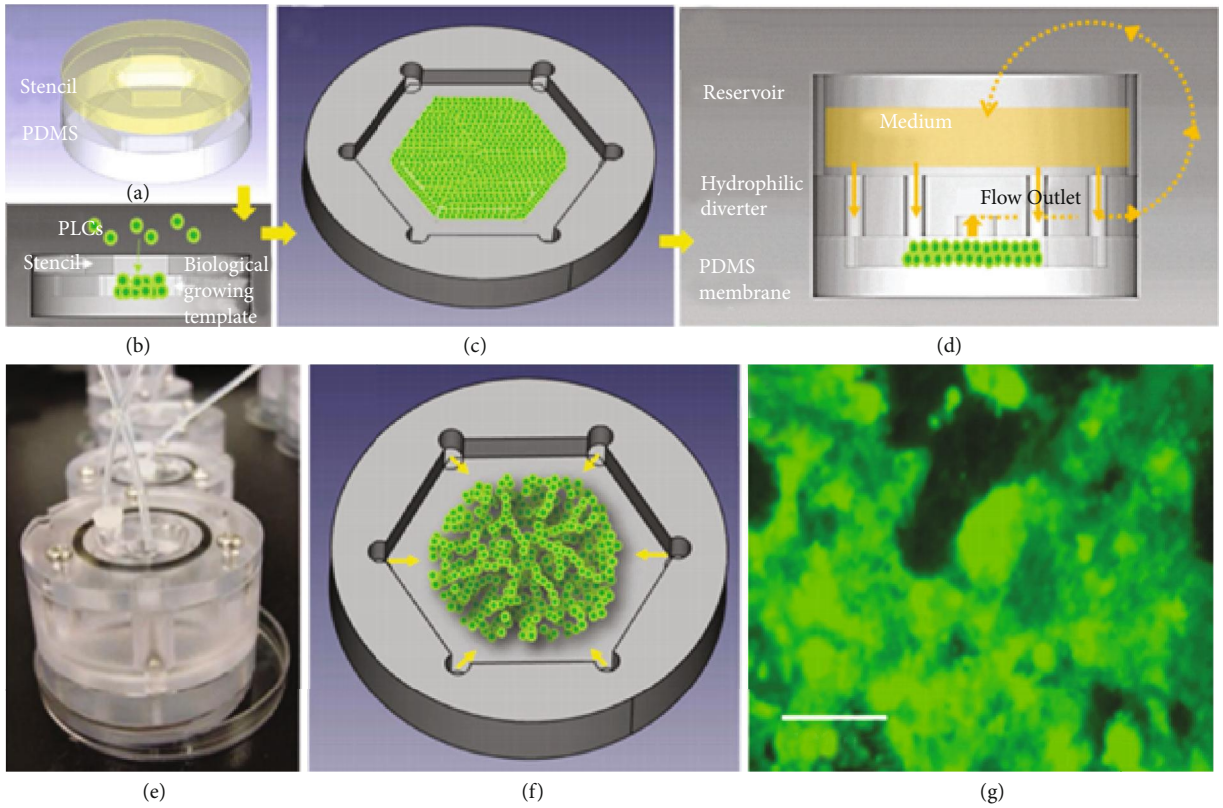

Figure 5: Design principles of a tissue incubator. Multilayered PLCs were deposited on PDMS membrane through a stencil (a) to create a biological growing template (b) and a hexagonal contour (c). After overnight culture, the stencil was removed, and a hydrophilic diverter was assembled with a reservoir to create micro-/macrocirculation (d). The hydrophilic diverter provides PLCs with vertical anchorage. (e) Photograph of the entire device. (f) Schematic diagram of the radial flow. (g) Liver-on-a-chip (LOC) shows the cell viability (green). Reproduced (or adapted) with permission [42], ©2017, Wiley Online Library.

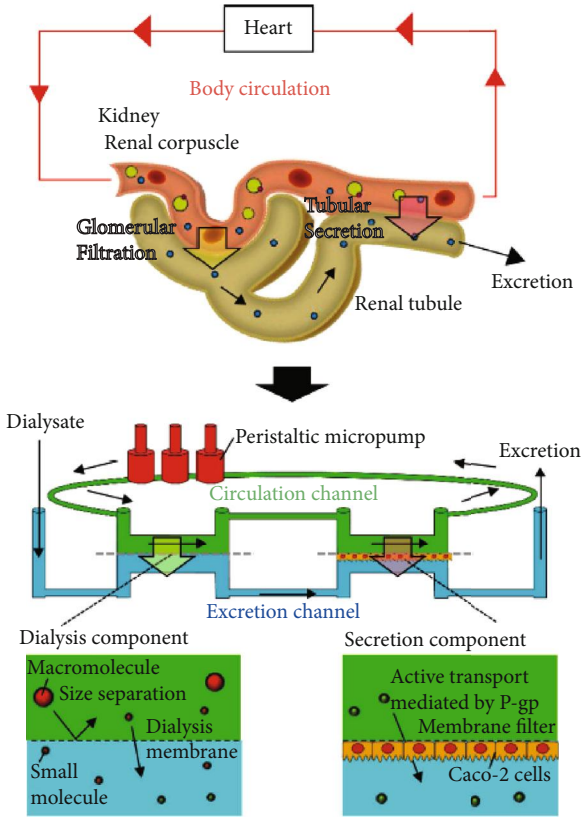

FIGURE 6: Renal excretion in the human body and the microfluidic kidney model which mimics the glomerular filtration and tubular secretion in the kidney. Reproduced (or adapted) with permission [45], ©2018, J-STAGE.

predicting drug effects, interactions, and toxicity. A microfluidic kidney-on-a chip device mimicked the differentiation of human-induced pluripotent stem cells (hiPSC) into mature podocytes that express markers for this phenotype. The device was fabricated through stereolithography using SU-8, silicon master mold, and PDMS. Four microchannels with two layers separated by a porous membrane created an ECM-cell interface to provide the appropriate culture media and to apply fluid shear stress (FSS). The array has proven to closely resemble the physiological behavior of *in vivo* environments. The authors have tested two different dosage assays under shear stress condition: (i) a daily gentamicin dose as a classic oral administration and (ii) a continuous infusion regimen. The cell mortality was 2% higher with the continuous regimen, which predicated that a normal regimen of 7-14 days would show a different pharmacokinetic profile. Also, the cell injury protein levels depended on the drug administration regimen. The study proved that one drug can lead to various outcomes and potentially damage kidney cells, depending on the way it is administered [54].

Primary cell lines cultured in the *in vitro* systems lack maintaining their physiological functions over an extended time. Induced pluripotent stem cells or immortalized cells have demonstrated to reproduce the proximal tubule characteristics. They are able to differentiate into podocytes and maintain the primary kidney cell functions for prolonged periods. A microfluidic device that uses podocytes cocultured with proximal tubule cells to mimic an accurate renal tubule has been proposed. Musah et al. [58] fabricated PDMS molds for developing microvascular channels and a porous membrane using stereolithography. The study differentiated hiPSC into podocytes for 35 days and improved the classical seeding. The upregulation of mature podocyte genes and downregulation of nephron progenitors confirmed a mature lineage, while the efficiency of differentiation was up to 90%. The podocytes were cultured on the top of the membrane and the glomerular endothelial cells on the opposite side of the membrane, separated by a glomerular basement membrane (GBM) to recapitulate the physiology and mechanical properties of the glomerular capillary. For five subsequent days, the cells were exposed to different concentrations of adriamycin (doxorubicin), a chemotherapeutic drug used to treat cancer. The results showed a dose-dependent toxicity through the quantification of albumin and inulin in the glomerular chip confirming a direct correlation of the drug-induced, dose-dependent cell damage. Moreover, cell destruction, higher urinary clearance, and albumin uptake were demonstrated within this platform [58].

The kidney proximal tubule plays a role in the absorption of nutrients, such as water and glucose, and secretes xenobiotics and protein-bound metabolites. Its cells, HPTECs, are frequently used to investigate the nephrotoxicity of several classes of drugs, including antibiotics and antiretrovirals [59]. Other studies evaluated a 3D tubular ECM scaffold to accurately reproduce the kidney's microenvironment and provide *in vivo*-like results [49, 60].

A study in 2016 described a 3D microphysiological system (MPS) consisting of a PDMS base with a collagen scaffold coated with an extracellular matrix (ECM) that resembled the human proximal tubule, which was used for growing PTECs for seven days. The authors analyzed the aquaporins and the sodium-glucose cotransporter-2 (SGLT2) inhibitors, a glucose uptake receptor, to prove the cell polarization in comparison to 2D models. The major contribution of this study was the assessment of metabolic competency in the case of ammonia biosynthesis and vitamin D biotransformation. The transportation of organic anionic solutes was sensitive to specific transport inhibitors, and the glucose reabsorption was 10-fold higher than that of previous reports and downregulated by the SLGT2 specific inhibition. This suggests that the device may be considered as a high-fidelity model that allows fundamental drug metabolism research [49].

In a recent study, the Nortis® device, with a chamber coated with type IV collagen, and an ECM to grow human primary PTECs, was explored. The device was applied to predict polymyxin (PMB) nephrotoxicity using injury biomarkers such as kidney injury molecule-1 (KIM-1), calbindin, clusterin, osteoactivin, VEGF, and α-GST. PTECs and immortalized cell lines were cultured and incubated in the chambers for 12 hours in the presence of the flow. Cell viability was determined by immunostaining. The authors concluded that the detection of biomarkers was fourfold higher than the controls after exposing PTECs to increasing concentrations of PMB and its analogs (NAB739 or NAB741) for 24 hours. This model has demonstrated a

Table 2: Summary of recent advancements of kidney-on-a-chip devices including the type of drug, the application, the applied cell, and the kinetics.

Drug type	Applications	Applied cell lines	Kinetics	Ref(s)
Gentamicin	Nephrotoxicity	MDCK	24 hrs	[54]
Vitamin D	Biotransformation	PTECs	>28 days	[49]
Polymyxin B	Nephrotoxicity	PTECs	14 days	[60]
Doxorubicin	Biodistribution	MDCK	—	[64]
	Nephrotoxicity, Nephrogenesis	NPC, EPCs	22 days	[61]
Cisplatin	Nephrotoxicity	Renal adenocarcinoma cell culture	24 hrs	[65]
Ciclosporin A	Nephrotoxicity, bioprinting	Convoluted renal proximal tubules	65 days	[47]
Adriamicin	Nephrotoxicity	hiPSC	>21 days	[58]

MDCK: Madin-Darby canine kidney; PTECS: proximal tubule epithelial cells; NPC: nephron progenitor cells; EPCs: endothelial progenitor cells; hiPSC: human-induced pluripotent stem cells.

capacity to detect drug toxicity within 24 hours of exposure [60].

Homan et al. (2016), on the other hand, developed a renal proximal tubule (PT) by combining bioprinting and organ-on-a-chip principles. The model consisted of a bioprinted silicon gasket with an open tubule to perfuse the cells (Figures 7(a)–7(d)). The ECM used in this study was composed of fibrinogen, gelatin, and two enzymes (thrombin and transglutaminase) that enabled the rapid solidification of the matrix around the 3D structures. Cell media and PTECs were perfused through the 3D convoluted tubular architecture on a chip through an external peristaltic pump (Figure 7(b), iv). By monitoring the variations of cell morphology, the nephrotoxicity of cyclosporine A (CysA) (typically used for transplant patients) was shown to be dose-dependent on CysA to induced damage. Moreover, the 3D PT and the perfused cells improved their albumin uptake and the albumin receptor, megalin. The platform tested over 65 days has proven to have a more extensive cell functionality than 2D cultures. The authors concluded that the model could be used for drug screening and disease modelling [47].

Homan et al. [61] later fabricated a millifluidic chip using silicone-based ink and gelatin for evaluating doxorubicin, a chemotherapeutic drug. H9 human embryonic stem cells (ESCs) were seeded into this device to develop organoids under controlled FSS. While the model was not used for any specific application, it has shown potential for studying kidney development, diseases, and regeneration [61].

Nephrotoxicity related to drugs has a significant patient morbidity and mortality rate, particularly on those exposed to a broad range of prescribed drugs, such as antibiotics, analgesics, and chemotherapeutic agents. The development of new approaches for the safety screening of drugs and other toxic compounds is therefore vital. Rayner et al. created a tunable human renal vascular-tubular platform (hRVTU) by a photolithography technique using PMMA layers separated by a collagen membrane. The authors developed a vascularized renal tubule using cells isolated from a single donor: HUVECs seeded into the top channel, human kidney epithelial cells (HKMECs) into the bottom channel, and fetal human kidney pericytes, into the collagen matrix [44, 45, 47, 49]. The platform has not been used for testing any drug; however, the model could hold great promise for studying kidney diseases and for drug development [62].

Kidney cells contain ion channels which control the ion concentration by absorption or secretion into the urine. To assess the functionality of ion channels in kidney-on-a-chip devices, Aschenbrenner et al. developed a low-cost device manufactured by 3D printing using acrylonitrile butadiene styrene (ABS) to measure the Ca^{++} flux. The device is composed of an inlet, a chamber, and an outlet, with a zigzag-shaped microfluidic channel. Transfected human embryonal kidney-derived (HEK293) cells with the capsaicin (a pungent alkaloid from chili peppers) receptor TRPV1 were seeded in the chamber and incubated overnight under standard conditions. Using cell morphology imaging during chemical stimulation with capsaicin, the fluorescence intensity showed a consistent increase with an increase in the intracellular calcium concentration. The authors concluded that the model was reliable for ion analysis [63].

It is, indeed, challenging to effectively reproduce the kidney's sophisticated microvessels and their physiology. A reported kidney-on-chip has modelled the microvessels for the evaluation of anticancer drugs. Bogorad et al. [64] employed a platform to study the pharmacokinetics and transport of doxorubicin in MDCK cells. The model contained perfusable microvessels to obtain fluorescence images to quantify drug transport at different time points. The developed microdevice recreated the structure and physiology of kidney cells. The results could be compared with previous reports describing renal cell receptor polarization explored through real-time imaging and quantitative analysis of doxorubicin permeability [64].

Other studies integrated sensors within the organ-on-a-chip devices for monitoring the drug-induced nephrotoxicity *in situ*. Additionally, the detection instruments such as smartphone-based fluorescence readers offer beneficial features in the monitoring of drugs. Cho et al. [65] incorporated a fluorescence nanoparticle immunocapture/immuneagglutination assay into a kidney-on-a-chip coupled to a smartphone-based microscope to evaluate the cytotoxicity of cisplatin on renal adenocarcinoma cells. The device consisted of three layers of PDMS with an inlet and outlet holes. The three layers were patterned onto glass, and the bottom substrate was etched in order to measure the analytes of interest. When the proximal tubular

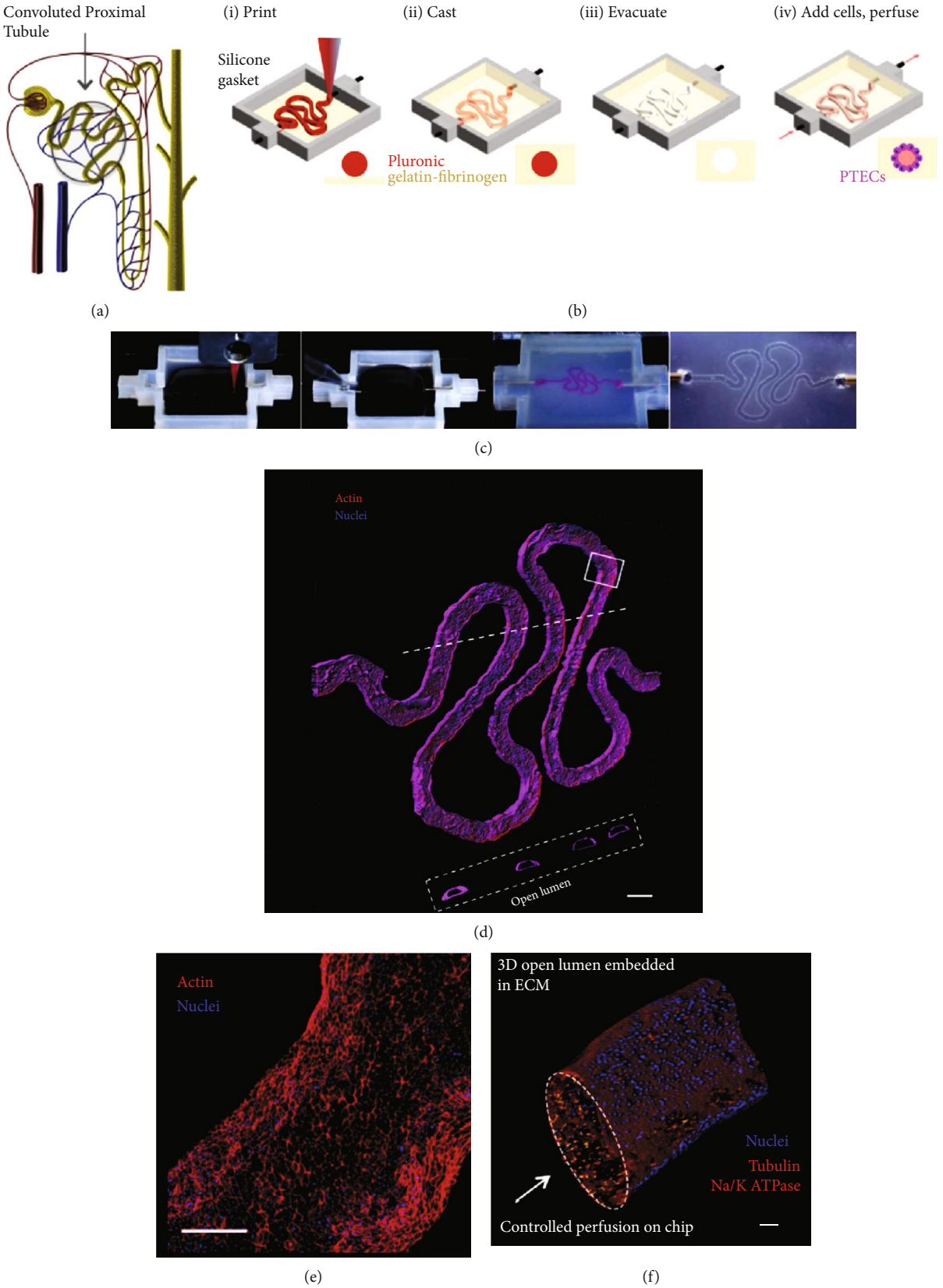

Figure 7: 3D convoluted renal proximal tubule on a chip. (a) Schematic of a nephron highlighting the convoluted proximal tubule; (b, c) corresponding schematics and images of different steps in the fabrication of 3D convoluted, perusable proximal tubules; (d–f) a 3D rendering of the printed convoluted proximal tubule acquired by confocal microscopy. Reproduced (or adapted) with permission [47], ©2016, Nature.

cells in the kidney are exposed to toxins, their brush border membrane released γ-glutamyl transpeptidase (GGT) into the lumen which was recognized by a sensor. The results established that with increasing cisplatin concentrations, the fluorescence intensity also increased. Furthermore, with the increase of cisplatin, γ-glutamyl transpeptidase antigens were released into the media; hence, cell viability decreases [65].

One of the major limitations for the development of kidney-on-chip devices is the lack of human podocytes, which are the main component of the glomerulus. With recent advances in the differentiation of podocytes from human pluripotent stem cells, and their coculture with renal parenchyma, this challenge is expected to be overcome. However, further research in this area is required. Moreover, development of more realistic 3D models that could integrate the glomerulus, the proximal tubular-like cells, and nephron-like cells is still on the horizon of research accomplishment. Such platforms would ideally mimic the human kidney and reproduce the biological processes of the kidney for the preclinical assessment of candidate drugs.

2.3. Lung-on-Chip. In mammals, the lungs are part of the lower respiratory system. Their composition includes airways, multiple branched blood vessels, and two main zones: the conducting zone, where the air enters, and the respiratory zone, where the exchange of oxygen and carbon dioxide occurs. The main parts are the bronchus, bronchiole, and alveoli, and each compartment has epithelial cells and a basement membrane. Within the alveoli, alveolar type I and type II cells exist. The alveolus is the smallest functional unit of the lung and provides a large surface area for gas exchange [66]. The biomimetics (and bioenergetics) of the lungs represent a unique challenge, as it includes several types of cells and mechanical forces since a periodic mechanical axis force is exerted with each respiratory cycle, and this dynamic mechanical force is difficult to recreate *in vitro* [67]. However, development of accurate lung tissue is critical to understanding the effects of drugs, toxins, and pathogens in such airways, as well as the understanding of infectious diseases which impact respiratory function.

Some models have used suspended gels to create the basal lung membrane. Humayun et al. [68] developed a microfluidic device using PMMA micromilling consisting of three chambers: (i) an upper microchamber for achieving an air-liquid interface and seeded with EC, (ii) a middle matrigel-collagen layer, and (iii) a lower chamber cultured with smooth muscle cells (SMC) (Figure 8). These chambers kept the cells functional and alive for 31 days, as measured by morphological markers, including ZO-1 tight junctions and F-actin [68]. Such cell stability allows further analysis of the lungs and impacts the measurement of a drug on lung functions.

Another device created by Stucki et al. [69] integrated respiration movements. The design has a bioartificial alveolar barrier, with a thin, porous, and flexible PDMS membrane. On this membrane, epithelial cells were cultured on the apical side and endothelial cells on the basal side. To generate a microdiaphragm, the membrane was stretched downwards into the pneumatic part and connected to pneumatic microchannels (Figure 9). The microdiaphragm applied a reproducible 3D cyclic strain to the cells to mimic the movements of the diaphragm (Figure 9). The study demonstrated that mechanical stress affected the permeability of the epithelial barrier [69]. Some of the latest examples of lung-on-chip platforms for drug discovery, development, and analysis are thoroughly reviewed in this article (Table 3).

2.3.1. Analysis of Drugs in Lung-on-Chip Devices. Air-borne toxins may affect the integrity of the epithelial barrier. During a study conducted by Liu et al. [70], they exposed lung cells to different levels of polluted air or cigarette smoke. Their device was fabricated by soft lithography with a middle PMMA layer having through-hole arrays. Each hole was pipetted agarose-gelatin and epithelial cells. In the upper chamber, these cells were always in contact with air or different air contaminants. Such accurate microdevices aided in the analysis of different lung injuries. In this study, the authors obtained a mimetic lung injury that induced an inflammatory response in the lung cells [70]. This device has the specific capabilities of the human lung to evaluate and predict drug toxicity *in vitro*.

A potential limitation of this device was that the applied cells used originated from adenocarcinoma human alveolar basal epithelial cells. Addressing the potential limitations of the model would require using primary human alveolar epithelial cells from a long-term culture.

Huh [71] created a microfluidic device that replicated the microarchitecture and dynamic microenvironment of the alveolar-capillary unit of the living human lung. The study introduced inflammatory insults, including proinflammatory cytokines and *E. coli* bacteria, into the upper alveolar compartment, to recapitulate the cellular immune response to microbial infection in human lung alveoli. This activated the endothelial cells on the opposite side of the membrane and resulted in the increased expression of adhesion molecules. This was followed by adhesion of human neutrophils circulating in the lower vascular channel to the endothelium and the subsequent transmigration across the tissue layers into the airspace [71]. This human breathing lung-on-a-chip, microengineered model has the potential to evaluate environmental toxins, such as silica nanoparticles.

The creation of devices that involve airways permits the analysis of lung inflammation and the testing of drugs. In the work of Benam et al. (2016), the microdevice consisted of two parallel PDMS channels divided by a porous PS membrane coated on both sides with type I collagen, on which epithelial (top air channel) or endothelial (bottom blood channel) cells were cultured to create a tissue-tissue interface. The study analyzed the structural features of the cell barriers with high mimetic results for 4-6 weeks. With this model, the authors induced an asthmatic phenotype and chronic obstructive pulmonary disease (COPD) and treated the cells with IL-13. Major molecular characteristics of asthma, including IL-8, RANTES, cellular damage, and goblet cells, were measured. The study reported a subsequent treatment of rheumatoid arthritis with tofacitinib to inhibit the signaling pathway of IL-13 or dexamethasone. The results were consistent with clinical findings, which indicated that the

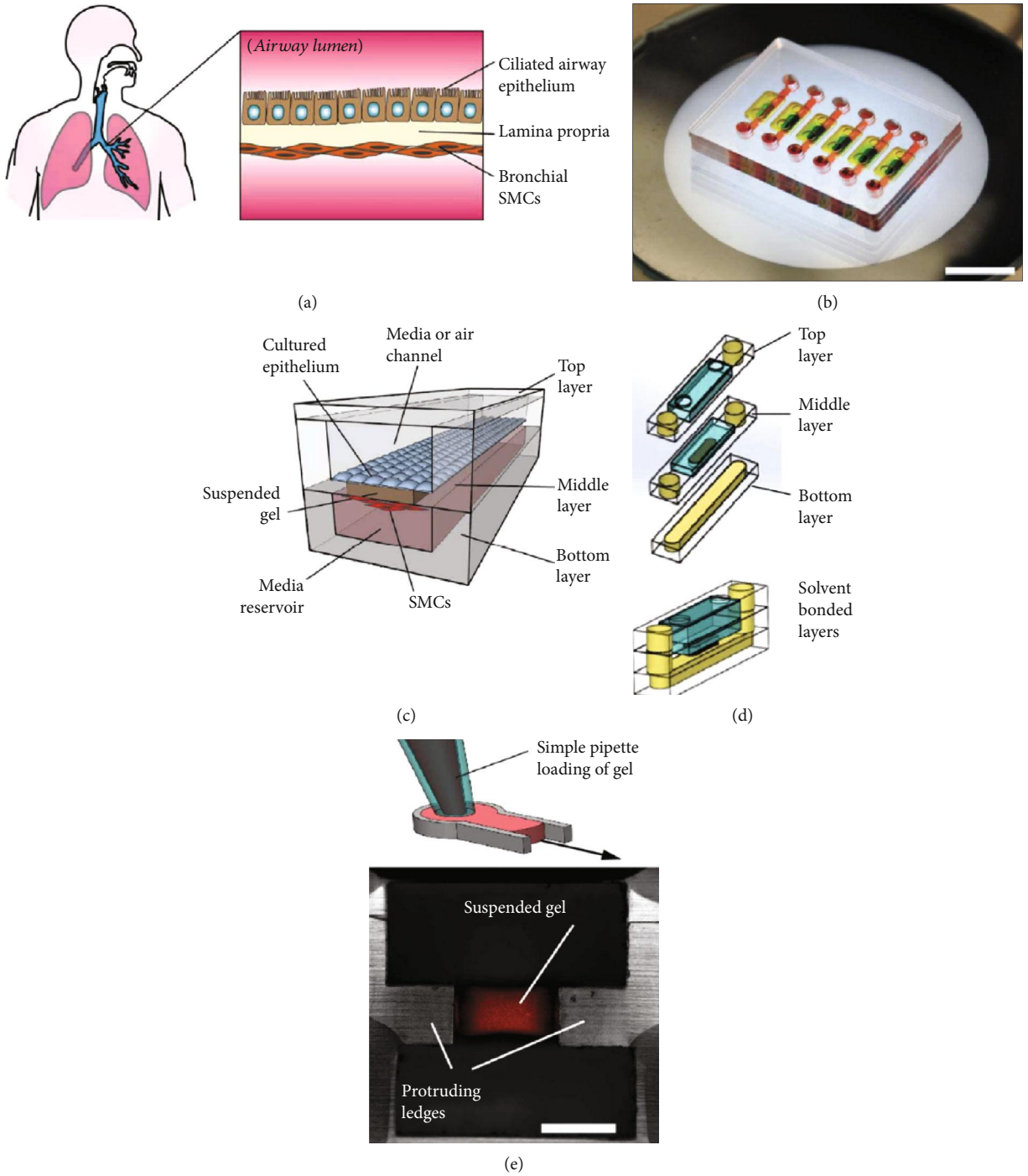

Figure 8: Lung airway-on-a-chip device design and fabrication. (a) Schematic of airway lumen tissue structure. (b) Photograph of an assembled lung airway microdevice (scale bar = 10 mm). (c) Lung airway microdevice schematic design. (d) Exploded view of the three PMMA layers. (e) The suspended hydrogel is introduced into the middle layer. Magnified image of the device cross-section (scale bar = 500 μm). Reproduced (or adapted) with permission [68], ©2018, Royal Society of Chemistry.

specific inhibitor, tofacitinib, restored normal cilia and reduced the cytokine production in comparison to corticosteroid administration, which was ineffective [67].

Pulmonary thrombosis affects 650,000–700,000 persons annually in the United States of America (USA), of which approximately 10% is due to an inopportune diagnosis. There is an absence of effective *in vitro* or animal models for studying this disease that could lead to the development of new treatments. A device composed of two PDMS microchannels, separated with a porous, thin, and flexible PDMS membrane, was fabricated. The membrane was coated with an ECM, which emulated the interaction between endothelial cells and the alveolus in the human lung (Figure 10). This model used whole human blood instead of a cell culture

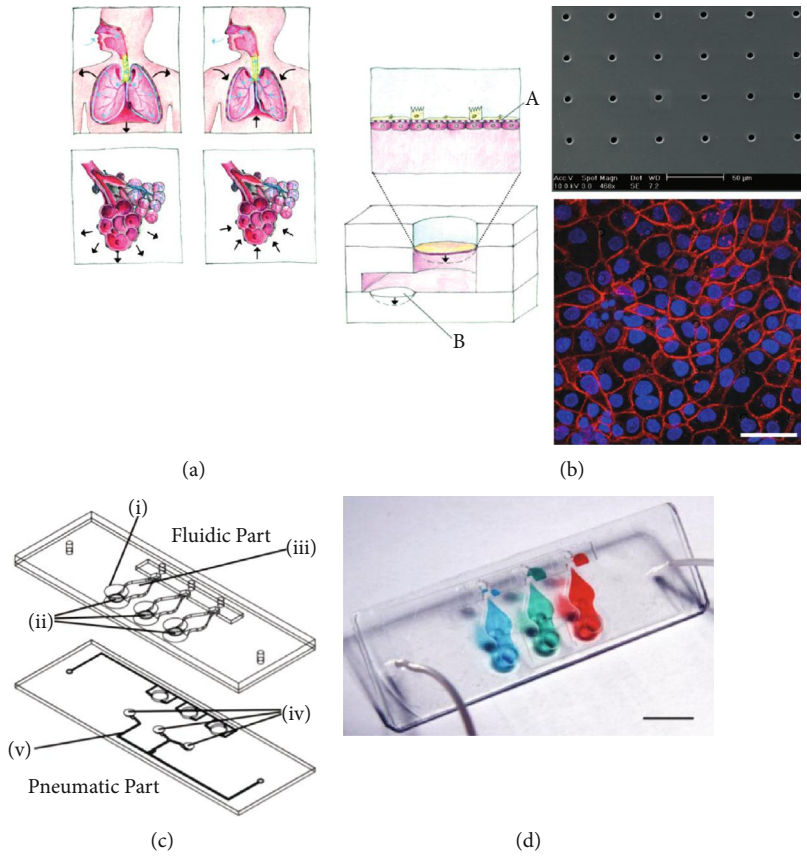

Figure 9: Design of the lung-on-a-chip. (a) In vivo, inspiration is controlled by the diaphragm. (b) In vitro, the 3D cyclic mechanical strain of the bioartificial alveolar membrane (A) induced by a microdiaphragm; (B) the bioartificial alveolar membrane is shown in the upper microscope picture. (c) The fluidic part consists of (i) alveolar cell culture wells, (ii) membranes, (iii) basolateral chambers, (iv) microdiaphragms, and (v) pneumatic microchannels. (d) Photograph of the lung-on-a-chip (scale bar, 10 mm). Reproduced (or adapted) with permission [69], ©2015, Royal Society of Chemistry.

Table 3: Summary of recent advancements in lung-on-a-chip systems including the type of drug, the application, the applied cell lines, and kinetics.

Drug type	Application	Applied cell lines	Kinetics	Ref(s)
Gefitinib	Antitumoral drug	A549, HFL1, and HUVEC	5 days	[73]
Parmodulin-2	Antithrombotic drug	hAEC and HUVEC	12 days	[72]
Tofacitinib	Anti-inflammatory drug	hAEC	5 weeks	[67]
ZnO and TiO_2 nanoparticles	Nanotoxicity	hAEC and HUVEC	3 days	[76]

A549 is an adenocarcinomic human alveolal basal epithelial cell. HFL1: human fetal lung fibroblasts; HUVECs: human umbilical cord cells; hAEC: primary human alveolar cells; ZnO: zinc oxide; TiO_2: titanium dioxide.

medium, leading to a device that could evaluate antithrombotic drugs *in vitro* [72]. In this work, the authors induced platelet activation and clot formation in the presence of fluid shear conditions by collagen exposure. As it occurs within *in vivo* systems, when the endothelium was stimulated by inflammatory cytokines, it promoted platelet recruitment and thrombus formation. A drug candidate, parmodulin-2 (PM2), was tested for the treatment of this injury. The drug possessed antithrombotic and anti-inflammatory properties as a result of the inactivation of protease-activated receptor-1, a peptide that mediates tissue inflammation and coagulation abnormalities. In this model, the drug indicated a potent protective and antithrombotic effect on human lung cells [72].

Gefitinib is an anticancer drug that inhibits the epidermal growth factor receptor tyrosine kinase (EGFR-TKIs) and which benefits non-small-cell lung cancer (NSCLC) patients. The drug is a tyrosine kinase inhibitor of the EGFR that regulates basic cellular functions, such as proliferation, migration, and differentiation, which play a role in the etiology of solid tumors. However, the initial drug resistance has become challenging. A research group introduced a lung tumor model with the cultured A549 lung cancer cell line and

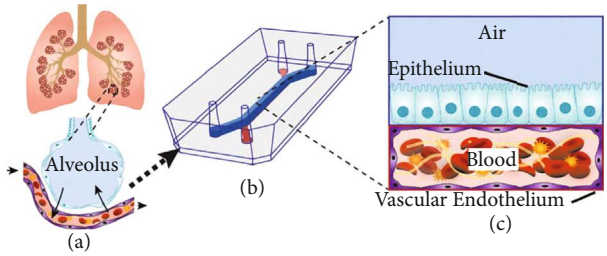

FIGURE 10: Microengineered model of human pulmonary thrombosis-on-chip. (a) A conceptual schematic of the human lung showing that the alveoli interact with the neighboring blood vessels during hemostasis or pulmonary dysfunction. (b) Engineering drawing of the microdevice. (c) Graphic illustration showing how the top compartment (1 mm wide and 1 mm tall) is cultured with human primary alveolar epithelial cells and the entire bottom chamber (1 mm wide and 250 mm tall) lined with human endothelial cells forming a lumen. Reproduced (or adapted) with permission [72], ©2017, American Society for Clinical Pharmacology and Therapeutics.

human fetal lung fibroblasts. In this study, the authors created a microfluidic device with a nanofiber membrane made from polylactic-co-glycolic acid (PLGA) and PDMS (Figures 11(a) and 11(b)). The electrospun PLGA membrane was designed to be biocompatible, porous, and permeable. The toxicity of gefitinib, an anticancer drug, was evaluated by testing the cell viability of the cocultured human non-small-cell lung cancer cells (A549), human fetal lung fibroblasts (HFL1), and HUVECs (Figures 11(c)–11(e)). A459 cells are typically sensitive to gefitinib; however, when cocultured with HFL1, it was found that these cells helped in the survival of the cancerous cells, despite the presence of the drug. When A549, HFL1, and HUVEC cells were cocultured, A549 stimulated the invasion of tumoral cells causing the death of HUVECs. This lung-on-a-chip device successfully simulated the tumor microenvironment and alveolar biochemical factors to evaluate the toxicity of a drug for personalized medicine [73].

Nanotechnology has been emerging as an important tool for many novel applications in the biomedical field. However, exposure to nanoparticles (NPs) has generated pulmonary diseases, such as asthma, pulmonary edema, emphysema, and lung cancer [74]. Titanium oxide (TiO_2) is considered safe; however, zinc oxide (ZnO) NPs induce toxicity to human lung cells by causing damage to the alveolar epithelial cells and human alveolar adenocarcinoma [75]. A recent study evaluated the toxicity of ZnO and TiO_2 in a lung-on-a-chip device, measuring reactive oxygen stress and apoptosis of the epithelial and endothelial cells. The device consisted of two parallel channels lined with human pulmonary alveolar cells and a lower chamber with human umbilical endothelial cells. In the middle channel, matrigel coverture mimicked a basal membrane. The NPs were delivered to the epithelial cells mimicking acute pulmonary nanoparticle exposure. Both nanoparticles showed dose-dependent toxicity on the two cell lines causing apoptosis. The ZnO particles showed higher membrane permeability due to cell destruction by oxygen species [75].

In line with these findings, another study introduced a mathematical model and practical device experiments predicting the nano- and microparticle delivery to the cell within microfluidic devices by closely mimicking the airways of the lungs [76]. ZnO and TiO_2 particles with diameters of $d \leq 700$ nm were spread in the air flow using different flow rates. The results confirmed that ZnO NPs were more toxic than TiO_2, showing higher reactive oxygen species and permeability. The system has accurately mimicked acute pulmonary nanoparticle exposure.

Despite numerous advancements in the development of lung-on-chip devices, there are still many challenges associated with the development of 3D *in vitro* lung models. Various designs and fabricated devices will further an understanding of organ physiology, drug toxicity, and drug interactions. Nevertheless, the lung-on-a-chip models need to use pluripotent stem cells, provide an appropriate biological environment to maintain the cell functions over extended periods of time, and incorporate ventilation mechanics into the miniaturized lung-on-chip platforms. These platforms could lead to the development of integrated systems to study the clinical course of lung diseases and to evaluate novel therapeutic strategies.

2.4. Gut-on-Chip. The first stage in the pharmacokinetics of a drug is the absorption of that drug. In that perspective, the route of administration of the drug is of great importance. Oral medications arrive at the gut that is covered by a membrane. The close interaction of the gut with ingested food, xenobiotics, and drugs induces the rupture and absorption of the consumed materials. The intestine contains villi and microvilli on the epithelial cells, which promote secretion, cellular adhesion, and absorption by increasing the surface area, among other factors [77]. The many functions of the gut, including peristaltic movements and intestinal microbiota which pertain, pose a great level of complexity, hence challenging their replication on static models. Single-dose and repeat-dose testing in toxicological studies is typically developed during the preclinical phases of drug development for identifying the effects of a drug on functions in the gut, including intestinal motility, nausea and emetic reflex, and absorption. *In vitro* cell culture techniques use a monolayer of human colon adenocarcinoma cells (Caco-2) and the human colorectal adenocarcinoma cell line (HT-29) to predict the rapid assessment of orally administered drugs. However, current *in vitro* models lack the careful mimicking of the tissue structure, the absence of microbiota [78], and the complexity of the gut functions, such as peristaltic movements and flow [79]. A considerable number of research studies have focused on the development of gut-on-a-chip devices and have attempted to closely model the characteristics of the intestine, including the microbiome [80]. Microfluidic organ-on-a-chip models of the human intestine are one of the most studied 3D models, as those platforms are very advanced in the integration of several cell lines, including Caco-2, HUVEC, myofibroblasts, primary intestinal epithelial cells, or immune cells. Such synergy allows researchers to evaluate drugs, diseases, microbiome interactions, colon cancer metastasis, and

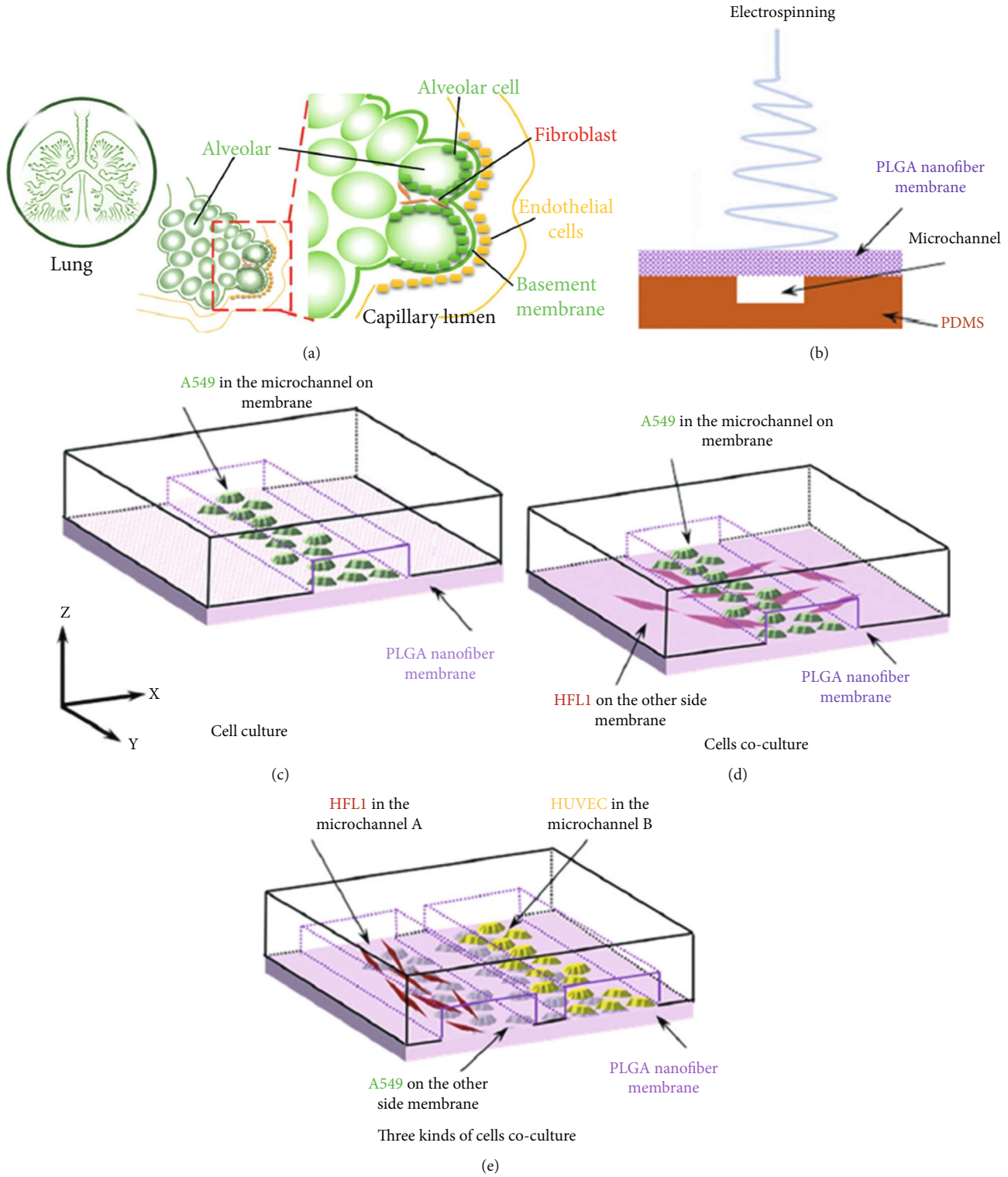

Figure 11: (a) Schematic diagram of the alveolar structure. (b) Schematic diagram of microfluidic chip with PLGA nanofiber membrane as substrate prepared by electrospinning. (c) Schematic diagram of culture of A549 cells on the chip. (d) Schematic diagram of the coculture of A549 cells and HFL1 cells. (e) Schematic diagram of the coculture of A549 cells, HFL1 cells, and HUVECs. Reproduced (or adapted) with permission [73], ©2018, Royal Society of Chemistry.

radiation effects in a single system. Some of the latest examples of gut-on-chip platforms for drug discovery, development, and analysis are thoroughly reviewed in this article (Table 4).

2.4.1. Analysis of Drugs in Gut-on-Chip Devices. Different devices with sophisticated microchannels and perfused chambers have been engineered where immune cells, gut

Table 4: Summary of recent advancements in gut-on-chip platforms including the type of drug, the applications, the applied cell lines, and the kinetics.

Drug type	Applications	Applied cell lines	Kinetics	Ref(s)
DMOG	Drug interaction Radiation-g	Caco-2 HUVEC	5 days	[84]
Isofosfamid, verapamil	Pharmacokinetics	Caco-2	11 days	[93]
Midazolam, indomethacin	Pharmacokinetics Toxicity	PiEC, human myofibroblast, Caco-2	21 days	[94]
Paracetamol	Toxicity	Caco-2, HepG2	14 days	[140]
Mariskat	Efficacy	Caco-2, hIEC	24 days	[141]
Rifampicin, ketoconazole	Pharmacokinetics	HiPCs	34 days	[142]

DMOG: dimethyloxaloyl; Caco-2: colon adenocarcinoma cells; HUVECs: human umbilical vein endothelial cells; PiEC: primary intestinal epithelial cells; HepG2: human hepatocellular carcinoma cells; hIEC: human intestinal epithelial cells; HiPCs: hormone independent prostate cells.

microbiome, and pathogens were cocultured, while fluids that deliver nutrients, drugs, and other compounds were flowing under controlled peristaltic-like motion. These devices mimic the human intestinal microenvironment and emulate many physiological and pathophysiological functions of the gut. They are used to study gastrointestinal infections, immune-microbiome inflammatory diseases (inflammatory bowel disease), ileus disease, celiac disease, colorectal cancer, etc., and to understand disease mechanisms. Some human enzymes, including CYP450, CYP2C9, CYP2D6, and CYP3A4, are the most important isoforms of P450 enzymes in phase 1 drug metabolism in humans [81]. The activity of such enzymes can be carefully studied within gut-on-chip devices. Furthermore, understanding the interactions between the gut cells, microbiota, and pathogens with drugs is crucial. Application of 3D microfluidic devices has opened windows of opportunity to predict the efficacy and safety of new and existing drugs. This technology has been used to develop human gut-on-a-chip models that emulate the human intestinal structure to culture human Caco-2 cells, commensal and pathogenic microorganisms, and immune cells inside its cyclic mechanical forces thereby emulating an *in vivo* intestine [82].

A microfluidic gut-on-a-chip model was developed to analyze and provide new insights on the pathophysiology of inflammatory gut diseases, including bowel disease and ileus, and to determine the bacterial overgrowth. The authors fabricated the device from flexible PDMS with three microchannels, where the central channel has an ECM-coated porous membrane that was seeded with the cells. Caco-2 cells were cultured under peristaltic movements and were exposed to the flow of the culture medium through the upper and lower microchannels to promote the formation of villi structures. The platform was intended for the growth of the gut microbiome and for drug assessment. Moreover, the platform was used to evaluate the effects of probiotics and antibiotics, confirming that peristaltic forces play an important role in the gut biome preventing overpopulation [79, 83]. In the gene analysis, it was observed that cells cultured with the microfluidic devices change the expression of 22,097 genes compared to static cultures. Moreover, the addition of probiotic bacteria for 72 h in the gut-on-chip exhibited a different profile compared to chips without bacteria. When the enteroinvasive *E. coli* bacteria were introduced to the system, the microbiota also protected the height of the villi and decreased the lesion area [83].

To address the mimetic capacity of microfluidic devices in gut cells, most of the available studies have demonstrated the natural structure of the intestine layers (Figure 12(a)). One such study is that of Jalili-Firoozinezhad et al. [84] in which the villus intestinal epithelium polarization with ZO-1 tight junctions and an apical brush border were created within a gut-on-chip device. The authors also mimicked the production of mucus and alkaline phosphatase or sucrase-isomaltase within the platform. The effect of γ-radiation on villus morphology, cytotoxicity, apoptosis, and ROS was studied in this platform. The study confirmed that cells exposed to γ-irradiation induce changes in intracellular ROS and cause disruption of epithelial and endothelial integrity. Moreover, dimethyloxalylglycine (DMOG) used as pretreatment shielded the gut cells and diminished the harmful effects of radiation (Figures 12(b) and 12(c)) [84].

Shim et al. (2017) fabricated a generic gut-on-chip device consisting of three layers of PDMS with a membrane incorporating a collagen scaffold to mimic the intestinal villi, providing a reservoir for cell culture and fluid shear to improve cell differentiation and the physiological functions of the gut. The first layer was equipped with reservoirs for storing media, the second layer with fluidic channels made from a wafer mold to replicate the villi, and the third layer with a hole at the center. The microfluidic chip resembled the human intestine, with villi-shape structures. Caco-2 cells were seeded, stained with phalloidin and DAPI, and cultured under gravity flow for 14 days. Cells from this line were used due to the physical and physiological resemblance they share with gut cells [77]. Cell morphology examination showed that the cells were able to reproduce the villi structure and the fluidic shear in the 3D chip. The authors concluded that the villi had an important reduction in height, maybe due to contraction of the Caco-2 cells, degradation by protease proteins, and also due to the fluidic shear. However, exposing cells to the perfusion culture improved their metabolic activity, confirming that the gut-on-a-chip device could work as a platform for assessment of drug absorption and metabolism [77].

A more sophisticated model that mimicked the human intestine was developed by Villenave et al. [85]. The multilayer platform was composed of two microchannels

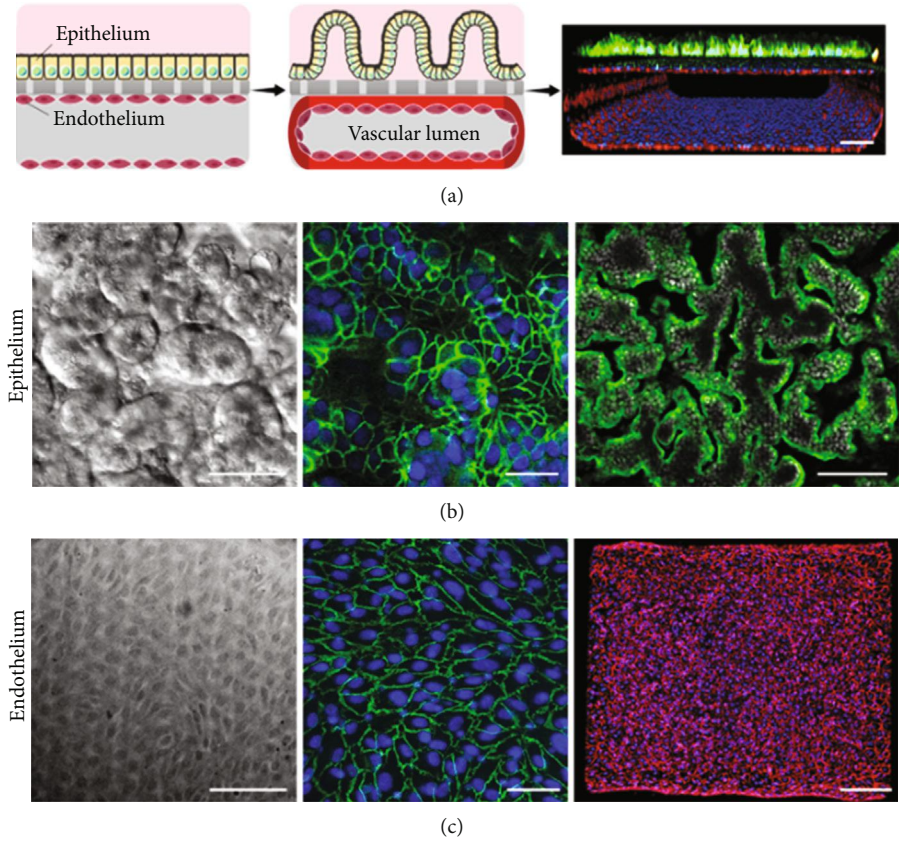

FIGURE 12: (a) Schematic showing the human intestinal epithelium and endothelium when initially plated on opposite sides of the matrix-coated porous membrane within the two-channel microfluidic device. (b) Microscopic views showing the villus morphology of the human intestinal epithelium and the immunofluorescence staining of the junction protein. (c) Microscopic views showing the planar morphology of the human endothelium and views of the immunofluorescence staining of the associated proteins. Reproduced (or adapted) with permission [84], ©2018, Nature.

separated by a porous membrane and was fabricated through lithography using a previously reported method [79, 82]. Outside the channels were two vacuum chambers that were used to simulate intestinal forces and movements within the device (Figures 13(a) and 13(b)). The membrane was cultured/coated with human Caco-2 intestinal epithelial cells for six days (Figure 13(c)). In this study, coxsackievirus B1 (CVB1) was used to infect the gut cells and subsequently to evaluate the reaction. Once the intestine cells had grown on the porous membrane, the virus was activated, and the response of the infection was measured through luminescence assays and real-time polymerase chain reaction (RT-qPCR). Results from the luminescent assay and the morphological analysis indicated that the device could be used successfully to monitor the behavior of the infection. It was also concluded that peristalsis facilitates infection downstream due to the flow and that the response varies in time according to the route of the infection and depending on the flow direction [85].

A substantial number of studies report that Caco-2 and HT-29 cell lines isolated from tumor sites can anchor several gene mutations with each passage, which might not accurately represent the human intestine. Therefore, other cell types could be cultured within gut-on-chip devices, including organoids. In particular, human intestinal organoids (HIOs) derived from either human biopsy or iPSC were repeatedly reported in the literature [86]. Kasendra et al. [87] developed a human small intestine-on-chip containing primary intestinal epithelium cells isolated from biopsy-derived human organoids, which resembled the intestinal epithelium and showed efficient monolayer formation when gut microvascular endothelial cells were seeded within the lower chamber. The device was fabricated from PDMS with a porous ECM-coated PDMS membrane, as described previously (Figure 14(a)) [79, 82, 83]. The formation of villi-like structures could be improved by using chemical gradients of growth factors, such as Wnt-3A, responding, and noggin, though the exact mechanism of the formation of villi-like structures remains unclear [87].

Using flow cytometry, Workman et al. [88] have shown that HIOs obtained from iPS cocultured with mesenchymal cells can be incorporated into a gut-on-chip platform. The device was fabricated using PDMS with a microchannel architecture, and the membrane was produced on a silicon mold. The organoids were stained and seeded under flow conditions for ten days, and the cells were polarized and used to assess the effect of interferon- (IFN-) γ. The chips were analyzed microscopically, and villi-like projections were observed, demonstrating that they belong to the gut lineage cells [88].

Recent studies describe how drug metabolism could also occur in the intestine during absorption induced by the gut

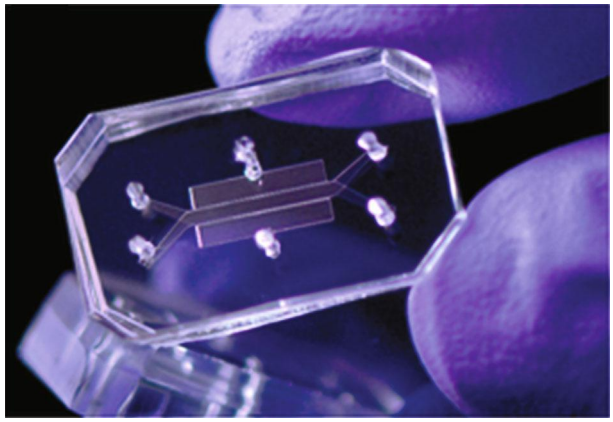

(a)

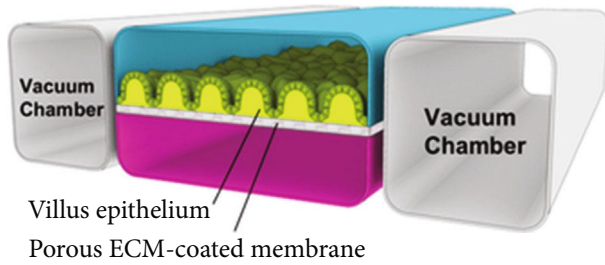

(b)

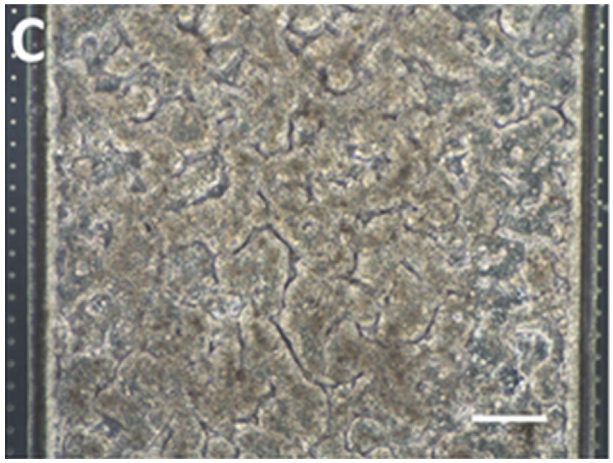

(c)

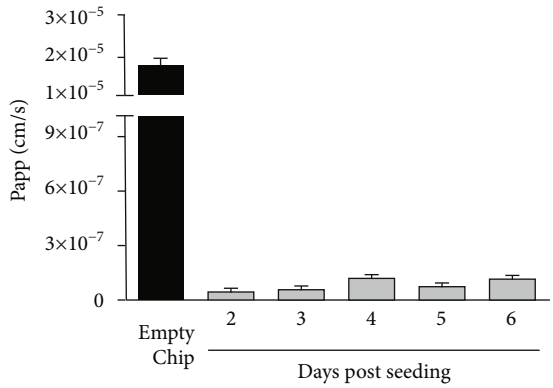

(d)

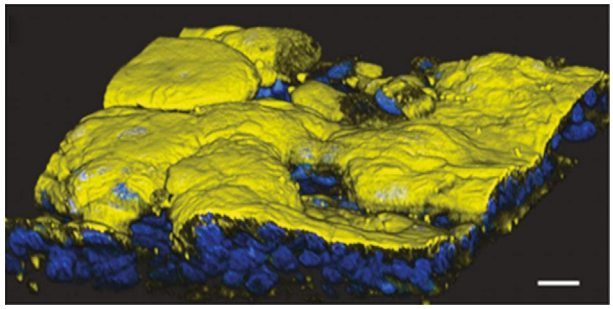

(e)

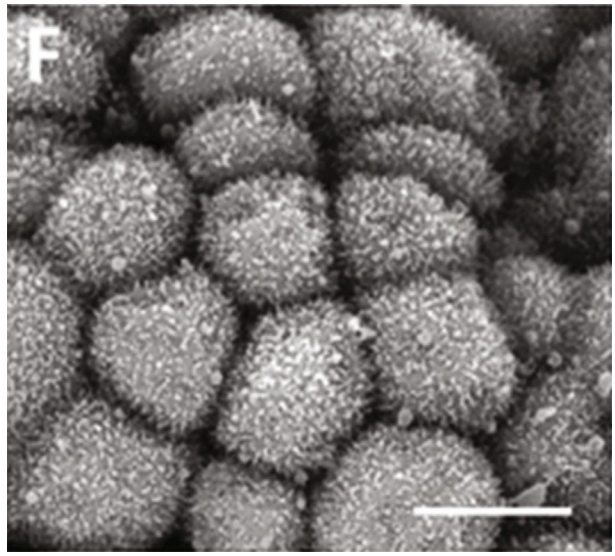

(f)

Figure 13: Gut-on-a-chip microfluidic device. (a) Photograph and (b) schematic of the device. (c) Micrograph of human Caco-2 intestinal epithelial cells cultured in the device. (d) Apparent permeability (Papp) of the epithelium assessed by adding fluorescent inulin-FITC. (e) Confocal immunofluorescence micrograph of human villus intestinal epithelium formed inside the gut-on-a-chip and stained for villin (yellow). (f) SEM micrographs of the apical surface of the villus epithelium. Reproduced (or adapted) with permission [85], ©2017, Public Library of Science.

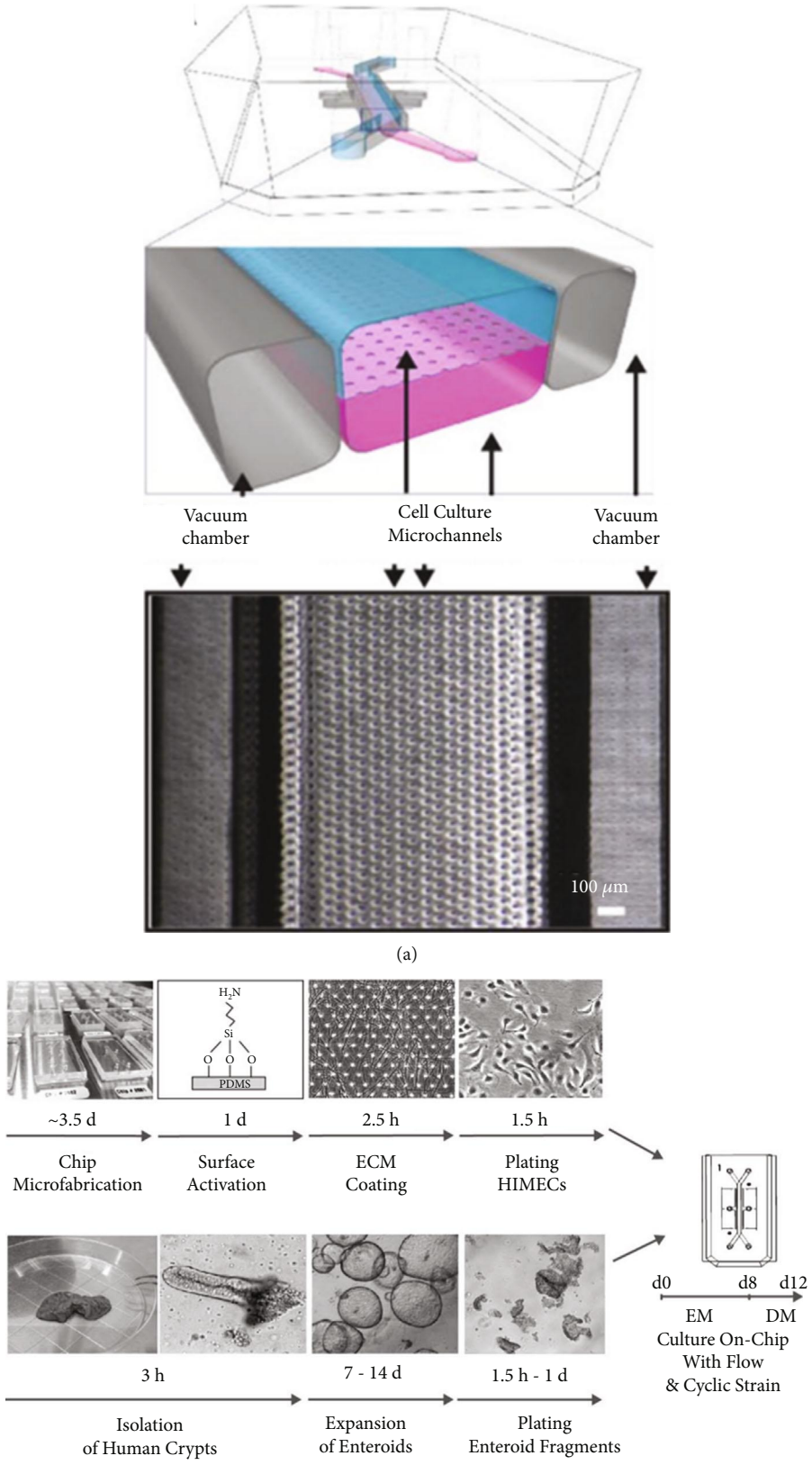

Figure 14: Fabrication of the primary human intestine chip. (a) A schematic microdevice showing the upper epithelium (blue), the lower microvascular cells (pink), and the porous membrane in-between. The different microfluidic channels and some components are shown. (b) Schematic representation of the procedure involved in the establishment of microfluidic cocultures (epithelium and endothelium). Reproduced (or adapted) with permission [87], ©2018, Nature.

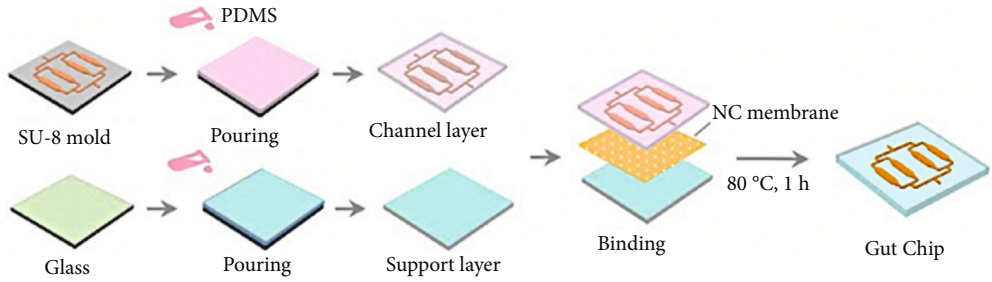

Figure 15: Fabrication process of the biomimetic human gut-on-a-chip. The channel layer and the support layer were made of PDMS, and the middle layer was fabricated of nitrocellulose. Reproduced (or adapted) with permission [93], ©2018, Wiley Online Library.

microbiome [89–92]. Guo et al. reported a device that consisted of three layers: a channel layer, a central porous layer of collagen I and nitrocellulose (NC), and a support layer derived from PDMS (Figure 15). Using Caco-2 cells in the microfluidic model, the authors analyzed the CYP3A4 and CYP2C9 enzymes and their expression levels. Both proteins showed an increase in the expression level within the 3D *in vitro* system after five days in comparison to the static cultures. SEM images confirmed that the membrane offered functionality for cell growth, and a high protein-binding capability, which improved cell adhesion. Also, the study confirmed that the model promotes the expression of the CYP3A4 and CYP2C9 in Caco-2 cells influenced by the porous NC membrane [93]. To verify their functionality, they evaluated the metabolism of verapamil and ifosfamide. The principal metabolite of verapamil produced by CYP3A4/CYP3A5 is *N*-norverapamil, and the CYP3A4/CYP2B6 metabolite derived from ifosfamide is 2-DCE-IFM. Within the device, the detection of both metabolites occurred on day 5, showing a higher cell efficiency compared with the monolayer culture.

Another study used the same cytochromes as Guo and coworkers to verify the expression and functionality of the CYP45 isoforms on the transformation of midazolam, rifampicin, ketoconazole, and indomethacin within a 3D *in vitro* platform. The multicellular 3D primary human intestinal tissue model consisted of a layer of cultured cells, such as human primary cells, polarized gut epithelium, and adult human intestinal myofibroblasts. The study confirmed the toxicity and inflammation responses of the epithelial cells due to the presence of indomethacin. Furthermore, an upregulation of inflammatory genes and epithelial cell death, as a result of the toxic effect of the tumor necrosis factor alpha (TNF-α) and LDH, was recorded within this 3D platform [94].

Some other promising models measure the efficiency of the gut barrier to perform drug transport studies and other xenobiotic agents in real time using Caco-2 cells and electrodes for transepithelial electrical resistance [95]. In one of these studies, a device consisting of eight microchambers was designed with a commercial Teflon membrane coated with thiolene to ensure effective bonding between the chip layers. Caco-2 cells were seeded under medium flow for 9-10 days. A cell viability test was performed after staining the cells for one day. The results confirmed that the device could be used as a functional drug transport model [95]. This miniaturized intestine-on-chip was found to be a promising platform for the detection of duodenum cell injuries and infections, among others.

The close mimicking of the gut's microenvironment is crucial for studying the metabolism of drugs. The addition of microbiota to the devices provides new perspectives and physiological models for a wide range of diseases. An abundance of Firmicutes and Bacteroidetes phyla are responsible for several gut functions, including absorption, metabolism, and excretion. Classical models including explants or transwells are not suitable for drug development due to their limited culture lifespan. Higher accuracy in the recreation of the microenvironment of the gut within the device may be critical to the discovery and metabolic assessment of drugs or nutraceuticals.

2.5. Heart-on-Chip. The cardiovascular system is a complex model of muscle tissue, blood vessels, and blood constituents. Cardiac muscle tissue is composed of organized cardiomyocytes (CMs) that contain a single nucleus in the center of the cell and connected to one another by intercalated discs that contain the gap junctions and the desmosomes that are important for cardiac muscle contraction. Cardiovascular diseases (CVDs) are among the most significant leading cause of premature death in developed countries. Several drugs cause cardiac toxicity, which manifests as proarrthymia in patients with or without clinical symptoms and leading to hemodynamic deterioration, syncope, or death [96]. Because of drug-related cardiac complications, the assessment of cardiovascular safety during drug development is of paramount importance. Therefore, there is a high demand for new drugs to prevent or treat CVDs. Nevertheless, the drug development for CVDs is hindered by the lack of adequate models to correctly mimic the cardiac muscle. Additionally, many drugs for the treatment of other organs or diseases have side effects or adverse reactions on cardiac tissue, which is a primary risk to consider during diverse drug development. For example, fenfluramine, developed to treat obesity, seldane for treating allergies, and rofecoxib, to be used as analgesic, have adverse effects on the cardiovascular system [97].

Recent advances in microfluidics and stem cell research provide an opportunity to recreate the cellular microenvironment to allow stem cell differentiation and an evaluation of their behavior. One of the most significant challenges in this area of research is to have a scaffold with a particular

Table 5: Summary of recent advancements in cardiotoxicity modelling and testing including the type of drug, the application, the applied cell lines, and the kinetics.

Drug type	Application	Applied cell lines	Kinetics	Ref(s)
DXR	Toxicity	HUVECs and hiPSC-CMs	33 days	[56]
	Pharmacokinetics and toxicity	hCMs and HepG2	24 hours	[100]
Isoprenaline	Toxicity	CMs and hiPSC-derived CMs	6 days	[101]
TiO_2 and Ag nanoparticles	Cardiotoxicity	CMs and NRVMs	35 hrs	[103]

DXR: doxorubicin; HUVECs: human umbilical vein endothelial cells; hiPSC: human-induced pluripotent stem cells; CMs: cardiomyocytes; hCMs: human primary cardiomyocytes; HepG2: human hepatocellular carcinoma; NRVMs: neonatal rat ventricular myocytes; TiO_2: titanium dioxide; Ag: silver.

architecture that mimics the cardiac tissue reproducing the hierarchical structure of the native myocardium with all its functions, including mechanical contractions, molecular transport, electrical activity, and specific responses to drug stimulation [98]. Heart-on-chip devices should reproduce the cellular organization level in a living heart through a very well-assembled and aligned tissue structure [99]. Additionally, there is a need for the integration of blood vessels to produce cardiovascular organoids [56]. Heart-on-chips based on the use of cardiac organoids can mimic the heart's main functions, including the synchronous contraction, the transport of nutrients and oxygen, and the removal of waste products, making them useful devices for testing potential therapeutic agents [56]. Some of the latest examples of heart-on-chip platforms for drug discovery, development, and analysis are thoroughly reviewed in this article (Table 5).

2.5.1. Analysis of Drugs in Heart-on-Chip Devices. Cardiac toxicity is responsible for nearly half of new drug recalls. The recent development of heart-on-chip platforms to evaluate drug toxicity has provided the potential to replicate a human-like response to compounds known to affect the heart's physiology. Zhang et al. fabricated a 3D endothelialized microfibrous scaffold using a bioprinter, a bioink, and cells (Figure 16). GelMA, a mixture of alginate, gelatin, and a photoinitiator, was used as bioink. HUVECs were resuspended in the ink, bioprinted through continuous deposition, and cultured for 15 days, resembling a blood vessel. After 33 days, cardiomyocytes and hiPSC-cardiomyocytes, with their respective medium, were seeded and incubated over each scaffold and exposed to doxorubicin, an anticancer drug. With a microfluidic perfusion bioreactor, the endothelialized-myocardium-on-chip model was used as a platform for cardiovascular drug screening. The toxic effects of doxorubicin on cardiomyocytes and endothelial cells were associated with the drug dose. It was concluded that the combination of bioprinting, microfluidics, and stem cells in this platform was useful for developing next-generation human organ models for personalized drug screening to mitigate drug-induced cardiovascular toxicity [56]. The development of these bioprinted 3D scaffolds, where cell lineages can interact together to recapitulate the organ physiology, could subsequently be used for *in vitro* drug testing and for mechanistic biological studies.

An integrated heart/cancer-on-chip (iHCC) to reproduce the side effects of anticancer drugs was created using a few main components: a PDMS perfusion layer and a control layer and a peristaltic pump. These components of the platform were fundamental, as the flow was created in the closed-circuit loop providing circulation within the culture chambers (Figure 17). The chip was developed using soft lithography and was used for the culture of human primary cardiomyocytes (hCMs) and HepG2 and for their subsequent treatment with doxorubicin for 24 hours. Based on the findings of this study, the platform offered the possibility of culturing different cells and recapitulated physiological and pathological conditions for the evaluation of drug toxicity [100].

In another study, Marsano et al. developed a beating heart-on-chip that can generate functional 3D microcardiac tissues. The device was equipped with two compartmentalized PDMS microchambers separated by a PDMS membrane. The top compartment was subdivided into a central channel and two side channels. Cardiomyocytes and human iPSC-derived cardiomyocytes were suspended into a matrix of fibrin gel in the central channel, while the culture medium was replenished through the side channels and generated a 3D cell construct. By pressurizing the bottom compartment, the PDMS membrane deformed, thereby compressing the 3D cell construct (Figure 18). A cyclic pressure signal mimicked systolic and diastolic phases. This study demonstrated a method to generate mature and functional 3D cardiac microconstructs. Cyclic mechanical stimulation was found to improve the maturation of the microengineered cardiac tissues (μECTs) [101]. This microfluidic platform could be used to evaluate the cardiac microphysiological system by assessing the effects of drugs on cardiac cells.

Nowadays, the use of engineered nanomaterials (ENM) is in constant rise, potentially posing unknown health responses when inhaled. Therefore, developing prevention strategies and treatments against these nanoscaled materials is an important research area in the event that they are harmful to the human body. TiO_2 NPs are widely used in sunscreens, cosmetics, paints, tiles, etc. TiO_2 NPs may result in ROS production, causing oxidative stress, inflammation, and the risk of cancer [102]. The study of the biosafety of nanoparticles and the toxic effects of TiO_2 requires a device that can provide an environment and conditions which mimic that of real tissues. In the case of the heart, it requires an ECM, along with a movement-contraction mechanism. A muscle-inspired aligned nanofiber was produced by electrospinning using a mixture of polycaprolactone (PCL) and polydopamine (PDA) [103]. The device consisted of four layers: (i) a gelatin layer over a PDMS base which was used as support for the scaffold and the cardiomyocytes, (ii) a PDMS layer, (iii) a thin

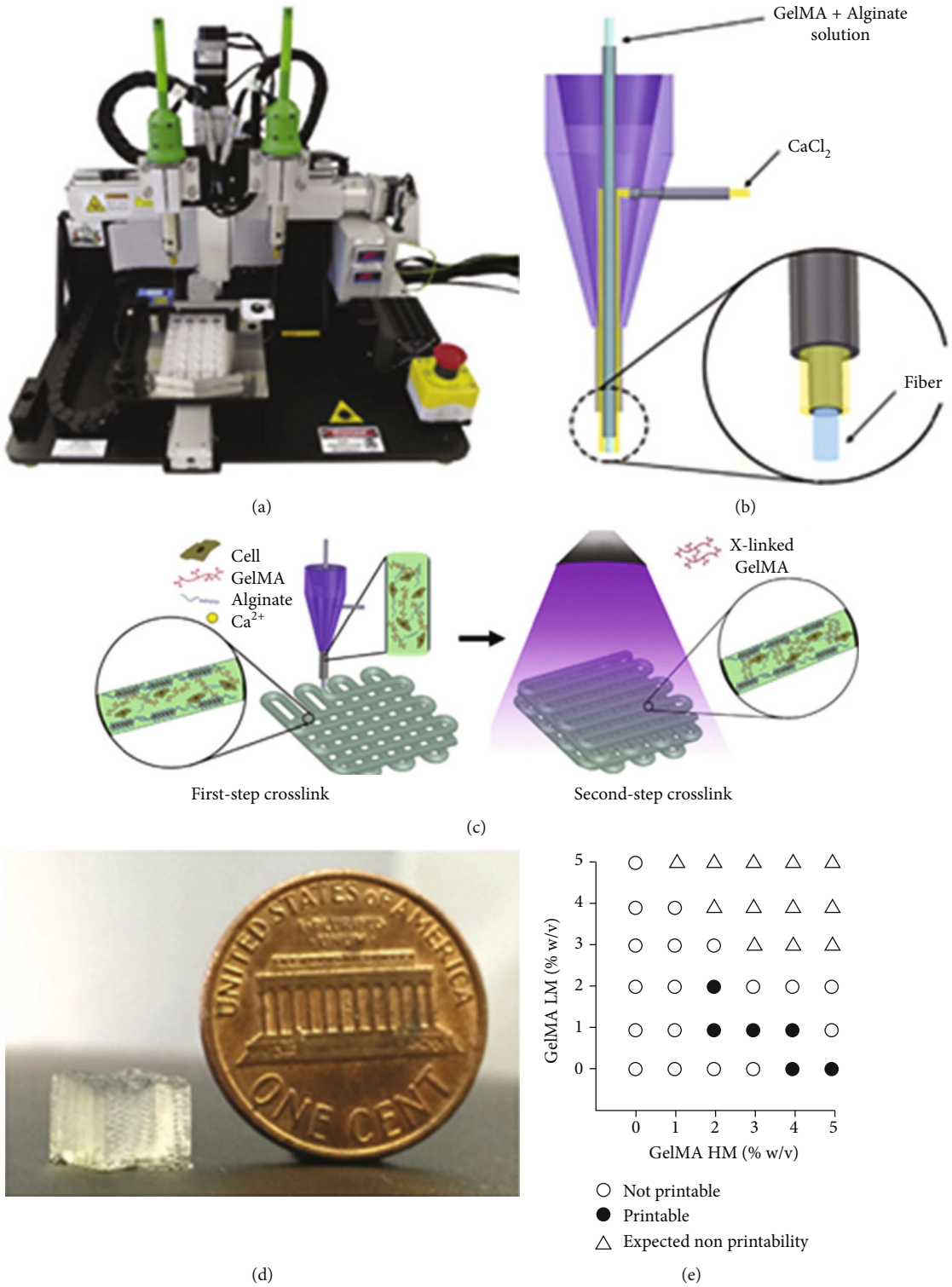

FIGURE 16: (a) Organovo Novogen MMX bioprinter. (b) Schematic of the coaxial needle where the bioink is delivered from the core, and the ionic crosslinking $CaCl_2$ solution is sheathed on the side. (c) Schematic diagrams showing the two-step crosslinking process, with $CaCl_2$ followed by UV illumination. (d) Photograph of a bioprinted cubic microfibrous scaffold. (e) Bioink optimization where conditions of printability and nonprintability for different concentrations of GelMA-HM and GelMA-LM were analyzed. Reproduced (or adapted) with permission [56], ©2016, Elsevier.

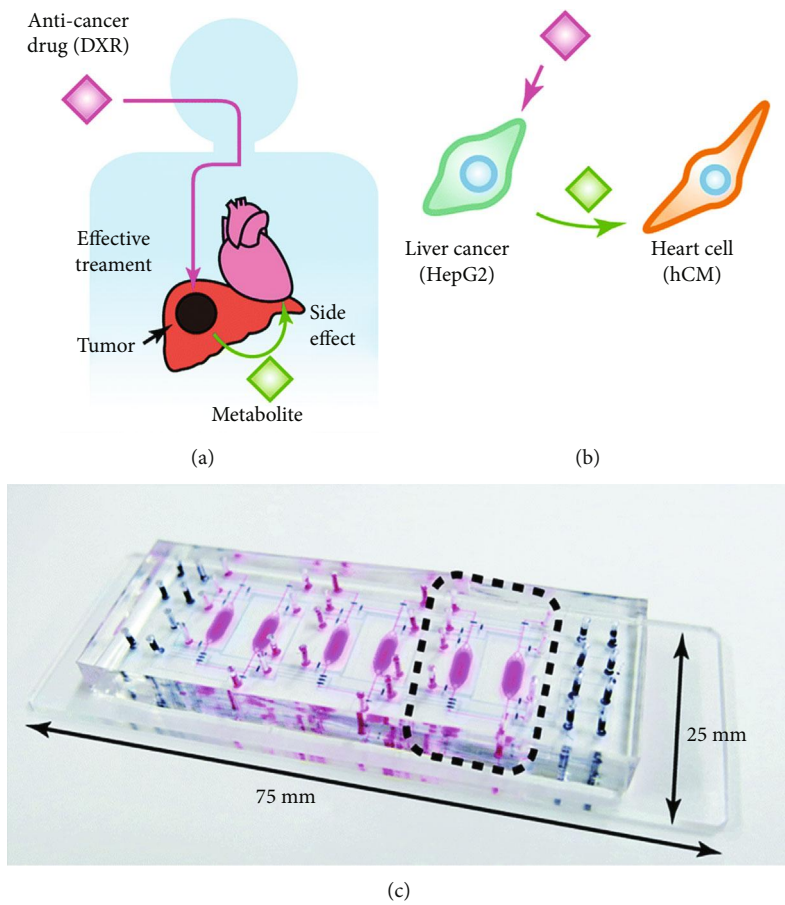

Figure 17: Integrated heart/cancer on a chip, (a, b) Communication between liver cancer cells and healthy heart cells through exchange of metabolites and the side effects of an anticancer drug. (c) Photograph of an actual iHCC fabricated on a glass slide. Reproduced (or adapted) with permission [100], ©2017, Royal Society of Chemistry.

sensor film (responsible for the contractions), and (iv) a lower PDMS layer. Neonatal rat ventricular myocytes (NRVMs), grown on the scaffold, were developed into a mature and functional tissue. TiO_2 NPs and silver (Ag) were added directly to the scaffold. The collected data established that high doses of TiO_2 NPs (100 μg/mL) affected the contractile function and damaged the tissue structure after 48 hours of exposure [103].

The structural colors of living flora and fauna have inspired researchers to develop hydrogels, nanoshells, filaments, and several bioinspired materials [104–107]. To mimic the color shift mechanism of chameleons, Fu et al. (2018) created a heart-on-chip system using such bioinspired materials. The hydrogel scaffolds were fabricated using colloidal crystal templates prepared with silicon dioxide (SiO_2) nanoparticles assembled on glass slides. GelMA was subsequently infiltrated into the templates, polymerized with UV light, and etched with hydrofluoric acid. Silicon patterned wafers were used to obtain colored hydrogels that were disinfected with UV light before seeding with cardiomyocytes isolated from rat pups. The biohybrid colored hydrogel contained perfused microfluidic chambers to provide the medium and the drug solution to the living cells (Figure 19). The platform was used to evaluate isoproterenol, a drug used for mild or transient episodes of bradycardia and heart block. The authors featured this system in a study of the microphysiological monitoring of biological systems and for drug screening [99].

The complexity of the anatomical and physiological structure of the heart muscle has been a major driving parameter for the fabrication of new devices that track cardiac impulses, analyze mechanical properties, and mimic some of the main atrophic characteristics. Development of a system that optimizes 3D cell seeding, while maintaining the electrophysiologic characteristics and mimicking the blood flux, represents an excellent opportunity to understand the pathogenesis of certain chemotherapeutic treatments. The adverse effects of chemotherapeutic drugs are not well-studied due to the time-lapse of *in vitro* assays and insufficient knowledge regarding the continuous monitoring of such drugs.

2.6. Skin-on-Chip. Skin is the largest organ of the body and is comprised of epidermis, dermis, and hypodermis layers, which are mainly comprised of keratinocytes, fibroblasts, and adipocytes, respectively. The epidermis is in charge of preventing the entry of exogenous materials and pathogens, while the dermis protects internal organs and regulates water evaporation. The human skin serves as a physiological barrier to safeguard the internal organs. Since the skin is an outer barrier, it is constantly exposed to many chemical substances and

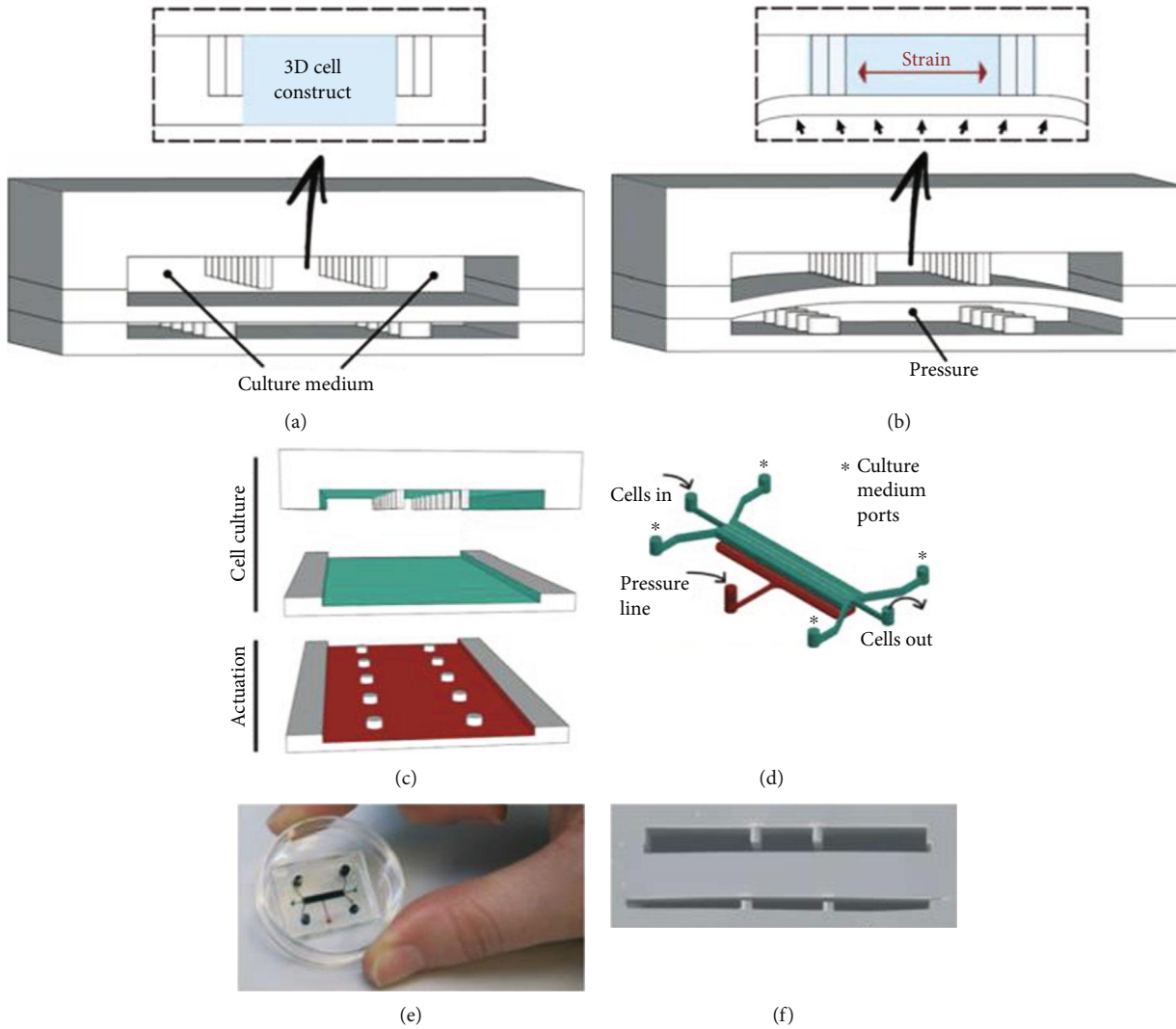

Figure 18: Design of the 3D heart-on-a-chip microdevice. (a) The device uses two compartmentalized PDMS chambers. (b) By pressurizing the bottom compartment, the compression transduces into a uniaxial strain applied to the 3D cell construct. (c) Inside view of the PDMS chambers. (d) 3D sketch of both compartments. (e) Picture of an actual 3D heart-on-chip device. (f) Scanning electron microscopy image of a cross-section of the device (scale bar, 500 μm). Reproduced (or adapted) with permission [101], ©2016, Royal Society of Chemistry.

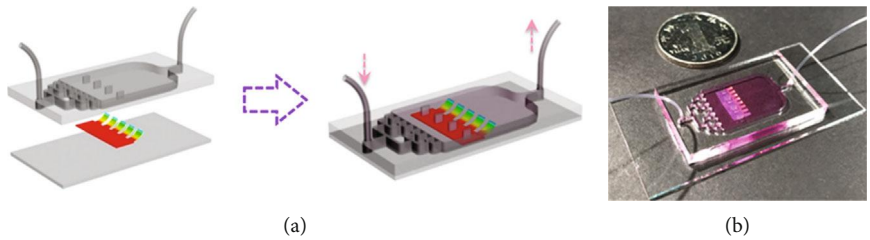

Figure 19: The applications of the biohybrid structural color hydrogels in a heart-on-a-chip system. (a) Schematic of the construction of the heart-on-a-chip by integrating the biohybrid structural color hydrogel into a bifurcated microfluidic system. (b) Image of the biohybrid structural color hydrogel integrated heart-on-a-chip. Reproduced (or adapted) with permission [99], ©2018, American Association for the Advancement of Science.

biological agents, including cosmetics, skin detergents, UV light, pathogenic microorganisms, and environmental pollutants [108]. Animal models have been extensively used to evaluate cosmetics and diverse drugs. Nevertheless, the ethical considerations, high costs, time-consuming processes, the limited ability to represent the real human physiology and metabolism, and the impossibility of performing quantitative studies remain as main drawbacks for drug testing and disease

modelling. To overcome these limitations, the development of 3D microfluidic platforms, where cells are cultured in an ECM as better simulators of skin functions, is gaining attention [109].

During drug testing in this organ, the complexity of the diffusion at the several layers of skin represents a significant disadvantage in animal or 2D models. Percutaneous-dermal absorption requires three steps: penetration of the compound to a skin layer, permeation through the layers, and resorption into blood circulation. The chemical interaction with the hydrophilic nature of the skin must be tested in an accurate 3D model that leads to the analysis of drug interactions. One of the standard tests for skin permeation of drugs or transdermal delivery systems is the diffusion cell apparatus, also known as the Franz diffusion cell [110, 111]. In this overview, the latest skin-on-chip technologies are summarized, including those that improved on the Franz diffusion cell analysis. Some of the latest examples of skin-on-chip platforms for drug discovery, development, and analysis are thoroughly reviewed in this article (Table 6).

2.6.1. Analysis of Drugs in Skin-on-Chip Devices. Recent advances in microfluidic cell culture systems enable the construction of *in vitro* human skin models that can be used to evaluate the toxicity of drugs and other compounds [112]. Current skin models have been developed to evaluate the efficacy of drugs and the effect of UV radiation and of aging by using keratinocytes, fibroblasts, melanocytes, and stem cells to better reproduce the physiology of the skin. Wufuer et al. (2016) developed a skin-on-chip device to mimic the structures and functional responses of human skin [108]. The model comprised of three PDMS and two porous membrane layers to coculture human epidermal keratinocytes (HaCaT), human skin fibroblasts (HS27), and HUVECs mimicking the epidermis, dermis, and the endothelium layers. Skin inflammation and edema were induced by perfusing TNF-α through the dermal layer (Figure 20). The model analyzed the expression levels of proinflammatory cytokines and the efficacy of dexamethasone, a drug used for treating inflammation and edema, in order to demonstrate the functionality of the system. The results showed that IL-1β, IL-6, and IL-8 levels increased with 25 ng/mL and 50 ng/mL of dexamethasone but decreased with 100 ng/mL of dexamethasone, confirming the dose-dependent effectiveness of the anti-inflammatory drug.

Mori et al. [113] fabricated a 3D skin-on-a-chip microdevice with perfusable vascular channels coated with endothelial cells that comprised a skin equivalent fixed to a culture device connected to an external pump and tubes. The skin equivalent contained normal human dermal fibroblasts (NHDFs), normal human epidermal keratinocytes (NHEKs), and HUVECs. The authors evaluated the percutaneous absorption of the model drugs, caffeine and isosorbide dinitrate (ISDN), through the skin equivalent layer during the perfusion of Dulbecco's modified Eagle's medium (DMEM) in the vascular channels. Its feasibility was demonstrated by measuring the permeation of the applied drugs through the vascular channels. Both drugs reached the vascular channels after ~5 min of drug application and took ~30 min to reach the skin equivalent. These results confirmed that the model can be used for the development of skin treatments and cosmetics.

Lee et al. (2017) described the construction of a 3D multicellular microfluidic chip for an *in vitro* skin model. The device consisted of two layers of PDMS. The bottom layer consists of microfluidic channels for vascular cells, and the top layer contained a skin cell culture chamber. The chip, controlled by gravitational effects, was placed on a platform tilted at a certain angle to induce a specific flow. The results suggested that the presence of flow plays a crucial role in maintaining the viability of cells. The 3D skin chip with vascular structures can be a valuable *in vitro* model for reproducing the interactions between the different components of the skin tissue. It operates in a more physiologically realistic manner in demonstrating the consumption of oxygen and homogenous diffusion of glucose, which enables the system for assessing the reaction of the skin to cosmetic products and drugs [109].

A recent innovative study tested the efficacy of penicillin and neutrophil migration in human tissue infected with *Staphylococcus aureus*. This device has three compartments: a column, a blood channel, and a migration zone. The fabrication was done by soft photolithography on PDMS cured overnight and bonded to the glass-bottomed well plates. The skin tissue was taken from a human skin microbiopsy and autologous blood (Figures 21(a) and 21(b)). The infection model involved a pretreatment of the biopsy with the bacteria which was subsequently injected into the device. The authors initially measured neutrophil migration on the middle section of the chip, interpreted as activation of the cells in the presence of the pathogen. The very interesting result revealed that the time of migration correlates with a pattern of infection. Additionally, the study provided the efficacy test of the penicillin, showing bacterial clearance and indirect attenuation of neutrophil migration over time [114].

The Franz diffusion cell approach is the most common methodology to evaluate drug permeation *in vitro*; however, the test suffers from poor reproducibility [115]. To overcome that limitation, Lukács et al. [116] designed and fabricated a skin-on-chip device by using PMMA and polylactic acid (PLA) through 3D printing to evaluate caffeine penetration. The microfluidic diffusion chamber contained two skin holders with layers for a skin sample or membrane (Figures 22(a) and 22(b)). The authors simultaneously ran the *in vivo* experiments using the Franz diffusion system, in order to compare the results of caffeine absorption. The data showed that both tests provided similar C_{max} values, while more advanced systems are needed to assess and evaluate drug formulations [116].

In a similar study, Alberti et al. [117] tested the diffusion of caffeine, salicylic acid, and testosterone on human primary fibroblasts and keratinocytes in a microfluidic skin permeation platform validated by the Franz diffusion cell. The system was composed of a multichambered microfluidic chip fabricated by the thermal bonding of three thermoplastic layers and six polytetrafluoroethylene (PTFE) membrane disks or human skin punches and twelve silicone membrane connectors. This innovative design permitted the accumulation of perfused media in a 96-well plate. The permeability coefficient (Kp) of caffeine was $0.83^{\circ}\mathrm{cm\,h^{-1}}$ and $0.94^{\circ}\mathrm{cm\,h^{-1}}$ for the skin platform and Franz cells, respectively. The Kp value for salicylic acid

Table 6: Summary of recent advancements in skin-on-chip and drug testing including the type of drug, the application, the applied cell lines, and the kinetics.

Drug type	Application	Applied cell lines	Kinetics	Ref(s)
Dexamenthasone	Efficacy	HaCaT, HUVEC, HS27	3 days	[108]
	Efficacy	GM-3348, HUVEC, human macrophages (primary cell culture)	Over 48 hrs	[123]
Caffeine ISDN	Absorption	HUVEC, NHDFs, NHEKs	10 days	[113]
Penicillin	Efficacy	Human skin biopsy, peripheral human blood	>24 hrs	[114]
Caffeine	Diffusion	Rat skin cells	—	[116]
Caffeine Salicylic acid Testosterone	Diffusion	N/TERT-1, human primary fibroblast	—	[117]
TNPs	Toxicity	HaCaT	48-72 hrs	[121]

HaCaT: human epidermal keratinocytes; HUVECs: human umbilical vein endothelial cells; HS27 and GM-3348: human fibroblast; ISDN: isosorbide dinitrate; NHDFs: normal human dermal fibroblasts; NHEKs: normal human epidermal keratinocytes; N/TERT-1: keratinocytes; TNPs: titanium dioxide nanoparticles.

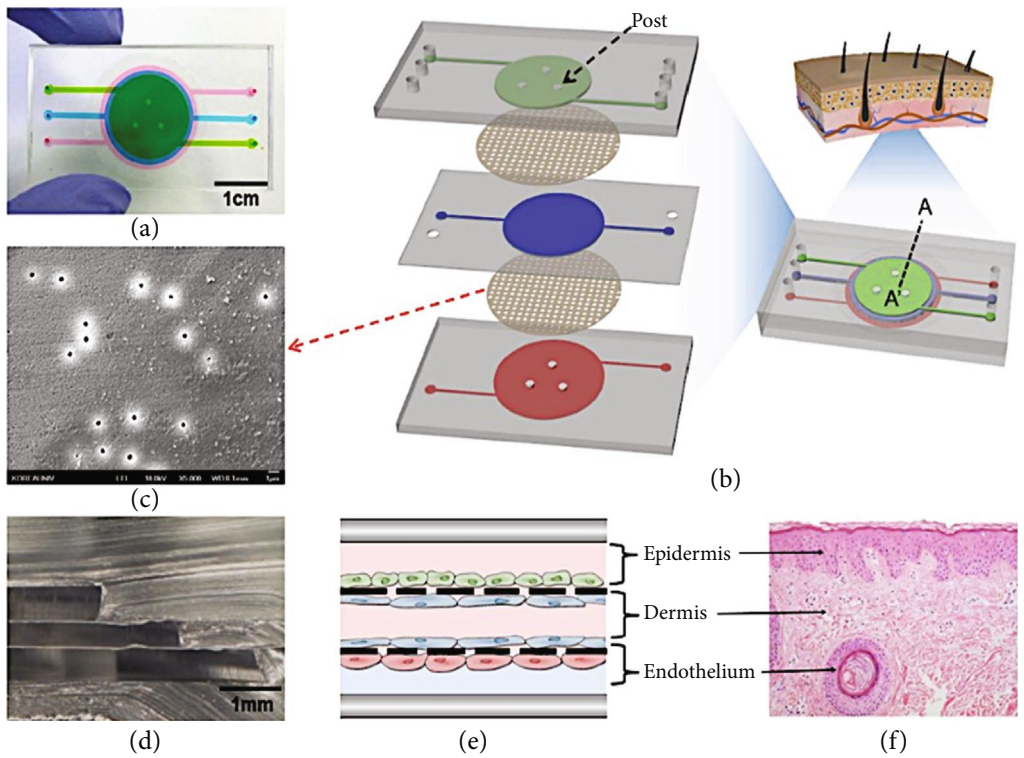

Figure 20: Description of the microfluidic device. (a) Image of a skin-on-a-chip device filled with fluid in three different colors. (b) 3D scheme of the skin-on-a-chip system comprising three PDMS layers and two PET porous membranes (footprint: 48 mm × 26 mm; height: 7 mm). (c) SEM image of PET porous membranes (pore size: 0.4 μm) obtained from Transwell. (d) Cross-sectional image of A–A′. (e) Schematic of the skin-on-a-chip system, including three separate channels with four vertically stacked cell layers. (f) Representative histological skin section stained with hematoxylin and eosin to indicate the cellular organization of skin. Reproduced (or adapted) with permission [108], ©2016, Nature.

was 11°cm h^{-1} and 10°cm h^{-1} and for testosterone 8.2°cm h^{-1} and 9.2°cm h^{-1}, confirming that the permeation test of the microfluidic system was highly accurate and similar to the Franz model [117].

Ramadan et al. [118] further corroborated these findings using an air-liquid interface and transepithelial electrical resistance (TEER) probes to evaluate the effects of lipopolysaccharides and UV irradiation on the cell growth and tight junction formation allowing a more realistic *in vivo* culture environment. The findings of this study indicated that dynamic perfusion allowed for an increase of cell viability for up to 17 days [118].

More recently, Alexander et al. [119] fabricated a skin-on-chip integrated with a sensor to evaluate the TEER and the extracellular acidification rate (EAR) integrating an automated air-liquid interface. The biochip device was comprised

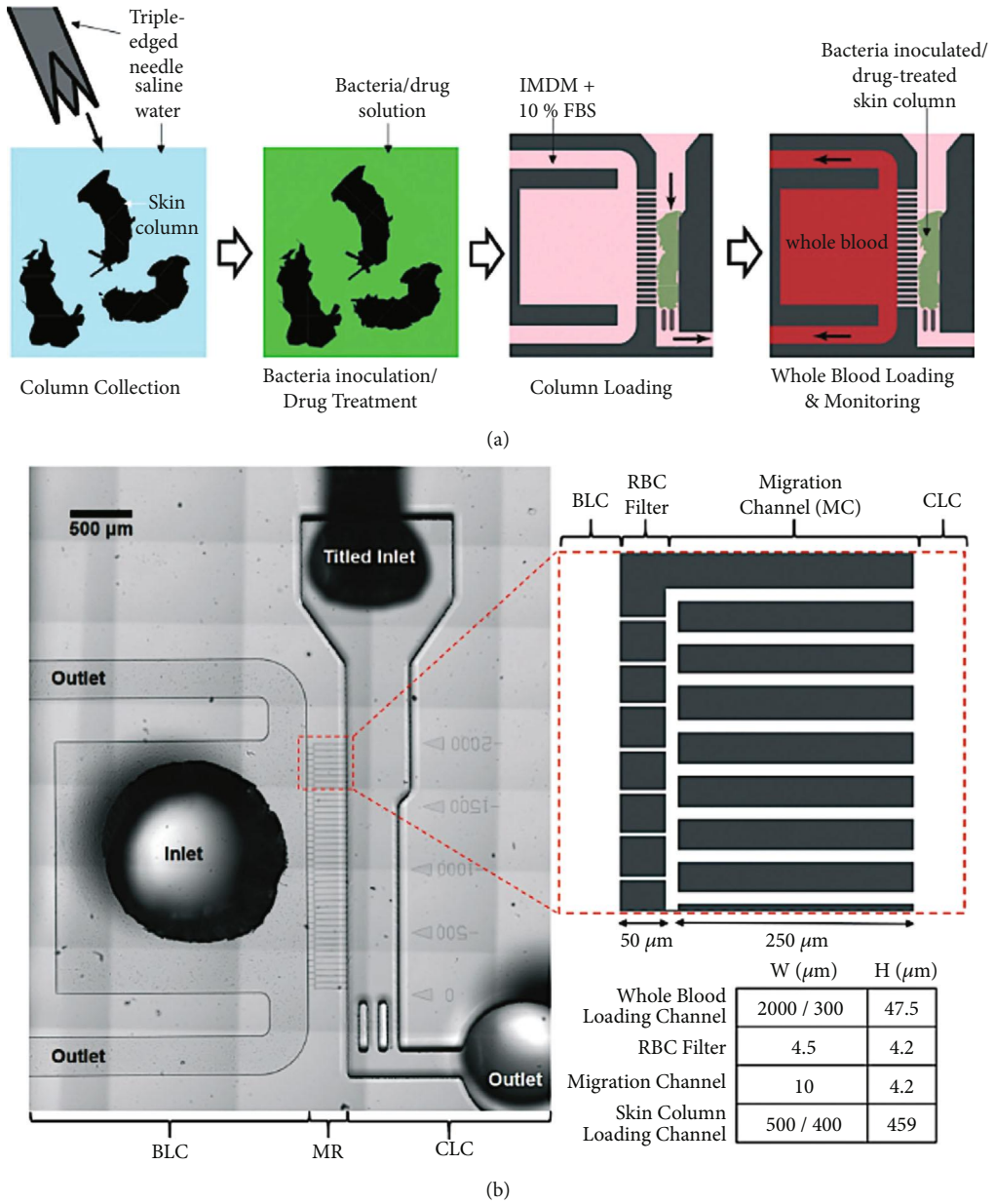

FIGURE 21: *Ex vivo* skin-on-a-chip assay for the diagnosis of skin and soft tissue infections. (a) Schematics of the human skin and blood sample loading. (b) Microfluidic design of *ex vivo* skin-on-a-chip. Left shows the bright field image of *ex vivo* skin-on-a-chip. Top-right represents the design of the migration channel (MC). Bottom-right shows the dimension of ex vivo skin-on-a-chip components: whole blood loading channel (BLC), red blood cell (RBC) filter, MC, and skin column loading channel (CLC). Reproduced (or adapted) with permission [114], ©2018, Royal Society of Chemistry.

of membranes that were inserted into the culture chamber where murine fibroblast cells and medium were perfused through an inlet opening into the chamber formed below the membrane. Pores at the bottom of the membrane allowed for the passive diffusion of fresh nutrients to the basal layer of cells and of the waste products from the cells. Nutrient-depleted medium was then pumped out of the chamber through an outlet (Figures 23(a) and 23(b)). The device used TEER sensors to continuously monitor the cells noninvasively. This study was a proof-of-concept that demonstrated the capability of the custom-made device to maintain stable culture conditions to be used as a screening platform for the evaluation of drug candidates and to understand their mode of action [119].

The skin experiences constant physical stimuli including stretching. Exposure to excessive physical stimuli stresses the skin and can accelerate aging. In the study of Lim et al., the effect of physical stress was studied to generate knowledge on skin aging using a skin equivalent model of aged wrinkled skin-on-a-chip (WSOC). To create this platform, two PDMS layers were constructed through soft lithography. The first structure contained chambers and a magnet placed on an aluminum mold with a hole for the magnet placement. The second mold was responsible for communicating channels

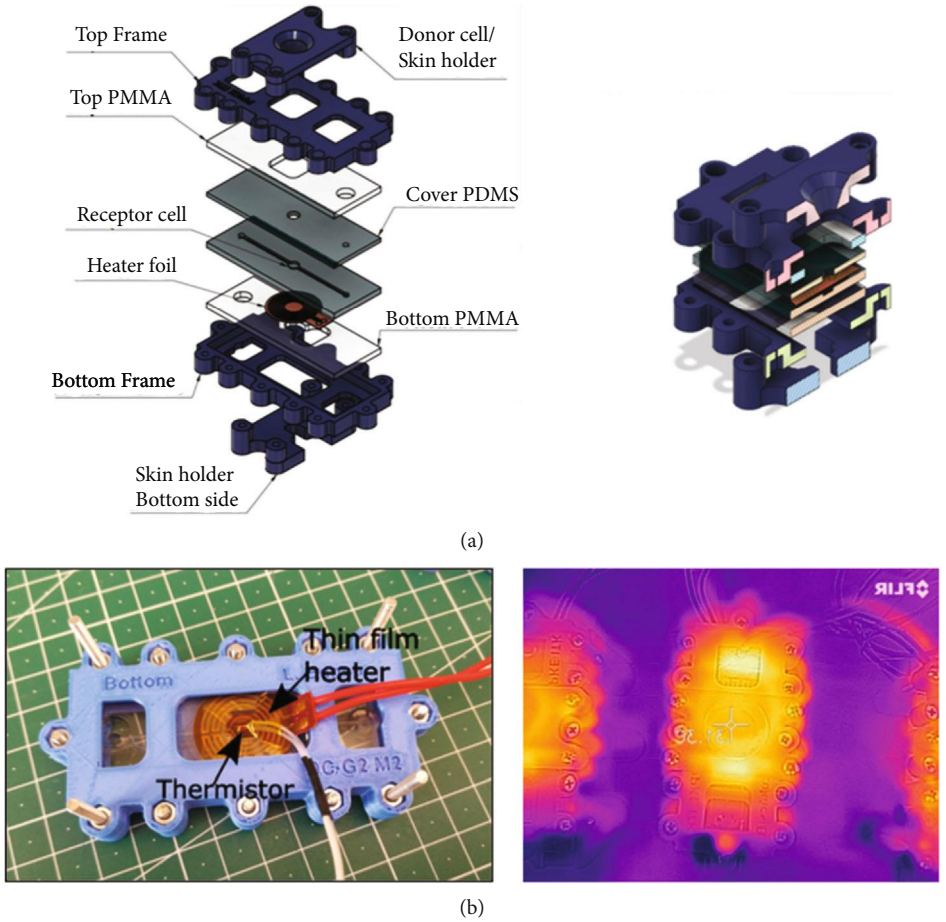

FIGURE 22: : Schematic view of the microfluidic diffusion chamber. (a) Layer by layer view. (b) The bottom side of the chip and temperature control measurement. Reproduced (or adapted) with permission [116], ©2018, MDPI.

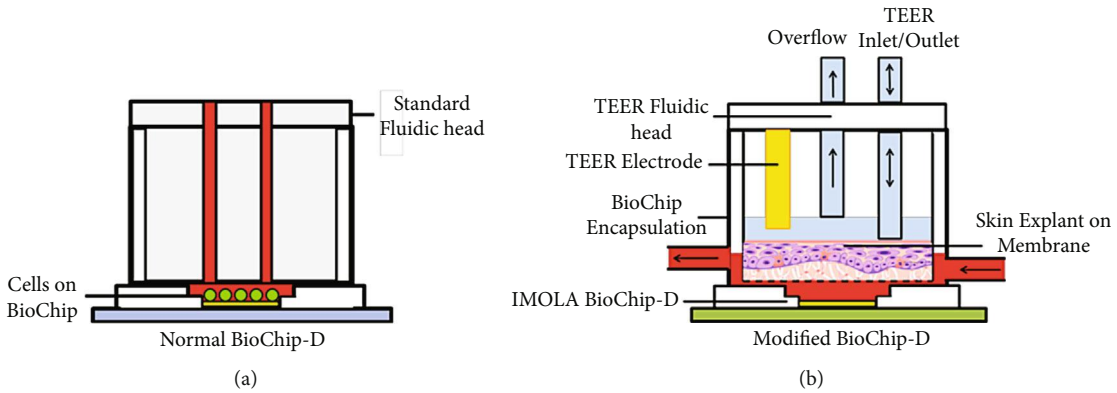

FIGURE 23: Schematic diagrams: (a) standard biochip with fluidic head and (b) modified biochip. Reproduced (or adapted) with permission [119], ©2018, MDPI.

between chambers. The device provided a platform to study the effects of antiwrinkle drugs used in cosmetic applications. The model allowed human fibroblasts and keratinocytes to be perfused with other elements to form 3D skin equivalents that were then stretched for 12 h per day at either 0.01 or 0.05 Hz for up to seven days to form WSOC. After seven days of constant stress, the results demonstrated an increase in collagen and fibronectin within the ECM expressed by fibroblasts. Fibroblasts are known to be responsible for the formation of resilient and elastic skin. Keratinocytes, which are responsible for the production of keratin, were notably decreased when compared with the control, unstretched skin tissue. The experiment showed positive results for the replication of an *in vitro* skin aging model. Moreover, the

platform could be applied for antiwrinkle cosmetics and medicines [112].

Many commercial sunblock products use organic or inorganic UV filters to block harmful UV rays. TiO_2 and ZnO are commonly used as UV blockers in sunscreens, but despite the protection they provide against cutaneous phototoxicity, these chemicals can cause oxidative stress-mediated toxicity in cells by absorbing UV radiation after direct exposure to UV sunblockers [120]. McCormick et al. [121] developed a skin model to evaluate the toxicity of titanium dioxide nanoparticles (TNPs) and the effect of UV irradiation. The chip was made from PDMS, while quartz plates and 96-well plates were used to expose the HaCaT to UV and TNPs as shown in Figures 24(a)–24(d). The study demonstrated that TNPs absorbed a wide range of UV-A and UV-B wavelengths protecting the cells when exposed to UV irradiation. The live/dead staining cell test showed an IC_{50} (50% viability) value of 35.6 mJ/cm^2 when they were exposed to UV without TNPs [121]. Overall, these results provide valuable information for the study of nanoparticle toxicity and drug testing.

The versatility of the microfluidic systems gives flexibility to the function of such devices. In that perspective, Hakimi et al. [122] fabricated a handheld skin printer with several microfluidic compartments and a cartridge that contains bioinks and a cross-linker for wound healing application (Figures 25(a)–25(c)). The cartridge was 3D printed using a resin, integrated Luer lock connectors, and wells (Figure 25). The bioinks were prepared with different formulations based on fibrinogen, hyaluronic acid, alginate, collagen type I, and keratinocytes allowing the deposition of sheets that were cross-linked at the site of deposition. The position of the cartridge allowed the coordination of the flow rates when it was delivered to the skin. *In vivo* assays, performed in animal models, demonstrated that cells added to the bioink and *in situ* delivered enhanced granulation tissue formation and increased wound healing. This portable device can also be used to deliver compounds and/or drugs for *in situ* wound healing [122].

Similarly, in a recent study, Biglari et al. [123] developed a skin wound-on-chip model to assess the anti-inflammatory effect of macrophages and dexamethasone on wound healing during inflammation induced with TNF-α. The device, fabricated with PDMS, consisted of three channels: two lateral channels for human dermal fibroblast (GM-3348) and human macrophages from primary cell culture and an inner channel for endothelial cells (HUVEC). Macrophages were also cocultured with HUVECs and fibroblasts to simulate an inflammatory condition. In addition, dexamethasone was used to test the efficacy on reducing the TNF-α-induced inflammation on damaged fibroblasts. The authors found that the macrophages produced cytokines that induced fibroblast differentiation to myofibroblasts during the wound healing process, while dexamethasone increased vascularization. The wound-on-chip model may help to gain insight into the mode of action of a drug in wound healing and the potential for a preclinical test for new drugs and cosmetics [123].

Skin-on-a-chip devices are perhaps the most advanced systems in the category of organ-on-chip. They represent successful platforms for wound regeneration, drug testing, and toxic agent testing, including UV light, allergens, and cosmetics. Skin-on-a-chip platforms can replicate injuries or induced-disease environments through the incorporation of several cell lines. The addition of biosensors can measure compounds in real-time during examinations of drug penetration or drug toxicity. Despite tremendous efforts, certain challenges with respect to the cell microenvironment and full cellular compatibility assays are yet to be addressed. The majority of studies use primary cell cultures, cell lines (human and animal-derived), differentiated induced pluripotent stem cells (iPSCs), or a combination of them, within the same device. Mimicking the real microenvironment is necessary to control these variables and their compatibility with a validation system. Another challenge is the long-lasting cultures that may require cell heterogenicity and delivery of nutrients. Most devices could maintain a viable skin system over 30 days. However, for studying extended treatment efficacy, drug permeability, and toxicity over time, a longer culture period is needed. Another limitation of the current 3D *in vitro* skin models is that they do not recapture the human skin architecture and physiology. In particular, an ideal model must be comprised of epidermis and dermis layers and the presence of vascular structures for the diffusion of nutrients and signaling molecules. Furthermore, the present devices lack the long-term survival of competent full-thickness skin. We believe that a 3D skin chip with vascular structures can be a valuable *in vitro* model for reproducing the interactions between different components of the skin tissue and thus function as a more physiologically realistic platform for testing skin reactions to cosmetic products and drugs.

2.7. Brain-on-Chip. The brain is the most sophisticated component of the central nervous system (CNS). It is comprised of about 86 billion neurons, the electrically excitable cells that receive signals from the body's sensory organs and then output information to the organs, communicating in trillions of synaptic connections. Apart from the neurons, the CNS is comprised of numerous other cells, including astrocytes, oligodendrocytes, and microglia that fulfil a crucial role for many functions of the body. Unlike other cells, neurons do not divide, and neither do they die off to be replaced by new ones. Research regarding brain development is still limited, as the main models that have been used are animal models. Such models have limitations, including high cost, time-consuming and labor-intensive procedures, and experimental variations [124]. To overcome those limitations, systems capable of imitating the *in vivo* neuronal plasticity must be developed [125]. As an alternative, biomedical research has attempted to mimic this complex human organ using traditional 2D cultures. Expectedly, such platforms are far from realistically representing the physiology of the brain, especially the neuronal plasticity, and the effective blood-brain barrier (BBB), a selective diffusion barrier that protects the brain from the effects of numerous drugs [126]. This barrier involves a vascular endothelial layer that interacts with astrocytes and neurons and plays a vital role in evaluating drug delivery and drug toxicity. Thus, this barrier has been used

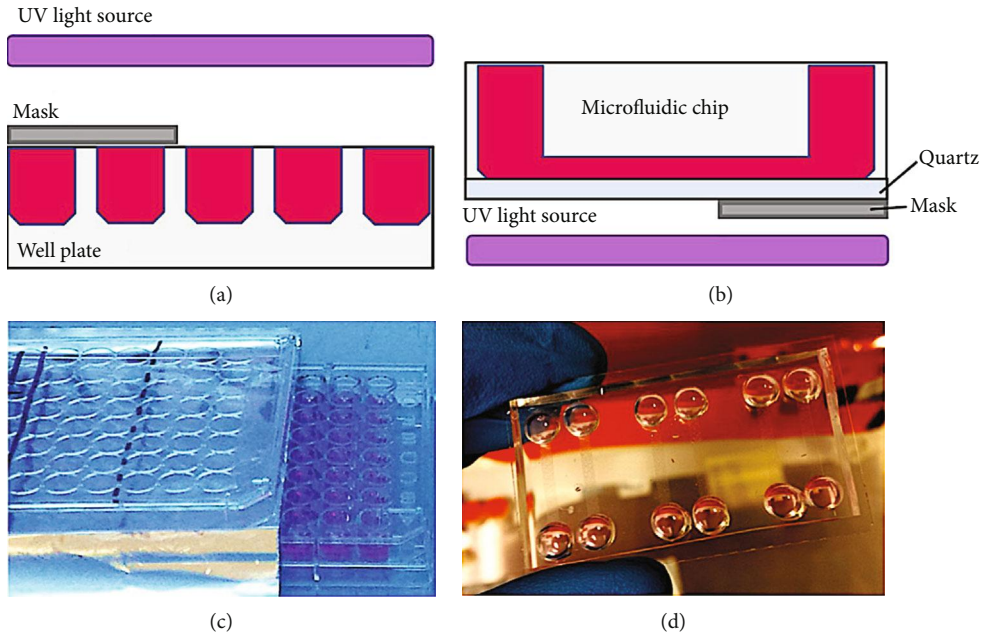

FIGURE 24: Diagram of different UV exposure methods, with (a) top-down UV from the biosafety cabinet on a 96-well plate and (b) bottom-up UV from the light table on a microfluidic chip. Photographs of (c) well plate and (d) microfluidic device. Reproduced (or adapted) with permission [121], ©2019, American Institute of Physics.

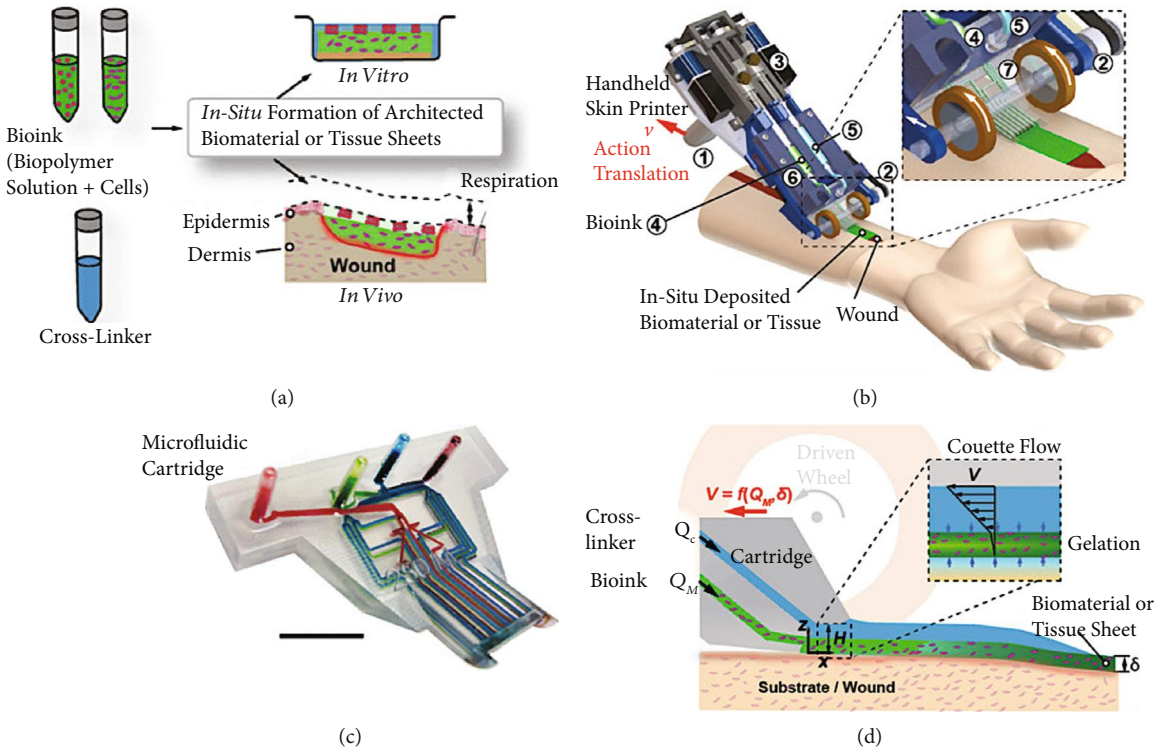

FIGURE 25: Handheld skin printer: (a) schematic diagram illustrating working principle of handheld bioprinter. (b) Rendered image of handheld bioprinter. (c) Photograph of 3D printed microfluidic cartridge. Scale bar 10 mm. (d) Schematic sideview image showing sheet formation between moving microfluidic cartridge and deposition surface or wound. Inset indicates fluid velocity profiles in bioink (green) and cross-linker layers (blue). Reproduced (or adapted) with permission [122], ©2018, Royal Society of Chemistry.

Table 7: Summary of recent advancements in *in vitro* models in brain toxicity testing including the type of drug, the application, the applied cell lines, and the kinetics.

Drug type	Application	Applied cell lines	Kinetics	Ref(s)
Amyloid-β	Toxicity (disease mimic)	Neural progenitor suspension (cortical rat cells)	Over 10 days	[125]
CXCL12, SLIT2-N	Chemotactic effect	Progenitor hNT2, primary hNPC, hBMECs	8 weeks	[143]
Antihuman transferrin receptor (MEM-189), MoAb	Transcytosis	TY10, hBPCT, hAst		[131]
Dextran	Permeability	Astrocytes (pup), primary cortical cells (rat), HUVEC	Over 7 days	[130]
		hCMEC/D3	Over 4 days	[144]

CXCL12, SLIT2-N: chemokines; hNT2: human teratocarcinoma cells; hNPC: human fetal neural progenitor cells; hBMECs, TY10: human brain microvascular endothelial cells; MoAb: monoclonal antibody; hBPCT: human brain pericyte; hAst: human astrocytes; HUVECs: human umbilical vein endothelial cells; hCMEC/D3: human cerebral microvascular endothelial cell line; TEER: transendothelial electrical resistance.

to study the mechanisms of degenerative diseases, including Alzheimer's disease (AD), Parkinson's disease (PD), and amyotrophic sclerosis (AS). Recently, 3D models based on microfluidics have become widely applied to study brain functions and neurotoxicity for the purpose of drug discovery. Such devices facilitate cell-cell interactions by resembling fundamental dynamic conditions of the native brain environment. Some of the latest examples of brain-on-chip platforms for drug discovery, development, and analysis are thoroughly reviewed in this article (Table 7).

2.7.1. Analysis of Drugs in Brain-on-Chip Devices. Brain-on-chip technology is aimed at modelling brain tissue in order to test and predict the effects of certain drugs, to establish new treatments to reverse or prevent neurodegenerative diseases (such as AD and PD), and to screen candidate therapeutic drugs for toxicity. AD is the most common type of dementia and affects tens of millions of people worldwide [127]. The monomeric amyloid-β is a peptide associated with a variety of biological brain functions; however, its soluble oligomers accumulate and form senile plaques that are implicated in the pathogenesis of AD. Research has featured the effects of amyloid-β peptides on the neuronal body of the brain. Park et al. (2015) developed a microfluidic chip that was based on 3D neurospheroids that could closely mimic the *in vivo* brain microenvironment by providing a constant flow of fluid. The PDMS chip contained a concave microwell array for the formation of homogeneous neurospheroids having a uniform size with 3D cytoarchitecture. The osmotic micropump system was connected to an outlet to provide a continuous flow of medium at the interstitial flow level [125]. When the flow on the spheroids was reduced, the size differentiation was inversely accelerated. Traditional mature molecules like beta-III tubulin showed an increase when the active interstitial flow was induced. By providing a 3D cytoarchitecture and interstitial flow, the chip mimicked the microenvironment of a normal brain and those of AD patients, facilitating the investigation of amyloid-β effects on 3D neural tissue. Furthermore, modelling the blood-brain barrier was necessary, as it is a critical structure between the central nervous system and the rest of the body. The authors tested the toxicity of amyloid-β protein on neurospheroids under dynamic or static conditions for 7 days. By using this platform, it was confirmed that neurospheroids cultured under dynamic conditions showed a larger size than those cultured under static conditions, while the amyloid-β reduced cell viability under static conditions. Moreover, the fluidic model also demonstrated that the treatment with amyloid-β decreased the synapsing levels, and it permeated deeper than static assays, which enhanced the biomimetic disease modelling [125].

As was mentioned, the BBB is a selective diffusion barrier within the brain. It is comprised of several cell types that together with tight junctions can protect the brain from the passage of drugs or other compounds directly into the brain [128]. Advances in microfluidic and nanofabrication have contributed to the development of *in vitro* BBB-on-chip platforms that are unique tools for studying the physiology of the brain, neurodegenerative diseases, neurotoxic compounds, and drug discovery. Brown et al. [129] designed a microfluidic device introduced as a neurovascular unit (NVU) comprised of both a vascular chamber and a brain chamber separated by a porous PDMS membrane, allowing cell-to-cell communication between endothelial cells, astrocytes, and pericytes. The NVU had four crucial design features that helped mimic the BBB: (i) adjustable flow on both sides of the barrier, (ii) low media-to-cell volume, (iii) scaffolding to orient and support multiple cell types, and (iv) easy adjustment of the device orientation. The upper layer was used for perfusion, loading, and sampling for the brain compartment with pericytes, neurons, astrocytes, and ED ECM (collagen 1) [129]. The shear stress increased the expression of tight junction molecules and successful dextran permeability through the mimetic BBB. A limitation of this model was the use of PDMS that impedes cell adhesion due to its hydrophobicity. While the device was not used to test any drug, it was demonstrated to have potential to be used for drug discovery due to its close resemblance to the structure of the BBB.

In a 3D neurovascular device, Adriani et al. [130] explored further the mimicking of the BBB. The barrier was made from PDMS by soft lithography and bonded to glass coverslips. The device was composed of four channels connected to cell culture media and a hydrogel scaffold arranged with nine trapezoidal structures. Three different cell types were seeded within the device, namely, astrocytes, primary cortical cells, and HUVEC cells. This simultaneous cell culture allowed a permeability assessment of the *in vitro* BBB. Dextran label particles were introduced to the system to

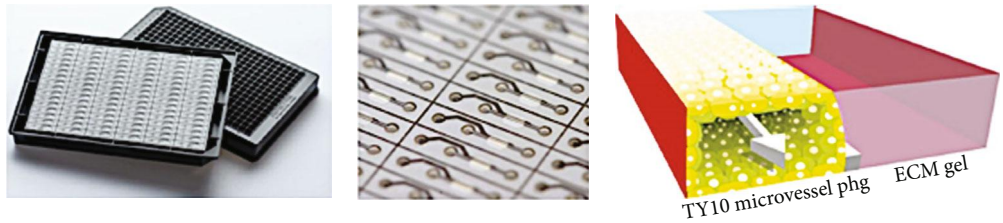

(a) (b) (c)

Figure 26: OrganoPlate device platform. (a) Schematic of the two-lane OrganoPlate. (b) Zoom-in of the bottom of the two-lane OrganoPlate. (c) 3D schematic of the chip. Reproduced (or adapted) with permission [131], ©2018, Springer.

assess the permeability of the endothelial barrier. The structure, natural function, and maturation of each cell type were measured with specific cell markers. The permeability of dextran in cocultures was higher than the respective monolayers. Nevertheless, the device suffered from certain limitations due to the HUVEC differential species of the cells forming leakier barriers that do not mimic the BBB [130].

Another *in vitro* BBB model was developed in a high-throughput membrane-free microfluidic platform. Due to the intrinsic hydrophobicity of PDMS that impedes cell adhesion and can cause nonspecific absorption of proteins and hydrophobic analytes, Wevers et al. [131] chose a commercial microfluidic platform (Figure 26(a)) that employs optical quality glass and polymers that are biocompatible and low compound-absorbing. In this platform, a two-channel OrganoPlate was used for seeding human brain pericytes (hBPCT), human brain microvascular endothelial cells (TY10), and human astrocyte (hAst) cell lines for the evaluation of antibody BBB-shuttle models. In this assay, the transcytosis across the BBB was assessed by the introduction of an antihuman transferrin receptor (MEM-189 mIgG1). The platform allowed for the patterning of ECM gel (Figure 26(c)) through surface tension. A blood vessel was grown adjacent to that gel, and a channel was used to insert the astrocytes and pericytes (Figure 26(b)). The system was free of artificial membranes and accommodated fluid flow through the blood vessels, while allowing fluid phase sampling of molecules that penetrated the endothelial and matrix layers. The tests were performed through the antibody transcytosis assay and Meso scale discovery (MSD). The results showed that the passaging of antibody MEM-189 through the BBB model was approximately twofold higher than the control antibody, indicating that the model can serve as a strong method to study the passage of large molecules and the antibody penetration of brain endothelial cells [131].

Organophosphates (OPs) are one of the principal constituents of insecticides, pesticides, and biological weapons (nerve agents). OP-based compound exposure may occur through direct contact, inhalation, or ingestion. OPs can cause varying levels of toxicity, whose symptoms include diarrhea, nausea, vomiting, sweating, muscle tremors, confusion, drowsiness, seizures, and brain damage [132]. The BBB restricts delivery and permeability of many pharmaceuticals and blood-borne compounds to the central nervous system. However, some OPs can penetrate through the BBB, inhibiting acetylcholinesterase activity, and therefore causing neurotoxicity. Emerging BBB-on-chip models represent a promising alternative to evaluate neurotoxic compounds. Recently, Koo et al. [133] reported a bioprinted 3D platform to study the toxicity of OPs. A microfluidic chip (OrganoPlate) was used to coculture immortalized murine brain endothelial cells, immortalized murine brain neuroblastoma, murine astrocytes, and murine microglia cells (Figures 27(a)–27(c)) to evaluate the *in vitro* neurotoxicity of four OPs: dimethyl methylphosphonate (DMMP), diethyl methylphosphate (DEMP), diethyl cyanophosphonate (DECP), and diethyl chlorophosphate (DCP). The acetylcholinesterase assay showed that DMMP and DEMP can penetrate through the BBB and inhibit acetylcholinesterase activity only at higher concentrations, while DECP and DCP showed strong toxicity even at lower concentrations, inhibiting both acetylcholinesterase and cell viability. These results are similar to the results from *in vivo* counterpart assays [133].

In another report, Shah et al. used a 3D brain-on-a-chip system to evaluate the effect of nitrophenyl isopropyl methylphosphonate (NIMP), commonly called Sarin gas. A commercial MEA device (a tool used for neuronal network studies) with integrated microscopes was used to evaluate the protective effect of pyridostigmine bromide (PB). PB is a drug capable of restoring the enzymatic activity of acetylcholinesterase, when the neurons are exposed to OPs. It was used during the Gulf War as a pretreatment from the harmful effects of nerve agents. Human iPSC-derived neurons and astrocytes pretreated with PB were cultured on the chip and monitored for 35 days. The results showed a higher toxic effect on the cells exposed to NIMP and the cells pretreated with PB, than those cells exposed only to DMSO. Therefore, it is likely that PB does not have the ability penetrate the BBB [134].

In brain cancer, the cells grow to form a mass of tissue that interferes with brain functions. One of the most common types of brain cancer is a glioblastoma. The *in vitro* cancer-on-chip models have been used to study the biological processes of the disease and to evaluate the efficacy of drug therapies. Fan et al. [135] developed a device to study a very aggressive cancer type known as glioblastoma multiform (GlBM). The chip was made of 3-(trimethoxysilyl)propyl methacrylate (TMSPMA) and poly(ethylene glycol)diacrylate (PEGDA) hydrogels fabricated by soft lithography. The GlBM cells (U87) were cultured in the PEGDA hydrogel which formed 3D spheroids within seven days. The effectiveness of two anticancer drugs, pitavastatin and irinotecan, was studied, together with the drug response over the surface of

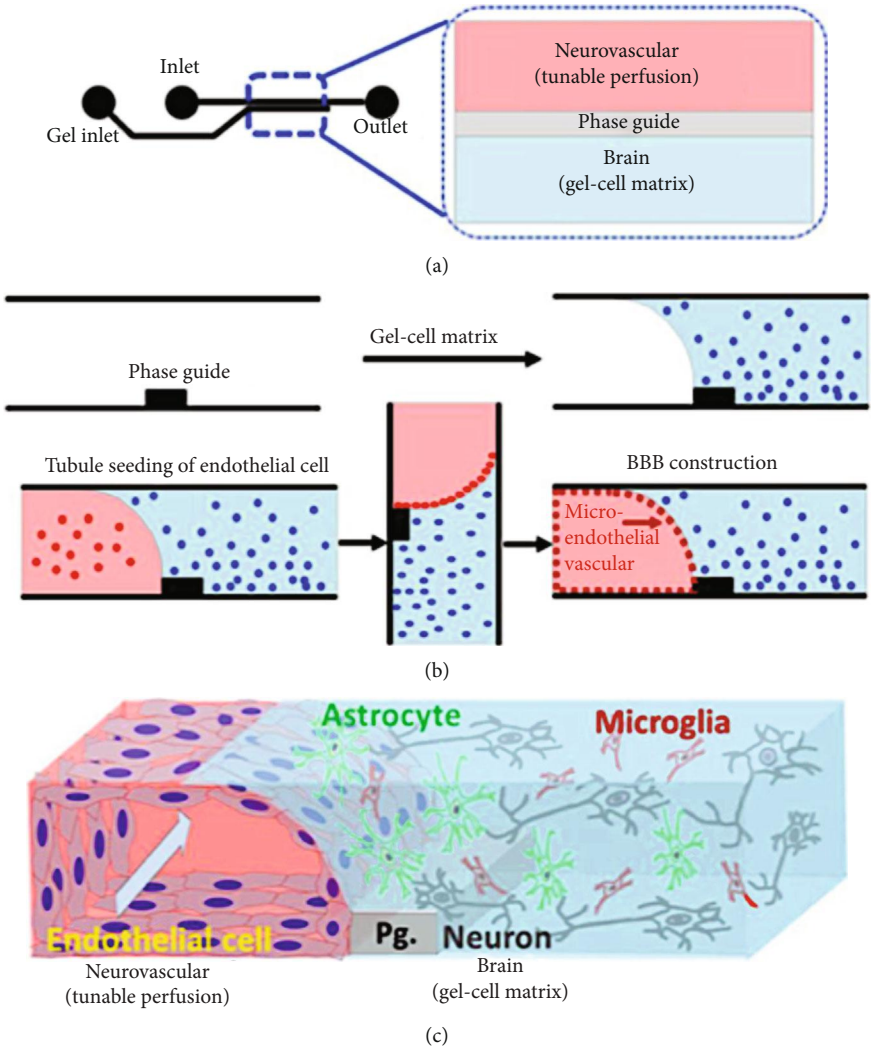

Figure 27: 3D brain construction for high content OP toxicity screening; (a) structure and format application of in vitro culture ware, (b) experimental procedure for constructing 3D neurovascular/brain compartment, and (c) scheme of 3D tetraculture for brain on chip. Reproduced (or adapted) with permission [133], ©2018, Nature.

the spheroids. The results showed that the drugs were diffused through the porous hydrogel matrix into the microwells. Also, it was confirmed that the combination of the two drugs was more effective in reducing the size of the GlBM spheroids, compared with either drug in isolation [135]. All these features provide a key ability to studying drug delivery, as well as determining the pharmacokinetics and pharmacodynamics of new drugs and therapies in the brain.

The high interaction of the cells in the brain requires a considerable research effort to recreate the heterogenicity of cellular communications in microfluidic devices. However, the advances are significant to study the brain barrier drug permeability *in situ* and provide real-time measurement of compounds through the addition of biosensors. This achievement was representative of the enormous need for an accurate brain-on-chip system. Fabrication methods in the future must improve the ability to integrate a better microenvironment for the scaffold-neuronal cells in this complex organ. Furthermore, brain functions are strongly related to, and coordinated by, the entire body; hence, a realistic brain physiology could only be studied in the context of other organs, including the endocrine and circulatory systems.

3. Conclusions and Perspectives

This comprehensive review provides a thorough analysis of the latest advancements in the area of organ-on-chip devices aimed at drug discovery, development, and/or assessment. The latest strategies and achievements reported in the literature highlighting key-playing organs including the liver, kidney, lung, gut, heart, skin, and brain were examined. In addition, the fabrication strategies and the specific application of each device, as well as advantages and disadvantages of each system, were reviewed. Despite the immense advances in the area, there remain a number of significant challenges yet to be addressed with respect to the organ-on-chip devices. Standardization and optimization of the manufacturing methods rely highly on the characteristics of the respective organ, including the anatomical structure, cell interaction, morphology, and basal molecular expression, as

well as the design of the devices, mathematical fluidic modelling, and biocompatibility of the materials used in fabrication, among others.

Another challenge is to facilitate cell heterogenicity. Most studies use immortalized cell lines, primary cell culture, and cell explants, as well as animal or human cells. This may lead to noncomparable results with questionable reproducibility and accuracy that might, in turn, be incompatible with the actual organ. The selection of cells is crucial and should be decided depending on the aim of each developed model. Moreover, high cell viability and long-lasting cell cultures are vital to further explore the potential of these devices. While the majority of the studies have not achieved culture periods longer than 30 days, it is evident that microfluidic systems with continuous flux and automatized circulation could significantly enhance the periodicity of cell viability and culture. Furthermore, frequent supplementation of each specific cell media and mimicked physiological fluid or blood substitute could play a major role in the metabolic functions of the organs. Another important aspect in the fabrication and function of organ-on-chip devices is the validation process. Most studies to date lack the validation step and a close or contemporaneous comparison with the actual organ. A multidisciplinary research approach could dramatically impact all of the involved elements in such devices and would present a major step forward in carefully mimicking human organs. The success of organ-on-chip devices in drug development, drug metabolism, toxicity, safety, and efficacy assays in preclinical trials depends on overcoming each of the mentioned experimental challenges.

Abbreviations

2-DCE-IFM: 2-Deschloroethyl-ifosfamide metabolite
MTT: 3-(4,5-Dimethylthiazol-2-yl)-2,5-diphenyltetrazolium bromide
TMSPMA: 3-(Trimethoxysilyl)propyl methacrylate
DAPI: 4,6-Diamidino-2-phenylindole
ABS: Acrylonitrile butadiene styrene
AKD: Acute kidney disease
A549: Adenocarcinomic human alveolar basal epithelial cells
α-GST: Alpha glutathione *S*-transferase
AD: Alzheimer's disease
ATCC: American Type Culture Collection
AS: Amyotrophic sclerosis
MEM-189 mIgG1: Antihuman transferrin receptor
BLC: Blood loading channel
BBB: Blood-brain barrier
Ca^{++}: Calcium cation
$CaCl_2$: Calcium chloride
CMs: Cardiomyocytes
CVDs: Cardiovascular diseases
CNS: Central nervous system
CKD: Chronic kidney disease
COPD: Chronic obstructive pulmonary disease
Caco-2: Colon adenocarcinoma cells
CLC: Column loading channel
CVB1: Coxsackievirus B1
CysA: Cyclosporin A
CYP450: Cytochrome P450
CYP2D6: Cytochrome P450 family 2, subfamily D, polypeptide 6
CYP2E1: Cytochrome P450 family 2, subfamily E, polypeptide 1
CYP3A4: Cytochrome P450 family 3, subfamily A, polypeptide 4
CYP2B6: Cytochrome P450 family 2, subfamily B, polypeptide 6
CYP2C9: Cytochrome P450 family 2, subfamily C, polypeptide 9
DCP: Diethyl chlorophosphate
DECP: Diethyl cyanophosphonate
DEMP: Diethyl methylphosphate
DMMP: Dimethyl methylphosphonate
DMSO: Dimethyl sulfoxide
DMOG: Dimethyloxalylglycine
DXR: Doxorubicin
DILI: Drug-induced liver injury
DMEM: Dulbecco's modified Eagle's medium
ESCs: Embryonic stem cells
EA.hy926: Endothelial cells
ENM: Engineered nanomaterials
EGFR-TKIs: Epidermal growth factor receptor tyrosine kinase
ECs: Epithelial cells
SU-8: Epoxy-based negative photoresist
EAR: Extracellular acidification rate
ECM: Extracellular matrix
F-actin: Filamentous-actin (protein)
FSS: Fluidic shear stress
FITC: Fluorescent isothiocyanate
FEP: Fluorinated ethylene-propylene
GelMA: Gelatin methacryloyl
GelMA-HM: Gelatin methacryloyl-high degree
GelMA-LM: Gelatin methacryloyl-low degree
GlBM: Glioblastoma multiform
GBM: Glomerular basement membrane
GFR: Glomerular filtration rate
HepaRG: Hepatic biprogenitor cell line
HBV: Hepatitis B virus
HNF4a: Hepatocyte nuclear factor 4 alpha
HiPCs: Hormone independent prostate cells
HAEC: Human aortic endothelial cell line
hAst: Human astrocytes
TY10: Human brain microvascular endothelial cell
hBMECs: Human brain microvascular endothelial cells
hBPCT: Human brain pericytes
hCMEC/D3: Human cerebral microvascular endothelial cell line
HT-29: Human colorectal adenocarcinoma cell line
HEK293: Human embryonal kidney-derived
HaCaT: Human epidermal keratinocytes
HFL1: Human fetal lung fibroblasts
hNPC: Human fetal neural progenitor cells

GM-3348: Human fibroblast
HS27: Human fibroblasts
LX-2: Human hepatic stellate cell
HepG2: Human hepatocellular carcinoma
HepG2/C3: Human hepatocellular carcinoma/complement factor 3
U937: Human histiocytic lymphoma cell line
hiPSC: Human-induced pluripotent stem cells
hIEC: Human intestinal epithelial cells
HIOs: Human intestinal organoids
HK-2: Human kidney epithelial cells
HKMECs: Human kidney microvascular endothelial cells
HK8160: Human Kupffer cells
hCMs: Human primary cardiomyocytes
HPTECs: Human proximal tubular epithelial cells
hRVTU: Human renal vascular-tubular platform
hNT2: Human teratocarcinoma cells
HUVECs: Human umbilical vein endothelial cells
HIF PHDs: Hypoxia inducible factor prolyl hydroxylase
iPSCs: Induced pluripotent stem cells
iHCC: Integrated heart/cancer on a chip
IFN: Interferon
IFN-α: Interferon-alpha
IL-13: Interleukin-13
IL-8: Interleukin-8
ISDN: Isosorbide dinitrate
N/TERT-1: Keratinocytes
KIM-1: Kidney injury molecule-1
LDH: Lactate dehydrogenase
LSEC: Liver sinusoidal endothelial cell
LOC: Liver-on-a-chip
LSOC: Liver-sinusoid-on-a-chip
MDCK: Madin-Darby canine kidney
MSD: Meso scale discovery
mRNA: Messenger ribonucleic acid
miR-122: Micro-RNA-122
μECTs: Microengineered cardiac tissues
MEA: Microelectrode array
MPS: Microphysiological system
MC: Migration channel
MoAb: Monoclonal antibody
MRP2: Multidrug resistance protein 2
NPs: Nanoparticles
NRVMs: Neonatal rat ventricular myocytes
NPC: Nephron progenitor cells
NVU: Neurovascular unit
Nrf2: NF-E2-related transcription factor
NC: Nitrocellulose
NIMP: Nitrophenyl isopropyl methylphosphonate
NAFLD: Nonalcoholic fatty liver disease
NPCs: Nonparenchymal cells
NSCLC: Non-small-cell lung cancer
NHEKs: Normal epidermal keratinocytes
NHDFs: Normal human dermal fibroblasts
OPs: Organophosphates
PD: Parkinson's disease
PM2: Parmodulin-2
PBM: Peripheral blood mononuclear cells
LLC-PK1: Pig kidney cells
PEGDA: Poly(ethylene glycol) diacrylate
PLGA: Poly(lactide-co-glycolide)
PMMA: Poly(methylmethacrylate)
PCL: Polycaprolactone
PC: Polycarbonate
PDA: Polydiacetylene
PDMS: Polydimethylsiloxane
PET: Polyethylene terephthalate
PLA: Polylactic acid
PMB: Polymyxin B
PS: Polystyrene
PTFE: Polytetrafluoroethylene
hAEC: Primary human alveolar cells
Hu8150: Primary human hepatocytes
PiEC: Primary intestinal epithelial cells
PLCs: Primary liver cells
Wnt-3A: Protein
p53: Protein 53
UGT1A1: Protein coding gene
PT: Proximal tubule
PTECs: Proximal tubule epithelial cells
PB: Pyridostigmine bromide
ROS: Reactive oxygen species
RT-qPCR: Real-time polymerase chain reaction
RBC: Red blood cells
RANTES: Regulated on activation, normal T cell expressed and secreted
RBF: Renal blood flow
RPTEC: Renal proximal tubule epithelial cells
RES: Reticuloendothelial system
SEM: Scanning electron microscopy
SiO2: Silicon dioxide
Ag: Silver
SMC: Smooth muscle cells
SGLT2: Sodium-glucose cotransporter-2
SULT1A1: Sulfotransferase 1A1
3D: Three-dimensional
TiO2: Titanium dioxide
TNPs: Titanium dioxide nanoparticles
TEER: Transepithelial electrical resistance
TRPV1: Transient receptor potential V1
TEM: Transmission electron microscopy
TNF-α: Tumor necrosis factor alpha
2D: Two-dimensional
UV: Ultraviolet
VEGF: Vascular endothelial growth factor
WSOC: Wrinkled skin-on-a-chip
ZnO: Zinc oxide
ZO-1: Zonula occludens-1
GGT: γ-Glutamyl transpeptidase.

Conflicts of Interest

The authors declare no conflict of interest.

Authors' Contributions

Aida Rodriguez-Garcia and Jacqueline Oliva-Ramirez have contributed equally to this work.

Acknowledgments

The authors would like to acknowledge the financial and technical support of Writing Lab, TecLabs, and Tecnológico de Monterrey for the production of this work. The graphical abstract was created by BioRender software through a licensed subscription.

Supplementary Materials

The supplementary file includes graphical abstract of the manuscript. *(Supplementary Materials)*

References

[1] B. Zhang, A. Korolj, B. F. L. Lai, and M. Radisic, "Advances in organ-on-a-chip engineering," *Nature Reviews Materials*, vol. 3, no. 8, pp. 257–278, 2018.

[2] J. Park, I. Wetzel, I. Marriott et al., "A 3D human triculture system modeling neurodegeneration and neuroinflammation in Alzheimer's disease," *Nature Neuroscience*, vol. 21, no. 7, pp. 941–951, 2018.

[3] M. E. Katt, A. L. Placone, A. D. Wong, Z. S. Xu, and P. C. Searson, "In vitro tumor models: advantages, disadvantages, variables, and selecting the right platform," *Frontiers in Bioengineering and Biotechnology*, vol. 4, 2016.

[4] I. W. Mak, N. Evaniew, and M. Ghert, "Lost in translation: animal models and clinical trials in cancer treatment," *American Journal of Translational Research*, vol. 6, no. 2, pp. 114–118, 2014.

[5] Q. Wu, J. Liu, X. Wang et al., "Organ-on-a-chip: recent breakthroughs and future prospects," *Biomedical Engineering Online*, vol. 19, no. 1, p. 9, 2020.

[6] Y. S. Zhang, K. Yue, J. Aleman et al., "3D bioprinting for tissue and organ fabrication," *Annals of Biomedical Engineering*, vol. 45, no. 1, pp. 148–163, 2017.

[7] S.-S. Yoo, "3D-printed biological organs: medical potential and patenting opportunity," *Expert Opinion on Therapeutic Patents*, vol. 25, no. 5, pp. 507–511, 2015.

[8] W. Peng, P. Datta, B. Ayan, V. Ozbolat, D. Sosnoski, and I. T. Ozbolat, "3D bioprinting for drug discovery and development in pharmaceutics," *Acta Biomaterialia*, vol. 57, pp. 26–46, 2017.

[9] S. H. Lee and J. H. Sung, "Organ-on-a-chip technology for reproducing multiorgan physiology," *Advanced Healthcare Materials*, vol. 7, no. 2, article 1700419, 2018.

[10] R. K. Kankala, S.-B. Wang, and A.-Z. Chen, "Microengineered organ-on-a-chip platforms towards personalized medicine," *Current Pharmaceutical Design*, vol. 24, no. 45, pp. 5354–5366, 2018.

[11] H. Kimura, Y. Sakai, and T. Fujii, "Organ/body-on-a-chip based on microfluidic technology for drug discovery," *Drug Metabolism and Pharmacokinetics*, vol. 33, no. 1, pp. 43–48, 2018.

[12] S. E. Park, A. Georgescu, and D. Huh, "Organoids-on-a-chip," *Science*, vol. 364, no. 6444, pp. 960–965, 2019.

[13] G. Tuschl, B. Lauer, and S. O. Mueller, "Primary hepatocytes as a model to analyze species-specific toxicity and drug metabolism," *Expert Opinion on Drug Metabolism & Toxicology*, vol. 4, no. 7, pp. 855–870, 2008.

[14] W. B. Jakoby and I. H. Pastan, *Methods in Enzymology: Cell Culture*, Academic Press, New York, NY, USA, 1979.

[15] T. Mseka, J. R. Bamburg, and L. P. Cramer, "ADF/cofilin family proteins control formation of oriented actin-filament bundles in the cell body to trigger fibroblast polarization," *Journal of Cell Science*, vol. 120, no. 24, pp. 4332–4344, 2007.

[16] J. Rodés, J. P. Benhamou, A. Blei et al., *Textbook of Hepatology: From Basic Science to Clinical Practice*, Wiley-Blackwell Publishing, 3rd edition, 2008, https://www.wiley.com/en-us/Textbook+of+Hepatology&;3A+From+Basic+Science+to+Clinical+Practice&2C+3rd+Edition-p-9781405181518.

[17] L. DeLeve, "Hepatic microvasculature in liver injury," *Seminars in Liver Disease*, vol. 27, no. 4, pp. 390–400, 2007.

[18] T. Adachi, H. Nakagawa, I. Chung et al., "Nrf2-dependent and -independent induction of ABC transporters ABCC1, ABCC2, and ABCG2 in HepG2 cells under oxidative stress," *Journal of Experimental Therapeutics and Oncology*, vol. 6, no. 4, pp. 335–348, 2007.

[19] K. P. Kanebratt and T. B. Andersson, "Evaluation of HepaRG cells as an in vitro model for human drug metabolism studies," *Drug Metabolism and Disposition*, vol. 36, no. 7, pp. 1444–1452, 2008.

[20] S. J. Lee, Y. J. Lee, and K. K. Park, "The pathogenesis of drug-induced liver injury," *Expert Review of Gastroenterology and Hepatology*, vol. 10, no. 10, pp. 1175–1185, 2016.

[21] A. Choe, S. K. Ha, I. Choi, N. Choi, and J. H. Sung, "Microfluidic gut-liver chip for reproducing the first pass metabolism," *Biomedical Microdevices*, vol. 19, no. 1, 2017.

[22] Y. Wang, W. Su, L. Wang et al., "Paper supported long-term 3D liver co-culture model for the assessment of hepatotoxic drugs," *Toxicology Research*, vol. 7, no. 1, pp. 13–21, 2018.

[23] N. S. Bhise, V. Manoharan, S. Massa et al., "A liver-on-a-chip platform with bioprinted hepatic spheroids," *Biofabrication*, vol. 8, no. 1, article 014101, 2016.

[24] B. Corrado, V. Gregorio, G. Imparato, C. Attanasio, F. Urciuolo, and P. A. Netti, "A three-dimensional microfluidized liver system to assess hepatic drug metabolism and hepatotoxicity," *Biotechnology and Bioengineering*, vol. 116, no. 5, pp. 1152–1163, 2019.

[25] A. M. Ortega-Prieto, J. K. Skelton, S. N. Wai et al., "3D microfluidic liver cultures as a physiological preclinical tool for hepatitis B virus infection," *Nature Communications*, vol. 9, no. 1, 2018.

[26] A. A. Zakhariants, O. A. Burmistrova, M. Y. Shkurnikov, A. A. Poloznikov, and D. A. Sakharov, "Development of a specific substrate—inhibitor panel (liver-on-a-chip) for evaluation of cytochrome P450 activity," *Bulletin of Experimental Biology and Medicine*, vol. 162, no. 1, pp. 170–174, 2016.

[27] A. A. Zakharyants, O. A. Burmistrova, and A. A. Poloznikov, "The use of human liver cell model and cytochrome P450 substrate—inhibitor panel for studies of dasatinib and warfarin interactions," *Bulletin of Experimental Biology and Medicine*, vol. 162, no. 4, pp. 515–519, 2017.

[28] A. J. Foster, B. Chouhan, S. L. Regan et al., "Integrated in vitro models for hepatic safety and metabolism: evaluation of a human liver-chip and liver spheroid," *Archives of Toxicology*, vol. 93, no. 4, pp. 1021–1037, 2019.

[29] T. J. Long, P. A. Cosgrove, R. T. Dunn II et al., "Modeling therapeutic antibody-small molecule drug-drug interactions using a three-dimensional perfusable human liver coculture platform," *Drug Metabolism and Disposition*, vol. 44, no. 12, pp. 1940–1948, 2016.

[30] U. Sarkar, K. C. Ravindra, E. Large et al., "Integrated assessment of diclofenac biotransformation, pharmacokinetics, and omics-based toxicity in a three-dimensional human liver-immunocompetent coculture system," *Drug Metabolism and Disposition*, vol. 45, no. 7, pp. 855–866, 2017.

[31] N. Tsamandouras, T. Kostrzewski, C. L. Stokes, L. G. Griffith, D. J. Hughes, and M. Cirit, "Quantitative assessment of population variability in hepatic drug metabolism using a perfused three-dimensional human liver microphysiological system," *Journal of Pharmacology and Experimental Therapeutics*, vol. 360, no. 1, pp. 95–105, 2017.

[32] C. Rowe, M. Shaeri, E. Large et al., "Perfused human hepatocyte microtissues identify reactive metabolite-forming and mitochondria-perturbing hepatotoxins," *Toxicology In Vitro*, vol. 46, pp. 29–38, 2018.

[33] B. Delalat, C. Cozzi, S. Rasi Ghaemi et al., "Microengineered bioartificial liver chip for drug toxicity screening," *Advanced Functional Materials*, vol. 28, no. 28, article 1801825, 2018.

[34] W. R. Proctor, A. J. Foster, J. Vogt et al., "Utility of spherical human liver microtissues for prediction of clinical drug-induced liver injury," *Archives of Toxicology*, vol. 91, no. 8, pp. 2849–2863, 2017.

[35] R. Jellali, T. Bricks, S. Jacques et al., "Long-term human primary hepatocyte cultures in a microfluidic liver biochip show maintenance of mRNA levels and higher drug metabolism compared with Petri cultures," *Biopharmaceutics & Drug Disposition*, vol. 37, no. 5, pp. 264–275, 2016.

[36] A. A. Poloznikov, S. V. Nikulin, A. A. Zakhariants et al., ""Branched tail" oxyquinoline inhibitors of HIF prolyl hydroxylase: early evaluation of toxicity and metabolism using liver-on-a-chip," *Drug Metabolism Letters*, vol. 13, no. 1, pp. 45–52, 2019.

[37] J. Theobald, A. Ghanem, P. Wallisch et al., "Liver-kidney-on-chip to study toxicity of drug metabolites," *ACS Biomaterials Science & Engineering*, vol. 4, no. 1, pp. 78–89, 2017.

[38] J. Deng, X. Zhang, Z. Chen et al., "A cell lines derived microfluidic liver model for investigation of hepatotoxicity induced by drug-drug interaction," *Biomicrofluidics*, vol. 13, no. 2, article 024101, 2019.

[39] S. Prill, D. Bavli, G. Levy et al., "Real-time monitoring of oxygen uptake in hepatic bioreactor shows CYP450-independent mitochondrial toxicity of acetaminophen and amiodarone," *Archives of Toxicology*, vol. 90, no. 5, pp. 1181–1191, 2016.

[40] H. Pein, A. Ville, S. Pace et al., "Endogenous metabolites of vitamin E limit inflammation by targeting 5-lipoxygenase," *Nature Communications*, vol. 9, no. 1, p. 3834, 2018.

[41] S. Mi, X. Yi, Z. du, Y. Xu, and W. Sun, "Construction of a liver sinusoid based on the laminar flow on chip and self-assembly of endothelial cells," *Biofabrication*, vol. 10, no. 2, article 025010, 2018.

[42] Y.-S. Weng, S. F. Chang, M. C. Shih, S. H. Tseng, and C. H. Lai, "Scaffold-free liver-on-a-chip with multiscale organotypic cultures," *Advanced Materials*, vol. 29, no. 36, p. 1701545, 2017.

[43] S. K. Nigam, W. Wu, K. T. Bush, M. P. Hoenig, R. C. Blantz, and V. Bhatnagar, "Handling of drugs, metabolites, and uremic toxins by kidney proximal tubule drug transporters," *Clinical Journal of the American Society of Nephrology*, vol. 10, no. 11, pp. 2039–2049, 2015.

[44] R. Huang, W. Zheng, W. Liu, W. Zhang, Y. Long, and X. Jiang, "Investigation of tumor cell behaviors on a vascular microenvironment- mimicking microfluidic chip," *Scientific Reports*, vol. 5, no. 1, article 17768, 2015.

[45] Y. Sakuta, I. Takehara, K.-i. Tsunoda, and K. Sato, "Development of a microfluidic system comprising dialysis and secretion components for a bioassay of renal clearance," *Analytical Sciences*, vol. 34, no. 9, pp. 1073–1078, 2018.

[46] E. J. Weber, A. Chapron, B. D. Chapron et al., "Development of a microphysiological model of human kidney proximal tubule function," *Kidney International*, vol. 90, no. 3, pp. 627–637, 2016.

[47] K. A. Homan, D. B. Kolesky, M. A. Skylar-Scott et al., "Bioprinting of 3D convoluted renal proximal tubules on perfusable chips," *Scientific Reports*, vol. 6, no. 1, article 34845, 2016.

[48] T. T. G. Nieskens and A.-K. Sjögren, "Emerging in vitro systems to screen and predict drug-induced kidney toxicity," *Seminars in Nephrology*, vol. 39, no. 2, pp. 215–226, 2019.

[49] M. Adler, S. Ramm, M. Hafner et al., "A quantitative approach to screen for nephrotoxic compounds in vitro," *Journal of the American Society of Nephrology*, vol. 27, no. 4, pp. 1015–1028, 2016.

[50] M. J. Ryan, G. Johnson, J. Kirk, S. M. Fuerstenberg, R. A. Zager, and B. Torok-Storb, "HK-2: an immortalized proximal tubule epithelial cell line from normal adult human kidney," *Kidney International*, vol. 45, no. 1, pp. 48–57, 1994.

[51] G. Gstraunthaler, W. Pfaller, and P. Kotanko, "Biochemical characterization of renal epithelial cell cultures (LLC-PK1 and MDCK)," *American Journal of Physiology-Renal Physiology*, vol. 248, no. 4, pp. F536–F544, 1985.

[52] M. A. Perazella, "Renal vulnerability to drug toxicity," *Clinical Journal of the American Society of Nephrology*, vol. 4, no. 7, pp. 1275–1283, 2009.

[53] J. Sateesh, K. Guha, A. Dutta, P. Sengupta, and K. Srinivasa Rao, "Design and analysis of microfluidic kidney-on-chip model: fluid shear stress based study with temperature effect," *Microsystem Technologies*, vol. 25, no. 7, pp. 2553–2560, 2019.

[54] S. Kim, S. C. LesherPerez, B. . C. Kim et al., "Pharmacokinetic profile that reduces nephrotoxicity of gentamicin in a perfused kidney-on-a-chip," *Biofabrication*, vol. 8, no. 1, article 015021, 2016.

[55] S. Musah, N. Dimitrakakis, D. M. Camacho, G. M. Church, and D. E. Ingber, "Directed differentiation of human induced pluripotent stem cells into mature kidney podocytes and establishment of a glomerulus chip," *Nature Protocols*, vol. 13, no. 7, pp. 1662–1685, 2018.

[56] Y. S. Zhang, A. Arneri, S. Bersini et al., "Bioprinting 3D microfibrous scaffolds for engineering endothelialized myocardium and heart-on-a-chip," *Biomaterials*, vol. 110, pp. 45–59, 2016.

[57] L. Yang, S. V. Shridhar, M. Gerwitz, and P. Soman, "Anin vitrovascular chip using 3D printing-enabled hydrogel casting," *Biofabrication*, vol. 8, no. 3, article 035015, 2016.

[58] S. Musah, A. Mammoto, T. C. Ferrante et al., "Mature induced-pluripotent-stem-cell-derived human podocytes reconstitute kidney glomerular-capillary-wall function on a chip," *Nature Biomedical Engineering*, vol. 1, no. 5, p. 0069, 2017.

[59] L. H. Lash, "Role of bioactivation reactions in chemically induced nephrotoxicity," in *Drug Metabolism Handbook*, pp. 761–781, Wiley Online Library, 2008.

[60] E. J. Weber, K. A. Lidberg, L. Wang et al., "Human kidney on a chip assessment of polymyxin antibiotic nephrotoxicity," *JCI Insight*, vol. 3, no. 24, 2018.

[61] K. A. Homan, N. Gupta, K. T. Kroll et al., "Flow-enhanced vascularization and maturation of kidney organoids in vitro," *Nature Methods*, vol. 16, no. 3, pp. 255–262, 2019.

[62] S. G. Rayner, K. T. Phong, J. Xue et al., "Reconstructing the human renal vascular–tubular unit in vitro," *Advanced Healthcare Materials*, vol. 7, no. 23, article 1801120, 2018.

[63] D. Aschenbrenner, O. Friedrich, and D. F. Gilbert, "3D printed lab-on-a-chip platform for chemical stimulation and parallel analysis of ion channel function," *Micromachines*, vol. 10, no. 8, p. 548, 2019.

[64] M. I. Bogorad and P. C. Searson, "Real-time imaging and quantitative analysis of doxorubicin transport in a perfusable microvessel platform," *Integrative Biology*, vol. 8, no. 9, pp. 976–984, 2016.

[65] S. Cho, A. Islas-Robles, A. M. Nicolini, T. J. Monks, and J. Y. Yoon, "In situ, dual-mode monitoring of organ-on-a-chip with smartphone-based fluorescence microscope," *Biosensors and Bioelectronics*, vol. 86, pp. 697–705, 2016.

[66] J. A. Zepp and E. E. Morrisey, "Cellular crosstalk in the development and regeneration of the respiratory system," *Nature Reviews Molecular Cell Biology*, vol. 20, no. 9, pp. 551–566, 2019.

[67] K. H. Benam, R. Villenave, C. Lucchesi et al., "Small airway-on-a-chip enables analysis of human lung inflammation and drug responses in vitro," *Nature Methods*, vol. 13, no. 2, pp. 151–157, 2016.

[68] M. Humayun, C.-W. Chow, and E. W. K. Young, "Microfluidic lung airway-on-a-chip with arrayable suspended gels for studying epithelial and smooth muscle cell interactions," *Lab on a Chip*, vol. 18, no. 9, pp. 1298–1309, 2018.

[69] A. O. Stucki, J. D. Stucki, S. R. R. Hall et al., "A lung-on-a-chip array with an integrated bio-inspired respiration mechanism," *Lab on a Chip*, vol. 15, no. 5, pp. 1302–1310, 2015.

[70] X.-J. Liu, S. W. Hu, B. Y. Xu et al., "Microfluidic liquid-air dual-gradient chip for synergic effect bio-evaluation of air pollutant," *Talanta*, vol. 182, pp. 202–209, 2018.

[71] D. Huh, "A human breathing lung-on-a-chip," *Annals of the American Thoracic Society*, vol. 12, Supplement 1, pp. S42–S44, 2015.

[72] A. Jain, R. Barrile, A. van der Meer et al., "Primary human lung alveolus-on-a-chip model of intravascular thrombosis for assessment of therapeutics," *Clinical Pharmacology & Therapeutics*, vol. 103, no. 2, pp. 332–340, 2018.

[73] X. Yang, K. Li, X. Zhang et al., "Nanofiber membrane supported lung-on-a-chip microdevice for anti-cancer drug testing," *Lab on a Chip*, vol. 18, no. 3, pp. 486–495, 2018.

[74] J. Jia'en Li, S. Muralikrishnan, C.-T. Ng, L.-Y. L. Yung, and B.-H. Bay, "Nanoparticle-induced pulmonary toxicity," *Experimental Biology and Medicine*, vol. 235, no. 9, pp. 1025–1033, 2010.

[75] M. Zhang, C. Xu, L. Jiang, and J. Qin, "A 3D human lung-on-a-chip model for nanotoxicity testing," *Toxicology Research*, vol. 7, no. 6, pp. 1048–1060, 2018.

[76] H. Moghadas, M. S. Saidi, N. Kashaninejad, and N. T. Nguyen, "Challenge in particle delivery to cells in a microfluidic device," *Drug Delivery and Translational Research*, vol. 8, no. 3, pp. 830–842, 2018.

[77] K.-Y. Shim, D. Lee, J. Han, N.-T. Nguyen, S. Park, and J. H. Sung, "Microfluidic gut-on-a-chip with three-dimensional villi structure," *Biomedical Microdevices*, vol. 19, no. 2, p. 37, 2017.

[78] X. He, D. O. Mishchuk, J. Shah, B. C. Weimer, and C. M. Slupsky, "Cross-talk between E. coli strains and a human colorectal adenocarcinoma- derived cell line," *Scientific Reports*, vol. 3, no. 1, p. 3416, 2013.

[79] H. J. Kim, D. Huh, G. Hamilton, and D. E. Ingber, "Human gut-on-a-chip inhabited by microbial flora that experiences intestinal peristalsis-like motions and flow," *Lab on a Chip*, vol. 12, no. 12, pp. 2165–2174, 2012.

[80] W. Shin, L. A. Hackley, and H. J. Kim, ""Good fences make good neighbors": how does the human gut microchip unravel mechanism of intestinal inflammation?," *Gut Microbes*, vol. 11, no. 3, pp. 581–586, 2020.

[81] F. P. Guengerich, "Cytochrome P450 and chemical toxicology," *Chemical Research in Toxicology*, vol. 21, no. 1, pp. 70–83, 2008.

[82] H. J. Kim and D. E. Ingber, "Gut-on-a-chip microenvironment induces human intestinal cells to undergo villus differentiation," *Integrative Biology*, vol. 5, no. 9, pp. 1130–1140, 2013.

[83] H. J. Kim, H. Li, J. J. Collins, and D. E. Ingber, "Contributions of microbiome and mechanical deformation to intestinal bacterial overgrowth and inflammation in a human gut-on-a-chip," *Proceedings of the National Academy of Sciences of the United States of America*, vol. 113, no. 1, pp. E7–E15, 2016.

[84] S. Jalili-Firoozinezhad, R. Prantil-Baun, A. Jiang et al., "Modeling radiation injury-induced cell death and countermeasure drug responses in a human gut-on-a-chip," *Cell Death & Disease*, vol. 9, no. 2, p. 223, 2018.

[85] R. Villenave, S. Q. Wales, T. Hamkins-Indik et al., "Human gut-on-a-chip supports polarized infection of coxsackie B1 virus in vitro," *PLoS One*, vol. 12, no. 2, article e0169412, 2017.

[86] J. R. Spence, C. N. Mayhew, S. A. Rankin et al., "Directed differentiation of human pluripotent stem cells into intestinal tissue in vitro," *Nature*, vol. 470, no. 7332, pp. 105–109, 2011.

[87] M. Kasendra, A. Tovaglieri, A. Sontheimer-Phelps et al., "Development of a primary human Small Intestine-on-a-Chip using biopsy- derived organoids," *Scientific Reports*, vol. 8, no. 1, p. 2871, 2018.

[88] M. J. Workman, J. P. Gleeson, E. J. Troisi et al., "Enhanced utilization of induced pluripotent stem cell–derived human intestinal organoids using microengineered chips," *Cellular and Molecular Gastroenterology and Hepatology*, vol. 5, no. 4, pp. 669–677.e2, 2018.

[89] S. P. Claus, S. L. Ellero, B. Berger et al., "Colonization-induced host-gut microbial metabolic interaction," *mBio*, vol. 2, no. 2, 2011.

[90] D.-H. Yoo, I. S. Kim, T. K. van le, I. H. Jung, H. H. Yoo, and D. H. Kim, "Gut microbiota-mediated drug interactions between lovastatin and antibiotics," *Drug Metabolism and Disposition*, vol. 42, no. 9, pp. 1508–1513, 2014.

[91] A. Sharma, M. M. Buschmann, and J. A. Gilbert, "Pharmacomicrobiomics: the holy grail to variability in drug response?," *Clinical Pharmacology & Therapeutics*, vol. 106, no. 2, pp. 317–328, 2019.

[92] M. Renouf and S. Hendrich, "Bacteroides uniformis is a putative bacterial species associated with the degradation of the isoflavone genistein in human feces," *The Journal of Nutrition*, vol. 141, no. 6, pp. 1120–1126, 2011.

[93] Y. Guo, Z. Li, W. Su, L. Wang, Y. Zhu, and J. Qin, "A biomimetic human gut-on-a-chip for modeling drug metabolism in intestine," *Artificial Organs*, vol. 42, no. 12, pp. 1196–1205, 2018.

[94] L. R. Madden, T. V. Nguyen, S. Garcia-Mojica et al., "Bioprinted 3D primary human intestinal tissues model aspects of native physiology and ADME/Tox functions," *iScience*, vol. 2, pp. 156–167, 2018.

[95] H.-Y. Tan, S. Trier, U. L. Rahbek, M. Dufva, J. P. Kutter, and T. L. Andresen, "A multi-chamber microfluidic intestinal barrier model using Caco-2 cells for drug transport studies," *PLoS One*, vol. 13, no. 5, article e0197101, 2018.

[96] M. Hiraoka, "Mechanisms of drug-induced cardiac toxicity," in *Electrical Diseases of the Heart*, I. Gussak, C. Antzelevitch, A. A. M. Wilde, P. A. Friedman, M. J. Ackerman, and W. K. Shen, Eds., pp. 691–704, Springer, London, UK, 2008.

[97] H. Savoji, M. H. Mohammadi, N. Rafatian et al., "Cardiovascular disease models: a game changing paradigm in drug discovery and screening," *Biomaterials*, vol. 198, pp. 3–26, 2019.

[98] N. Annabi, K. Tsang, S. M. Mithieux et al., "Highly elastic micropatterned hydrogel for engineering functional cardiac tissue," *Advanced Functional Materials*, vol. 23, no. 39, pp. 4950–4959, 2013.

[99] F. Fu, L. Shang, Z. Chen, Y. Yu, and Y. Zhao, "Bioinspired living structural color hydrogels," *Science Robotics*, vol. 3, no. 16, 2018.

[100] K.-i. Kamei, Y. Kato, Y. Hirai et al., "Integrated heart/cancer on a chip to reproduce the side effects of anti-cancer drugs in vitro," *RSC Advances*, vol. 7, no. 58, pp. 36777–36786, 2017.

[101] A. Marsano, C. Conficconi, M. Lemme et al., "Beating heart on a chip: a novel microfluidic platform to generate functional 3D cardiac microtissues," *Lab on a Chip*, vol. 16, no. 3, pp. 599–610, 2016.

[102] M. R. Gwinn and V. Vallyathan, "Nanoparticles: health effects—pros and cons," *Environmental Health Perspectives*, vol. 114, no. 12, pp. 1818–1825, 2006.

[103] S. Ahn, H. A. M. Ardoña, J. U. Lind et al., "Mussel-inspired 3D fiber scaffolds for heart-on-a-chip toxicity studies of engineered nanomaterials," *Analytical and Bioanalytical Chemistry*, vol. 410, no. 24, pp. 6141–6154, 2018.

[104] F. Fu, Z. Chen, Z. Zhao et al., "Bio-inspired self-healing structural color hydrogel," *Proceedings of the National Academy of Sciences*, vol. 114, no. 23, pp. 5900–5905, 2017.

[105] M. Yang, H. Chan, G. Zhao et al., "Self-assembly of nanoparticles into biomimetic capsid-like nanoshells," *Nature Chemistry*, vol. 9, no. 3, pp. 287–294, 2017.

[106] B. Bharti, A. L. Fameau, M. Rubinstein, and O. D. Velev, "Nanocapillarity-mediated magnetic assembly of nanoparticles into ultraflexible filaments and reconfigurable networks," *Nature Materials*, vol. 14, no. 11, pp. 1104–1109, 2015.

[107] A. R. Studart, "Additive manufacturing of biologically-inspired materials," *Chemical Society Reviews*, vol. 45, no. 2, pp. 359–376, 2016.

[108] M. Wufuer, G. H. Lee, W. Hur et al., "Skin-on-a-chip model simulating inflammation, edema and drug-based treatment," *Scientific Reports*, vol. 6, no. 1, article 37471, 2016.

[109] S. Lee, S. P. Jin, Y. K. Kim, G. Y. Sung, J. H. Chung, and J. H. Sung, "Construction of 3D multicellular microfluidic chip for an in vitro skin model," *Biomedical Microdevices*, vol. 19, no. 2, p. 22, 2017.

[110] A. L. M. Ruela, A. G. Perissinato, M. E. . S. Lino, P. S. Mudrik, and G. R. Pereira, "Evaluation of skin absorption of drugs from topical and transdermal formulations," *Brazilian Journal of Pharmaceutical Sciences*, vol. 52, no. 3, pp. 527–544, 2016.

[111] M.-A. Bolzinger, S. Briançon, J. Pelletier, and Y. Chevalier, "Penetration of drugs through skin, a complex rate-controlling membrane," *Current Opinion in Colloid & Interface Science*, vol. 17, no. 3, pp. 156–165, 2012.

[112] H. Y. Lim, J. Kim, H. J. Song et al., "Development of wrinkled skin-on-a-chip (WSOC) by cyclic uniaxial stretching," *Journal of Industrial and Engineering Chemistry*, vol. 68, pp. 238–245, 2018.

[113] N. Mori, Y. Morimoto, and S. Takeuchi, "Skin integrated with perfusable vascular channels on a chip," *Biomaterials*, vol. 116, pp. 48–56, 2017.

[114] J. J. Kim, F. Ellett, C. N. Thomas et al., "A microscale, full-thickness, human skin on a chip assay simulating neutrophil responses to skin infection and antibiotic treatments," *Lab on a Chip*, vol. 19, no. 18, pp. 3094–3103, 2019.

[115] S.-F. Ng, J. J. Rouse, F. D. Sanderson, V. Meidan, and G. M. Eccleston, "Validation of a static Franz diffusion cell system for in vitro permeation studies," *AAPS PharmSciTech*, vol. 11, no. 3, pp. 1432–1441, 2010.

[116] B. Lukács, Á. Bajza, D. Kocsis et al., "Skin-on-a-chip device for ex vivo monitoring of transdermal delivery of drugs—design, fabrication, and testing," *Pharmaceutics*, vol. 11, no. 9, p. 445, 2019.

[117] M. Alberti, Y. Dancik, G. Sriram et al., "Multi-chamber microfluidic platform for high-precision skin permeation testing," *Lab on a Chip*, vol. 17, no. 9, pp. 1625–1634, 2017.

[118] Q. Ramadan and F. C. W. Ting, "In vitro micro-physiological immune-competent model of the human skin," *Lab on a Chip*, vol. 16, no. 10, pp. 1899–1908, 2016.

[119] F. Alexander, S. Eggert, and J. Wiest, "Skin-on-a-chip: transepithelial electrical resistance and extracellular acidification measurements through an automated air-liquid interface," *Genes*, vol. 9, no. 2, p. 114, 2018.

[120] P. Tucci, G. Porta, M. Agostini et al., "Metabolic effects of TiO_2 nanoparticles, a common component of sunscreens and cosmetics, on human keratinocytes," *Cell Death & Disease*, vol. 4, no. 3, article e549, 2013.

[121] S. McCormick, L. E. Smith, A. M. Holmes et al., "Multiparameter toxicity screening on a chip: effects of UV radiation and titanium dioxide nanoparticles on HaCaT cells," *Biomicrofluidics*, vol. 13, no. 4, article 044112, 2019.

[122] N. Hakimi, R. Cheng, L. Leng et al., "Handheld skin printer: in situ formation of planar biomaterials and tissues," *Lab on a Chip*, vol. 18, no. 10, pp. 1440–1451, 2018.

[123] S. Biglari, T. Y. L. le, R. P. Tan et al., "Simulating inflammation in a wound microenvironment using a dermal wound-on-a-chip model," *Advanced Healthcare Materials*, vol. 8, no. 1, article 1801307, 2019.

[124] D. Pamies, T. Hartung, and H. T. Hogberg, "Biological and medical applications of a brain-on-a-chip," *Experimental Biology and Medicine*, vol. 239, no. 9, pp. 1096–1107, 2014.

[125] J. Park, B. K. Lee, G. S. Jeong, J. K. Hyun, C. J. Lee, and S. H. Lee, "Three-dimensional brain-on-a-chip with an interstitial level of flow and its application as an in vitro model of Alzheimer's disease," *Lab on a Chip*, vol. 15, no. 1, pp. 141–150, 2015.

[126] Y. I. Wang, H. E. Abaci, and M. L. Shuler, "Microfluidic blood-brain barrier model provides in vivo-like barrier properties for drug permeability screening," *Biotechnology and Bioengineering*, vol. 114, no. 1, pp. 184–194, 2017.

[127] G.-F. Chen, T. H. Xu, Y. Yan et al., "Amyloid beta: structure, biology and structure-based therapeutic development," *Acta Pharmacologica Sinica*, vol. 38, no. 9, pp. 1205–1235, 2017.

[128] M. Tajes, E. Ramos-Fernández, X. Weng-Jiang et al., "The blood-brain barrier: structure, function and therapeutic approaches to cross it," *Molecular Membrane Biology*, vol. 31, no. 5, pp. 152–167, 2014.

[129] J. A. Brown, V. Pensabene, D. A. Markov et al., "Recreating blood-brain barrier physiology and structure on chip: a novel neurovascular microfluidic bioreactor," *Biomicrofluidics*, vol. 9, no. 5, article 054124, 2015.

[130] G. Adriani, D. Ma, A. Pavesi, R. D. Kamm, and E. L. K. Goh, "A 3D neurovascular microfluidic model consisting of neurons, astrocytes and cerebral endothelial cells as a blood-brain barrier," *Lab on a Chip*, vol. 17, no. 3, pp. 448–459, 2017.

[131] N. R. Wevers, D. G. Kasi, T. Gray et al., "A perfused human blood–brain barrier on-a-chip for high-throughput assessment of barrier function and antibody transport," *Fluids and Barriers of the CNS*, vol. 15, no. 1, p. 23, 2018.

[132] A. Adeyinka and L. Pierre, *Organophosphates*, StatPearls: Treasure Island, 2019.

[133] Y. Koo, B. T. Hawkins, and Y. Yun, "Three-dimensional (3D) tetra-culture brain on chip platform for organophosphate toxicity screening," *Scientific Reports*, vol. 8, no. 1, p. 2841, 2018.

[134] J. Shah, H. Enright, D. Lam et al., *Evaluating the organophosphate NIMP on a 3D-brain-on-a-chip system*, Lawrence Livermore National Lab.(LLNL), 2019.

[135] Y. Fan, D. T. Nguyen, Y. Akay, F. Xu, and M. Akay, "Engineering a brain cancer chip for high-throughput drug screening," *Scientific Reports*, vol. 6, no. 1, article 25062, 2016.

[136] L.-D. Ma, Y. T. Wang, J. R. Wang et al., "Design and fabrication of a liver-on-a-chip platform for convenient, highly efficient, and safe in situ perfusion culture of 3D hepatic spheroids," *Lab on a Chip*, vol. 18, no. 17, pp. 2547–2562, 2018.

[137] Y. Liu, K. Hu, and Y. Wang, "Primary hepatocytes cultured on a fiber-embedded PDMS chip to study drug metabolism," *Polymers*, vol. 9, no. 12, p. 215, 2017.

[138] A. A. Poloznikov, A. A. Zakhariants, S. V. Nikulin et al., "Structure-activity relationship for branched oxyquinoline HIF activators: effect of modifications to phenylacetamide "tail"," *Biochimie*, vol. 133, pp. 74–79, 2017.

[139] J. Theobald, M. A. Abu el Maaty, N. Kusterer et al., "In vitro metabolic activation of vitamin D3 by using a multi-compartment microfluidic liver-kidney organ on chip platform," *Scientific Reports*, vol. 9, no. 1, p. 4616, 2019.

[140] D. W. Lee, S. K. Ha, I. Choi, and J. H. Sung, "3D gut-liver chip with a PK model for prediction of first-pass metabolism," *Biomedical Microdevices*, vol. 19, no. 4, p. 100, 2017.

[141] A. Skardal, M. Devarasetty, S. Forsythe, A. Atala, and S. Soker, "A reductionist metastasis-on-a-chip platform for in vitro tumor progression modeling and drug screening," *Biotechnology and Bioengineering*, vol. 113, no. 9, pp. 2020–2032, 2016.

[142] D. Onozato, M. Yamashita, A. Nakanishi et al., "Generation of intestinal organoids suitable for pharmacokinetic studies from human induced pluripotent stem cells," *Drug Metabolism and Disposition*, vol. 46, no. 11, pp. 1572–1580, 2018.

[143] O. Kilic, D. Pamies, E. Lavell et al., "Brain-on-a-chip model enables analysis of human neuronal differentiation and chemotaxis," *Lab on a Chip*, vol. 16, no. 21, pp. 4152–4162, 2016.

[144] T. D. Brown, M. Nowak, A. V. Bayles et al., "A microfluidic model of human brain (μHuB) for assessment of blood brain barrier," *Bioengineering & Translational Medicine*, vol. 4, no. 2, article e10126, 2019.

Hindawi
Advances in Polymer Technology
Volume 2020, Article ID 7163985, 18 pages
https://doi.org/10.1155/2020/7163985

Research Article

Magnetic Colloidal Particles in Combinatorial Thin-Film Gradients for Magnetic Resonance Imaging and Hyperthermia

Sumera Khizar,[1] Nasir Mahmood Ahmad,[1] Hassan Saleem,[2] Muhammad Asif Hamayun,[3] Sadia Manzoor,[3] Noureddine Lebaz,[4] and Abdelhamid Elaissari[4]

[1]*Polymer Research Lab, School of Chemical and Materials Engineering (SCME), National University of Sciences and Technology (NUST), H-12 Sector, Islamabad 44000, Pakistan*
[2]*Islamabad Diagnostic Center, Islamabad 44000, Pakistan*
[3]*Department of Physics, COMSATS University, Park Road, Islamabad 45550, Pakistan*
[4]*Univ Lyon, University Claude Bernard Lyon-1, CNRS, LAGEPP-UMR 5007, F-69622 Lyon, France*

Correspondence should be addressed to Nasir Mahmood Ahmad; nasir.ahmad@scme.nust.edu.pk

Received 27 March 2020; Revised 20 May 2020; Accepted 4 June 2020; Published 14 July 2020

Guest Editor: Samira Hosseini

A stable oil-in-water (O/W) magnetic emulsion was prepared by the emulsification of organic ferrofluid in an aqueous media, and its theranostic applications were investigated. The synthesis and characterization of the organic ferrofluid were carried out comprising of superparamagnetic maghemite nanoparticles with oleic acid coating stabilized in octane. Both exhibit spherical morphology with a mean size of 6 nm and 200 nm, respectively, as determined by TEM. Thermogravimetric analysis was carried out to determine the chemical composition of the emulsion. The research work described here is novel and elaborates the fabrication of thin-film gradients with 5, 10, 15, and 20 bilayers by layer-by-layer technique using polydimethyl diallyl ammonium chloride (PDAC) and prepared magnetic colloidal particles. The thin-film gradients were characterized for their roughness, morphology, and wettability. The developed gradient films and colloids were explored in magnetic resonance imaging (MRI) and hyperthermia. T1- and T2-weighted images and their corresponding signal intensities were obtained at 1.5 T. A decreasing trend in signal intensities with an increase in nanoparticle concentration in colloids and along the gradient was observed in T2-weighted images. The hyperthermia capability was also evaluated by measuring temperature rise and calculating specific absorption rates (SAR). The SAR of the colloids at 259 kHz, 327 kHz, and 518 kHz were found to be 156 W/g, 255 W/g, and 336 W/g, respectively. The developed magnetic combinatorial thin-film gradients present a significant potential for the future efficient simultaneous diagnostic and therapeutic bioapplications.

1. Introduction

The significant advancement in nanotechnology made possible the production and designing of multifunctional hybrid biomaterials that are highly appropriate for biomedical applications [1]. The development of magnetically engineered colloids is of great interest because of their unique properties and has emerged as promising functional tools for bioapplications for simultaneous diagnostic and therapeutic (theranostic) purposes. Their capability of being manipulated under an external magnetic field provides controllable means of magnetically tagging biomolecules, effective bioseparation, and biosensing, magnetic resonance imaging (MRI) contrast enhancement, and targeted drug delivery [2, 3]. In addition, response to an alternating magnetic field allows the transfer of magnetic energy to the particles in the form of heat, opening the opportunity of being used as an important approach to successful cancer therapy [4].

Among various magnetic nanoparticles, superparamagnetic nanoparticles of single domains of about 5–20 nm as mean diameter particularly magnetite (Fe_3O_4) and maghemite (γ-Fe_2O_3) are promising candidates for biomedical applications due to their biocompatibility [5]. These are widely explored in cancer theranostic bioapplications because of their high magnetic moment, low toxicity, biologically tolerated in a broad range of concentrations, and

synthesis through simplest, economical, and convenient methods using ferric and ferrous salts such as nitrates, chlorides, sulphates, perchlorates, etc. [6]. Recently, magnetic nanoparticles (MNP) coated with biopolymers have gained much attention due to biocompatible, biodegradable, and nontoxic properties of polymers. The organic/inorganic surface coating around iron oxide nanoparticles is essential for biomedical applications. It brings stoichiometric modifications on the surface of nanoparticles, good colloidal stability, and low toxicity in the biological environment and biocompatibility of oxide nanoparticles [7]. Hence, suitable chemical design of magnetic polymer colloids is extremely important in order to make them appealing for magnetic resonance imaging for diagnosis, therapeutic actions of drug delivery, and hyperthermia for combined imaging-guided therapeutics [8].

Depending upon the application, there are several methods to prepare polymeric magnetic nanoparticles among which emulsion technique is the most common and oldest technique [9]. This approach is based on the encapsulation of iron oxide nanoparticles into a biodegradable polymer matrix for improving particle stability and functionalization. In this direction, polyesters such as poly(lactic-co-glycolic acid) (PLGA), polycaprolactone (PCL), polylactic acid (PLA), and polyethylene glycol (PEG) have been reported due to their exceptional characteristics such as biodegradability and biocompatibility [7]. The surface functionalization of the nanoparticles affects the solubility and biodistribution of the colloids inside the body and has a direct influence on imaging capabilities and magnetic behavior of the nanoparticles [10]. Regarding cancer diseases, these colloids are also used as an effective tool for therapy, such as drug delivery and hyperthermia. Furthermore, the employment of magnetic polymer colloids to design multifunctional biothin films by incorporating various materials to obtain molecular-level control presents numerous biomedical applications. The layer-by-layer (LBL) self-assembled multilayer (SAMu) biothin films are not only useful for diagnostics but are also helpful in directing therapeutic agents by focusing on an external magnetic field to the target zone [11]. A broad range of stimuli-responsive thin films have been fabricated and are used as a point-of-care diagnostic devices that can be routinely applied in everyday clinical practice. Thin films of nickel ferrites and chitosan were fabricated by the LBL technique and investigated for their ability to generate an intensity difference using blood as a test liquid; however, T1 and T2 images were not explored in detail [12]. Using the same manual fabrication protocol, thin films were designed, fabricated, and characterized but the magnetic behavior of the films was not tested [13].

In some nanosystems, a combinatorial investigation is best performed in which gradients were incorporated into the thin films for fabricating lab-on-a-chip type films. The development of such combinatorial and high-throughput strategy can eliminate sample preparation steps and permit the development of a disposable chip for a dipstick-like approach toward molecular diagnostics. The combinatorial technique is used not only for identifying new compositions but also for the rapid optimization of the characteristics of the material. The combinatorial approach shows a variation in composition, thickness, and functionality in a single library and allows simultaneous synthesis and screening of large arrays of different materials [14].

Efficient research methods and strategies have been developed for combinatorial fabrication of thin films and their high-throughput characterization. Most frequently, physical and chemical vapor deposition techniques have been applied for the rapid combination of libraries where wide-ranging compositional variation is generated [15].

The current study aims at preparing oil-in-water (O/W) magnetic emulsion by emulsification of organic ferrofluid in an aqueous media. The organic ferrofluid prepared by the coprecipitation method was stabilized in octane. This magnetic fluid was then emulsified in an aqueous solution containing a surfactant to obtain a stable emulsion of magnetic colloidal particles. Multiple techniques were used to characterize the magnetic nanoparticles and the magnetic polymer colloids. In addition, biothin-film gradients were designed and fabricated using magnetic colloidal particles and PDAC solution through the layer-by-layer technique and were characterized to study their morphology/texture and growth. T1- and T2-weighted images of a colloidal suspension of nanoparticles with different iron concentrations were obtained. To the best of our knowledge, combinatorial thin-film gradients were never explored for an in vitro MRI study. Heating response of the prepared magnetic emulsion was also observed for hyperthermia treatment. This research work is the first detailed work dedicated to the fabrication of combinatorial thin-film gradients using the layer-by-layer technique which can be a promising technique in the future for disposable lab-on-chip as a dipstick approach for ultrasensitive molecular imaging of bioanalytes. The technique used for the fabrication of combinatorial thin-film gradients is simple, economical, environmentally friendly, and not time consuming. The developed combinatorial thin-film gradients can further be analyzed as a reservoir for therapeutic drug for in vitro drug release and as a biomimetic multifunctional assembly to develop a point-of-care on chip technology.

2. Materials and Methods

2.1. Materials. $FeCl_2{\cdot}4H_2O$, $FeCl_3{\cdot}6H_2O$, HCl (35%), NH_3 (20%), oleic acid, octane, and polydimethyl diallyl ammonium chloride PDAC (20 wt.% solution) of analytical grade were purchased from Sigma-Aldrich (Germany). Sodium dodecyl sulphate (SDS) used as an anionic surfactant was purchased from Sigma-Aldrich (Germany). Concentrated sulphuric acid (H_2SO_4) (Sigma-Aldrich, 95-98% purity) and potassium dichromate (Scharlau, reagent grade) were used for cleaning the glass substrate. Glass microslides as a substrate for the fabrication of films are from Thermo Fisher Scientific. Ultrapure water was used for the preparation of all solutions. All chemicals/materials were of analytical grades and used as received.

2.2. Synthesis of Magnetic Emulsion

2.2.1. Preparation of Aqueous Ferrofluid. Coprecipitation is a simple and convenient technique to prepare magnetic nanoparticles based on the reduction of metallic elements under

different salt conditions [6]. The ferrofluid synthesis was carried out at 20°C in a thermostatically controlled 500 mL reactor equipped with a mechanical stirring system consisting of a three-branched Teflon anchor. Ferrous and Ferric chlorides were first dissolved in hydrochloric acid (1 M). When the dissolution of the iron salts was completed with the formation of an orange homogeneous solution, the concentrated ammonia solution (20%) was quickly added to the reactor with vigorous stirring at 1000 rpm. The immediate appearance of a black precipitate corresponds to the formation of iron oxide. The coprecipitation reaction is continued in an ammoniac medium for one hour. The pH of the reaction medium was then close to 9.

2.2.2. Preparation of Organic Ferrofluid. The above prepared aqueous ferrofluid was kept under slow stirring in the preparation reactor. The oleic acid was then added directly to the reactor. One hour later, the entire reaction medium was recovered in a beaker. Octane was gradually incorporated into the beaker using a pipette. The mixture was then placed on a magnetic stirring plate for two hours. The iron oxide nanoparticles coated with oleic acid spontaneously pass from the ammoniac phase to the organic phase, which results in very clear phase separation between a clear lower phase (aqueous phase) and an upper phase constituted by the organic ferrofluid.

2.2.3. Preparation of (O/W) Magnetic Emulsion. The first step was to prepare a starting polydisperse emulsion of ferrofluid referred to as "preemulsion." This preemulsion was obtained by gradually incorporating the organic ferrofluid in an aqueous solution containing a surfactant (SDS) with moderate stirring. The prepared magnetic emulsion was highly sheared before performing a magnetic sorting process to obtain narrow size distribution. Octane was removed via evaporation process using rotary evaporation. The final magnetic emulsion was then dispersed in the SDS solution for further characterization and usage.

2.3. Designing Strategy for Fabrication of Combinatorial Thin-Film Gradients. The basic principle of the layer-by-layer technique is the deposition of a substrate such as glass slides in polyelectrolyte and charged colloids solution having opposite charges as presented in Figure 1. Glass slides were first cleaned by overnight dipping in chromic solution (10 wt.% aqueous potassium dichromate: conc. H_2SO_4 50 : 50 *v*/*v*) by which they got negative charges on their surface. In this technique, glass slides were first dipped in positive polyelectrolyte solution for 10 minutes followed by rinsing in ultrapure water twice for five minutes. This results in the first positive layer with the removal of unbound molecules on the glass slide. Then, the glass slides were exposed to the negatively charged solution (solution of prepared magnetic emulsion) again for ten minutes followed by rinsing in ultrapure water twice for five minutes. This results in a single bilayer formation on the substrate that includes one bilayer of polyelectrolyte and magnetic colloids. The number of bilayers deposited is determined by the number of cycles that the substrate undertakes. Following this scheme, combinatorial thin-film gradients were fabricated by varying the exposed surface of the substrate to the solution of polyelectrolyte and magnetic colloids by changing the solution level. Combinatorial thin-film gradients were fabricated having four distinct regions with 5, 10, 15, and 20 bilayers on a glass substrate. The dipping level of the solution is changed after the completion of every 5 bilayers to make gradients in the films.

2.4. Characterization Techniques. The average hydrodynamic diameter (D_h), particle size distribution, and surface charge of the magnetic nanoparticles were determined by Malvern Zetasizer (Nano ZS, Malvern Instruments Limited, U.K). The measurements were carried out in a 1 mM NaCl solution at 25°C. The physical size of the prepared nanoparticles was examined using Transmission Electron Microscopy (TEM, Netherland) with a Philips CM120 microscope at the "Centre Technologique des Microstructures" (CT) at the University of Lyon (Villeurbanne, France). Thermogravimetric analysis of organic ferrofluid and colloids was achieved by the thermogravimetric analyzer (NETZSCH–TG209F1 Iris® ASC, Germany) in the inert atmosphere from room to 600°C temperature at the heating rate of 10°C/min. The magnetic properties of dried magnetic colloids were studied at room temperature by using a vibrating sample magnetometer (Automatic Bench of Magnetic Measurements-ABMM (UK) at the University of Lyon, Villeurbanne, France).

Detailed analysis to determine surface properties of the thin films including film morphology, distribution of colloids, and covered area was observed using low-vacuum analytical scanning electron microscopy (SEM, JEOL JSM 6490LA, Japan) at an accelerating voltage of 20 kV at various magnifications. Morphology and nanostructures of the prepared films were obtained by an atomic force microscope (AFM, Jeol JSPM-5200, Germany) operating in AC or tapping mode, using a commercially available silicon probe. All samples were also imaged using AFM in tapping mode with magnetic force microscopy (MFM) in hover mode under ambient conditions to observe the deposition of bilayers in each section. The contact angle of different sections of the gradient was measured by using drop shape analyzer DSA 25 (KRUSS Advanced 1.8.0.4, Germany) based on the sessile drop technique. To measure the contact angle, a 10-15 μL drop of ultrapure water was placed on the surface of a glass slide using a needle. The angle between the liquid/vapor interface and the solid/liquid interface (i.e., contact angle) was measured by using the ADVANCE software installed in the drop shape analyzer. Film thickness was measured by optical profilometer (NANOVEA PS-50, USA) by moving the probe along the substrate (glass slide) having self-assembly of thin films to acquire the surface height.

2.5. Magnetic Resonance Imaging (MRI) of Magnetic Colloids and Thin-Film Gradients. To study the diagnostic capability of magnetic colloids and their films, MRI was carried out by using a clinical MRI machine (GE SIGNA EXPLORER, USA) of 1.5 Tesla having a FOV of 22 cm and an aperture of 60 cm. Samples were prepared with

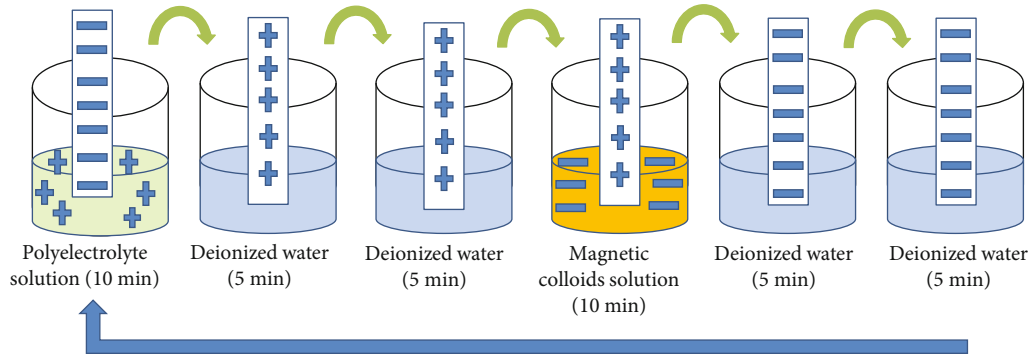

Figure 1: Fabrication of combinatorial thin-film gradients using the layer-by-layer technique.

different concentrations in water in glass vials designated as A0, A1, A2, A3, A4, and A5. T1- and T2-weighted images were obtained with different values of MRI field echo (FE) sequences (TR and TE) to study signal intensity. All samples were placed in the MRI machine on the top of the multichannel body coil. Contrast images were analyzed using host software SV 25 available in MRI machine, and region of interest (ROI) was calculated with the statistical tool K-PACS Workstation (Version 1.5). Water was used as a control to compare the contrast of colloids.

MRI of thin films was also performed using T1 and T2 sequences with different values of MRI field echo (FE) sequences (TR and TE). Glass microslide was immersed in ultrapure water in a custom made polyacrylic cell. Then, the cell is placed inside a magnetic coil to obtain MRI images. The same region of interest was taken in every section of the films having 5, 10, 15, and 20 bilayers, and uncoated region was taken as a reference. The intensity data was measured in Hounsfield units based on the number of pixels contained within the ROI. The relative intensity of each section was measured by taking the mean values of the intensity. All the images were taken in axial mode (along the z-axis) with a slice thickness of 4 mm and a spacing of 1 mm.

2.6. Hyperthermia Study. To study the heating effect of the prepared magnetic colloids, hyperthermia measurement of the prepared magnetic emulsion was done by Nanotheric Magnetherm 1.5 induction unit, operating at different frequencies. The temperature of the field coils was maintained by circulating water at 12°C. A small quantity (1 mL) of the magnetic emulsion was taken in an Eppendorf tube and placed in an insulating cylindrical container under an alternating magnetic field. Temperature rise was noted for a specific time with the "Neoptix optical fiber" temperature sensor. SAR values were calculated by using Equation (1) [16].

$$\mathrm{SAR} = \frac{cM}{m} \cdot \frac{dT}{dt}, \tag{1}$$

where c is the specific heat of the sample, M is the total mass of the sample (in grams), and m is the mass of magnetic nanoparticles (in grams). dT/dt is the initial linear slope of the sample temperature profile obtained by a linear fitting of the experimental data over the short time interval.

3. Results and Discussion

The salient overview of the experimental work is presented in Figure 2 to highlight magnetic colloidal particles and the potential bioapplications of combinatorial thin-film gradients fabricated by using the layer-by-layer technique for MRI analysis and magnetic hyperthermia. MRI analysis showed that the developed film gradients enable us to perform imaging experiments in a single step for disposable lab-on-chip as a dipstick approach for diagnostic applications, and magnetic colloids deposited in film gradients are considered as T2 contrast agents. Hyperthermia measurements of magnetic colloidal particles showed a significant heating effect in an alternating magnetic field to exhibit their suitability for therapeutic applications. The present research has significant potential for advances in polymer technology to design and develop magnetic colloidal particles and their combinatorial thin films for future efficient simultaneous diagnostic and therapeutic bioapplications.

3.1. TEM and Dynamic Light Scattering (DLS) Analysis of Aqueous Ferrofluid and Magnetic Emulsion. The aqueous ferrofluid synthesized by coprecipitation was analyzed by TEM. It was observed that particles were well dispersed with minor aggregation due to the absence of any stabilizer that weakens the magnetic interactions between the particles [17]. No stabilizing agent was used during the synthesis to get superparamagnetic nanoparticles. Agglomeration of particles was due to the attractive forces between the magnetic nanoparticles [18]. Some partial aggregation is probably caused by the preparation of the samples for TEM measurement. The observed clusters may also be attributed to the capillary forces during the drying process of the droplet deposited on the grid before TEM analysis. Results of the TEM analysis in Figure 3(a) showed that the magnetic nanoparticles were spherically shaped and uniformly distributed in size with a mean diameter in number (D_n) of around 6.6 nm and 8 nm as a mean diameter in weight (D_w). The polydispersity index (PDI) was calculated by the analysis of the TEM plate and it was found to be 1.2 (PDI = D_w/D_n). The small size of the particles indicates that the nanoparticles were in the superparamagnetic regime [19]. Figure 3(b) shows the size distribution of aqueous ferrofluid nanoparticles which was carried out using dynamic light scattering

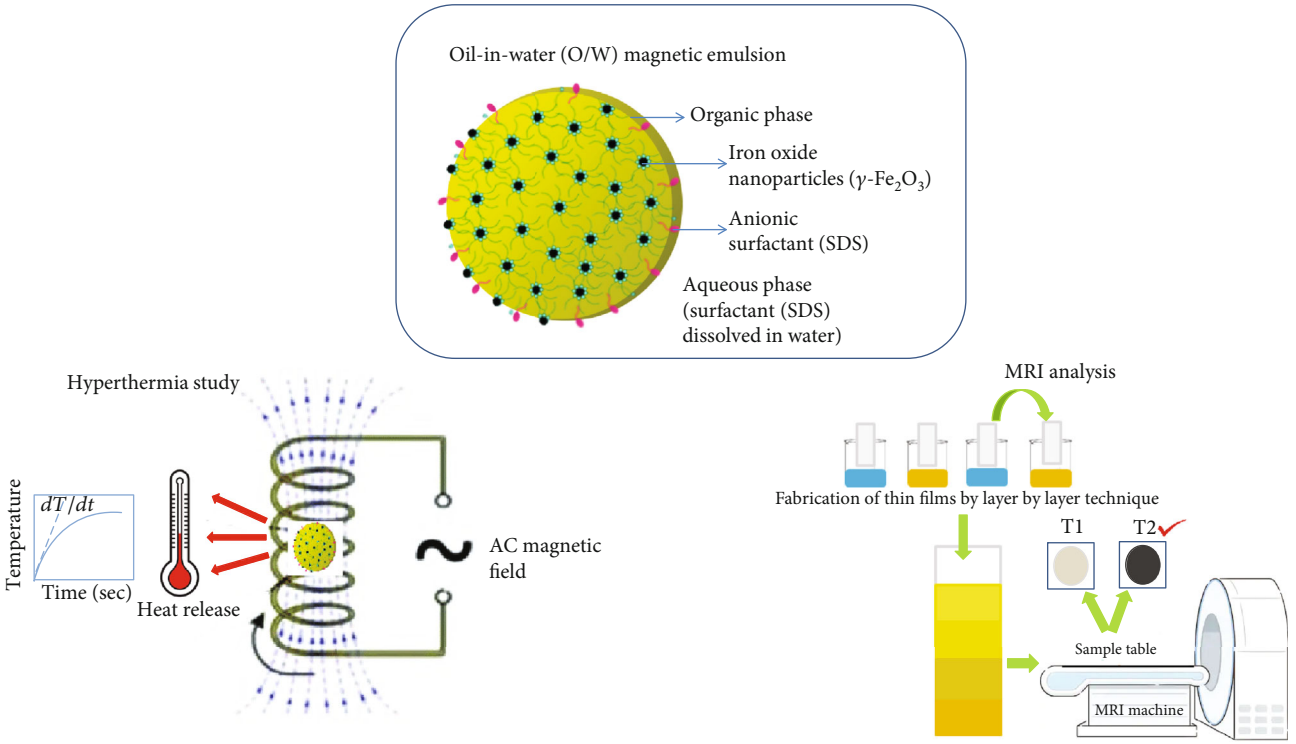

Figure 2: The overview of the magnetic colloidal particle and potential application of combinatorial thin-film gradients fabricated by using the layer-by-layer technique for MRI analysis and colloids for magnetic hyperthermia.

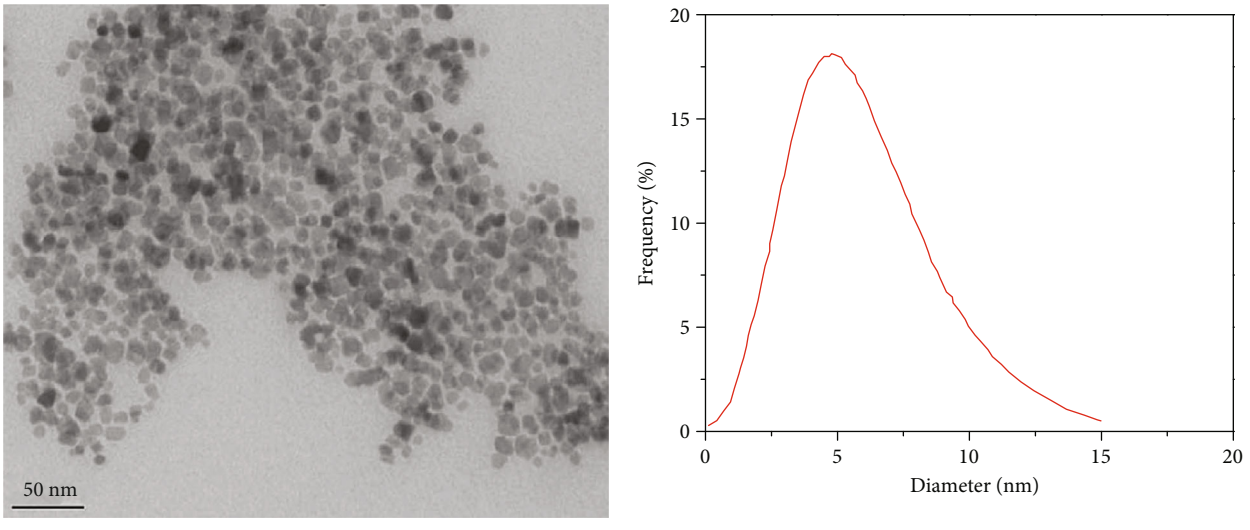

(a) (b)

Figure 3: (a) TEM analysis of the prepared aqueous iron oxide nanoparticles. (b) Dynamic light scattering (DLS) analysis of highly diluted aqueous ferrofluid.

analysis (DLS). The mean hydrodynamic size of the magnetic nanoparticles was found to be around 5 nm which was in agreement with TEM analysis. The narrow size distribution was due to the spherical morphology and negligible magnetic agglomeration [17].

The prepared colloidal particles were also determined by TEM to observe their morphology, structure, and size. TEM images proved the colloidal stability of the particles without aggregation [17]. Figure 4(a) shows the spherical shape of the particles having a smooth surface texture and of nanometric size around 200 nm. The average hydrodynamic particle size was found to be 200 nm with a polydispersity index of 0.023 (Figure 4(b)). The lower value of PDI indicates the monodispersity of the system with an excellent colloidal stability [20]. The zeta potential is the measure of repulsive forces between particles, and its value indicates the colloidal

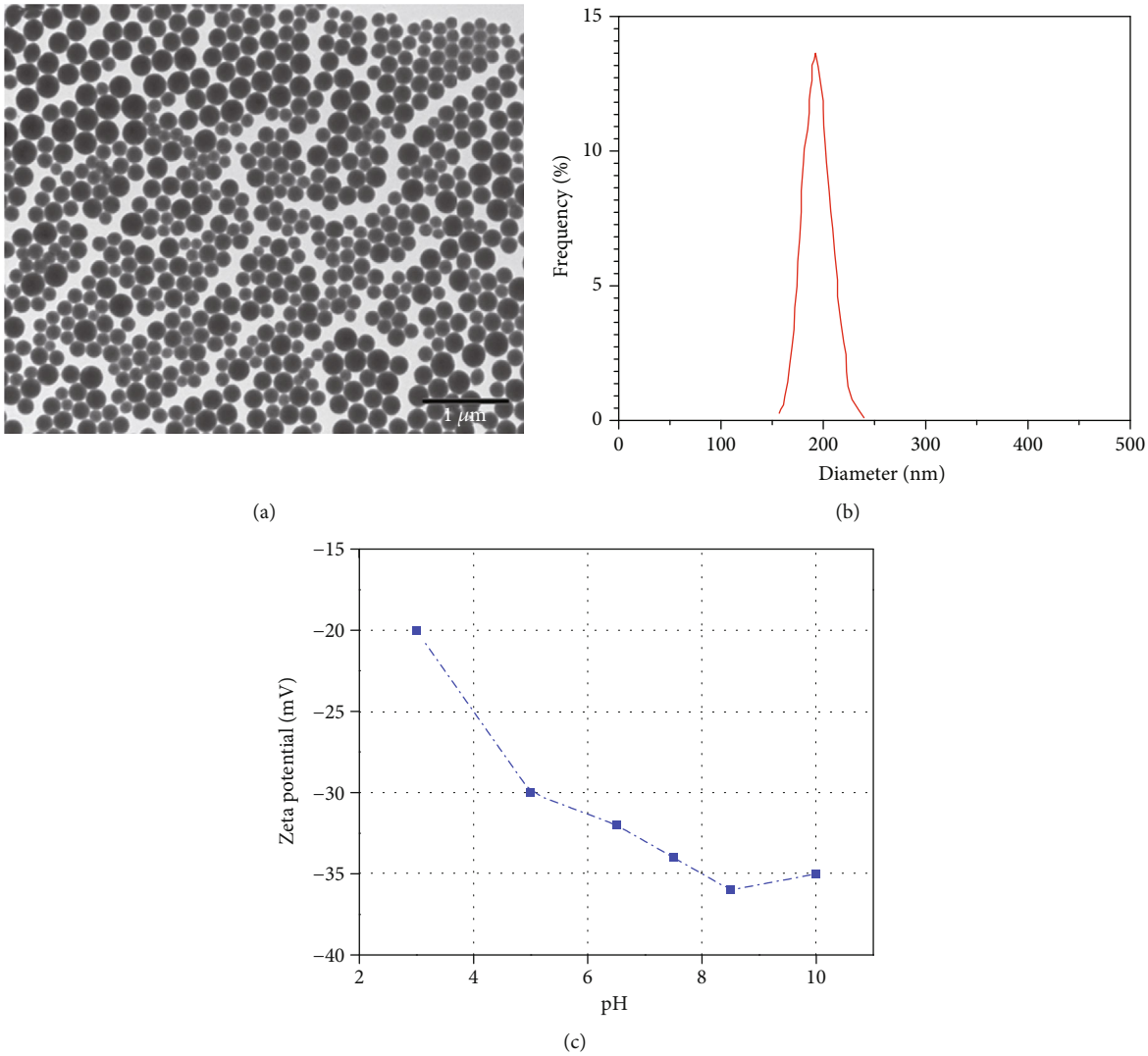

Figure 4: (a) TEM image of the magnetic emulsion. (b) Particle size distribution of the prepared magnetic emulsion via dynamic light scattering technique. (c) Evolution of the zeta potential of the magnetic emulsion as a function of pH.

dispersion stability [21]. Zeta potential of the prepared emulsion as a function of pH was found to be between -20 and -36 mV as shown in Figure 4(c). The observed negative zeta potential was attributed to SDS sulphate groups present on the surface of the magnetic nanoparticles.

3.2. TGA of Organic Ferrofluid and Magnetic Emulsion. For the present study, the objective of thermogravimetric analysis (TGA) was to determine the chemical composition and thermal behavior of the organic ferrofluid and magnetic emulsion based on thermal decomposition. The TGA was used for quantitative analysis to determine both organic and inorganic phases. The TGA profile of pure oleic acid typically exhibited single-step thermal degradation with the maximum rate at around 280°C as several studies reported in the literature [22–24]. In the present work, the TGA was carried out in the range of room temperature to 600°C in an inert atmosphere with a heating rate of 10°C/min. Figure 5 shows the thermal behavior of the organic ferrofluid, illustrating the variations of the residual masses of the samples with the increasing temperature. About 20% of weight loss between 25°C and 550°C is attributed to the degradation of oleic acid in organic ferrofluid [25]. It was also observed that the weight loss is composed of two steps, and this is in good agreement with the reported literature [24]. The first weight loss of about 3% between 25°C and 250°C was due to the loss of oleic acid that acts as an outer layer. The second weight loss of about 17% was attributed to the loss of the oleic acid layer (inner layer) strongly bound to the magnetic nanoparticles because of the covalent bond formation that is related to the affinity between the carboxylic group of oleic acid and ferric and ferrous ions on iron oxide nanoparticles [26, 27]. The amount of maghemite in ferrofluid can be estimated from the residual mass percentages. TGA curve shows that the oleic acid would completely decompose when the temperature reached 550°C. According to mass loss data from the TGA for organic ferrofluid, the maghemite content in the ferrofluid was found to be 80%, showing that the formulation containing 20 wt.% oleic acid with respect to total

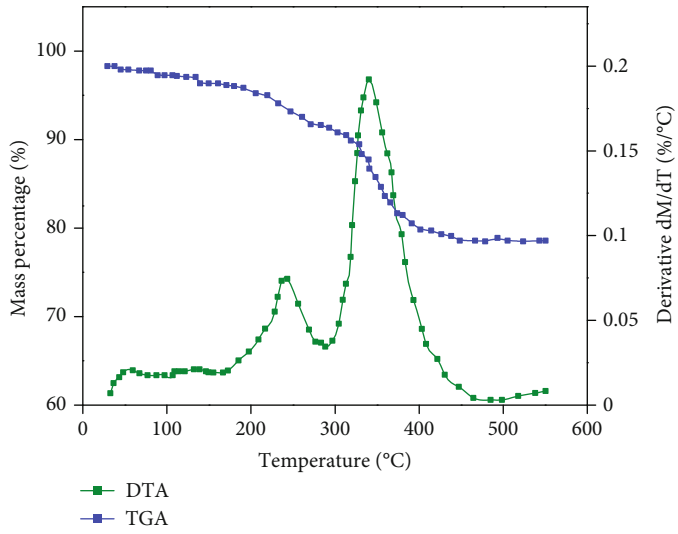

Figure 5: Thermogravimetric analysis (TGA) and differential thermal analysis (DTA) of dried organic ferrofluid.

formulation weight [24, 28, 29]. There were two endotherm peaks observed in DTA (differential thermal analysis) corresponding to the weight loss in two steps in the range of 200°C to 500°C that confirmed the formation of a bilayer of oleic acid on the maghemite surface. The outer layer which was physically adsorbed on the inner layer gets decomposed at a lower temperature while the inner layer that was strongly bonded to the particle surface undergoes decomposition at higher temperature [30]. The second endotherm was observed at around 350°C revealing the complete decomposition of oleic acid.

The iron content in the prepared magnetic emulsion was also determined by thermogravimetric analysis (TGA). This technique consists of measuring the loss of mass of the analyzed sample (in powder form) by thermal degradation of ferrofluid [31]. The crude magnetic emulsion was washed extensively before TGA; this removed all the impurities including the physically adsorbed outer layer of oleic acid. Since oleic acid was used in high excess, therefore, free molecules of oleic acid that formed the outer layer were mainly oriented to the water interface. It resulted in single-step degradation unlike the two-step degradation observed in the case of organic ferrofluid. There was no significantly different thermal change observed as noted in these studies. It is expected that similar trends of thermal degradation of oleic acid took place in the prepared magnetic emulsion. Figure 6 shows that about 25% of the weight loss was due to the degradation of oleic acid in ferrofluid droplets found in the magnetic emulsion [30]. The thermograms for magnetic emulsion show that the loss of mass was gradual. A broad endotherm peak was observed around 350°C that corresponds to the complete degradation of surfactants. Thus, a mass loss using TGA demonstrated that magnetic emulsion was found to be composed of 75% of iron oxides and 25 wt.% oleic acid that remained bound to nanoparticles and could not be washed off [32].

3.3. Magnetization Measurement of Organic Ferrofluid and Emulsion. The saturation magnetization of the ferrofluid is shown in Figure 7. It was determined by extrapolation (magnetic field-H $\rightarrow \infty$) of the line obtained by plotting magnetization – M = f (1/H) and was close to 55 emu/g. This value was close to the theoretically saturated magnetization of maghemite (M_s = 76 emu/g) and reflects the excellent magnetic properties of iron oxide nanoparticles [33]. Differences between experimental and theoretical values were frequently reported in the literature and justified by the existence of defects in the crystal structure or the presence of nonmagnetic compounds incorporated during emulsion formulation [34]. In our case, this difference was mainly attributed to magnetically inactive oleic acid used to prepare organic ferrofluid, which accounts for almost 20% of the total mass of the organic ferrofluid [35]. Considering the composition of the magnetic emulsion, the saturation magnetization reached 40 emu/g, revealing that the superparamagnetic behavior of the magnetic particles was retained after emulsification[33].

3.4. Combinatorial Thin-Film Thickness. The thickness of self-assembled combinatorial thin film gradients depends on the number of bilayers of adsorbed polyelectrolyte and magnetic colloidal particles [36]. Film thickness was measured by optical profilometer, and it was clearly shown in Figure 8 that the thickness varies with the number of bilayers. The thickness increases almost linearly after the deposition of every five bilayers. Less increase in the thickness after the deposition of five bilayers could be due to the substrate effect [37]. The total thickness of films having 5, 10, 15, and 20 bilayers was 50 μm, 82 μm, 142 μm, and 232 μm, respectively. The film thickness increasing with bilayers shows uniform growth of PDAC/magnetic colloids thin films with a distinct interface between coated and uncoated surfaces.

3.5. Scanning Electron Microscopy (SEM) of Combinatorial Thin-Film Gradients. Film morphology, distribution of colloidal particles, and area coverage were determined by SEM at various magnifications. The oppositely charged particles adsorbed onto the substrates have increased with the increase

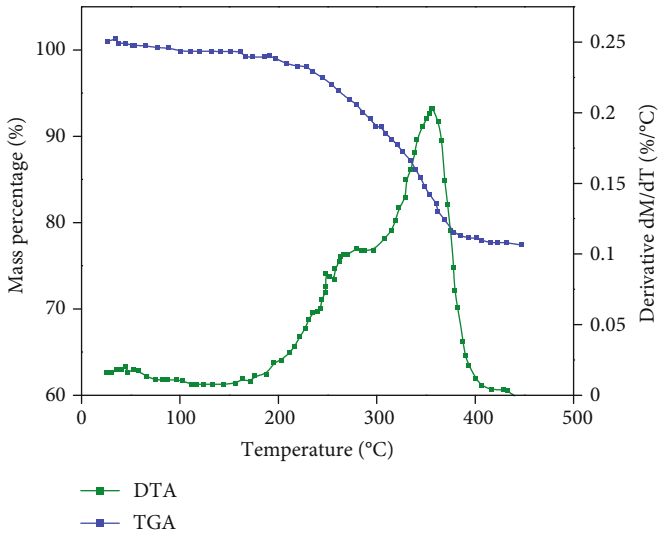

Figure 6: Thermogravimetric analysis (TGA) and differential thermal analysis (DTA) of prepared magnetic emulsion.

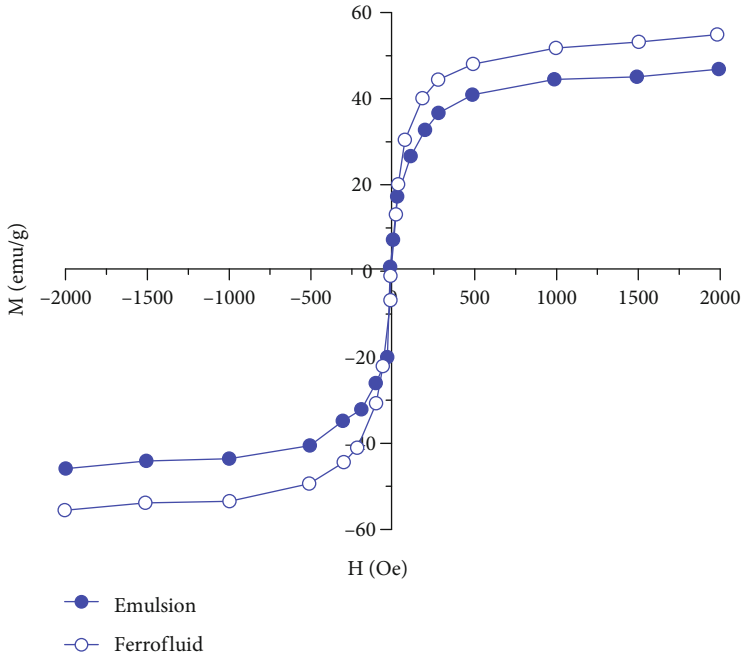

Figure 7: Magnetization versus magnetic field for organic ferrofluid (empty markers) and magnetic emulsion (full markers) under a dried state.

in the number of bilayers. SEM images also revealed agglomeration of particles due to electrostatic attraction between oppositely charged polyelectrolytes showed in Figure 9. The gradient films of PDAC and negatively charged colloids in different bilayer sections undergo charge overcompensation phenomenon that was directly related to layer-by-layer adsorption of particles in successive steps [38]. Increasing the number of washing steps or varying the substrate can lead to a uniform distribution of opposite charges and ensure uniformity in film deposition [39].

Oppositely charged colloids deposited in the first layer served as sites for the second layer. The surface adsorption and agglomeration of magnetic colloidal particles progressively increased with the number of bilayer colloids [40]. In 5 bilayers, much less fractions of glass slide surface area were covered as compared to 10, 15, and 20 bilayers due to substrate effect [37].

Electrostatic interactions between negatively charged magnetic colloidal particles and positively charged PDAC played an important role in the growth of thin films. Thus, one may easily tune the characteristics of the thin films by controlling the colloids concentration on the surface. The magnetic colloidal particles were directly adsorbed on the glass slide without any change in their properties, such as size

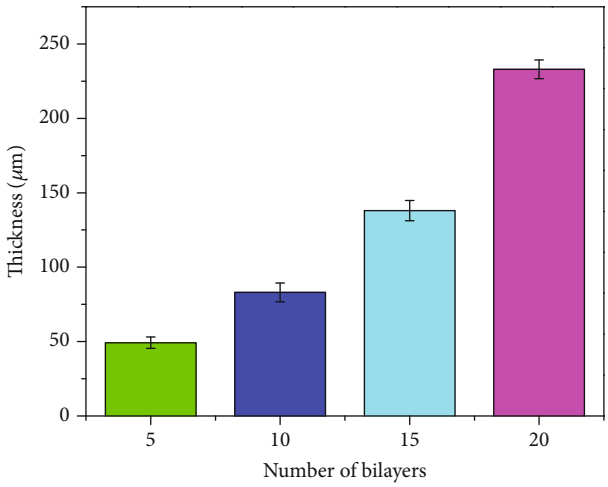

Figure 8: Thickness profile of combinatorial thin-film gradients having 5, 10, 15, and 20 bilayers.

and shape; these are very important for in vitro applications of the films [13].

3.6. Contact Angle of Combinatorial Thin-Film Gradients. Figure 10 shows a decrease in contact angle values with an increase in the number of bilayers that was necessary for T2-weighted MRI contrast agents. The decrease in contact angle with bilayers confirms the phenomenon of charge overcompensation in growing thin films [41] and an increase in hydrophilicity of films that results in greater interaction of water molecules with the fabricated films. There was a regular decrease in contact angle with an increasing number of bilayers. The decreasing trend of contact angle in fabricated gradient films can be attributed to a higher colloidal particles deposition [40]; this is highly important for MRI [13].

3.7. Quantitative Analysis of Topography of Combinatorial Thin-Film Gradients by Atomic Force Microscopy (AFM) and Magnetic Force Microscopy (MFM). AFM and MFM imaging were achieved for each section of the combinatorial thin-film gradient deposited on a glass slide. Figures 11 and 12 shows the AFM and MFM images of thin-film gradients of magnetic colloidal particles. AFM images show the increasing coverage and agglomeration in 3D images as the number of bilayers increases [40]. The gradient trend can be seen from the AFM results in Figure 11 showing that, as the number of bilayers increases, the number of particles deposited also increases along the substrate. It was also observed that the deposition of particles in each section of bilayers (5, 10, 15, and 20) was nonlinear. This type of nonlinear deposition has been observed in the case of the LBL technique [42]. In addition, the distribution of particles on substrates became more uniform with the increase in the number of film bilayers. It is clearly evident that with the increase in the number of bilayers, there is a significant increase in the deposition of magnetic colloidal particles on the surface of the prepared films via a self-assembly process. The number of adsorption sites increased with the number of bilayers indicated the increase in thickness and roughness of the surface [13, 43]. As a consequence, an increase in the number of deposited colloidal particles with the increase in the number of bilayers leads to the increase in surface roughness along the substrate for 5, 10, and 15 bilayers; this is in agreement with the reported literature [12, 13]. But we observed a slightly different behavior of gradient films with 20 bilayers. The surface with 20 bilayers observed to be relatively smoother as compared to surfaces with 5, 10, and 15 bilayers. The root-mean-square values (R_q) of surface roughness were 19.1 nm, 41.2 nm, 47.5 nm, and 34 nm for 5, 10, 15, and 20 bilayers, respectively, whereas average roughness (R_a) values were 12.2 nm, 29.8 nm, 39.2 nm, and 27.3 nm for 5, 10, 15, and 20 bilayers, respectively. The surface roughness of films with 20 bilayers is lower as compared to 5, 10, and 15 bilayers, and that anomaly may be attributed to various factors that affect the resolution of the surface roughness measurement. The AFM system noise effects limit the vertical resolution, and the tip radius effect limits the spatial resolution [44]. Due to these effects, film gradients with 20 bilayers showed a decrease in R_a and R_q values. Tip geometry directly correlates to the roughness value [45]. When the tip is sharp, it obtains an accurate feature of the surface. But as the tip becomes blunt, it cannot approach the bottom of the sample, so it obtains a skewed feature of the surface. In short, as the tip radius increases, the roughness value decreases. In the tapping mode, AFM tip sharpness degraded more than 80%, and its diameter changed significantly as its tip end got damaged progressively during the scans which affect the roughness measurements. The system noise is equally important since when the noise gets mixed into the AFM results; the AFM cannot accurately measure the accurate roughness [46]. The charge on the polyelectrolyte, substrate-PDAC interactions, and substrate dipping time in polyelectrolytes also affected the adsorption behavior in LBL thin films [47]. Agglomeration of colloidal particles was due to the electrostatic interactions between oppositely charged polyelectrolytes on the surface.

MFM images of different sections of bilayers were also carried out to characterize and localize magnetic nanoparticles at the nanoscale as shown in Figure 12. It was clearly evidenced from the MFM images that individual magnetic nanoparticles cannot be detected by MFM because the magnetic field is directly proportional to the diameter of the particles and thus very small. MFM contrast was generated by the interaction between the MFM probe and the magnetic field close to the sample surface. These local nanoscale magnetic interactions cause deflection of the probe which produces a measurable signal monitored for the magnetic imaging of the sample [48]. The phase image contrast represents magnetic force gradient mapping. MFM images of combinatorial gradient films showed that, as the number of bilayers increases, brighter features were higher. An increase in density can be seen through the contrast caused by the magnetic properties of the surface being characterized. Thus, the MFM images showed the magnetic field distribution of a sample on the nanoscale, and no extensive sample preparation is needed. In each section of bilayers, agglomeration of particles in the form of clusters

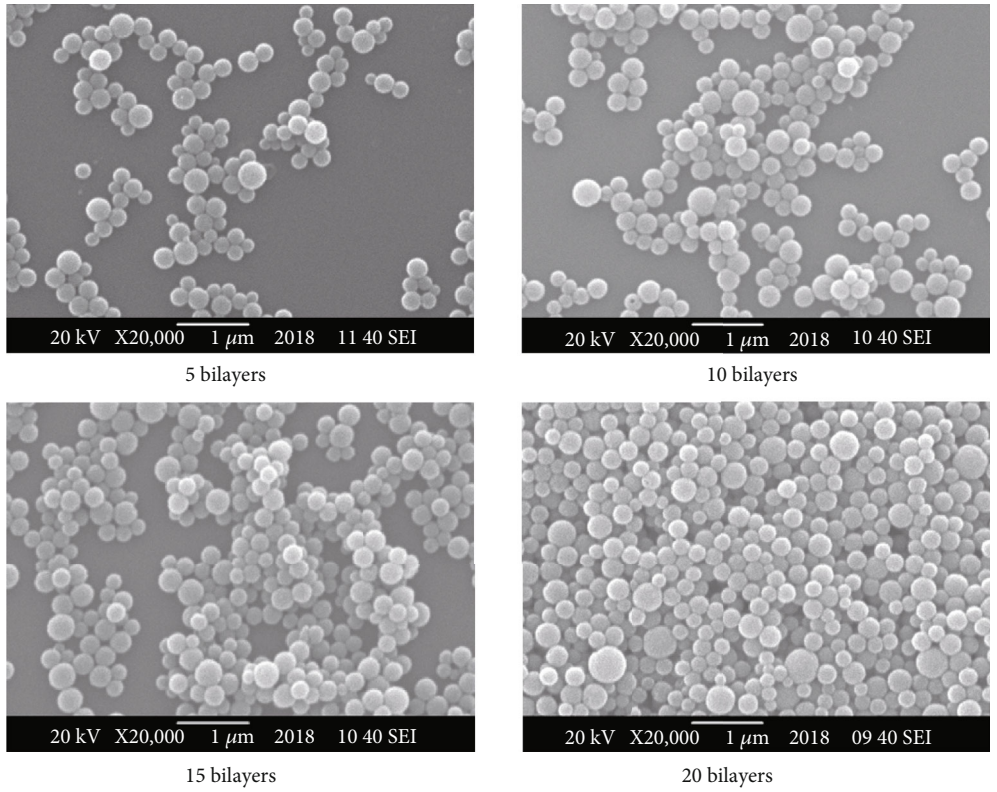

Figure 9: SEM micrographs of combinatorial thin-film gradients of PDAC and magnetic colloidal particles.

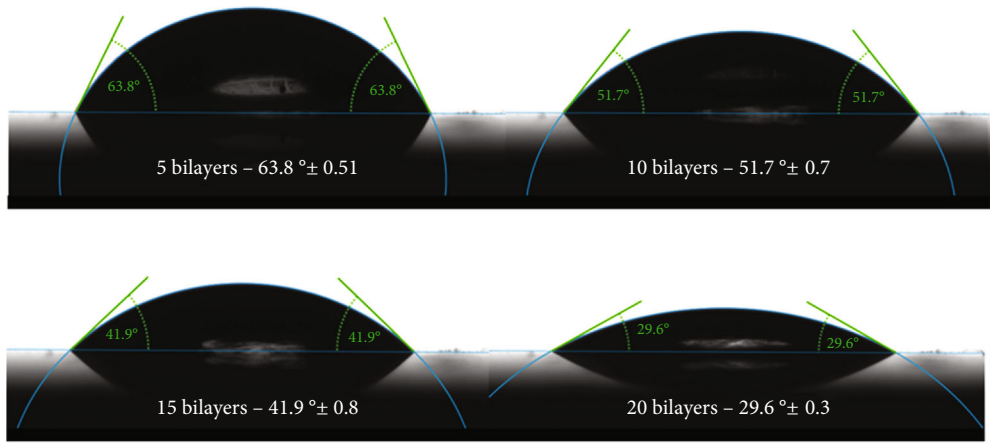

Figure 10: Contact angle measurements of combinatorial thin-film gradients.

was successfully imaged. From the MFM images, one can see the phase shift in terms of degrees resulting from the tip and sample interactions [49]. As the number of adsorbed colloids increases with the number of bilayers, there can be an increase in the interaction between the tip and the substrate that causes the shift in the oscillation of the cantilever. The difference in phase angle between free and interacting cantilever oscillation causes a phase shift that increases with increasing bilayers. The larger the phase shift, the better the magnetic properties of the samples [50]. A negative phase shift over small magnetic domains was observed in MFM images. This was due to attractive interactions between the probe and the magnetic domain. In addition, the magnetically induced phase shift can have both positive and negative regions over a single magnetic domain when the probe-magnetic domain distance is small, rather than being a unidirectional effect [48].

3.8. MRI Analysis of Magnetic Colloids and Combinatorial Thin-Film Gradients. MRI is a very time consuming and expensive diagnostic investigation as compared to other methods such as X-ray and computed tomography (CT). There are no known side effects of MRI scans because it does not involve any kinds of radiations, but it uses magnetism that can distort images of the patients having heart

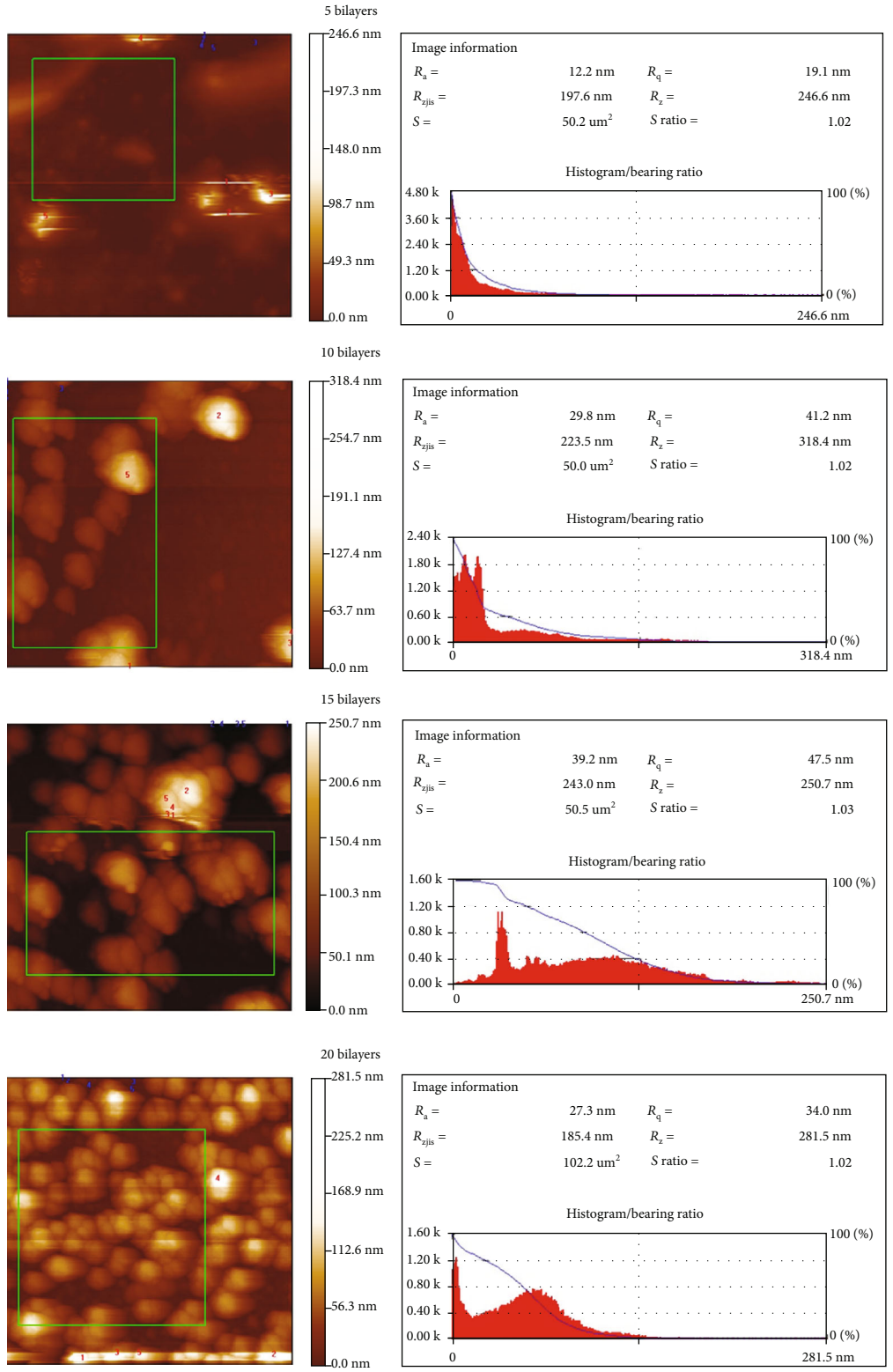

Figure 11: AFM images of combinatorial thin-film gradients of PDAC and prepared magnetic colloidal particles.

pacemakers, metal implants, metal chips, or clips that can interact with the magnet. MRI contrast agents can cause an allergic reaction, flushing sensations, coldness, headache, itching, nausea in patients, and distortion of images obtained by MRI scanners due to the presence of metallic chips, surgical clips, or any other foreign metallic material inside the body. Out of all these side effects, claustrophobia is one of the dominant sensations during MRI scanning in which the patient feels uncomfortable due to the fear of being enclosed or trapped. MRI is also not suitable for patients having

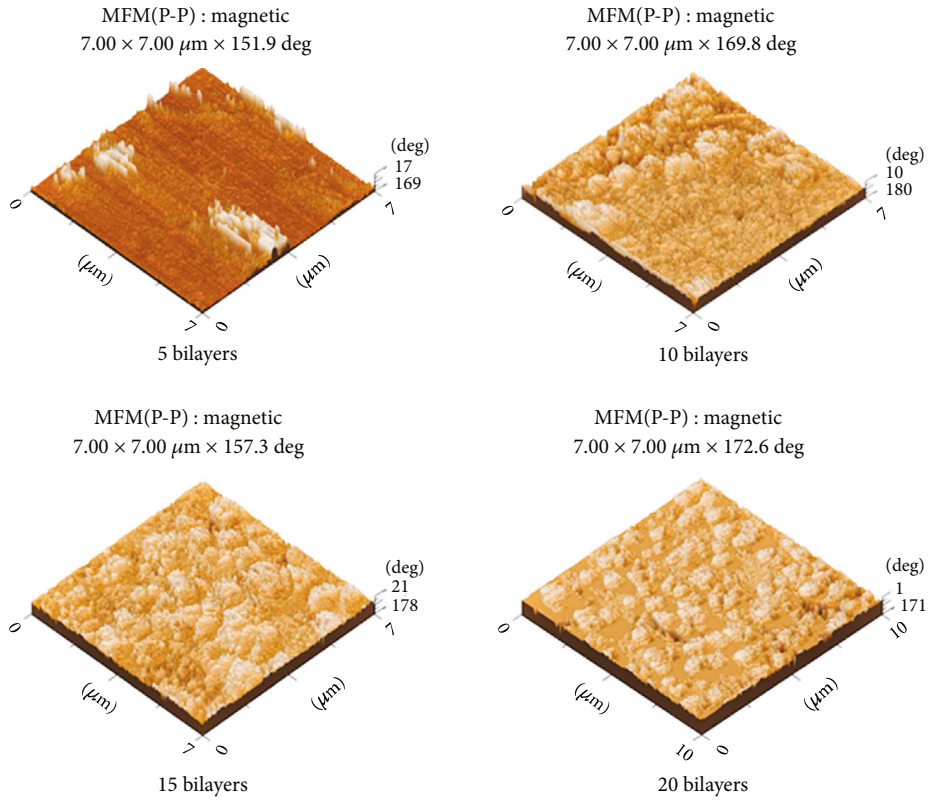

Figure 12: MFM images of combinatorial thin-film gradients of PDAC and prepared magnetic colloidal particles.

asthma, anemia hypotension, and sickle cell disease. Different other methods are used for imaging like X-ray, CT, and positron emission tomography (PET), but MRI is the safest procedure to produce images of the body structures. The main advantage of the present work is the in vitro noninvasiveness diagnosis of biological fluids using combinatorial thin-film gradients. The developed technique lessens the time and expense of the MRI procedure and reduces animal experimentation. The development of such films permits the advancement of the easiest sample application, economic, reproducible, and a disposable chip for dipstick-like approach towards molecular diagnostics.

3.8.1. Effect of Iron Concentration of Colloids on Imaging. Magnetic nanoparticles are considered as T2 contrast agents because they reduced the spin-spin relaxation time [51]. For this purpose, the experimental work carried out to determine the extent to which these particles would enhance the contrast of an MRI image through T1 and T2 sequences. T2 was characterized by spin-spin relaxation time in which the transverse component of the magnetization vector exponentially decayed towards its equilibrium value of zero in MRI. On the other hand, T1 was the spin-lattice relaxation in which longitudinal components of the magnetization vector exponentially recovered to its initial value. Both T1 and T2 are different for different tissues.

MRI characteristics of the prepared O/W emulsion were investigated at various concentrations of iron in the water. Glass vial containing only water was used as a control to compare the contrast capability of the emulsion. These samples were exposed to a magnetic field, a radiofrequency pulse that causes atoms spin and relax after the pulse stops. This relaxation time was detected by the scanners and mathematically converted into an image. The MRI contrast capability of all the samples having different concentrations was analyzed and compared to water. MRI images represent the placement of samples inside the MRI machine. The MRI images were recorded, and equal region of interest (ROI) was drawn manually to obtain average intensity data based on the number of pixels within ROI. Graphs were made using concentrations of iron and acquired ROI intensity. T1-weighted images were obtained by varying TR values (420, 520, 620, 720, and 820 ms) keeping TE fixed at 20 ms, and T2-weighted images were obtained at different TE values (45, 75, 105, 135, and 165 ms) at constant TR 5000 ms.

Figure 13 characterizes the comparison of the average intensity of various samples in the case of T1- and T2-weighted images at TE 75 ms and TR 520 ms. It was observed that all the samples were better T2 contrast agents, as there was no significant effect of concentration on T1 intensity. Also, the T2 negative contrast capability increases with an increase in the concentration of iron in samples that is in good agreement with the reported literature [52, 53]. Compared to water which appeared brighter, T2-weighted images of magnetic colloids appeared to be darker. T2 intensity values of samples indicated their sensitivity as MRI contrast agents.

The T1- and T2-weighted images were obtained through T1 and T2 sequences. As the iron concentration increases in water, signal intensity decreases significantly from higher to

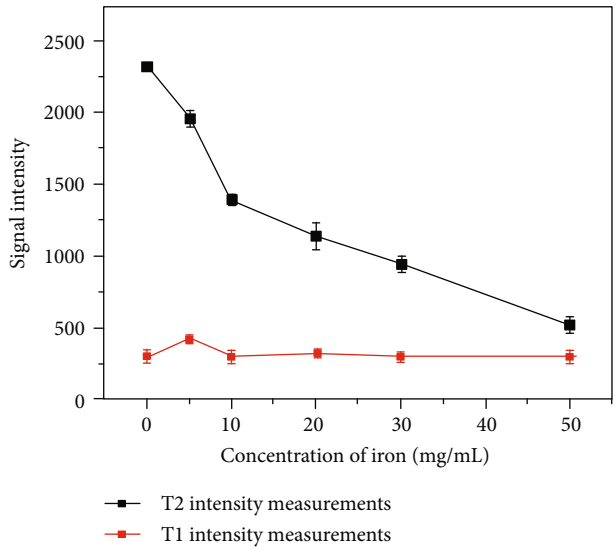

Figure 13: T2 (TE = 75 ms; TR = 5000 ms) and T1 (TE = 20 ms; TR = 520 ms) intensity measurements for various samples. Intensity data is taken as mean intensity within three ROI measurements in terms of intensities of pixels generated from the MRI experiment.

lower values; this is in agreement with the reported values [54–56]. It showed the potential of the prepared emulsion as negative contrast agents. MRI signal intensity varies with TE values. The energy exchanged between protons in water increased with the concentration that resulted in the enhancement of the T2 relaxation rate. An increase in iron concentration creates inhomogeneity in an externally applied field that leads to the dephasing of the magnetic moments and eventually T2 shortening [57]. The lower intensity values compared to water indicated a negative contrast property of these formulations in the case of T2 sequences. The nature of surface coating or functionality on the magnetic nanoparticles also affected the relaxivity of magnetic colloids. It can also be concluded that the emulsification of magnetic nanoparticles in an aqueous phase in this formulation increased the hydrophilicity of particles that allowed greater proximity of water molecules to the nanoparticles, leading to a shortening of T2 relaxation. Hydrophilic and hydrophobic nature of coating affects the degree of hydration and thus their ability to generate contrast in MRI imaging [58]. The surface coating of magnetic particles also prevents the aggregation of particles and thus reduces the interparticle distance that leads to a shortening of the T2 relaxation rate. Relaxivities were strongly affected by particle aggregation [59].

From the results of the signal intensity of T1-weighted images, it was revealed that the concentration of iron did not significantly affect the degree of contrast in T1-weighted images. Thus, the prepared magnetic colloidal particles were considered as T2 contrast agents rather than T1. Surface modification of magnetic nanoparticles influenced the imaging capabilities, hence also affected the T1 relaxivity [58]. It was observed that a sufficient amount of iron is required to generate contrast in MRI and to improve the visibility of internal body structures in MRI [60]. Magnetic resonance imaging contrast agents also induce noticeable relaxation time change in the atoms of body tissues after oral or intravenous administration. The intensity data obtained from MRI images suggest that these formulations could be helpful to develop more effective contrast agents for diagnosis and can be explored for various biomedical applications. Thus, the T2 has strong relaxivity that resulted in a strong variation in T2 signal intensity in the prepared colloids. The mean signal intensity data for all the samples were calculated, and the bar graphs of the mean signal intensity values along with standard deviation values were plotted for each TE sequence (45, 75, 105, 135, and 165 ms) at TR 5000 ms. Signal intensity showed a constant decreasing trend for all the samples at all TE values, which was observed from Figure 14.

3.8.2. MRI Analysis of Combinatorial Thin-Film Gradients. The objective of the present work was also to investigate combinatorial thin-film gradients for their efficacy as contrast imaging agents via MRI to evaluate whether these films were able to generate any contrast. MRI was carried out using a clinical 1.5 T MRI machine. Glass slides having gradients were immersed in a test liquid (ultrapure water) and examined at room temperature. An uncoated region was taken as a reference to compare the difference between the contrasts generated by the gradients. The axial MRI images of thin films were obtained which showed five different regions in combinatorial thin-film gradients (uncoated, 5, 10, 15, and 20 bilayers). The results indicated that magnetic colloids in combinatorial thin films can generate contrast. Signal intensity decreased with the increase in the number of bilayers from 5 to 20. The decrease in signal intensity along the gradient was due to an increase in the number of particles deposited on the slide and a decrease in contact angle that enhances the interaction of water molecules and colloids [13]. An increase in the number of particles adsorbed in thin films along the gradient from 5 to 20 bilayers was evident from SEM results, due to which there is a decrease in MRI intensity count. Due to the hydrophilic nature of the films, it is considered highly efficient to generate contrast in the images formed in MRI scans. Furthermore, functionalization of the surface of magnetic nanoparticles enables their use as multifunctional particles in cancer treatment and multimodality imaging.

Agglomeration of magnetic colloids upon interaction with bioanalytes results in an increase or decrease of MRI intensity, thus showing their potential capability as a contrast agent and forms the base of detection [57]. In the case of combinatorial thin-film gradients, agglomeration was due to the self-assembly of particles rather than interaction with analytes. This study revealed that the combinatorial thin-film gradients of adsorbed magnetic colloids on glass microslides have assisted in decreasing the contrast of the image formed by MRI [52, 53]. This work has significant prospects to enhance and improve the future point-of-care lab-on-chip to develop highly efficient imaging via surface-based MRI of a wide variety of molecules and cells present in the sample of the blood pool such as white blood cells, red blood cells, and platelets. The development of combinatorial gradient thin films eradicated the necessity of injecting magnetic colloids

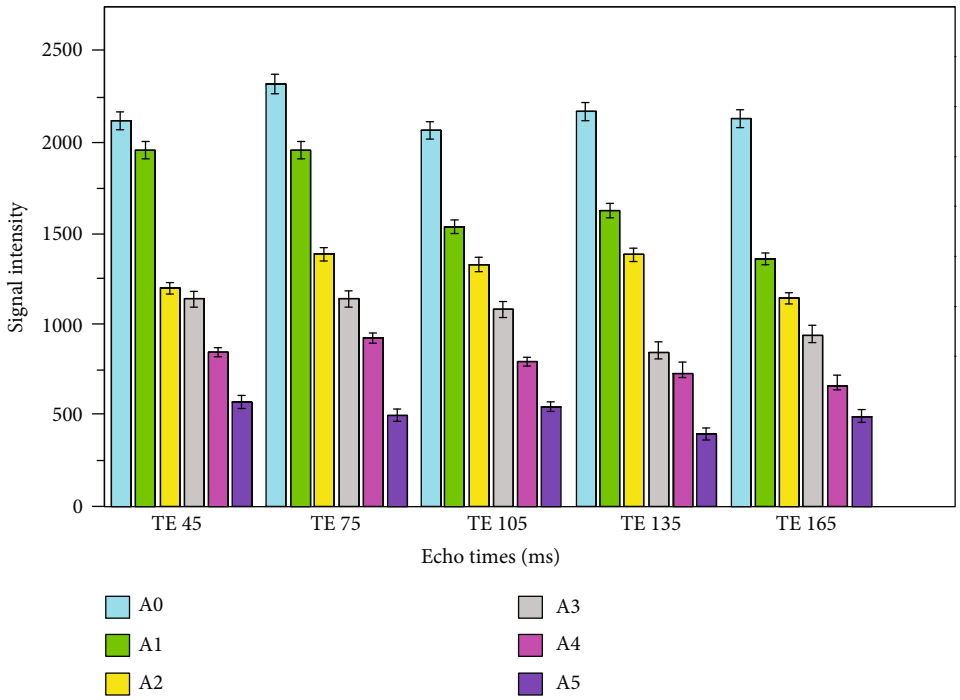

Figure 14: Mean signal intensity graph of different samples for TE 45, 75, 105, 135, and 165 ms and TR = 5000 ms.

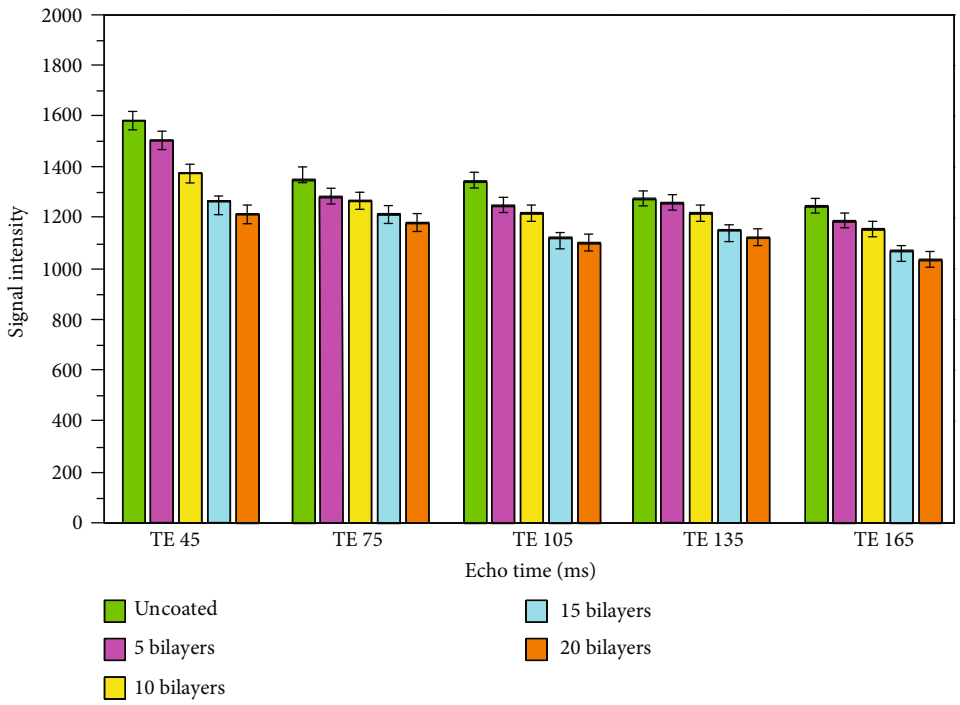

Figure 15: Mean signal intensity graph of combinatorial thin-film gradients for TE 45, 75, 105, 135, and 165 ms and TR = 5000 ms.

into a living body as contrast agents and prevents the association of living organisms in experimentations. Thin films can be fabricated with specific receptors that respond to certain cells which further improve cellular visualization. Difference in contrast in combinatorial thin-film gradients significantly enhances the sensitivity of the films and allows their usage in microfluidic lab-on-chip MRI systems. The mean signal intensity values of uncoated, 5, 10, 15, and 20 bilayer sections in combinatorial gradient thin films were calculated, and the graphs of the mean signal intensity values with standard deviations were constructed against T2 sequence (TE 45, 75, 105, 135, and 165 ms). A persistent decreasing trend in

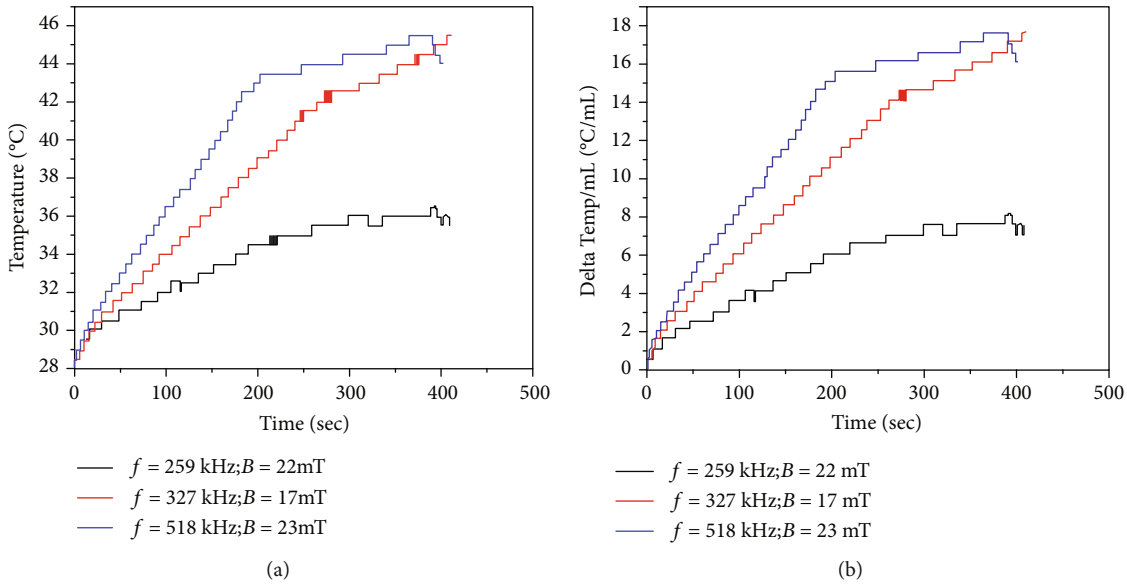

Figure 16: Heating curves of magnetic emulsion taken at different values of AC magnetic field parameters. (a) Hyperthermia measurements of 1 mL of sample. (b) Change in temperature per mL of magnetic emulsion.

intensity was observed at all TE sequences as shown in Figure 15.

3.9. Hyperthermia Measurement of Magnetic Colloidal Particles. This part of the study aimed at evaluating the heating capability of colloidal particles (magnetic emulsion) as hyperthermia mediators. The heating profiles of the sample were estimated and plotted as a function of time, shown in Figures 16(a) and 16(b). The sample was placed in a small vial, inserted in an insulated container to confirm adiabatic condition. Measurements were made at different frequencies (259 kHz, 22 mT; 327 kHz, 17 mT; and 518 kHz, 23 mT) for a specific time (400 sec). The temperature rises with increasing frequency up to a certain limit and then becomes constant [61]. In the present work, maghemite nanoparticles of 6.6 nm as mean size were emulsified in aqueous solution. This mean particle size was less than the critical mean size required for maximum hyperthermia effect (15-18 nm) [62]. The emulsification of organic ferrofluid hinders the heating effect and thus provides better control over the therapeutics. The high heat capacity of the surfactant ensures that the temperature rise was reasonable to avoid overheating, and surface functionalization of nanoparticles regulates the heating performance in hyperthermia. Low content of surfactant over the magnetic nanoparticles had better heating efficacy. There was a maximum temperature rise of 17°C at 518 kHz. As the frequency decreases, there was a different degree of heating observed. Starting from the normal body temperature (37°C), there was a temperature rise of 7°C at 259 kHz, which was suitable for hyperthermia. These results were in concordance with the previously reported values [63]. SAR values at 259 kHz, 327 kHz, and 518 kHz were found to be 156 W/g, 255 W/g, and 336 W/g, respectively. The magnetic emulsion had low SAR values due to the nonmagnetic part in the prepared emulsion and large hydrodynamic size [16].

4. Conclusions

Aqueous and organic ferrofluids consisting of maghemite nanoparticles were prepared by using the coprecipitation method. Single emulsion technique was devised to emulsify these nanoparticles in an aqueous medium. The particle size of nanoparticles and their colloidal particles were determined by TEM and found to be 6 nm and 200 nm, respectively. The iron oxide contents were measured by TGA and found to be 75% in the magnetic emulsion. The saturation magnetization of maghemite nanoparticles was 55 emu/g, which was higher than its colloidal solution due to surface modification. Combinatorial thin-film gradients were also fabricated using a layer-by-layer self-assembly method using PDAC and the prepared magnetic emulsion. The thin films were analyzed by scanning electron microscopy, atomic, and magnetic force microscopy that showed overall an increase in surface coverage with an increase in a number of bilayers. Film thickness was also measured and showed linear deposition of colloidal particles along the substrate. The diagnostic capability of these films and colloids were evaluated by obtaining T1- and T2-weighted images using water as the test liquid. A negative contrast was enhanced as the concentration of iron increases in the samples. Film gradients showed a decreasing trend in intensity with an increase in the number of bilayers. Thus, the developed magnetic combinatorial thin-film gradients from prepared magnetic colloids could be served as a noninvasive medical imaging modality that can be used as a dipstick approach in routine clinical diagnosis. Hyperthermia measurements indicated a significant heating effect of magnetic colloids in alternating magnetic field showed their suitability for therapeutic applications.

Abbreviations

O/W: Oil-in-water

LBL: Layer-by-layer
SAMu: Self-assembled multilayer
PDAC: Polydimethyl diallyl ammonium chloride
SDS: Sodium dodecyl sulphate
MRI: Magnetic resonance imaging
ROI: Region of interest
TE: Echo time
TR: Repetition time
SAR: Specific absorption rate.

Data Availability

The experimental data used to support the findings of this study are available from the corresponding author upon request.

Conflicts of Interest

The authors declare that there are no conflicts of interest regarding the publication of this paper.

Authors' Contributions

Sumera Khizar carried out the experimental work and drafted the manuscript. Nasir M. Ahmad designed and coordinated this research as a principal investigator. Abdelhamid Elaissari assisted in magnetic colloid synthesis, Hassan Saleem carried out MRI studies, and Muhammad Asif Hamayun and Sadia Manzoor participated to perform hyperthermia studies. All the authors read and approved the final manuscript.

Acknowledgments

The authors acknowledge the support of the NUST Research Directorate for support of present work. Sumera Khizar acknowledges the financial support of HEC for the scholarship and the IRSIP program (grant No. 9046) for visiting LAGEPP-UMR, University Claude Bernard Lyon-1, Lyon, France. Dr. Nasir M. Ahmad acknowledges the support of Higher Education Commission (HEC) NRPU (grant No. 3526 and 6020).

References

[1] J. D. Simpson, S. A. Smith, K. J. Thurecht, and G. Such, "Engineered polymeric materials for biological applications: overcoming challenges of the bio-nano interface," *Polymers*, vol. 11, no. 9, article 1441, 2019.

[2] J. Pellico, C. M. Ellis, and J. J. Davis, "Nanoparticle-based paramagnetic contrast agents for magnetic resonance imaging," *Contrast Media & Molecular Imaging*, vol. 2019, article 1845637, pp. 1–13, 2019.

[3] Y. Liu, P. Yin, J. Chen, B. Cui, C. Zhang, and F. Wu, "Conducting polymer-based composite materials for therapeutic implantations: from advanced drug delivery system to minimally invasive electronics," *International Journal of Polymer Science*, vol. 2020, Article ID 5659682, 16 pages, 2020.

[4] S. S. Hayek, "Synthesis and characterization of CeGdZn-ferrite nanoparticles as magnetic hyperthermia application agents," *Advances in Materials Science and Engineering*, vol. 2019, 8 pages, 2019.

[5] T. Guo, M. Lin, J. Huang et al., "The recent advances of magnetic nanoparticles in medicine," *Journal of Nanomaterials*, vol. 2018, Article ID 7805147, 8 pages, 2018.

[6] R. M. Kadhim, E. E. Al-Abodi, and A. F. Al-Alawy, "Synthesis and characterization of magnetic iron oxide nanoparticles by co-precipitation method at different conditions," *Journal of Engineering*, vol. 24, no. 10, 2018.

[7] D. Lombardo, M. A. Kiselev, and M. T. Caccamo, "Smart nanoparticles for drug delivery application: development of versatile nanocarrier platforms in biotechnology and nanomedicine," *Journal of Nanomaterials*, vol. 2019, Article ID 3702518, 26 pages, 2019.

[8] S. Khizar, N. M. Ahmad, N. Ahmed, S. Manzoor, and A. Elaissari, "Encapsulation of doxorubicin in magnetic-polymer hybrid colloidal particles of Eudragit E100 and their hyperthermia and drug release studies," *Polymers for Advanced Technologies*, vol. 31, no. 8, pp. 1732–1743, 2020.

[9] N. Ahmed, N. M. Ahmad, H. Fessi, and A. Elaissari, "In vitro MRI of biodegradable hybrid (iron oxide/polycaprolactone) magnetic nanoparticles prepared via modified double emulsion evaporation mechanism," *Colloids and Surfaces B: Biointerfaces*, vol. 130, pp. 264–271, 2015.

[10] M. K. Lima-Tenório, E. A. G. Pineda, N. M. Ahmad et al., "Aminodextran polymer-functionalized reactive magnetic emulsions for potential theranostic applications," *Colloids and Surfaces B: Biointerfaces*, vol. 145, pp. 373–381, 2016.

[11] J. Xing, Y. Cai, Y. Wang, H. Zheng, and Y. Liu, "Synthesis of polymer assembled mesoporous $CaCO_3$ nanoparticles for molecular targeting and pH-responsive controlled drug release," *Advances in Polymer Technology*, vol. 2020, Article ID 8749238, 8 pages, 2020.

[12] M. A. Hassan, M. Saqib, H. Shaikh, N. M. Ahmad, and A. Elaissari, "Magnetically engineered smart thin films: toward lab-on-chip ultra-sensitive molecular imaging," *Journal of Biomedical Nanotechnology*, vol. 9, no. 3, pp. 467–474, 2013.

[13] A. Ahsan, A. Aziz, M. A. Arshad et al., "Smart magnetically engineering colloids and biothin films for diagnostics applications," *Journal of Colloid Science and Biotechnology*, vol. 2, no. 1, pp. 19–26, 2013.

[14] I. Takeuchi, J. Lauterbach, and M. J. Fasolka, "Combinatorial materials synthesis," *Materials Today*, vol. 8, no. 10, pp. 18–26, 2005.

[15] A. Ludwig, "Discovery of new materials using combinatorial synthesis and high-throughput characterization of thin-film materials libraries combined with computational methods," *NPJ Computational Materials*, vol. 5, no. 1, p. 70, 2019.

[16] F. Reyes-Ortega, A. V. Delgado, E. K. Schneider, B. L. Checa Fernandez, and G. R. Iglesias, "Magnetic nanoparticles coated with a thermosensitive polymer with hyperthermia properties," *Polymers*, vol. 10, no. 1, p. 10, 2018.

[17] M. R. Ghazanfari, S. F. Shams, M. R. Jaafari, and M. Kashefi, "Multi-successive-step pH sensitive procedure: survey of dominant formation mechanism of therapeutic SPIONs," *Ceramics International*, vol. 45, no. 5, pp. 6030–6036, 2019.

[18] M. Circu, A. Nan, G. Borodi, J. Liebscher, and R. Turcu, "Refinement of magnetite nanoparticles by coating with organic stabilizers," *Nanomaterials*, vol. 6, no. 12, p. 228, 2016.

[19] G. Kandasamy, S. Surendran, A. Chakrabarty, S. N. Kale, and D. Maity, "Facile synthesis of novel hydrophilic and

carboxyl-amine functionalized superparamagnetic iron oxide nanoparticles for biomedical applications," *RSC Advances*, vol. 6, no. 102, pp. 99948–99959, 2016.

[20] Y. Tyagi and N. V. S. Madhav, "Smart innovative approach for designing fluvoxamine loaded bio-nanosuspension for the management of depression," *International Journal of Applied Pharmaceutics*, vol. 11, no. 1, p. 191, 2019.

[21] M. H. Hidayat Chai, N. Amir, N. Yahya, and I. M. Saaid, "Characterization and colloidal stability of surface modified zinc oxide nanoparticle," *Journal of Physics: Conference Series*, vol. 1123, article 012007, 2018.

[22] L. A. García-Zapateiro, J. M. Franco, C. Valencia, M. A. Delgado, and C. Gallegos, "Viscous, thermal and tribological characterization of oleic and ricinoleic acids-derived estolides and their blends with vegetable oils," *Journal of Industrial and Engineering Chemistry*, vol. 19, no. 4, pp. 1289–1298, 2013.

[23] M. Seyhan, W. Kucharczyk, U. E. Yarar et al., "Interfacial surfactant competition and its impact on poly(ethylene oxide)/Au and poly(ethylene oxide)/Ag nanocomposite properties," *Nanotechnology, Science and Applications*, vol. 10, pp. 69–77, 2017.

[24] N. V. Jadhav, A. I. Prasad, A. Kumar et al., "Synthesis of oleic acid functionalized Fe_3O_4 magnetic nanoparticles and studying their interaction with tumor cells for potential hyperthermia applications," *Colloids and Surfaces B: Biointerfaces*, vol. 108, pp. 158–168, 2013.

[25] M. M. Rahman, F. Montagne, H. Fessi, and A. Elaissari, "Anisotropic magnetic microparticles from ferrofluid emulsion," *Soft Matter*, vol. 7, no. 4, pp. 1483–1490, 2011.

[26] T. Gong, D. Yang, J. Hu, W. Yang, C. Wang, and J. Q. Lu, "Preparation of monodispersed hybrid nanospheres with high magnetite content from uniform $Fe_{3O}4$ clusters," *Colloids and Surfaces A: Physicochemical and Engineering Aspects*, vol. 339, no. 1-3, pp. 232–239, 2009.

[27] F. Montagne, O. Mondain-Monval, C. Pichot, H. Mozzanega, and A. Elaïssari, "Preparation and characterization of narrow sized (O/W) magnetic emulsion," *Journal of Magnetism and Magnetic Materials*, vol. 250, pp. 302–312, 2002.

[28] J. Mosafer, K. Abnous, M. Tafaghodi, A. Mokhtarzadeh, and M. Ramezani, "In vitro and in vivo evaluation of anti-nucleolin-targeted magnetic PLGA nanoparticles loaded with doxorubicin as a theranostic agent for enhanced targeted cancer imaging and therapy," *European Journal of Pharmaceutics and Biopharmaceutics*, vol. 113, pp. 60–74, 2017.

[29] C. W. Lai, F. W. Low, M. F. Tai, and S. B. Abdul Hamid, "Iron oxide nanoparticles decorated oleic acid for high colloidal stability," *Advances in Polymer Technology*, vol. 37, no. 6, pp. 1712–1721, 2018.

[30] R. P. Araújo-Neto, E. L. Silva-Freitas, J. F. Carvalho et al., "Monodisperse sodium oleate coated magnetite high susceptibility nanoparticles for hyperthermia applications," *Journal of Magnetism and Magnetic Materials*, vol. 364, pp. 72–79, 2014.

[31] R. Y. Hong, B. Feng, X. Cai et al., "Double-miniemulsion preparation of Fe_3O_4/poly(methyl methacrylate) magnetic latex," *Journal of Applied Polymer Science*, vol. 112, no. 1, pp. 89–98, 2009.

[32] J. Mosafer, K. Abnous, M. Tafaghodi, H. Jafarzadeh, and M. Ramezani, "Preparation and characterization of uniform-sized PLGA nanospheres encapsulated with oleic acid-coated magnetic-Fe_3O_4 nanoparticles for simultaneous diagnostic and therapeutic applications," *Colloids and Surfaces A: Physicochemical and Engineering Aspects*, vol. 514, pp. 146–154, 2017.

[33] A. K. Singh, O. N. Srivastava, and K. Singh, "Shape and size-dependent magnetic properties of Fe_3O_4 nanoparticles synthesized using piperidine," *Nanoscale Research Letters*, vol. 12, no. 1, p. 298, 2017.

[34] A. Kumar, P. Kumar, G. Rana, M. S. Yadav, and R. P. Pant, "A study on structural and magnetic properties of NixZn1-xFe_2O_4 ($0 \le x \le 0.6$) ferrite nanoparticles," *Applied Science Letters*, vol. 1, no. 2, pp. 33–36, 2015.

[35] T. Kim and M. Shima, "Reduced magnetization in magnetic oxide nanoparticles," *Journal of Applied Physics*, vol. 101, no. 9, article 09M516, 2007.

[36] M. Logar, B. Jancar, D. Suvorov, and R. Kostanjšek, "In situ-synthesis of Ag nanoparticles in polyelectrolyte multilayers," *Nanotechnology*, vol. 18, no. 32, article 325601, 2007.

[37] S. S. Shiratori and M. F. Rubner, "pH-dependent thickness behavior of sequentially adsorbed layers of weak polyelectrolytes," *Macromolecules*, vol. 33, no. 11, pp. 4213–4219, 2000.

[38] M. Ulmeanu, M. Zamfirescu, and R. Medianu, "Self-assembly of colloidal particles on different surfaces," *Colloids and Surfaces A: Physicochemical and Engineering Aspects*, vol. 338, no. 1-3, pp. 87–92, 2009.

[39] M. M. de Villiers, D. P. Otto, S. J. Strydom, and Y. M. Lvov, "Introduction to nanocoatings produced by layer-by-layer (LbL) self-assembly," *Advanced Drug Delivery Reviews*, vol. 63, no. 9, pp. 701–715, 2011.

[40] A. G. Osorio, G. B. Machado, M. B. Pereira et al., "Synthesis and characterization of magnetic carbon nanotubes/silsesquioxane nanocomposite thin films," *Applied Surface Science*, vol. 371, pp. 9–15, 2016.

[41] J. B. Schlenoff and S. T. Dubas, "Mechanism of polyelectrolyte multilayer growth: charge overcompensation and distribution," *Macromolecules*, vol. 34, no. 3, pp. 592–598, 2001.

[42] R. K. Iler, "Multilayers of colloidal particles," *Journal of Colloid and Interface Science*, vol. 21, no. 6, pp. 569–594, 1966.

[43] S.-L. Ou, W.-J. Liu, Y.-H. Chang et al., "Structure, magnetic property, surface morphology, and surface energy of $Co_{40}Fe_{40}V_{10}B_{10}$ films on Si(100) substrate," *Applied Sciences*, vol. 10, no. 2, p. 449, 2020.

[44] F. Ruffino and M. G. Grimaldi, "Morphological characteristics of Au films deposited on Ti: a combined SEM-AFM study," *Coatings*, vol. 8, no. 4, p. 121, 2018.

[45] I. Misumi, K. Naoi, K. Sugawara, and S. Gonda, "Profile surface roughness measurement using metrological atomic force microscope and uncertainty evaluation," *Measurement*, vol. 73, pp. 295–303, 2015.

[46] R. Buzio, E. Gnecco, C. Boragno et al., "Self-affine properties of cluster-assembled carbon thin films," *Surface Science*, vol. 444, no. 1-3, pp. L1–L6, 2000.

[47] A. Jung, N. Ha, N. Kim et al., "Multiple transfer of layer-by-layer nanofunctional films by adhesion controls," *ACS Applied Materials & Interfaces*, vol. 11, no. 51, pp. 48476–48486, 2019.

[48] C. S. Neves, P. Quaresma, P. V. Baptista et al., "New insights into the use of magnetic force microscopy to discriminate between magnetic and nonmagnetic nanoparticles," *Nanotechnology*, vol. 21, no. 30, article 305706, 2010.

[49] X. Li, W. Lu, Y. Song et al., "Quantitatively probing the magnetic behavior of individual nanoparticles by an AC field-modulated magnetic force microscopy," *Scientific Reports*, vol. 6, no. 1, article 22467, 2016.

[50] L. Yue, Y. Jin, W. Zhang, and D. J. Sellmyer, "Magnetic force microscopy study of Zr_2Co_{11}-based nanocrystalline materials: effect of Mo addition," *Journal of Nanomaterials*, vol. 2015, 5 pages, 2015.

[51] N. A. Navolokin, S. V. German, A. B. Bucharskaya et al., "Systemic administration of polyelectrolyte microcapsules: where do they accumulate and when? In vivo and ex vivo study," *Nanomaterials*, vol. 8, no. 10, p. 812, 2018.

[52] M. W. Marashdeh, B. Ababneh, O. M. Lemine et al., "The significant effect of size and concentrations of iron oxide nanoparticles on magnetic resonance imaging contrast enhancement," *Results in Physics*, vol. 15, article 102651, 2019.

[53] J. S. Basuki, A. Jacquemin, L. Esser, Y. Li, C. Boyer, and T. P. Davis, "A block copolymer-stabilized co-precipitation approach to magnetic iron oxide nanoparticles for potential use as MRI contrast agents," *Polymer Chemistry*, vol. 5, no. 7, pp. 2611–2620, 2014.

[54] L. M. Ali, P. Marzola, E. Nicolato et al., "Polymer-coated superparamagnetic iron oxide nanoparticles as T_2 contrast agent for MRI and their uptake in liver," *Future Science*, vol. 5, no. 1, article FSO235, 2019.

[55] C. Sanson, O. Diou, J. Thévenot et al., "Doxorubicin loaded magnetic polymersomes: theranostic nanocarriers for MR imaging and magneto-chemotherapy," *ACS Nano*, vol. 5, no. 2, pp. 1122–1140, 2011.

[56] D. M. A. Neto, R. M. Freire, J. Gallo et al., "Rapid sonochemical approach produces functionalized Fe_3O_4 nanoparticles with excellent magnetic, colloidal, and relaxivity properties for MRI application," *The Journal of Physical Chemistry C*, vol. 121, no. 43, pp. 24206–24222, 2017.

[57] Y. Zhang, J. Cheng, and W. Liu, "Characterization and relaxation properties of a series of Monodispersed magnetic nanoparticles," *Sensors*, vol. 19, no. 15, article 3396, 2019.

[58] W. Zhang, L. Liu, H. Chen et al., "Surface impact on nanoparticle-based magnetic resonance imaging contrast agents," *Theranostics*, vol. 8, no. 9, pp. 2521–2548, 2018.

[59] H. T. Ta, Z. Li, Y. Wu et al., "Effects of magnetic field strength and particle aggregation on relaxivity of ultra-small dual contrast iron oxide nanoparticles," *Materials Research Express*, vol. 4, no. 11, article 116105, 2017.

[60] G. Rostoker, M. Laroudie, R. Blanc et al., "Signal-intensity-ratio MRI accurately estimates hepatic iron load in hemodialysis patients," *Heliyon*, vol. 3, no. 1, article e00226, 2017.

[61] N. Griffete, J. Fresnais, A. Espinosa, D. Taverna, C. Wilhelm, and C. Ménager, "Thermal polymerization on the surface of iron oxide nanoparticles mediated by magnetic hyperthermia: implications for multishell grafting and environmental applications," *ACS Applied Nano Materials*, vol. 1, no. 2, pp. 547–555, 2018.

[62] N. Rescignano, Y. González-Alfaro, E. Fantechi et al., "Design, development and characterization of a nanomagnetic system based on iron oxide nanoparticles encapsulated in PLLA-nanospheres," *European Polymer Journal*, vol. 62, pp. 145–154, 2015.

[63] C. Yadel, A. Michel, S. Casale, and J. Fresnais, "Hyperthermia efficiency of magnetic nanoparticles in dense aggregates of cerium oxide/iron oxide nanoparticles," *Applied Sciences*, vol. 8, no. 8, p. 1241, 2018.

Hindawi
Advances in Polymer Technology
Volume 2020, Article ID 7310657, 14 pages
https://doi.org/10.1155/2020/7310657

Research Article

Polymethacrylate Sphere-Based Assay for Ultrasensitive miRNA Detection

Samira Hosseini,[1,2] **Patricia Vázquez-Villegas**,[1] **Richard C. Willson**,[3,4,5] **Marco Rito-Palomares**,[5] **Margarita Sanchez-Dominguez**,[6] **Leo H. Koole**,[6] **Marc J. Madou**,[7,8,9] **and Sergio O. Martínez-Chapa**[1]

[1]*Escuela de Ingenierı́a y Ciencias, Tecnologico de Monterrey, Ave. Eugenio Garza Sada 2501, Monterrey 64849, NL, Mexico*
[2]*Writing Lab, TecLabs, Vicerrectoría de Investigación y Transferencia de Tecnología, Tecnologico de Monterrey, Ave. Eugenio Garza Sada 2501, Monterrey 64849, NL, Mexico*
[3]*University of Houston, Department of Chemical and Biomolecular Engineering, Houston, TX 77204, USA*
[4]*University of Houston, Department of Biology and Biochemistry, Houston, TX 77204, USA*
[5]*Escuela de Medicina y Ciencias de Salud, Tecnologico de Monterrey, Avenida Ignacio Morones Prieto 3000 Poniente, 64710 Monterrey, NL, Mexico*
[6]*Centro de Investigación en Materiales Avanzados, S. C. (CIMAV), Unidad Monterrey, Parque de Investigación e Innovación Tecnológica, Apodaca, NL 66628, Mexico*
[7]*Faculty of Health, Medicine and Life Sciences, Maastricht University, Maastricht, Netherlands*
[8]*University of California, Department of Biomedical Engineering, Irvine, CA 92697, USA*
[9]*University of California, Department of Mechanical and Aerospace Engineering, Irvine, CA 92697, USA*

Correspondence should be addressed to Samira Hosseini; samira.hosseini@tec.mx

Received 3 July 2019; Revised 26 October 2019; Accepted 11 November 2019; Published 1 April 2020

Academic Editor: Leandro Gurgel

Although microRNAs (miRNAs) have emerged as increasingly important target analytes, their biorecognition remains challenging due to their small size, high sequence homology, and low abundance in clinical samples. Nanospheres and microspheres have also gained increasing attention in biosensor applications due to their high specific surface area and the wide variety of compositions available. In this study, chemically designed and synthesized microspheres with active functional groups were used to promote effective miRNA immobilization resulting in better biorecognition. Upon conjugation with fluorescence-labeled complimentary probes, acylate-based spheres have indirectly detected MiR159, offering significantly enhanced analytical sensitivity, specificity, and accuracy while yielding a considerably low limit of detection (LOD) of 40 picomolar. Furthermore, MiR159 presence, which is known to be inversely correlated to breast cancer incidence and progression, was successfully detected in a competitive assay, which is promising for upgrading the current assay to clinical use.

1. Introduction

MicroRNAs (miRNAs) are short regulatory ribonucleic acids (RNAs) ranging from 18 to 25 nucleotides in length [1]. Overexpression or underexpression of miRNAs is associated with various diseases and with distinct stages of specific illnesses [2–6]. Monitoring changes in expression levels of miRNAs is invaluable for timely initiation of treatment and/or for monitoring the effectiveness of an ongoing treatment [7–9]. MiRNAs are challenging targets for biorecognition due to their small size, high levels of sequence homology, and semistable secondary structures [10]. Routinely applied strategies for detection of miRNAs including northern blot, microarrays, or real-time polymerase chain reaction (PCR) require complex equipment and data analysis, while they are costly and not always available in every clinical setup [8, 11]. Moreover, several reports indicate insufficient specificity and sensitivity

when dealing with these techniques which add to the existing challenges of miRNA detection [12].

Nano/microspheres have drawn a great deal of interest in immunoassays due to their key advantageous features including (i) amenability to screening and multiplexing; (ii) significantly larger specific surface area in comparison with two-dimensional (2D) platforms which facilitate higher analyte-surface interaction; and (iii) high spatial freedom for interaction with biomolecules of interest [13–21]. miRNA detection using different particle types are reported in the literature [22, 23]. A wide range of particles were used for the purpose of miRNA detection including magnetic, carbon, graphene oxide, silver, and copper particles [24–30]. Quantum dots-encoded microbeads (Qbeads) introduce another strategy for detection of miRNAs [31, 32]. While these technologies opened windows of opportunity for effective detection of miRNAs, a vast majority of them involve time-consuming functionalization steps, expensive reagents, complicated procedures, and sophisticated laboratory setups [12]. Even then, the stability of the modified bioreceptive surfaces is not guaranteed, as they might lose their functionality over time [33, 34].

In this work, we describe a proof-of-concept strategy that involves cross-linked polymethacrylate microspheres of different sizes as bioreceptor surfaces for miRNA detection based on nucleotide hybridization. The polymer-based microspheres possess tailored physical and chemical properties. While offering a large surface area for analyte-surface interaction, the spheres are benefited from the inherent presence of carbonyl (-C=O), hydroxyl (-OH), and aromatic groups that further promotes biomolecular interactions. This makes the functionalization and surface activation steps unnecessary. Microspheres were integrated into a conventional 96-well plate for a one-step hybridization assay for biorecognition of Cy3-labeled miR159 as the target analyte, using a complementary amino-modified DNA capture probe. Moreover, synthetic unlabeled miR159 was detected in a competitive assay as a further proof-of-concept since the concentration of miR159 in blood serum is inversely correlated to the breast cancer incidence and progression in humans [35]. This straightforward strategy for the first time allows a routine analytical assay to detect microRNAs in the picomolar (pM) range without any amplification.

2. Materials and Methods

2.1. Chemicals and Reagents. Sodium citrate ($Na_3C_6H_5O_7$), sodium chloride (NaCl), hydrochloric acid (HCl), sodium dodecyl sulfate (SDS), polysorbate 20 (Tween 20), toluidine blue (TB), sodium hydroxide (NaOH), acetic acid (AcOH), nuclease-free water, and bovine serum albumin (BSA) were purchased from Sigma Aldrich (St. Louis, MO, USA). Capture probe, amino-modified DNA (5′-TTTAAGGAGCTCacatacgcgggcc-3′/amino modifier/), target Cy3-labeled analyte miR159 (5′-GAGCUCCUUAAAguuaaaca-3′/Cy3/), synthetic target miRNA159 (5′-GAGCUCCUUAAAguuaaaca-3′) and the noncomplementary negative control, Cy3-tagged miR-lin4 (5′-acaccugggcucuccggguac-3′/Cy3/), were purchased from Integrated DNA Technologies (Coralville, IA, USA). The uppercase and lowercase letters in the biomolecules represent complementary and noncomplementary nucleotides, respectively (amino modifier is a primary amine with no spacer arm).

2.2. Microsphere Synthesis. Polymethacrylate microspheres were synthesized in a suspension by polymerization (Geleen, the Netherlands) with monomers methyl methacrylate (MMA), 2 hydroxylethylmethacrylate (HEMA), 4-iodo-benzyloxo-ethyl methacrylate (4-IEMA), and tetraethyleneglycol dimethacrylate (TEGDMA). Details of particle synthesis and characterization (storage stability, hemo- and cyto-compatibility, structure, and absence of leachable components) have previously been reported [36, 37]. Spheres were sieved and size-sorted as follows: MMS-1 (200–400 μm); MMS-2 (400–600 μm); MMS-3 (600–700 μm); and MMS-4 (700–900 μm) (Figure 1). The spheres are slightly hydrophilic and relatively dense (~1.3 g/mL) which are advantageous features for biorecognition applications, as the conjugated particles will sink in aqueous media without clustering. This, in turn, maximizes the contact with the analyte of interest.

2.3. Morphology, Size Distribution, Surface Area, and Raman Spectroscopy Analyses. A scanning electron microscope equipped with a field emission gun (FESEM, JEOL, JSM7600F, USA) was used for the morphological analysis of platinum-coated spheres from different size categories. The acceleration voltage of the instrument was 0.5 kV. The size distribution of each size category was calculated from optical microscope images of 500 ± 5 randomly selected spheres from each group (OLYMPUS, BX51TRF, Japan). The specific surface area of each size category (per 10 mg) was calculated from the size distribution analysis (Figure 1) [36]. Raman spectra were recorded on a Raman Spectrometer, LabRAM HR Evolution (Horiba, Japan), coupled to an Olympus BX-4 microscope. The wavelength used to excite the sample was 532 nm, which was provided with a Nd:YAG laser as an irradiation source. The specific conditions were as follows: laser ND filter 25%, accumulation time of 3 s, 6 accumulations, 600 lines/mm grating (500 nm), a hole of 50 micrometers.

2.4. Topography Analysis of Microspheres before and after miRNA Immobilization. The surface of the microspheres before and after miRNA immobilization was analyzed by atomic force microscopy (AFM, Asylum Research MFP3D SA) in the tapping mode in air. An Asylum Research model AC240TS-R3 rectangular tip was used to analyze the surface. The scans covered areas of 60×60 μm and 1×1 μm with a speed interval from 0.20 to 0.50 Hz. The frequency of the first nominal resonance was 70 kHz, the nominal spring constant was 2 N/m, and the nominal curvature radius was 9 ± 2 nm. Prior to AFM analysis, samples of microspheres were incubated in hybridization solution (1 μM of capture probe and 1 μM of the Cy3-miRNA analyte) for 2 hours followed by washing two times with SSC and 0.01X SSC, respectively.

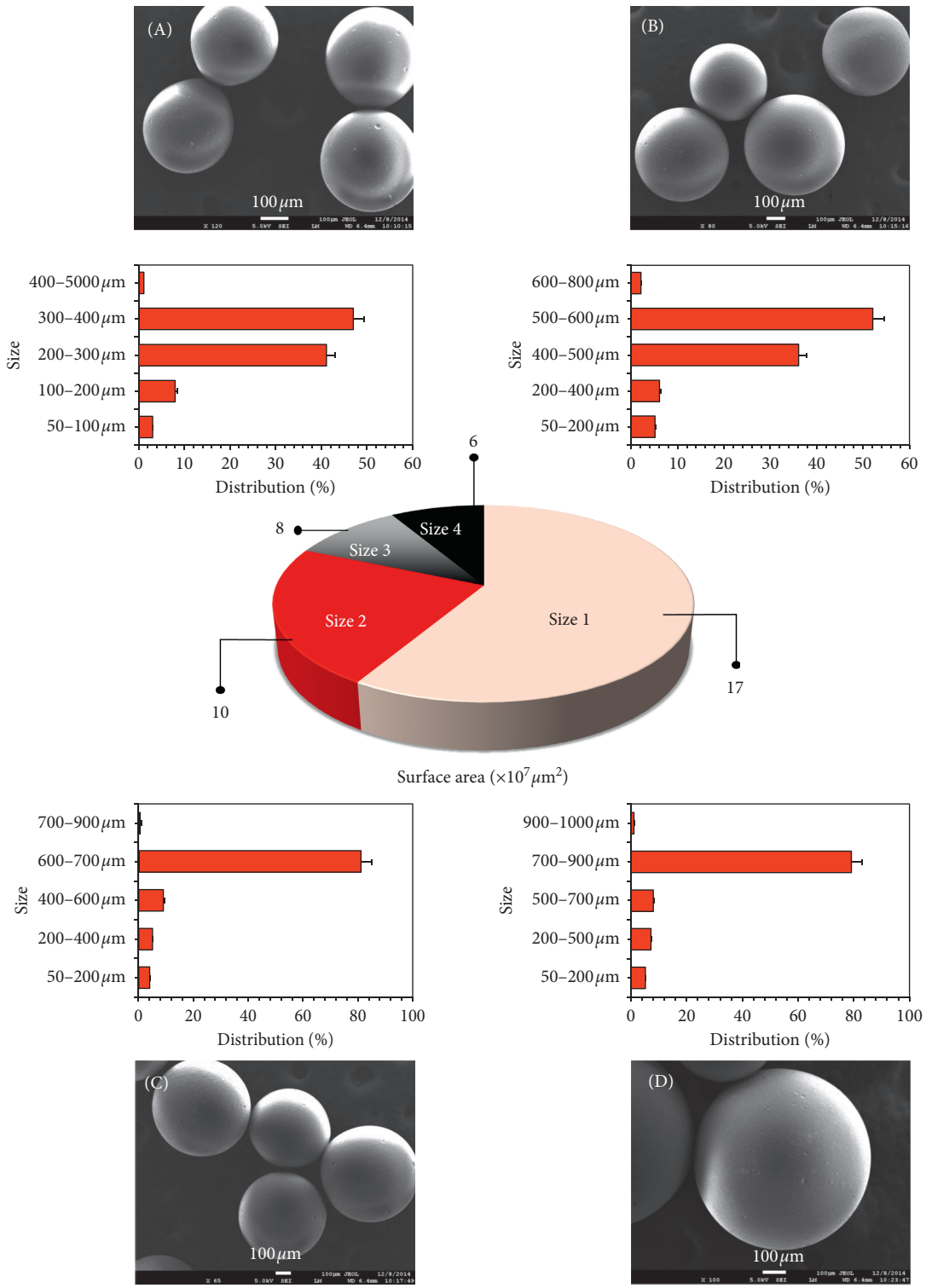

Figure 1: SEM images of the spheres from different size categories along with their size distributions: (a) MMS-1 (200–400 μm); (b) MMS-2 (400–600 μm); (c) MMS-3 (600–700 μm); (d) MMS-4 (700–900 μm). Specific surface area measurement for 10 mg of each size group is presented in the center.

2.5. Oligonucleotide Immobilization and Toluidine Blue Titration. The ability of the microspheres in accommodating miRNAs on their surface was assessed via a toluidine blue assay. The assay was calibrated prior to readout using calibration solutions of 2 μM, 4 μM, 6 μM, 8 μM, and 10 μM TB. Microspheres (10 mg) were incubated in a 1 μM solution of the capture probe (200 μL, 37°C, 2 h) followed by thorough washing with sodium saline citrate (SSC). This method was previously reported in the literature and was thoroughly tested [38–40]. Toluidine blue (TB) titration was used to

confirm the presence of the oligonucleotide capture probes bonded to the surface of the microspheres. This technique relies on the pH-dependent electrostatic interaction between TB dyes and nucleotide phosphate groups (Figure 2(a)) [38]. Spheres of different size categories (10 mg) were immersed in 8 mL of 0.5 mM TB and 0.1 mM NaOH solution for 2 hr, followed by washing the spheres in 0.1 mM NaOH for the complete removal of noncomplexed TB dye. The spheres were subsequently incubated in 3 mL of acidic solution (50% AcOH in distilled water) for 45 minutes in order to strip the complexed TB molecules into the acid solution for measurement at 635 nm by using a Jenway (Stone, Staffordshire, UK) spectrophotometer.

2.6. Buffer Preparation for the Analytical Assay. The stock solution of 20 times concentrated SSC (20X, 3 M NaCl, 0.3 M $Na_3C_6H_5O_7$, pH adjusted to 7 using HCl) and subsequent dilutions of this buffer (5X and 0.01X) were prepared with nuclease-free water (Sigma Aldrich, St. Louis, MO, USA). All dilutions were filtered with sterile 0.2 μm syringe filters (Corning, Corning, NY, USA). The capture probe solution was initially prepared in nuclease-free water and was diluted in SSC buffer to 10 μM. This concentration was utilized as the stock solution for further dilutions of the capture probe. The solutions of SSC and 0.01X SSC have been used as the washing buffers after incubation with the capture probe and hybridization miRNA, respectively. A blocking buffer containing (1%, w/v) BSA, (0.02%, w/v) SDS, and (0.05%, w/v) Tween 20 in 5X SSC was used to reduce the chance of nonspecific binding.

2.7. Indirect and Competitive Hybridization Assays. A predetermined amount of the spheres (10 mg) was loaded into the wells of conventional 96-well plates (Corning, NY, USA). As control, the indirect assay was also conducted in the conventional 96-well plate without spheres. To minimize experimental variability, all the assays were performed under the exact same conditions and by using the same batch of buffers. The miRNA probes were physically immobilized on the surface of the spheres. The spheres were loaded inside a 96-well plate, and each well was charged with 200 μL solution of capture probe (1 μM). The incubation was carried out for 2 hr at 37°C. All the wells were thoroughly washed with SSC buffer (3 times, 200 μL) and were charged with blocking buffer (200 μL) to avoid nonspecific binding. The incubation was carried out for 1 hr at 37°C followed by a complete washing process with SSC buffer. Each well has subsequently received 200 μL of the analyte solution (2 hr at 37°C). Analyte solutions (Cy3-miR159) were prepared by diluting the original concentration (100 μM) with 0.01X SSC buffer in order to achieve a concentration range as follows: 1000 nM, 100 nM, 10 nM, 1 nM, 100 pM, 10 pM, and 1 pM. To avoid fluorescent bleaching, from this step onwards, the assay was performed in a dark room. The assay was finalized by another round of washing (0.01X SSC) before readout. The fluorescence intensity of the Cy3 label was measured with 530/25 nm and 590/35 nm excitation and emission filters, respectively. The readout was performed with an integration time of 0.1 s and 120% sensitivity in a Synergy 2 microplate reader (BioTek Instruments, Inc., Winooskin, VT, USA).

Since the concentration of the target analyte is inversely correlated with breast cancer, a competitive hybridization assay was additionally performed to assess the potentials of the developed assay. Synthetic miR159 was detected in competition with Cy3-labeled miR159. In this procedure, 10 mg of microspheres (MMS- 3 as the representative group) was loaded in each well of a 96-well plate and coated with capture probe at 1 μM. The fluorescence-labeled miRNA (Cy3-miR159) was diluted to 100 nM and 1000 nM, while synthetic miR159 was diluted to 0 nM, 10 nM, 100 nM, and 1000 nM. Competitive binding was performed using the same buffers and at the same incubation time and temperatures as reported above. Relative fluorescent intensity was calculated by dividing intensity (for each concentration of the untagged miRNA) by the negative outcomes (calculated in the absence of untagged miRNA).

2.8. Calibration and Evaluation of the Assay. Calibration of the assay was performed with capture probe (1 μM) and different concentrations of the target analyte (1000 nM, 100 nM, 10 nM, 1 nM, 100 pM, 10 pM, and 1 pM). Calibration curves were plotted by conversion of the data to the logarithmic scale. Negative replicates were conducted with the noncomplementary Cy3-labeled miR-lin4 as hybridizing miRNA ($n = 10$). Cutoff values for each individual size category of the microspheres were calculated as twice that of the mean values of the negative controls [41]. Only readouts with intensity outcomes above cutoff values were interpreted as positives.

A total number of 80 positive and 40 negative replicates were conducted to obtain important parameters such as analytical sensitivity, specificity, and accuracy of the assay. Calculations were performed following the equations below considering the negative/positive readouts in comparison with the total number of the conducted replicates [42]:

$$\begin{aligned} \text{sensitivity} &= \frac{\text{TP}}{\text{TP} + \text{FN}} \times 100, \\ \text{specificity} &= \frac{\text{TN}}{\text{TN} + \text{FP}} \times 100, \\ \text{accuracy} &= \frac{\text{TP} + \text{TN}}{\text{total replicates}} \times 100. \end{aligned} \tag{1}$$

Variables in these equations are as follows:

True positive (TP)

True negative (TN)

False positive (FP)

False negative (FN)

Limit of detection (LOD) for each size category was determined as 3 times the average standard deviation (s, in the case of lowest miRNA concentration) divided by the slope of the calibration curve (m) following the given equation [34, 43–48]:

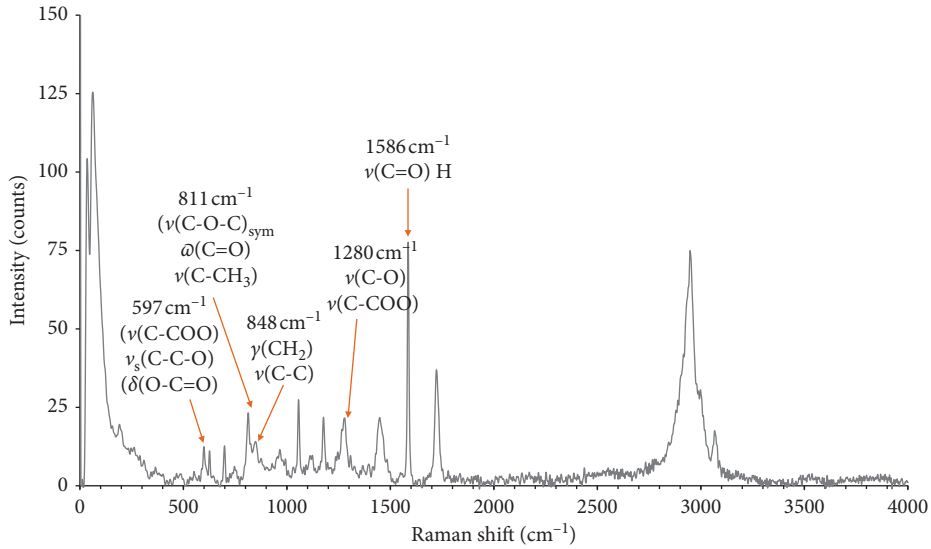

Figure 2: Raman analysis of the polymethacrylate spheres with the assigned peaks.

$$\text{LoD} = \frac{3 \times s}{m}. \quad (2)$$

The conventional assay conducted without spheres was also calibrated and carefully evaluated.

3. Results and Discussion

3.1. Morphology, Size Distribution, and Surface Area of the Spheres. Microspheres of different size groups were imaged by SEM, and representative morphologies are presented in Figures 1(a)–1(d). The recorded morphologies were found to be smooth, and the dimensions of the spheres were within the expected range as the sieved groups. Uniform spheres with consistent surface morphologies allow the interpretation to be focused on the effects of specific surface area and chemistry of the spheres for biomolecule immobilization.

Diameter range and size distribution (graphs in Figures 1(a)–1(d)) were calculated for each size group of the spheres by using optical images. Subsequently, the specific surface area for each size category was carefully calculated (for 10 mg of the microsphere) from the respective size distributions. The surface area ranged from 6×10^7 to 17×10^7 μm^2 (Figure 1, the central pie chart). As expected, the highest surface area per mass was offered by the smallest spheres (MMS-1), and the lowest specific surface area per mass was measured for the largest spheres (MMS-4). In principle, the higher specific surface area enhances the analyte-surface interaction resulting in higher probability of the biomolecular coupling and subsequent biorecognition [33, 49].

3.2. Raman Spectroscopy Analyses of the Spheres. Figure 2 shows the Raman spectrum of the microspheres. It should be noted that there is no signal from the C=C stretching mode from the methacrylic group, normally around 1640 cm^{-1}, indicative of successful copolymerization (an evidence for no free monomers) [50, 51]. Several signals were assigned to functional groups of the different polymers involved in synthesis of the spheres. The signal at 597 cm^{-1} may correspond to PMMA polymer (ν(C-COO), ν_S(C-C-O)) [52] as well as to p-HEMA (δ(O-C=O)) [53]. The peak at 811.8 cm^{-1} can be assigned to several signals from p-HEMA (ν(C-O-C)$_{sym}$, ϖ(C=O) or ν(C-CH$_3$)) [4]. Also arising from p-HEMA, the signal at 848 cm^{-1} can be assigned to γ(CH$_2$) or ν(C-C) [53]. The deformation localized on the OCH$_2$-CH$_2$OH part of the p-HEMA molecule can be seen at 955 cm^{-1} [53]. The signal at 1280.5 cm^{-1} can be assigned to ν(C-O) and ν(C-COO) from PMMA. At 1448.8 cm^{-1} [52], deformation from (C-CH$_2$) of p-HEMA can be observed [53]. The aromatic ring stretch from p-IEMA is shown at 1586.41 cm^{-1} [54]. Another signal from the carbonyl is observed at 1719.8 cm^{-1} (ν(C=O) H bonded from p-HEMA or p-TEGDMA) [55]. The wide band around 2949 cm^{-1} arises from several signals from PMMA (ν_S(C-H) of O-CH$_3$ with ν_S(C-H) of α-CH$_3$ and ν_a(CH$_2$)) [52]. Finally, the shoulder at 3065 cm^{-1} may arise from the iodobenzyl part of p-IEMA or various signals from PMMA and p-TEGDMA [52, 55].

3.3. Toluidine Blue (TB) Titration. The presence of negatively charged nucleotide strands on the surface of the spheres was investigated by a TB assay. As described before, each TB molecule contains an aromatic cation segment and a chloride anion (Figure 3(a)). A pH-sensitive adsorption/desorption mechanism leads to the ionization of the TB dye in the alkaline environment (Figure 3(a), step 1). Positively charged TB then binds to the negative $-PO_4^-$ groups of the miRNAs (Figure 3(a), step 2) and desorbs upon subsequent lowering of the pH (Figure 3(a), step 3). Concentration of the TB dyes measured by UV-Vis is expected to be proportional to the concentration of the capture probes on the surface of the microspheres.

Figure 3(b) shows a highly linear calibration plot for TB assay with predetermined concentrations of TB in acidic

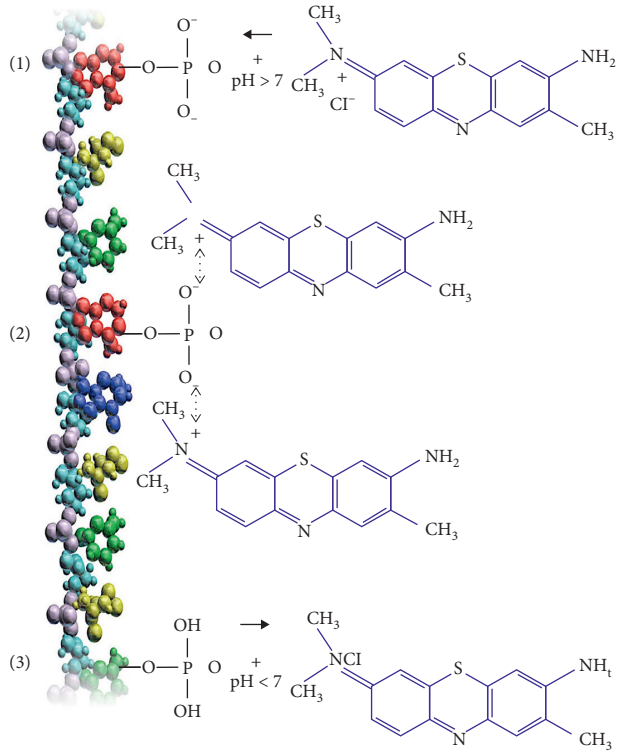

(a)

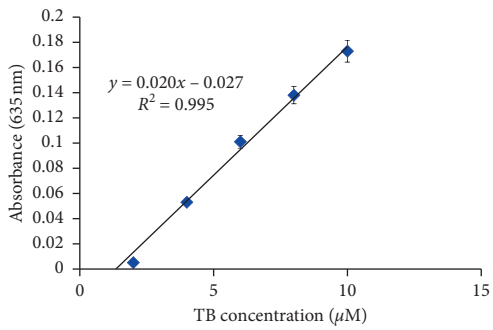

(b)

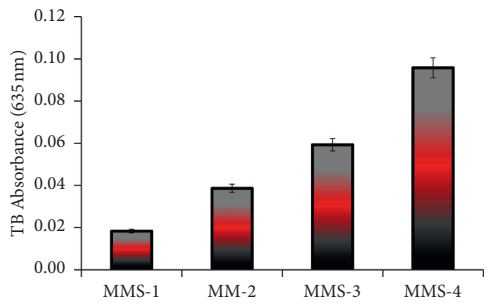

(c)

MMS groups	Surface area per 10 μg (mm^2)	TB bound (mM/mm^2)	Capture probe concentration (nM/mm^2)	Capture probe concentration (in 10 μg of the spheres) (nM)
1	170	95.0	3.80	645.8
2	100	171.1	6.84	684.4
3	80	226.1	9.04	723.5
4	60	330.3	13.21	792.7

(d)

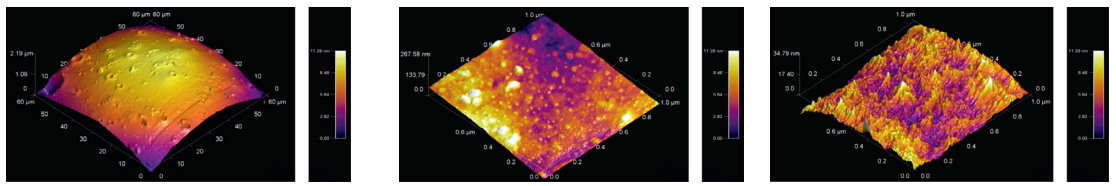

(e) (f) (g)

Figure 3: TB analysis for indirect confirmation of the presence of capture probe on the surface of the spheres: (a) adsorption and desorption mechanisms of the TB molecules to the $-PO_4^-$ groups of the nucleotide available on the surface of the spheres via alteration of the pH from the alkaline to acidic environment; (b) calibration curve plotted by titration of the TB assay using different concentrations of the calibration solutions (2 μM, 4 μM, 6 μM, 8 μM, and 10 μM); (c) TB absorbance per mm^2 of the surface measured by spectroscopic UV-Vis (635 nm); and (d) breakdown calculations of the TB assay. AFM analysis ((e) 60 μm) and zoomed-in view ((f) 10 μm) of the microspheres prior to immobilization and ((g) 10 μm) after surface attachment of the hybrid strands which shows the clear alteration of the surface roughness.

solution. While the concentration of TB is considered proportional to the concentration of the capture probe on the surface of the spheres, it is important to note that the results of TB assay is a comparative means for such correlation. Figure 3(c) represents the TB absorbance on 10 mg of the spheres from different size groups. As can be observed, the TB absorbance increases as the size of the spheres increases, which demonstrates that a higher particle size encourages a higher number of TB dye molecules to bind to the captured strands on the surface even though a lower total surface area is offered by the larger sizes. The latter is explained by the fact that spatial freedom for an efficient interaction between capture probes and TB molecules increases as the dimension of the spheres increases [49, 56, 57]. The approximate size of the TB molecules (≈0.7 to 1.1 nm) is in the range of the length of a horizontally oriented single miRNA strand (≈1 nm) on the beads so the more the space for maneuvering between the strands, the easier it is for TB to bind [58, 59]. Presumably available surface functionalities reacted with miRNA strands; thus, the inter-miRNA distance on the smaller particle size microspheres would make the TB diffusion rather difficult which is not the case when the larger sphere size is applied. In Figure 3(d), a breakdown calculation of the TB assay is provided. This analysis provides an approximate concentration of TB dyes per mm^2 of the spheres' surface. Every strand of the capture probe consists of 25 nucleotides with individual $-PO_4^-$ groups. It is known that TB is highly interactive towards anionic sulfates, carboxylates, and phosphate groups [60]. If the interaction between positively charged TB and negative $-PO_4^-$ groups occurs in a 1 : 1 ratio, TB absorbance would be proportional to the capture probes present on each mm^2 of the spheres' surface (Figure 3(d)); thus the number of capture probes that are immobilized on the total surface of the spheres can be indirectly calculated (Figure 3(d)).

3.4. Topography Analysis of the Spheres before and after miRNA Immobilization. Surface topography of the microspheres was analyzed by AFM to study surface changes (roughness and surface area) before and after miRNA immobilization. AFM analysis (presented in Figures 3(e) and 3(f), before miRNA immobilization, and Figures 3(g), after immobilization) shows a clear alteration in the topography of the surface between pristine surfaces (Figures 3(e) and 3(f), zoomed-in view) and the surfaces after miRNA immobilization (Figure 3(g)). An increased surface roughness (from 6.8 nm to 41.2 nm) was recorded for surfaces of the spheres before and after miRNA immobilization, respectively. As a result of coupling in the hybrid strand, a capture probe shares 12 nucleotides with tagged miRNA analyte. Therefore, the coupled strand contains a total of 33 nucleotides. Knowing the approximate size of each nucleotide (~1 nm), the size of the hybrid strand can be roughly calculated (~33 nm). This number closely corresponds to the improved surface roughness analyzed by AFM (34.4 nm). Additionally, the recorded surface area was found to be ~100-fold greater when comparing surface-immobilized spheres with those before immobilization (from 1 μm^2 to 100.6 μm^2). Such enhancement in the surface area is a direct function of the hybrid strands present on the surface of the bioreceptive microspheres.

3.5. Performance Analysis of the Microspheres in Indirect Detection of miR159. Figure 4(a) shows the calibration curves plotted in a logarithm scale for each microsphere size group conducted in varied concentrations of the labeled miRNA. Increasing correlation coefficient values are observed for MMS-1, MMS-3, and MMS-4, respectively. Figures 4(b) and 4(c) depict fluorescence images of the spheres after detection of 1 nM and 100 nM of the labeled analyte, respectively. According to these images, partial clustering of the spheres has seemingly limited complete analyte-surface interaction. Incorporation of gentle mixing/shaking systems could be a suitable method to allow better accessibility of the spheres to the entire sample volume and to enhance the detection signal further.

Figure 4(d) provides a detection performance comparison among different size groups of the spheres in contrast to their cutoff values (twice the mean values of the negative outcomes, presented in red). The detection signals in this chart are plotted with their original values without subtracting the cutoff values for detailed performance comparison among the size groups. As can be seen, the MMS-1, MMS-2, and MMS-3 groups of the microspheres offered higher detection signal in comparison with the largest size category (MMS-4), when subtracting the cutoff values from the actual detection signals. The overall signal intensity obtained from the developed assay in this study falls within the previously reported values for successful detection of miRNAs using a solid-phase hybridization assay [7, 61]. None of the previously reported detection methods, however, rely on conventional ELISA for the detection miRNAs, which is the point of the current study.

3.6. Performance of the Microspheres in a Competitive Assay. The performance of the spheres was further assessed in a competitive assay. In this protocol, concentration of the fluorescently tagged Cy3-miR159 remained constant, while the concentration of the untagged synthetic miR159 (target analyte) was varied, resulting in decreased fluorescence intensity as the concentration of the target analyte increased. Figure 4(e) represents the result of the competitive assay, which was conducted with the MMS-3 category of the spheres as representative. Concentrations of the untagged miRNA (x-axis) are presented in the logarithm scale, while the y-axis depicts the relative fluorescence intensity. The systematic decrease in fluorescence intensity as a result of increased concentration of the untagged miRNAs provides a clear proof-of-concept that the proposed hybridization assay is an easy and reliable method for quantification of miR159 within this conventional platform.

3.7. Possible Analyte-Surface Interactions. The surface of the microspheres promotes a variety of interaction types between the analyte of interest and the surface. Figure 4(f) schematizes

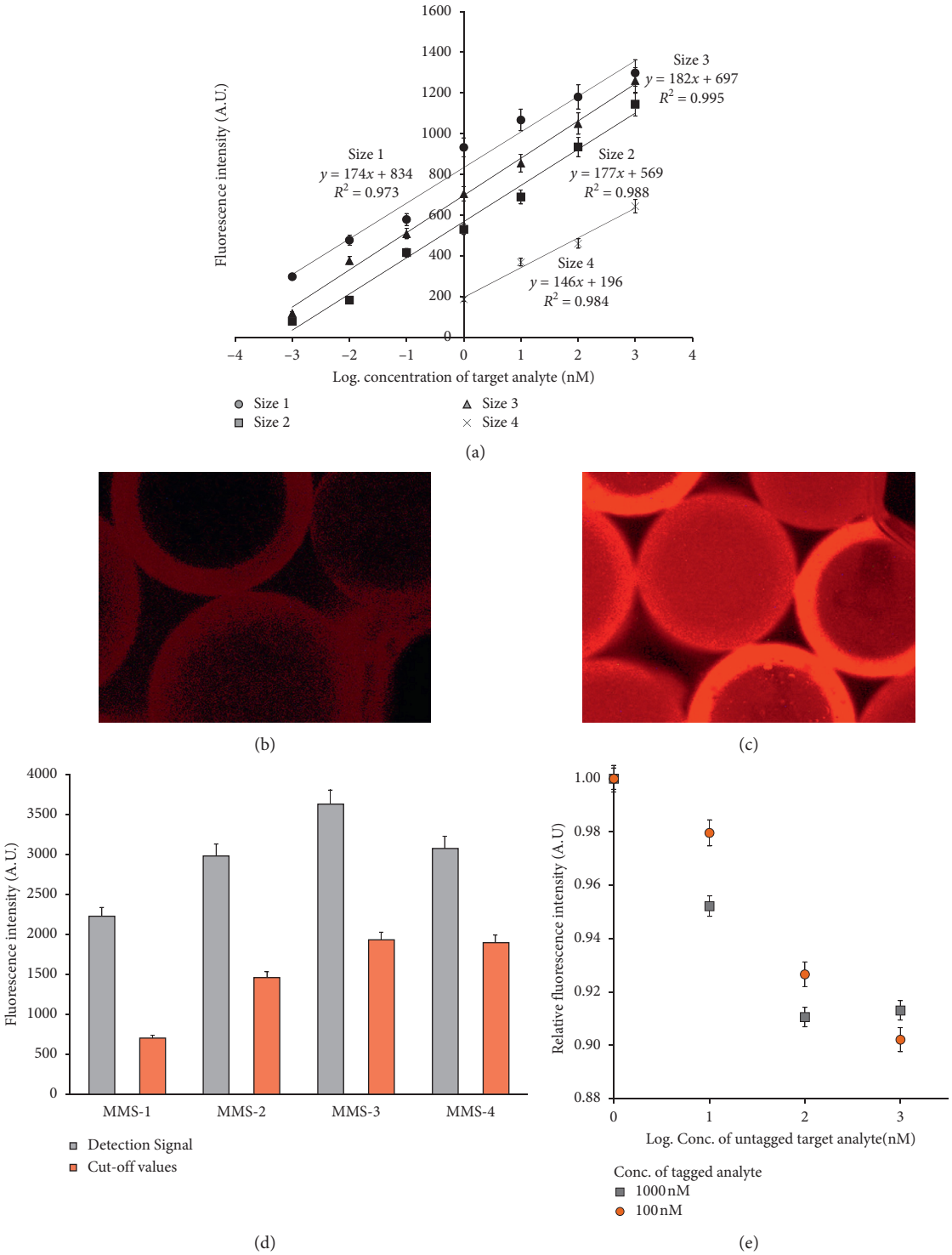

Figure 4: Continued.

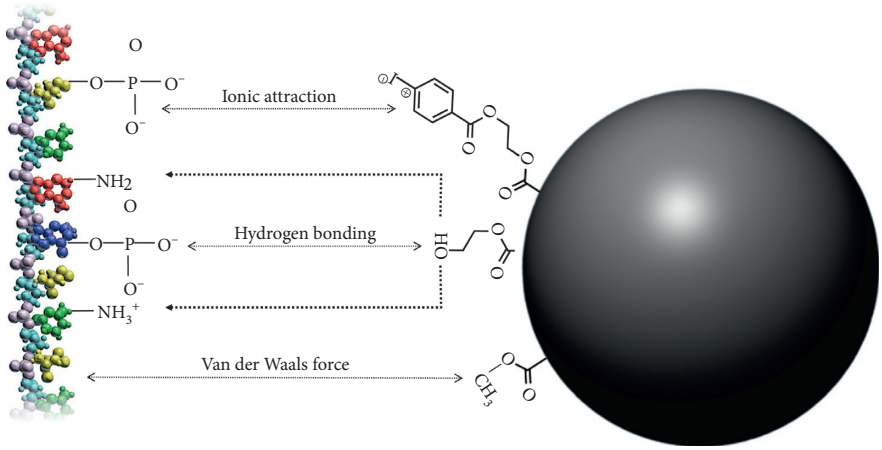

(f)

FIGURE 4: Performance analysis of the microspheres for detection of miR159: (a) calibration curves plotted for different size categories of the spheres in varied concentrations of the labeled miRNA (1 nM, 10 nM, 100 nM and 1000 nM, 100 pM, 10 pM, and 1 pM); (b, c) fluorescence images of the spheres (MMS-3 as the representative) after detection of 1 nM and 100 nM of the labeled miRNA, respectively; (d) performance analysis of the spheres via indirect detection of miRNA in comparison to the cutoff values, which are twice that of the average negative controls calculated for different size categories (concentration of the labeled miRNA = 1 nM); (e) relative fluorescence signal resulting from competitive assay conducted with a mixture of fluorescent Cy3-miR159 (concentration: 1000 nM or 100 nM) and non-conjugated miR159 at different concentrations (1000, 100, and 10 nM); and (f) schematic representation of the possible physical interactions between the sphere's surface and a capture probe.

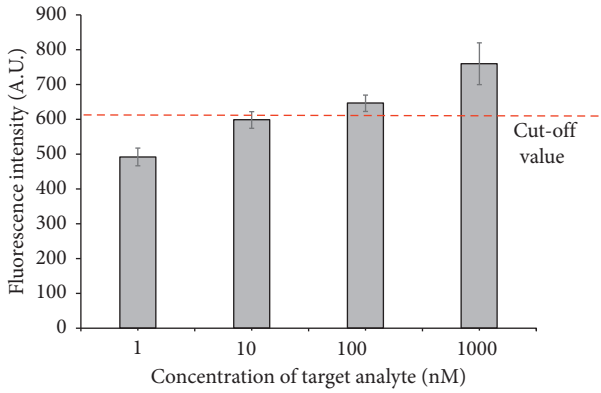

(a)

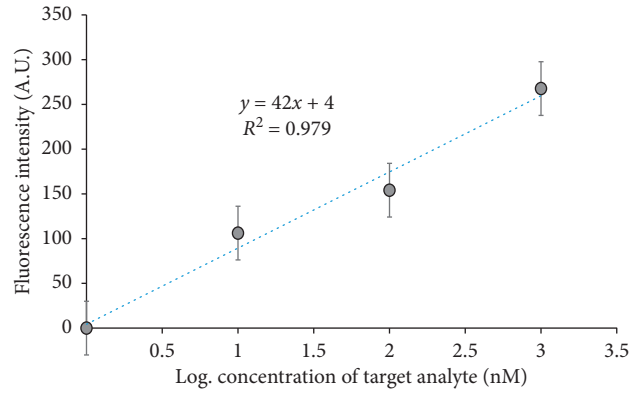

(b)

Detection status	96-wellplate +	96-wellplate −
Positive (TP, FP)	10	8
Negative (FN, TN)	10	2
Total	20	10

Evaluation parameters	96-wellplate
Sensitivity (%)	50
Specificity (%)	80
Accuracy (%)	40
LoD (nM)	15×10^3

(c)

FIGURE 5: Performance evaluation of conventional 96-well plates: (a) performance analysis of the conventional well plate in miRNA detection (concentration of the labeled miRNA = 1 nM); (b) ELISA calibration curve plotted for varied concentrations of the labeled miRNA (1 nM, 10 nM, 100 nM, and 1000 nM); (c) evaluation of the assay and calculated analytical sensitivity, specificity, accuracy, and LOD.

the possible physical interactions between the engineered surface of the spheres and the nucleotide strands. Hydrogen bonding (H-bond) between the $-PO_4^-$ and the $-NH_2$ groups of the capture probe and -OH groups of the spheres has the highest likelihood. The H-bond occurs between the H atoms of the spheres' -OH groups (O and H are covalently bound) and the N and O atoms of the miRNAs with lone-pair electrons. Furthermore, aromatic rings of the spheres can involve negatively charged $-PO_4^-$ groups of the biomolecules in ionic attraction (electrostatic interaction) [62]. Moreover, carbonyl groups (-C=O) of the spheres could promote van der Waals forces in interaction with the biomolecules [63].

Table 1: Calculated analytical sensitivity, specificity, accuracy, and LOD of the microspheres in miRNA detection.

Detection status	MMS-1		MMS-2		MMS-3		MMS-4	
	+	−	+	−	+	−	+	−
Positive (TP, FP)	20	1	20	3	20	3	20	3
Negative (FN, TN)	0	9	0	8	0	7	0	7
Total	20	10	20	10	20	10	20	10
Sensitivity (%)	100		100		100		100	
Specificity (%)	90		80		70		70	
Accuracy (%)	93		90		86		90	
LOD (pM)	90		40		50		2×10^6	

Table 2: Comparison of the current method with the commercial technologies for miRNA detection.

Platform	Time (min)	Complexity	Accessibility	Specificity	Sensitivity	LOD	References
Gel electrophoresis assays	~280	Moderately complex depending on the assay type	Highly accessible in regular laboratory setups	Standard procedure may induce a chance for nonspecific binding; DNA fragments of interest must be gel-purified and verified to avoid nonspecific bindings	Not suitable for detecting low concentrations	Depends on the assay type (picomolar rage)	[80, 81]
Polymerase chain reaction (PCR)	~35	Complex, expensive, time-consuming, and labor-intensive	Not amenable to many laboratory setups	Highly specific	Accuracy can be compromised by contamination causing amplification of spurious DNA products	Femtomolar range	[65]
Real time polymerase chain reaction (RT-PCR/ qRT-PCR)	~120	Primer design, normalization, and optimization techniques are complex	Involves challenging and individualized processes		High-throughput quantification of miRNAs is error prone		[65, 82]
Polymethacrylate sphere-based assay	~240	Simple and straightforward	Highly accessible in regular laboratory setups	Moderately specific	Highly sensitive	Picomolar range	Current study

Additionally, hydrophobic interaction can play a major role in attracting miRNAs to the surface [62, 64], since the monomers involved in chemical synthesis of the spheres are mostly hydrophobic in their nature [37]. This multitude of physical attraction can strongly influence the biomolecular immobilization and subsequent detection of the miRNAs. Noteworthy that the inherent presence of the surface functional groups on the spheres also promotes covalent attachment of biomolecules to the surface via application of zero-length cross-linking agents or spacer [49, 56].

3.8. Evaluation of the Assay. The assay conducted in a conventional 96-well plate without microspheres was conducted and evaluated for its performance in miRNA detection. Figure 5 provides a detailed analysis of the conventional assay in detection of miR159: (A) detection performance; (B) calibration analysis; and (C) evaluation of the assay. The conventional assay in a 96-well plate shows a rather low detection ability in comparison with the obtained cutoff values that correspond to the negative controls (Figure 5(a)). While the calibration plot refers to a standard linearity level, the assay has proven to suffer from low analytical sensitivity (50%), low accuracy (40%), and unacceptable LOD (Figure 5(c)). A comparison between performance of the 96-well plate with and without microspheres shows a significant detection enhancement due to the presence of microspheres (Figure 5(c)). In particular, size 3 group of the spheres marks a 10-fold higher fluorescence intensity in comparison with that of conventional assay

which enables the detection of challenging biomolecules as miRNAs by *gold standard* technique.

Table 1 summarizes the evaluation parameters for the assay conducted with integrated microspheres. As can be seen, application of the spheres within the conventional assay resulted in 100% analytical sensitivity regardless of the size category. MMS-1, in particular, improved the analytical specificity considerably. Except for MMS-4, all size categories have shown LODs within a picomolar range which is highly desirable for miRNA detection. In the case of MMS-4, recorded standard deviation for lowest concentration of the analyte contributed to the LOD outcome which is not as favorable as those of other size groups. It is noteworthy that the high TB absorption by this size category (MMS-4) does not guarantee its better performance in the analytical assay since the evaluation parameters are also the function of key elements such as the negative control, the calibration curve's slope, and the standard deviation.

While a vast number of reports in the literature provides insight into biodiagnosis strategies, sensitive, selective, accessible, and cost-effective miRNA detection remains a challenge [65]. Circulating miRNAs are present in blood at ng/mL levels. This, according to the length of a fragment, corresponds to a molecular concentration within a picomolar range [66]. Taking the abundance of miRNAs into account, a high level of sensitivity and selectivity is required to detect these challenging bioentities in an effective manner. While several efforts have introduced new methodologies or modified strategies for ultrasensitive targeting miRNAs [67–79], the conventional detection is currently performed by gel electrophoresis assays, polymerase chain reaction (PCR), and real-time polymerase chain reaction (RT-PCR/qRT-PCR). Table 2 provides a comparison between different aspects of commercially applied techniques in comparison with the proposed method here. This table summarizes time, complexity, accessibility, specificity, sensitivity, and LOD for these techniques. While the presented strategy in this study is not as powerful as PCR or qRT-PCR (comparison of the LOD in Table 2), it can be widely accessible in any laboratory setup. This, however, is not the case for PCR/RT-PCR, which is typically operated with highly sophisticated machinery. Further LOD enhancement of the presented strategy can be achieved by incorporating shaking/mixing techniques that would allow spheres to have higher chance of interaction with biomolecules. Comparatively, the proposed strategy offers the least complexity of operation. 96-well plates are available almost in any laboratory setup, and lab technicians familiar with gold standard detection methods could carry out the assay protocols without further training. Most importantly, PCR/RT-PCR is far more inexpensive when compared to the proposed assay while its accuracy might be compromised by contamination.

4. Conclusion

In this work, we have demonstrated a proof-of concept methodology for miRNA detection. Methacrylate microspheres were integrated into a 96-well plate, and immobilized DNA probes were used to capture and detect miR159 within a picomolar range. All important parameters of the assay including analytical sensitivity, specificity, accuracy, and the limit of detection were improved due to the presence of the spheres. This is particularly promising as this simple integration offers the chance of biorecognition for challenging biomolecules including miRNAs within a conventional platform that is typically available in any laboratory setup. Application of the polymer microspheres hold a great potential as they are cost-effective bioreceptive platforms that can be mass-produced in desirable size ranges and with controlled properties depending on the type of desired biorecognition.

Data Availability

All data are presented within the manuscript.

Conflicts of Interest

The authors declare no conflicts of interest.

Authors' Contributions

Samira Hosseini and Patricia Vázquez-Villegas contributed equally to the work. Marc Madou was responsible for conceptualization. Samira Hosseini, Patricia Vázquez-Villegas, and Margarita Sanchez-Dominguez were involved in formal analysis. Sergio Martínez-Chapa carried out funding acquisition. Samira Hosseini, Patricia Vázquez-Villegas, and Leo Koole performed methodology. Marco Rito-Palomares was responsible for project administration. Marco Rito-Palomares and Leo Koole provided resources. Samira Hosseini, Richard Willson, Leo Koole, Marc Madou, and Sergio Martínez-Chapa supervised the study. Samira Hosseini and Marc Madou wrote the original draft. Margarita Sanchez-Dominguez wrote and edited the manuscript.

Acknowledgments

The authors wish to acknowledge the financial support of Tecnológico de Monterrey, Bioprocess and Synthetic Biology Chair (Grant 0821C01004). The authors also would like to acknowledge the financial support of Tecnologico de Monterrey, Mexico, for the special grant (grant number: 002EICII01) awarded to the Nano-sensors and Devices Focus Group, School of Engineering and Sciences, Tecnologico de Monterrey, Monterrey, Mexico. The authors would also like to acknowledge Dr. Oscar E. Vega and Dr. J. Alejandro Arizpe-Zapata (CIMAV S.C. Unidad Monterrey) for conducting AFM analysis and Raman measurements, respectively.

References

[1] K. A. Cissell and S. K. Deo, "Trends in microRNA detection," *Analytical and Bioanalytical Chemistry*, vol. 394, no. 4, pp. 1109–1116, 2009.

[2] N. E. Larkey, L. Zhang, S. S. Lansing, V. Tran, V. L. Seewaldt, and S. M. Burrows, "Förster resonance energy transfer to

impart signal-on and -off capabilities in a single microRNA biosensor," *The Analyst*, vol. 141, no. 22, pp. 6239–6250, 2016.

[3] Y. H. Roh, S. J. Sim, I.-J. Cho, N. Choi, and K. W. Bong, "Vertically encoded tetragonal hydrogel microparticles for multiplexed detection of miRNAs associated with Alzheimer's disease," *The Analyst*, vol. 141, no. 15, pp. 4578–4586, 2016.

[4] Y. Li, J. Zhang, J. Zhao, L. Zhao, Y. Cheng, and Z. Li, "A simple molecular beacon with duplex-specific nuclease amplification for detection of microRNA," *The Analyst*, vol. 141, no. 3, pp. 1071–1076, 2016.

[5] F. Degliangeli, P. P. Pompa, and R. Fiammengo, "Nanotechnology-based strategies for the detection and quantification of MicroRNA," *Chemistry—A European Journal*, vol. 20, no. 31, pp. 9476–9492, 2014.

[6] J. Liu, X. Jiang, R. Zhang et al., "MXene-enabled electrochemical microfluidic biosensor: applications toward multicomponent continuous monitoring in whole blood," *Advanced Functional Materials*, vol. 29, no. 6, Article ID 1807326, 2019.

[7] N. E. Larkey, C. K. Almlie, V. Tran, M. Egan, and S. M. Burrows, "Detection of miRNA using a double-strand displacement biosensor with a self-complementary fluorescent reporter," *Analytical Chemistry*, vol. 86, no. 3, pp. 1853–1863, 2014.

[8] M. de Planell-Saguer and M. C. Rodicio, "Analytical aspects of microRNA in diagnostics: a review," *Analytica Chimica Acta*, vol. 699, no. 2, pp. 134–152, 2011.

[9] Y.-S. Borghei, M. Hosseini, M. R. Ganjali, and S. Hosseinkhani, "Label-free fluorescent detection of microRNA-155 based on synthesis of hairpin DNA-templated copper nanoclusters by etching (top-down approach)," *Sensors and Actuators B: Chemical*, vol. 248, pp. 133–139, 2017.

[10] F. Causa, A. Aliberti, A. M. Cusano, E. Battista, and P. A. Netti, "Supramolecular spectrally encoded microgels with double strand probes for absolute and direct miRNA fluorescence detection at high sensitivity," *Journal of the American Chemical Society*, vol. 137, no. 5, pp. 1758–1761, 2015.

[11] Z. Lu, L. Zhang, Y. Deng, S. Li, and N. He, "Graphene oxide for rapid microRNA detection," *Nanoscale*, vol. 4, no. 19, pp. 5840–5842, 2012.

[12] J.-J. Li, Q. Xi, W.-F. Du, R.-Q. Yu, and J.-H. Jiang, "Label-free fluorescence detection of microRNA based on target induced adenosine2-coralyne-adenosine2 formation," *The Analyst*, vol. 141, no. 8, pp. 2384–2387, 2016.

[13] J. Raez, D. R. Blais, Y. Zhang et al., "Spectroscopically encoded microspheres for antigen biosensing," *Langmuir*, vol. 23, no. 12, pp. 6482–6485, 2007.

[14] R. Bellisario, R. J. Colinas, and K. A. Pass, "Simultaneous measurement of antibodies to three HIV-1 antigens in newborn dried blood-spot specimens using a multiplexed microsphere-based immunoassay," *Early Human Development*, vol. 64, no. 1, pp. 21–25, 2001.

[15] H. Dai, J. Zhu, Z. Yang et al., "A paramagnetic microspheres based automation-friendly rapid chemiluminescent immunoassay method for sensitive detection of chicken interferon-γ," *Chemical Communications*, vol. 49, no. 17, pp. 1708–1710, 2013.

[16] C. C. Hsu, C. E. Wobus, E. K. Steffen, L. K. Riley, and R. S. Livingston, "Development of a microsphere-based serologic multiplexed fluorescent immunoassay and a reverse transcriptase PCR assay to detect murine norovirus 1 infection in mice," *Clinical and Vaccine Immunology*, vol. 12, no. 10, pp. 1145–1151, 2005.

[17] A. J. Johnson, A. J. Noga, O. Kosoy, R. S. Lanciotti, A. A. Johnson, and B. J. Biggerstaff, "Duplex microsphere-based immunoassay for detection of anti-West Nile virus and anti-St. Louis encephalitis virus immunoglobulin M antibodies," *Clinical and Vaccine Immunology*, vol. 12, no. 5, pp. 566–574, 2005.

[18] P. Du and P. Liu, "Novel smart yolk/shell polymer microspheres as a multiply responsive cargo delivery system," *Langmuir*, vol. 30, no. 11, pp. 3060–3068, 2014.

[19] H. Weng, X. Huang, M. Wang, X. Ji, and X. Ge, "Formation of cagelike sulfonated polystyrene microspheres via swelling-osmosis process and loading of CdS nanoparticles," *Langmuir*, vol. 29, no. 49, pp. 15367–15374, 2013.

[20] O. Mero, M.-T. Sougrati, J.-C. Jumas, and S. Margel, "Engineered magnetic core-shell SiO_2/Fe microspheres and "Medusa-like" microspheres of SiO_2/iron oxide/carbon nanofibers or nanotubes," *Langmuir*, vol. 30, no. 32, pp. 9850–9858, 2014.

[21] C. Zhang, J. Luo, L. Ou et al., "Fluorescent porous carbazole-decorated copolymer monodisperse microspheres: facile synthesis, selective and recyclable detection of iron (III) in aqueous medium," *Chemistry—A European Journal*, vol. 24, no. 12, pp. 3030–3037, 2018.

[22] T. A. Taton, C. A. Mirkin, and R. L. Letsinger, "Scanometric DNA array detection with nanoparticle probes," *Science*, vol. 289, no. 5485, pp. 1757–1760, 2000.

[23] A. H. Alhasan, D. Y. Kim, W. L. Daniel et al., "Scanometric microRNA array profiling of prostate cancer markers using spherical nucleic acid-gold nanoparticle conjugates," *Analytical Chemistry*, vol. 84, no. 9, pp. 4153–4160, 2012.

[24] L. Jiang, D. Duan, Y. Shen, and J. Li, "Direct microRNA detection with universal tagged probe and time-resolved fluorescence technology," *Biosensors and Bioelectronics*, vol. 34, no. 1, pp. 291–295, 2012.

[25] L. Wang, Y. Cheng, H. Wang, and Z. Li, "A homogeneous fluorescence sensing platform with water-soluble carbon nanoparticles for detection of microRNA and nuclease activity," *The Analyst*, vol. 137, no. 16, pp. 3667–3672, 2012.

[26] H. Dong, J. Zhang, H. Ju et al., "Highly sensitive multiple microRNA detection based on fluorescence quenching of graphene oxide and isothermal strand-displacement polymerase reaction," *Analytical Chemistry*, vol. 84, no. 10, pp. 4587–4593, 2012.

[27] S. W. Yang and T. Vosch, "Rapid detection of MicroRNA by a silver nanocluster DNA probe," *Analytical Chemistry*, vol. 83, no. 18, pp. 6935–6939, 2011.

[28] B.-Z. Chi, R.-P. Liang, W.-B. Qiu, Y.-H. Yuan, and J.-D. Qiu, "Direct fluorescence detection of microRNA based on enzymatically engineered primer extension poly-thymine (EPEPT) reaction using copper nanoparticles as nano-dye," *Biosensors and Bioelectronics*, vol. 87, pp. 216–221, 2017.

[29] A. E. Prigodich, O.-S. Lee, W. L. Daniel, D. S. Seferos, G. C. Schatz, and C. A. Mirkin, "Tailoring DNA structure to increase target hybridization kinetics on surfaces," *Journal of the American Chemical Society*, vol. 132, no. 31, pp. 10638–10641, 2010.

[30] R. Liu, Q. Wang, Q. Li, X. Yang, K. Wang, and W. Nie, "Surface plasmon resonance biosensor for sensitive detection of microRNA and cancer cell using multiple signal amplification strategy," *Biosensors and Bioelectronics*, vol. 87, pp. 433–438, 2017.

[31] X. Qu, H. Jin, Y. Liu, and Q. Sun, "Strand displacement amplification reaction on quantum dot-encoded silica bead

for visual detection of multiplex MicroRNAs," *Analytical Chemistry*, vol. 90, no. 5, pp. 3482–3489, 2018.

[32] O. A. Goryacheva, A. S. Novikova, D. D. Drozd et al., "Water-dispersed luminescent quantum dots for miRNA detection," *TrAC Trends in Analytical Chemistry*, vol. 111, pp. 197–205, 2019.

[33] S. Hosseini, F. Ibrahim, I. Djordjevic, and L. H. Koole, "Recent advances in surface functionalization techniques on polymethacrylate materials for optical biosensor applications," *The Analyst*, vol. 139, no. 12, pp. 2933–2943, 2014.

[34] S. Hosseini and F. Ibrahim, *Current Optical Biosensors in Clinical Practice: Novel Polymeric Biochips for Enhanced Detection of Infectious Diseases*, Springer, Berlin, Germany, 2016.

[35] A. R. Chin, M. Y. Fong, G. Somlo et al., "Cross-kingdom inhibition of breast cancer growth by plant miR159," *Cell Research*, vol. 26, no. 2, pp. 217–228, 2016.

[36] S. Hosseini, M. M. Aeinehvand, S. M. Uddin et al., "Microsphere integrated microfluidic disk: synergy of two techniques for rapid and ultrasensitive dengue detection," *Scientific Reports*, vol. 5, no. 1, 2015.

[37] K. Saralidze, C. van Hooy-Corstjens, L. Koole, and M. Knetsch, "New acrylic microspheres for arterial embolization: combining radiopacity for precise localization with immobilized thrombin to trigger local blood coagulation," *Biomaterials*, vol. 28, no. 15, pp. 2457–2464, 2007.

[38] S. Sano, K. Kato, and Y. Ikada, "Introduction of functional groups onto the surface of polyethylene for protein immobilization," *Biomaterials*, vol. 14, no. 11, pp. 817–822, 1993.

[39] I. Djordjevic, N. R. Choudhury, N. K. Dutta, S. Kumar, E. J. Szili, and D. A. Steele, "Polyoctanediol citrate/sebacate bioelastomer films: surface morphology, chemistry and functionality," *Journal of Biomaterials Science, Polymer Edition*, vol. 21, no. 2, pp. 237–251, 2010.

[40] S. Hosseini, F. Ibrahim, I. Djordjevic, and L. H. Koole, "Polymethyl methacrylate-co-methacrylic acid coatings with controllable concentration of surface carboxyl groups: a novel approach in fabrication of polymeric platforms for potential bio-diagnostic devices," *Applied Surface Science*, vol. 300, pp. 43–50, 2014.

[41] S. Alcon, A. Talarmin, M. Debruyne, A. Falconar, V. Deubel, and M. Flamand, "Enzyme-linked immunosorbent assay specific to dengue virus type 1 nonstructural protein NS1 reveals circulation of the antigen in the blood during the acute phase of disease in patients experiencing primary or secondary infections," *Journal of Clinical Microbiology*, vol. 40, no. 2, pp. 376–381, 2002.

[42] E. M. Linares, C. S. Pannuti, L. T. Kubota, and S. Thalhammer, "Immunospot assay based on fluorescent nanoparticles for dengue fever detection," *Biosensors and Bioelectronics*, vol. 41, pp. 180–185, 2013.

[43] S. J. Reinholt, A. Sonnenfeldt, A. Naik, M. W. Frey, and A. J. Baeumner, "Developing new materials for paper-based diagnostics using electrospun nanofibers," *Analytical and Bioanalytical Chemistry*, vol. 406, no. 14, pp. 3297–3304, 2014.

[44] A. Shrivastava and V. Gupta, "Methods for the determination of limit of detection and limit of quantitation of the analytical methods," *Chronicles of Young Scientists*, vol. 2, no. 1, p. 21, 2011.

[45] N. Swamy, K. N. Prashanth, and K. Basavaiah, "Titrimetric and spectrophotometric assay of diethylcarbamazine citrate in formulations using iodate and iodide mixture as reagents," *Brazilian Journal of Pharmaceutical Sciences*, vol. 51, no. 1, pp. 43–52, 2015.

[46] M. Gad, H. Zaazaa, S. Amer, and M. Korany, "Static headspace gas chromatographic method for the determination of residual solvents in cephalosporins," *RSC Advances*, vol. 5, no. 22, pp. 17150–17159, 2015.

[47] S. M. Bauer, M. Gehringer, and S. A. Laufer, "A direct enzyme-linked immunosorbent assay (ELISA) for the quantitative evaluation of Janus Kinase 3 (JAK3) inhibitors," *Analytical Methods*, vol. 6, no. 21, pp. 8817–8822, 2014.

[48] A. G. Pereira, F. B. D'Avila, P. C. L. Ferreira, M. G. Holler, R. P. Limberger, and P. E. Fröehlich, "Determination of cocaine, its metabolites and pyrolytic products by LC-MS using a chemometric approach," *Analytical Methods*, vol. 6, no. 2, pp. 456–462, 2014.

[49] J. M. Goddard and J. H. Hotchkiss, "Polymer surface modification for the attachment of bioactive compounds," *Progress in Polymer Science*, vol. 32, no. 7, pp. 698–725, 2007.

[50] J. L. Koenig, *Spectroscopy of Polymers*, Elsevier, Amsterdam, Netherlands, 1999.

[51] T. H. Qazi, R. Rai, and A. R. Boccaccini, "Tissue engineering of electrically responsive tissues using polyaniline based polymers: a review," *Biomaterials*, vol. 35, no. 33, pp. 9068–9086, 2014.

[52] E. Evlyukhin, L. Museur, M. Traore, C. Perruchot, A. Zerr, and A. Kanaev, "A new route for high-purity organic materials: high-pressure-ramp-induced ultrafast polymerization of 2-(hydroxyethyl) methacrylate," *Scientific Reports*, vol. 5, p. 18244, 2015.

[53] C. C. Bonang and S. M. Cameron, "Resonance Raman and hyper-Raman scattering from monosubstituted benzenes," *Chemical Physics Letters*, vol. 187, no. 6, pp. 619–622, 1991.

[54] C. Navarra, M. Cadenaro, A. Frassetto, L. Fontanive, R. Di Lenarda, and L. Breschi, "Degree of conversion of self-etch adhesives: in situ micro-Raman analysis," *Operative Dentistry*, vol. 41, no. 5, pp. 501–510, 2016.

[55] K. Thomas, M. Sheeba, V. Nampoori, C. Vallabhan, and P. Radhakrishnan, "Raman spectra of polymethyl methacrylate optical fibres excited by a 532 nm diode pumped solid state laser," *Journal of Optics A: Pure and Applied Optics*, vol. 10, Article ID 055303, 2008.

[56] Y. Bai, C. G. Koh, M. Boreman et al., "Surface modification for enhancing antibody binding on polymer-based microfluidic device for enzyme-linked immunosorbent assay," *Langmuir*, vol. 22, no. 22, pp. 9458–9467, 2006.

[57] S. Hosseini, F. Ibrahim, I. Djordjevic et al., "Synthesis and processing of ELISA polymer substitute: the influence of surface chemistry and morphology on detection sensitivity," *Applied Surface Science*, vol. 317, pp. 630–638, 2014.

[58] J. Jebaramya, M. Ilanchelian, and S. Prabahar, "Spectral studies of toluidine blue o in the presence of sodium dodecyl sulfate," *Sensors*, vol. 21, p. 22, 2009.

[59] H. G. Hansma, I. Revenko, K. Kim, and D. E. Laney, "Atomic force microscopy of long and short double-stranded, single-stranded and triple-stranded nucleic acids," *Nucleic Acids Research*, vol. 24, no. 4, pp. 713–720, 1996.

[60] G. Sridharan and A. Shankar, "Toluidine blue: a review of its chemistry and clinical utility," *Journal of Oral and Maxillofacial Pathology*, vol. 16, no. 2, pp. 251–255, 2012.

[61] H. Arata, H. Komatsu, A. Han, K. Hosokawa, and M. Maeda, "Rapid microRNA detection using power-free microfluidic chip: coaxial stacking effect enhances the sandwich hybridization," *The Analyst*, vol. 137, no. 14, pp. 3234–3237, 2012.

[62] J.-Y. Yoon, H.-Y. Park, J.-H. Kim, and W.-S. Kim, "Adsorption of BSA on highly carboxylated microspheres-quantitative effects of surface functional groups and

interaction forces," *Journal of Colloid and Interface Science*, vol. 177, no. 2, pp. 613–620, 1996.

[63] S. H. Lee and E. Ruckenstein, "Adsorption of proteins onto polymeric surfaces of different hydrophilicities-a case study with bovine serum albumin," *Journal of Colloid and Interface Science*, vol. 125, no. 2, pp. 365–379, 1988.

[64] A. Kondo and K. Higashitani, "Adsorption of model proteins with wide variation in molecular properties on colloidal particles," *Journal of Colloid and Interface Science*, vol. 150, no. 2, pp. 344–351, 1992.

[65] T. Tian, J. Wang, and X. Zhou, "A review: microRNA detection methods," *Organic & Biomolecular Chemistry*, vol. 13, no. 8, pp. 2226–2238, 2015.

[66] S. O. Kelley, "What are clinically relevant levels of cellular and biomolecular analytes?" *ACS Sensors*, vol. 2, no. 2, pp. 193–197, 2017.

[67] M. N. Islam, M. K. Masud, N.-T. Nguyen et al., "Gold-loaded nanoporous ferric oxide nanocubes for electrocatalytic detection of microRNA at attomolar level," *Biosensors and Bioelectronics*, vol. 101, pp. 275–281, 2018.

[68] H. Yang, A. Hui, G. Pampalakis et al., "Direct, electronic microRNA detection for the rapid determination of differential expression profiles," *Angewandte Chemie International Edition*, vol. 48, no. 45, pp. 8461–8464, 2009.

[69] M. N. Islam, S. Moriam, M. Umer et al., "Naked-eye and electrochemical detection of isothermally amplified HOTAIR long non-coding RNA," *The Analyst*, vol. 143, no. 13, pp. 3021–3028, 2018.

[70] M. K. Masud, M. N. Islam, M. H. Haque et al., "Gold-loaded nanoporous superparamagnetic nanocubes for catalytic signal amplification in detecting miRNA," *Chemical Communications*, vol. 53, pp. 8231–8234, 2017.

[71] K. M. Koo, L. G. Carrascosa, M. J. A. Shiddiky, and M. Trau, "Amplification-free detection of gene fusions in prostate cancer urinary samples using mRNA-gold affinity interactions," *Analytical Chemistry*, vol. 88, no. 13, pp. 6781–6788, 2016.

[72] K. M. Koo, L. G. Carrascosa, M. J. A. Shiddiky, and M. Trau, "Polyextensions of miRNAs for amplification-free electrochemical detection on screen-printed gold electrodes," *Analytical Chemistry*, vol. 88, no. 4, pp. 2000–2005, 2016.

[73] H. Lee, J.-E. Park, and J.-M. Nam, "Bio-barcode gel assay for microRNA," *Nature Communications*, vol. 5, no. 1, p. 3367, 2014.

[74] C. Wang, Q. Ding, P. Plant et al., "Droplet digital PCR improves urinary exosomal miRNA detection compared to real-time PCR," *Clinical Biochemistry*, vol. 67, pp. 54–59, 2019.

[75] B. Tian, Z. Qiu, J. Ma et al., "On-particle rolling circle amplification-based core-satellite magnetic superstructures for microRNA detection," *ACS Applied Materials & Interfaces*, vol. 10, no. 3, pp. 2957–2964, 2018.

[76] R. Tian, Y. Li, and J. Bai, "Hierarchical assembled nanomaterial paper based analytical devices for simultaneously electrochemical detection of microRNAs," *Analytica Chimica Acta*, vol. 1058, pp. 89–96, 2019.

[77] Z.-Z. Yang, Z.-B. Wen, X. Peng, Y.-Q. Chai, W.-B. Liang, and R. Yuan, "A novel fluorescent assay for the ultrasensitive detection of miRNA-21 with the use of G-quadruplex structures as an immobilization material for a signal indicator," *Chemical Communications*, vol. 55, no. 45, pp. 6453–6456, 2019.

[78] J. Wang, J. Lu, S. Dong et al., "An ultrasensitive electrochemical biosensor for detection of microRNA-21 based on redox reaction of ascorbic acid/iodine and duplex-specific nuclease assisted target recycling," *Biosensors and Bioelectronics*, vol. 130, pp. 81–87, 2019.

[79] T. Xue, W. Liang, Y. Li et al., "Ultrasensitive detection of miRNA with an antimonene-based surface plasmon resonance sensor," *Nature Communications*, vol. 10, p. 28, 2019.

[80] https://www.thermofisher.com/mx/es/home/life-science/pcr/real-time-pcr/real-time-pcr-learning-center/real-time-pcr-basics/benefits-fast-real-time-pcr.html.

[81] A. Drabik, A. Bodzoń-Kułakowska, and J. Silberring, "Gel electrophoresis," in *Proteomic Profiling and Analytical Chemistry*, P. Ciborowski and J. Silberring, Eds., pp. 115–143, Elsevier, Boston, MA, USA, 2nd edition, 2016.

[82] E. Varkonyi-Gasic, R. Wu, M. Wood, E. F. Walton, and R. P. Hellens, "Protocol: a highly sensitive RT-PCR method for detection and quantification of microRNAs," *Plant Methods*, vol. 3, no. 1, p. 12, 2007.

Hindawi
Advances in Polymer Technology
Volume 2020, Article ID 9040535, 21 pages
https://doi.org/10.1155/2020/9040535

Review Article

Essential Oils-Loaded Electrospun Biopolymers: A Future Perspective for Active Food Packaging

Shahla Ataei,[1] **Pedram Azari**,[2,3] **Aziz Hassan**,[1] **Belinda Pingguan-Murphy**,[2] **Rosiyah Yahya**,[1] **and Farina Muhamad**[2]

[1]*Department of Chemistry, University of Malaya, 50603 Kuala Lumpur, Malaysia*
[2]*Department of Biomedical Engineering, Faculty of Engineering, University of Malaya, 50603 Kuala Lumpur, Malaysia*
[3]*Centre for Applied Biomechanics, Department of Biomedical Engineering, Faculty of Engineering, University of Malaya, 50603 Kuala Lumpur, Malaysia*

Correspondence should be addressed to Shahla Ataei; sh.ataei.k@gmail.com and Farina Muhamad; farinamuhamad@um.edu.my

Received 15 October 2019; Accepted 13 December 2019; Published 21 February 2020

Guest Editor: Samira Hosseini

The growth of global food demand combined with the increased appeal to access different foods from every corner of the globe is forcing the food industry to look for alternative technologies to increase the shelf life. Essential oils (EOs) as naturally occurring functional ingredients have shown great prospects in active food packaging. EOs can inhibit the growth of superficial food pathogens, modify nutritious values without affecting the sensory qualities of food, and prolong the shelf life when used in food packaging as an active ingredient. Since 2016, various reports have demonstrated that combinations of electrospun fibers and encapsulated EOs could offer promising results when used as food packaging. Such electrospun platforms have encapsulated either pure EOs or their complexation with other antibacterial agents to prolong the shelf life of food products through sustained release of active ingredients. This paper presents a comprehensive review of the essential oil-loaded electrospun fibers that have been applied as active food packaging material.

1. Introduction

For many decades, synthetic polymers have dominated food packaging industry due to their favourable properties such as softness, lightness, and transparency. So far, petrochemical-based plastics such as polyethylene terephthalate (PET), polyvinylchloride (PVC), polyethylene (PE) [1], polypropylene (PP) [2], polystyrene (PS) [3], and polyamide (PA) [4] have been extensively used as packaging materials as a result of their low cost of synthesis, decent mechanical performance, lack of permeability to oxygen, carbon dioxide, anhydride, and aromatic compounds as well as heat sealability, all of which contribute to food preservation and waste reduction. Despite several desirable properties, the usage of conventional plastics needs to be restricted since their long degradation cycles pose serious ecological threats to the environment. Therefore, it is increasingly important to employ novel biodegradable raw materials. Although complete replacement of conventional plastics with eco-friendly plastics is impossible to achieve, at least for specific applications such as food packaging, the use of biobased active food packaging seems to be a realistic solution. Active food packaging is a new method to prolong the shelf life of food products and to maintain of their safety, quality, and integrity. According to the European regulation (EC) No. 450/2009, active packaging consists of systems that interact with the food as they would absorb substances such as moisture, carbon dioxide, or odour from packaged food or release desired materials such as antimicrobial, antioxidant compounds or flavours into the packaged food (European Commission 2009) [5]. Despite the importance of active food packaging, there are limitations associated with the existing polymeric materials to serve as optimal active packaging and modifications are necessary. Such modifications involve addition

of other additives such as antimicrobial and antioxidant agents which are required.

EOs derived from different parts of aromatic plants have been extensively researched for being a natural product and their nutritional health benefits. The main interest in EOs lies in their various therapeutic properties, namely, antioxidant, antimicrobial, antitumour, analgesic, insecticidal, antidiabetic, and anti-inflammatory [6–9]. As of 2019, the number of published papers regarding essential oils in food industry is almost 800 papers, indicating the use of EOs as biopreservatives in all types of foods [10].

EOs hold great potential for active food packaging applications as they can be directly added to the food products or incorporated into food packaging for gradual release during transportation and storage to improve shelf life and preservation [11]. Although EOs have been demonstrated as an alternative to chemical preservatives in active food packaging systems, they are associated with certain limitations that need to be resolved for successful incorporation in active food packaging systems. High volatility, low aqueous solubility, and intense smell are the major shortcomings that have limited the usage of EOs in food industry. Therefore, the encapsulation of oils has been considered as a key solution in food packaging. Recent advances in encapsulation technology have improved the stability of sensitive components during production, through a reduction in evaporation and degradation of volatile compounds as well as firmer control over the capsules' dimensions, shape, and morphology during the encapsulation process [12, 13]. These methods carry out chemical encapsulation through ionic gelation, simple and complex coacervation, cocrystallization, interfacial polymerization, molecular inclusion, entrapment in liposomes, and ionic gelation plus electrostatic interactions [14].

Among the various approaches for nanoencapsulation, electrospinning is a versatile, easy to operate method for continuous fabrication of nanostructures [15]. Electrospun membranes exhibit a fibrous morphology with large surface area to volume ratio, high porosity, and fiber diameters in the range of nano to micron, all of which are favourable properties for the sustained release of active ingredients from the packaging membrane to the surface of the food [16]. While electrospinning is widely applied in the fields of tissue engineering [17], wound dressing [18], enzyme immobilization [19], and electrode materials [20], its application as food packaging is only recently explored [21]. These recent advances in applications of loaded electrospun membranes in active food packaging call for a review on this topic. Although there are several reviews on relevant topics, the subject has the potential to be reviewed on its own merits.

Fernández-López and Viuda-Martos studied application of EOs in food systems [10]. Ribeiro-Santos et al. reviewed application of EOs incorporated into films and coatings in food packaging. Films containing EOs are usually produced via casting method [22]. In another study, São Pedro et al. reviewed nanoencapsulation of EOs into lipid carriers such as solid lipid nanoparticles, liposomes, and nanoemulsions for drug delivery systems. They concluded significant improvement in antimicrobial activity of EOs [23]. In the above-mentioned reviews, the authors have emphasized the potential of EOs to be used as a part of packaging materials or their direct incorporation into the food matrix. However, this review focuses on EOs, as effective protective antimicrobials, and their incorporation in active food packaging through electrospinning. The properties of the polymeric matrices, main active components of Eos, and encapsulation through electrospinning are reviewed. The main objective of this review is to provide a broad insight into the potential applications of electrospun nanofibers encapsulating EOs as active food packaging materials. To the best knowledge of the authors, there is no review available on application of encapsulated EOs in food packaging using electrospinning technique.

2. Essentials Oils (EOs) for Active Food Packaging

EOs are produced by angiospermic plants and have found various usages in different industries [24]. Among all the plant species, only aromatic plants are sources of EOs. Aromatic plants form about 10% of plant species (over 17,000) and are well distributed around world [25]. EOs are secondary metabolites which could be derived from different plant organs including flowers (jasmine, rose, chamomile, violet, and lavender), buds (clove), leaves (thyme, eucalyptus, salvia, and rosemary), fruits (star anise), twigs (*Luma chequen*), bark (cinnamon), seeds (cardamom), wood (sandal), rhizome, and roots (ginger), all of which have the potential to be applied in food packaging as antimicrobial and antioxidant agents [26–30].

The chemical composition and quality of EOs depend on characteristics of the source plant such as growth conditions, variety, geographical origin, age, season, and condition of the plant when harvested. Extraction method, analysis conditions, and processing chemicals can also affect their properties [31–34]. Their extraction yield is usually very low (about 1%) which makes them valuable rare substances. EOs consist of concentrated lipophilic volatile aroma compounds including terpenes, terpenoids, and phenol-derived aromatic and aliphatic components. The phenolic compounds in EOs can diminish or almost eliminate the presence of microorganisms and minimize lipid oxidation [35].

The natural extracts of EOs are classified as Generally Recognized as Safe (GRAS) by the US Food and Drug Administration (FDA) and received approval for safety and effectiveness [36]. Therefore, in food related application, they are more suitable alternatives to synthetic antioxidants such as butylated hydroxytoluene (BHT) or butylated hydroxyanisole (BHA) which might have a carcinogenic effect [36].

These oils are substances accountable for the active function of packaging with the flexibility to be settled in a different container or be directly added to the packaging material. In either of the cases, the release of the oils during transportation and storage leads to increased shelf life.

Electrospun-loaded EOs could be the answer to market demands as they allow foods to reach the consumers with

their original or enhanced organoleptic properties, increased shelf life, and improved safety [37–40]. The packaging materials produced in these systems can contain active ingredients designed for sustained release during storage or transportation to delay food deterioration.

Table 1 summarizes the essential oils that have been successfully used in food packaging for improved efficiency.

3. Electrospinning and Nanoencapsulation in Active Food Packaging

Electrospinning which was first patented by Cooley and Morton in 1902 is a straightforward method for producing continuous micro- and nanofibers [62]. Unlike the conventional methods of fiber production which are based on application of mechanical force, electrospinning uses high-voltage electrostatic repulsive force for drawing and fiber stretching. Therefore, via electrospinning, it is possible to obtain fibers with diameters in the range of nanometres [63]. A typical electrospinning device is made up of a high voltage power source, a pump with tuneable feeding rate, a capillary as spinneret, and a collector. High voltage power source oppositely charges the capillary (commonly more than 10 kV) and the collector creating the pulling force for whipping instability [63]. When the charges building up within the polymer solution accumulate to a critical amount, a jet starts initiation from the capillary tip. The jet undergoes uniaxial stretching and thinning, while moving toward the oppositely charged collector and solvent evaporation is happening in the meantime. Once the jet reaches the collector, all the solvent should be evaporated, and formation of micro- or nanofibrous morphologies should have taken place. There are two sets of parameters that affect the morphology of the electrospinning products: intrinsic parameters such as solution viscosity, solvent evaporation rate, and conductivity of the polymer solution and processing parameters which include applied voltage, feeding rate, collector shape and texture, and collection distance [64]. Figure 1 shows the various aspects involved in production of encapsulated electrospun fibers including EO extraction (Figure 1(a)), complexation and solution preparation (Figure 1(b)), and a typical electrospinning system (Figure 1(c)). Several other techniques such as phase separation, bicomponent extrusion, template synthesis, drawing, centrifugal spinning, and melt blowing have been reported to produce polymeric micro/nanofibers [65–69]. However, for food applications, most of these methods suffer from various shortcomings such as difficulty of control, lack of applicability to a wide range of materials, and exposure to chemicals affecting the stability of sensitive nutrients and prohibiting their usage due to toxicity concerns [70–72]. Due to their size and high specific surface area, electrospun nanofibers have an edge in encapsulation efficiencies and demonstrate major potential for applications requiring controlled release of active ingredients, while exhibiting appropriate levels of biodegradability and biocompatibility [73]. The electrospun antimicrobial membranes are fabricated by adding antimicrobial agents into the polymer solution followed by electrospinning. Although the incorporation of EOs into nanofibers was demonstrated earlier, there was no report on the application of electrospun-loaded EOs for antimicrobial packaging materials until 2016 [74]. Biopolymers such as polyvinyl alcohol (PVA) [75], chitosan (CS) [74], polycarbonate (PC) [76], and polyethylene oxide (PEO) [77] have been popular options for encapsulation of EOs through electrospinning because of their excellent properties in generating nanofibers and membranes [21].

Within the last few years, nanoencapsulation of biological compounds in carrier materials has found its way to food technology as a simple yet effective technique for modification of the quality of food and preservation [78]. Encapsulation is effective in enhancing the stability and solubility of EOs as well as masking their strong flavour. Due to the hydrophobicity, instability, and volatility of EOs, they usually cannot be directly added to electrospinning solution and a carrier substance such as cyclodextrins (CDs), liposomes (LO), and CS is usually required [79, 80].

3.1. Encapsulation of Cinnamon Essential Oil (CEO). CEO is a plant-derived antimicrobial substance of which FDA has categorized it as GRAS. Its protective qualities do not disturb the physicochemical or nutritious properties of the food. CEO exhibits a broad spectrum of antimicrobial activity against a variety of microorganisms through prevention of cell wall biosynthesis, functions of membrane, and specific enzyme activities [81]. Encapsulation of CEO protects it from harsh environmental conditions, extends the shelf life, and allows controlled release of the active compound [82].

Conn et al. reported successful use of CEO as an antimicrobial agent against common microorganisms [83, 84]. CEO was encapsulated into β-cyclodextrin (β-CD) before incorporation in electrospun PVA fibers. CDs are cyclic oligosaccharides produced through enzymatic conversion of starch and exhibit nontoxic and biodegradable characteristics. Several studies have reported the use of CDs for food-related applications [85–87]. CDs are composed of α-1,4-linked glucopyranose units and form a shortened cone-like structure cavity. As a result of their unique chemical structure, they form noncovalent host-guest inclusion complexes with EOs, CEO/β-CD inclusion complex (CEO/β-CD-IC), enhancing their solubility, chemical stability, and bioavailability and protecting them from oxidation [88]. The mechanism behind the complexation is the displacement of the high-enthalpy water molecules occupying the cavity, with a guest molecule of proper polarity and dimensions [89, 90]. Therefore, they are often used to encapsulate various types of food additives and essential oils [89].

β-CD is the most commonly used member of CDs which is a hydrophobic molecule capable of entrapping EOs within its inner cavity [91]. A novel antimicrobial membrane electrospun based on PVA, CEO, indicated molecular interactions amongst PVA, CEO, and β-CD, resulting in enhancement in thermal stability of CEO and masking its special flavour. Thermogravimetric analysis of PVA/CEO/β-CD nanofibers indicated a shift of the second weight loss peak to higher temperature (110–160°C) due to possible formation of chemical or hydrogen bonds between PVA and CEO. The inhibition zone of nanofibers based on PVA/CEO/

Table 1: Essential oils incorporated in food packaging applications.

Essential oil combinations	Properties	Food product	Applied film material
Rosemary [41]	Antimicrobial	Chicken	Cellulose acetate
Cinnamon clove [42]	Antimicrobial	Bakery	Cassava starch
Lemon, thyme, and cinnamon [43]	Antibacterial	NA	Chitosan
Cinnamon, winter savory, and oregano [44]	Antimicrobial	Bologna and ham	Alginate
Bergamot [45]	Antifungal and antibacterial	NA	Chitosan
Garlic, rosemary, and oregano [46]	Antimicrobial	NA	Whey protein isolate (WPI)
Oregano [47]	Antimicrobial (against *S. aureus*, *Shewanella putrefaciens*, and *Yersinia enterocolitica*) and antioxidant	NA	Quince seed mucilage
Oregano [48]	Antimicrobial	Pizza	Cellulosic resin
Oregano [49]	Antimicrobial	Ripened sheep cheese model	Polypropylene (PP) and polyethylene terephthalate (PET)
Oregano and thyme [50]	Antimicrobial (against *Pseudomonas* spp. and *coliform bacteria*)	Fresh ground beef	Soy protein
Oregano [51]	Antimicrobial	Fresh beef	Whey protein isolate (WPI)
Mixture of oregano, pimento berry, and lemongrass (mix A) and mixture of nutmeg, lemongrass, and citral (mix B) [52]	Antimicrobial (against *L. monocytogenes*)	Fresh broccoli	Methylcellulose (MC) and blend of polycaprolactone/alginate (PCL/ALG)
Ginger, turmeric, and plai [53]	Antioxidant	NA	Fish skin gelatin
Satureja hortensis [54]	Antibacterial and antioxidant	NA	k-Carrageenan
Oregano and pimento [55]	Antioxidant	Whole beef muscle	Milk protein
Clove [56]	Antibacterial	Fish	Gelatin chitosan
Clove [57]	Antibacterial and antioxidant	Sardine patties	Sunflower protein concentrate
Linalool or methyl chavicol [39]	Antimicrobial	Cheddar cheese	Low-density polyethylene (LDPE)
Oregano and bergamot [58]	Antimicrobial	Formosa plum	Hydroxypropyl methylcellulose and limonene constituent EO
Cinnamon and mustard [59]	Antibacterial	Tomatoes	Zein
Limonene constituent EO, lemongrass, and oregano [60]	Antimicrobial	Strawberries	Chitosan
Peppermint, red thyme, chitosan, and lemon [61]	Flavouring	Strawberry	Chitosan

β-CD was reported to be wider than that of PVA/CEO. The entrapment of CEO into the cavities of β-CD improved the solubility of CEO and led to a more effective release into the agar medium [92]. Moreover, water contact angle results indicated that addition of CEO/β-CD reduced the hydrophobicity of the nanofibrous membrane. Perhaps that explains the excellent antimicrobial properties of the PVA/CEO/β-CD nanofibrous film against both Gram-positive and Gram-negative bacteria. According to the report, it effectively extended the shelf life of strawberries and showed potential for active food packaging applications. Furthermore, the electrospun membranes are managed to incorporate greater amount of CEO compared to casted film which resulted in enhanced antimicrobial activity.

Rieger and Schiffmann investigated the antimicrobial property of electrospun CS/cinnamaldehyde/PEO nanofibers against *E. coli* [74]. It was demonstrated that the inherent antibacterial properties of chitosan combined with the quick release of cinnamaldehyde (CA) achieved elevated inactivation rates against *Escherichia coli* and *Pseudomonas aeruginosa* [74].

Wen et al. for the first time reported the use of polylactic acid (PLA) and CEO as antimicrobial food packaging material. CEO/β-CD-IC was successfully produced through coprecipitation method and modified the thermal stability of CEO. PLA was the selected polymer matrix since it is an FDA approved bioplastic as food-contact material [83, 93]. The CEO/β-CD-IC was encapsulated into PLA nanofibers by electrospinning [94]. The electrospun biodegradable PLA/CEO/β-CD nanofilm demonstrated better antimicrobial activity, against *Escherichia coli* and *Staphylococcus aureus*, compared to PLA/CEO nanofilm. The results indicated that PLA/CEO/β-CD fiber efficiently increased the shelf life of pork, suggesting a potential application in active food packaging [94].

Liu et al. studied the effect CEO contents (1%, 1.5%, 2%, and 2.5% v/v) on the efficiency of encapsulation, nanoparticle dimensions, and antibacterial activity of CS nanoparticles loaded in PLA. CS nanoparticles as the carriers of CEO were added to the PLA solution followed by electrospinning. The obtained electrospun fibers were capable of sustained release of CEO [95]. The study suggested that addition of CEO could enhance the antibacterial activity of the PLA/CS-CEO fibers. The optimal composition was reported to be PLA/CS-CEO-1.5, which showed the greatest antibacterial activity against *E. coli* and *S. aureus* (99.3% and

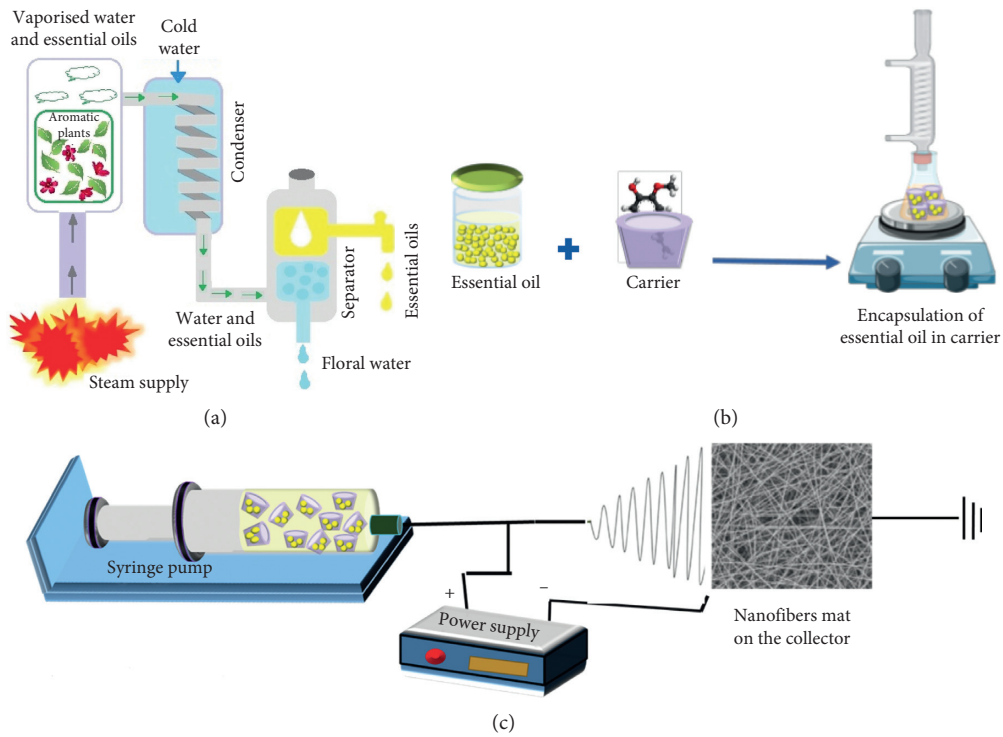

Figure 1: An overview of fabrication of essential oils-loaded electrospun nanofibers for active food packaging. (a) Extraction of essential oils. (b) Complexation with career and incorporation in electrospinning solution. (c) Electrospinning of composite solution.

98.4%, resp.) during the incubation period. The observation was a result of high crystallinity of CEO and its strong interactions with CS which lowered the solubility of PLA and allowed the CEO to exhibit a similar antimicrobial activity even at slower release rate [96].

Lin et al. reported encapsulation of CEO/β-CD/proteoliposomes into polyethylene oxide (PEO) nanofibers to study their antimicrobial behavior against *Bacillus cereus* (*B. cereus*) [97]. *B. cereus* is one of the major sources of contamination and spoilage in meat products [98]. *B. cereus* shows high adaptability to extreme environments (acidic, alkaline, and high temperature) [99]. Nanoantibacterial liposomes, artificial lipid vesicles, are microscopic morphologies made up of a central section enclosed by concentric phospholipid bilayers embedding aqueous cores. They are capable of encapsulating both hydrophilic substances in the inner aqueous section and hydrophobic matters within lipid bilayers and amphiphilic molecules at the lipid/water interface [88]. Proteoliposomes tend to agglomerate and shed when they come into a direct contact with food surface, as a result reducing the bioactivity of encapsulated substances. In addition, the hydrophobic nature of nanoliposomes has a negative effect on their encapsulation efficiency (EE) of EOs. Therefore, for further enhancement of the EE and stability of CEO in proteoliposomes, β-cyclodextrin (β-CD) is added to the system.

The physicochemical stability of CEO proteoliposomes was significantly enhanced by introduction of β-CD. Taking advantage of bacterial protease secreted from *B. cereus*, the controlled release of CEO from proteoliposomes was achieved via proteolysis of protein in proteoliposomes. Additionally, the antibacterial efficiency of CEO/β-CD proteoliposomes against *B. cereus* was improved as a result of their stability by encapsulation in nanofibers. The nanofibrous combination showed satisfactory antibacterial efficiency as active food packaging for beef against *B. cereus* without any impact on sensory quality while extending the shelf life.

Figure 2(a) shows the steps involved in preparation of CEO/β-CD (Figure 2) proteoliposomes and their incorporation in PEO spinning solution, while Figure 2(b) displays *B. cereus* proteinase-triggered CEO release from proteoliposomes. The CEO/β-CD proteoliposomes can precisely prevent bacterial multiplication by the stimulus-response of casein to bacterial protease in presence of *B. cereus*.

The combination of EO and lysozyme (LYS) when used as antimicrobial packaging can decrease the dose of EO besides extending the application of LYS-derived packaging material. Feng et al. reported a novel antimicrobial electrospun nanofilm based on PVA/β-cyclodextrin/CEO/LYS, where the combination of CEO and LYS was acting as antimicrobial agent [75]. LYS is a natural antimicrobial enzyme classified as GRAS which is usually derived from chicken egg white [100, 101]. LYS exhibits antimicrobial action toward Grampositive bacteria through splitting the bonds between N-acetylmuramic acid and N-acetylglucosamine of the peptidoglycan in the cell wall [102]. In this study, CEO was selected for its antimicrobial activity against bacteria (*L. monocytogenes* and *S. enteritidis*) and molds (*A. niger (ATCC1015)* and *Penicillium (CICC41489)*). The choice of PVA as the electrospinning matrix was because of its

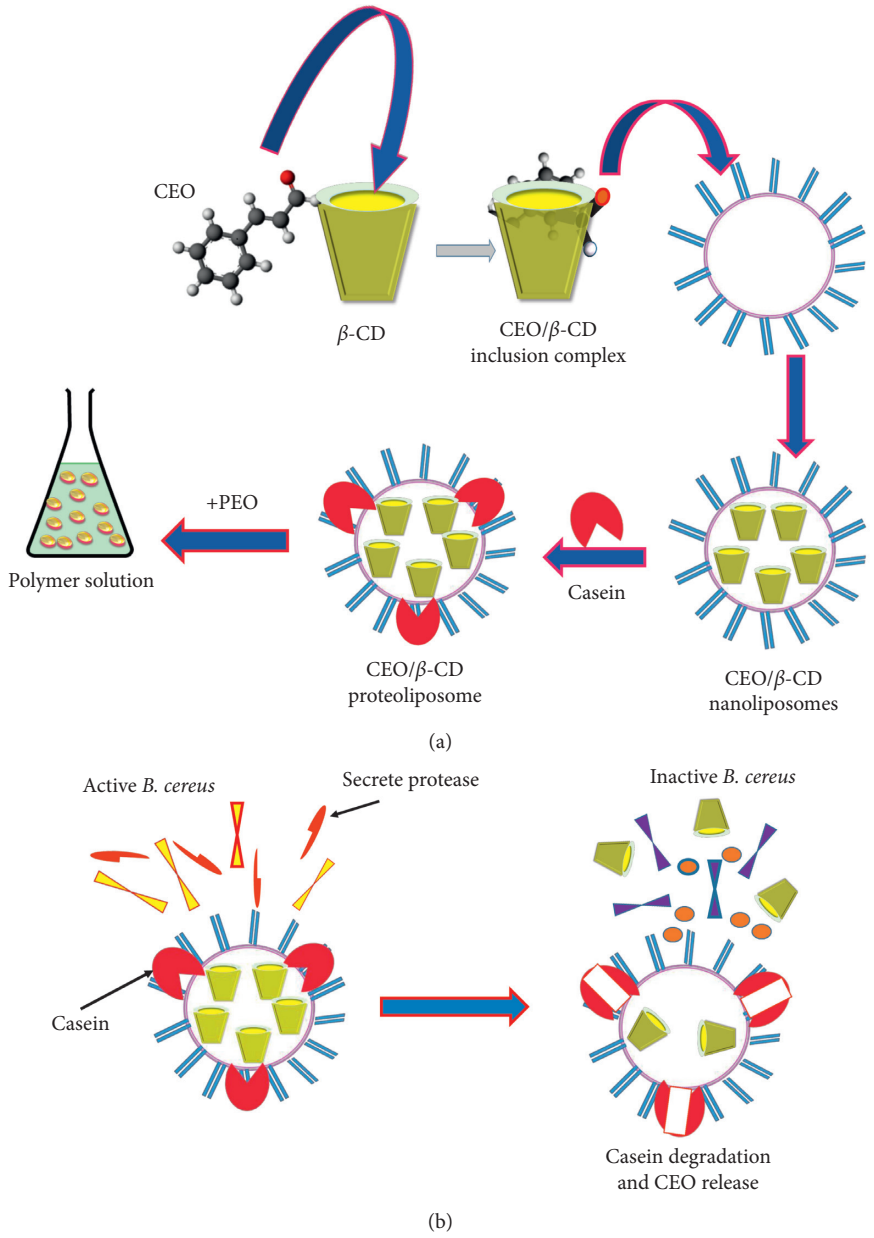

Figure 2: Encapsulation of CEO in β-CD and PEO and their antibacterial activity against *B. cereus*. (a) Preparation of CEO/β-CD proteoliposomes and incorporation in PEO spinning solution. (b) Schematic of *B. cereus* proteinase-triggered CEO release from CEO/β-CD proteoliposomes.

solubility in water soluble and biocompatibility as it has been extensively used in food preservation [103]. Furthermore, PVA could be applied without usage of organic solvents, thereby preventing the denaturation of LYS [104]. The aim of their study was to reduce the dosage of CEO in the packaging material without affecting antimicrobial action. The study suggested that the concentration of antimicrobial agent consisting 2% CEO and 0.25% LYS (w/w) in PVA matrix has a decent performance as food packaging material.

Shao et al. fabricated ultrafine PVA/permutite/CEO membranes via electrospinning [105]. PVA doped with permutite powder was applied as polymer matrix and CEO was encapsulated as the antibacterial component. Permutite is a nontoxic highly stable aluminosilicate which can be engaged in reversible interactions with various types substances including gas molecules [106]. The fabricated membranes were characterized for physicochemical properties such as morphology, porosity, surface area, tensile, and chemical interaction. Furthermore, the antibacterial action of the as-prepared films was explored for fruit packaging by using fresh cut strawberries. Fresh cut fruits hold a large share of the market since they only require partial processing without any additional preparation [107]. However, being susceptible to microorganisms such as mold, yeast, and fungi remains to be the major problem for the fresh cut fruit [108]. The release behavior in electrospun

membranes is diffusion controlled as it is physically adsorbed by polymeric matrix and very low activation energy is required for the release process [109]. Such property finds importance at lower temperatures (4–6°C), where the release of EOs at low temperatures will hardly achieve the minimum concentration required for preservation [110]. In the study, differential scanning calorimetry and pore distribution results suggested weak physical interactions between the CEO and the fibers as a result of mesoporous adsorption (15.77 J/g and 37.7 J/g) which can benefit the release of CEO at low temperature. The authors concluded that PVA/permutite/CEO fibrous films have the potential to delay the rapid corruption of strawberries during storage.

3.2. Encapsulation of Eugenol Essential Oil. Eugenol (4-allyl-2-methoxyphenol), most abundantly found component in clove oil, nutmeg oil, and cinnamon oil, has been successfully applied in food preservation, cosmetics manufacturing, and traditional medicine. Several researches have confirmed antibacterial, antioxidant, anti-inflammatory, and local anesthetic properties of eugenol [111]. Presence of high contents of phenolic compounds such as eugenol in volatile oils exhibits strong antioxidant properties [112]. Eugenol is a yellow oily liquid which exhibits lipid peroxidation induced by reactive oxidase system (ROS) because of its radical scavenging activity [35, 36, 113]. Like other EOs, eugenol also suffers from high volatility and poor water solubility. Therefore, encapsulation of eugenol is necessary to increase its effectiveness and longer shelf life [114]. Kayaci et al. in a joint research demonstrated that the EE of the volatile active agents such as menthol, vanillin, eugenol, geraniol, and allyl isothiocyanate was only effective when used with CD inclusion complexes (CD-IC) [15, 115–118]. One of the challenges in encapsulation is to incorporate higher amounts of the active ingredient in the polymeric matrix [115, 119]. When electrospun polymers appear as carrier matrix, the amount of the active ingredients in CD system is often limited to 5% of the fabricated membrane's weight. This is due to difficulty of electrospinning uniform nanofibers from polymeric solution containing higher amounts of CD. This research group recently focused on nanofibrous webs encapsulating much higher amounts of active agents (loading of ~10% (w/w) or more with respect to fibrous CD matrix). They reported that production of polymer-free electrospinning from only CD systems was spun [120–123].

Celebioglu et al. prepared excessively concentrated aqueous CD solutions (160% (w/v)) [124]. They prepared inclusion complexes between eugenol (guest molecule) and cyclodextrins (host molecules) at a molar ratio of 1 : 1 CD : eugenol followed by electrospinning to obtain nanofibrous webs (eugenol/CD). Since dimensions and form of the CD cavity are a significant parameter for formation of effective inclusion complexation, three different CD derivatives were applied in this work. The three modified CDs, namely, hydroxypropyl-beta-cyclodextrin (HP-β-CD), hydroxypropyl-gamma-cyclodextrin (HP-γ-CD), and methyl-beta-cyclodextrin (M-β-CD), were used to create inclusion complexes with eugenol. The resulting electrospun eugenol/CD samples showed self-standing and flexible characteristics as a mat web and displayed rapid solubility in water. Figure 3 demonstrates the chemical structure of modified CDs, eugenol, and schematic illustration of the inclusion complexation formation between CD and eugenol. Moreover, thermal stability of eugenol was enhanced for eugenol/CD/IC (up to ~310°C) in comparison with pure eugenol (up to ~200°C). Furthermore, eugenol/CD exhibited effective antioxidant activities. The strongest interactions within the complex were observed between M-β-CD and eugenol compared to the other two host CD molecules (HP-β-CD and HP-γ-CD) for eugenol/CD samples. The authors suggested potentials for their membranes in food related and oral-care applications.

Liposomal encapsulation of eugenol is an alternative way to decrease the damage to eugenol at processing and storage phase. Liposome containing eugenol is a natural and effective antioxidant that can encapsulate hydrophobic and lipophilic drugs [125]. However, liposomal instability as a major drawback can affect their efficiency as an antioxidant. Furthermore, conventional liposomes often have low EE and instability of vesicle aggregation, fusion, or rupture, all of which pose serious challenges to the commercial exploitation of eugenol liposomes as an industrial antioxidant. Therefore, the stability of eugenol liposome can affect the performance of the final product as active food packaging material. The stability of liposomes is being improved through various strategies such as polymer-coated liposomes, hydrogel-liposome composites, and nanoparticle-stabilized liposomes [126–128].

Cui et al. reported an undemanding method to form an antioxidant based on novel complexes of liposome encapsulated SiO_2-eugenol. SiO_2-eugenol forms a supramolecular assembly with a core of colloidal particles covered by a lipid shell [127]. SiO_2 nanoparticles in food industry serve as an additive which can provide stiff support for the lipid bilayer thin film to enhance physical stability of liposome [129]. Besides being porous, the hydrophilic property of SiO_2 nanoparticles facilitates absorption when volatilization occurs [130, 131]. There are few reports of immobilization of liposome on electrospun nanofibers for food preservation [132, 133]. While SiO_2-eugenol liposomes could not be electrospun on their own, their combination with PEO could be electrospun and showed great potential as food packaging material [103, 134]. Cui et al. reported production of a novel electrospun membrane based on PEO and SiO_2-eugenol liposomes [135]. Figure 4 shows schematic illustration of liposomes-encapsulated SiO_2-eugenol.

The study explored application of SiO_2 as an architectural template for liposomes which could bring promising prospects to application of eugenol-based antioxidant. As a proof of concept, their electrospun membranes were exposed in contact with beef over a period of 60 days and exhibited excellent antioxidant activity.

Munteanu et al. investigated the biodegradation and tensile properties of PLA membranes coated with antimicrobial and antioxidant CS-EO complexes [136]. Chitosan has exhibited significant antibacterial action against various pathogens such as *Klebsiella pneumoniae*, *Escherichia coli*,

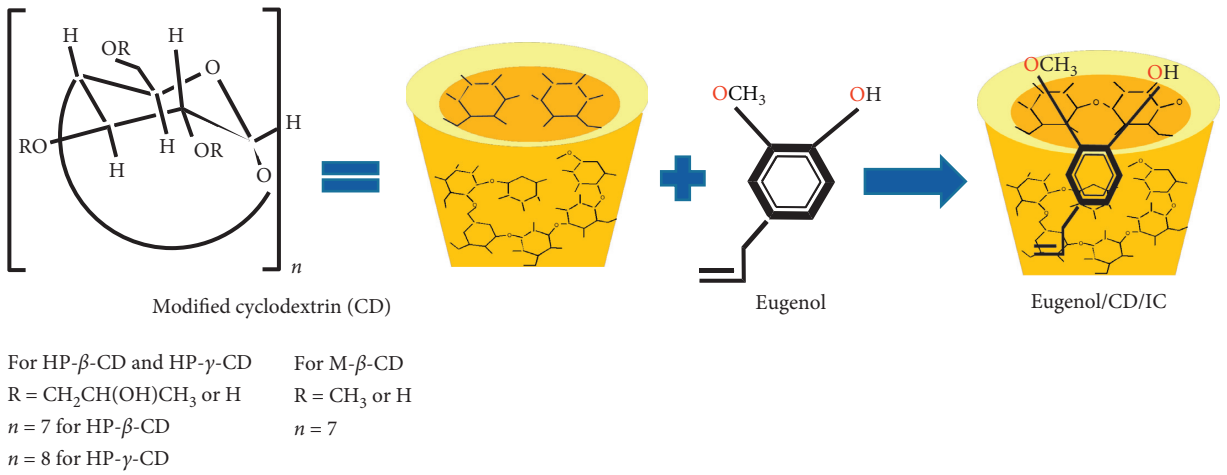

Figure 3: Chemical structure of modified CD [125], eugenol, and schematic illustration of IC formation between CD and eugenol.

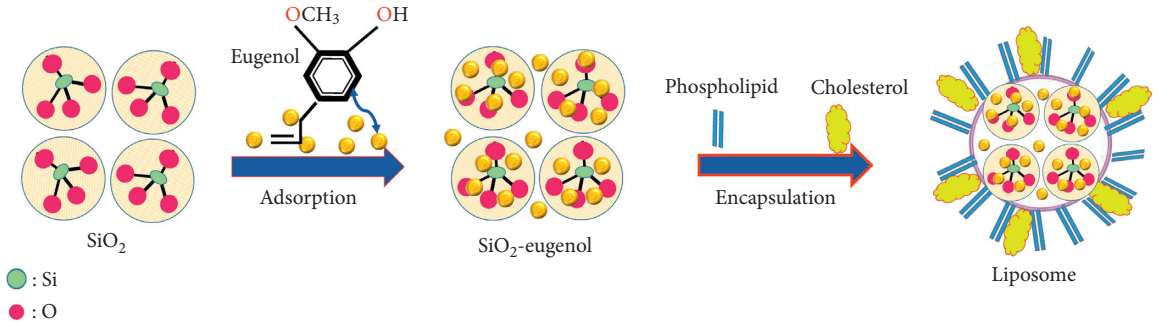

Figure 4: Schematic illustration of liposomes-encapsulated SiO_2-eugenol.

Staphylococcus aureus, and *Pseudomonas aeruginosa* [137]; therefore, it has been a popular subject of studies in antibacterial coatings [138]. It also can encapsulate other antibacterial agents such as nisin [139], which could further enhance the antimicrobial action of the packaging coatings [140]. PLA electrospun membranes were coated with bioformulations containing the essential and vegetable oils, that is, clove and argan oils loaded into CS. 99% of the argan oil is composed of acylglycerols, while the antioxidant constituents are tocopherols, squalene, sterols, and phenols [141, 142]. Eugenol as the major volatile constituent of clove oil (about 80%) is accountable for its antioxidant and antimicrobial properties [143]. The study involved coaxial electrospraying of encapsulated CS over the electrospun PLA membrane which was placed on the metallic collector. Based on the report when high molecular weight CS was used, the coaxial electrospinning produced beaded CS nanofibers with the oil encapsulated and distributed along the beaded fibers. On the other hand, use of lower molecular weight CS led to electrospraying loaded chitosan nanoparticles and providing smoother surface. The PLA films coated with CS-EO formulations exhibited higher antibacterial activity compared to the films coated only with CS. The clove oil's antibacterial activity was higher than argan oil due to its higher phenolic content. The beaded fibers showed better antibacterial activity compared to nanoparticles perhaps due to the higher specific surface area of the rougher nanofibrous morphology of the coating layer.

Melendez-Rodriguez et al. encapsulated eugenol within the pores of mesoporous silica nanoparticles (MCM-41) by vapor adsorption [144]. Subsequently, for the first time, electrospinning technique was applied to include MCM-41 particles containing eugenol into poly(3-hydroxybutyrate-co-3-hydroxyvalerate) (PHBV). To fabricate continuous films, the produced electrospun fibers were thermally treated at 155°C. The resultant PHBV films filled with eugenol-loaded mesoporous silica nanoparticles revealed increased mechanical strength, adequate thermal resistance, and good barrier properties to water vapor and limonene. According to their results, they suggested that the films can be used in the form of coatings or interlayers for active food packaging applications.

Cui et al. evaluate the antibacterial activity of clove oil-loaded chitosan nanoparticles (CO@CNPs) and gelatin electrospun nanofibers against *E. coli* O157:H7 biofilms on cucumbers [145]. Once CO@CNPs were used at 30% (w/v), *E. coli* O157:H7 population reduced to approximately 99.98% and high antibacterial activity was achieved after 8 hours. Following this, electrospinning was applied to incorporate the prepared CO@CNPs into gelatin nanofibers. After applying 9 mg/mL gelatin/CO@CNPs treatment for 24 h, the population of *E. coli* O157:H7 biofilm decreased to almost 99.99% in vitro. The results confirmed that treatment of the gelatin/CO@CNPs nanofibers could maintain the flavour and color of cucumber for more than 4 days. Based

on their results, both CO@CNPs and gelatin/CO@CNPs nanofibers at specified amount showed significant destruction effect on *E. coli* O157:H7 biofilms in vitro.

3.3. Encapsulation of Thyme Essential Oil (TEO) and Thymol (THY). TEO, a plant secondary metabolite possessing safe and nontoxic properties, is derived from thymus vulgaris. TEO exhibits excellent antibacterial action against a wide spectrum of bacteria such as *Escherichia coli* O157:H7, *Salmonella enterica* subsp. *enterica serovar Enteritidis CICC 21482 (S. enteritidis)*, and *Salmonella typhimurium CICC 22956 (S. typhimurium)* [146]. However, TEO suffers from several shortcomings such as volatility, hydrophobicity, and special flavour which highlight the need for encapsulation which is usually achieved through a coprecipitation of TEO into *ß*-CD [91].

THY is also the major volatile component of essential oils derived from plants belonging to the Lamiaceae family. It is a monoterpene usually found in oregano and thyme; however, its preservation and delivery applications remain to be a challenge due to its hydrophobic and volatile nature. It is registered in European flavouring list and classified as GRAS by FDA [147]. THY exhibits antimicrobial action against a wide range of microorganisms such as bacteria, fungi, and yeasts [148–150] through its capacity to disturb the lipid bilayer of the cell membrane and could increase membrane permeability [151]. THY is typically used for food preservation and control of postharvest decay of fresh produce [152, 153].

Lin et al. reported production of gelatin nanofibers containing TEO/β-cyclodextrin ε-polylysine nanoparticles (TCPNs) for controlling the propagation of *Campylobacter jejuni* (*C. jejuni*) [154]. *C. jejuni* is the major source of contamination on poultry surface which poses huge threats to human health. Moreover, *C. jejuni* is a zoonotic pathogen that lives as a symbiotic microorganism in the digestive tract of the poultry [113]. During poultry slaughter, *C. jejuni* can leak and rupture through external channel and cause meat contamination. The *C. jejuni* contaminated meat is known to be the main cause of human campylobacteriosis which accounts for 8.4% of the diarrheal diseases [155].

C. jejuni meat contaminations may not be completely inactivated as it shows high resistance against some frequently used antibiotics such as cephalosporins, quinolones, and gentamicin [156] and the demand for an efficient natural antibacterial agent to replace chemical antibiotics frequently used in meat industry. Since *C. jejuni* primarily contaminates meat surface, an antimicrobial packaging has a great potential to inhibit its reproduction.

A simple TEO/β-CD-IC is not effective against *C. jejuni* as β-CD has an electroneutral nature and its absorption onto negatively charged bacterial cell wall is limited. To address this issue ionic gelation was applied to adsorb cationic biopolymers onto the surface of TEO/β-CD-IC [157]. In the study, ε-polylysine (ε-PLY), a biodegradable cationic biological metabolite with outstanding antibacterial properties, was selected to prepare TEO/β-CD ε-polylysine nanoparticles (TCPNs) [158]. The presence of $-NH_2$ along the ε-PLY chains improves nanoparticle binding onto negatively charged bacterial cell wall leading to an acceleration in the apoptosis process [159]. Antibacterial nanofibers were obtained by adding TCPNs into the polymer matrix via electrospinning. The prepared membranes showed outstanding antimicrobial action against *C. jejuni*, through membranolysis. The results confirmed that damaged cell membrane and proteins leakage of *C. jejuni* were results of antimicrobial activity of nanoparticles. Chicken samples packed in the antimicrobial membranes possessed lower aerobic bacterial count and thiobarbituric acid (TBA). Total volatile basic nitrogen (TVBN) and pH values were lower as well without any adverse effect on color, texture, and sensory evaluation, signaling bright prospects for the membranes in poultry preservation.

Aytac et al. reported encapsulation of THY/γ-CD-IC into in electrospun zein nanofibrous web for food packaging application [160]. Two different molar ratios THY/γ-CD (1 : 1 and 2 : 1, resp.) were prepared and encapsulated into electrospun zein nanofibers. Figure 5 shows the chemical structure of THY, schematic representation of γ-CD, and THY/γ-CD-IC formation. The choice of γ-CD was due to its lack of adverse effects on nutrient absorption in food products and nutraceutical applications [161]. Successful formation of complex between THY and γ-CD at both molar ratios was reported. Cyclodextrin inclusion complexes of thymol (THY/CD-IC) have been demonstrated to be applicable in pork meat systems to prevent oxidation and enhance meat stability at high relative humidity (up to 75%) for long storage periods [162–165].

However, it is worth mentioning that the release of THY was higher than that from zein-THY/γ-CD-IC nanofibrous membranes (2 : 1). Similarly, zein-THY/γ-CD-IC nanofibrous membranes (2 : 1) had stronger antibacterial activity against *E. coli* and *S. aureus*. In brief, zein-THY/γ-CD-IC nanofibrous membranes were most efficient at decreasing the bacterial count in meat stored over a 5-day period at 4°C. Thus, these membranes exhibit great potential as antibacterial food packaging material.

Zhang et al. encapsulated THY in poly(lactide-co-glycolide), PLGA fiber through core-shell coaxial electrospinning [166]. PLGA which is known for its biodegradability and controlled delivery properties [167] has the capability of encapsulating hydrophobic substances and had shown great potential in enhancing the efficiency of delivery in food systems [168, 169]. The study indicated that nanofibers with good core-shell structure were formed and volatile THY was encapsulated successfully. The results demonstrated that PLGA can efficiently suppress the volatilization of THY, so the encapsulated thymol gradually evaporates into the fruits and vegetables storage environment. In their work, the antibacterial and fruit preservation ability of the nanofiber films were tested by strawberry. The results suggested that the produced membranes efficiently inhibit bacterial, fungal, and yeast growth to extend the shelf life of fruits. This novel biocompatible antibacterial packaging material would have a huge application prospect for food preservation.

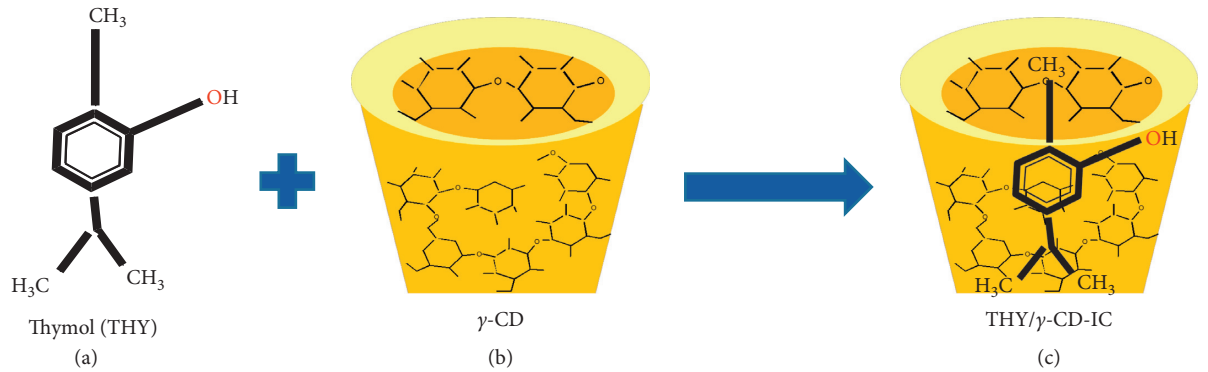

Figure 5: The chemical structure of (a) THY, (b) schematic representation of γ-CD, and (c) THY/γ-CD-IC formation.

Table 2: Encapsulation of the EOs into different carriers and matrixes with their antimicrobial activities for food or food packaging.

Matrix	Essential oil (guest)	Carrier (host)	Food evaluated	Action	Findings
PVA [84]	CEO	β-CD	Strawberries	Antibacterial against Gram-positive and Gram-negative bacteria (*S. aureus* and *E. coli*)	(1) Addition of CEO/β-CD caused to increase water contact angle and more hydrophilicity of the nanofibrous film (2) Enhanced antimicrobial action compared with that of casted films (3) The molecular interaction among PVA, CEO, and β-CD modified the thermal stability of CEO (4) Electrospinning achieved incorporation of greater amounts CEO in the membrane and enhanced antimicrobial action compared to film casting
PEO [74]	Cinnamaldehyde	CS	NA	Antimicrobial against *E. coli* and *Pseudomonas aeruginosa*	(1) The release of CA from CS/CA (0.5 and 5.0%)/PEO nanofibrous membranes directly affected cytotoxicity against *P. aeruginosa* (within three hours, 81 ± 4% of the *P. aeruginosa* was deactivated)
PLA [94]	CEO	β-CD-IC	Pork	Antibacterial against *E. coli* and *S. aureus*	(1) The CEO/β-CD-IC was prepared by the coprecipitation (2) Formation of CEO/β-CD-IC considerably improved the thermal stability and antimicrobial activity of CEO (3) The electrospun PLA/CEO/β-CD nanofibers showed outstanding antimicrobial action against both Gram-positive and Gram-negative bacteria (4) Electrospinning achieved incorporation of greater amounts CEO in the membrane and enhanced antimicrobial action compared to film casting
PLA [95]	CEO	CS	NA	Antibacterial against *E. coli and S. aureus*	The optimal composition found to be PLA/CS-CEO-1.5, which exhibited the highest antibacterial activity for a long time
PEO nanofibers [97]	CEO	β-CD proteoliposomes	Beef and meat production preservation	Antibacterial against *B. cereus*	(1) The antibacterial effect of CEO/β-CD proteoliposomes against *B. cereus* increased, and their stability enhanced due to encapsulation (2) The physicochemical stability and the EE of CEO proteoliposomes were significantly enhanced through introduction of β-CD

Table 2: Continued.

Matrix	Essential oil (guest)	Carrier (host)	Food evaluated	Action	Findings
PVA [75]	CEO/LYS	β-CD	NA	Antibacterial against *L. monocytogenes* and *Salmonella enteritidis*. Antifungal against *Aspergillus niger* and *Penicillium*	(1) The suitable CEO and LYS concentrations were as 2% (w/w) and 0.25% (w/w), respectively (2) The molecular interactions among PVA, β-CD, CEO, and LYS modified the thermal stability of CEO and LYS (3) The minimum inhibition concentration (MIC) against *L. monocytogenes* and *S. enteritidis* was approximately 0.8–1 mg/mL (4) Minimum bactericidal concentration (MBC) was approximately 6-7 $mg{\cdot}mL^{-1}$
PVA doped with permutite powder [105]	CEO	PVA/permutite	Fresh cut fruits (strawberry)	Antibacterial	(1) The nanofibrous mat exhibited high porosity with the pore size distribution ranging from 1.7 nm to 56.7 nm (2) DSC and pore distribution analysis indicated presence of weak physical interactions between the CEO and nanofibers due to mesoporous adsorption (15.77 J/g and 37.7 J/g) which helps release of CEO at low temperature
Eugenol/ CD/IC-NW (self-standing (without matrix) [124]	Eugenol	CD/IC	NA	Antioxidant	(1) Volatility nature of eugenol was preserved (~70–95%) in eugenol/ CD inclusion complex nanofibrous webs (eugenol/CD/IC-NW) (2) Thermal stability of eugenol for eugenol/CD/IC-NW increased up to ~310°C from ~200°C (3) The eugenol/CD/IC-NW showed rapid aqueous dissolution, contrary to poor water solubility of eugenol (4) The strongest complexation was between M-β-CD and eugenol compared to other two host CD molecules (HP-β-CD and HP-γ-CD) (5) The electrospun eugenol/CD/ IC-NW samples exhibited improved antioxidant action compared to eugenol in its pure form (6) Radical scavenging property of eugenol/CD/IC-NW was enhanced compared to eugenol in its pure form
PEO [135]	SiO_2-eugenol	Liposome	Beef	Antioxidant	Liposomes containing SiO_2-eugenol was immobilized on electrospun nanofibers. This system exhibited outstanding antioxidant action on beef during 60-day storage

Table 2: Continued.

Matrix	Essential oil (guest)	Carrier (host)	Food evaluated	Action	Findings
PLA [136]	Clove containing 80% eugenol (essential oil) and argan oils (vegetable oils)	CS	NA	Antibacterial and antioxidant	(1) The samples prepared with Chit-H showed higher roughness of the coating layer compared to samples prepared with Chit-L (2) Chit-H samples showed higher antibacterial action compared to Chit-L, for either of the oils, due to the higher specific surface area of the rougher morphology of the coating layer (3) The clove oil had better antibacterial activity than argan oil, in combination with both chitosan types (4) Chit-H samples showed higher antibacterial activity compared with Chit-L, in combination with both types of oil (5) PLA coated with chitosan-oil formulations had higher antibacterial action than the films coated with pure CS (6) The chitosan-clove oil combination showed higher antioxidant action compared to pure CS coating.
PHBV films [144]	Eugenol	Mesoporous silica nanoparticles	NA	Antimicrobial against *S. aureus* and *E. coli*	(1) The incorporation of eugenol EO on MCM-41 significantly increased plasticization on PHBV and a reduction in its crystallinity (2) The mechanical strength of the PHBV films and barrier properties were enhanced (3) The incorporation of MCM-41 with eugenol caused slight reduction in ductility
Gelatin nanofibers [145]	Clove oil	CS	Cucumber	Antibacterial against *E. coli* O157:H7	Approximately 99.98% reduction in *E. coli* O157:H7 population was obtained after 8 hours of treatment, when CO@CNPs were used at 30% (w/v)
Gelatin [154]	TEO	β-CD ε-polylysine	Chicken	Antimicrobial against *C. jejuni*	(1) The TCPNs loaded gelatin nanofibers (TEGNs) exhibited exceptional antimicrobial action against *C. jejuni* on chicken (2) The TEGNs packaged chicken samples had lower aerobic bacterial count, TBA, TVBN, and pH values without undesirable effect on color, texture, and sensory evaluation
Zein [160]	THY/γ-CD-IC	Zein	Meat	Antimicrobial against *E. coli* and *S. aureus*	(1) THY/γ-CD-IC (2 : 1) exhibited higher preservation rate and stability than THY/γ-CD-IC (1 : 1) (2) Zein-THY/γ-CD-IC-NF (2 : 1) contained more THY as indicated by TGA (3) THY/γ-CD-IC (2 : 1) had higher stability. The released amount of THY from zein-THY/γ-CD-IC-NF (2 : 1) was more than zein-THY-NF and zein-THY/γ-CD-IC-NF (1 : 1) (4) Antibacterial action of zein-THY/γ-CD-IC-NF (2 : 1) was greater than zein-THY-NF and zein-THY/γ-CD-IC-NF (1 : 1)

Table 2: Continued.

Matrix	Essential oil (guest)	Carrier (host)	Food evaluated	Action	Findings
PLGA [166]	THY	PLGA nanofiber	Fruits	Inhibition of the growth of bacteria, fungi, and yeast	Due to core-shell morphology, THY encapsulated in the PLGA nanofiber is slowly released to inhibit the growth of bacteria on the surface of food
PEO [174]	TTO	β-CD-IC	Beef	Antibacterial against *E. coli O157:H7*	(1) The highest antibacterial action against *E. coli* O157:H7 was observed on the beef for 7 d, at 4°C or 12°C (2) The flavour values significantly enhanced in plasma-treated TTO/β-CD-IC PEO nanofibers compared with the control groups (3) TTO/β-CD-IC at concentrations of 30% and 40% exhibited great antibacterial action leading to a 99.94% and 99.96% decrease in population after 24 hours
Gelatin [176]	PO	Gelatin	NA	Antibacterial against *E. coli* and *S. aureus*	(1) The combination of PO and CO in gelatin nanofiber showed overall improved bioactivities compared to PO or CO alone (2) The surface hydrophobicity of nanofibers was enhanced with the addition of EOs (3) The addition of EO was reported to improve mechanical flexibility of electrospun mats with the ability to tune tensile modulus and strength of nanofibers
	CO	Gelatin	NA	Antioxidant	
CS [191]	CHEO	CS	Beef	Antibacterial against *L. monocytogenes*	(1) The cell membrane permeability of *L. monocytogenes* increased (2) Respiratory metabolism of *L. monocytogenes* was prevented (3) The slow release of CHEO from CHEO/CS/NF achieved an antibacterial inhibition efficiency of 99.91 to 99.97% between 4°C and 25°C (4) In presence of antioxidant agents in ECHO/CS/NF, the value of TBARS in treated beef was 0.135 MDA/kg
Gelatin [193]	MO	CS	Cheese	Antibacterial against *L. monocytogenes* and *S. aureus*	Nanofibers have high antibacterial effect at 4°C and 25°C with negligible effect on surface color

3.4. Encapsulation of Tea Tree Oil (TTO), Peppermint Oil (PO), Chamomile Oil (CO), Chrysanthemum Essential Oil (CHEO), and Moringa Oil (MO). TTO is a natural essential oil which is composed of several organic substances such as terpene hydrocarbons, terpene alcohols, and terpene phenols. There are several reports regarding antimicrobial and anticancer properties of TTO [170, 171]. However, like other EOs, the application of TTO remains limited due to its chemical instability in exposure to air and high temperatures [172]. Therefore, forming noncovalent inclusion complex with β-CD as an antibacterial agent paves the way toward stability [173].

Cui et al. studied the incorporation of TTO/β-CD-IC, as antibacterial agent into electrospun PEO, to fabricate antibacterial packaging material [174]. As mentioned earlier, TTO is not completely soluble in aqueous PEO solution and the volatilization of TTO would intensify during the electrospinning which might create further problems regarding quick release during storage [175]. Therefore, in the study, the β-CD and TTO were used as a host guest to create water-soluble inclusion complex. The membranes were subjected to plasma treatment, and after the treatment the efficiency of antibacterial agent release from PEO nanofibers was improved appropriately. The plasma treated electrospun membranes exhibited the highest antibacterial activity against *E. coli* O157:H7 on the beef for a period of 7 days, with inhibition efficiently of 99.99% at either 4°C or 12°C. According to their results, the plasma-treated PEO nanofibers containing TTO/β-CD prolong the shelf life of beef and sustain its sensory quality which suggests a bright prospect in food preservation.

Tang et al. fabricated gelatin nanofibers incorporating two kinds of EOs, that is, peppermint essential oil (PO) and chamomile essential oil (CO), for potential edible packaging application [176]. PO has excellent antimicrobial property, which made it the subject of several studies in food preservation, pharmaceuticals, and wound dressing [177–179]. CO on the other hand is mostly used in medicinal tea, cosmetics, perfumery, and food industry due to its calming, antibacterial, and antioxidant properties [180–183]. Gelatin nanofibers loaded with PO and CO were successfully produced with morphological homogeneity and smoothness. All the gelatin nanofibers containing PO, CO, or their combination showed enhanced antibacterial action proportionate to EO content against *Escherichia coli* (*E. coli*) and *Staphylococcus aureus* (*S. aureus*) as well as certain antioxidant property. Incorporation of CO resulted in improved antioxidant activity, while the antibacteria activity against *E. coli* and *S. aureus* was better for the nanofibers containing EO. The mixture of PO and CO in gelatin nanofiber showed overall better bioactivities compared to the samples that contained only one of them. Addition of EOs enhanced the surface hydrophobicity of nanofibers based on water contact angle results. This is important since the high hydrophilicity and sensitivity to moisture of gelatin are one of its major drawbacks as packaging material [184]. Therefore, it is not surprising that researches have been focused on blending gelatin with other hydrophobic materials to eliminate its drawbacks for food packaging applications [185, 186]. Along with hydrophobic polymers, EOs could be an alternative to be incorporated in gelatin-based packaging for improvement of bioactivities as well as the required physical properties [187]. The high surface area to volume ratio and the nanostructure of electrospun nanofibers were shown to improve the sustained release of bioactive ingredients to food surface and intensify the bioactive actions [16, 84]. Furthermore, the addition of EO is reported to enhance mechanical flexibility of electrospun membranes and to control tensile modulus and strength. The mentioned phenomena are achieved through affecting morphology and diameter of nanofibers by inducing rearrangement of protein network and cross-links between the polymer chains and some constituents of EOs [5]. Finally, the cytotoxicity test demonstrated the noncytotoxicity of gelatin nanofibers incorporated with PO and CO, thus indicating the potential of the gelatin/EOs nanofibers as prospective food packaging.

Chrysanthemum essential oil (CHEO) is an aromatic oil extracted from chrysanthemum which has antioxidant and anti-inflammatory properties [188]. Chrysanthemum has cardiovascular protective functions and can prevent a variety of diseases such as hypertension, atherosclerosis, and coronary heart disease [189, 190].

Lin et al. incorporated CHEO into CS nanofibers (CS/NF) using electrospinning [191].

Since CHEO had a negative effect on phosphofructokinase activity, hexokinase, and pyruvate kinase in *L. monocytogenes* cells, antibacterial properties of CHEO against *L. monocytogenes* increased. The slow release of CHEO from CHEO/CS/NF effectively prolonged the antibacterial action. The antibacterial application of the CHEO nanofibers against *L. monocytogenes* was tested on beef. Beef parameters like thiobarbituric acid reactive substances (TBARS), pH values, and texture at different storage temperatures (4°C, 12°C, and 25°C) were evaluated. Due to the presence of antioxidant components in CHEO released from CHEO/CS/NF, the beef parameters like thiobarbituric acid reactive substances (TBARS) value in treated beef were lower (0.135 MDA/) comparing with the untreated sample. Moreover, pH value for beef sample packed with CHEO/CS/NF showed 6.43 (after 10 days of storage) that was lower than pH value of unpacked sample (7.05) at 4°C. They suggested a potential application in food packaging.

Moringa oil (MO), an essential oil derived from *Moringa oleifera*, is resistant to autooxidation. *Moringa oleifera* grows in South and Central America, Africa, Southeast Asia, and the Indian subcontinent [192]. Lin et al. fabricated MO-loaded chitosan nanoparticles (MO@CNPs) and loaded them into gelatin nanofibers for biocontrol of *L. monocytogenes* and *S. aureus* on cheese [193]. Beside the excellent physicochemical properties of nanofibers, they had outstanding antibacterial activity against *S. aureus* and *L. monocytogenes* on cheese at 4°C and 25°C and negligible impact on the surface color and sensory quality of cheese within 4 days of storage. Hence, the MO@CNPs loaded gelatin nanofiber demonstrated excellent antibacterial action as a candidate for further food application studies.

To summarize, Table 2 demonstrates successful encapsulation of the different EOs into various carriers and electrospun matrices with their food related properties. The relevant electrospinning parameters could be found in Table S1 in Supplementary Materials.

4. Conclusions

Growing consumer demand for safe and chemical-free natural products has improved the quality and safety of the products against pathogenic deterioration and lipid oxidation within their shelf life. Especial attention has been given to EOs as natural additives and antimicrobial and antioxidant agents classified as GRAS. In this regard, the study of EOs has great importance, since it has been proven that their antimicrobial activity can replace artificial preservatives. However, their low solubility in water, oxidation susceptibility, and volatilization have limited their use. The encapsulation technique is a beneficial way in improving the stability of EOs and thus their efficiency as antibacterial/antioxidant agents. The combination of electrospinning and nanoencapsulation EOs has allowed successful development of new antimicrobial packages for food preservation. These new nanoencapsulation techniques have attracted global interest in food packaging and research area due to the positive protection and environmental friendliness. As presented in the article, these new combinations take advantage of encapsulation and slow release properties of electrospun polymers as a potential new platform for stabilization of natural oils for food packaging.

While the initial results of loaded electrospun fibers for food packaging are promising, it should not be forgotten that

the composite nanofibers hugely depend on electrospinning process. Electrospinning despite various advantages has serious problems as well. Low production rate especially for aqueous polymeric solutions remains a major problem, along with limitations to selection of highly volatile organic solvents as well. Particularly, solvents must not have any adverse effect on the antimicrobial properties of the active ingredients or bring the risk of future side effects. Technical advancements in electrospinning in terms of process control and production rate within the last three decades have provided an opportunity to use nanofibers for more applications. However, electrospinning still needs lots of further innovations in order to upscale production rate and quality for food packaging application at industrial scale.

The current review demonstrated that electrospinning technology is a potential new platform for enhanced stabilization by encapsulation of natural oils in nanofibers. Whilst the initial results suggest great prospects for loaded nanofibers as food packaging, to produce a feasible product at industrial scale, loaded electrospun fibers require extensive processing.

Conflicts of Interest

The authors declare no conflicts of interest.

Acknowledgments

This research was funded by Fundamental Research Grant Scheme (FRGS) FP096-2018A and Research University Grant-Faculty Program GPF013A-2018. S. Ataei would like to acknowledge the University of Malaya for her appointment as Visiting Research Fellow (Ref. UM/PS-19308).

Supplementary Materials

Table S1: the electrospinning parameters used in related references. (*Supplementary Materials*)

References

[1] P. Tice, *Packaging Materials: 4. Polyethylene for Food Packaging Applications*, ILSI, Washington, DC, USA, 2003.

[2] S. Allahvaisi, *Polypropylene in the Industry of Food Packaging*, IntechOpen, London, UK, 2012.

[3] K. Cassidy and S. Elyashiv-Barad, "US FDA's revised consumption factor for polystyrene used in food-contact applications," *Food Additives and Contaminants*, vol. 24, no. 9, pp. 1026–1031, 2007.

[4] M. J. Elyashiv-Barad, S. Plant, and J. W. Strawbridge, *Plastics in Food Packaging*, John Wiley & Sons, Hoboken, NJ, USA, 2011.

[5] S. Yildirim, B. Röcker, M. K. Pettersen et al., "Active packaging applications for food," *Comprehensive Reviews in Food Science and Food Safety*, vol. 17, no. 1, pp. 165–199, 2018.

[6] A. Ocaña-Fuentes, E. Arranz-Gutiérrez, F. J. Señorans, and G. Reglero, "Supercritical fluid extraction of oregano (Origanum vulgare) essentials oils: anti-inflammatory properties based on cytokine response on THP-1 macrophages," *Food and Chemical Toxicology*, vol. 48, no. 6, pp. 1568–1575, 2010.

[7] V. S. Periasamy, J. Athinarayanan, and A. A. Alshatwi, "Anticancer activity of an ultrasonic nanoemulsion formulation of Nigella sativa L. essential oil on human breast cancer cells," *Ultrasonics Sonochemistry*, vol. 31, pp. 449–455, 2016.

[8] H.-F. Yen, C.-T. Hsieh, T.-J. Hsieh, F.-R. Chang, and C.-K. Wang, "In vitro anti-diabetic effect and chemical component analysis of 29 essential oils products," *Journal of Food and Drug Analysis*, vol. 23, no. 1, pp. 124–129, 2015.

[9] F. Brahmi, A. Abdenour, M. Bruno et al., "Chemical composition and in vitro antimicrobial, insecticidal and antioxidant activities of the essential oils of Mentha pulegium L. and Mentha rotundifolia (L.) Huds growing in Algeria," *Industrial Crops and Products*, vol. 88, pp. 96–105, 2016.

[10] J. Fernández-López and M. Viuda-Martos, "Introduction to the special issue: application of essential oils in food systems," *Foods*, vol. 7, no. 4, p. 56, 2018.

[11] C. M. Galanakis, "Recovery of high added-value components from food wastes: conventional, emerging technologies and commercialized applications," *Trends in Food Science & Technology*, vol. 26, no. 2, pp. 68–87, 2012.

[12] A. Jaworek, "Micro- and nanoparticle production by electrospraying," *Powder Technology*, vol. 176, no. 1, pp. 18–35, 2007.

[13] A. Jaworek and A. T. Sobczyk, "Electrospraying route to nanotechnology: an overview," *Journal of Electrostatics*, vol. 66, no. 3-4, pp. 197–219, 2008.

[14] J. Castro-Rosas, C. R. Ferreira-Grosso, C. A. Gómez-Aldapa et al., "Recent advances in microencapsulation of natural sources of antimicrobial compounds used in food—a review," *Food Research International*, vol. 102, pp. 575–587, 2017.

[15] F. Kayaci and T. Uyar, "Encapsulation of vanillin/cyclodextrin inclusion complex in electrospun polyvinyl alcohol (PVA) nanowebs: prolonged shelf-life and high temperature stability of vanillin," *Food Chemistry*, vol. 133, no. 3, pp. 641–649, 2012.

[16] Y. P. Neo, S. Swift, S. Ray, M. Gizdavic-Nikolaidis, J. Jin, and C. O. Perera, "Evaluation of gallic acid loaded zein submicron electrospun fibre mats as novel active packaging materials," *Food Chemistry*, vol. 141, no. 3, pp. 3192–3200, 2013.

[17] W.-J. Li, C. T. Laurencin, E. J. Caterson, R. S. Tuan, and F. K. Ko, "Electrospun nanofibrous structure: a novel scaffold for tissue engineering," *Journal of Biomedical Materials Research*, vol. 60, no. 4, pp. 613–621, 2002.

[18] R. A. Thakur, C. A. Florek, J. Kohn, and B. B. Michniak, "Electrospun nanofibrous polymeric scaffold with targeted drug release profiles for potential application as wound dressing," *International Journal of Pharmaceutics*, vol. 364, no. 1, pp. 87–93, 2008.

[19] M. R. El-Aassar, "Functionalized electrospun nanofibers from poly (AN-co-MMA) for enzyme immobilization," *Journal of Molecular Catalysis B: Enzymatic*, vol. 85-86, pp. 140–148, 2013.

[20] Q. Dong, G. Wang, H. Hu et al., "Ultrasound-assisted preparation of electrospun carbon nanofiber/graphene composite electrode for supercapacitors," *Journal of Power Sources*, vol. 243, pp. 350–353, 2013.

[21] J. A. Bhushani and C. Anandharamakrishnan, "Electrospinning and electrospraying techniques: potential food

based applications," *Trends in Food Science & Technology*, vol. 38, no. 1, pp. 21–33, 2014.

[22] R. Ribeiro-Santos, M. Andrade, N. R. d. Melo, and A. Sanches-Silva, "Use of essential oils in active food packaging: recent advances and future trends," *Trends in Food Science & Technology*, vol. 61, pp. 132–140, 2017.

[23] A. São Pedro, I. E. Santo, C. V. Silva, C. Detoni, and E. Albuquerque, "The use of nanotechnology as an approach for essential oil-based formulations with antimicrobial activity," in *Microbial Pathogens and Strategies for Combating Them*, A. Méndez-Vilas, Ed., vol. 2, pp. 1364–1374, Formatex Research Center Pulisher, Badajoz, Spain, 2013.

[24] R. Pavela, "Essential oils for the development of eco-friendly mosquito larvicides: a review," *Industrial Crops and Products*, vol. 76, pp. 174–187, 2015.

[25] K. Svoboda and R. Greenaway, "Investigation of volatile oil glands of Satureja hortensis L.(summer savory) and phytochemical comparison of different varieties," *The International Journal of Aromatherapy*, vol. 13, no. 4, pp. 196–202, 2003.

[26] W. A. Wannes, B. Mhamdi, J. Sriti et al., "Antioxidant activities of the essential oils and methanol extracts from myrtle (Myrtus communis var. italica L.) leaf, stem and flower," *Food and Chemical Toxicology*, vol. 48, no. 5, pp. 1362–1370, 2010.

[27] A. Dvaranauskaite, P. Venskutonis, C. Raynaud, T. Talou, P. Viskelis, and A. Sasnauskas, "Variations in the essential oil composition in buds of six blackcurrant (Ribes nigrum L.) cultivars at various development phases," *Food Chemistry*, vol. 114, no. 2, pp. 671–679, 2009.

[28] L. E. Hill, C. Gomes, and T. M. Taylor, "Characterization of beta-cyclodextrin inclusion complexes containing essential oils (trans-cinnamaldehyde, eugenol, cinnamon bark, and clove bud extracts) for antimicrobial delivery applications," *LWT—Food Science and Technology*, vol. 51, no. 1, pp. 86–93, 2013.

[29] J. Lv, H. Huang, L. Yu et al., "Phenolic composition and nutraceutical properties of organic and conventional cinnamon and peppermint," *Food Chemistry*, vol. 132, no. 3, pp. 1442–1450, 2012.

[30] C. Vallverdú, R. Vila, F. Tomi, M. Carhuapoma, J. Casanova, and S. Cañigueral, "Composition of the essential oil from leaves and twigs of Luma chequen," *Flavour and Fragrance Journal*, vol. 21, no. 2, pp. 241–243, 2006.

[31] A. I. Hussain, F. Anwar, S. T. Hussain Sherazi, and R. Przybylski, "Chemical composition, antioxidant and antimicrobial activities of basil (Ocimum basilicum) essential oils depends on seasonal variations," *Food Chemistry*, vol. 108, no. 3, pp. 986–995, 2008.

[32] M. Khajeh, Y. Yamini, N. Bahramifar, F. Sefidkon, and M. Reza Pirmoradei, "Comparison of essential oils compositions of Ferula assa-foetida obtained by supercritical carbon dioxide extraction and hydrodistillation methods," *Food Chemistry*, vol. 91, no. 4, pp. 639–644, 2005.

[33] P. S. Negi, "Plant extracts for the control of bacterial growth: efficacy, stability and safety issues for food application," *International Journal of Food Microbiology*, vol. 156, no. 1, pp. 7–17, 2012.

[34] L. Riahi, H. Chograni, M. Elferchichi, Y. Zaouali, N. Zoghlami, and A. Mliki, "Variations in Tunisian wormwood essential oil profiles and phenolic contents between leaves and flowers and their effects on antioxidant activities," *Industrial Crops and Products*, vol. 46, pp. 290–296, 2013.

[35] F. Bakkali, S. Averbeck, D. Averbeck, and M. Idaomar, "Biological effects of essential oils—a review," *Food and Chemical Toxicology*, vol. 46, no. 2, pp. 446–475, 2008.

[36] K.-K. Li, S.-W. Yin, X.-Q. Yang, C.-H. Tang, and Z.-H. Wei, "Fabrication and characterization of novel antimicrobial films derived from thymol-loaded zein-sodium caseinate (SC) nanoparticles," *Journal of Agricultural and Food Chemistry*, vol. 60, no. 46, pp. 11592–11600, 2012.

[37] D. Dainelli, N. Gontard, D. Spyropoulos, E. Zondervan-van den Beuken, and P. Tobback, "Active and intelligent food packaging: legal aspects and safety concerns," *Trends in Food Science & Technology*, vol. 19, pp. S103–S112, 2008.

[38] M. Ozdemir and J. D. Floros, "Active food packaging technologies," *Critical Reviews in Food Science and Nutrition*, vol. 44, no. 3, pp. 185–193, 2004.

[39] P. Suppakul, K. Sonneveld, S. W. Bigger, and J. Miltz, "Efficacy of polyethylene-based antimicrobial films containing principal constituents of basil," *LWT—Food Science and Technology*, vol. 41, no. 5, pp. 779–788, 2008.

[40] L. Vermeiren, F. Devlieghere, M. van Beest, N. de Kruijf, and J. Debevere, "Developments in the active packaging of foods," *Trends in Food Science & Technology*, vol. 10, no. 3, pp. 77–86, 1999.

[41] A. A. M. d. Melo, R. M. Geraldine, M. F. A. Silveira et al., "Microbiological quality and other characteristics of refrigerated chicken meat in contact with cellulose acetate-based film incorporated with rosemary essential oil," *Brazilian Journal of Microbiology*, vol. 43, no. 4, pp. 1419–1427, 2012.

[42] A. C. Souza, G. E. O. Goto, J. A. Mainardi, A. C. V. Coelho, and C. C. Tadini, "Cassava starch composite films incorporated with cinnamon essential oil: antimicrobial activity, microstructure, mechanical and barrier properties," *LWT—Food Science and Technology*, vol. 54, no. 2, pp. 346–352, 2013.

[43] Y. Peng and Y. Li, "Combined effects of two kinds of essential oils on physical, mechanical and structural properties of chitosan films," *Food Hydrocolloids*, vol. 36, pp. 287–293, 2014.

[44] M. Oussalah, S. Caillet, S. Salmiéri, L. Saucier, and M. Lacroix, "Antimicrobial effects of alginate-based films containing essential oils on Listeria monocytogenes and Salmonella typhimurium present in bologna and ham," *Journal of Food Protection*, vol. 70, no. 4, pp. 901–908, 2007.

[45] J. Hafsa, M. a. Smach, M. R. Ben Khedher et al., "Physical, antioxidant and antimicrobial properties of chitosan films containing Eucalyptus globulus essential oil," *LWT—Food Science and Technology*, vol. 68, pp. 356–364, 2016.

[46] A. C. Seydim and G. Sarikus, "Antimicrobial activity of whey protein based edible films incorporated with oregano, rosemary and garlic essential oils," *Food Research International*, vol. 39, no. 5, pp. 639–644, 2006.

[47] M. Jouki, F. T. Yazdi, S. A. Mortazavi, and A. Koocheki, "Quince seed mucilage films incorporated with oregano essential oil: physical, thermal, barrier, antioxidant and antibacterial properties," *Food Hydrocolloids*, vol. 36, pp. 9–19, 2014.

[48] D. A. Botre, N. d. F. F. Soares, P. J. P. Espitia, S. de Sousa, and I. R. T. Renhe, "Avaliação de filme incorporado com óleo essencial de orégano para conservação de pizza pronta," *Revista Ceres*, vol. 57, no. 3, pp. 283–291, 2015.

[49] V. Otero, R. Becerril, J. A. Santos, J. M. Rodríguez-Calleja, C. Nerín, and M.-L. García-López, "Evaluation of two antimicrobial packaging films against Escherichia coli O157:H7

strains in vitro and during storage of a Spanish ripened sheep cheese (Zamorano)," *Food Control*, vol. 42, pp. 296–302, 2014.

[50] Z. K. Emiroğlu, G. P. Yemiş, B. K. Coşkun, and K. Candoğan, "Antimicrobial activity of soy edible films incorporated with thyme and oregano essential oils on fresh ground beef patties," *Meat Science*, vol. 86, no. 2, pp. 283–288, 2010.

[51] K. G. Zinoviadou, K. P. Koutsoumanis, and C. G. Biliaderis, "Physico-chemical properties of whey protein isolate films containing oregano oil and their antimicrobial action against spoilage flora of fresh beef," *Meat Science*, vol. 82, no. 3, pp. 338–345, 2009.

[52] P. N. Takala, K. D. Vu, S. Salmieri, R. A. Khan, and M. Lacroix, "Antibacterial effect of biodegradable active packaging on the growth of Escherichia coli, Salmonella typhimurium and Listeria monocytogenes in fresh broccoli stored at 4°C," *LWT—Food Science and Technology*, vol. 53, no. 2, pp. 499–506, 2013.

[53] P. Tongnuanchan, S. Benjakul, and T. Prodpran, "Physico-chemical properties, morphology and antioxidant activity of film from fish skin gelatin incorporated with root essential oils," *Journal of Food Engineering*, vol. 117, no. 3, pp. 350–360, 2013.

[54] S. Shojaee-Aliabadi, H. Hosseini, M. A. Mohammadifar et al., "Characterization of antioxidant-antimicrobial κ--carrageenan films containing Satureja hortensis essential oil," *International Journal of Biological Macromolecules*, vol. 52, pp. 116–124, 2013.

[55] M. Oussalah, S. Caillet, S. Salmiéri, L. Saucier, and M. Lacroix, "Antimicrobial and antioxidant effects of milk protein-based film containing essential oils for the preservation of whole beef muscle," *Journal of Agricultural and Food Chemistry*, vol. 52, no. 18, pp. 5598–5605, 2004.

[56] J. Gómez-Estaca, A. López de Lacey, M. E. López-Caballero, M. C. Gómez-Guillén, and P. Montero, "Biodegradable gelatin-chitosan films incorporated with essential oils as antimicrobial agents for fish preservation," *Food Microbiology*, vol. 27, no. 7, pp. 889–896, 2010.

[57] P. R. Salgado, M. E. López-Caballero, M. C. Gómez-Guillén, A. N. Mauri, and M. P. Montero, "Sunflower protein films incorporated with clove essential oil have potential application for the preservation of fish patties," *Food Hydrocolloids*, vol. 33, no. 1, pp. 74–84, 2013.

[58] W. S. Choi, S. Singh, and Y. S. Lee, "Characterization of edible film containing essential oils in hydroxypropyl methylcellulose and its effect on quality attributes of "Formosa" plum (Prunus salicina L.)," *LWT*, vol. 70, pp. 213–222, 2016.

[59] J. Yun, X. Fan, X. Li, T. Z. Jin, X. Jia, and J. P. Mattheis, "Natural surface coating to inactivate Salmonella enterica serovar Typhimurium and maintain quality of cherry tomatoes," *International Journal of Food Microbiology*, vol. 193, pp. 59–67, 2015.

[60] K. D. Vu, R. G. Hollingsworth, E. Leroux, S. Salmieri, and M. Lacroix, "Development of edible bioactive coating based on modified chitosan for increasing the shelf life of strawberries," *Food Research International*, vol. 44, no. 1, pp. 198–203, 2011.

[61] Á. Perdones, I. Escriche, A. Chiralt, and M. Vargas, "Effect of chitosan-lemon essential oil coatings on volatile profile of strawberries during storage," *Food Chemistry*, vol. 197, pp. 979–986, 2016.

[62] S. Ramakrishna, K. Fujihara, W.-E. Teo, T. Yong, Z. Ma, and R. Ramaseshan, "Electrospun nanofibers: solving global issues," *Materials Today*, vol. 9, no. 3, pp. 40–50, 2006.

[63] Z.-M. Huang, Y.-Z. Zhang, M. Kotaki, and S. Ramakrishna, "A review on polymer nanofibers by electrospinning and their applications in nanocomposites," *Composites Science and Technology*, vol. 63, no. 15, pp. 2223–2253, 2003.

[64] L. Wannatong, A. Sirivat, and P. Supaphol, "Effects of solvents on electrospun polymeric fibers: preliminary study on polystyrene," *Polymer International*, vol. 53, no. 11, pp. 1851–1859, 2004.

[65] V. Lassalle and M. L. Ferreira, "PLA nano- and microparticles for drug delivery: an overview of the methods of preparation," *Macromolecular Bioscience*, vol. 7, no. 6, pp. 767–783, 2007.

[66] L. G. Gómez-Mascaraque, G. Sanchez, and A. López-Rubio, "Impact of molecular weight on the formation of electrosprayed chitosan microcapsules as delivery vehicles for bioactive compounds," *Carbohydrate Polymers*, vol. 150, pp. 121–130, 2016.

[67] S. Torres-Giner, A. Martinez-Abad, M. J. Ocio, and J. M. Lagaron, "Stabilization of a nutraceutical omega-3 fatty acid by encapsulation in ultrathin electrosprayed zein prolamine," *Journal of Food Science*, vol. 75, no. 6, pp. N69–N79, 2010.

[68] S. M. Jafari, *Nanoencapsulation Technologies for the Food and Nutraceutical Industries*, Academic Press, Cambridge, MA, USA, 2017.

[69] A. A. Almetwally, M. El-Sakhawy, M. Elshakankery, and M. Kasem, "Technology of nano-fibers: production techniques and properties-critical review," *Journal of the Textile Association*, vol. 78, pp. 5–14, 2017.

[70] S. Chakraborty, I.-C. Liao, A. Adler, and K. W. Leong, "Electrohydrodynamics: a facile technique to fabricate drug delivery systems," *Advanced Drug Delivery Reviews*, vol. 61, no. 12, pp. 1043–1054, 2009.

[71] A. López-Rubio, E. Sanchez, S. Wilkanowicz, Y. Sanz, and J. M. Lagaron, "Electrospinning as a useful technique for the encapsulation of living bifidobacteria in food hydrocolloids," *Food Hydrocolloids*, vol. 28, no. 1, pp. 159–167, 2012.

[72] R. Pérez-Masiá, J. M. Lagaron, and A. Lopez-Rubio, "Morphology and stability of edible lycopene-containing micro- and nanocapsules produced through electrospraying and spray drying," *Food and Bioprocess Technology*, vol. 8, no. 2, pp. 459–470, 2015.

[73] M. Eltayeb, P. K. Bakhshi, E. Stride, and M. Edirisinghe, "Preparation of solid lipid nanoparticles containing active compound by electrohydrodynamic spraying," *Food Research International*, vol. 53, no. 1, pp. 88–95, 2013.

[74] K. A. Rieger and J. D. Schiffman, "Electrospinning an essential oil: cinnamaldehyde enhances the antimicrobial efficacy of chitosan/poly(ethylene oxide) nanofibers," *Carbohydrate Polymers*, vol. 113, pp. 561–568, 2014.

[75] K. Feng, P. Wen, H. Yang et al., "Enhancement of the antimicrobial activity of cinnamon essential oil-loaded electrospun nanofilm by the incorporation of lysozyme," *RSC Advances*, vol. 7, no. 3, pp. 1572–1580, 2017.

[76] J. Wróblewska-Krepsztul, T. Rydzkowski, I. Michalska-Pożoga, and V. K. Thakur, "Biopolymers for biomedical and pharmaceutical applications: recent advances and overview of alginate electrospinning," *Nanomaterials*, vol. 9, no. 3, p. 404, 2019.

[77] K. A. Rieger, N. P. Birch, and J. D. Schiffman, "Electrospinning chitosan/poly(ethylene oxide) solutions with

essential oils: correlating solution rheology to nanofiber formation," *Carbohydrate Polymers*, vol. 139, pp. 131–138, 2016.

[78] I. Katouzian and S. M. Jafari, "Nano-encapsulation as a promising approach for targeted delivery and controlled release of vitamins," *Trends in Food Science & Technology*, vol. 53, pp. 34–48, 2016.

[79] M. Shrestha, T. M. Ho, and B. R. Bhandari, "Encapsulation of tea tree oil by amorphous beta-cyclodextrin powder," *Food Chemistry*, vol. 221, pp. 1474–1483, 2017.

[80] J.-h. Cheng, Y.-n. Hu, Z.-g. Luo, W. Chen, H.-m. Chen, and X.-c. Peng, "Preparation and properties of octenyl succinate β-cyclodextrin and its application as an emulsion stabilizer," *Food Chemistry*, vol. 218, pp. 116–121, 2017.

[81] E. N. Faikoh, Y.-H. Hong, and S.-Y. Hu, "Liposome-encapsulated cinnamaldehyde enhances zebrafish (Danio rerio) immunity and survival when challenged with Vibrio vulnificus and Streptococcus agalactiae," *Fish & Shellfish Immunology*, vol. 38, no. 1, pp. 15–24, 2014.

[82] Z. Fang and B. Bhandari, "Encapsulation of polyphenols—a review," *Trends in Food Science & Technology*, vol. 21, no. 10, pp. 510–523, 2010.

[83] R. E. Conn, J. J. Kolstad, J. F. Borzelleca et al., "Safety assessment of polylactide (PLA) for use as a food-contact polymer," *Food and Chemical Toxicology*, vol. 33, no. 4, pp. 273–283, 1995.

[84] P. Wen, D.-H. Zhu, H. Wu, M.-H. Zong, Y.-R. Jing, and S.-Y. Han, "Encapsulation of cinnamon essential oil in electrospun nanofibrous film for active food packaging," *Food Control*, vol. 59, pp. 366–376, 2016.

[85] G. Chen and B. Liu, "Cellulose sulfate based film with slow-release antimicrobial properties prepared by incorporation of mustard essential oil and β-cyclodextrin," *Food Hydrocolloids*, vol. 55, pp. 100–107, 2016.

[86] C. López-de-Dicastillo, M. Jordá, R. Catalá, R. Gavara, and P. Hernández-Muñoz, "Development of active polyvinyl alcohol/β-cyclodextrin composites to scavenge undesirable food components," *Journal of Agricultural and Food Chemistry*, vol. 59, no. 20, pp. 11026–11033, 2011.

[87] M. Jawaid and S. K. Swain, *Bionanocomposites for Packaging Applications*, Springer, Berlin, Germany, 2018.

[88] C. Sebaaly, C. Charcosset, S. Stainmesse, H. Fessi, and H. Greige-Gerges, "Clove essential oil-in-cyclodextrin-in-liposomes in the aqueous and lyophilized states: from laboratory to large scale using a membrane contactor," *Carbohydrate Polymers*, vol. 138, pp. 75–85, 2016.

[89] E. M. M. Del Valle, "Cyclodextrins and their uses: a review," *Process Biochemistry*, vol. 39, no. 9, pp. 1033–1046, 2004.

[90] J. Szejtli, "Introduction and general overview of cyclodextrin chemistry," *Chemical Reviews*, vol. 98, no. 5, pp. 1743–1754, 1998.

[91] C. Samperio, R. Boyer, W. N. Eigel et al., "Enhancement of plant essential oils' aqueous solubility and stability using alpha and beta cyclodextrin," *Journal of Agricultural and Food Chemistry*, vol. 58, no. 24, pp. 12950–12956, 2010.

[92] H. M. C. de Azeredo, "Antimicrobial nanostructures in food packaging," *Trends in Food Science & Technology*, vol. 30, no. 1, pp. 56–69, 2013.

[93] H. Samsudin, H. Soto-Valdez, and R. Auras, "Poly(lactic acid) film incorporated with marigold flower extract (Tagetes erecta) intended for fatty-food application," *Food Control*, vol. 46, pp. 55–66, 2014.

[94] P. Wen, D.-H. Zhu, K. Feng et al., "Fabrication of electrospun polylactic acid nanofilm incorporating cinnamon essential oil/β -cyclodextrin inclusion complex for antimicrobial packaging," *Food Chemistry*, vol. 196, pp. 996–1004, 2016.

[95] Y. Liu, S. Wang, R. Zhang, W. Lan, and W. Qin, "Development of poly(lactic acid)/chitosan fibers loaded with essential oil for antimicrobial applications," *Nanomaterials*, vol. 7, no. 7, p. 194, 2017.

[96] M. Kashiri, Y. Maghsoudlo, and M. Khomeiri, "Incorporating Zataria multiflora Boiss. essential oil and sodium bentonite nano-clay open a new perspective to use zein films as bioactive packaging materials," *Food Science and Technology International*, vol. 23, no. 7, pp. 582–596, 2017.

[97] L. Lin, Y. Dai, and H. Cui, "Antibacterial poly(ethylene oxide) electrospun nanofibers containing cinnamon essential oil/beta-cyclodextrin proteoliposomes," *Carbohydrate Polymers*, vol. 178, pp. 131–140, 2017.

[98] M. C. Ribeiro, M. da Silva Fernandes, A. Yoshiteru Kuaye, R. Jimenez-Flores, and M. Gigante, "Preconditioning of the stainless steel surface affects the adhesion of Bacillus cereus spores," *International Dairy Journal*, vol. 66, pp. 108–114, 2017.

[99] S. Kumari and P. K. Sarkar, "Bacillus cereus hazard and control in industrial dairy processing environment," *Food Control*, vol. 69, pp. 20–29, 2016.

[100] İ. Ünalan, F. Korel, and A. Yemenicioğlu, "Active packaging of ground beef patties by edible zein films incorporated with partially purified lysozyme and Na2EDTA," *International Journal of Food Science & Technology*, vol. 46, no. 6, pp. 1289–1295, 2011.

[101] K. S. Doosh and S. M. Abdul-Rahm, "Effect of lysozyme isolated from hen egg white in elongation the shelf life of Iraqi soft cheese made from buffalo milk," *Pakistan Journal of Nutrition*, vol. 13, no. 11, pp. 635–641, 2014.

[102] C. B. Amara, N. Eghbal, P. Degraeve, and A. Gharsallaoui, "Using complex coacervation for lysozyme encapsulation by spray-drying," *Journal of Food Engineering*, vol. 183, pp. 50–57, 2016.

[103] L. Ge, Y.-s. Zhao, T. Mo, J.-r. Li, and P. Li, "Immobilization of glucose oxidase in electrospun nanofibrous membranes for food preservation," *Food Control*, vol. 26, no. 1, pp. 188–193, 2012.

[104] D.-z. Yang, Y.-h. Long, and J. Nie, "Release of lysozyme from electrospun PVA/lysozyme-gelatin scaffolds," *Frontiers of Materials Science in China*, vol. 2, no. 3, pp. 261–265, 2008.

[105] P. Shao, Z. Yan, H. Chen, and J. Xiao, "Electrospun poly(-vinyl alcohol)/permutite fibrous film loaded with cinnamaldehyde for active food packaging," *Journal of Applied Polymer Science*, vol. 135, no. 16, p. 46117, 2018.

[106] J. Wu, C. Yu, and Q. Li, "Regenerable antimicrobial activity in polyamide thin film nanocomposite membranes," *Journal of Membrane Science*, vol. 476, pp. 119–127, 2015.

[107] A. Baselice, F. Colantuoni, D. A. Lass, G. Nardone, and A. Stasi, "Trends in EU consumers' attitude towards fresh-cut fruit and vegetables," *Food Quality and Preference*, vol. 59, pp. 87–96, 2017.

[108] M. Oliveira, M. Abadias, J. Usall, R. Torres, N. Teixidó, and I. Viñas, "Application of modified atmosphere packaging as a safety approach to fresh-cut fruits and vegetables—a review," *Trends in Food Science & Technology*, vol. 46, no. 1, pp. 13–26, 2015.

[109] J. Xiao, C. Shi, H. Zheng et al., "Kafirin protein based electrospun fibers with tunable mechanical property, wettability, and release profile," *Journal of Agricultural and Food Chemistry*, vol. 64, no. 16, pp. 3226–3233, 2016.

[110] H. H. Kara, F. Xiao, M. Sarker et al., "Antibacterial poly(lactic acid) (PLA) films grafted with electrospun PLA/allyl isothiocyanate fibers for food packaging," *Journal of Applied Polymer Science*, vol. 133, no. 2, 2016.

[111] S. Phunpee, S. Saesoo, I. Sramala et al., "A comparison of eugenol and menthol on encapsulation characteristics with water-soluble quaternized β-cyclodextrin grafted chitosan," *International Journal of Biological Macromolecules*, vol. 84, pp. 472–480, 2016.

[112] K. P. Anthony, S. A. Deolu-Sobogun, and M. A. Saleh, "Comprehensive assessment of antioxidant activity of essential oils," *Journal of Food Science*, vol. 77, no. 8, pp. C839–C843, 2012.

[113] H. Cetin Babaoglu, A. Bayrak, N. Ozdemir, and N. Ozgun, "Encapsulation of clove essential oil in hydroxypropyl β-cyclodextrin for characterization, controlled release, and antioxidant activity," *Journal of Food Processing and Preservation*, vol. 41, no. 5, Article ID e13202, 2017.

[114] H. M. C. Marques, "A review on cyclodextrin encapsulation of essential oils and volatiles," *Flavour and Fragrance Journal*, vol. 25, no. 5, pp. 313–326, 2010.

[115] T. Uyar, J. Hacaloglu, and F. Besenbacher, "Electrospun polyethylene oxide (PEO) nanofibers containing cyclodextrin inclusion complex," *Journal of Nanoscience and Nanotechnology*, vol. 11, no. 5, pp. 3949–3958, 2011.

[116] F. Kayaci, Y. Ertas, and T. Uyar, "Enhanced thermal stability of eugenol by cyclodextrin inclusion complex encapsulated in electrospun polymeric nanofibers," *Journal of Agricultural and Food Chemistry*, vol. 61, no. 34, pp. 8156–8165, 2013.

[117] F. Kayaci, H. S. Sen, E. Durgun, and T. Uyar, "Functional electrospun polymeric nanofibers incorporating geraniol-cyclodextrin inclusion complexes: high thermal stability and enhanced durability of geraniol," *Food Research International*, vol. 62, pp. 424–431, 2014.

[118] Z. Aytac, S. Y. Dogan, T. Tekinay, and T. Uyar, "Release and antibacterial activity of allyl isothiocyanate/β-cyclodextrin complex encapsulated in electrospun nanofibers," *Colloids and Surfaces B: Biointerfaces*, vol. 120, pp. 125–131, 2014.

[119] Z. Aytac, S. I. Kusku, E. Durgun, and T. Uyar, "Quercetin/β-cyclodextrin inclusion complex embedded nanofibres: slow release and high solubility," *Food Chemistry*, vol. 197, pp. 864–871, 2016.

[120] Z. Aytac, Z. I. Yildiz, F. Kayaci-Senirmak, N. O. San Keskin, T. Tekinay, and T. Uyar, "Electrospinning of polymer-free cyclodextrin/geraniol-inclusion complex nanofibers: enhanced shelf-life of geraniol with antibacterial and antioxidant properties," *RSC Advances*, vol. 6, no. 52, pp. 46089–46099, 2016.

[121] Z. Aytac, Z. I. Yildiz, F. Kayaci-Senirmak et al., "Fast-dissolving, prolonged release, and antibacterial cyclodextrin/limonene-inclusion complex nanofibrous webs via polymer-free electrospinning," *Journal of Agricultural and Food Chemistry*, vol. 64, no. 39, pp. 7325–7334, 2016.

[122] Z. Aytac, Z. I. Yildiz, F. Kayaci-Senirmak, T. Tekinay, and T. Uyar, "Electrospinning of cyclodextrin/linalool-inclusion complex nanofibers: fast-dissolving nanofibrous web with prolonged release and antibacterial activity," *Food Chemistry*, vol. 231, pp. 192–201, 2017.

[123] A. Celebioglu, F. Kayaci-Senirmak, S. İpek, E. Durgun, and T. Uyar, "Polymer-free nanofibers from vanillin/cyclodextrin inclusion complexes: high thermal stability, enhanced solubility and antioxidant property," *Food & Function*, vol. 7, no. 7, pp. 3141–3153, 2016.

[124] A. Celebioglu, Z. I. Yildiz, and T. Uyar, "Fabrication of electrospun eugenol/cyclodextrin inclusion complex nanofibrous webs for enhanced antioxidant property, water solubility, and high temperature stability," *Journal of Agricultural and Food Chemistry*, vol. 66, no. 2, pp. 457–466, 2018.

[125] D. Pornpattananangkul, L. Zhang, S. Olson et al., "Bacterial toxin-triggered drug release from gold nanoparticle-stabilized liposomes for the treatment of bacterial infection," *Journal of the American Chemical Society*, vol. 133, no. 11, pp. 4132–4139, 2011.

[126] G. A. T. Kaminski, M. R. Sierakowski, R. Pontarolo, L. A. d. Santos, and R. A. d. Freitas, "Layer-by-layer polysaccharide-coated liposomes for sustained delivery of epidermal growth factor," *Carbohydrate Polymers*, vol. 140, pp. 129–135, 2016.

[127] W. Liu, W. Liu, A. Ye et al., "Environmental stress stability of microencapsules based on liposomes decorated with chitosan and sodium alginate," *Food Chemistry*, vol. 196, pp. 396–404, 2016.

[128] L. M. P. Montenegro, J. B. Griep, F. C. Tavares, D. H. de Oliveira, D. Bianchini, and R. G. Jacob, "Synthesis and characterization of imine-modified silicas obtained by the reaction of essential oil of Eucalyptus citriodora, 3-aminopropyltriethoxysilane and tetraethylorthosilicate," *Vibrational Spectroscopy*, vol. 68, pp. 272–278, 2013.

[129] J. H. Cui, Y. Liang, D. Yang, and Y. Liu, "Facile fabrication of rice husk based silicon dioxide nanospheres loaded with silver nanoparticles as a rice antibacterial agent," *Scientific Reports*, vol. 6, no. 1, p. 21423, 2016.

[130] K. Okada, T. Tomita, Y. Kameshima, A. Yasumori, and K. J. D. MacKenzie, "Porous properties of coprecipitated Al_2O_3-SiO_2 xerogels prepared from aluminium nitrate nonahydrate and tetraethylorthosilicate," *Journal of Materials Chemistry*, vol. 9, no. 6, pp. 1307–1312, 1999.

[131] H. Ziyang, Z. Lan, and L. Guangchao, "Study on fabrication and properties of porous HA/SiO_2 composite coating on titanium substrate," *Acta Chimica Sinica*, vol. 70, no. 3, pp. 235–240, 2012.

[132] Z. Li, H. Kang, N. Che et al., "Controlled release of liposome-encapsulated Naproxen from core-sheath electrospun nanofibers," *Carbohydrate Polymers*, vol. 111, pp. 18–24, 2014.

[133] N. C. Wickremasinghe, V. A. Kumar, and J. D. Hartgerink, "Two-step self-assembly of liposome-multidomain peptide nanofiber hydrogel for time-controlled release," *Biomacromolecules*, vol. 15, no. 10, pp. 3587–3595, 2014.

[134] I. Peinado, M. Mason, A. Romano, F. Biasioli, and M. Scampicchio, "Stability of β-carotene in polyethylene oxide electrospun nanofibers," *Applied Surface Science*, vol. 370, pp. 111–116, 2016.

[135] H. Cui, L. Yuan, W. Li, and L. Lin, "Antioxidant property of SiO_2-eugenol liposome loaded nanofibrous membranes on beef," *Food Packaging and Shelf Life*, vol. 11, pp. 49–57, 2017.

[136] B. Munteanu, L. Sacarescu, A.-L. Vasiliu et al., "Antioxidant/antibacterial electrospun nanocoatings applied onto PLA films," *Materials*, vol. 11, no. 10, p. 1973, 2018.

[137] K. Divya, S. Vijayan, T. K. George, and M. S. Jisha, "Antimicrobial properties of chitosan nanoparticles: mode of action and factors affecting activity," *Fibers and Polymers*, vol. 18, no. 2, pp. 221–230, 2017.

[138] M. Gällstedt, A. Brottman, and M. S. Hedenqvist, "Packaging-related properties of protein- and chitosan-coated

paper," *Packaging Technology and Science*, vol. 18, no. 4, pp. 161–170, 2005.

[139] S.-I. Hong, J.-W. Lee, and S.-M. Son, "Properties of polysaccharide-coated polypropylene films as affected by biopolymer and plasticizer types," *Packaging Technology and Science*, vol. 18, no. 1, pp. 1–9, 2005.

[140] C. H. Lee, D. S. An, H. J. Park, and D. S. Lee, "Wide-spectrum antimicrobial packaging materials incorporating nisin and chitosan in the coating," *Packaging Technology and Science*, vol. 16, no. 3, pp. 99–106, 2003.

[141] H. Berrougui, M. Cloutier, M. Isabelle, and A. Khalil, "Phenolic-extract from argan oil (Argania spinosa L.) inhibits human low-density lipoprotein (LDL) oxidation and enhances cholesterol efflux from human THP-1 macrophages," *Atherosclerosis*, vol. 184, no. 2, pp. 389–396, 2006.

[142] M. Kouidri, A. K. Saadi, A. Noui, and F. Medjahed, "The chemical composition of argan oil," *International Journal of Advanced Studies in Computers, Science and Engineering*, vol. 4, no. 1, p. 24, 2015.

[143] K. Chaieb, H. Hajlaoui, T. Zmantar et al., "The chemical composition and biological activity of clove essential oil, Eugenia caryophyllata (Syzigium aromaticum L. Myrtaceae): a short review," *Phytotherapy Research*, vol. 21, no. 6, pp. 501–506, 2007.

[144] B. Melendez-Rodriguez, K. J. Figueroa-Lopez, A. Bernardos et al., "Electrospun antimicrobial films of poly(3-hydroxybutyrate-co-3-hydroxyvalerate) containing eugenol essential oil encapsulated in mesoporous silica nanoparticles," *Nanomaterials*, vol. 9, no. 2, p. 227, 2019.

[145] H. Cui, M. Bai, M. M. A. Rashed, and L. Lin, "The antibacterial activity of clove oil/chitosan nanoparticles embedded gelatin nanofibers against Escherichia coli O157:H7 biofilms on cucumber," *International Journal of Food Microbiology*, vol. 266, pp. 69–78, 2018.

[146] H. Cui, C. Ma, C. Li, and L. Lin, "Enhancing the antibacterial activity of thyme oil against Salmonella on eggshell by plasma-assisted process," *Food Control*, vol. 70, pp. 183–190, 2016.

[147] A. Marchese, I. E. Orhan, M. Daglia et al., "Antibacterial and antifungal activities of thymol: a brief review of the literature," *Food Chemistry*, vol. 210, pp. 402–414, 2016.

[148] L. Rivas, M. J. McDonnell, C. M. Burgess et al., "Inhibition of verocytotoxigenic Escherichia coli in model broth and rumen systems by carvacrol and thymol," *International Journal of Food Microbiology*, vol. 139, no. 1-2, pp. 70–78, 2010.

[149] M. A. Numpaque, L. A. Oviedo, J. H. Gil, C. M. García, and D. L. Durango, "Thymol and carvacrol: biotransformation and antifungal activity against the plant pathogenic fungi Colletotrichum acutatum and Botryodiplodia theobromae," *Tropical Plant Pathology*, vol. 36, no. 1, pp. 3–13, 2011.

[150] P. S. Chavan and S. G. Tupe, "Antifungal activity and mechanism of action of carvacrol and thymol against vineyard and wine spoilage yeasts," *Food Control*, vol. 46, pp. 115–120, 2014.

[151] L.-H. Wang, Z.-H. Zhang, X.-A. Zeng, D.-M. Gong, and M.-S. Wang, "Combination of microbiological, spectroscopic and molecular docking techniques to study the antibacterial mechanism of thymol against Staphylococcus aureus: membrane damage and genomic DNA binding," *Analytical and Bioanalytical Chemistry*, vol. 409, no. 6, pp. 1615–1625, 2017.

[152] D. Valero, J. M. Valverde, D. Martínez-Romero, F. Guillén, S. Castillo, and M. Serrano, "The combination of modified atmosphere packaging with eugenol or thymol to maintain quality, safety and functional properties of table grapes," *Postharvest Biology and Technology*, vol. 41, no. 3, pp. 317–327, 2006.

[153] C. O. Pérez-Alfonso, D. Martínez-Romero, P. J. Zapata, M. Serrano, D. Valero, and S. Castillo, "The effects of essential oils carvacrol and thymol on growth of Penicillium digitatum and P. italicum involved in lemon decay," *International Journal of Food Microbiology*, vol. 158, no. 2, pp. 101–106, 2012.

[154] L. Lin, Y. Zhu, and H. Cui, "Electrospun thyme essential oil/gelatin nanofibers for active packaging against Campylobacter jejuni in chicken," *LWT*, vol. 97, pp. 711–718, 2018.

[155] P. Umaraw, A. Prajapati, A. K. Verma, V. Pathak, and V. P. Singh, "Control of Campylobacter in poultry industry from farm to poultry processing unit: a review," *Critical Reviews in Food Science and Nutrition*, vol. 57, no. 4, pp. 659–665, 2017.

[156] W. C. Silva, B. N. Targino, R. S. Mendonça, A. S. Sant'Ana, and H. M. Hungaro, "Campylobacter: an overview of cases, occurrence in food, contamination sources, and antimicrobial resistance in Brazil," *Food Reviews International*, vol. 34, no. 4, pp. 364–389, 2018.

[157] A. Pant and J. S. Negi, "Novel controlled ionic gelation strategy for chitosan nanoparticles preparation using TPP-β-CD inclusion complex," *European Journal of Pharmaceutical Sciences*, vol. 112, pp. 180–185, 2018.

[158] H. Lu, L. Zou, Y. Xu, and Y. V. Li, "Controlled dispersion of multiwalled carbon nanotubes modified by hyperbranched polylysine," *Journal of Applied Polymer Science*, vol. 135, no. 19, p. 46249, 2018.

[159] M. Rizwan, R. Yahya, A. Hassan et al., "Synthesis of a novel organosoluble, biocompatible, and antibacterial chitosan derivative for biomedical applications," *Journal of Applied Polymer Science*, vol. 135, no. 9, p. 45905, 2018.

[160] Z. Aytac, S. Ipek, E. Durgun, T. Tekinay, and T. Uyar, "Antibacterial electrospun zein nanofibrous web encapsulating thymol/cyclodextrin-inclusion complex for food packaging," *Food Chemistry*, vol. 233, pp. 117–124, 2017.

[161] Z. Li, M. Wang, F. Wang et al., "γ-cyclodextrin: a review on enzymatic production and applications," *Applied Microbiology and Biotechnology*, vol. 77, no. 2, pp. 245–255, 2007.

[162] P. A. P. Cevallos, M. P. Buera, and B. E. Elizalde, "Encapsulation of cinnamon and thyme essential oils components (cinnamaldehyde and thymol) in β-cyclodextrin: effect of interactions with water on complex stability," *Journal of Food Engineering*, vol. 99, no. 1, pp. 70–75, 2010.

[163] Z. Aytac and T. Uyar, "Antioxidant activity and photostability of α-tocopherol/β-cyclodextrin inclusion complex encapsulated electrospun polycaprolactone nanofibers," *European Polymer Journal*, vol. 79, pp. 140–149, 2016.

[164] F. Tao, L. E. Hill, Y. Peng, and C. L. Gomes, "Synthesis and characterization of β-cyclodextrin inclusion complexes of thymol and thyme oil for antimicrobial delivery applications," *LWT—Food Science and Technology*, vol. 59, no. 1, pp. 247–255, 2014.

[165] I. Mourtzinos, N. Kalogeropoulos, S. E. Papadakis, K. Konstantinou, and V. T. Karathanos, "Encapsulation of nutraceutical monoterpenes in β-cyclodextrin and modified starch," *Journal of Food Science*, vol. 73, no. 1, pp. S89–S94, 2008.

[166] Y. Zhang, Y. Zhang, Z. Zhu, X. Jiao, Y. Shang, and Y. Wen, "Encapsulation of thymol in biodegradable nanofiber via coaxial eletrospinning and applications in fruit

preservation," *Journal of Agricultural and Food Chemistry*, vol. 67, no. 6, pp. 1736–1741, 2019.

[167] H. K. Makadia and S. J. Siegel, "Poly lactic-co-glycolic acid (PLGA) as biodegradable controlled drug delivery carrier," *Polymers*, vol. 3, no. 3, pp. 1377–1397, 2011.

[168] C. Gomes, R. G. Moreira, and E. Castell-Perez, "Poly (DL-lactide-co-glycolide) (PLGA) nanoparticles with entrapped trans-cinnamaldehyde and eugenol for antimicrobial delivery applications," *Journal of Food Science*, vol. 76, no. 2, pp. N16–N24, 2011.

[169] L. M. Silva, L. E. Hill, E. Figueiredo, and C. L. Gomes, "Delivery of phytochemicals of tropical fruit by-products using poly (DL-lactide-co-glycolide) (PLGA) nanoparticles: synthesis, characterization, and antimicrobial activity," *Food Chemistry*, vol. 165, pp. 362–370, 2014.

[170] R. F. Lins, W. R. Lustri, S. Minharro, A. Alonso, and D. de Sousa Neto, "On the formation, physicochemical properties and antibacterial activity of colloidal systems containing tea tree (Melaleuca alternifolia) oil," *Colloids and Surfaces A: Physicochemical and Engineering Aspects*, vol. 497, pp. 271–279, 2016.

[171] D. J. Ireland, S. J. Greay, C. M. Hooper et al., "Topically applied Melaleuca alternifolia (tea tree) oil causes direct anticancer cytotoxicity in subcutaneous tumour bearing mice," *Journal of Dermatological Science*, vol. 67, no. 2, pp. 120–129, 2012.

[172] O. Catanzano, M. C. Straccia, A. Miro et al., "Spray-by-spray in situ cross-linking alginate hydrogels delivering a tea tree oil microemulsion," *European Journal of Pharmaceutical Sciences*, vol. 66, pp. 20–28, 2015.

[173] F. d. S. Oliveira, T. S. d. Freitas, R. P. d. Cruz et al., "Evaluation of the antibacterial and modulatory potential of α-bisabolol, β-cyclodextrin and α-bisabolol/β-cyclodextrin complex," *Biomedicine & Pharmacotherapy*, vol. 92, pp. 1111–1118, 2017.

[174] H. Cui, M. Bai, and L. Lin, "Plasma-treated poly(ethylene oxide) nanofibers containing tea tree oil/beta-cyclodextrin inclusion complex for antibacterial packaging," *Carbohydrate Polymers*, vol. 179, pp. 360–369, 2018.

[175] F. A. P. Scacchetti, E. Pinto, and G. M. B. Soares, "Functionalization and characterization of cotton with phase change materials and thyme oil encapsulated in beta-cyclodextrins," *Progress in Organic Coatings*, vol. 107, pp. 64–74, 2017.

[176] Y. Tang, Y. Zhou, X. Lan et al., "Electrospun gelatin nanofibers encapsulated with peppermint and chamomile essential oils as potential edible packaging," *Journal of Agricultural and Food Chemistry*, vol. 67, no. 8, pp. 2227–2234, 2019.

[177] R. Liang, S. Xu, C. F. Shoemaker, Y. Li, F. Zhong, and Q. Huang, "Physical and antimicrobial properties of peppermint oil nanoemulsions," *Journal of Agricultural and Food Chemistry*, vol. 60, no. 30, pp. 7548–7555, 2012.

[178] I. Liakos, L. Rizzello, H. Hajiali et al., "Fibrous wound dressings encapsulating essential oils as natural antimicrobial agents," *Journal of Materials Chemistry B*, vol. 3, no. 8, pp. 1583–1589, 2015.

[179] B. P. Chumpitazi, G. L. Kearns, and R. J. Shulman, "Review article: the physiological effects and safety of peppermint oil and its efficacy in irritable bowel syndrome and other functional disorders," *Alimentary Pharmacology & Therapeutics*, vol. 47, no. 6, pp. 738–752, 2018.

[180] M. H. H. Roby, M. A. Sarhan, K. A.-H. Selim, and K. I. Khalel, "Antioxidant and antimicrobial activities of essential oil and extracts of fennel (Foeniculum vulgare L.) and chamomile (Matricaria chamomilla L.)," *Industrial Crops and Products*, vol. 44, pp. 437–445, 2013.

[181] S. Agatonovic-Kustrin, D. Babazadeh Ortakand, D. W. Morton, and A. P. Yusof, "Rapid evaluation and comparison of natural products and antioxidant activity in calendula, feverfew, and German chamomile extracts," *Journal of Chromatography A*, vol. 1385, pp. 103–110, 2015.

[182] F. Duman, I. Ocsoy, and F. O. Kup, "Chamomile flower extract-directed CuO nanoparticle formation for its antioxidant and DNA cleavage properties," *Materials Science and Engineering: C*, vol. 60, pp. 333–338, 2016.

[183] A. Cvetanović, J. Švarc-Gajić, P. Mašković, S. Savić, and L. Nikolić, "Antioxidant and biological activity of chamomile extracts obtained by different techniques: perspective of using superheated water for isolation of biologically active compounds," *Industrial Crops and Products*, vol. 65, pp. 582–591, 2015.

[184] Z. A. N. Hanani, Y. H. Roos, and J. P. Kerry, "Use and application of gelatin as potential biodegradable packaging materials for food products," *International Journal of Biological Macromolecules*, vol. 71, pp. 94–102, 2014.

[185] F. M. Fakhouri, D. Costa, F. Yamashita et al., "Comparative study of processing methods for starch/gelatin films," *Carbohydrate Polymers*, vol. 95, no. 2, pp. 681–689, 2013.

[186] S. F. Hosseini, M. Rezaei, M. Zandi, and F. Farahmandghavi, "Bio-based composite edible films containing Origanum vulgare L. essential oil," *Industrial Crops and Products*, vol. 67, pp. 403–413, 2015.

[187] M. Ahmad, S. Benjakul, T. Prodpran, and T. W. Agustini, "Physico-mechanical and antimicrobial properties of gelatin film from the skin of unicorn leatherjacket incorporated with essential oils," *Food Hydrocolloids*, vol. 28, no. 1, pp. 189–199, 2012.

[188] P.-D. Duh, "Antioxidant activity of water extract of four Harng Jyur (Chrysanthemum morifolium Ramat) varieties in soybean oil emulsion," *Food Chemistry*, vol. 66, no. 4, pp. 471–476, 1999.

[189] C.-K. Lii, Y.-P. Lei, H.-T. Yao et al., "Chrysanthemum morifolium Ramat. reduces the oxidized LDL-induced expression of intercellular adhesion molecule-1 and E-selectin in human umbilical vein endothelial cells," *Journal of Ethnopharmacology*, vol. 128, no. 1, pp. 213–220, 2010.

[190] F. Khallouki, M. Hmamouchi, C. Younos, R. Soulimani, J. M. Bessiere, and E. M. Essassi, "Antibacterial and molluscicidal activities of the essential oil of Chrysanthemum viscidehirtum," *Fitoterapia*, vol. 71, no. 5, pp. 544–546, 2000.

[191] L. Lin, X. Mao, Y. Sun, G. Rajivgandhi, and H. Cui, "Antibacterial properties of nanofibers containing chrysanthemum essential oil and their application as beef packaging," *International Journal of Food Microbiology*, vol. 292, pp. 21–30, 2019.

[192] M. Nadeem and M. Imran, "Promising features of Moringa oleifera oil: recent updates and perspectives," *Lipids in Health and Disease*, vol. 15, no. 1, p. 212, 2016.

[193] L. Lin, Y. Gu, and H. Cui, "Moringa oil/chitosan nanoparticles embedded gelatin nanofibers for food packaging against Listeria monocytogenes and Staphylococcus aureus on cheese," *Food Packaging and Shelf Life*, vol. 19, pp. 86–93, 2019.

Hindawi
Advances in Polymer Technology
Volume 2020, Article ID 6861205, 16 pages
https://doi.org/10.1155/2020/6861205

Review Article

Recent Advances in Carbon Nanotubes for Nervous Tissue Regeneration

Carlos Redondo-Gómez,[1] **Rocío Leandro-Mora**,[2] **Daniela Blanch-Bermúdez**,[2] **Christopher Espinoza-Araya**,[2] **David Hidalgo-Barrantes**,[2] **and José Vega-Baudrit**[1,2]

[1]*National Laboratory of Nanotechnology LANOTEC, 1174-1200 Pavas, San José, Costa Rica*
[2]*Faculty of Exact and Natural Sciences, National University of Costa Rica (UNA), Heredia, Costa Rica*

Correspondence should be addressed to José Vega-Baudrit; jvegab@gmail.com

Received 10 October 2019; Revised 5 December 2019; Accepted 19 December 2019; Published 11 February 2020

Guest Editor: Ernesto Di Maio

Regenerative medicine has taken advantage of several nanomaterials for reparation of diseased or damaged tissues in the nervous system involved in memory, cognition, and movement. Electrical, thermal, mechanical, and biocompatibility aspects of carbon-based nanomaterials (nanotubes, graphene, fullerenes, and their derivatives) make them suitable candidates to drive nerve tissue repair and stimulation. This review article focuses on key recent advances on the use of carbon nanotube- (CNT-) based technologies on nerve tissue engineering, outlining how neurons interact with CNT interfaces for promoting neuronal differentiation, growth and network reconstruction. CNTs still represent strong candidates for use in therapies of neurodegenerative pathologies and spinal cord injuries.

1. Introduction

The emergent field of nanomedicine proposes the application of precisely engineered nanomaterials for the prevention, diagnosis, and therapy of certain diseases, including neurological pathologies [1]. These pathologies occur when basic units of the nervous system start to deteriorate. In these nerve cells, alterations cause them to function abnormally, which results in demise of cell functions. Initial symptoms of neuronal deterioration may include loss of coordination or the ability to remember names, which may worsen over time if a large number of neurons deteriorate [2]. Due to the complexity of the nervous system, recovering function of the injured nerves or repairing damages associated to neurodegenerative conditions is still a major challenge in the biomedical field. Neurodegenerative diseases affect over 90,000 people every year, from which spinal cord injuries alone affect 10,000 people yearly. Alzheimer's and Parkinson's disease are the most common neurological diseases and occur in more than 5 million and 1.2 million Americans, respectively [3]. Considering the high amount of nerve repair procedures being currently conducted, as well as an increasing and ageing world population, the number of patients in need of neural implants to improve the regeneration of damaged tissue will only substantially increase over the years.

Neuroregeneration is the regrowth, restoration, or repair of degenerated nerves and nervous tissues, associated with the production of new axons, neurons, glia, myelin, and synapses. The nervous system is divided into the peripheral nervous system (PNS), which has the innate capability for self-repair and regeneration, while the central nervous system (CNS) is unable to self-repair and regenerate. Silicon-based materials are the most common for peripheral nerve implants; being studied since the 1960s, they have been used as a model system giving fundamental insight on nerve tissue regeneration.

Silicone has been implemented in the diagnosis, monitoring, and continuous treatment of nerve tissue damages [4]. Silicone been primarily used due to its biocompatibility, flexibility, and wide availability in different dimensions. However, their low impermeability and general inert

properties do not actively prompt neural tissue regeneration and have led to research on substitute materials [5]. Today, the treatment for damages in the CNS (i.e., spinal cord) consists on physical therapy to help patients with limited mobility without a full regain and restoration of the tissue and motor function [6].

Although still narrow, the application of nanotechnology and nanomaterials to neuroscience has experienced an impressive growth over the past decades, with an increasing amount of studies proposing scaffolds based on nanomaterial as strategies to regenerate nerve cells and tissues [7]. An ideal scaffold for neural tissue application shall exhibit electrical activity to stimulate cell outgrowth, biodegradability, and bioactivity for growth factor delivery; interestingly, a number of nanomaterials exhibit some of these properties and have proved relative long-term success when implanted [8].

Carbon-based nanomaterials (CBNs) have shown great potential when interacting with neurons and nerve tissues [9–11]. The discovery and manipulation of innovative nanomaterials, like fullerenes and graphene, but especially carbon nanotubes (CNTs), are likely to have a major impact on neuroregenerative techniques and in the biomedical applications in general. CNTs have shown to interact with the nervous system promoting the neural development. Furthermore, the outstanding mechanical, thermal, and conductive properties make CNTs very promising for other technological fields as conductive composites and sensors [12]. This work intends to review some recent uses of CNTs in nerve regeneration. We start providing an overview of nerve architectures and recent progresses on carbon-based nanomaterials for regenerative therapies and neuron repair. We finish the review with some closing remarks on biocompatibility and toxicity challenges of CNTs when used as part of these therapies.

2. Central and Peripheral Nerve Regeneration

The human nervous system consists of the central nervous system (CNS) and the peripheral nervous system (PNS), which at the same time is composed of two cell types, neurons and neuroglia. Neurons are the brain's nerve cells that transmit information from electrical and chemical signals throughout the nervous system, while neuroglia are the most numerous cells and their purpose is to aid the function of neurons. Within these cells, there are Schwann cells in the PNS and astrocytes and oligodendrocytes in the CNS. Researchers have shown that functional and structural recovery of the nerves depends on both extrinsic and intrinsic factors [13].

2.1. Peripheral Nervous System Repair. The PNS consists of a complex collection of spinal nerves, brain nerves, and neuron clusters called ganglia. These cells interact with other tissues transmitting sensory messages to and from the spinal cord [14]. The PNS has the ability to slowly regenerate on its own (axon growth 0.5–1 mm/day); in case of small injuries, nerve axons can regenerate by proliferating Schwann cells and macrophages to remove cellular debris from the injury side. Schwann cells infiltrate in the injury to stimulate and guide the new forming axon across the damaged nerve [15]. On the other hand, larger injuries need to be surgically treated, commonly using an autologous nerve implant. While extrinsic factors contemplate the environment at the injury site, intrinsic factors like the size of the injury and the ability of the neurons to regenerate by the synthesis of growth factors influence PNS regeneration [14–16]. In general, tissue engineering together with nanotechnology, aim to create innovative materials to help accelerate the PNS recovery since the delay in tissue regrowth may lead to muscle atrophy.

2.2. Central Nervous System Repair. The CNS includes the brain and the spinal cord, it is responsible of interpreting and conducting signals as well as providing stimulation to the PNS and from there to other tissues [17]. In contrast to the PNS, the CNS does not support full tissue regeneration; this leads to permanent loss of functions that can cause several physical and cognitive complications. Many factors such as the environment surrounding the CNS injuries and lack of neuronal regeneration capacity prevent cells from regenerating. Axonal regrowth is constrained by supporting cells, like myelinating oligodendrocytes, that create a growth inhibitor environment due to the formation of glial scar tissue and the lack of Schwann cells to promote axonal growth [18]. Therefore, the overall regeneration strategies for CNS are to reactivate gliosis while promoting tissue regeneration, where nanomaterials incorporated as part of current implants may help with [6].

3. Current Materials for Nerve Tissue Regeneration and Stimulation

Neurological implants' success in enhancing survival of damaged neurons, axons growth, and neuronal synaptic signal transmission is key to face the functional impairment that caused neuronal loss or degeneration. Basically, any strategy developed to fix an injury on the CNS should focus on regrowing injured axons, the plastic remodeling of neuronal circuitry, and the construction of new neurons [7].

Upgrades in material synthesis have allowed to develop artificial nerve conduits built of absorbable synthetic materials. Materials like polyhydroxybutyrate (PHB), polylactic acid (PLA), or polyglycolic acid (PGA) are being investigated as biodegradable-absorbable synthetic polymers for neural cell growth and axon organization. In fact, absorbable synthetics (PLA and PGA), and nonabsorbable synthetics like poly lactic-co-glycolic acid (PLGA), are already used for nerve regeneration. These three polymers are mechanically fragile and lack regions suitable for further chemical modification [19]; in any case, they have been FDA-approved for use in several neuron repair devices.

3.1. Polycaprolactone- (PCL-) Based Materials. PCL has gained considerable interest in the field of nerve regeneration research. The main features of this biodegradable

polyester are its ease of manipulation and low processing costs. Its high processability is given by the great solubility this substance has in many organic solvents and that its crystalline nature enables easy formability at low temperatures. Neurolac® (Polyganics Inc., the Netherlands) is a PCL nerve conduit approved by the FDA [20].

Other PCL co-polymers like the biodegradable polycaprolactone fumarate (PCLF) have recently allowed the fabrication of CNT composites [21]. These PCLF-CNT scaffolds not only exhibited excellent suitability to culture neuroblastic PC-12 cells (that can easily differentiate into neuron-like cells), but also allowed for good cell growth, differentiation, and electrical stimulation, which reflected in a neurite extension and promoted cellular migration and intracellular connections, which are all critical cellular behaviours for nerve regeneration [21].

3.2. Collagen-Based Materials. Collagen comprises a large family of proteins with a wide range of biomedical uses including peripheral nerve repair. When the purified collagen becomes weakly antigenic, it exhibits a smooth microgeometry and transmural permeability, both support the diffusion processes through collagen matrices [22]. Collagen type I constitutes an essential structural component of the extracellular matrix and has been employed at fabricating nerve repair conduits. Of over a dozen nerve conduits, currently, FDA-approved three are made of collagen type I: NeuraGen, NeuroMatrix, and NeuroFlex [22].

The first semipermeable type I collagen nerve guidance conduit approved by the FDA was NeuraGen® (Integra Life Sciences Corporation, Plainsboro, NJ, USA). A medical study on peripheral nerve reconstruction reported the clinical experience of using this implant, in which patients tolerated splinting and exercise without negative clinical repercussions. In another research, this conduit was compared with direct suture repair, in patients with complete traumatic nerve injuries. Results showed that patients who were treated with NeuraGen® had less postoperative pain than those treated with direct suture repair. The main conclusion was that nerve repair using the NeuraGen® is a quite effective method of joining severed nerves [23]. As collagen-based nerve repair conduits still lack good mechanical stability, the possibility to reinforce them with CNTs seems appealing; in fact, this might improve their electrical conductivity, thus exhibiting good viability of neuronal cells as has been demonstrated in similar biomaterials [24].

4. Carbon Nanomaterials for Nerve Tissue Regeneration

Nanosized materials and nanoscale technologies seem to challenge many traditional paradigms in Materials Science. Since the discovery of CNTs by Sumio lijima in 1991, scientific literature on the physical and chemical properties of nanomaterials, especially carbon-based nanomaterials (CBNs), has grown significantly and so has the use of CBNs in nerve regeneration applications (Figure 1).

CBNs offer unequal advantages, like high electrical conductivity, high surface-volume ratio, powerful mechanical strength, and chemical stability [25]. CBNs are held in high esteem in the biomedical materials community, and constant efforts have been made to integrate them into existing materials and devices like cellular sensors, tissue scaffold reinforcements, and drug delivery systems [26]. Fullerenes, graphene and carbon nanotubes (CNTs) are the most studied CBNs; they have attracted significant attention regarding their unique optical, electronic, mechanical, thermal, and chemical properties [27].

4.1. Fullerenes. Fullerenes are CBNs of great importance in biomedical research. Since their discovery in 1985, it was evident that this polyaromatic, symmetrical, and hollow spherical cage C_{60} molecule was meant to find a number of versatile applications in antiviral therapies [28], energy production, flat panel displays, semiconductors, environmental technologies, cosmetics [29], and food industry [30]. C_{60} has been recently used as an in vitro vehicle for therapeutic astrocyte delivery to neural lesions [31]. PCL and C_{60} were electrospun into 200 nm diameter nanofibers that showed good cell attachment and promising potential as drug delivery devices (Figure 2) [31].

4.2. Graphene. Graphene is a polycyclic aromatic molecule that is composed of a two-dimensional sheet of sp^2-bonded carbon atoms. This dimensional feature grants graphene and its derivative graphene oxide (GO) with high elasticity, conductivity, remarkable mechanical strength, rapid heterogeneous electron transfer, and high surface area [26]. Graphene is considered a versatile building block for functional nanoelectronics, energy storage, and production [33] as well as antibacterial [34], biosensing [35], and anticancer therapies [11].

Different amounts of layers grant the graphene with different properties, going from one-layered graphene to multilayered graphene structures [36], and interaction between these graphene-based nanomaterials and neurons have been recently explored [35]. In a recent study by Pampaloni and coworkers, it is shown that single-layer graphene (SGL) can tune astrocytes excitability and increases neuronal firing by altering membrane-associated functions in vitro. The authors hypothesize that graphene restricts the mobility of K^+ ions in close proximity to the SGL surface, but only when SLG is deposited on electrically insulating substrates. In this fashion, graphene properties might affect neuronal information processing (Figure 3) [35].

4.3. Carbon Nanotubes (CNTs). Carbon nanotubes (CNTs) are most widely used in nerve regeneration CBN to date [22]. Different from other CBNs, CNTs exhibit tunable physical (length, diameter, single-walled SWCNTs, vs multiwalled MWCNTs, chirality) [38] and chemical properties (surface functionalization and high electrochemical surface area) [26]. CNTs can be envisioned as cylinders made of rolled-up

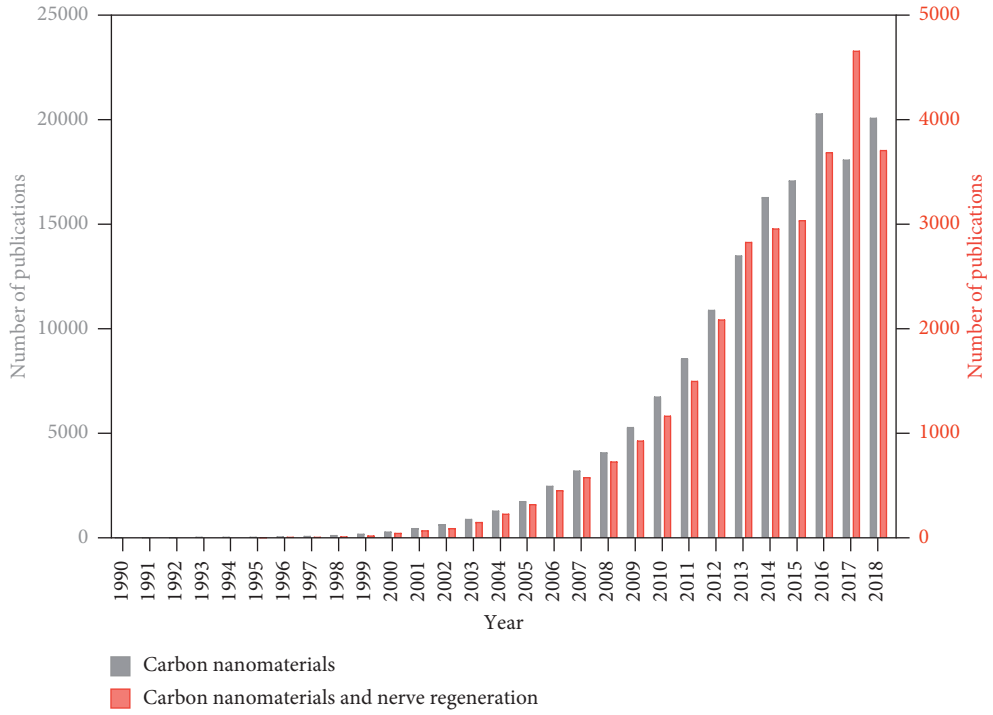

Figure 1: Increasing trend of reports on carbon nanomaterials (grey) and carbon nanomaterials and nerve regeneration (red). A google scholar search was performed on either "carbon nanomaterials" or "carbon nanomaterials and nerve regeneration" on the specified time period.

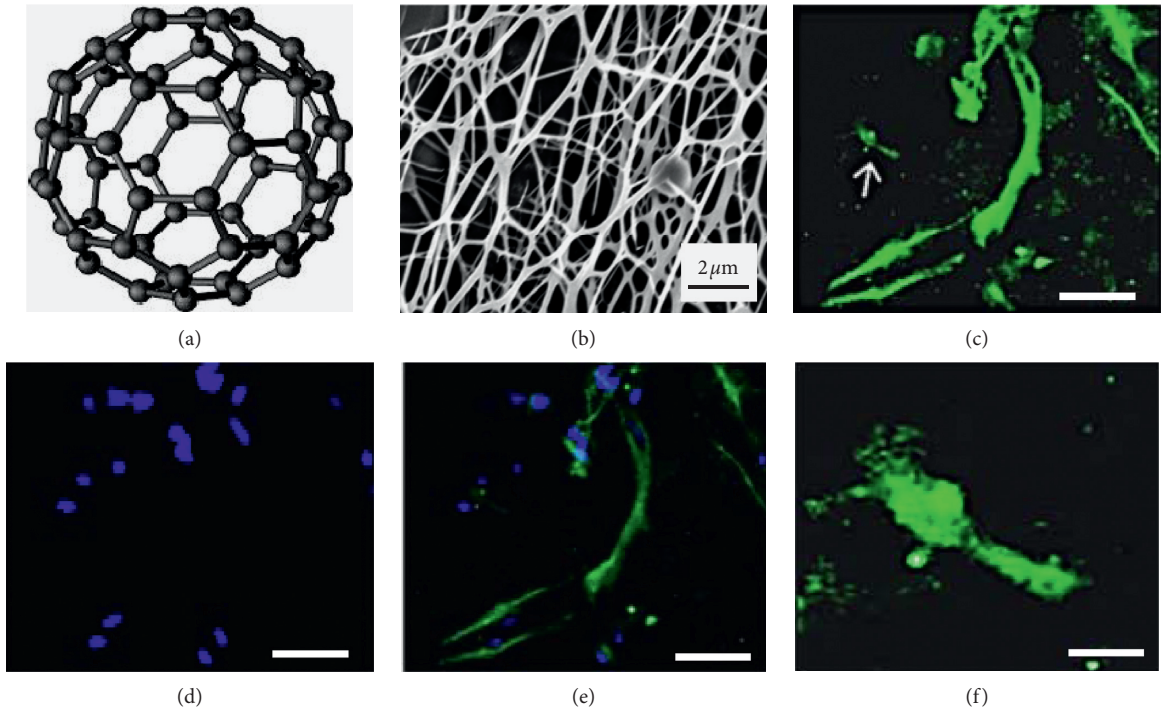

Figure 2: (a) Representation of C_{60} fullerene [32]. (b) SEM images of PCL-fullerene nanoscaffolds fabricated by electrospinning. (c–e) Immunocytochemical micrographs of astrocytes cultures on the scaffolds and labeled with antiglial fibrillary acidic protein antibody (antiGFAP, green) and Hoechst dyes (blue, scale bar: 50 μm). (f) Magnification images of cells pointed with an arrow in (c) (scale bar: 25 μm) [31].

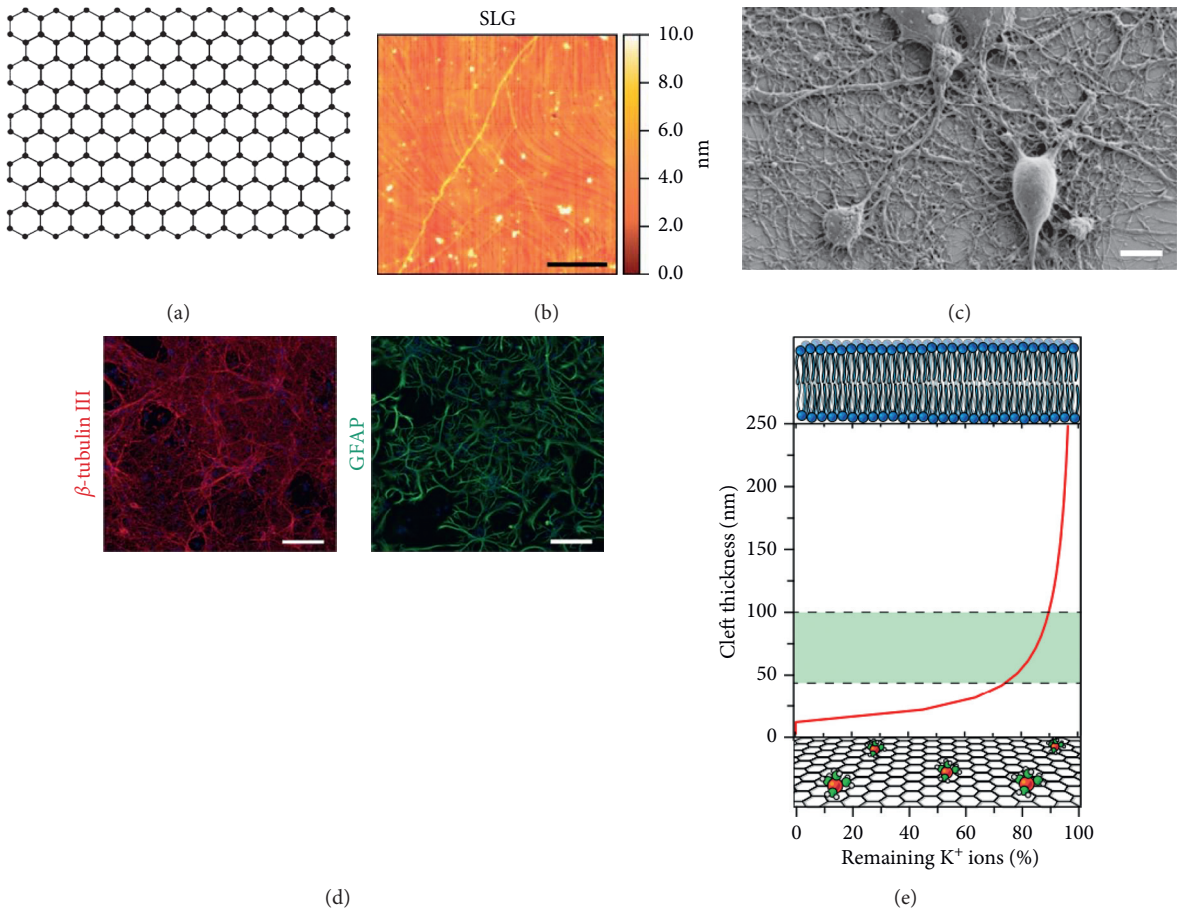

Figure 3: (a) Molecular representation of graphene [37]. (b) AFM topography of single-layer graphene (SGL, scale bar: 5 μm). (c) Scanning electron micrograph depicting hippocampal neuron morphology cultured onto SLG (scale bar: 10 μm). (d) Fluorescent microscopy images showing dissociated hippocampal networks labelled with class III β-tubulin (for neurons) in red and GFAP (for astrocytes) in green (scale bar: 100 μm). (e) Sketch of the local amount of K+ depletion in the space between the cell membrane and the SLG surface (membrane/surface cleft) due to graphene trapping as function of cleft thickness. The light green region shows the extrapolated K+ depletion values (red line) within the range of the estimated cleft dimensions (40–100 nm). See Reference [35] for more details.

graphene layers with diameters in the nanometer scale (Figure 4). CNTs possess an extended conjugated sp^2 carbon network that renders a π-electron system which extends over the nanostructure originating either highly conducting CNTs or semiconducting ones; this also provides tunable band gaps compatible with neural activity [9]. The following section addresses the specific use of CNTs in neural regeneration and stimulation in deeper detail.

5. CNTs for Neural Regeneration and Stimulation

CNTs are generating an attractive approach in the treatment of neural pathologies and nerve tissue damaged. On top of their aforementioned capabilities, CNTs show morphological similarity to neurites, and small CNT bundles have dimensions similar to those of dendrites (the branched extensions of neuron cells), enhancing possibilities for not only probing, repairing, stimulating, or reconfiguring neural networks [9] but also gaining insights into basic mechanisms of neuronal functions [10]. Success on the application of CTNs is strongly connected to the ability to control the interaction between them and the neurons' changes in ionic conductance and synaptic transmission, this being a perk when incorporated into electrodes and conductive probes [1, 40]. In the following sections, we provide a comprehensive view of the use of CNTs in neural regeneration and stimulation.

5.1. Improving CNTs Neurocompatibility. CNTs are synthesized through a number of treatments that renders them positive or negative charged and be further modified to incorporate various functional groups via covalent [41] and noncovalent pathways [42].

Incorporation of hydrophilic polymers such as polyethylene glycol (PEG) increases CNT solubility in aqueous solution, and increasing their biocompatibility and facilitating the fabrication of CNT-based medical materials and common use polymers such as poly-ethyleneimine (PEI) and poly-L-ornithine (PLO) have been reported to promote neural attachment and subsequent neurite outgrowth; these noncovalent functionalization examples represent a valuable

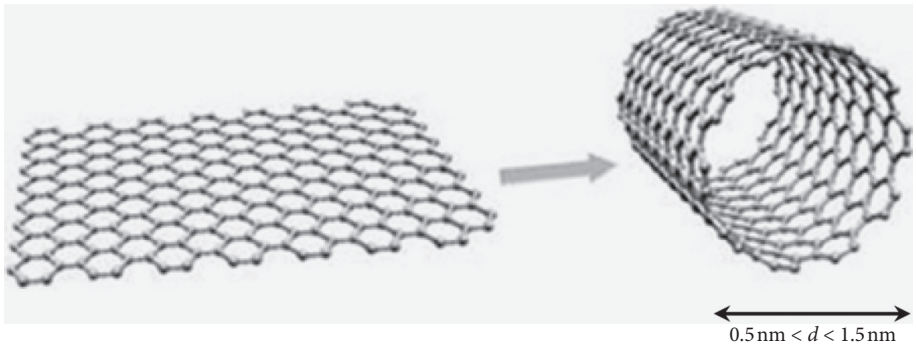

(a)

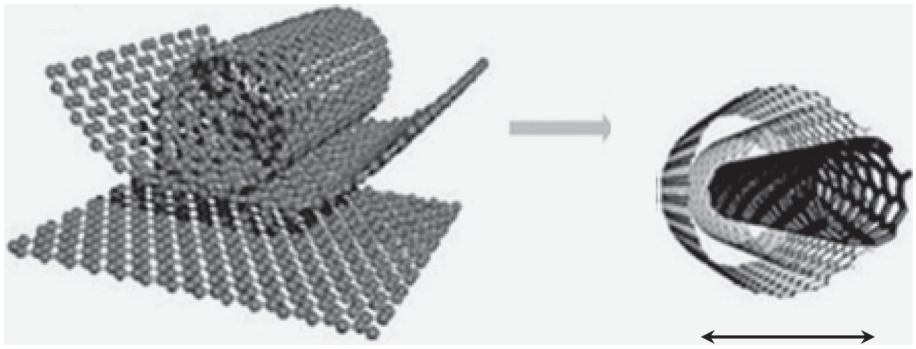

(b)

Figure 4: Representation of a typical (A) single-walled carbon nanotube (SWCNT) and a multiwalled carbon nanotube (MWCNT) (adapted from reference [39]).

resource when manufacturing the coating for neural interface devices [43, 44]. Use of CNTs decorated with these poly-cations generally promotes neuron growth, and this is most likely due to an enhanced electrostatic interaction between the CNTs and the plasma membrane of neural cells that has a negative charge [45]. Recent biofunctionalization approaches [46] appear as promising alternatives for increasing CNTs water solubility and further neuron growth stimulation and cell membrane incorporation.

5.2. CNTs Application Strategies. The literature reports on two possible strategies to control neural cell functions through biofunctionalized CNTs. One is through the addition of soluble stand-alone CNTs directly to neuronal cell culture medium, while the other one involves CNTs surface modification for further attachment substrates such as scaffolds. The first strategy requires a direct application of the CNTs to the nerve tissue allowing the carbon structures to interact directly with nerve culture and to expand or disperse within the cells.

The second strategy employs CNTs as modifiers (either surface or bulk) of other materials to enhance their neurofunctionality as part of multicomposite scaffolds, implantable devices cell guiding matrices, and enhancing activity of other components such as the therapeutic drugs (small molecules), proteins (neurotrophic factors or extracellular matrix (ECM) components), and nucleic acids (siRNA, miRNA, pDNA, etc.) [43].

Properties like roughness, charge, polarity, and chemistry of CNT scaffolds, can alter the affinity of neurons linked to CNT-containing surfaces. Direct interactions between neurites and CNTs act as an exoskeleton, with more membrane/material tight junction formation. Greater surface area of CNT significantly results in stronger charge injection capacity and lesser interfacial impedance as they help in electrochemical coupling via electron transfer between CNTs and neurites [5, 44, 47, 48].

5.3. Neural Response Mechanisms to CNTs. CNTs have demonstrated to play an important role mediating interactions between neurons and their environment. When used as a scaffold, CNTs act not only as a reservoir of adsorbed proteins, but also play a dynamic role in boosting neuronal electrical performance. Observed discontinuous and tight contacts between MWCNT or SWNT bundles and neuronal membranes favor the hypothesis of a direct electrical coupling (Figure 5). The work of Cellot et al. demonstrate that meshwork of MWCNTs outside neurons is in intimate contact with a small area of the neuritic membranes, this

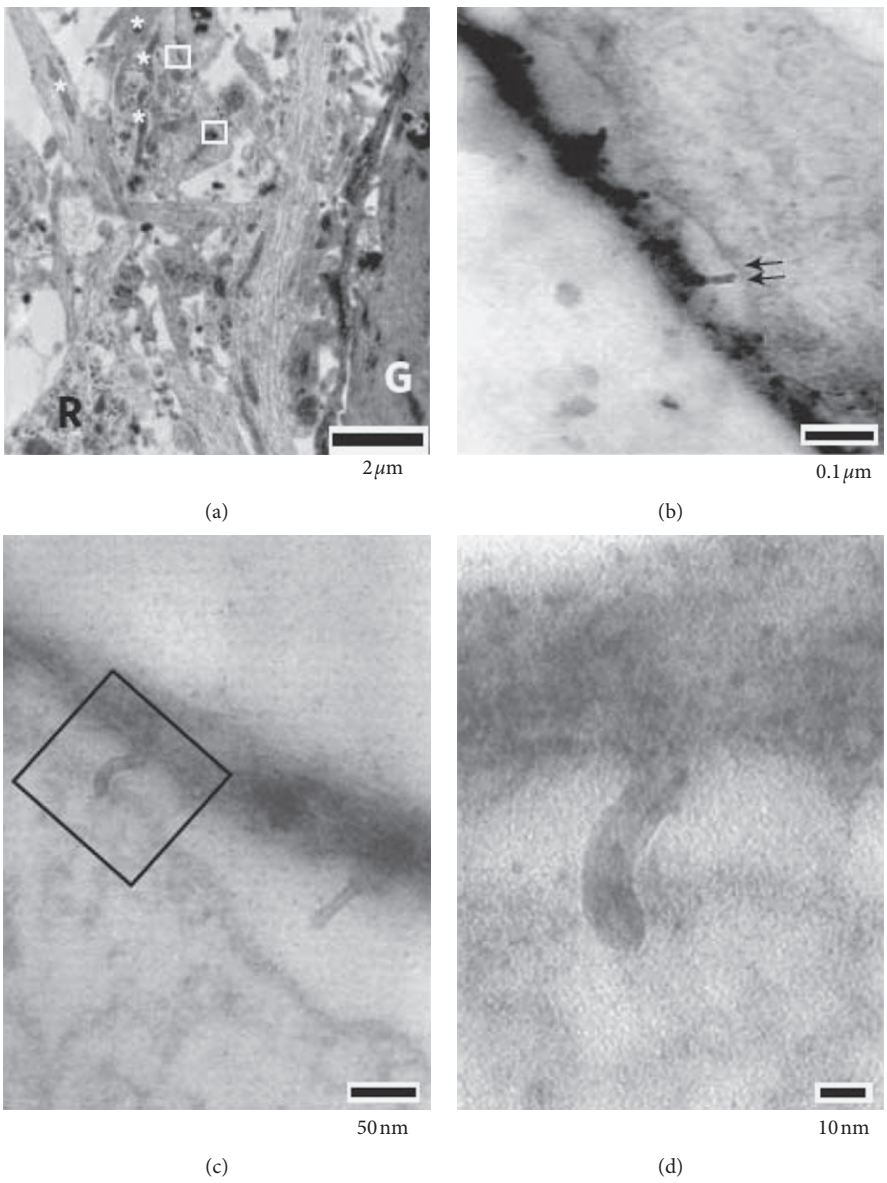

Figure 5: Interaction between MWCNTs and neurons. (a) Transmission electron micrographs (TEM) sections of neurons grown on MWCNTs showing functional synaptic contacts (rectangular box). (b) Arrows indicate MWCNT-membrane contacts on this TEM section from (a). (c, d) High-magnification micrographs from a section consecutive to those of (b) illustrating how MWCNTs 'pinch' neuronal membranes [10].

report constitutes the very first attempt at linking electrical phenomena in nanomaterials to neuron excitability [10].

Hippocampal neurons cultured on MWCNTs were studied by Fabbro et al. [49] demonstrating an increase in expression of paxillin, this membrane protein is involved in focal adhesions-mediated intracellular signaling pathways, demonstrating that electrophysiological cues provided by CNTs can be translated into specific neuronal signals. However, more detailed mechanistic studies between the neuronal tissue and CNTs interface are still required to engineer further applications of CBNs [5, 48, 50]. Some recent applications are presented in the following section.

5.4. Selected Applications. CNTs have been incorporated in the design and manufacturing of several biomedical technologies. A number of comprehensive reviews on the use of CNTs for neuron regeneration can be found in the literature [7, 15, 22, 51]. This section aims to present recent examples of CNT-based materials used as scaffolds (hard printed or in the form of hydrogels) for neuron culture and conduits for nerve reconstruction. Most of the following subsections detail CNT-based materials applied to peripheral nerve studies; nevertheless, the first example is remarkable as it shows a rare example of CNT-mediated cortical regeneration.

5.4.1. Transparent CNT-Based Substrates for Cortical Functional Regeneration. Pampaloni and coworkers have recently reported on the preparation of optically transparent CNT-based substrate (tCNTs) consisting of MWCNT carpets grown on fused silica substrates [52]. tCNTs not only favor dissociated primary neurons network formation and function (Figure 6(a)) but also boost the spontaneous synaptic activity of hippocampal neurons. In this report, tCNTs were used to support the growth of intact or lesioned entorhinal-hippocampal complex organotypic cultures (EHCs: 3D explants of the CNS in which the overall functional and anatomical neuronal connections are preserved [53]), finding that the CNT-based material induces the sprouting of functionally active fibers crossing lesioned areas (Figures 6(b) and 6(c)).

5.4.2. 3D Printing Nanoconductive MWCNT Scaffolds for Nerve Regeneration. Aminated MWCNTs have been recently been incorporated in a poly(ethylene glycol) diacrylate (PEGDA) matrix [54]. This report shows how CNTs can be easily incorporated in emerging 3D printing technologies to render scaffolds that support differentiation and growth of neural cells while having microelectroporous characteristics, and the manufacturing process is depicted in Figure 7.

In this study on MWCNT-PEGDA scaffolds, concentration of CNTs was evaluated, finding that proliferation at 0.02% of amine-containing MWCNT was the highest after four days of culture, whereas the highest proliferation of neural stem cells (NSCs) in all the concentration groups occurred in the 0.1% amine-containing MWCNT scaffolds. This proliferation was obtained until day seven, and the researchers believe that this delay was caused by the adaptation process of the NSCs to the substrate. Higher concentrations of MWCNTs in the printed scaffolds showed a higher positive charge which could promote a better development and greater nerve cell growth [54].

5.4.3. CNT-Interfaced Glass Fiber Scaffold for Regeneration of Transected Sciatic Nerve. Peripheral nerve injuries are common in clinical settings, yet the possibility of the nerve to regenerate spontaneously will vary according to the severity of the injury, which will be limited if the injury is too severe. The study by Ahn et al. addresses this issue by fabricating a phosphate glass microfiber (PGF) scaffold that incorporates aminated CNT [55].

The researchers performed a surface coupling of aminated CNTs to aligned PGF bundles and used the resulting fibers as interfacing material for neuron physical guidance. In vivo cell guidance studies were performed after wrapping the CNT-PGF substrate around poly(l/d-lactic acid) (PLDLA) electrospun nanofibers. The nerve guidance device was made in the shape of a cylindrical tube (as shown in Figure 8) and tested in a rat sciatic injury model [55], exhibiting good neural interaction, cell viability, and physicochemical integrity. Finally, the implant displays effectiveness in restoring motor functions, indicating that the muscle in the animal was functionally improved as a result of the CNT interfacing, as the scaffold-crossing axons reinnervated into the gastrocnemius muscles [55].

5.4.4. Polysaccharide/CNT Hydrogel Hybrid as Neuronal Growth Substrates. Hydrogels are attracting much attention in biomedical applications given their molecular-scale control over mechanical and bioresponsive properties [56]. Most hydrogels still lack good mechanical strength and electrical conductivity, thus limiting their biomedical applications, but CNT hydrogels hybrids have emerged as candidates to overcome this. These composite hydrogels have rapidly gained attention in developing regenerative therapies for skeletal muscles and cardiac and neural cells [57].

A recent study by Wu et al. explores the potential of chitin-based composite hydrogels incorporating MWCNTs [58]. These hybrid hydrogels originated from a chitin/NaOH/urea aqueous solution blended with modified MWCNTs. Hydrogel bulk consisted on bundles of chitin nanofibers and carbon nanostructures that were stabilized through intermolecular forces like hydrogen bonding and electrostatic and hydrophobic interactions (Figure 9), that also contribute to refrain CNT release from the hydrogel scaffold. The resulting hydrogels showed improvements in thermal stability, a better hemocompatibility, good mechanical properties, while slowing down biodegradability rates, and the swelling ratio compared to control chitin hydrogels [58]. On top of these improvements, in vitro evaluation of Schwann cells was performed, resulting in a successful proliferation of the neuronal cells with little cytotoxicity and neurotoxicity, displaying a promising potential as neuronal growth substrates for peripheral nerve regeneration [58].

5.4.5. Nerve Guide Conduits Based on Protein/CNT Composites. The study presented by Mottaghitalab et al. introduced a clever nerve guide conduit (NGC) design that merged the mechanical advantages of the naturally occurring proteins silk fibroin (SF) and SWCNTs for use in nerve grafts. The resulting conduit showed stable chemical, physical, and electroconductivity properties due to its uniformity; plus the addition of fibronectin containing nanofibers (FN) through a electrospinning process rendered an addition extracellular matrix guidance for neuron growth and migration (Figure 10). FN conferred the SF/SWNTs NGCs conduits bioactivity allowing the growth and adhesion of U373 cell lines. NGCs were studied in vivo, implanted to 10 mm left sciatic nerve defects in rats, resulting in nerve regeneration in the proximal regions of the implants after five weeks. In both SF/SWNT and SF/SWNT/FN NGCs, more myelinated axons were present as well as higher nerve conduction velocities, indicating a functional recovery for the injured nerves [59].

6. Biocompatibility and Neurotoxicity of CNTs

Academic communities and regulatory agencies have grown in concern about the adverse effects of CNT-based materials and nanomaterials in general. Factors such as particle concentration, exposure route (injection, ingestion, and

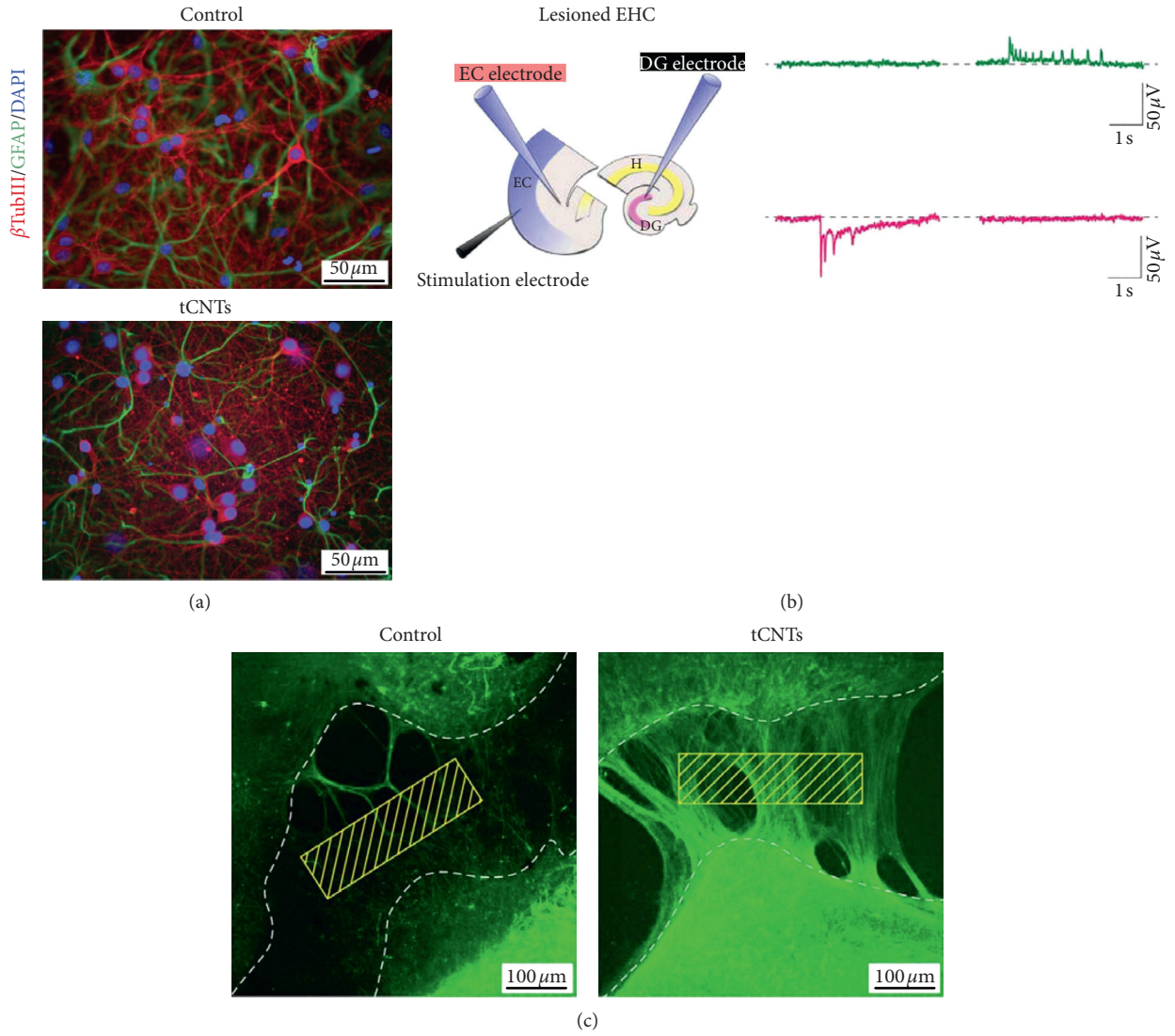

Figure 6: (a) Fluorescent micrographs of dissociated primary cells networks grown on glass control substrates (top) and on tCNTs substrates (bottom) (β-tubulin III, red: neurons; GFAP, green: astrocytes; DAPI, blue: cell nuclei). (b) tCNTs induce the sprouting of functionally active fibers crossing lesioned areas in entorhinal-hippocampal complex organotypic cultures (EHCs). (a) Entorhinal cortex/dentate gyrus (EC/DG) intercommunication ability through the perforant pathway (PP) transection in intact and lesioned EHC using a stimulation electrode inserted into the EC superficial layer. (c) Representative confocal images showing the sprouting of SMI32-positive axon fibers (in green) crossing the gap area [52].

inhalation [60]), particle size, particle distribution, particle agglomeration, and surface adsorbability and attachment are pivotal to comprehend the huge variability in the nanotoxicity studies of CNTs [61].

Most of these studies CNTs have been developed on stand-alone CNTs (i.e., suspended in physiological circulating fluids) generating accumulation-related adverse reactions in the tissues [62]. Nonetheless, when CNTs are firmly surface-immobilized (by either covalent or noncovalent approaches), it seems that there is no or there is little cytotoxicity [61]; that is the case of devices commonly inserted in the CNS/PNS directly in contact with neurons. Therefore, CNTs show in general good compatibility in vivo with neuronal tissues.

The most cautious way to use CNT would be to prevent them from entering the organism freely [60]. Examples like the one discussed in Section 5.4.4 or other CNT-hydrogel systems [63] comprise the trapping of free CNTs within the hydrogel network, thus limiting standalone CNTs release.

As long as CNTs remain firmly attached to a surface or their release is hampered, collateral diseases (such as cardiopulmonary diseases, inflammation and fibrosis, among others [64, 65]) can be prevented. Then factors like superficial load, distribution of the functional groups of the CNTs, and manufacture methods [65, 66] and their relation to toxicological responses can be discussed, as we describe in the following section.

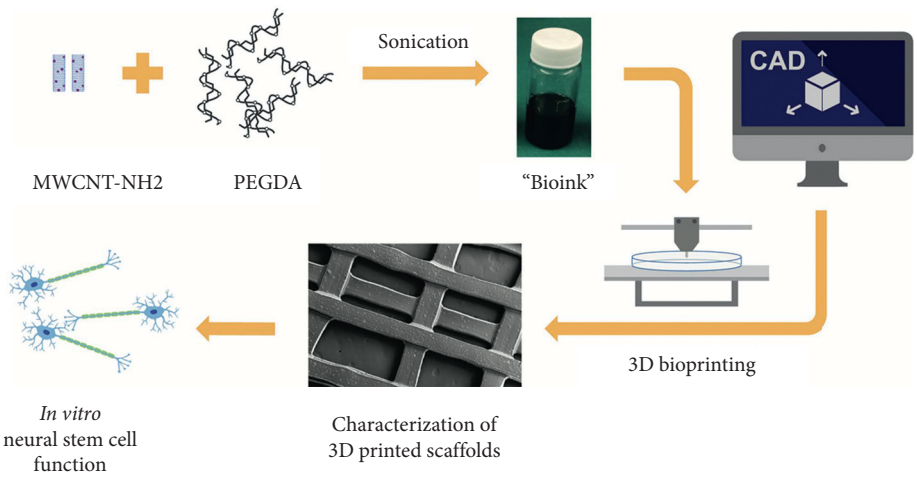

Figure 7: Representation of the manufacturing process of 3D-printing nanoconductive MWCNT-PEGDA scaffolds [54].

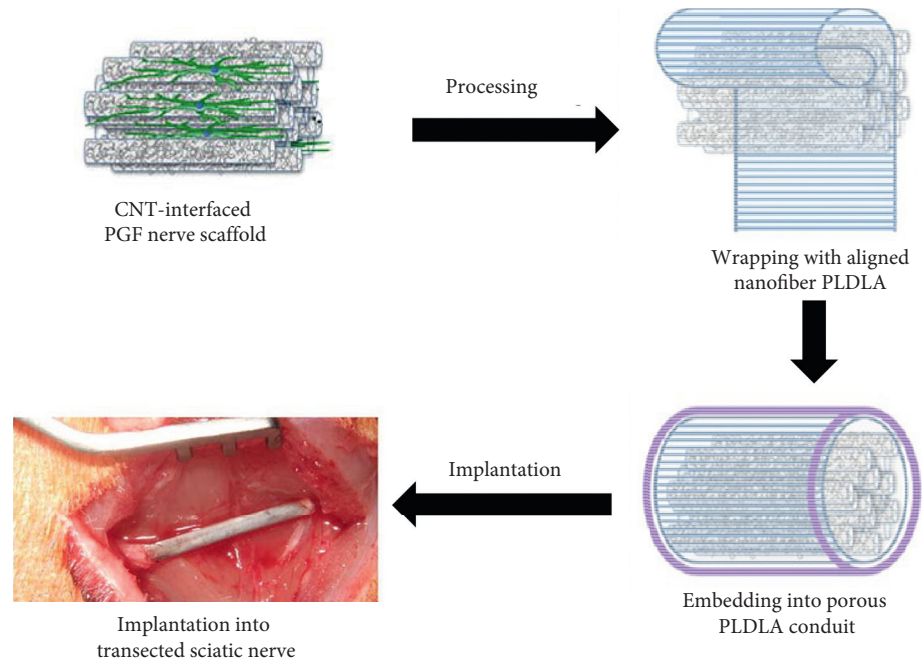

Figure 8: Functionality of a CNT-interfaced PGF scaffold used as nerve conduit. The aligned PGF bundle interfaced with CNTs for neurite outgrowth (adapted from reference [55]).

6.1. CNTs Neurotoxicity Related to Manufacturing and Functionalisation. As previously mentioned, CNT can be manufactured by different methods (arc discharge, chemical vapor deposition, and laser ablation of graphite among others) which generate a wide spectrum of CNT lengths, number of walls, chiralities, and most importantly impurities. Despite the fact that a number of studies highlight toxic effects in cells upon exposure to stand-alone CNTs, these adverse effects are largely due to heavy metal nanoparticles (Fe, Co, Ni, Y) produced during their synthesis [67].

Further functionalization steps tend to remove these metals and also to reduce CNTs' tendency to bundle, thus improving further biodistribution and lowering inflammatory responses compared to pristine CNTs [67–70]. Table 1 shows some toxicity-related effects as consequence of different CNTs solubilizing and functionalisation treatments in biological tissues with special emphasis on neuron related reports [67, 92].

On top of the chemical nature of impurities in CNTs, the number of walls, length, and chirality also influence their toxicity and behavior at biointerfaces [93, 94]. Depending on these physical characteristics, their cell interaction mechanism can be altered and generate different immunological responses [95, 96]. Several studies have shown a lower immune response as CNT length decreases, since short CNT can cross cell membranes more easily, whereas longer CNTs remain bundled in the

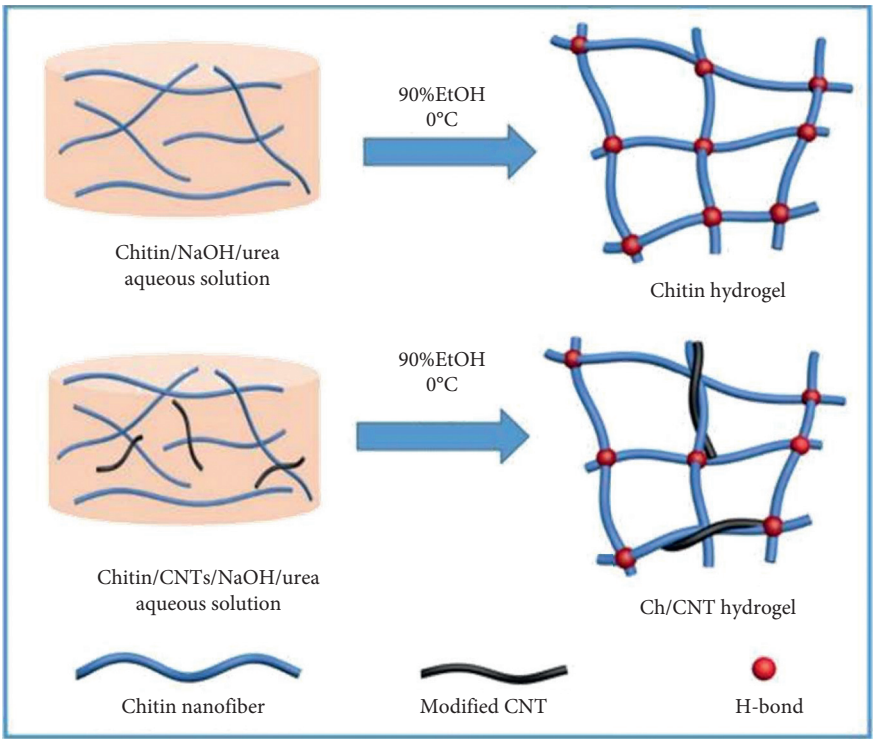

Figure 9: Schematic representation of the synthesis process of chitin-MWCNT hydrogel hybrids [58].

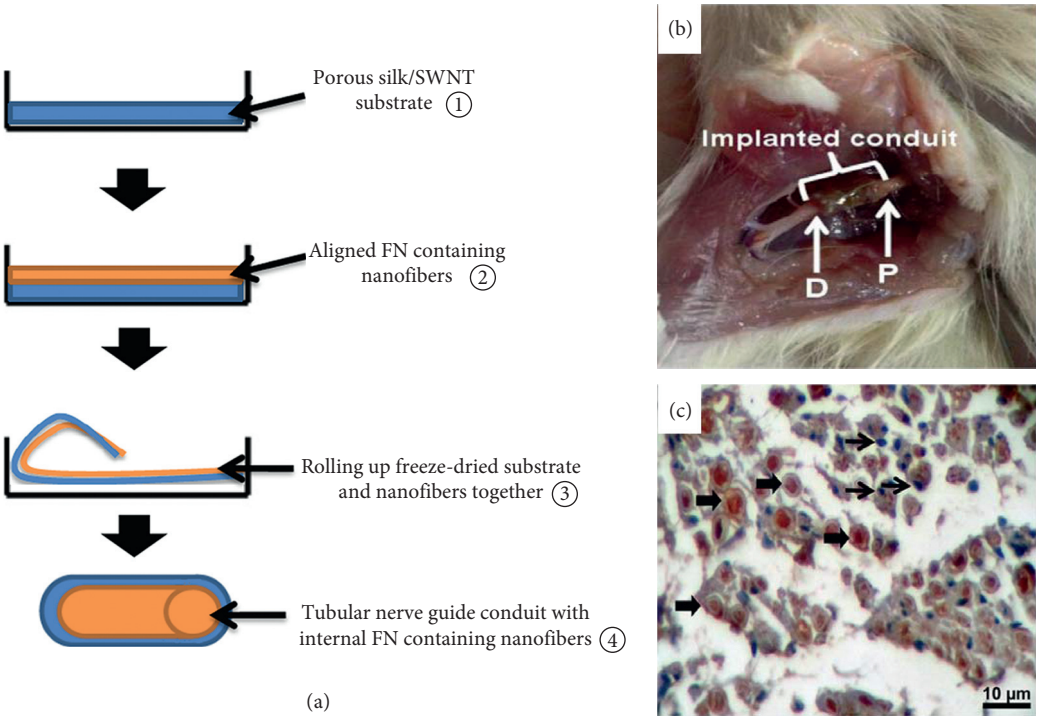

Figure 10: (a) Schematic representation of rolling up protocol for nerve guide conduit (NGC) containing SF/SWNT/FN. (1) Porous SF/SWNT substrates. (2) Aligned FN containing nanofibers prepared by electrospinning on substrate. (3) Rolling up the complex. (4) Tubular NGC with internal aligned nanofibers coated by porous Silk/SWNT substrate. (b) Implanted SF/SWNT/FN. conduit in left sciatic nerve defects in a rat model after 5 weeks implantation. (c) Cross sections of regenerated nerves taken from SF/SWNT/FN nerve conduit after 5 weeks. Wide arrows: myelinated axon. Narrow arrows: Schwann cells (adapted from reference [59]).

Table 1: Toxicity study of various carbon nanotubes solubilization and functionalisation schemes of biological interest.

Small molecules as solubilizing agents	Toxicity	Reference
Tetrahydrofuran	Tumorigen, mutagen	[71]
Dichlorocarbene	Harmful	[71]
Anthracene	Possible tumor promoter	[72]
Pyrene	Carcinogenic, mutagenic	[73]
Zn-porphyrin	Unknown, likely safe	[74]
Phenylethyl alcohol	Topical irritant	[75]
n-octyl-β-d-glucoside	Unknown	[76]
n-decanoyl-*N*-methylglucamide	Unknown	[76]
Triaminopyrimidine	Unknown	[77]
Lysophosphatidylcholine	Unknown	[77]
Barbituric acid	Not pharmacologically active	[78]
Sodium cholate	Unknown	[76]
Taurine	Safe up to ~28.57 mg/mL	[79]
Thiolated organosilane	Unknown	[80]
Macromolecules as solubilizing agents	**Toxicity**	**Reference**
Chitosan	Mostly safe	[81]
Helical amylase	Unknown	[82]
Poly(phenyleneethynylene)	Possible antimicrobial properties	[83]
Poly(aminobenzene sulfonic acid)	Hazardous to blood, nervous system, liver	[84]
PAA	Severely irritating and corrosive	[85]
PEG	Acute oral and dermal	[84]
Sulfonated polyaniline	Unknown	[86]
Functionalisation approach	**Toxicity**	**Reference**
MWCNT-NH_3^+	Weak transient inflammatory response on glial cells	[87]
^{13}C enriched SWCNTs + Tween-80 1%	Moderate (mouse lungs and liver), biodistribution study	[88]
PEG-modified SWCNTs	Mostly safe (spinal cord injury)	[89]
[^{111}In]DTPA-MWCNTs	Not determined (blood-brain barrier in vitro model)	[90]
PEG-oligodeoxynucleotide (CpG)	Mostly safe (glioma tumor model)	[91]

PEG: polyethylene glycol; PAA: poly(acrylic acid); DTPA: diethylenetriaminepentaacetic acid.

extracellular space [97] often generating reactive oxygen species (ROS), thus triggering oxidative stress response on cells [93].

6.2. Neuron Interaction Mechanisms. So far, it is understood that there are two possible mechanisms that CNTs can present to enter neurons or potential host cells: active transport through endocytosis/phagocytosis and passive transport or simple diffusion (also known as nanopenetration) [92].

Both mechanisms are presented in Figure 11, where the absorption of CNTs using the deformation of the plasma membrane to form a vesicle that internalizes into the cytoplasm is resented [98, 99]. Phagocytosis is a process similar to endocytosis but is characterized by its specialized exogenous material of greater size as bacteria or microorganisms. Both mechanisms are dependent on energy (ATP) and temperature [100, 101].

Nanopenetration is a passive mechanism that allows the CNT to cross the membrane without the need to generate a vesicle, and it can be compared with the simple diffusion that some substances of interest for the membrane present [102]. The results of several studies of both mechanisms suggest that they can generate different immune reactions, as they activate a number of transport routes at the same time and also DNA damage can be involved at some point [102].

A number of studies have tested how a number of small and macromolecules can travel across the blood-brain barrier (BBB) [103]; in fact, CNTs are no exception to this. When ^{13}C-enriched SWCNTs were administered to mice, it was found they accumulate in the animal's brain, but showing little or no acute toxicity while also accumulating in liver, lung, and spleen, organs where CNTs persistence may lead to long-term toxicity effects [88].

MWCNTs are also able to cross the BBB as the work of Kafa et al. demonstrated. In this study, radiolabeled MWCNTs were intravenously administered to a murine model in order to study the molecular mechanism mediating CNTs crossing the BBB, finding that micropinocytosis is the prevalent internalization mechanism, and therefore transcellular uptake is hypothesized as the primary mechanism behind the BBB crossing [90].

Gastrointestinal administration of SWCNTs can lead to accumulation across the BBB, it also known that SWCNTs tend to accumulate in neurons' lysosomes. Yang et al. took advantage of these observations to treat Alzheimer's disease model mice by delivering acetylcholine using the CNTs [104]. This study based the release of cargo based on a pH change in neuron lysosomes, but it has been demonstrated that CNTs can be enzymatically degraded by peroxidases in immune cells, glia cells, and the extracellular space as well [67]; therefore, lessening concerns about their use in neuron therapies.

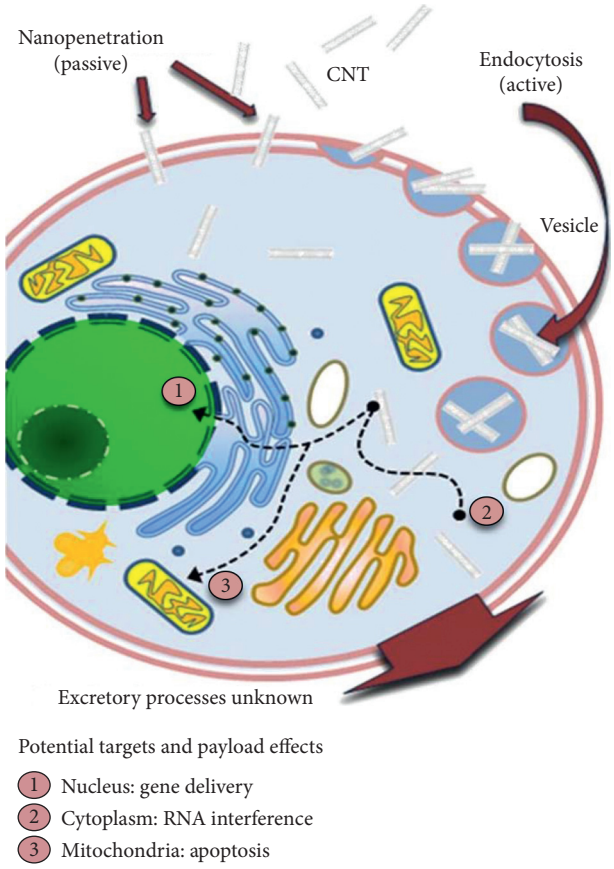

Figure 11: Schematics showing endocytosis and nanopenetration mechanisms of stand-alone CNTs [92].

7. Concluding Remarks and Future Perspectives

This review has examined how CBNs have been recently applied to nervous tissue regeneration. Research on nervous system repair continues to use CNTs in the pursue of novel therapies for treating nerve damage and neurodegenerative pathologies. It was found that most of the literature reports on neuronal applications of CNTs happen to take place on nervous cell lines or PNS; therefore, more research focused on CNS regeneration should be developed despite its complexity.

Even though initial safety concerns about stand-alone CNTs toxicity limited their use in neuronal applications, more and more studies show how these issues can be bypassed by controlling CNTs firm attachment to a substrate. Further nanotoxicological and pharmacokinetic studies are required, but it is highly advised for these reports to include extensive details of CNTs physical and chemical characterization of the CBN; its impurities and surface characteristics in order to systematically homogenize the, quite contradictory, outcome results. In this regard, more studies should be carried out on the relation between toxicity and shape, size, functional groups, and release of CNT when integrated into devices.

As more control over CNT behavior is gained, the better comprehension of their interactions with neurons will be gained. This will facilitate a more efficient CNT incorporation a part of devices like nerve conduits, sensors, and micro and nanoelectromechanical systems (NEMS and MEMS). It is likely that future studies involving neuronal application of CNTs explore the benefits of combining different forms of CBNs, allowing for sensors and micro and nanoelectromechanical systems (NEMS and MEMS) with increased functionality and levels of complexity.

Current advances on additive manufacturing technologies like 3D printing will allow for increasing complexity of CNT based materials, this will provide improved compatibility and functionality of CNT-containing system when designed to match the intricacies of the CNS. Additive manufacturing technologies will also allow for the precise and reproducible merging of CNTs with biologically relevant cues like proteins and biodegradable biopolymers, thus improving the application of CNTs in the commission of nervous regeneration.

Conflicts of Interest

The authors declare no conflicts of interest.

Authors' Contributions

Conceptualization was done by J. V. Investigation was done by R. L., D. B., C. E., D. H., and C. R. Original draft was prepared by R. L., D. B., C. E., D. H., and C. R. Review and editing were performed by R. L., D. B., C. E., D. H., and C. R. C. R., J. V. supervised the study. J. V and C. R received the funding.

Acknowledgments

This research was funded by LANOTEC-CeNAT and the Ministry of Science Technology and Telecommunications of the Republic of Costa Rica (PINN-MICITT).

References

[1] A. Nunes, K. Al-Jamal, T. Nakajima, M. Hariz, and K. Kostarelos, "Application of carbon nanotubes in neurology: clinical perspectives and toxicological risks," *Archives of Toxicology*, vol. 86, no. 7, pp. 1009–1020, 2012.

[2] D. C. Rubinsztein, "The roles of intracellular protein-degradation pathways in neurodegeneration," *Nature*, vol. 443, no. 7113, pp. 780–786, 2006.

[3] A. Ajetunmobi, A. Prina-Mello, Y. Volkov, A. Corvin, and D. Tropea, "Nanotechnologies for the study of the central nervous system," *Progress in Neurobiology*, vol. 123, pp. 18–36, 2014.

[4] G. R. D. Evans, "Peripheral nerve injury: a review and approach to tissue engineered constructs," *The Anatomical Record*, vol. 263, no. 4, pp. 396–404, 2001.

[5] L. A. Pfister, M. Papaloïzos, H. P. Merkle, and B. Gander, "Nerve conduits and growth factor delivery in peripheral nerve repair," *Journal of the Peripheral Nervous System*, vol. 12, no. 2, pp. 65–82, 2007.

[6] J. T. Seil and T. J. Webster, "Electrically active nanomaterials as improved neural tissue regeneration scaffolds," *Wiley Interdisciplinary Reviews: Nanomedicine and Nanobiotechnology*, vol. 2, no. 6, pp. 635–647, 2010.

[7] A. Fabbro, M. Prato, and L. Ballerini, "Carbon nanotubes in neuroregeneration and repair," *Advanced Drug Delivery Reviews*, vol. 65, no. 15, pp. 2034–2044, 2013.

[8] T. J. Webster, M. C. Waid, J. L. McKenzie, R. L. Price, and J. U. Ejiofor, "Nano-biotechnology: carbon nanofibres as improved neural and orthopaedic implants," *Nanotechnology*, vol. 15, no. 1, pp. 48–54, 2004.

[9] C. J. Serpell, K. Kostarelos, and B. G. Davis, "Can carbon nanotubes deliver on their promise in biology? Harnessing unique properties for unparalleled applications," *ACS Central Science*, vol. 2, no. 4, pp. 190–200, 2016.

[10] G. Cellot, E. Cilia, S. Cipollone et al., "Carbon nanotubes might improve neuronal performance by favouring electrical shortcuts," *Nature Nanotechnology*, vol. 4, no. 2, pp. 126–133, 2009.

[11] C. C. Liu, J. J. Zhao, R. Zhang et al., "Multifunctionalization of graphene and graphene oxide for controlled release and targeted delivery of anticancer drugs," *American Journal of Translational Research*, vol. 9, no. 9, pp. 5197–5219, 2017.

[12] A. Fabbro, S. Bosi, L. Ballerini, and M. Prato, "Carbon nanotubes: artificial nanomaterials to engineer single neurons and neuronal networks," *ACS Chemical Neuroscience*, vol. 3, no. 8, pp. 611–618, 2012.

[13] J. S. Belkas, M. S. Shoichet, and R. Midha, "Peripheral nerve regeneration through guidance tubes," *Neurological Research*, vol. 26, no. 2, pp. 151–160, 2004.

[14] N. Zhang, H. Yan, and X. Wen, "Tissue-engineering approaches for axonal guidance," *Brain Research Reviews*, vol. 49, no. 1, pp. 48–64, 2005.

[15] A. Fraczek-Szczypta, "Carbon nanomaterials for nerve tissue stimulation and regeneration," *Materials Science and Engineering: C*, vol. 34, pp. 35–49, 2014.

[16] J. S. H. Taylor and E. T. W. Bampton, "Factors secreted by schwann cells stimulate the regeneration of neonatal retinal ganglion cells," *Journal of Anatomy*, vol. 204, no. 1, pp. 25–31, 2004.

[17] C. Zhao, A. Tan, G. Pastorin, and H. K. Ho, "Nanomaterial scaffolds for stem cell proliferation and differentiation in tissue engineering," *Biotechnology Advances*, vol. 31, no. 5, pp. 654–668, 2013.

[18] K. Liu, A. Tedeschi, K. K. Park, and Z. He, "Neuronal intrinsic mechanisms of axon regeneration," *Annual Review of Neuroscience*, vol. 34, no. 1, pp. 131–152, 2011.

[19] E. Biazar, "Types of neural guides and using nanotechnology for peripheral nerve reconstruction," *International Journal of Nanomedicine*, vol. 839, 2010.

[20] M. Perán, M. García, E. Lopez-Ruiz, G. Jiménez, and J. Marchal, "How can nanotechnology help to repair the body? Advances in cardiac, skin, bone, cartilage and nerve tissue regeneration," *Materials*, vol. 6, no. 4, pp. 1333–1359, 2013.

[21] Z. Zhou, X. Liu, W. Wu et al., "Effective nerve cell modulation by electrical stimulation of carbon nanotube embedded conductive polymeric scaffolds," *Biomaterials Science*, vol. 6, no. 9, pp. 2375–2385, 2018.

[22] K. M. Oprych, R. L. D. Whitby, S. V. Mikhalovsky, P. Tomlins, and J. Adu, "Repairing peripheral nerves: is there a role for carbon nanotubes?," *Advanced Healthcare Materials*, vol. 5, no. 11, pp. 1253–1271, 2016.

[23] G. Jia, H. Wang, L. Yan et al., "Cytotoxicity of carbon nanomaterials: single-wall nanotube, multi-wall nanotube, and fullerene," *Environmental Science & Technology*, vol. 39, no. 5, pp. 1378–1383, 2005.

[24] R. A. MacDonald, C. M. Voge, M. Kariolis, and J. P. Stegemann, "Carbon nanotubes increase the electrical conductivity of fibroblast-seeded collagen hydrogels," *Acta Biomaterialia*, vol. 4, no. 6, pp. 1583–1592, 2008.

[25] Z. Zhu, L. Garcia-Gancedo, A. J. Flewitt, H. Xie, F. Moussy, and W. I. Milne, "A critical review of glucose biosensors based on carbon nanomaterials: carbon nanotubes and graphene," *Sensors*, vol. 12, no. 5, pp. 5996–6022, 2012.

[26] C. Cha, S. R. Shin, N. Annabi, M. R. Dokmeci, and A. Khademhosseini, "Carbon-based nanomaterials: multifunctional materials for biomedical engineering," *ACS Nano*, vol. 7, no. 4, pp. 2891–2897, 2013.

[27] N. Choudhary, S. Hwang, and W. Choi, "Carbon nanomaterials: a review," in *Handbook of Nanomaterials Properties*, pp. 709–769, Springer, Berlin, Germany, 2014.

[28] R. F. Schinazi, R. Sijbesma, G. Srdanov, C. L. Hill, and F. Wudl, "Synthesis and virucidal activity of a water-soluble, configurationally stable, derivatized C60 fullerene," *Antimicrobial Agents and Chemotherapy*, vol. 37, no. 8, pp. 1707–1710, 1993.

[29] S.-R. Chae, Y. Watanabe, and M. R. Wiesner, "Comparative photochemical reactivity of spherical and tubular fullerene nanoparticles in water under ultraviolet (UV) irradiation," *Water Research*, vol. 45, no. 1, pp. 308–314, 2011.

[30] A. Husen and K. Siddiqi, "Carbon and fullerene nanomaterials in plant system," *Journal of Nanobiotechnology*, vol. 12, no. 1, p. 16, 2014.

[31] M. Srikanth, R. Asmatulu, K. Cluff, and L. Yao, "Material characterization and bioanalysis of hybrid scaffolds of carbon nanomaterial and polymer nanofibers," *ACS Omega*, vol. 4, no. 3, pp. 5044–5051, 2019.

[32] A. Nasri, A. Boubaker, B. Hafsi, W. Khaldi, and A. Kalboussi, "High-sensitivity sensor using C60-single molecule transistor," *IEEE Sensors Journal*, vol. 18, no. 1, pp. 248–254, 2018.

[33] S. He and W. Chen, "3D graphene nanomaterials for binder-free supercapacitors: scientific design for enhanced performance," *Nanoscale*, vol. 7, no. 16, pp. 6957–6990, 2015.

[34] P. Kumar, P. Huo, R. Zhang, and B. Liu, "Antibacterial properties of graphene-based nanomaterials," *Nanomaterials*, vol. 9, no. 5, p. 737, 2019.

[35] N. P. Pampaloni, M. Lottner, M. Giugliano et al., "Single-layer graphene modulates neuronal communication and augments membrane ion currents," *Nature Nanotechnology*, vol. 13, no. 8, pp. 755–764, 2018.

[36] M. Pumera, "Graphene-based nanomaterials and their electrochemistry," *Chemical Society Reviews*, vol. 39, no. 11, p. 4146, 2010.

[37] A. I. Rusanov, "Thermodynamics of graphene," *Surface Science Reports*, vol. 69, no. 4, pp. 296–324, 2014.

[38] P.-C. Ma, N. A. Siddiqui, G. Marom, and J.-K. Kim, "Dispersion and functionalization of carbon nanotubes for polymer-based nanocomposites: a review," *Composites Part A: Applied Science and Manufacturing*, vol. 41, no. 10, pp. 1345–1367, 2010.

[39] R. Vidu, M. Rahman, M. Mahmoudi, M. Enachescu, T. D. Poteca, and I. Opris, "Nanostructures: a platform for brain repair and augmentation," *Frontiers in Systems Neuroscience*, vol. 8, p. 91, 2014.

[40] P. Gupta and D. Lahiri, "Aligned carbon nanotube containing scaffolds for neural tissue regeneration," *Neural Regeneration Research*, vol. 11, no. 7, pp. 1062–1603, 2016.

[41] C. Gao, Z. Guo, J.-H. Liu, and X.-J. Huang, "The new age of carbon nanotubes: an updated review of functionalized

carbon nanotubes in electrochemical sensors," *Nanoscale*, vol. 4, no. 6, pp. 1948–1963, 2012.

[42] Y. Zhou, Y. Fang, and R. Ramasamy, "Non-covalent functionalization of carbon nanotubes for electrochemical biosensor development," *Sensors*, vol. 19, no. 2, p. 392, 2019.

[43] J.-Y. Hwang, U. S. Shin, W.-C. Jang, J. K. Hyun, I. B. Wall, and H.-W. Kim, "Biofunctionalized carbon nanotubes in neural regeneration: a mini-review," *Nanoscale*, vol. 5, no. 2, pp. 487–497, 2013.

[44] K. Matsumoto, C. Sato, Y. Naka, R. Whitby, and N. Shimizu, "Stimulation of neuronal neurite outgrowth using functionalized carbon nanotubes," *Nanotechnology*, vol. 21, no. 11, Article ID 115101, 2010.

[45] A. Sucapane, G. Cellot, M. Prato, M. Giugliano, V. Parpura, and L. Ballerini, "Interactions between cultured neurons and carbon nanotubes: a nanoneuroscience vignette," *Journal of Nanoneuroscience*, vol. 1, no. 1, pp. 10–16, 2009.

[46] C. Redondo-Gómez, F. Orozco, P.-L. Michael Noeske, V. Soto-Tellini, Y. R. Corrales-Ureña, and J. Vega-Baudrit, "Cholic acid covalently bound to multi-walled carbon nanotubes: improvements on dispersion stability," *Materials Chemistry and Physics*, vol. 200, pp. 331–341, 2017.

[47] V. Lovat, D. Pantarotto, L. Lagostena et al., "Carbon nanotube substrates boost neuronal electrical signaling," *Nano Letters*, vol. 5, no. 6, pp. 1107–1110, 2005.

[48] N. W. S. Kam, E. Jan, and N. A. Kotov, "Electrical stimulation of neural stem cells mediated by humanized carbon nanotube composite made with extracellular matrix protein," *Nano Letters*, vol. 9, no. 1, pp. 273–278, 2009.

[49] A. Fabbro, A. Sucapane, F. M. Toma et al., "Adhesion to carbon nanotube conductive scaffolds forces action-potential appearance in immature rat spinal neurons," *PLoS One*, vol. 8, no. 8, Article ID e73621, 2013.

[50] P. A. Tran, L. Zhang, and T. J. Webster, "Carbon nanofibers and carbon nanotubes in regenerative medicine," *Advanced Drug Delivery Reviews*, vol. 61, no. 12, pp. 1097–1114, 2009.

[51] Y. Zhang, Y. Bai, and B. Yan, "Functionalized carbon nanotubes for potential medicinal applications," *Drug Discovery Today*, vol. 15, no. 11-12, pp. 428–435, 2010.

[52] N. P. Pampaloni, I. Rago, I. Calaresu et al., "Transparent carbon nanotubes promote the outgrowth of enthorinodentate projections in lesioned organ slice cultures," *Developmental Neurobiology*, pp. 1–16, 2019.

[53] A. Vlachos, D. Becker, P. Jedlicka, R. Winkels, J. Roeper, and T. Deller, "Entorhinal denervation induces homeostatic synaptic scaling of excitatory postsynapses of dentate granule cells in mouse organotypic slice cultures," *PLoS One*, vol. 7, no. 3, Article ID e32883, 2012.

[54] S.-J. Lee, W. Zhu, M. Nowicki et al., "3D printing nano conductive multi-walled carbon nanotube scaffolds for nerve regeneration," *Journal of Neural Engineering*, vol. 15, no. 1, Article ID 016018, 2018.

[55] H.-S. Ahn, J.-Y. Hwang, M. S. Kim et al., "Carbon-nanotube-interfaced glass fiber scaffold for regeneration of transected sciatic nerve," *Acta Biomaterialia*, vol. 13, pp. 324–334, 2015.

[56] Y. S. Zhang and A. Khademhosseini, "Advances in engineering hydrogels," *Science*, vol. 356, no. 6337, 2017.

[57] A. Vashist, A. Kaushik, A. Vashist et al., "Advances in carbon nanotubes-hydrogel hybrids in nanomedicine for therapeutics," *Advanced Healthcare Materials*, vol. 7, no. 9, Article ID 1701213, 2018.

[58] S. Wu, B. Duan, A. Lu, Y. Wang, Q. Ye, and L. Zhang, "Biocompatible chitin/carbon nanotubes composite hydrogels as neuronal growth substrates," *Carbohydrate Polymers*, vol. 174, pp. 830–840, 2017.

[59] F. Mottaghitalab, M. Farokhi, A. Zaminy et al., "A biosynthetic nerve guide conduit based on silk/SWNT/fibronectin nanocomposite for peripheral nerve regeneration," *PLoS One*, vol. 8, no. 9, Article ID e74417, 2013.

[60] J. Simon, E. Flahaut, and M. Golzio, "Overview of carbon nanotubes for biomedical applications," *Materials*, vol. 12, no. 4, p. 624, 2019.

[61] L. Yan, F. Zhao, S. Li, Z. Hu, and Y. Zhao, "Low-toxic and safe nanomaterials by surface-chemical design, carbon nanotubes, fullerenes, metallofullerenes, and graphenes," *Nanoscale*, vol. 3, no. 2, pp. 362–382, 2011.

[62] C.-W. Lam, J. T. James, R. McCluskey, S. Arepalli, and R. L. Hunter, "A review of carbon nanotube toxicity and assessment of potential occupational and environmental health risks," *Critical Reviews in Toxicology*, vol. 36, no. 3, pp. 189–217, 2006.

[63] R. Bellingeri, F. Alustiza, N. Picco et al., "In vitro toxicity evaluation of hydrogel-carbon nanotubes composites on intestinal cells," *Journal of Applied Polymer Science*, vol. 132, no. 5, p. 41370, 2015.

[64] X. Chen, J. Fang, Y. Cheng et al., "Biomolecular interaction analysis for carbon nanotubes and for biocompatibility prediction," *Analytical Biochemistry*, vol. 505, pp. 1–7, 2016.

[65] N. M. Bardhan, D. Ghosh, and A. M. Belcher, "Carbon nanotubes as in vivo bacterial probes," *Nature Communications*, vol. 5, no. 1, p. 4918, 2014.

[66] C. Ge, J. Du, L. Zhao et al., "Binding of blood proteins to carbon nanotubes reduces cytotoxicity," *Proceedings of the National Academy of Sciences*, vol. 108, no. 41, pp. 16968–16973, 2011.

[67] M. Baldrighi, M. Trusel, R. Tonini, and S. Giordani, "Carbon nanomaterials interfacing with neurons: an in vivo perspective," *Frontiers in Neuroscience*, vol. 10, 2016.

[68] R. Singh, D. Pantarotto, D. McCarthy et al., "Binding and condensation of plasmid DNA onto functionalized carbon nanotubes: toward the construction of nanotube-based gene delivery vectors," *Journal of the American Chemical Society*, vol. 127, no. 12, pp. 4388–4396, 2005.

[69] R. Singh, D. Pantarotto, L. Lacerda et al., "Tissue biodistribution and blood clearance rates of intravenously administered carbon nanotube radiotracers," *Proceedings of the National Academy of Sciences*, vol. 103, no. 9, pp. 3357–3362, 2006.

[70] G. Pagona and N. Tagmatarchis, "Carbon nanotubes: materials for medicinal chemistry and biotechnological applications," *Current Medicinal Chemistry*, vol. 13, no. 15, pp. 1789–1798, 2006.

[71] H. Hu, B. Zhao, M. A. Hamon, K. Kamaras, M. E. Itkis, and R. C. Haddon, "Sidewall functionalization of single-walled carbon nanotubes by addition of dichlorocarbene," *Journal of the American Chemical Society*, vol. 125, no. 48, pp. 14893–14900, 2003.

[72] T. G. Hedderman, S. M. Keogh, G. Chambers, and H. J. Byrne, "In-depth study into the interaction of single walled carbon nanotubes with anthracene and p -terphenyl," *The Journal of Physical Chemistry B*, vol. 110, no. 9, pp. 3895–3901, 2006.

[73] D. M. Guldi, G. M. A. Rahman, N. Jux et al., "Functional single-wall carbon nanotube nanohybrids associating SWNTs with water-soluble enzyme model systems," *Journal of the American Chemical Society*, vol. 127, no. 27, pp. 9830–9838, 2005.

[74] F. Cheng and A. Adronov, "Noncovalent functionalization and solubilization of carbon nanotubes by using a conjugated Zn–porphyrin polymer," *Chemistry—A European Journal*, vol. 12, no. 19, pp. 5053–5059, 2006.

[75] S. Dumonteil, A. Demortier, S. Detriche et al., "Dispersion of carbon nanotubes using organic solvents," *Journal of Nanoscience and Nanotechnology*, vol. 6, no. 5, pp. 1315–1318, 2006.

[76] A. Ishibashi and N. Nakashima, "Individual dissolution of single-walled carbon nanotubes in aqueous solutions of steroid or sugar compounds and their Raman and near-IR spectral properties," *Chemistry—A European Journal*, vol. 12, no. 29, pp. 7595–7602, 2006.

[77] A. P. Roberts, A. S. Mount, B. Seda et al., "In vivo biomodification of lipid-coated carbon nanotubes by *Daphnia magna*," *Environmental Science & Technology*, vol. 41, no. 8, pp. 3025–3029, 2007.

[78] A. Ikeda, Y. Tanaka, K. Nobusawa, and J.-I. Kikuchi, "Solubilization of single-walled carbon nanotubes by supramolecular complexes of barbituric acid and triaminopyrimidines," *Langmuir*, vol. 23, no. 22, pp. 10913–10915, 2007.

[79] X. Wang, X. Y. Deng, H. F. Wang et al., "Bio-effects of water soluble taurine multi-wall carbon nanotubes on lungs of mice," *Zhonghua Yu Fang Yi Xue Za Zhi*, vol. 41, pp. 85–90, 2007.

[80] M. Bottini, A. Magrini, N. Rosato, A. Bergamaschi, and T. Mustelin, "Dispersion of pristine single-walled carbon nanotubes in water by a thiolated organosilane: application in supramolecular nanoassemblies," *The Journal of Physical Chemistry B*, vol. 110, no. 28, pp. 13685–13688, 2006.

[81] J. Tkac, J. W. Whittaker, and T. Ruzgas, "The use of single walled carbon nanotubes dispersed in a chitosan matrix for preparation of a galactose biosensor," *Biosensors and Bioelectronics*, vol. 22, no. 8, pp. 1820–1824, 2007.

[82] O.-K. Kim, J. Je, J. W. Baldwin, S. Kooi, P. E. Pehrsson, and L. J. Buckley, "Solubilization of single-wall carbon nanotubes by supramolecular encapsulation of helical amylose," *Journal of the American Chemical Society*, vol. 125, no. 15, pp. 4426-4427, 2003.

[83] J. Mao, Q. Liu, X. Lv et al., "A water-soluble hybrid material of single-walled carbon nanotubes with an amphiphilic poly(phenyleneethynylene): preparation, characterization, and photovoltaic properties," *Journal of Nanoscience and Nanotechnology*, vol. 7, no. 8, pp. 2709–2718, 2007.

[84] B. Zhao, H. Hu, A. Yu, D. Perea, and R. C. Haddon, "Synthesis and characterization of water soluble single-walled carbon nanotube graft copolymers," *Journal of the American Chemical Society*, vol. 127, no. 22, pp. 8197–8203, 2005.

[85] A. Liu, T. Watanabe, I. Honma, J. Wang, and H. Zhou, "Effect of solution pH and ionic strength on the stability of poly(acrylic acid)-encapsulated multiwalled carbon nanotubes aqueous dispersion and its application for NADH sensor," *Biosensors and Bioelectronics*, vol. 22, no. 5, pp. 694–699, 2006.

[86] H. Zhang, H. X. Li, and H. M. Cheng, "Water-soluble multiwalled carbon nanotubes functionalized with sulfonated polyaniline," *The Journal of Physical Chemistry B*, vol. 110, no. 18, pp. 9095–9099, 2006.

[87] G. Bardi, A. Nunes, L. Gherardini et al., "Functionalized carbon nanotubes in the brain: cellular internalization and neuroinflammatory responses," *PLoS One*, vol. 8, no. 11, Article ID e80964, 2013.

[88] S.-T. Yang, W. Guo, Y. Lin et al., "Biodistribution of pristine single-walled carbon nanotubes in vivo†," *The Journal of Physical Chemistry C*, vol. 111, no. 48, pp. 17761–17764, 2007.

[89] J. A. Roman, T. L. Niedzielko, R. C. Haddon, V. Parpura, and C. L. Floyd, "Single-walled carbon nanotubes chemically functionalized with polyethylene glycol promote tissue repair in a rat model of spinal cord injury," *Journal of Neurotrauma*, vol. 28, no. 11, pp. 2349–2362, 2011.

[90] H. Kafa, J. T.-W. Wang, N. Rubio et al., "The interaction of carbon nanotubes with an in vitro blood-brain barrier model and mouse brain in vivo," *Biomaterials*, vol. 53, pp. 437–452, 2015.

[91] D. Zhao, D. Alizadeh, L. Zhang et al., "Carbon nanotubes enhance CpG uptake and potentiate antiglioma immunity," *Clinical Cancer Research*, vol. 17, no. 4, pp. 771–782, 2011.

[92] C. P. Firme and P. R. Bandaru, "Toxicity issues in the application of carbon nanotubes to biological systems," *Nanomedicine: Nanotechnology, Biology and Medicine*, vol. 6, no. 2, pp. 245–256, 2010.

[93] D. Mohanta, S. Patnaik, S. Sood, and N. Das, "Carbon nanotubes: evaluation of toxicity at biointerfaces," *Journal of Pharmaceutical Analysis*, vol. 9, no. 5, pp. 293–300, 2019.

[94] R. Alshehri, A. M. Ilyas, A. Hasan, A. Arnaout, F. Ahmed, and A. Memic, "Carbon nanotubes in biomedical applications: factors, mechanisms, and remedies of toxicity," *Journal of Medicinal Chemistry*, vol. 59, no. 18, pp. 8149–8167, 2016.

[95] K. Kostarelos, "Rational design and engineering of delivery systems for therapeutics: biomedical exercises in colloid and surface science," *Advances in Colloid and Interface Science*, vol. 106, no. 1–3, pp. 147–168, 2003.

[96] A. Nel, "Toxic potential of materials at the nanolevel," *Science*, vol. 311, no. 5761, pp. 622–627, 2006.

[97] Y. Sato, A. Yokoyama, K.-I. Shibata et al., "Influence of length on cytotoxicity of multi-walled carbon nanotubes against human acute monocytic leukemia cell line THP-1 in vitro and subcutaneous tissue of rats in vivo," *Molecular BioSystems*, vol. 1, no. 2, p. 176, 2005.

[98] M. Marsh and H. T. McMahon, "The structural era of endocytosis," *Science*, vol. 285, no. 5425, pp. 215–220, 1999.

[99] G. J. Doherty and H. T. McMahon, "Mechanisms of endocytosis," *Annual Review of Biochemistry*, vol. 78, no. 1, pp. 857–902, 2009.

[100] N. W. S. Kam, Z. Liu, and H. Dai, "Carbon nanotubes as intracellular transporters for proteins and DNA: an investigation of the uptake mechanism and pathway," *Angewandte Chemie International Edition*, vol. 45, no. 4, pp. 577–581, 2006.

[101] N. W. Shi Kam, T. C. Jessop, P. A. Wender, and H. Dai, "Nanotube molecular transporters: internalization of carbon nanotube–protein conjugates into mammalian cells," *Journal of the American Chemical Society*, vol. 126, no. 22, pp. 6850-6851, 2004.

[102] M. Pacurari, X. J. Yin, J. Zhao et al., "Raw single-wall carbon nanotubes induce oxidative stress and activate MAPKs, AP-1, NF-κB, and akt in normal and malignant human mesothelial cells," *Environmental Health Perspectives*, vol. 116, no. 9, pp. 1211–1217, 2008.

[103] R. Daneman and A. Prat, "The blood-brain barrier," *Cold Spring Harbor Perspectives in Biology*, vol. 7, no. 1, 2015.

[104] Z. Yang, Y. Zhang, Y. Yang et al., "Pharmacological and toxicological target organelles and safe use of single-walled carbon nanotubes as drug carriers in treating Alzheimer disease," *Nanomedicine: Nanotechnology, Biology and Medicine*, vol. 6, no. 3, pp. 427–441, 2010.

Hindawi
Advances in Polymer Technology
Volume 2020, Article ID 6163904, 12 pages
https://doi.org/10.1155/2020/6163904

Review Article

Perspectives, Tendencies, and Guidelines in Affinity-Based Strategies for the Recovery and Purification of PEGylated Proteins

Luis Alberto Mejía-Manzano, Patricia Vázquez-Villegas, and José González-Valdez

Tecnologico de Monterrey, School of Engineering and Science, Av. Eugenio Garza Sada 2501 Sur, Monterrey, NL 64849, Mexico

Correspondence should be addressed to José González-Valdez; jose_gonzalez@tec.mx

Received 11 July 2019; Accepted 23 December 2019; Published 25 January 2020

Guest Editor: Margarita S. Dominguez

In recent years, the effective purification of PEGylated therapeutic proteins from reaction media has received particular attention. Although several techniques have been used, affinity-based strategies have been scarcely explored despite the fact that, after PEGylation, marked changes in the molecular affinity parameters of the modified molecules are observed. With this in mind, future contributions in the bioseparation of these polymer-protein conjugates are expected to exploit affinity in chromatographic and nonchromatographic techniques which will surely derive in the integration of different operations. However, this will only occur as novel ligands which are simultaneously found. As it will be mentioned, these novel ligands may be screened or designed. In both cases, computer-aided tools will support their identification or development. Additionally, ligand discovery by high-throughput screening (HTS) is believed to become a fast, economic, and informative technology that will aid in the mass production of ligands along with genetic engineering and related technologies. Therefore, besides analyzing the state of the art in affinity separation strategies for PEGylated molecules, this review proposes a basic guideline for the selection of adequate ligands to provide information and prospective on the future of affinity operations in solving this particular bioengineering problem.

1. Introduction

The chemical or physical attachment of polyethylene glycol (PEG) to a molecule or a therapeutic protein is defined as PEGylation [1–3]. Among the benefits that have been associated to this strategy at a general therapeutic level are the increase in protein solubility, size, and thermal and mechanical stability [4], which confer proteolysis resistance and a reduction in renal clearance, immunogenicity, and toxicity [5]. In 2017, the global market of PEGylated therapeutic proteins was valued at US$ 10, 388 million with an estimated compound annual growth rate (GAGR) of 6.9% from 2018 to 2025 [6]. To date, there are more than 12 FDA-cleared PEG-modified drugs and about 30 more in research and/or clinical trials [7].

The PEG used in PEGylation can be linear or branched with diverse sizes, depending on the size of the biomolecule to be modified [7]. Polymer molecular weights of 40 to 60 kDa are preferred [2]. To do so, PEG is functionalized with different chemical groups (i.e., amino, hydroxyl, imidazole, histidine, thiol, disulfide, carboxylic, hydrophobic, or electrostatic residues) [8]. Depending on the kind of reaction used, PEGylation can be classified into noncovalent or covalent, and the last one is subdivided into random or site-specific [9]. Noncovalent PEGylation exploits hydrophobic or ionic interactions to form coordination complexes between the protein and the polymer [9]; however, these are scarcely used because the PEG coating can be easily removed [10]. On the contrary, covalent techniques involve the formation of fixed chemical bonds which can be site-specific in some cases. PEG-carboxylates, PEG-carbonates, or PEG activated with N-hydroxysuccinimide are examples of agents that lead to random or unspecific PEGylations [9]. Among the strategy examples to obtain site-specific conjugation, we can find N-terminal thiol bridging or enzymatic PEGylations [9]. Although a site-specific modification is always preferred, it can be expensive, it is not always feasible, or it may require

a high expertise and development time [11]. Furthermore, if the molecule presents several of these target-specific sites, the reaction tends to produce PEGylated species that vary in modification degree (number of attached chains) and positional isomerism [11] as it occurs with random PEGylation. In this context, the mono-PEGylated conjugate is usually the most adequate isomer regarding the desired properties and biological activity for its therapeutic function. Thus, the recovery and purification of the right conjugate with the desired yield and purity result in a sophisticated and resource-consuming procedure.

Current separation methods to purify the mono-PEGylated conjugates can be classified into two main groups: chromatographic and nonchromatographic techniques [12]. Within the nonchromatographic techniques, ultrafiltration has been applied in the recovery of PEGylated ovalbumin, bovine serum albumin, α-lactalbumin, and ribonuclease A (RNase A) [13], with the disadvantages of obtaining low recoveries and the high cost of the membranes. On their part, aqueous two-phase systems (ATPS) have demonstrated to be a promising technique in the fractionation of PEGylated proteins in PEG-phosphate systems [14, 15], but until now, the operation has not been carried out at pilot or industrial scales. Polyacrylamide gel electrophoresis (PAGE) is used mainly for the characterization or analysis of the modified molecules, requiring the use of an additional step to remove the dyes used in the staining of the proteins [12].

On the contrary, chromatographic techniques are still the preferred method for PEGylated conjugate purification. Size exclusion chromatography (SEC) has been effective to remove low molecular weight impurities and nonreacted proteins, nevertheless SEC has been unable to distinguish between conjugates and positional isomers causing poor resolution, high buffer consumption, large sample dilution, and long processing times [16, 17]. Ion exchange chromatography (IEX) takes advantage of protein charge modification due to PEG shielding, that is to say, the covering of the protein surface and the loss of a positive charge for each linked PEG chain [18]. However, the negative aspects of this methodology are low dynamic binding capacity of proteins with long PEG chains [19], short support lifetimes, and low column loads. On its part, reverse phase chromatography (RPC) has been applied for the analysis of PEG-conjugates in HPLC systems more than in preparative levels because the high temperatures and the use of organic solvents in the mobile phase cause protein denaturation [16]. Hydrophobic interaction chromatography (HIC) has been successfully implemented for the recovery of modified proteins with different degrees of PEGylation, but in this method, free PEG is also linked to the stationary phase, and there is a lack of predictive understanding of molecule retention which makes HIC not suitable for its use at large scales [20].

One of the discussed aspects of protein PEGylation is the change in the affinity parameters of the protein after its reaction. In this sense, affinity-based separations might be an effective and attractive option in the purification of protein-polymer conjugates considering the high selectivity that characterizes the interactions involved. This review analyzes different studies about the effects of PEGylation on the affinity of the modified molecules and presents current reports on affinity-based purification strategies for these conjugates. Distinctive tools in the screening/design and production of novel ligands are also referred. Future trends and challenges in the bioseparations of PEGylated proteins by affinity methods are elucidated, and a guide procedure to select the adequate ligand and operation for the purification of a PEG-modified protein is proposed.

2. Effects of PEGylation on Protein Affinity

As it has been mentioned, PEGylation has been used as a strategy to reduce the immunogenicity of some therapeutic biomolecules, proteins, or antibodies and to diminish dose frequency in patients [4]. In general terms, the affinity of PEGylated proteins towards biological agents is affected and is expected to change depending on the extent of the PEGylation procedure, [21] but there is still a lack of understanding on how this occurs. In this aspect, some reports have registered a decrement on the affinity of the PEGylated enzyme towards its biological counterpart. For instance, native ribonuclease A (RNase A) had a dissociation constant (k_d) of 7.6×10^{-8} M, while modified RNase A with 4 and 9 PEG molecules had k_d of 1.3×10^{-7} M and 1.2×10^{-6} M, respectively [22]. Chapman [4] concluded from his research with antibodies that affinity is reduced in random PEGylation more severely employing amine-reactive chemistries and in the cases when two or more attached PEG molecules per antibody molecule are found. He also reports a 50% inhibition of the Fc (fragment crystallizable) receptor binding in the antibody when 25% of the available amines were modified by random PEGylation. Furthermore, Fc activity was more affected than the antigenic binding activity. This report describes, as well, that, in site-specific PEGylation of complete antibodies or antibody fragments, the affinity binding is retained. However, it also suggests that binding loss may be caused by ionic interference rather than affinity interference [4]. In summary, Chapman states that the changes in affinity vary in every case depending on the protein size, surface density, length of the PEG chains, and of course the PEGylation strategy used [4]. All these factors have an accumulative effect, and the closer the modification site is to the binding or active site, the most severe is the effect in its affinity. In those cases in which affinity loss occurs during the PEGylation of some drugs, the negative effect may be compensated through the application of the multivalence concept (the binding of more than one biomolecule to a macroligand) as it has been observed in the conjugation of PEGylated ligands to nanoparticles [23].

3. Current Advances in the Purification of PEGylated Proteins through Affinity Procedures

Affinity-based bioseparations are techniques that exploit a biological recognition phenomenon, which is reversible and

specific, to achieve the separation of one or several of the desired biomolecules from their contaminants [24]. Such procedures require operations such as chromatography, precipitation, membrane-based purifications, and two-phase extractions. [24] These can also be grouped as affinity nonchromatographic and chromatographic techniques. The essential steps in a protein affinity-based bioseparation (regardless of the operation type) are (1) the capture of the protein with the ligand (which can be free or linked to a particular matrix), (2) washing or separation of the contaminants of the mixture, and (3) elution or recovery of the target protein [25].

Even when affinity bioseparations have been highly demanded for the isolation of pharmaceutical proteins, their use in polymer-protein conjugates recovery has been poorly studied. The change in affinity properties has been mainly addressed in chromatographic techniques mostly because chromatography will continue to be the preferred method for biopharmaceutical purification because of its high-resolution capabilities [26].

Affinity chromatography (AC) is a selective and powerful purification operation which is based on a highly specific biological interaction between a target and a ligand [27–30]. The advantages attributed to AC are high selectivity and specificity, high sample concentration, high level of purification (greater than 1,000-fold), scalability [31], conservation of biological activity using gentle operations, and time saving. Until now, the applications of affinity chromatography for the purification of PEGylated proteins after a PEGylation reaction are scarce. There are only two works dealing to some extent with affinity chromatography of PEG-modified proteins. In one of these works, the purification of 20 kDa mono-PEGylated lysozyme with heparin affinity chromatography was optimized through an experimental design [32], and the elution curves for the operation were later simulated [33]. The other studies deal with the PEGylation of ligands in AC supports or resins, with the aim of improving their stability using as model concanavalin and protein A [34, 35].

Regarding possible ligands for PEGylated proteins, the discovery of induced immunogenicity in patients and animals administered with PEG-protein conjugates was the antecedent for the identification and isolation of anti-PEG antibodies [36]. The existing anti-PEG antibodies are of IgG and IgM isotypes, and several of them are available commercially (Table 1). However, much has been questioned regarding their specificity [37], but in current studies, interesting conclusions have been obtained. One of them is that none of the monoclonal or polyclonal anti-PEG antibodies are totally methoxy or backbone-specific, so these show relative specificities. For example, the anti-PEG antibodies inducted by HO-PEG-proteins target the backbone but not the hydroxyl end-group [38, 39]. In those antibodies raised against metoxi-PEG (mPEG)-proteins, the affinity depends on the hydrophobicity of their end-groups and the backbone lengths of the polymers, so anti-mPEGs presented a few hundreds of times more affinity for 10 kDa mPEG than for mTEG (tri(ethylene glycol) monomethyl ether) [38]. The reported applications using anti-PEG antibodies enclose diagnosis, analysis, and quantification of both PEG and PEGylated proteins. Only in one work, the anti-PEG antibody PEG B-47 (rabbit IgG1 monoclonal antibody) was used as part of an immunoaffinity purification, and the antibody was bound to streptavidin-coated magnetic beads for the capture of the MK-2662 peptide PEGylated with 40 kDa branched PEG at C-terminus [40]. The captured peptide was digested and injected in 2D-HPLC followed by a triple-quadrupole mass spectrometer detector [40]. However, in this work, the peptide is destroyed making the application fundamentally analytic, which is not recommended if peptide recovery is wanted. In the same way, our research group is attempting to use anti-PEG antibodies as selective ligands in PEG-protein downstream processes but from a preparative perspective.

Approaches on using affinity chromatography for carrying out PEGylation reactions with better effectiveness (denominated affinity on-column PEGylation or solid-phase PEGylation) have also been performed. This methodology consists on integrating the reaction and purification operations in a single step with the goal of doing a more site-specific PEGylation and protecting the active or binding site in enzymes or proteins from PEG alteration [41]. The protein is adsorbed onto the affinity matrix, and then PEGylation is performed during protein retention [42]. Table 2 shows examples in which solid-phase PEGylation with affinity chromatography has been applied to important therapeutic proteins. On-column PEGylation ensures the catalytic activity after the PEG-modification, especially in proteins with modifiable amino acids in the binding site as it happens with the presence of lysines, which can be attacked during N-terminal PEGylation [8]. As consequence, protein biological activity is more conserved than in random PEGylation. Table 2 displays, for the most part, relative bioactivities greater than 50%, whereas in unplanned PEG conjugations, the achieved bioactivity is only 40% or even null. In general, solid-phase PEGylation has improved yields for the mono-PEGylated protein in comparison to liquid-phase PEGylation [44, 46]. Furthermore, on-column PEGylation represents an attractive integration of operations obtaining a desirable product with less downstream steps [47] in less time and with guaranteed biological activity. Nevertheless, this is not always true since in some cases, affinity changes between the nonmodified and the mono-PEGylated product are not enough to resolve both proteins in the elution step of the AC [44, 45]. Also, when multiple conjugates are formed due to the high number of modifiable amino acids in the protein surface [42], a second purification chromatography (SEC or IEX) could be mandatory.

In general, the affinity property for the isolation of PEGylated proteins has only been exploited with chromatography in a small number of works. The integration of PEGylation and chromatography is a common approach with the aim of improving PEGylation yields and reducing isomer appearance. However, the use and study of preparative affinity chromatography needs to be encouraged.

Table 1: Commercial anti-PEG antibodies and recommended applications.

Antibody	Isotype	Class	Source	Company	Specificity	Suggested applications
B-47	G	Monoclonal	Rabbit	RabMAb®	Metoxi-PEG of conjugates	ELISA, WB, IHC
PEG-2-128	M	Monoclonal	Rabbit	RabMAb®	PEG backbone	ELISA, WB
RM105	G	Monoclonal	Rabbit	RabMAb®	Metoxi-PEG	ICC, WB, ELISA, IHC, flow Cyt, IP
5D6-3	G1	Monoclonal	Mouse	RabMAb®	PEG backbone	ELISA, WB
PA5-32247	G	Polyclonal	Rabbit	Thermo Fisher Scientific®	PEG	WB
09F02	G3	Monoclonal	Mouse	Lifespan BioSciences®	PEG	ELISA
THE™ PEG antibody	M	Monoclonal	Mouse	Lifespan BioSciences®	PEG backbone and conjugates	ELISA, IHC, IP, WB
E11	G1	Monoclonal	Mouse	Lifespan BioSciences®	PEG backbone	ELISA
3.3	G1	Monoclonal	Mouse	Lifespan BioSciences®	PEG backbone and conjugates	ELISA, WB, flow Cyt
6.3	G1	Monoclonal	Mouse	Lifespan BioSciences®	PEG backbone	ELISA, WB, flow Cyt
15-2b	G2	Monoclonal	Mouse	Lifespan BioSciences®	Metoxi-PEG	ELISA, WB, flow Cyt
r33G	G3	Monoclonal	Rat	Lifespan BioSciences®	PEG backbone	ELISA
AGP3	M	Monoclonal	Mouse	Lifespan BioSciences®	PEG backbone	ELISA, WB, flow Cyt, IHC
rAGP6	M	Monoclonal	Mouse	Lifespan BioSciences®	PEG backbone	ELISA, WB
PEGPAB-01	G	Polyclonal	Rabbit	Lifespan BioSciences®	PEG	WB

ELISA: enzyme-linked immunosorbent assay, WB: western blot, IHC: immunohistochemistry, ICC: immunocytochemistry, and IP: immunoprecipitation.

Table 2: Affinity solid-phase PEGylation of some important proteins.

Protein	Affinity support	Used PEG reagent	Mono-PEGylated yield (%)	Formation of multi-PEGylated	Relative bioactivity[a] (%)	Reference
L-Asparaginase	L-Asparagine Sepharose CL-4B	5 kDa cyanuric chloride mPEG	—	No	50.2[b]	[43]
Catalase	Procion Red Sepharose CL-4B	6 kDa cyanuric chloride mPEG	—	No	46.5[c]	[43]
Recombinant fibroblast growth factor 2 (FGF-2)	Heparin Sepharose	20 kDa mPEG butyraldehyde	58.3	No	105.4[d]	[44]
Recombinant human keratynocite growth factor 1 (RhKGF-1)	Heparin Sepharose	20 kDa mPEG butyraldehyde	40	No	89.6[d]	[45]
His-tagged recombinant staphylokinase (trSak)	Ni^{2+}-IDA Sepharose 4FF	Succinimidyl carbonate mPEG (5,10, 20 kDa)	5 kDa > 40 10 kDa > 30 20 kDa > 28	Yes (di-PEG) in PEGylation with 5 and 10 kDa	5 kDa > 83[e] 10 kDa > 81 20 kDa > 75	[42]

[a]Kept bioactivity after PEGylation respect to bioactivity of the unmodified protein. Bioactivity was measured in a different way for each protein. [b]Measured absorbance at 500 nm of ammonia with Nessler's method. [c]Spectrophotometrical measure of the decrease in absorbance of H_2O_2 at 240 nm. [d]Mitogenic activity measured by NIH3T3 cell proliferation assay. [e]*In vitro* bioactivity was measured as the diameter of the halo around the well in Petri dishes with the fibrinogen powder.

4. Future Trends and Perspectives in the Affinity Purification of PEGylated Proteins

Future advances in the affinity purification of PEGylated proteins will be highlighted in two main pathways. One being the search or generation of novel ligands for PEG-modified proteins and the second one centered in the development of nonchromatographic affinity strategies. Regarding the first aspect, there are still very few known ligands for PEGylated proteins (basically heparin and anti-PEG or anti-PEGylated protein antibodies). This leads to promote the search or design of novel ligands at high production levels. The strategies to look for novel ligands will be addressed in the next section of this review.

Regarding the need of nonchromatographic affinity techniques, the unit operations considered until now are aqueous two-phase systems (ATPS), affinity-membrane separations, affinity precipitation, and magnetic strategies (Figure 1). ATPS are a promising liquid-liquid recovery operation for their simplicity, economy, having low energy consumption, high scalability potential, and preservation of the biological activity [48–50]. Affinity ATPS have been used to separate a great variety of proteins, molecules, and cells [51, 52], but there is an opportunity

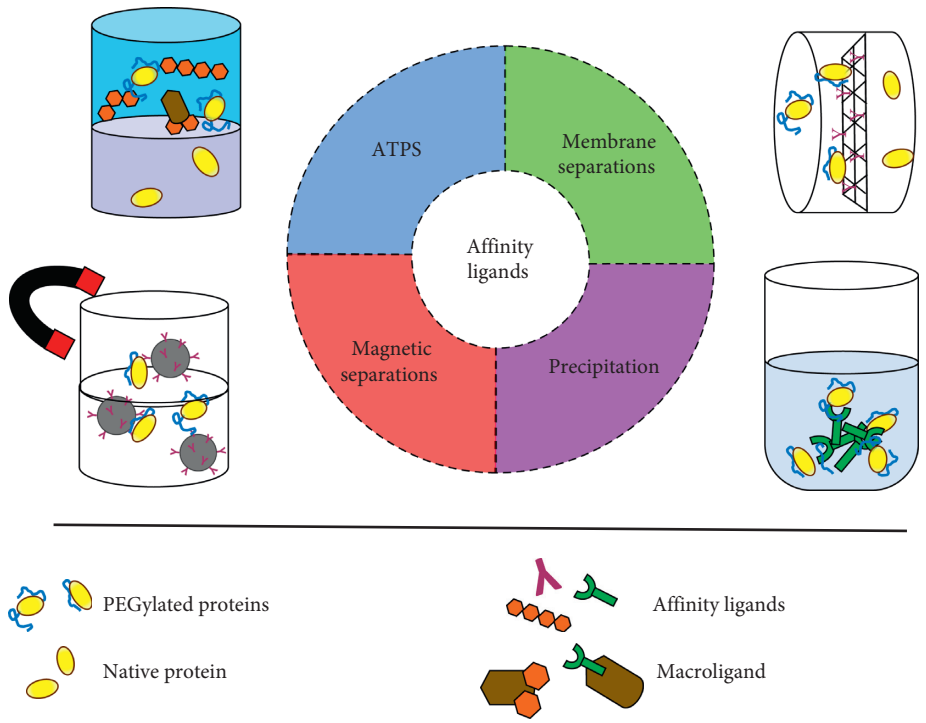

Figure 1: Potential nonchromatographic affinity-based strategies to be highlighted in the future recovery and purification of PEG-modified proteins.

area for PEG-modified proteins. In affinity-ATPS, the preferred systems have been PEG-dextran systems using antibodies, enzymes, or binding molecules as affinity elements. Affinity ATPS may be constructed for the purification of PEGylated proteins using the already known ligands for them.

It should be mentioned that by themselves, some individual PEGylated proteins (mono-PEGylated RNase A and α-lactalbumin) have showed preference for the top-phase (or PEG-rich phase) in PEG-phosphate systems [15, 53], but the use of affinity ligands may increase the recovery of these proteins in the PEG-rich phase. Incorporation of anti-PEGylated protein antibodies as ligands of PEG-modified proteins could favor the partitioning of these conjugates toward a determined phase. Reports about partitioning of antibodies in PEG-phosphate systems have shown that the polymers with low molecular weights favor the antibody partitioning in the PEG-rich phase unlike of systems using large PEGs in which antibodies are found in the salt-rich phase ($K_P < 1$). However, in this last case, the use of neutral salts like NaCl modifies the recovery of antibodies to the upper phase minimizing the polymer exclusion effects [54]. In PEG-dextran systems, antibodies partition to the bottom dextran-rich phase, but the use of some ligands for the antibody or modified PEGs [55] has enabled the partition of these antibodies to the top PEG-rich phase. With this in mind, further studies should be performed on the partition of those antibodies intended to be used for the primary recovery of PEGylated proteins to identify those systems in which these conjugates could be recovered. As it has been seen with most antibody partitioning studies, similar results could be expected leading to a good application for these purposes.

Affinity filtration, on its part, retains a protein that normally would pass through the membrane pores with the use of an affinity ligand. Its advantage is the specificity combined with the speed and the high-volume processing capacity of the membranes [56]. During the last few decades, affinity membranes have been coupled with chromatographic equipment giving place to membrane affinity chromatography (MAC) and to monolithic supports. MAC offers less risk of fouling or clogging and faster separations at semipreparative level [57].

Another alternative for the purification of PEGylated proteins is affinity precipitation. This technique can be defined as the specific and scalable solid-liquid separation of an insoluble substance (precipitate) induced by chemical or physical changes [58]. Temperature, pH, and salt concentration are factors involved in precipitate formation. For PEG-proteins, three different formats of affinity precipitation can be proposed: simple one-ligand, mixed-ligand and macroligand, or indirect precipitation. One and mixed-ligand formats can be categorized as primary or direct precipitation [58], where a unique and selective ligand (e.g., anti-PEGylated protein antibody) is used for capturing PEGylated proteins (Figure 2(a)). Mixed-ligand formats require a mixture of two ligands (e.g., anti-PEGylated protein and native protein antibodies) to fractionate the PEGylation reaction with different sedimentary velocities. Here, the separation is characterized basically for the ability of a first ligand to recognize only PEGylated proteins and a second ligand that recognizes the native unreacted protein

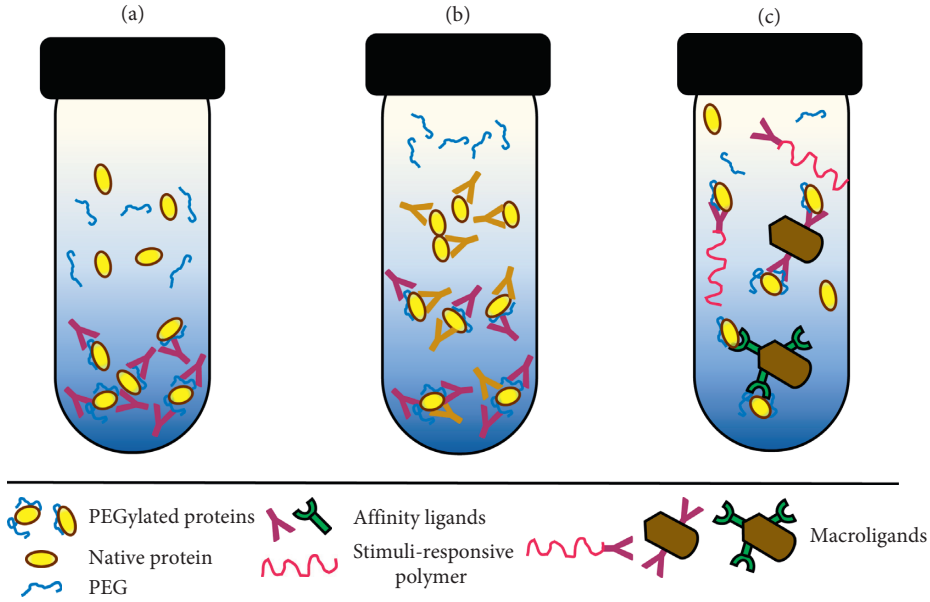

Figure 2: Proposed designs for the affinity precipitation of PEGylated proteins.

(Figure 2(b)). To be successful, the fractionation according with the size of the complexes could be achieved through gradual precipitation. In the third format, macroligands, which are bifunctional agents formed by a first molecule and the ligand, in which the first molecule can be a biomolecule (e.g., protein A, tags, and carrier proteins) binding one or several ligands (Figure 2(c)); stimuli-responsive polymers belong to this group and are well represented by acrylamide copolymers [59]. Application of stimuli-responsive polymers would have to be evaluated in the case of PEG-proteins due to the interactions between the polymers and the protein.

Magnetic affinity separations are characterized as simple, fast, gentle, versatile, scalable, and automated processes [60, 61]. For proteins, there are two modes of affinity magnetic separations: direct and indirect. In the direct method, the ligand must be coupled to the magnetic particle to capture the target protein; in the indirect method, the ligand and magnetic particles are added separately, leaving the ligand the function to interfere in the union of the target and the magnetic particle [60]. Nowadays, magnetic particles and separators are available commercially; the particles are sold with functional groups, in activated forms or with the embedded ligands, which make their procurement and use relatively easy. The application of the presented affinity nonchromatographic separation for PEGylated proteins will be conditioned by overcoming some hurdles such as abundance, recycling, and stability of the ligand in the purification media, so as the use of an efficient methodology for conjugate tracking and characterization.

The use of nanoparticles may be interesting in affinity-based separations of PEGylated proteins because of the multivalency and high avidity that nanoparticles present [23]. Through this route, PEGylated angiotensin II receptor type 1 has been bound to multivalent nanoparticle counterbalancing the affinity loss (up to 600-fold affinity decrease) caused by PEG-modification [62]. Ligands for PEG-proteins such as anti-PEGylated protein antibodies or those developed in the future might be immobilized firstly on nanoparticles (Figure 3) and in this way, improve the affinity capacity of the nonchromatographic technique and affinity loss and recoverability of the ligand.

A general trend in bioseparations is the design of simple one-stage operations commonly called process integration [63]. Many of the described nonchromatographic options can be combined with each other or with chromatography (as in MAC) in a unique purification stage and increase the efficiency of the individual operations until reaching the observed performance of chromatographic techniques. This integration is not restricted only to separation stages but also to production as it is visualized in "solid-phase PEGylation." Following the trend of process integration, affinity magnetic ATPS or so-called magnetic extraction phases (MEP) are not far away from being considered for the recovery of PEGylated proteins as well. Works dealing with this alternative for a mixture of lysozyme and ovalbumin have already been assayed [64]. In this work, a cationic magnetic adsorbent and a nonionic surfactant (Triton X-114) are added to the protein mixture. The magnetic adsorbent captured lysozyme, and a biphasic system is later formed heating at 30°C and excluding the magnetic particles to the lower surfactant-rich phase. The top-phase is eliminated, and lysozyme was eluted and separated of the magnetic particles increasing temperature again. The purity (>80%) and yield (74%) of the lysozyme are then comparable to those where only the magnetic cation exchange was performed [64]. In this context, this integral approach results interesting if applied to PEGylated proteins since modified and native proteins may be separated from the reaction media in a first phase elimination to later elute each protein isomer, varying the process conditions. Another appropriate combination might be affinity ATPS and precipitation, in which selective recognition of PEGylated proteins

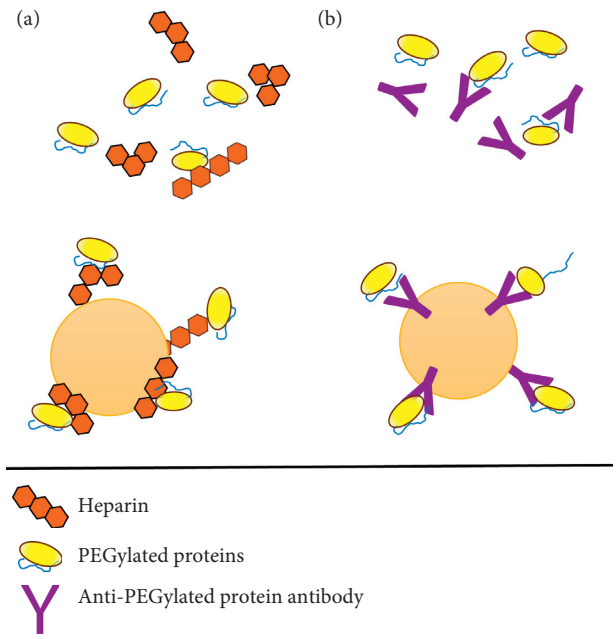

Figure 3: Improved affinity by immobilizing PEGylated protein ligands on multivalent nanoparticles.

with a macroligand would be partitioned to the upper phase in a PEG-salt or PEG-dextran system [25] and later performing the separation of this phase to have a precipitation induced by a mild change in the system.

As conclusion, trends point to the development of nonchromatographic affinity techniques and their integration in the recovery of proteins modified with PEG, including the use of multiple ligands or macroligands.

5. Guidelines in the Selection and Development of Affinity Purification Strategies for PEGylated Proteins

When a protein affinity purification method is needed and the experience in downstream processing is limited, a common query is how to choose the best strategy to do this. This same doubt is not foreign to PEGylated protein purification. Considering that the ligand and unit operation selections must be based firstly on getting a fast, economic, and practical purification process, one starting point to choose the best strategy is to know if the PEGylation procedure for a protein has already been reported and if it keeps part of the required biological activity. Although this can seem redundant, for novel PEGylated proteins, it constitutes a way of knowing if a joint PEGylation-separation process is feasible or if it should focus solely on its purification. If the PEGylation strategy and activity of the protein have been widely studied, the procedure will focus exclusively on purification. On the contrary, PEGylation and purification should be treated at the same time with the aim to achieve effectiveness in both processes, and this last might lead to the use of solid-phase PEGylation. This is recommended especially when the protein possesses in its binding site amino acids susceptible to alteration under a particular PEGylation chemistry. One alternative for overcoming this is engineered mutations, as long as the knowledge and costs allow it.

Following the line in which a PEGylation tactic has been preset, a second question is how much protein needs to be purified. The response steers to decide between a nonchromatographic or chromatographic technique since nonchromatographic operations are oriented to obtain large amounts of protein at low costs although resolution and purity may be somewhat compromised [65]. However, the decision on what technique should be used is closely related to how abundant and expensive is the ligand and if the ligand is commercially available. So, for costly and/or low-production ligands, AC is a suitable alternative, especially if the recovery of the ligand has not been addressed. Storage, sterilization feasibility, and stability are other factors regarding the ligand that can influence the decision [27]. In this point, other questions related to the ligand must be fulfilled (Figure 4). The first question in ligand selection involves having evidence of the existence of any ligands for the protein. It may be an antibody or even the target of its biological function. When the ligand is very expensive, unknown, scarce, or not isolated, one first trial is the use of pre-existing affinity chromatographic supports. This alternative can be cheap, rapidly developed, powerful, and functional if there is any evidence or suspected affinity interaction between the support and the target molecule. A clear example of this application is the purification of mono-PEGylated lysozyme with heparin chromatography which can be regarded as an example of novel applications of existing supports for protein purification [32]. Among the most common affinity supports that can be tried to purify proteins are Heparin Sepharose, Lectin Sepharose, Blue Sepharose, Gelatin Sepharose, Lysine Sepharose, Streptavidin Sepharose, Protein A Sepharose, and IMAC Sepharose.

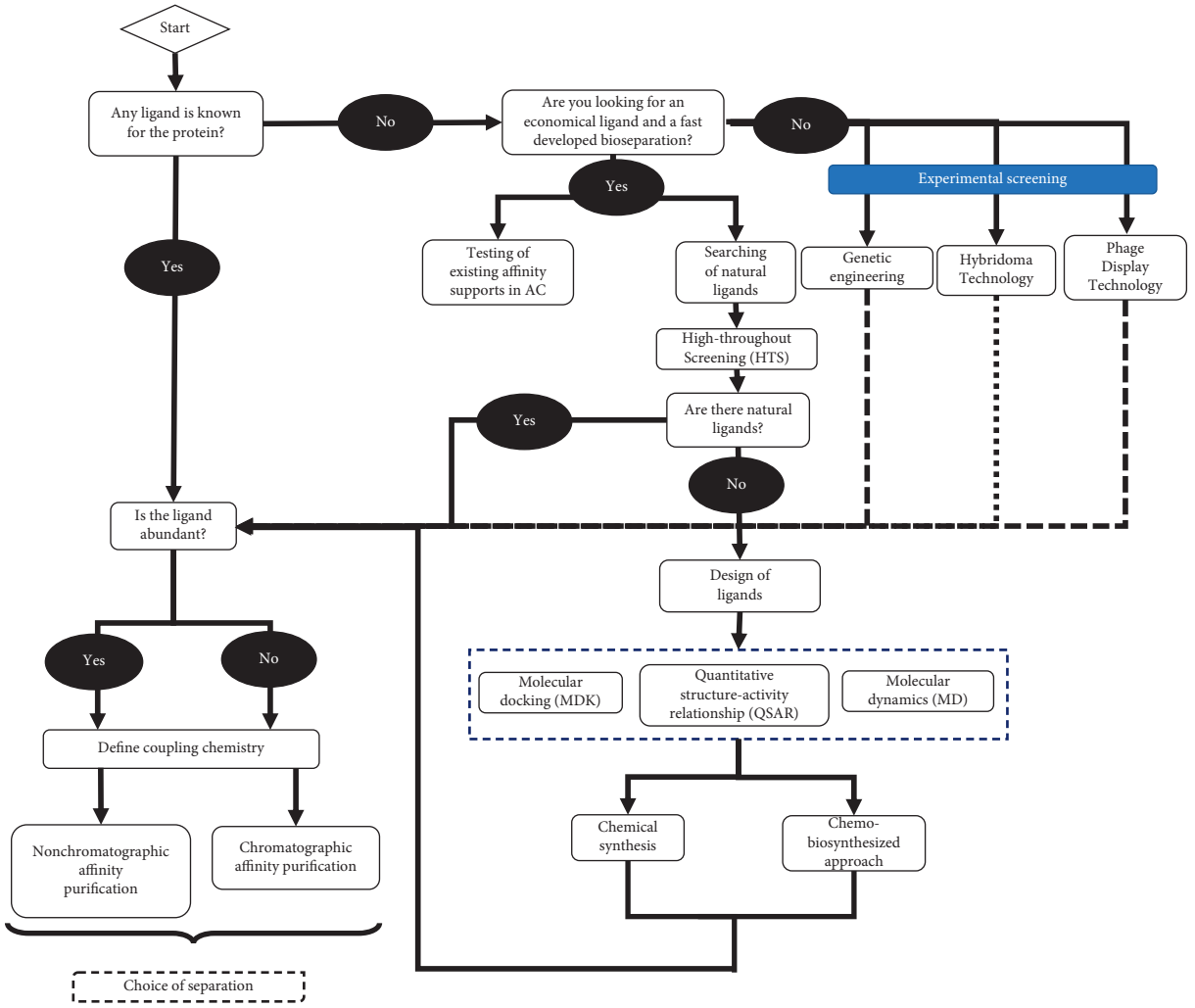

Figure 4: Ligand selection for an affinity-based bioseparation for PEGylated proteins.

If no separation in those pre-existing affinity chromatographic supports is detected, the next alternative is to localize a ligand. The identification of a potential ligand can be reached through two main strategies: searching for natural ligands and to design them.

In the first approach, traditional experimental searching involves genetic engineering, antibody production platforms, and high-throughput screening (HTS). On its part, antibody production can be done by exploiting the traditional method of the hybridoma technology, which consists in the creation of a hybrid cell combining a B cell of the spleen of an immunized animal with its antigen and a myeloma cell, with high reproduction of the new cell [66, 67]. However, one drawback of this option is time consumption. On the contrary, a nontested technology yet is phage display, cloning genes of Fab antibody regions in a vector, which transforms a bacterium using a bacteriophage [66, 68]. On their part, aptamers, which are oligonucleotides of ribonucleic acid (RNA) or single-strand deoxyribonucleic acid (ssDNA) with three-dimensional structure, also represent viable ligands with high thermal stability and low immunogenicity, capable to be bound with high specificity to proteins [69]. The aptamers have the advantage of being synthetized in great quantities with accuracy at large scale in less time and recognizing a wide spectrum of molecules or biomolecules in comparison with antibodies [69]. In fact, their implementation for the capture of proteins, specifically plasma-derived factors VII, H, and IX, in chromatography has already started [70]. Mutation of ligand gene sequences, alteration of the epitope, or affinity site in antibodies are another options. When the designated ligands are based on mimicking a natural binding, those are called biomimetic affinity ligands [25]; these may be created by chemical, enzymatic, or combined synthesis of their *posteriori* design and prediction. However, it is essential to have in mind the time investment, cost, and low yields that these synthesis methods may present depending on the nature availability and complexity of these compounds or raw materials.

On the contrary, high-throughput screening techniques (HTST) seem to be a safer and direct choice for screening ligands. This approach, emerged around the end of the 1990's, gained importance in drug discovery inside the pharmaceutical industry [71]. It is based on the assaying of a larger number of candidate compounds (10,000 or even

100,000) against specific targets. [72] Putative compounds are taken from existing libraries of natural molecules or biomolecules. Their benefits include fast testing, low cost, and high-quality data [71]. Some of these characteristics are relative because workstations and automated devices are expensive, and maintenance is mandatory.

As it can be appreciated in Figure 4, when natural ligands are not located and the tridimensional structure and sequence of the protein are known, mimetic ligands may be chemically synthetized, biosynthesized, or chemo-biosynthetized. The design of ligands implies the synthesis of a novel chemical or biochemical ligand (*in silico*), not previously known. Ligand design can be helped by computational tools as it is described as follows.

Ligand definition can be assisted by computer-aided screening (CAS), computer-aided drug design (CADD), [73] and/or high-throughput screening techniques (HTST). CAS or CADD tests several molecules or biomolecules as possible ligands with tools such as molecular docking (MDK), molecular dynamics (MD), and quantitative structure-activity relationship (QSAR). MDK is a method emerged in the 1980's, which attempts to find interactions between molecules [74] as putative ligands and predicts the binding affinity changing their orientation [75]. The used software for MDK is Auto Dock, Dock, Gold, V Life MDS, and Flex X. On its part, MD simulation is a predictive computational method which allows to understand the structure, folding, conformations, and behavior in biological systems of a specific biomolecule, involving iterative numerical calculations of forces that consider molecules as a set of atoms connected by strings (bounds) governed under classical laws of motion [76]. There are several free and commercial packages used for MD like GROMACS, GROMOS, AMBER, NAMD, CHARMM, COSMOS, and ORAC [77]. MD assists MDK with putative structures of the ligand or target and the estimation of the binding free energies. However, it is also important to mention the limitations when these two modelling tools are considered in ligand design. For example, the need of training and the long time that simulations can take (i.e., weeks or even months in some cases) but setting aside those aspects predicted binding constants are not always accurate since multiple factors (temperature, pH, and environment) can impact the quality of simulations and allosterism can occur in some ligand-target interactions [77]. QSAR has been more widely employed in medical chemistry, and it generates a model that describes the activity as a function of several descriptors of the molecule structure [78]. These descriptors can be constitutional (i.e., molecular weight, atoms number, and bond type), electrostatic, topological (number of bonds, valence electrons, and atom connectivity data), or geometrical [78, 79]. In all these computer-aided tools, experimental execution will be the best way to confirm the obtained results by simulation. Due to the strengths and weaknesses cited for each specific tool in the screening or ligand development, some authors agree to make an integration, for example, an initial CAS or CADD followed by other experimental options like HTS [73]. Reiterative selection processes are suggested too like the case of CAS/CADD-HTS-CAS/CADD processes. The success of these tools in ligand definition will depend heavily on having the right experience in the field as well as the resources for investment [27]. It should be mentioned that related results might be lengthy and costly as much as experimental searching. As mentioned previously, the synthesis or biosynthesis of these proposed ligands must go hand-in-hand with organic chemistry synthesis or biochemical synthesis.

In this same line, after the selection of the ligand (independently of its search or design), and in correlation with the protein abundance and requirements, the choice of the purification operation should be performed. As it has been said, when ligands and proteins are in high amounts, nonchromatographic affinity techniques are recommended. However, there is not yet a guide to select a specific operation between these, so the best option must be selected through experimentation by trial-and-error.

Another consideration is the immobilization method of the ligands when these require to be fixed to a support (i.e., resin, membrane, or particles). At first, the available chemical groups in the affinity ligand must be checked to perform the immobilization as well as to know the chemistry in the support or beads even if these have been previously activated for a particular function and application conditions. The omission of these considerations might result on a decrease in target binding, ligand degradation, or presence of unspecific interactions with contaminants. For PEGylated proteins, hydrophobic, or ionic groups could entail nonspecific interactions. Tentative analysis using docking algorithms can also predict these situations.

Immobilization methods can be classified basically into two branches: covalent and noncovalent methods. The first offers a chemical stable and durable bond between the support and the ligand avoiding leakage of this last during the normal operation. Covalent methods are performed between immobilized ligands with amine groups and supports having N`N-carbonyldiimidazole, cyanogen bromide, N-hydroxysuccinimide, or tresyl/tosyl chloride and between sulfhydryl groups with supports having divinylsulfone, epoxy, bromoacetyl, yodoacetyl, maleimide, and tosyl chloride groups [29, 80]. The associated drawbacks of these covalent immobilizations are improper orientation or steric hindrance because these are not site-directed. However, there are also covalent site-directed attachments, which increase the functionality of the ligands [81]. Inside this group, we can find metal-carrying supports (e.g., iminodiacetic or nitrilotriacetic acids) or attachment via protein bridges. In antibodies, the carbohydrate residues are oxidized with periodate and then bound to hydrazine or amine-activated supports, which might be the most efficient option of those described. However, care must be taken in doing this since overoxidizing promotes denaturing, and oligosaccharide moieties can result damaged in the purified ligands [82]. On their part, noncovalent immobilization tactics rely on a physical and temporal adsorption of the ligand with the

support, and the ligand can be retained under conditions of elution of the target. Modified avidin/streptavidin, protein A or G supports are used for this purpose. A disadvantage is that a large amount of ligand can be needed due to loss [80].

In brief, the guide proposed here for the operation selection of an affinity-based-strategy for the recovery and/or purification of PEG-modified proteins is founded in the previous knowledge of the protein properties, its PEGylation process, the availability of known ligands, and previously described immobilization methods. Also, multidisciplinary support (computational techniques, genetic engineering, and organic/biochemical synthesis) is suggested, but economic resources, experience, and time are critical factors in the decision about its use and involvement degree.

6. Conclusion

The recovery and purification of PEGylated proteins continue to be a challenge, despite the fact that several techniques have been studied and employed. Although affinity loss has been reported in many cases after PEGylation reactions, the change in this property of the modified proteins can be exploited for their purification. In this context, affinity-based strategies are envisioned as the future of the recovery and purification of PEG-modified proteins due to their selectivity and specificity. So far, affinity chromatography has been the unique affinity-based bioseparation tested for PEGylated proteins. Selection and abundance of the ligand and the type of technique will be key points in the successful implementation of affinity separations for PEG-protein conjugates. Until now, only two potential ligands have been identified for PEGylated proteins: anti-PEG antibodies and heparin. Therefore, the search or design of novel ligands is fundamental for the growth of this area. At this point, high-throughput screening and several computer-aided tools (i.e., molecular docking, molecular dynamics, and quantitative structure-activity relationship) could be very useful. In the same way, large-scale production of ligands can be promoted through phage display, aptamer production, and genetic engineering along with traditional chemical organic synthesis and biosynthesis. Nonchromatographic affinity techniques like precipitation, aqueous two-phase systems, and membrane and magnetic separations are expected to emerge in this context with integrated operations that will surely improve the yields of the desired PEGylated protein conjugate, saving resources and reducing processing times.

Conflicts of Interest

The authors declare that they have no conflicts of interest.

Acknowledgments

This work was supported by the Bioprocess Research Chair (0020209I13) and the FEMSA Biotechnology Center at Tecnologico de Monterrey.

References

[1] F. M. Veronese and A. Mero, "The impact of PEGylation on biological therapies," *BioDrugs*, vol. 22, no. 5, pp. 315–329, 2008.

[2] R. W. Payne, B. M. Murphy, and M. C. Manning, "Product development issues for PEGylated proteins," *Pharmaceutical Development and Technology*, vol. 16, no. 5, pp. 423–440, 2011.

[3] C. Ginn, H. Khalili, R. Lever, and S. Brocchini, "PEGylation and its impact on the design of new protein-based medicines," *Future Medicinal Chemistry*, vol. 6, no. 16, pp. 1829–1846, 2014.

[4] A. P. Chapman, "PEGylated antibodies and antibody fragments for improved therapy: a review," *Advanced Drug Delivery Reviews*, vol. 54, no. 4, pp. 531–545, 2002.

[5] X. Zhang, H. Wang, Z. Ma, and B. Wu, "Effects of pharmaceutical PEGylation on drug metabolism and its clinical concerns," *Expert Opinion on Drug Metabolism & Toxicology*, vol. 10, no. 12, pp. 1691–1702, 2014.

[6] Allied Market Research, "PEGylated protein therapeutics market by product type (colony stimulating factor, interferon, erythropoietin (EPO), recombinant factor VIII, monoclonal antibody, enzyme, and others) by application (cancer, Autoimmune disease, Hepatitis, Multiple Sclerosis, Hemophilia, Gastrointestinal disorder, and others) by sales channel (hospital pharmacy, online provider, and retail pharmacy)—global opportunity analysis and industry forecast, 2018-2025," 2018.

[7] P. Bailon and W. Berthold, "Polyethylene glycol-conjugated pharmaceutical proteins," *Pharmaceutical Science & Technology Today*, vol. 1, no. 8, pp. 352–356, 1998.

[8] M. J. Roberts, M. D. Bentley, and J. M. Harris, "Chemistry for peptide and protein PEGylation," *Advanced Drug Delivery Reviews*, vol. 64, pp. 116–127, 2012.

[9] G. Pasut and F. M. Veronese, "State of the art in PEGylation: the great versatility achieved after forty years of research," *Journal of Controlled Release*, vol. 161, no. 2, pp. 461–472, 2012.

[10] A. A. D'souza and R. Shegokar, "Polyethylene glycol (PEG): a versatile polymer for pharmaceutical applications," *Expert Opinion in Drug Delivery*, vol. 13, no. 9, pp. 461–472, 2016.

[11] F. M. Veronese and G. Pasut, "PEGylation, successful approach to drug delivery," *Drug Discovery Today*, vol. 10, no. 21, pp. 1451–1458, 2008.

[12] K. Mayolo-Deloisa, J. González-Valdez, D. Guajardo-Flores, O. Aguilar, J. Benavides, and M. Rito-Palomares, "Current advances in the non-chromatographic fractionation and characterization of PEGylated proteins," *Journal of Chemical Technology & Biotechnology*, vol. 86, no. 1, pp. 18–25, 2011.

[13] J. R. Molek and A. L. Zydney, "Ultrafiltration characteristics of pegylated proteins," *Biotechnology and Bioengineering*, vol. 95, no. 3, pp. 474–482, 2006.

[14] C. Delgado, F. Malik, B. Selisko, D. Fischer, and G. E. Francis, "Quantitative analysis of polyethylene glycol (PEG) in PEG-modified proteins/cytokines by aqueous two-phase systems," *Journal of Biochemical and Biophysical Methods*, vol. 29, no. 3-4, pp. 237–250, 1994.

[15] J. González-Valdez, J. L. F. Cueto, and M. Rito-Palomares, "Potential application of aqueous two-phase systems for the fractionation of RNase A and α-Lactalbumin from their PEGylated conjugates," *Journal of Chemical Technology & Biotechnology*, vol. 86, no. 1, pp. 26–33, 2011.

[16] M. Cisneros-Ruiz, K. Mayolo-Deloisa, M. Rito-Palomares, and T. M. Przybycien, "Separation of PEGylated variants of ribonuclease A and apo-α-lactalbumin via reversed phase

chromatography," *Journal of Chromatography A*, vol. 1360, pp. 309–316, 2014.

[17] S. Jevševar, M. Kunstelj, and V. G. Porekar, "PEGylation of therapeutic proteins," *Biotechnology Journal: Healthcare Nutrition Technology*, vol. 5, no. 1, pp. 113–128, 2010.

[18] S. Yamamoto, S. Fujii, N. Yoshimoto, and P. Akbarzadehlaleh, "Effects of protein conformational changes on separation performance in electrostatic interaction chromatography: unfolded proteins and PEGylated proteins," *Journal of Biotechnology*, vol. 132, no. 2, pp. 196–201, 2007.

[19] N. Yoshimoto and S. Yamamoto, "PEGylated protein separations: challenges and opportunities," *Biotechnology Journal*, vol. 7, no. 5, pp. 592-593, 2012.

[20] D. Pfister and M. Morbidelli, "Process for protein PEGylation," *Journal of Controlled Release*, vol. 180, pp. 134–149, 2014.

[21] J. M. Harris and R. B. Chess, "Effect of pegylation on pharmaceuticals," *Nature Reviews Drug Discovery*, vol. 2, no. 3, pp. 214–221, 2003.

[22] F. M. Veronese, P. Caliceti, O. Schiavon, and L. Sartore, "Preparation and properties of monomethoxypoly (ethylene glycol)-modified enzymes for therapeutic applications," in *Poly (Ethylene Glycol) Chemistry*, H. Milton H, Ed., Springer, New York, NY, USA, pp. 127–137, 1992.

[23] K. Park, "Ligand affinity: multivalency counterbalances PEGylation," *Journal of Controlled Release*, vol. 194, p. 351, 2014.

[24] N. Labrou and Y. D. Clonis, "The affinity technology in downstream processing," *Journal of Biotechnology*, vol. 36, no. 2, pp. 95–119, 1994.

[25] K. Mondal and M. N. Gupta, "The affinity concept in bioseparation: evolving paradigms and expanding range of applications," *Biomolecular Engineering*, vol. 23, no. 2-3, pp. 59–76, 2006.

[26] A. T. Hanke and M. Ottens, "Purifying biopharmaceuticals: knowledge-based chromatographic process development," *Trends in Biotechnology*, vol. 32, no. 4, pp. 210–220, 2014.

[27] M. Urh, D. Simpson, and K. Zhao, "Affinity chromatography: general methods," in *Methods in Enzymology 463 Guide to protein purification*, R. R. Burgess and M. P. Deutscher, Eds., vol. 463, pp. 417–438, Elsevier, Alpharetta, GA, USA, 2009.

[28] G. Fassina, "Affinity Chromatography," in *Encyclopedia of Life Sciences*, pp. 1–3, Nature Publishing Group, London, UK, 2001.

[29] D. S. Hage and P. F. Ruhn, "An introduction to affinity chromatography," in *Handbook of Affinity Chromatography*, D. S. Hage and J. Cazes, Eds., vol. 39, pp. 2–13, Taylor & Francis CRC Press, Boca Raton, FL, USA, 2005.

[30] G. Fassina, M. Ruvo, G. Palombo, A. Verdoliva, and M. Marino, "Novel ligands for the affinity-chromatographic purification of antibodies," *Journal of Biochemistry and Biophysical Methods*, vol. 49, no. 1-3, pp. 481–490, 2001.

[31] J. Fitzgerald, P. Leonard, E. Darcy, and R. O'Kennedy, "Immunoaffinity chromatography," in *Protein Chromatography: Methods and Protocols*, D. Walls and S. T. Loughran, Eds., pp. 35–59, Humana Press, Totowa, NJ, USA, 2011.

[32] L. A. Mejía-Manzano, M. E. Lienqueo, E. J. Escalante-Vázquez, M. Rito-Palomares, and J. A. Asenjo, "Optimized purification of mono-PEGylated lysozyme by heparin affinity chromatography using response surface methodology," *Journal of Chemical Technology and Biotechnology*, vol. 92, no. 10, pp. 2554–2562, 2017.

[33] L. A. Mejía-Manzano, G. Sandoval, M. E. Lienqueo, P. Moisset, M. Rito-Palomares, and J. A. Asenjo, "Simulation of mono-PEGylated lysozyme separation in heparin affinity chromatography using a general rate model," *Journal of Chemical Technology and Biotechnology*, vol. 93, no. 7, pp. 1980–1987, 2017.

[34] Z. Wen and B. Niemeyer, "Preparation and characterization of PEGyated concanavalin a for affinity chromatography with improved stability," *Journal of Chromatography B*, vol. 879, no. 20, pp. 1732–1740, 2011.

[35] J. González-Valdez, A. Yoshikawa, J. Weinberg, J. Benavides, M. Rito-Palomares, and T. M. Przybicien, "Toward improving selectivity in affinity chromatography with PEGylated affinity ligands: the performance of PEGylated protein A," *Biotechnology Progress*, vol. 30, no. 6, pp. 1364–1379, 2014.

[36] R. P. Garay and J. P. Labaune, "Immunogenicity of polyethylene glycol (PEG)," *The Open Conference Proceedings Journal*, vol. 2, no. 1, pp. 104–107, 2011.

[37] H. Schellekens, W. E. Hennink, and V. Brinks, "The immunogenicity of polyethylene glycol: facts and fiction," *Pharmaceutical Research*, vol. 30, no. 7, pp. 1729–1734, 2013.

[38] M. G. P. Saifer, L. D. Williams, M. A. Sobczyk, S. J. Michaels, and M. R. Sherman, "Selectivity of binding of PEGs and PEG-like oligomers to anti-PEG antibodies induced by methoxyPEG-proteins," *Molecular Immunology*, vol. 57, no. 2, pp. 236–246, 2014.

[39] P. Zhang, F. Sun, S. Liu, and S. Jiang, "Anti-PEG antibodies in the clinic: current issues and beyond PEGylation," *Journal of Controlled Release*, vol. 244, pp. 184–193, 2016.

[40] Y. Xu, J. T. Mehl, R. Bakhtiar, and E. J. Woolf, "Immunoaffinity purification using anti-PEG antibody followed by two-dimensional liquid chromatography/tandem mass spectrometry for the quantification of a PEGylated therapeutic peptide in human plasma," *Analytical Chemistry*, vol. 82, no. 16, pp. 6877–6886, 2010.

[41] C. J. Fee and J. M. Van Alstine, "PEG-proteins: reaction engineering and separation issues," *Chemical Engineering Science*, vol. 61, no. 3, pp. 924–939, 2006.

[42] J. Wang, Y. Wang, T. Hu et al., "An oriented adsorption strategy for efficient solid phase PEGylation of recombinant staphylokinase by immobilized metal-ion affinity chromatography," *Process Biochemistry*, vol. 47, no. 1, pp. 106–112, 2012.

[43] E. T. Baran, N. Özer, and V. Hasirci, "Solid-phase enzyme modification via affinity chromatography," *Journal of Chromatography B*, vol. 794, no. 2, pp. 311–322, 2003.

[44] Z. Huang, C. Ye, Z. Liu et al., "Solid-phase N-terminus PEGylation of recombinant human fibroblast growth factor 2 on heparin-sepharose column," *Bioconjugate Chemistry*, vol. 23, no. 4, pp. 740–750, 2012.

[45] Z. Huang, G. Zhu, C. Sun et al., "A novel solid-phase site-specific PEGylation enhances the in vitro and in vivo biostability of recombinant human keratinocyte growth factor 1," *PloS One*, vol. 7, no. 5, Article ID e36423, 2012.

[46] X. Suo, C. Zheng, P. Yu, X. Lu, G. Ma, and Z. Su, "Solid phase pegylation of hemoglobin," *Artificial Cells, Blood Substitutes, and Biotechnology*, vol. 37, no. 4, pp. 147–155, 2009.

[47] B. K. Lee, J. S. Kwon, H. J. Kim, S. Yamamoto, and E. K. Lee, "Solid-phase PEGylation of recombinant interferon α-2a for site-specific modification: process performance, characterization, andin VitroBioactivity," *Bioconjugate Chemistry*, vol. 18, no. 6, pp. 1728–1734, 2007.

[48] S. Raja, V. R. Murty, V. Thivaharan, V. Rajasekar, and V. Ramesh, "Aqueous two phase systems for the recovery of biomolecules–a review," *Science Technology*, vol. 1, no. 1, pp. 7–16, 2011.

[49] A. M. Goja, H. Yang, M. Cui, and C. Li, "Aqueous two-phase extraction advances for bioseparation," *Journal of Bioprocess Biotechnology*, vol. 4, no. 1, pp. 1–8, 2019.

[50] A. L. Grilo, M. Raquel Aires-Barros, and A. M. Azevedo, "Partitioning in aqueous two-phase systems: fundamentals, applications and trends," *Separation & Purification Reviews*, vol. 45, no. 1, pp. 68–80, 2016.

[51] L. J. Karr, S. G. Shafer, J. M. Harris, J. M. Van Alstine, and R. S. Snyder, "Immuno-affinity partition of cells in aqueous polymer two-phase systems," *Journal of Chromatography A*, vol. 354, pp. 269–282, 1986.

[52] F. Ruiz-Ruiz, J. Benavides, O. Aguilar, and M. Rito-Palomares, "Aqueous two-phase affinity partitioning systems: current applications and trends," *Journal of Chromatography A*, vol. 1244, pp. 1–13, 2012.

[53] J. González-Valdez, M. Rito-Palomares, and J. Benavides, "Effects of chemical modifications in the partition behavior of proteins in aqueous two-phase systems: a case study with RNase A," *Biotechnology Progress*, vol. 29, no. 2, pp. 378–385, 2013.

[54] A. M. Azevedo, P. A. J. Rosa, I. F. Ferreira, and M. R. Aires-Barros, "Chromatography-free recovery of biopharmaceuticals through aqueous two-phase processing," *Trends in Biotechnology*, vol. 27, no. 4, pp. 240–247, 2009.

[55] P. A. J. Rosa, A. M. Azevedo, I. F. Ferreira et al., "Affinity partitioning of human antibodies in aqueous two-phase systems," *Journal of Chromatography A*, vol. 1162, no. 1, pp. 103–113, 2007.

[56] R. Hatti-Kaul and B. Mattiason, *Transgenic Plants: A Production System for Industrial and Pharmaceutical Proteins*, M. Owen and J. Pen, Eds., John Wiley & Sons, England, UK, 1996.

[57] H. Zou, Q. Luo, and D. Zhou, "Affinity membrane chromatography for the analysis and purification of proteins," *Journal of Biochemical and Biophysical Methods*, vol. 49, no. 1-3, pp. 199–240, 2001.

[58] F. Hilbrig and R. Freitag, "Protein purification by affinity precipitation," *Journal of Chromatography B*, vol. 790, no. 1-2, pp. 79–90, 2003.

[59] F. Hilbrig, G. Stocker, J.-M. Schläppi, H. Kocher, and R. Freitag, "Utilization of group specific ligands in the downstream processing of proteins by affinity precipitation," *Food and Bioproducts Processing*, vol. 84, no. 1, pp. 28–36, 2006.

[60] I. Safarik and M. Safarikova, "Magnetic techniques for the isolation and purification of proteins and peptides," *Biomagnetic Research and Technology*, vol. 2, no. 7, pp. 1–17, 2004.

[61] L. Borlido, A. M. Azevedo, A. C. A. Roque, and M. R. Aires-Barros, "Magnetic separations in biotechnology," *Biotechnology Advances*, vol. 31, no. 8, pp. 1374–1385, 2013.

[62] R. Hennig, K. Pollinger, J. Tessmar, and A. Goepferich, "Multivalent targeting of AT1 receptors with angiotensin II-functionalized nanoparticles," *Journal of Drug Targeting*, vol. 23, no. 7-8, pp. 681–689, 2015.

[63] R. N. D'Souza, A. M. Azevedo, M. R. Aires Barros et al., "Emerging technologies for the integration and intensification of downstream bioprocesses," *Pharmaceutical Bioprocessing*, vol. 1, no. 5, pp. 423–440, 2013.

[64] J. S. Becker, O. R. T. Thomas, and M. Franzreb, "Protein separation with magnetic adsorbents in micellar aqueous two-phase systems," *Separation and Purification Technology*, vol. 65, no. 1, pp. 46–53, 2009.

[65] M. N. Gupta, "Purification of natural occurring biomaterials," in *Natural-Based Polymers for Biomedical Applications*, R. L. Reis, N. Neves, J. F. Mano, M. E. Gomes, A. P. Marques, and H. S. Azevedo, Eds., Woodhead Publishing in Materials, Cambridge, England, 2008.

[66] L. S. Carvalho, O. B. da Silva, G. C. de Almeida, J. D. de Oliveira, N. S. Parachin, and T. S. Carmo, "Production Processes for Monoclonal Antibodies," in *Fermentation Processes*, A. Faustino Jozala, Ed., InTechOpen, Rijeka, Coratia, 2017.

[67] C. Zhang, *Antibody Methods and Protocols*, G. Proetzel and H. Ebersbach, Eds., pp. 117–135, Humana Press, Totowa, NJ, USA, 2012.

[68] G. L. Verdine, T. N. Grossmann, R. E. Moellering, T. H. J. Yeh, Y. R. Y. Liang, and Y. Oak, "Bifunctional stapled polypeptides and uses thereof," U.S. Patent and Trademark Office, Washington, DC, USA, U.S. Patent No. 9,163,330, 2015.

[69] K.-M. Song, S. Lee, and C. Ban, "Aptamers and their biological applications," *Sensors*, vol. 12, no. 1, pp. 612–631, 2012.

[70] C. Forier, E. Boschetti, M. Ouhammouch et al., "DNA aptamer affinity ligands for highly selective purification of human plasma-related proteins from multiple sources," *Journal Of Chromatography A*, vol. 1489, pp. 39–50, 2017.

[71] R. Macarron, M. N. Banks, D. Bojanic et al., "Impact of high-throughput screening in biomedical research," *Natural Review Drug Discovery*, vol. 10, pp. 188–195, 2011.

[72] P. Szymański, M. Markowicz, and E. Mikiciuk-Olasik, "Adaptation of high-throughput screening in drug discovery—toxicological screening tests," *International Journal of Molecular Science*, vol. 13, no. 1, pp. 427–452, 2011.

[73] S. J. Y. Macalino, V. Gosu, S. Hong, and S. Choi, "Role of computer-aided drug design in modern drug discovery," *Archives of Pharmacal Research*, vol. 38, no. 9, pp. 1686–1701, 2015.

[74] Y. Z. Chen and D. G. Zhi, "Ligand-protein inverse docking and its potential use in the computer search of protein targets of a small molecule," *Proteins: Structure, Function, and Genetics*, vol. 43, no. 2, pp. 217–226, 2001.

[75] B. Mukesh and K. Rakesh, "Molecular docking: a review," *International Journal of Ayurveda Research*, vol. 2, no. 6, pp. 1746–1751, 2011.

[76] S. A. Adcock and J. A. McCammon, "Molecular dynamics: survey of methods for simulating the activity of proteins," *Chemical Reviews*, vol. 106, no. 5, pp. 1589–1615, 2006.

[77] D. Vlachakis, E. Bencurova, N. Papangelopoulos, and S. Kossida, "Current state-of-the-art molecular dynamics methods and applications," *Advances in Protein Chemistry and Structural Biology*, vol. 94, pp. 269–313, 2014.

[78] A. Dudek, T. Arodz, and J. Galvez, "Computational methods in developing quantitative structure-activity relationships (QSAR): a review," *Combinatorial Chemistry & High Throughput Screening*, vol. 9, no. 3, pp. 213–228, 2006.

[79] A. Cherkasov, E. N. Muratov, D. Fourches et al., "QSAR modeling: where have you been? Where are you going to?" *Journal of Medicinal Chemistry*, vol. 57, no. 12, pp. 4977–5010, 2014.

[80] A. C. Moser and D. S. Hage, "Immunoaffinity chromatography: an introduction to applications and recent developments," *Bioanalysis*, vol. 2, no. 4, pp. 769–790, 2010.

[81] M. Nisnevitch and M. A. Firer, "The solid phase in affinity chromatography: strategies for antibody attachment," *Journal of Biochemical and Biophysical Methods*, vol. 49, no. 1-3, pp. 467–480, 2001.

[82] A. Makaraviciute and A. Ramanaviciene, "Site-directed antibody immobilization techniques for immunosensors," *Biosensors and Bioelectronics*, vol. 50, pp. 460–471, 2013.

Hindawi
Advances in Polymer Technology
Volume 2019, Article ID 5067028, 10 pages
https://doi.org/10.1155/2019/5067028

Research Article

Development and Characterization of PEGylated Chromatographic Monoliths as a Novel Platform for the Separation of PEGylated RNase A Isomers

Calef Sánchez-Trasviña,[1] **Marco Rito-Palomares**,[2] **and José González-Valdez**[1]

[1]*Tecnologico de Monterrey, School of Engineering and Science, Av. Eugenio Garza Sada 2501 Sur, Monterrey, NL 64849, Mexico*
[2]*Tecnologico de Monterrey, Escuela de Medicina y Ciencias de la Salud, Av. Morones Prieto 3000 Pte, Monterrey, NL 64710, Mexico*

Correspondence should be addressed to José González-Valdez; jose_gonzalez@tec.mx

Received 7 June 2019; Accepted 6 August 2019; Published 12 December 2019

Guest Editor: Marco Lopez

PEGylated or polyethylene glycol-modified proteins have been used as therapeutic agents in different diseases. However, the major drawback in their procurement is the purification process to separate unreacted proteins and the PEGylated species. Several efforts have been done to separate PEGylation reactions by chromatography using different stationary phases and modified supports. In this context, this study presents the use of chromatographic monoliths modified with polyethylene glycol (PEG) to separate PEGylated Ribonuclease A (RNase A). To do this, Convective Interaction Media (CIM) Ethylenediamine (EDA) monolithic disks were PEGylated using three PEG molecular weights (1, 10, and 20 kDa). The PEGylated monoliths were used to separate PEGylated RNase A modified, as well, with three PEG molecular weights (5, 20, and 40 kDa) by hydrophobic interaction chromatography. Performance results showed that Bovine Serum Albumin (BSA) can bind to PEGylated monoliths and the amount of bound BSA increases when ammonium sulfate concentration and flow rate increase. Furthermore, when PEGylated RNase A was loaded into the PEGylated monoliths, PEG–PEG interactions predominated in the separation of the different PEGylated species (i.e., mono and di-PEGylated). It was also observed that the molecular weight of grafted PEG chains to the monolith impacts strongly in the operation resolution. Interestingly, it was possible to separate, for the first time, isomers of 40 kDa PEGylated RNase A by hydrophobic interaction chromatography. This technology, based on PEGylated monoliths, represents a new methodology to efficiently separate proteins and PEGylated proteins. Besides, it could be used to separate other PEGylated molecules of biopharmaceutical or biotechnological interest.

1. Introduction

During the last decades, several proteins have been used to treat different diseases where their high biological activity and high specificity have been demonstrated. However, some of these kinds of proteins have unfavorable properties such as low solubility, instability, and rapid clearance by the human body [1]. In this context, PEGylation has been one of the most successful strategies to overcome these drawbacks [2]. PEGylation is the covalent attachment of an activated polyethylene glycol (PEG) molecule to a protein [3]. This modification forms a steric barrier against proteolytic enzymes or antibodies, increases thermal stability, reduces immune response, and also increases the molecular size of the protein that enhances the circulation and clearance times in the human body [4, 5]. The first commercial PEGylated protein, for human consumption, was launched 30 years ago and since then several PEGylated drugs have been approved by the FDA [2].

In a common PEGylation reaction, several conjugates with different PEG chains attached to them are obtained. With this, the reaction mixture contains unreacted protein, mono-PEGylated and di-PEGylated proteins (sometimes even poly-PEGylated conjugates), and unreacted PEG [4, 6]. However, the PEGylated species have different effectiveness and activity levels and, the desired conjugate is usually the mono-PEGylated protein, which presents a higher biological activity and the best pharmacokinetic properties. The di-PEGylated protein or those conjugates with higher PEGylation degrees are less biologically active mainly because the active site becomes hindered by the PEG chains [6, 7]. For this reason, it is highly desirable to separate the mono-PEGylated protein from the other species. Nonetheless, its separation is a hard issue and an interesting

engineering problem because the physical and chemical properties are similar to those of the undesired products. In this context, chromatographic methods have represented the most attractive and effective alternative for their separation since it can exploit the different properties altered during the PEGylation reaction [4].

The chromatographic methods that have been used to separate mono-PEGylated proteins are hydrophobic interaction (HIC), anion exchange (AEX), size exclusion (SEC), and cation exchange (CEX) chromatographies [4, 6, 8]. Our research group has been working extensively in the separation of PEGylated proteins. In 2009 Cisneros-Ruiz et al. [9] separated PEGylated from unPEGylated Ribonuclease A (RNase A) using activated CH sepharose 4B media; in 2014 Hernández–Martínez and Aguilar [6] used PEG-modified Sepharose 6B supports with 550, 2000, and 5000 g mol^{-1} PEGs to separate the same PEGylated enzyme finding that the PEG–PEG interactions between the PEGylated support and the PEGylated proteins promoted their separation; in 2016 Mayolo-Deloisa et al. [4] analyzed the separation of PEGylated RNase A, β-lactoglobulin, and lysozyme by HIC between conventional (toyopearl butyl 650C and butyl sepharose) and monolithic (CIM C4 A) supports, they found that monolithic supports are a suitable alternative to traditional chromatographic media for the separation of PEGylated proteins.

The last two mentioned works present a guideline for a new idea: to combine the advantages of a chromatographic PEGylated support with the features of a monolithic one: PEGylated monoliths. Chromatographic monoliths, considered 4th generation chromatographic materials, consist of a single piece of highly open porous material. Monoliths can be used in all chromatographic modes. This kind of chromatographic supports can be operated at high convective flow rates since they possess small micropores and mesopores that allow low backpressures at high eluent flow rates [10]. These advantages have been used to purify oligonucleotides, proteins, PEGylated proteins, and other biotechnological products [11]. Another crucial advantage of monoliths is their tunable chemical, physical, and biological properties since they can present different chemical groups that can be functionalized with an extensive range of molecules to create supports with novel ligands [12]. In their work, Almedia et al. [13] modified monoliths with two ligands (lysine and cadaverine) for the recuperation of minicircle DNA. In this work, monoliths with ethylenediamine (EDA) groups were PEGylated using different PEG molecular weights. The PEGylated monoliths were used to separate PEGylated RNase A, a therapeutic protein with anticancer properties [14]. With this, it is possible to establish the basis of a new efficient platform to separate different PEGylated proteins for multiple applications.

2. Materials and Methods

2.1. Materials. Ribonuclease A, bovine serum albumin (BSA), sodium cyanoborohydride, hydrochloride acid, and Tris(hydroxymethyl)-aminomethane were bought from Sigma-Aldrich (St. Louis, MO, USA). Ammonium sulfate, dibasic potassium phosphate (K_2HPO_4), and monobasic potassium phosphate (KH_2PO_4) were purchased from J. T. Baker (Center Valley, PA, USA). Methoxy poly(ethylene glycol) propionaldehyde of nominal molecular masses of 1.0, 10.0, and 20.0 kDa came from JenKem Technologies (Allen, TX). CIM EDA disk monoliths were purchased from BIA Separations (Ajdovščina, Slovenia). Methanol of HPLC grade was purchased from Honeywell Burdick and Jackson (Morris Plains, NJ, USA). All other chemicals used were all at least of analytical grade.

2.2. Chromatographic Monolith PEGylation. CIM EDA disks (column volume, CV 0.34 mL) were PEGylated using three PEG molecular weights (1.0, 10.0, and 20.0 kDa) through reductive amination. To modify the monoliths, a syringe pump (Fusion 200, Chemyx Inc.) system was employed. The monoliths were washed with 10.0 mL of MilliQ (MQ) water at 1.0 mL/min, then equilibrated with 5.0 mL of a methanol solution at 10.0%, 20.0%, 50.0%, 75.0%, and 100.0% v/v at pH 6.0 using the same flow rate. Afterwards, 20.0 mL of methanol 100.0% v/v at pH 6.0 with 250.0 mM sodium cyanoborohydride and methoxy poly(ethylene glycol) propionaldehyde (mPEG) using a molar ratio 5 : 1 (amine : aldehyde active sites) [15] were passed through the disk at 0.1 mL/min during 24 hours. The monoliths were then washed with 5.0 mL of methanol pH 6.0 solutions at 100.0%, 75.0%, 50.0%, 20.0%, and 10.0 % v/v, 5.0 mL of water and 5.0 mL of ethanol 20.0% v/v at 1.0 mL/min consecutively. The experiments were carried out at room temperature, and the PEGylated monoliths were stored at 4°C until their use.

2.3. Monolith PEGylation Yield Calculation. The yield (or extent) of monolith PEGylation was determined by measuring free amine groups on the support using the same syringe pump system as mentioned before. Free amine groups were quantified using the method described by Noel et al., adapted to monoliths [16]. Briefly, the PEGylated monoliths were washed with 5.0 mL of MQ water and conditioned with 5.0 mL of MQ water at pH 3.0 at 1.0 mL/min. After this, 5.0 mL of a 50.0 mM orange II solution prepared with MQ water at pH 3.0 was pumped through the monoliths at 0.16 mL/min submerged in a water bath at 40°C. Then, the modified monoliths were air-dried. The unbound orange II molecules were removed, 25.0 mL of MQ water at pH 3.0 were pumped using a 1.0 mL/min flowrate. The bonded molecules were eluted using 90.0 mL of MQ water at pH 12.0 at 2.0 mL/min, collecting the fraction volume. The PEGylated monoliths were washed with 5.0 mL of MQ water and with an ethanol solution at 20.0% v/v. The pH of the collected volume was adjusted by the addition of 250.0 μL of 1.0 M HCl and the absorbance at 484 nm was measured using a microplate spectrophotometer (Biotek, VT, USA). The orange II concentration was determined with a calibration curve previously prepared (ε = 22.19 mM^{-1} cm^{-1}). The molar modification percentage was calculated according to the following equation:

$$\%\text{Modification} = \frac{\text{Total amino ligands } (\mu\text{mol}) - \text{Free amino ligands } (\mu\text{mol})}{\text{Total amino ligands } (\mu\text{mol})} * 100. \quad (1)$$

2.4. Adsorption Experiments. Because of the nature of the monolithic supports, the adsorption experiments on the PEGylated monoliths were performed only in dynamic mode. To do this, BSA was used as a protein model as used and preferred in similar experiments reported elsewhere [6, 17]. The breakthrough curves were obtained connecting the PEGylated monoliths to an Äkta Avant chromatography system (GE Healthcare, Uppsala, Sweden) and equilibrated with buffer B composed by 20.0 mM Tris–HCl pH 8.2 with 1.5 or 2.0 M of ammonium sulfate (AS). Protein solutions at different concentrations (1.0, 2.0, and 3.0 mg BSA/mL prepared en buffer B with 1.5 or 2.0 M AS) were loaded using a 50.0 mL superloop (GE Healthcare, Uppsala, Sweden) until the monoliths were saturated. The protein bonded was eluted with 20.0 mM Tris–HCl pH 8.2 buffer. The dynamic binding capacity (DBC) was obtained from the breakthrough curves for each PEGylated monolith as the amount of protein bonded per column volume when the outlet protein concentration reached 10% of the feed protein concentration. The 10% breakthrough ($DBC_{10\%}$) was calculated using the following equation:

$$DBC_{10\%} = \frac{1}{V_C}\int_0^{v_{10}} (C_F - C_{out})dv, \quad (2)$$

where V_C is the column volume in mL, V_{10} is the volume in mL applied at 10% breakthrough, C_F is the feed protein concentration in mg/mL and C_{out} is the outlet protein concentration in mg/mL. All experiments were carried out by triplicate and, the presented values correspond to the average of these results with their corresponding standard errors.

2.5. PEGylated RNase A Preparation. The PEGylation reactions were made according to the methodology reported by Mayolo-Deloisa et al. [4]. Briefly, 5.5 mL of an RNase A solution at a concentration of 3.0 mg/mL in a 100.0 mM sodium phosphate buffer at pH 5.1 + 100.0 mM of $NaBH_3CN$ were added to a vial containing 82.5 mg of mPEG with molecular weights of 5.0, 20.0, and 40.0 kDa. The reaction mixtures were stirred for 17 hours at 4°C, stopped by freezing at −20°C, and stored at this condition until their use.

2.6. Purification of PEGylated RNase A Conjugates by SEC. To obtain the PEGylated protein standards, the previously prepared PEGylation reactions were separated by SEC using an Äkta Prime Plus chromatography system (GE Healthcare, Uppsala, Sweden) equipped with a 5 mL injection loop, and an XK 2670 column packed with Superose 12 (70.0 × 2.6 cm, CV 320.0 mL). The mobile phase, a 10.0 mM sodium phosphate buffer at pH 7.2 + 150.0 mM potassium chloride was used to perform the isocratic elution at 1.0 mL/min. The fractions that presented absorbance at 280 nm were collected and concentrated using an Amicon chamber with a Diaflo ultrafiltration membrane of 3.0 kDa (Amicon Inc, MA, USA). The identity of each of the PEGylated and unreacted species has been previously confirmed and reported. Finally, the PEGylated protein was lyophilized and stored at −4°C [6]. These lyophilized PEGylated proteins were used as standards to carry out separation studies and peak identification in the PEGylated monoliths assays.

2.7. Separation of PEGylated RNase A through PEGylated Monoliths. The PEGylated monoliths were connected to an Äkta Avant System, equipped with a 0.1 mL injection loop. The experiments were performed at room temperature, using a flow rate equal to 1.0 mL/min. Buffer A, composed of 20.0 mM Tris–HCl pH 8.2 and phase B formed by phase A with 3.0 M of AS (due to low hydrophobicity of RNase A) were used in hydrophobic interaction mode.

The chromatographic runs were done using the following program: equilibration with phase B (10.0 CVs), injection (0.1 mL of PEGylation reaction without dilution), washing with phase B (3.0 CVs) and then immediately a step gradient was employed, 50% phase B (20.0 CVs), 20% phase B (17.5 CVs) and 0.0% phase B (20.0 CVs). The column eluent was monitored at 215 nm and also conductivity was measured throughout each run. All experiments were carried out by triplicate under the same conditions to allow performance comparison.

2.8. SDS–PAGE Analysis. As it will be mentioned later, two partially resolved peaks were observed for the 40.0 kDa PEGylated RNase A purification with the 20.0 kDa PEGylated monolith. To assess their identity, sodium dodecyl sulfate-polyacrylamide gel electrophoresis (SDS–PAGE) was performed according to the method reported by Mejia-Manzano et al. [18] using a 12.0% (w/v) Mini-PROTEAN precast gel (BIO-RAD, CA, USA). The desalted fractions containing the obtained peaks were mixed with 6x loading buffer and heated for 10 min at 99°C. The gel was silver-stained to detect proteins and a barium–iodine complex was used to visualize mPEG as it has been reported elsewhere [18].

2.9. A Combination of PEGylated Monoliths to Improve Separation. To improve the separation of PEGylated RNase A, two and three monoliths were placed consecutively into the Äkta Avant System in different orders. The use of consecutive monoliths is possible since the housing provided by BIA Separations can hold up to three monolithic disks. The PEGylated monolith configurations tried were: 10-20, 20-10, 1-10-20, and 20-10-1 kDa. The runs were performed using a flow rate of 2.0 mL/min and, the chromatographic program was the same as the previously described.

3. Results and Discussion

3.1. PEGylation Yield of Modified Monoliths. The separation and purification of PEGylated proteins has been a concern in different production schemes. In this work, monolithic disks were PEGylated through reductive amination to separate the different PEGylated RNase A species obtained after its conjugation reaction. Since EDA monoliths have primary amines and mPEG is activated with aldehyde groups, it is possible to graft the polymeric chains to the support using sodium cyanoborohydride as a reducing agent and methanol as protic solvent [19]. Besides, PEG is well soluble in methanol, even more than in water [20] and the solution viscosity is negligible at the PEG concentration used. The effectiveness of the PEGylation reaction on the monoliths for each PEG

Table 1: Molar modification percentage of EDA disk monoliths with PEG through reductive amination and dynamic binding capacity of the PEGylated monoliths.

PEG size (kDa)	Monolith molar modification (%)	Flow rate (mL/min)	$DBC_{10\%}$ (mg BSA/mL resin)			
			1		2	
			Ammonium sulfate (M)			
		BSA (mg/mL)	1.5	2	1.5	2
1	39.76	1	1.13 ± 0.05	2.67 ± 0.03	1.72 ± 0.05	3.21 ± 0.03
		2	1.68 ± 0.03	4.12 ± 0.14	2.71 ± 0.18	5.08 ± 0.05
		3	2.75 ± 0.02	5.09 ± 0.15	3.51 ± 0.18	6.85 ± 0.21
10	62.18	1	0.80 ± 0.02	2.72 ± 0.01	1.19 ± 0.04	2.92 ± 0.03
		2	1.33 ± 0.06	3.89 ± 0.04	1.92 ± 0.08	4.52 ± 0.04
		3	1.56 ± 0.03	5.07 ± 0.05	2.54 ± 0.07	5.75 ± 0.03
20	52.24	1	0.93 ± 0.01	3.18 ± 0.02	1.10 ± 0.02	3.02 ± 0.13
		2	1.90 ± 0.01	5.16 ± 0.01	2.20 ± 0.01	5.27 ± 0.03
		3	2.89 ± 0.05	6.26 ± 0.02	3.08 ± 0.19	6.88 ± 0.09

Data of $DBC_{10\%}$ presented represents the mean of three runs and their standard error.

molecular weight was determined indirectly by measuring the amount of unreacted primary amines using the orange II dye. This dye has the advantage to attach to primary amines via electrostatic charges under acidic conditions and can be released under alkaline conditions [16]. Table 1 shows the molar modification percentages of the PEGylated monoliths with different PEG sizes under the same experimental conditions. The amount of PEG molecules bound to the monoliths presents a maximum when using mPEG of 10.0 kDa and later decreases. This behavior shows the influence of PEG molecular weight in its linkage capability with the monolithic surface. At low molecular weights of mPEG (i.e., 1.0 kDa), the interactions between PEG chains and the amine groups on the monolithic surface are lower than those observed with the 10.0 kDa mPEG. On counterpart, at a high molecular weight of mPEG (i.e., 20.0 kDa), the polymeric chains attached to the support can probably change their structure to mushroom conformation [21] allowing steric effects and PEG–PEG interactions to hinder the contact between amine groups and free PEG chains thus avoiding the formation of new bonds between the polymer and the monolith. In this situation, the PEG–PEG interactions between the 20 kDa mPEG chains are more frequent due to its higher structural flexibility, allowing different spatial configurations that enhance the interactions between them [6]. Interestingly, the modification yield behavior obtained in this work differs from the data reported by Hernández–Martinez and Aguilar [6], where conclusions indicate that at higher PEG molecular weights, the modification percentage decreases on traditional resin supports. This different behavior could be associated with the different support structures. The high porous structure of monoliths allows better interactions between the mobile and stationary phases. Therefore, even using larger mPEG molecules (e.g., 10 kDa), the modification yield is not compromised. Lastly, since the modification percentage of PEGylated monoliths is molar, which means that the 20.0 kDa PEG chain has 20 times more glycol groups than the 1.0 kDa PEG chain, a difference in its chromatographic behavior is expected.

3.2. Adsorption Capacity of PEGylated Monoliths. A relevant parameter to determinate the performance of columns is their dynamic binding capacity (DBC). In this work, the DBC in HIC mode for each PEGylated monolith was determined using BSA as model protein under different operative conditions: flow rate, salt concentration, and feed protein concentration. Since the EDA monolithic disk is a weak anionic support [8], it was not possible to use it as a control in saturation curve experiments under the same conditions. The breakthrough curves, which show the rise of protein concentration in the effluent with time until this value reaches the same concentration of the feed [22], are presented in Figure 1. As seen, breakthrough curves present the same shape independently of the mPEG molecular weight attached to the monolith, this indicates that the protein adsorption process is the same in all three cases. However, at a high flow rate (i.e., 2.0 mL/min), the amount of BSA adsorbed by the PEGylated monoliths increases. This could be related to the transfer mechanism of the monolith: convective mass transfer. This behavior is opposite to that reported by Hernández–Martínez and Aguilar [6] since they used PEGylated Sepharose 6B, a porous bead material with a diffusion mass transfer.

On the other hand, when a 2.0 M concentration of AS was used, the PEGylated monoliths took more time to saturate than at the 1.5 M concentration, which means that the modified supports adsorb more BSA at higher AS concentrations. This behavior is observed because, at a high AS concentration, the hydrophobic regions of proteins become more exposed and promote more interactions with the grafted PEG chains in the monolith. When 1.5 M AS concentration is used, those hydrophobic regions are hindered even at high feed protein concentration, therefore a plateau-like curve is reached in a shorter time. Lastly, the polymer chain molecular weight attached to the monolith influences more the saturation times at 2.0 M SA. The hydrophobicity of PEG molecules increases with its molecular weight [23]. Therefore, at higher molecular weights, the hydrophobic interactions between the protein and the PEGylated monolith increase resulting in more proteins adsorbed into the support.

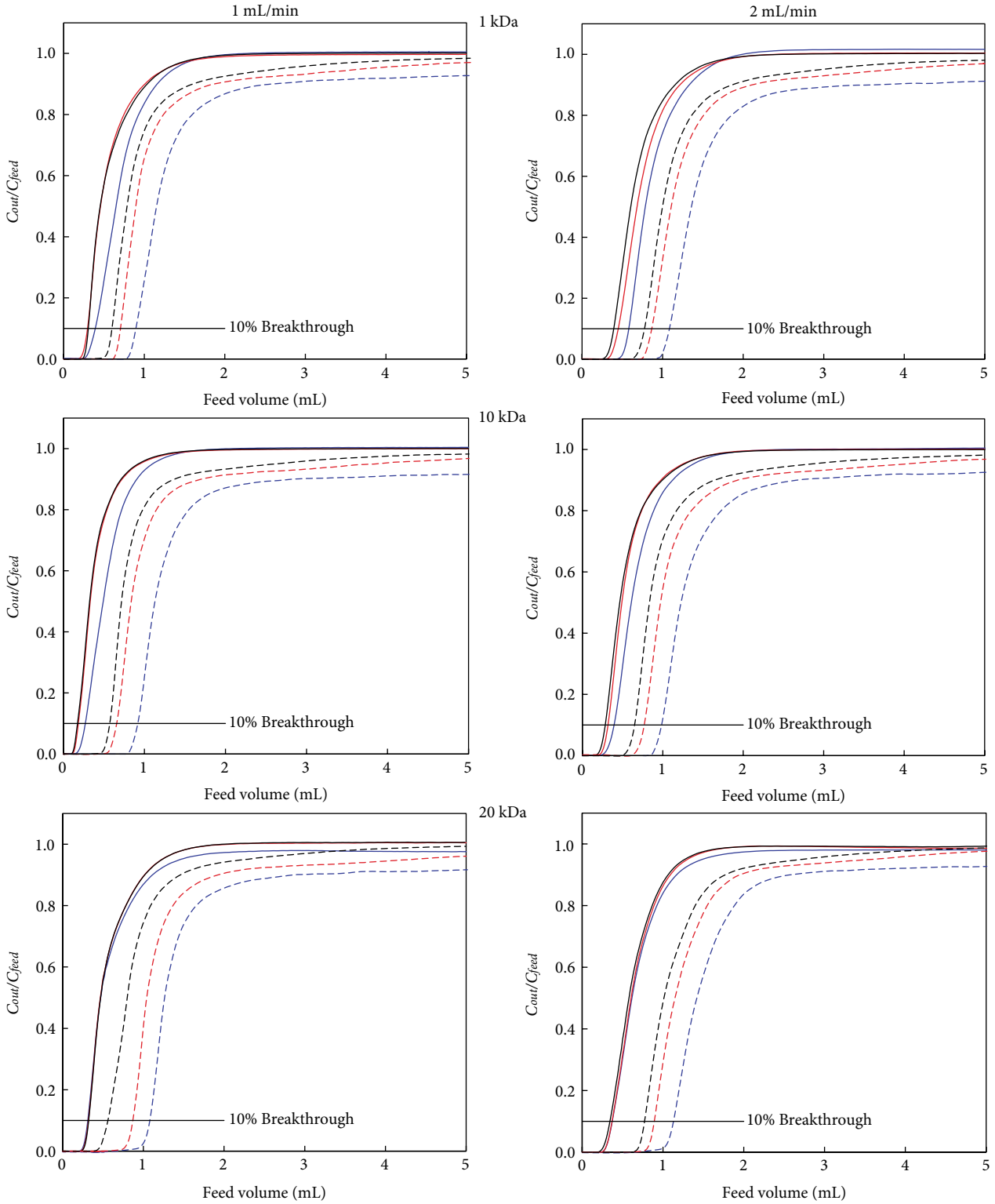

Figure 1: Breakthrough curves of PEGylated monoliths using BSA. The two ammonium sulfate concentrations used were 1.5 and 2.0 M and are represented by solid lines and dashed lines respectively. The color of the lines indicate the different BSA concentrations tested (blue lines, 1.0 mg/mL; red lines, 2.0 mg/mL and black lines, 3.0 mg/mL). Each column of graphs corresponds to each of the two Flow rates used (1.0 and 2.0 mL/min). All presented curves are the mean of three replicates.

In this same line, $DBC_{10\%}$ values for the PEGylated monoliths were determined (Table 1) for each one of the breakthrough curves shown in Figure 1. The $DBC_{10\%}$ of PEGylated monoliths increases with the rise of flow rate. This behavior is contrary to that reported by Hernánde–Martinez and Aguilar [6] due to the difference in mass transfer mechanism. The $DBC_{10\%}$ values in Table 1 are higher than those reported by Hernández–Martínez and Aguilar in their PEGylated Sepharose 6B. The convective mass transfer in monoliths plus the high available surface area from the monolithic structure and the hydrophobicity of PEG molecules allow better protein-support interactions and increase its adsorption capacity even at high flow rates. On the other hand, the higher DBC values were observed at high AS and fed protein concentration, which corresponds to the breakthrough curves behavior. Finally, the molecular weight of the PEG molecules grafted to the monolith showed a singular behavior. The PEGylated monolith with PEG of 10.0 kDa had the lowest DBC values while those modified with mPEG of 1.0 and 20.0 kDa showed, in general terms, similar values. This tendency could be attributed to the structural flexibility of the PEG chains since flexibility increases as the length does [24]. The PEG of 10.0 kDa attached to the monolith can modify its lineal structure into different spatial configurations. The different PEG configurations allow interactions hiding some hydrophobic regions that cannot bind to proteins or do so in a weaker way. A similar effect occurs with the 20.0 kDa PEG, but in spite of this phenomenon, its length allows adsorption of more proteins on its surface. For its part, the chain of 1.0 kDa PEG avoids other spatial configurations making its hydrophobic regions available for protein binding. The higher DBC values obtained were 6.85 ± 0.21 and 6.88 ± 0.09 mg/mL for the 1.0 kDa and 20.0 kDa PEGylated monoliths, respectively, at 2.0 mL/min, an AS concentration of 2.0 M and 3.0 mg/mL of BSA.

3.3. Capacity of PEGylated Monoliths to Separate PEGylated Proteins. The performance of the PEGylated monoliths to separate PEGylated proteins was evaluated using PEGylated RNase A. RNase A was conjugated with three PEG molecular weights to analyze the influence of the size of PEG chains attached to the protein in the separation of PEGylation reactions. As mentioned, DBC results indicated that at 2.0 mL/min the adsorption process has better performance; however, with PEGylated proteins, the amount of binding protein was lower at this particular flow rate (data not shown). Therefore, it was decided to use a volumetric flow rate of 1.0 mL/min in the subsequent experiments. Figure 2 shows the separation profiles of PEGylation reactions of RNase A. An important point to mention is that in previous reports, the PEGylation reaction is diluted in AS buffer before column injection [4, 6, 17] since proteins bind to HIC ligands at high salt concentrations and are eluted at low ones [25]. In this work, the reaction mixtures were not diluted in AS buffer before injection. Despite this, the PEGylated proteins were attached and separated using the PEGylated monoliths, showing that PEG–PEG interactions govern in this kind of chromatographic separation. In all cases, a small amount of

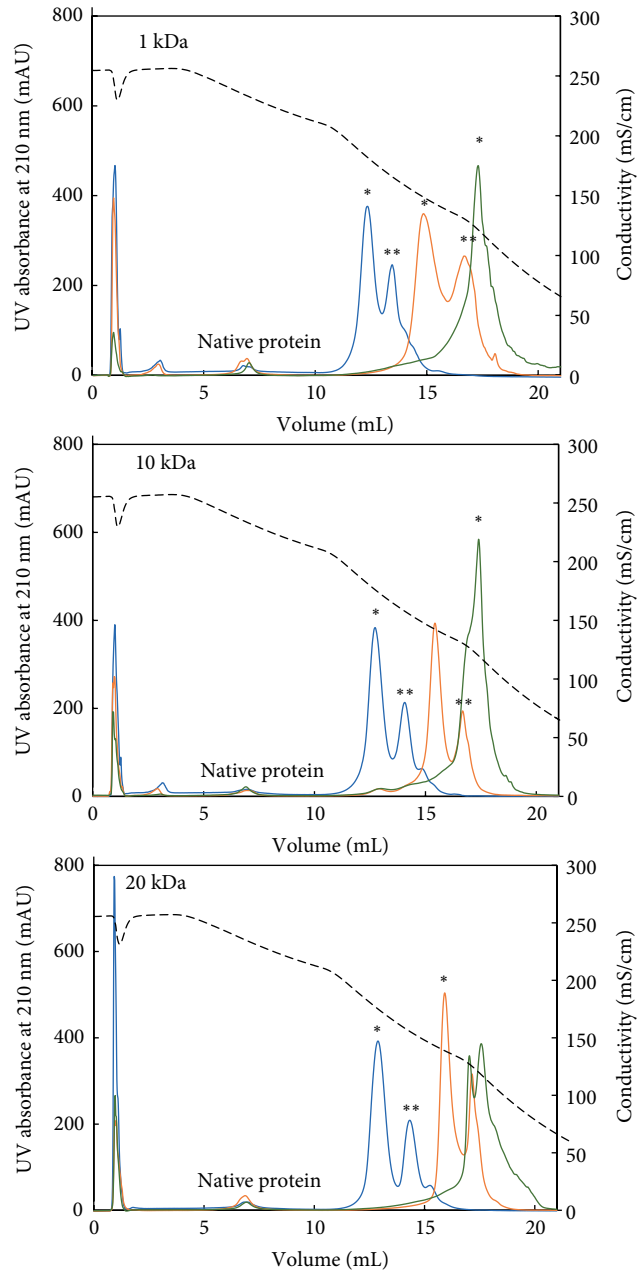

Figure 2: Separation of PEGylated Ribonuclease A using PEGylated monoliths. Chromatogram at 215 nm of Ribonuclease A PEGylation reactions with different PEG molecular weights 5.0 (blue line), 20.0 (orange line) and 40.0 kDa (green line) were separated using PEGylated monoliths modified with different PEG molecular weights 1.0, 10.0, and 20.0 kDa. Each experiment was carried out by triplicate. Conductivity was also measured and is presened in the chromatograms (black dashed line). *mono-PEGylated protein, **di-PEGylated protein.

the native protein binds weakly to the support, making its retention time different from that of the PEGylated species. On anion exchange chromatographic supports, protein PEGylation reduces their binding strength [26]. However, in PEGylated monoliths the effect is opposite because of the PEG–PEG interactions between the PEGylated protein

Table 2: Retention time and resolution factor (Rs) of PEGylated Ribonuclease A using PEGylated monoliths.

PEG MW in PEGylated monolith (kDa)	PEGylated Ribonuclease A								
	5 kDa			20 kDa			40 kDa		
	Retention time (mL)		Rs	Retention time (mL)		Rs	Retention time (mL)		Rs
	Mono-PEG	Di-PEG		Mono-PEG	Di-PEG		1st peak	2nd peak	
1	12.35	13.46	0.62 ± 0.03	14.95	16.7	0.94 ± 0.02	NA	NA	NA ± NA
10	12.83	14.19	0.95 ± 0.02	15.4	16.72	1.10 ± 0.04	NA	NA	NA ± NA
20	12.92	14.35	1.02 ± 0.01	15.94	17.17	1.04 ± 0.01	17.05	17.6	0.76 ± 0.01

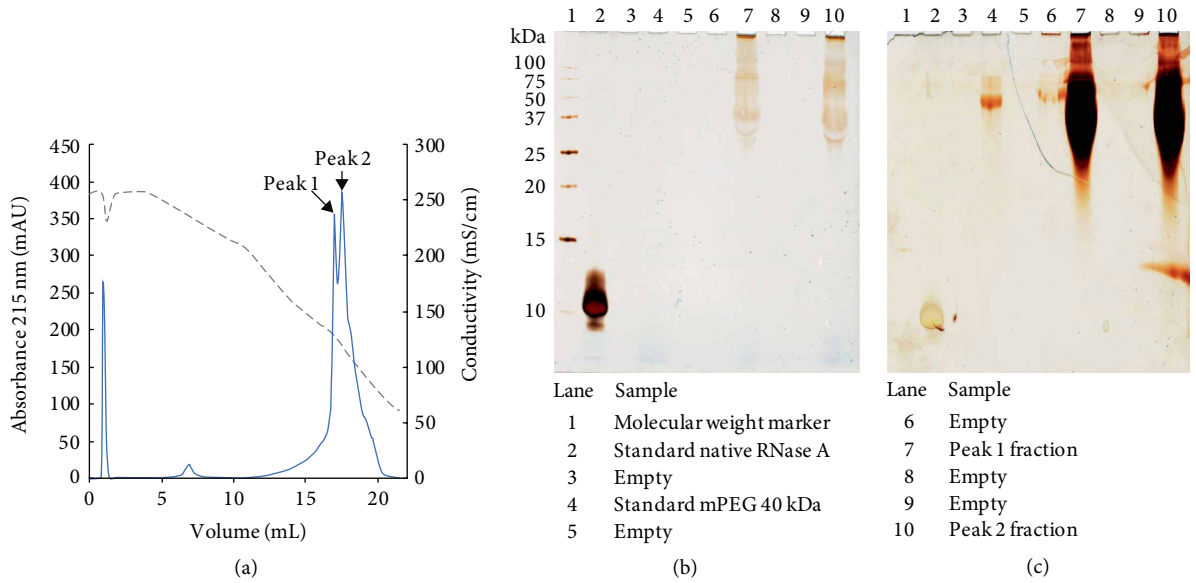

Figure 3: Separation and observation of 40.0 kDa PEGylated RNase A isomers using the 20.0 kDa PEGylated monolith. (a) Chromatogram at 215 nm of 40.0 kDa PEGylated RNase A in the 20.0 kDa PEGylated monolith using a step gradient elution. Buffer A: Tris–HCl 20.0 mM pH 8.2. Buffer B : Buffer A + 3.0 M ammonium sulphate. Loop 0.1 mL, Volumetric flow 1 mL min^{-1}. (b) Silver staining for protein detection of SDS–PAGE analysis of the chromatographic fractions. (c) I_2-$BaCl_2$ staining for mPEG detection of SDS–PAGE analysis of chromatographic fractions.

and the PEGylated monolith. In the separation process, the retention time (RT) of PEGylated RNase A depends strongly on the PEG molecular weight attached to the protein (Table 2), while the molecular weight of the PEG grafted to the monolith only shifts RT lightly. This behavior has an explanation in the fact that PEG molecules in the PEGylation mixture (i.e., free and protein-bound PEG) are more than the PEG molecules grafted to the monolith. Therefore, the strength of PEG–PEG interactions between the PEGylated species and the PEGylated monolith is very similar regardless of the PEG molecular weight attached to the support. On the other hand, when the molecular weight of the PEG attached to the protein increases, RT increases too (Table 2) since the amount of PEG–PEG interactions augments.

In terms of separation capacity, the resolution increases as the molecular weight of the polymer attached to the monolith increases (Figure 2 and Table 2). At high PEG molecular weights in the monolith, PEG–PEG interactions of the di-PEGylated species with the modified monolith are more extensive than the interactions of the mono-PEGylated species. Therefore, the di-PEGylated conjugate binds stronger in comparison with the other one, allowing a better separation between them.

Interestingly, when the 20.0 kDa PEGylated monolith was used to separate 40.0 kDa PEGylated RNase A, two peaks were obtained instead of one, which is usually expected (Figure 2). RNase A has a molecular weight of 13.68 kDa [27], therefore, the formation of a di-PEGylated conjugate is unlikely with a PEG of 40.0 kDa because of the produced steric hindrance. Once a PEG chain of this size is attached to the protein, it hinders other amino acid residues from reaction with other PEG molecules [1]. Hence, those two peaks could correspond to isoforms of the 40.0 kDa mono-PEGylated RNase A (i.e., conjugates with positional isomerism). To verify this point, silver and I_2-$BaCl_2$ staining of an SDS–PAGE gel of those peaks were analyzed. Figure 3 shows that those two peaks have the same profile and, due to their molecular weight, correspond to mono-PEGylated species and not to di-PEGylated species. The difference in retention times between the mono and the di-PEGylated species increases when the PEG MW attached to protein increases. For instance, with PEGylated RNase A of 5.0 and 20.0 kDa, the retention time difference changes from

Table 3: Retention time and resolution factor (Rs) of PEGylated Ribonuclease A using combined PEGylated monoliths in series.

PEGylated monoliths order (kDa)	PEGylated Ribonuclease A								
	5 kDa			20 kDa			40 kDa		
	Retention time (mL)		Rs	Retention time (mL)		Rs	Retention time (mL)		Rs
	Mono-PEG	Di-PEG		Mono-PEG	Di-PEG		1st peak	2nd peak	
10-20	13.41	14.79	1.06 ± 0.01	16.2	17.31	1.07 ± 0.02	17.30	17.73	0.67 ± 0.04
20-10	13.44	14.82	1.03 ± 0.01	16.22	17.33	0.97 ± 0.03	17.31	17.74	0.57 ± 0.05
1-10-20	13.76	15.08	1.06 ± 0.01	16.52	17.55	0.98 ± 0.04	17.53	17.97	0.52 ± 0.02
20-10-1	13.71	15.01	0.99 ± 0.01	16.46	17.53	0.85 ± 0.09	17.52	17.91	0.45 ± 0.00

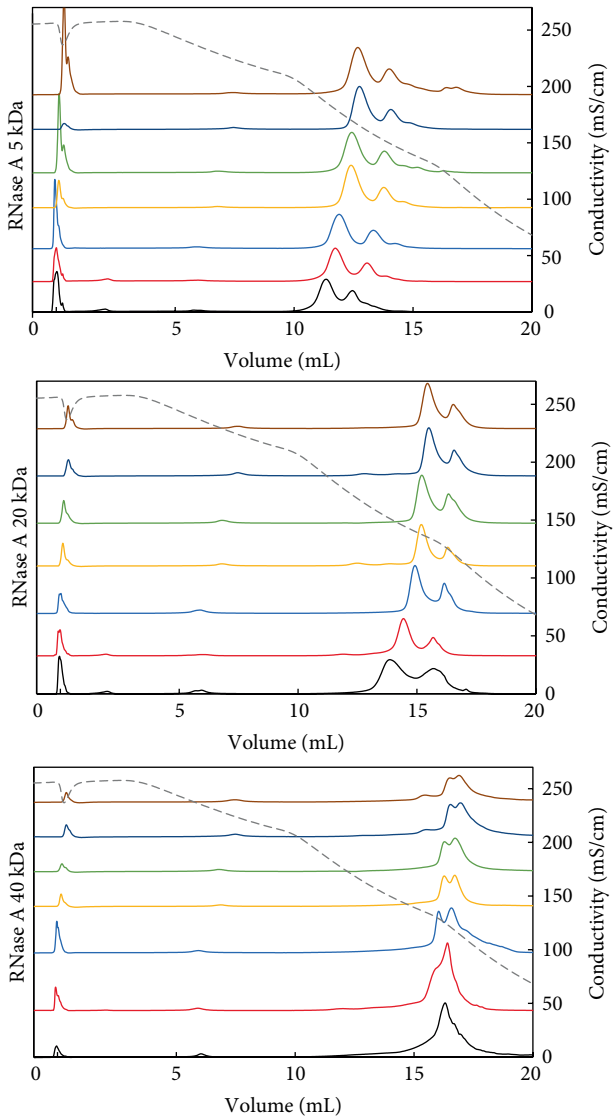

Figure 4: Comparison of PEGylated Ribonuclease A separation using different PEGylated monoliths series configurations. Ribonuclease A PEGylation reactions with PEG molecular weights of 5.0, 20.0, and 40.0 kDa were separated using PEGylated monoliths modified with PEGs of 1.0, 10.0, and 20.0 kDa in seven different configurations: 1.0 kDa (black line), 10.0 kDa (red line), 20.0 kDa (light blue line), 10.0-20.0 kDa (yellow line), 20.0-10.0 kDa (green line), 1.0-10.0-20.0 kDa (dark blue line), and 20.0-10.0-1.0 kDa (brown line). Each experiment was carried out by triplicate. Conductivity was also measured and is presented in the chromatograms (gray dashed line).

1.11 to 1.75 mL and, the retention time difference of both peaks in Figure 3 (PEGylated RNase A with 40 kDa) is only 0.55 mL. Therefore, it can be concluded that those peaks correspond to isomer species. Since proteins have several available reactive groups, the mPEG is probably binding to different residues on the protein [1]. The isomer separation of PEGylated proteins has been reported earlier using ion exchange chromatography [3, 8]. Nevertheless, to our knowledge, its separation by HIC has not been reported. PEGylation often results in a "charge-shielding effect" in which the PEG chains can reduce some of the electrostatic interactions between a PEGylated protein and a stationary phase due to steric hindrance [3]. In this work, a similar phenomenon occurs: "hydrophobicity-shielding effect" where depending on the PEGylation site, the hydrophobic interactions could change due to a masking effect of the hydrophobic or hydrophilic residues.

The separation of PEGylated RNase A from conjugation reactions has been studied previously. Mayolo-Deloisa et al. [4] separated PEGylated RNase A using a CIM C4 A monolithic disk, their best peak resolution was 1.16 and, in this work, the best resolution reached was of 1.1 ± 0.04. On the other hand, Hernández–Martínez and Aguilar [6] also achieved the separation of PEGylated RNase A conjugates using PEGylated sepharose 6B. However, their run-time and work volumes were at least two times larger than the used in this work.

3.4. Improving the PEGylated RNase A Separation. To achieve a better the separation between PEGylated species, two and three, of the previously described PEGylated monoliths, were placed serially in different configurations into the chromatographic system. Four combinations (10-20, 20-10, 1-10-20, and 20-10-1 kDa) were tested. Table 3 shows the peak resolution and retention times obtained for the different PEGylated species. The use of 2 or 3 sequential PEGylated monoliths allows the use of faster volumetric flow rates without affecting the retention time and resolution. Two flow rates (1.0 and 2.0 mL/min) were tested and, since this factor did not affect the chromatographic profiles (data not shown), a flow rate of 2.0 mL/min was used in the following experiments. In all cases, the use of more than one PEGylated monolith increased the retention time of the PEGylated species and this parameter was not affected by the order in which the disks were placed (Figure 4). When more than one modified support is used, the interactions between PEGylated proteins and the PEGylated supports are larger than those using a single disk.

Using more than one PEGylated monolith, the peak resolution was improved slightly only for the 5.0 kDa PEG-RNase A reaction. This is attributed to the nonuniformity of the PEG chain lengths due to the use of PEGylated monoliths with different PEG molecular weights. For the case of 20.0 and 40.0 kDa PEG-RNase A conjugates, the strength of the PEG–PEG interactions is not the same through the support and therefore, the proteins are eluted at different times inducing broader peaks and diminishing their resolution as it can be observed in Table 3 and Figure 4. Moreover, when the PEGylated monoliths are placed in decreasing PEG molecular weight order, the peak resolution falls. This phenomenon occurs because when the PEGylated protein is released from the 20.0 kDa PEGylated monolith, the salt concentration is not enough to bind the PEGylated protein to the 10.0 kDa PEGylated monolith and therefore, the PEG-RNase A species passes through and the peak resolution decreases.

These last experiments evidence the capability of using two or more monoliths at higher flow rates without observable changes in the separation behavior. In our particular case, to enhance the separation between the PEGylated RNase A species or other PEGylated proteins of biotechnological interest, it is necessary to use bigger PEGylated monoliths with the same PEG molecular weight.

4. Conclusions

As has been mentioned, the separation and purification of PEGylated proteins is a critical step in many production processes. For this reason, different chromatographic supports have been tested with varying results. In this work, a novel type of support was created and studied: PEGylated monoliths. Due to the chemistry of EDA disks, it was possible to PEGylate them using mPEG propionaldehyde via reductive amination showing that its modification degree depends on the length (molecular weight) of the mPEG to be attached. This reaction could be extrapolated to bigger monoliths with the same reactive groups to increase their workflow and processing capacity.

PEGylated monoliths are a suitable option to separate different proteins through HIC because: (1) it is possible to use them at high flow rates since their dynamic binding capacity does not decrease; (2) these modified supports take advantage of the hydrophobic PEG–PEG interactions between the PEGylated protein and the PEGylated monolith that predominate in the separation process; (3) sample preparation (dilution in a suitable buffer) is not necessary before injection, which means that it is possible to process larger sample volumes in less time and; (4) it is possible to separate PEGylated protein isoforms when long PEG chains are attached to both the monolith and the protein. On the other hand, in terms of resolution capacity, PEGylated monoliths with large PEG molecular weights allow a better separation of the PEGylated species.

This strategy based on PEGylated monoliths has a great potential to separate not only proteins or PEGylated proteins but also other PEGylated molecules of biopharmaceutical or biotechnological interest. Therefore, this represents a research opportunity area that requires the optimization of the monolith support PEGylation reactions to achieve better resolution capacities and to extrapolate its use to other molecules. In this way, a new and more efficient platform to separate and purify PEGylated proteins and other PEG conjugates can be established.

Data Availability

The experimental data used to support the findings of this study are available from the corresponding author upon request.

Conflicts of Interest

The authors declare that they have no conflicts of interest.

Acknowledgments

Calef Sánchez-Trasviña wishes to thank Alonso Ornelas-González and Marco Mata-Gómez for their technical support. The authors would like to thank the School of Engineering and Science and the FEMSA-Biotechnology Center at Tecnológico de Monterrey for their support through the Bioprocess Strategic Focus Group (0020209I13) and the National Council on Science and Technology of Mexico (CONACyT; project 242286). Calef Sánchez-Trasviña wishes to thank CONACyT, as well, for its support with scholarship 492276.

References

[1] D. Pfister and M. Morbidelli, "Process for protein PEGylation," *Journal of Controlled Release*, vol. 180, pp. 134–149, 2014.

[2] P. Zhang, F. Sun, S. Liu, and S. Jiang, "Anti-PEG antibodies in the clinic: current issues and beyond PEGylation," *Journal of Controlled Release*, vol. 244, pp. 184–93, 2016.

[3] N.-T. T. Nguyen, J. S. Lee, S. Yun, and E. K. Lee, "Separation of mono- and di-PEGylate of exenatide and resolution of positional isomers of mono-PEGylates by preparative ion exchange chromatography," *Journal of Chromatography A*, vol. 1457, pp. 88–96, 2016.

[4] K. Mayolo-Deloisa, J. González-Valdez, and M. Rito-Palomares, "PEGylated protein separation using different hydrophobic interaction supports: conventional and monolithic supports," *Biotechnology Progress*, vol. 32, pp. 702–707, 2016.

[5] N. Ulmer, D. Pfister, and M. Morbidelli, "Reactive separation processes for the production of PEGylated proteins," *Current Opinion in Colloid Interface Science*, vol. 31, pp. 86–91, 2017.

[6] A. Hernández–Martínez and O. Aguilar, "Chemical grafting of sepharose 6B and its use in the purification of PEGylated RNase A," *Separation and Purification Technology*, vol. 136, pp. 190–198, 2014.

[7] P. Madadkar, S. L. Nino, and R. Ghosh, "High-resolution, preparative purification of PEGylated protein using a laterally-fed membrane chromatography device," *Journal of Chromatography B*, vol. 1035, pp. 1–7, 2016.

[8] J. Gašperšič, A. Podgornik, P. Kramberger et al., "Separation of pegylated recombinant proteins and isoforms on CIM ion

exchangers," *Journal of Chromatography B*, vol. 1033, pp. 91–96, 2016.

[9] M. Cisneros-Ruiz, K. Mayolo-Deloisa, T. M. Przybycien, and M. Rito-Palomares, "Separation of PEGylated from unmodified ribonuclease A using sepharose media," *Separation and Purification Technology*, vol. 65, pp. 105–109, 2009.

[10] Y. Lv, T. C. Hughes, X. Hao et al., "A novel route to prepare highly reactive and versatile chromatographic monoliths," *Macromolecular Rapid Communications*, vol. 31, no. 20, pp. 1785–1790, 2010.

[11] T. Hall, D. C. Wood, and C. E. Smith, "Preparative and analytical chromatography of pegylated myelopoietin using monolithic media," *Journal of Chromatography A*, vol. 1041, no. 1–2, pp. 87–93, 2004.

[12] Y. Xin, J. Sakamoto, A. J. van der Vlies, U. Hasegawa, and H. Uyama, "Phase separation approach to a reactive polycarbonate monolith for "click" modifications," *Polymer*, vol. 66, pp. 52–57, 2015.

[13] A. M. Almeida, J. A. Queiroz, F. Sousa, and A. Sousa, "Minicircle DNA purification: performance of chromatographic monoliths bearing lysine and cadaverine ligands," *Journal of Chromatography B*, vol. 1118–1119, pp. 7–16, 2019.

[14] S. S. Kanwar and R. Kumar, "Ribonuclease as anticancer therapeutics," *Enzyme Engineering*, vol. 6, no. 1, pp. 1–8, 2017.

[15] R. F. Borch, M. D. Bernstein, and H. D. Durst, "Cyanohydridoborate anion as a selective reducing agent," *Journal of the American Chemical Society*, vol. 93, no. 12, pp. 2897–2904, 1971.

[16] S. Noel, B. Liberelle, L. Robitaille, and G. De Crescenzo, "Quantification of primary amine groups available for subsequent biofunctionalization of polymer surfaces," *Bioconjugate Chemistry*, vol. 22, pp. 1690–1699, 2011.

[17] M. A. Mata-Gómez, S. Yaman, J. A. Valencia-Gallegos, C. Tari, M. Rito-Palomares, and J. González-Valdez, "Synthesis of adsorbents with dendronic structures for protein hydrophobic interaction chromatography," *Journal of Chromatography A*, vol. 1443, pp. 191–200, 2016.

[18] L. A. Mejía-Manzano, K. Mayolo-Deloisa, C. Sánchez-Trasviña, J. González-Valdez, M. González-González, and M. Rito-Palomares, "Recovery of PEGylated and native lysozyme using an in situ aqueous two-phase system directly from the PEGylation reaction," *Journal of Chemical Technology and Biotechnology*, vol. 92, pp. 2519–2526, 2017.

[19] C. F. Lane, "Sodium cyanoborohydride – a highly selective reducing agent for organic functional groups," *Synthesis*, vol. 1975, no. 03, pp. 135–146, 1975.

[20] C. Özdemir and A. Güner, "Solubility profiles of poly(ethylene glycol)/solvents sytems, I: qualitative comparison of solubility parameter approaches," *European Polymer Journal*, vol. 43, no. 7, pp. 3068–3093, 2007.

[21] J. Jin, Y. Han, C. Zhang et al., "Effect of grafted PEG chain conformation on albumin and lysozyme adsorption: a combined study using QCM-D and DPI," *Colloids and Surfaces B: Biointerfaces*, vol. 136, pp. 838–844, 2015.

[22] F. C. de Sousa Junior, C. E. de Araújo Padilha, A. S. Chibério et al., "Modeling and simulation of breakthrough curves of recombinant 503 antigen using immobilized metal affinity expanded bed adsorption chromatography," *Separation and Purification Technology*, vol. 164, pp. 34–40, 2016.

[23] J. A. Asenjo and B. A. Andrews, "Aqueous two-phase systems for protein separation: a perspective," *Journal of Chromatography A*, vol. 1218, pp. 8826–8835, 2011.

[24] K. Abe, K. Higashi, K. Watabe et al., "Effects of the PEG molecular weight of a PEG-lipid and cholesterol on PEG chain flexibility on liposome surfaces," *Colloids and Surfaces A: Physicochemical and Engineering Aspects*, vol. 474, pp. 63–70, 2015.

[25] Z. Liu, S. R. Wickramasinghe, and X. Qian, "The architecture of responsive polymeric ligands on protein binding and recovery," *RSC Advances*, vol. 7, no. 44, pp. 27823–27832, 2017.

[26] M. Zhu and G. Carta, "Adsorption of polyethylene-glycolated bovine serum albumin on macroporus and polymer-grafted anion exchanger," *Journal of Chromatography A*, vol. 1326, pp. 29–38, 2014.

[27] J. González-Valdez, M. Rito-Palomares, and J. Benavides, "Effects of chemical modifications in the partition behavior of proteins in aqueous two-phase systems: a case study with RNase A," *Biotechnology Progress*, vol. 29, no. 2, pp. 378–385, 2013.